Contact Interactions of Silicone Masks During Nasal Continuous Positive Airway Pressure Therapy

By
Andrew Martin Sims

A thesis submitted for the degree of
Doctor of Philosophy

THE UNIVERSITY OF
NEW SOUTH WALES

SYDNEY · AUSTRALIA

Graduate School of Biomedical Engineering,
The University of New South Wales.

May 2012

Originality Statement

'I hereby declare that this submission is my own work and to the best of my knowledge it contains no materials previously published or written by another person, or substantial proportions of material which have been accepted for the award of any other degree or diploma at UNSW or any other educational institution, except where due acknowledgement is made in the thesis. Any contribution made to the research by others, with whom I have worked at UNSW or elsewhere, is explicitly acknowledged in the thesis. I also declare that the intellectual content of this thesis is the product of my own work, except to the extent that assistance from others in the project's design and conception or in style, presentation and linguistic expression is acknowledged.'

Signed:_____

Abstract

Obstructive Sleep Apnoea (OSA), characterised by repeated collapse of the pharyngeal airway during sleep, causes cessation of breathing followed by arousal, restoring normality. Continuous Positive Airway Pressure (CPAP) is a non-invasive, effective treatment for OSA where positive pressure is applied to the airway through a mask, maintaining patency. Nasal masks are commonly used, contacting the face across the upper lip, sides of the nose and the nasal bridge.

Despite health benefits, therapy compliance is sub-optimal, often due to poor mask fit and discomfort. Masks have been designed to conform to the facial profile, but have not taken into account facial deformations. The nature of facial deformations while undergoing CPAP therapy is unknown. This thesis investigates the contact interactions between the face and a nasal CPAP mask.

Magnetic Resonance Imaging (MRI) scans of the face were acquired of participants in the reference configuration and while undergoing CPAP therapy. The CPAP scan volume was registered onto the reference volume prior to surface generation for each state. Perpendicular deformation was measured from the reference facial profile to the deformed profile. Large facial deformations were measured at the sides of the nose (4.6 ± 1.6mm) and the upper lip (4.9 ± 1.8mm) with much smaller deformations at the nasal bridge (2.4 ± 0.2mm). When normalised by applied load and tissue thickness, no difference was found.

Finite Element Analysis (FEA) models of the face under CPAP therapy were prepared and validated against experimental data. The explicit FEA method was able to successfully engage the face and mask to simulate the application of CPAP therapy. An indentation study was performed to estimate the mechanical properties of subdermal fat using the Neo Hookean model ($\mu = 0.53 \pm 0.31$kPa). A model series was also prepared assuming the face to be rigid. Contact pressures were lower in the deformable models than in the rigid models. A linear association was found between these values at the sides of the nose and at the forehead.

These findings and techniques can be used to consider facial deformation in the development of future nasal CPAP masks to improve comfort and compliance to therapy.

Acknowledgements

I have really enjoyed and been stimulated by working on this research project, which happened to coincide with a significant period in my life. I am grateful and indebted to many people for their support, advice and assistance through the life of this project.

First and foremost I would like to thank my supervisors, Professors Klaus Schindhelm (UNSW and ResMed) and Anne Simmons (UNSW) for providing me the opportunity to undertake this work and Professor Mark Hoffman (UNSW) for agreeing to join the project as an advisor. I cannot speak highly enough of the wise and pragmatic support and counsel provided me, both professionally as we navigated through the vagaries of a multi faceted experimental research project and personally through births, deaths, health, illness and injury. I am still as excited today to be involved in clinically oriented biomechanics research as I was the day I started.

To all my friends and colleagues at ResMed, both in the Applied Research and Mask product development groups I would like to thank you all for your support, interest and encouragement in my work. There are some people I need to acknowledge personally for their assistance along the way. These are Gordon Malouf for his great advice and knowledge of the test equipment used when designing the CPAP MRI experimental arrangement, and his continued interest in this project, a pleasure to work with. I need to thank Dr Jeff Armitstead for his good humour and willingness to critically discuss any modelling issues throughout the life of the project, I am very grateful for this feedback along the way.

To my ResMed PhD research partners, Rachel and Questra, it has been a pleasure getting to know you both better during this time. Rachel, I wish you all the best in your new role and trust that the skills that you honed during your project will serve you well in your new endeavours. Qestra, thank you for your interest in all aspects of life and encouraging a sense of perspective. I only hope that I reflected the same back to you.

From the masks group I need to thank Philip Kwok, Philip Gunning and Sam Davidson for their confidence in my work and support of me in achieving this. Damien Mazzone, many thanks for being available for bouncing ideas around, your professionalism, high standards and your enthusiasm for this work. I look forward to working with you in the future. Tracey Bullivant, thank you for your continued interest and encouragement throughout the project. Lauren Portlock, thanks, life is never dull around you, I will shout you a caramello koala. Kai Stuebiger, I am grateful for your good humour and support. I owe you a drink, that is sure. Thanks to all the guys in the modelling lab. To my other colleagues, there are more than I

can name individually, that I have worked alongside, thanks for your good company, and a thriving work environment.

To my colleagues and friends at GSBME. Thank you for all of your input and criticism. In particular I need to thank Dr Socrates Dokos who has generously provided from his busy schedule, time and critical thought to review and suggest improvements to several parts of my work. Dr Ross Odell has provided well thought out criticism and suggestions which have been very helpful during experiment design, data presentation and troubleshooting. Prof John Whitelock has also given of his time to review parts of this work. To my PhD colleagues, Miganoosh, Amr, Huaying and Caroline, thanks for the opportunity to get to know you all and discuss each of our projects.

This project utilised several facilities, and I need to acknowledge my collaborators and the personnel who assisted and made those facilities available. For my collaborators in the indentation project at the University of Western Sydney, thank you for the opportunity to work with you and use your new scanner. I am grateful to Dr Tim Stait-Gardner and Professors John Morley and Bill Price. Additionally thanks to Lynette Fong for her work on this project.

Thank you to all the staff at the medical imaging facilities used at Prince of Wales Medical Research Institute, particularly Professor Caroline Rae and Kirsten Moffat, and at St Vincent's hospital.

I also owe a debt of gratitude to my participants for their willingness to participate in this project, and their enthusiasm to learn about my work.

The simulations performed in this project were run on a remote supercomputer. Thanks are due to the administration staff at National Computing Infrastructure (NCI) who were invaluable in assisting me develop the solution submission strategy and troubleshoot numerous 'interesting' licence issues.

Finally I would like to thank Robert Hood for his continued interest and encouragement in this project, his availability to review modelling strategies and finally his detailed proof reading. Thank you very much. Thanks also to Dr Norman Freund for being available to discuss troubleshooting strategies. A huge thanks to Kevin Harper for the extended email conversations as I found my way in LS-DYNA.

This now brings me to my friends, who supported and encouraged me in this work. Particular thanks to Norb and Amber, James and Jacky, Peter and Wendy, Nick and Megan as well as Greg and Jen, for their good humour and encouragement. Time for a BBQ I think. Thanks also to the guys from the mighty Lindfield All Age 5th grade reserve team - looking forward to next season, and our good friends at All Saints.

Lastly my family, to Dad, Mum, Robert, Louise and Alec thank you so much for all the support, love, babysitting, food and generally allowing me the time to complete this work. It is greatly appreciated. To Mark, Alina and Michael thanks for bearing with me during this project. To Chris for keeping in touch at crazy hours from San Diego. Finally to Natalie I am not even going to try listing things to thank her for, what more can I say than thank you, and I love you very much. To Matthew and Daniel, Dad will have more time to play now, and I look forward to that.

I continue to be grateful for being granted this opportunity to pursue this research project. I have benefited greatly from the support and encouragement of my family on all sides when making the decision to leave my previous job and study to direct my career towards the biomedical field. None more so than my extraordinary grandmother, Alison Sims, better known to me and my cousins as Granny. She had a great love of learning and would talk with great excitement often about looking forward to "seeing me in a velvet cap". Sadly she died in the latter half of my candidature, she will be missed.

Table of Contents

List of Figures

List of Tables

Acronym List

Part I

Introduction

Chapter 1

Introduction

Obstructive Sleep Apnoea (OSA) is a chronic and often undiagnosed condition where the sufferer's airway collapses during sleep, obstructing the airway and preventing regular breathing. This leads to a reduction of the blood oxygen saturation, continually rousing the body from the deeper restorative levels of sleep to regain patency of the airway and maintain efficient gas exchange in the respiratory system. The cycle may be repeated many times each night, and persist often with the sufferer unaware of the pathology or even the abnormal symptoms, often complaining of continued tiredness. Many times it is the sufferer's partner that is alarmed by the irregular breathing and cessation of breathing during sleep.

The ongoing holistic health effects of sleep apnoea are significant and relate to the individual, their relationships and society as a whole. The individual will often suffer extreme tiredness, their sleep is unrefreshing. Associations have been demonstrated with congestive heart failure, type 2 diabetes and metabolic syndrome. These in turn cause a host of pathological problems. OSA itself can be alarming for the partner of a sufferer as the pathological breathing and apnoea episodes can cause distress. Beyond the close family the extreme tiredness and lethargy that can be associated hinders the social interaction of the sufferer and places a strain on wider relationships. Finally, undiagnosed and untreated OSA can be costly to society in general with a potential to cause catastrophic and or fatal accidents. Recently (13/02/2008) a commuter flight carrying 43 passengers on a short flight from Honolulu, Hawaii to another island in the group deviated from their flight plan, did not acknowledge or respond to air traffic control directives and overshot the destination airport by 26 nautical miles while on autopilot . The probable cause of this incident as determined by the National Transportation Safety Board (2009) is as follows :

> The captain and first officer inadvertently falling asleep during the cruise phase of flight. Contributing to the incident were the captain's undiagnosed obstructive sleep apnoea and the flight crew's recent work

> schedules, which included several consecutive days of early-morning start times.

(National Transportation Safety Board, 2009)

Therefore, the problem of untreated sleep apnoea extends beyond the individual, and may affect many with potentially dire consequences.

A simple and very effective form of treatment for OSA is Continuous Positive Airway Pressure (CPAP) where positive pressure is applied to the airway through the wearing of a sealed face mask attached to a flow generator. This has the effect of creating an air splint in the airway, and inflating it like a balloon, and maintaining patency. Numerous patients have described how a new lease of life is achieved through the therapy creating improved relationships, increased efficiency at work, improved metabolic and cardiac function and eliminating daytime sleepiness.

Despite all these benefits that are offered by the therapy and few adverse events reported, a primary issue encountered is a general reluctance for people to be willing to sleep with the CPAP mask on. Reported side effects have included persistent red marks on the skin (erythema), claustrophobia, discomfort with the altered effort needed to breathe while on therapy, discomfort with the mask, inability to seal properly, resulting in annoying leaks which can prevent sleep or dry out the eyes. In the worst cases, soft tissue degradation has been encountered. All of these factors contribute to reducing the level of compliance to therapy.

A number of these issues such as general discomfort, leaks and skin marks relate to the fit of the mask to the face and the nature of the contact interface between the mask and the face. Since the advent of mass production of sleep apnoea masks, they have been designed to fit a range of faces. Masks have been designed using anthropometric measurements chosen to fit a range of the population. This has allowed for the development of very sophisticated mask systems, however complaints over comfort and fit still remain as the products develop. Improved patient compliance to therapy continues to be a major goal.

Despite the use of sophisticated anthropometric measurements in the development of the masks, the face has been effectively treated as a rigid body. While this has allowed the development and improvement of masks, the treatment of the face as a rigid body does not provide a means to realistically investigate the true nature of the contact between the face and the mask. In order to make the next step to intelligently guide the design of CPAP masks for improved comfort and therapy compliance, an approximation of the deformable interface between the mask and face is required.

This problem is the primary aim of the thesis. Mechanically, the face/mask is a complex system in the large deformation domain with interactions between non-linear materials. The thesis used medical imaging to estimate quasi-static facial deformations experienced by the CPAP user. These outputs were used develop non-linear Finite Element Analysis (FEA) models of the face to mask interface to estimate contact parameters such as pressure, and area of contact.

The purpose of the thesis is to open the investigation into contact interactions between the face and mask to form a foundation for more sophisticated and rigorous analysis of face to mask biomechanics. There is scope for parts of this work to be relevant in wider fields of research such as prosthetic limb - stump interfaces and contact loading of the skin in general. However this work will form a baseline foundation to enable equilibrium behaviour between mask and face to be predicted and provide an insight into the clinical behaviour of devices early in the design cycle, allowing the nature of the deformed contact to assist in guiding the design of further improved masks in the future to increase comfort, therapy compliance and then ultimately patient health, well-being and quality of life.

Chapter 2

Rationale

For 30 years, CPAP therapy has been a simple, effective and non-invasive treatment for OSA (Sullivan *et al.*, 1981). Positive airway pressure is continuously applied to the airway to create an air splint and prevent its collapse during sleep. The pressurised air is delivered to the airway by a system consisting of a flow generator, tubing and a fitted mask. Since the air in the system is positively pressured it is necessary to positively locate and fix the mask on the face to maintain a seal between the face and mask, and so effectively deliver therapy pressure.

Despite CPAP therapy being a safe and effective treatment for OSA there is a persistent reluctance to use or fully comply to the therapy among a portion of sufferers. Reported issues include poor sealing between the mask and face, erythema (red marks on the skin), general discomfort and in a few of the worst cases, skin breakdown. These issues relate to the fit and contact interactions between the face and the mask.

Though CPAP masks are designed using population specific anthropometric measurements to conform to the facial profile of the user, the facial elasticity or compliance to date has not been taken into account in the design of masks. The face has been assumed to be rigid. In reality both the cushion of the mask and the soft tissues of the face are highly compliant and mobile materials which will each deform significantly to an equilibrium configuration when in contact. The nature and extent of facial deformations while undergoing CPAP therapy is unknown. Therefore, the influence of the facial deformations on the contact parameters is correspondingly unknown.

The rationale for the thesis is twofold. Namely to investigate, describe and measure facial deformation under CPAP therapy, and then use this information to prepare and validate a virtual structural model of the patient taking into account facial deformations. The principal area of research is to provide a methodology that can be used to advance CPAP mask design by considering the biomechanical properties of the patient instead of just the mechanical properties of the mask. The greatest value of this approach is that it provides a means of estimating the facial

deformations and nature of the contact prior to the development of prototypes, and therefore, improve and expedite the product development cycle by estimating contact parameters *in silico*. The ultimate goal of this work is to improve mask quality and hence increase the patient comfort, compliance to therapy and ultimately increased well-being.

2.1 Hypothesis

That Magnetic Resonance Imaging (MRI) and FEA can be used to effectively simulate the mechanical and contact conditions experienced by patients while undergoing CPAP therapy.

2.2 Study Structure

Initially an anatomical MRI study was performed to investigate facial soft tissue deformations while undergoing CPAP therapy. Scans were acquired, providing information in both the reference and deformed configurations. The reference configuration data was used to develop the FEA models of the face, segmenting the superficial soft tissues into skin, subdermal fat and muscle tissues. Material properties for subdermal fat were sparse in literature, so a side project characterising the mechanical properties of subdermal fat under indentation loads was undertaken. This stream of work has been peer reviewed and published as (Sims *et al.*, 2010). The mechanical properties derived in this work were used as an input in the master facial FEA models. The CPAP FEA models were prepared and validated against the experimental data acquired from the scans of the participants. Contact parameters were able to be extracted from these models. To evaluate the predictive ability of the model an additional scan was performed using an alternate mask type. This was simulated using a facial model validated from the main study without any modifications.

The structure of the study is presented graphically in Figure 2.1.

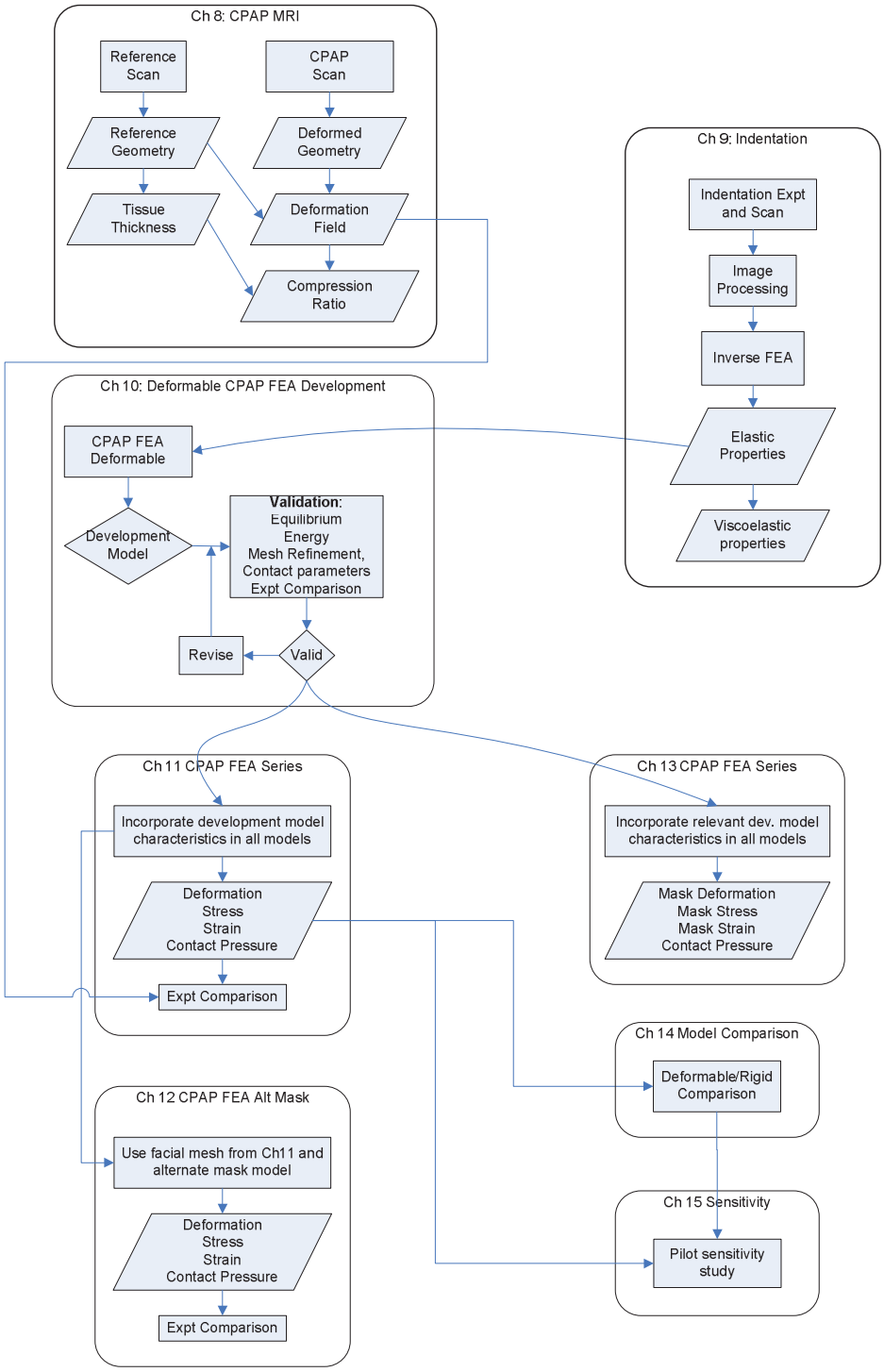

Figure 2.1: Project structure

Part II

Literature Review

Chapter 3

Sleep and Sleep Apnoea

Human life and correspondingly, brain activity, is spent alternating between the sleeping state and wakefulness (Culebras, 1996; Lee-Chiong Jr, 2008). Though precise details of its function remains uncertain, sleep is vital for general health and well-being and determining its precise purposes remains an active and growing field of research. Sleep medicine is now a thriving discipline with the potential to provide an immense benefit to the population in general (Culebras, 1996).

3.1 Wakefulness and Normal Sleep

The states of wakefulness and sleep are characterised by brain activity. In wakefulness a person is aware of themselves and their external environment and are able to interact with it. Conversely sleep is a state of unconsciousness characterised by a lack of awareness and interaction with surroundings. (Culebras, 1996; Lee-Chiong Jr, 2008).

Since the standardisation publication of Rechtschaffen *et al.* (1968), sleep has been classified into Rapid Eye Movement (REM) and Non Rapid Eye Movement (NREM) sleep, with NREM being divided into four progressively deeper numbered stages. In this publication they also prescribed a minimal set of recorded channels Electroencephalogram (EEG), Electro-oculogram (EOG) and Electromyogram (EMG) for Polysomnography (PSG), which has become the gold standard for classifying or staging sleep.

3.1.1 Muscle Tone During Sleep

The EMG signal from PSG recordings indicate that there is a progressive reduction in muscle tone during the successive stages of NREM sleep compared to the waking state. Finally there is a further significant reduction of the EMG signal and almost complete inhibition of muscle tone (atonia) during REM sleep (Walczak and Chokroverty, 1994). The atonia experienced during normal REM sleep inhibits or

paralyses all voluntary skeletal muscles with the exception of the orbital muscles and the diaphragm (Culebras, 1996). This is a protective mechanism which prevents acting out dreams and maintains the function of the respiratory system, which is critical to life.

3.2 Respiration Overview

The primary functions of the respiratory system are to breathe, transporting air in and out of the lungs, and the process of gas exchange of O_2 and CO_2 between the body and the atmosphere. These must be continuously maintained in order to sustain life, let alone function at a high level. The respiratory system is divided into two main components, the conducting portion, a highly branched tubular structure which transports the fluid and the respiratory portion where gas exchange occurs.

Breathing is achieved by alternating expansion and contraction of the lungs inducing pressure gradients between the lungs and the atmosphere causing the air to either flow into or out of the lungs through the conducting portion of the respiratory system. During inhalation the inspiratory muscles act together to increase the volume of the lungs, generating a negative pressure gradient from the atmosphere to the lungs, causing air to flow inwards. During exhalation the lung volume is reduced causing an increase of pressure in the lungs generating a negative pressure gradient from the lungs to the atmosphere causing air to flow outwards. Exhalation can be active or passive. Passive or quiet exhalation is accomplished without any voluntary muscle activity, the inspiratory muscles are simply relaxed and allowed to recoil to their neutral volume. Forced or active exhalation refers to the effort applied through the contraction of the expiratory muscles (abdominal and internal intercostals) to compress the lungs back to their neutral volume (Williams *et al.*, 1989b).During sleep the metabolism slows and the minute ventilation drops by about 15%. This primarily occurs through a reduction in the tidal volume, whereas the respiratory rate increases to compensate (Douglas *et al.*, 1982).

Deviations from the above description of normal respiration during sleep are referred to under the term Sleep Disordered Breathing (SDB). Though SDB covers a wide range of conditions, only obstructive apnoeas are of interest for this thesis.(American Academy of Sleep Medicine Task Force, 1999)

3.3 Obstructive Sleep Apnoea

Apnoea is a cessation of respiratory airflow. An apnoea can be classified as central or obstructive. In central apnoeas the airway remains patent but the effort to breathe is absent(Young *et al.*, 2002). Obstructive apnoeas on the other hand result from a physical collapse of the airway impeding airflow. An apnoea is commonly defined to be a cessation of airflow for a duration of at least 10s. Similarly a partial obstruction to flow is termed *hypopnoea*. Hypopnoea is defined as a reduction of airflow meeting at least one of the following requirements (Lawati *et al.*, 2009; American Academy of Sleep Medicine Task Force, 1999):

- $\geq$ 30 % reduction in airflow from a baseline for a duration $\geq$ 10 seconds accompanied by $\geq$ 4 % O_2 desaturation from a baseline
- $\geq$ 50 % reduction in airflow from a baseline for a duration $\geq$ 10 seconds accompanied by $\geq$ 3 % O_2 desaturation from a baseline or an arousal

The American Academy of Sleep Medicine Task Force (1999) recommendations define Obstructive Sleep Apnoea-Hypopnoea Syndrome (OSAHS) diagnostic criteria as follows:

> "The individual must fulfil criterion A or B, plus criterion C.
>
> A Excessive daytime sleepiness that is not better explained by other factors
>
> B Two or more of the following factors:
>
> - Choking or gasping during sleep
> - recurrent awakenings during sleep
> - unrefreshing sleep
> - daytime fatigue
> - impaired concentration
>
> C Overnight monitoring demonstrates five or more obstructed breathing events per hour during sleep. These events may include any combination of obstructive apnoeas/hypopnoeas or respiratory effort related arousals"

The above hourly count of apnoeic/hypopnoeic events is termed the Apnoea Hypopnoea Index (AHI) (American Academy of Sleep Medicine Task Force, 1999; Lawati *et al.*, 2009). The classification of the severity of OSA was recommended by the American Academy of Sleep Medicine Task Force (AASMTF) to consider both daytime sleepiness complaints and clinical data in the form of the AHI. The severity of OSA indicated by AHI and daytime sleepiness is classified as mild (AHI, 5-15), moderate (AHI, 15-30) and severe AHI $>$ 30. (American Academy of Sleep Medicine Task Force, 1999).

3.3.1 Aetiology

The underlying aetiology of OSA is understood to involve a mix of anatomical, neurological and mechanical factors that combine to restrict or collapse the airway, usually in the oropharynx (Sullivan *et al.*, 1981; Dempsey *et al.*, 2010). Anatomical factors that have been shown to influence the tendency for the airway to collapse relate to the bulk of the tissue surrounding the neck and airway (Banabilh *et al.*, 2009; Ryan and Love, 1996) as well as a tendency for the airway to be constricted in the oropharynx. Neurological contribution to the collapsibility of the airway includes the sleep induced atonia of the muscles of the head and neck, increasing tissue compliance. Mechanical conditions favouring apnoea include the weight of the soft tissue pressing on the airway, the mechanical properties of the surrounding soft tissues and the fluid flow properties in the airway.

Considering the commonly accepted aetiology that obstructive sleep apnoea is a passive phenomenon (Sullivan *et al.*, 1981), where a pressure drop is established in the airway with respect to the ambient atmospheric pressure during inspiration. This reduced pressure has the effect of drawing the soft palate and tongue in, hence restricting the airway. This is often exacerbated by the gravitational body forces applied to the soft tissues also compressing the soft tissues onto the airway. Since muscle atonia is induced during sleep, this tendency for the airway to be compressed is only resisted by the structure and arrangement of the soft tissues. As the airway is constricted this has the effect increasing airway resistance and reducing static pressure, therefore, increasing the pressure drop as greater effort is expended to inspire sufficient air. Eventually the airway will collapse with the tongue and soft palate completely occluding the airway, leading to apnoea. This concept is illustrated in figures 3.1a and 3.1b. (Sullivan *et al.*, 1981)

3.3.2 Pathophysiology

During obstructive apnoea, the airway has collapsed, the acute response to this obstruction is a reduction in the blood oxygen saturation, hypercapnia (increased CO_2) and rousing from deep levels of sleep. This was outlined by Sullivan *et al.* (1981), and is shown in Figure 3.2. Additionally, the increased respiratory muscular effort during obstructive episodes reduces intrathoracic pressure, systemic blood pressure, stroke volume and cardiac output (Shiomi *et al.*, 1991; Dempsey *et al.*, 2010). Conversely arousals following an apnoea lead to an immediate increase in arterial blood pressure (Dempsey *et al.*, 2010).

The reduction in oxygen saturation that is seen during apnoea has also been associated with pathological metabolism, in particular type 2 diabetes. Punjabi

(a) Normal state, muscle tone maintains airway patency despite pressure drop during inspiration

(b) Sleep apnoea episode, tongue and soft palate occlude the oropharynx

(c) Nasal Continuous Positive Airway Pressure providing a pneumatic splint to maintain patency during sleep

Figure 3.1: OSA schematic (ResMed Inc)

et al. (2002) found that the severity of glucose intolerance and insulin insensitivity is associated with the severity of OSA given by AHI. Similarly Ip *et al.* (2002) identified that AHI and minimum oxygen saturation were independently associated with insulin resistance. Babu *et al.* (2005) using continuous monitoring of very obese patients with type 2 diabetes found that compliance to proper CPAP therapy for more than 4 hours per day resulted in an reduction in glucose levels and improved insulin response.

OSA has been shown to be associated with chronic hypertension in numerous studies (Robinson *et al.*, 2004; Dempsey *et al.*, 2010). The causative nature of the link between OSA and hypertension and the associated health problems is a subject of great interest due to the potential public health benefits and associated health care cost savings from simple treatment. Peppard *et al.* (2000) found from the Wisconsin Cohort longitudinal study that there was a dose-response association between hypertension and SDB after accounting for Body Mass Index (BMI), age, sex, smoking, baseline status and body dimensions. In a further longitudinal study Marin *et al.* (2005) provided evidence for a causal link between OSA and cardiac outcomes. Their study compared the outcomes of groups of healthy and OSA patients men matched for age and BMI over a mean duration of 10 years. Some of the OSA patients refused CPAP therapy resulting in four groups for comparison, namely, CPAP treated OSA, untreated OSA, snorers and a control group. They found a) that there was an increased risk of fatal or non-fatal cardiovascular events in subjects with untreated severe OSA b) that there was a relation between the risk of cardiovascular events and AHI and c) significantly that the use of CPAP therapy reduces the risk.

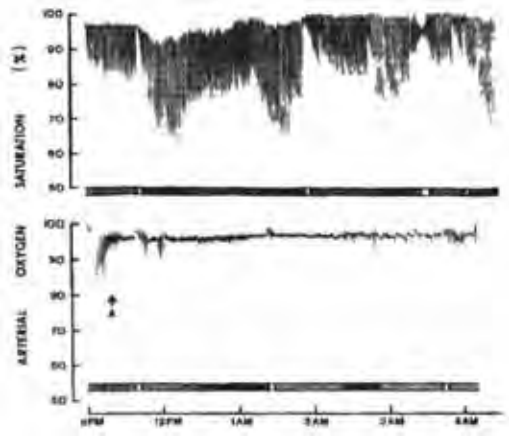

Figure 3.2: Blood oxygen saturation history over a nights PSG testing for the obstructed control recording (top) and CPAP therapy treatment (bottom) recording for the same patient (Sullivan *et al.*, 1981)

3.3.3 Symptoms and Comorbidities

OSAHS is typically manifested through a range of symptoms. Those that are directly related to the nature of sleep are primarily snoring, excessive daytime sleepiness, unrefreshing sleep and possibly alarm over irregular breathing from the partner of the sufferer during sleep. As mentioned previously in Section 3.3.2, OSAHS has a broad influence on the whole body's physiology, and can therefore, also be manifest in other apparently unrelated symptoms these could include hypertension, heart failure, myocardial infarction, depression, headaches at arousal, nocturia, diabetes and reflux among others (Schlosshan and Elliott, 2004). This broad influence on physiological response highlights the great benefits to the patient and society of increased awareness of OSAHS both in the general society and in speciality fields beyond sleep and respiratory medicine.

3.3.4 Epidemiology

Awareness of OSA has increased over the last 4 decades of research. The magnitude of the public health problem of OSA began to be realised in the 1990's as large scale population based studies such as Young *et al.* (Young *et al.*, 1993) reported a surprisingly large prevalence of 24% and 9% for men and women respectively in the Wisconsin Cohort Study. This was defined as an AHI ≥ 5 from PSG data from $n = 602$. The authors estimated that 4% of the male population and 2% of the female population have symptoms severe enough to be classed as Obstructive Sleep Apnoea Syndrome (OSAS) and require treatment. Similar results were found in other PSG population based studies around the world. Durán *et al.* (2001) reported that the prevalence in Spain of OSA over all ages of 26.2% and 28% for men and women

respectively . A further population based study in Busselton, Western Australia reported a prevalence of 26%. Undiagnosed OSAHS has been estimated at up to 80% of sufferers.

Further risk factors that have been identified for OSAHS include obesity, age, local anatomic characteristics, smoking, alcohol and familial disposition among others. Obesity, age and local characteristics will be expanded briefly below.

Obesity has been shown to be associated with OSA numerous times (Young *et al.*, 2002). Smith *et al.* (1985) demonstrated that a reduction in BMI in obese OSA sufferers was associated with a reduction in the AHI and improved sleep patterns and a reduction in daytime sleepiness, while no significant change was found in a control group. Schwartz *et al.* (1991) reported a reduction in the airway collapsibility as the critical pressure at which the airway collapsed was reduced following a reduction in BMI. The prevalence of obesity BMI > 30 in the United States as of 2008 was 32.2% and 35.5% in men and women respectively (Flegal *et al.*, 2010), encourageingly, this does reflect a reduction in the growth rate over the preceding decades.

Often the BMI has been used as an index of obesity. Its benefits are that it is an extremely simple calculated quantity, however it does not take into account body composition (*e.g.* increased muscle bulk) or localised deposition of adipose tissue. Local anatomic characteristics such as bulk of tissue or narrow pharyngeal airway can predispose people to OSAHS. Banabilh *et al.* (2009) as well as Lee *et al.* (2009) have published work significantly associating localised anthropometric measurements of the face and neck to the presence of OSA.

Prevalence of OSAHS among the elderly (> 65) has been estimated to be two to three times that of the middle aged population. Interestingly, Bixler *et al.* (1998) found that there was an increase in prevalence with age, but interestingly this was also accompanied by a reduction in the severity, as well as a greater portion being central apnoeas.

Considering the current trend of increasing obesity and an ageing population in many developed countries the diagnosed and undiagnosed population of OSAHS sufferers comprises a vast number of people. This places an enormous burden on both personal and societal demands for healthcare and its funding. This emphasises the importance of correct diagnosis and treatment of OSAHS and the possible impact that SDB can have on disparate health complaints, as the simple treatment of OSAHS can improve the symptoms of associated conditions therefore, avoiding possibly costly and invasive treatment options.

3.3.5 Treatment

There are a range of treatment options for OSAHS, these include mandibular advancement devices, surgery and CPAP. Mandibular advancement devices are used to hold the mandible in an advanced position to draw the soft tissue away from the airway to minimise the tendency to collapse. Surgery, obviously is an invasive and permanent treatment option. One of the available surgical treatment options is maxilla mandibular advancement which fractures and fixes the mandible in an advanced location, which also advances the soft tissue, opening the airway. Mihaescu *et al.* (2011) has shown via simulation the positive influence on breathing mechanics of the increased airway cross section. CPAP is a well known and effective therapy for OSAHS, it will be described in more detail below.

3.3.6 Continuous Positive Airway Pressure Therapy

Sullivan *et al.* (1981) demonstrated that the very simple and minimally invasive process of applying positive pressure to the airway of the patient was able to form an air splint and maintain patency for the duration of sleep. In his study, five patients were examined and the results were repeatable across all subjects. The application of positive airway pressure ranging from 4.5-10 cm H_2O prevented the collapse of the pharyngeal airway, and hence prevented the pathological reduction in O_2 saturation, and allowed a full and refreshing night's sleep. Clinical benefits were immediate with patients awaking refreshed and not experiencing any excessive daytime sleepiness. Additionally patients were able to sleep comfortably for a series of nights, so CPAP therapy did not prevent the onset of sleep in the absence of pathological tiredness.

This landmark study opened the way for the maturation of CPAP from a little known experimental technique to a widely used and valued therapy, providing increased vitality to a large group of patients around the world. The performance of CPAP therapy systems are now covered by international standards (ISO, 2007a,b).

While CPAP is an effective, non-invasive and easy to apply therapy, many users find that it takes some time acclimatising before being comfortable. This is primarily due to the strange sensation of breathing under positive pressure, where quiet exhalation is resisted and effort is required.

A modern CPAP system consists of a flow generator, tubing and a mask, with an option to include a humidifier in the system. Flow generators are advanced devices able to provide therapy over a pressure range of 4-20 cm H_2O as specified in the ISO standards (ISO, 2007a,b). Additionally features aimed to improve patient

compliance such as the gradual application of the therapy pressure during the onset of sleep.

CPAP masks are sophisticated components. There are three primary types of masks commonly available, these are nasal masks, full face masks and nasal pillows. Nasal masks consist of a roughly triangular frame and form a seal around from the nasal bridge, the sides of the nose and across the upper lip. Full face masks have been developed to provide treatment for patients that tend to breath through their mouth, or do not maintain a seal, allowing pressurised air to leak out of the mouth. Full face masks seal from the nasal bridge, around the side of the mouth and across the mental region anterior to the mandible. Nasal pillows are a completely different design where a slim line mask rests on the upper lip and profiled nozzles are inserted into the nares and seal on the interior surface.

In this thesis, nasal masks have been used for all experimental and modelling work, so no further discussion of full face or nasal pillows will be made. The masks used in the study are the ResMed Ultra Mirage II (UMII) and the ResMed Activa LT nasal masks.

UMII Mask Description

The ResMed UMII mask is shown in Figure 3.3. In order to accommodate a range of facial shapes, it is available in a range of sizes; shallow, standard, and large. The standard size UMII mask was used in this project.

The frame is moulded from a clear polycarbonate (Makrolon 2458) upon which all the other items are mounted. The Forehead support (FHS) and cushion are manufactured from Liquid Silicone Rubber (LSR). There is a considerable stiffness discrepancy between the components of the different materials. The main body of the frame forms a roughly triangular shape which fits around the nose. The depth of the section is sufficient to provide clearance from the pronasale to the tube opening for the supply air. A 3D swept tongue and groove joint is used to locate the cushion on the mask. A profiled clip is used to lock the cushion in place providing resistance against translation and rotation. The FHS is connected to the frame via the T-Bar. The frame/T-Bar connection is a pin joint with 4 circumferentially pitched ratchet detent positions, which engage with a cantilevered spring on the T-Bar. Bilateral clip housings are located laterally towards the base of the frame. These are the fastening locations for the headgear.

The cushion itself is a very complex component. It is moulded from LSR and comprises three main regions, namely the body, undercushion and membrane. The body comprises the bulk of the material of the cushion which is essentially a complex

Figure 3.3: ResMed UMII nasal CPAP mask

3D swept shape. This incorporates the interface with the frame through a 3D swept tongue and groove connection. The swept shape approximately follows the contour of the nasal region.

The undercushion is continuous with the body and is essentially a complex swept 3D cantilevered spring with a varying section profile, approximating a C-section. This acts as a non linear spring during engagement and under load.

The membrane is a lofted surface with varying thickness. In large parts it is very thin (0.3mm) and under the influence of a force conforms to the underlying shape of that portion of the face with which it is in intimate contact.

Attached to the T-Bar is the FHS, which is a moulded component with a frosted surface finish consisting of a pair of bilateral lofted pads of approximately trapezoidal profile which form a load path between the frame and the bearing surface of the forehead. Two bilateral oblique protrusions engage with the T-Bar through a conical bearing surface which is positively located with an interfering profile that is snapped through the T-Bar bearing surfaces.

Qualitative Engagement Description

As a patient puts on the mask, the following events occur as the mask engages with the face:

1. At some point the FHS will engage with the forehead.
2. Membrane makes contact with the skin around the nose
3. As the mask is advanced, the membrane stretches and conforms to the shape of the nose as well as rolling as it slides over the skin
4. At some point the undercushion may contact portions of the membrane, sandwiching it between the undercushion and the face. Thus engaging the undercushion as a non linear cantilevered spring, significantly changing the stiffness. The undercushion will roll and slide over the membrane as it engages, with some tendency to stick due to frictional effects.
5. Eventually the mask will seat itself on the tissue around the nose.
6. The system pressure in the mask may act on the underside of the membrane to assist in obtaining sealing with the face.

In a gross sense this will mean that the mask is simply supported with 3 points of support, namely, bilaterally with each of the FHS pads and the nasal region. Air pressure is applied to the interior of the mask and face. This would cause the mask to lift off the face but for headgear tension. Thus the mask is positively located onto the face by the headgear which acts as a preloaded spring.

3.3.7 Adverse Events

Despite nasal CPAP therapy being widely accepted and valued as an effective treatment for OSAHS, as with any therapy, it is not without side effects and occasional adverse events. Side effects can be physical and psychological, impacting on both the patient and their partner. Reported issues can be associated with the therapy itself, including dryness in the nose or mouth, bloating, nose bleeds and rhinorrhoea (Pepin *et al.*, 1995; Kakkar and Berry, 2007; Chai *et al.*, 2006; Nino-Murcia *et al.*, 1989). Similarly side effects associated with the mask include air leaks, discomfort, inflammation of the skin, sore or uncomfortable eyes , while other reported issues include headache, tinnitus and claustrophobia (Pepin *et al.*, 1995; Kakkar and Berry, 2007; Chai *et al.*, 2006; Nino-Murcia *et al.*, 1989; Jones *et al.*, 1994). Since this

project is focussed on the interactions between the mask and the face, some of these factors are expanded briefly.

It is essential that a mask be correctly fitted to create an effective seal between the mask and the face. The presence of leaks can be disconcerting and uncomfortable. In the case of leaking air near the nasal bridge, the leaking air jet can be directed into the eyes, which can lead to dry and sore eyes. Additionally mask leak can also be a source of noise which may be annoying for the patient and their partner hindering sleep. A poorly fitting mask may require increased headgear tension to hold the mask on the face tightly to eliminate or control leak.

Inflammation of the skin has been reported in a number of studies of patients using CPAP therapy and non invasive nasal ventilation. These include erythema and in extreme cases skin breakdown. There have been several extreme cases documented of full thickness skin necrosis across the nasal bridge from the use of nasal masks (Sleilati *et al.*, 2008; Smurthwaite and Ford, 1993) from extended continuous periods of use, refer to Figure 3.4. It must be noted that the case of Sleilati *et al.* (2008) required non invasive ventilation, rather than CPAP therapy for OSAHS, which requires higher headgear forces to locate the mask on the face. These cases highlight that excessive sustained loading applied to the skin through the mask, in the worst cases can lead skin breakdown. Therefore, aetiology and development mechanisms of pressure ulcers are relevant to this research. Pressure ulcers may develop either in the superficial or deep tissues, the latter is often referred to as Deep Tissue Injury (DTI). Superficial ulcers form in the skin following detachment of the skin layers and are usually associated with shear stresses within the skin and are often visible (Berlowitz and Brienza, 2007; Bouten *et al.*, 2003), DTI on the other hand is associated with a compressive state of loading and tissue deformation often near underlying bony prominences, which may progress to a clinically significant degree without presentation at the skin. Pressure ulcers are often clinically assessed using the National Pressure Ulcer Advisory Panel (NPUAP) Pressure Ulcer Staging System (Black *et al.*, 2007), which is summarised in Table 3.1. Historically, a common assumption arising from the work of (Landis, 1930) was that the onset of capillary bed closure occurred at a contact pressure of 32 mmHg 4.7kPa, leading to ischaemia and tissue degradation if unrelieved. Bouten *et al.* (2003) point out that capillary closure depends on local pressure gradients across capillary walls and not the applied pressure at an external surface of the body alone. Linder-Ganz and Gefen (2007), in a rat model, applied compressive pressures of up to 80 kPa to the gracilis muscle without occluding the capillary bed. Accompanying this experiment was an FEA model of muscle fascicles generated from a stained histological slide including muscle fibres, endomysium and capillaries. The muscle was subjected to

Table 3.1: NPUAP updated pressure ulcer staging system, reproduced from Black *et al.* (2007)

Stages	Description
Suspected DTI	Purple or maroon localized area of discolored intact skin or blood-filled blister due to damage of underlying soft tissue from pressure and/or shear. The area may be preceded by tissue that is painful, firm, mushy, boggy, warmer or cooler as compared to adjacent tissue.
Stage 1	Intact skin with non-blanchable redness of a localized area usually over a bony prominence. Darkly pigmented skin may not have visible blanching; its color may differ from the surrounding area.
Stage 2	Partial thickness loss of dermis presenting as a shallow open ulcer with a red pink wound bed, without slough. May also present as an intact or open/ruptured serum-filled blister.
Stage 3	Full thickness tissue loss. Subcutaneous fat may be visible but bone, tendon or muscle are not exposed. Slough may be present but does not obscure the depth of tissue loss. May include undermining and tunneling.
Stage 4	Full thickness tissue loss with exposed bone, tendon or muscle. Slough or eschar may be present on some parts of the wound bed. Often include undermining and tunneling.
Unstageable	Full thickness tissue loss in which the base of the ulcer is covered by slough (yellow, tan, gray, green or brown) and/or eschar (tan, brown or black) in the wound bed.

compressive pressure of up to 120 kPa which resulted in the capillary cross sectional area reducing by up to 71% without completely occluding any of the capillaries. The addition of shear to the loading of the muscle resulted in further total cross sectional area reduction and the occlusion of several capillaries, but only to a maximum of 46% of the capillaries in the Region of Interest (ROI). These results indicate that capillary closure and ischaemia is not the sole cause of DTI. Localised loading and deformation conditions are important including shear and any stress concentrations due to underlying morphology as well as the discrete properties of different tissue types. Superficial ulcers are more likely associated with shear forces at the skin surface and moisture than excessive contact pressure (Berlowitz and Brienza, 2007).

3.3.8 Therapy Compliance

Despite the clear benefits of CPAP therapy for the treatment of OSAHS and associated pathologies, the population compliance to this treatment is sub-optimal. There is wide variation in the published data for compliance to therapy. This can be seen in Table 3.2, which summarises reported compliance rates in a selection of recent and earlier studies. The range of compliance is from 29% to 90%. Different studies have used varying methods of determining compliance, including subjective interviews (Wolkove *et al.*, 2008), self reporting questionnaires (Nino-Murcia *et al.*,

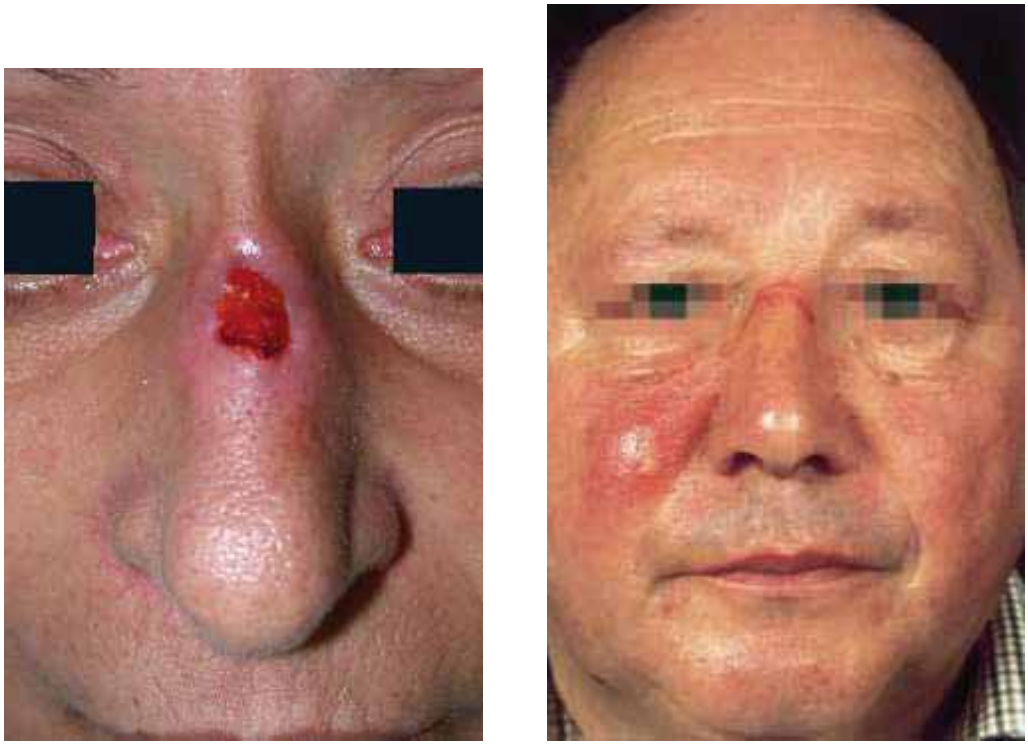

(a) Full thickness pressure sore requiring surgical treatment from the case study by Sleilati *et al.* (2008). This initiated over 2 days continuous ventilation.

(b) Erythema marks on the face over the cheek and across the nasal bridge (Verse, 2000).

Figure 3.4: Examples of skin marking and extreme skin degradation following nasal mask usage.

1989; Lojander *et al.*, 1999; Lindberg *et al.*, 2006; Richard *et al.*, 2007), derived from end points in studies (Marin *et al.*, 2005) , and objective data logging facilities built into the flow generators (Pepin *et al.*, 1995; Mortimore *et al.*, 1998; Sin *et al.*, 2002; Kribbs *et al.*, 1993). Therefore, while a significant portion of the population that is prescribed CPAP therapy are obtaining the benefits of increased health, vitality and quality of life (Sin *et al.*, 2002), there is scope for this to be improved.

Considering the side effects listed in Section 3.3.7, a number of issues relate to the fit of the mask on the face, these can influence the adherence or compliance to therapy. In the study of Lindberg *et al.* (2006) 26% of participants did not tolerate prescribed CPAP therapy citing primarily nasal or pharyngeal discomfort. While compliance to therapy will never be perfect, scope exists to improve this by reducing the impact of noted side effects of the therapy. Research into the nature of the contact interface between the mask and the face is explored.

Table 3.2: Compliance rates to CPAP therapy from a selection of studies

Study	Compliance	n
Nino-Murcia *et al.* (1989)	65%	139
Pepin *et al.* (1995)	88%	193
Mortimore *et al.* (1998)	90%	20
Lojander *et al.* (1999)	71%	151
Sin *et al.* (2002)	79%	296
Richard *et al.* (2007)	59%	232
Marin *et al.* (2005)	56%	667
Lindberg *et al.* (2006)	29%	38
Wolkove *et al.* (2008)	54%	80
Kribbs *et al.* (1993)	46%	35

3.4 Summary

OSAHS is a common condition in the general population with prevalence estimates up to 24%, with up to 80% of sufferers being undiagnosed. Over 30 years, CPAP has been shown to be a simple, effective, safe and non invasive treatment for OSAHS. Associations have been found between SDB and other conditions, which place a heavy burden on health care systems, including cardiac pathology and metabolic diseases. Therefore, considering both the latent undiagnosed population and associations with resource heavy conditions, there is great potential, with increased knowledge, for CPAP therapy to provide great benefit to society at large.

Despite the clear benefits provided to users, the adherence or compliance to therapy is sub-optimal, often estimated at about 65%. Reasons cited for non-compliance include discomfort from a poorly fitted mask, irritation from leaks as well as a general predisposition against wearing a mask on the face during sleep. The factors relating to the mask fit and leak are able to be studied and the knowledge gained used to continue the improvement of the quality and function of nasal CPAP masks.

3.5 Mask Design, Assumptions and Study Scope

CPAP masks are sophisticated medical devices whose performance criteria are specified by ISO standard (ISO, 2007b). There are a number of key anthropometric measurements on the face that are important in mask design and development. Sample measurements that are important in nasal mask design are the nasal width, nasal height and nasal root width. In addition to these measurements, 3D facial profile geometric information is used to assist generating a shape that is able to conform to and seal onto a variety of faces.

Inherent to this design methodology, though, is an assumption that the face is rigid, which correspondingly assumes that all of the deformation and strain energy is contained within the mask. This is patently not the case. In reality the face/mask interaction is one between the compliant soft tissues of the face and the compliant LSR components of the mask cushion and FHS. The soft tissues of the face are supported by the underlying skull and are relatively mobile on that support. Therefore, when the face and mask are engaged, they will adopt an intermediate equilibrium configuration with both the facial tissue and the mask deforming.

This assumption and deviation from reality defines the scope for the investigation and modelling of this project. The subsequent investigations seek to characterise the facial deformations experienced by the patient during CPAP therapy, which to the best of the author's knowledge is a novel measurement. These results are then used to both develop and validate finite element analyses which can be used to estimate contact mechanics.

Chapter 4

Head and Facial Anatomy

Section 3.3 introduced OSAHS and CPAP as a simple therapy, and concluded by outlining the direction of this research to characterise facial deformations and model the mechanical contact interactions between the patient's face and the mask. Therefore, it is appropriate to very briefly provide an overview of the anatomical structure of the head. Since nasal CPAP masks are applied to face, the region of interest for this study is limited to the superficial tissues of the face and its surrounds.

The head is a highly specialised assembly. Its form and structure provide mobility, protection and enable a high level of function across a variety of tasks. The primary functions that the head is involved in are:

- to house and protect the brain
- to provide entry and exit paths for the respiratory system
- to provide entry and preparation of food and fluid to the digestive system
- to house and protect sensory organs (eyes, ears, tongue, nose)
- to communicate via speech

4.1 Overview

The head consists of the skull and the attached soft tissues. It forms a complex shape which is closely linked with the wide range of functions listed above. The top of the head forms a convex curved surface with a relatively thin and even layer of soft tissue covering the skull known as the *scalp*. The anterior surface is known as the face. It is a complex shape incorporating both concave and convex surfaces which accommodate the eyes, nose and mouth.

Soft tissues cover the skull. The skin forms the continuous external surface of the body. It has a layered structure and is loosely attached to fatty deposits which are largely though not exclusively concentrated in subdermal tissue often referred to

as *panniculus adiposus*, *subcutis* or *hypodermis*. There are significant fatty deposits located in the face. Deep to the skin are the muscles of the head and face. These originate on the skull and insert also into the skull or in a number of cases insert into the overlying dermal tissue (Williams *et al.*, 1989b).

4.2 The Skull

The form of the head and face is dominated by the bony assembly of the skull, which is illustrated in Figure 4.1. It is the foundation that the muscles and superficial soft tissues are supported by and take their form from. The skull is the most complex bony structure in the body, consisting of 22 individual bones commonly grouped into two functional sets, the cranial and facial bones. Since this project deals with the contact interactions of the face and a nasal CPAP mask held onto the face. The regions of interest for this model are the surrounds of the contact area, the forehead and around the nose. Therefore, the modelling of the face will be localised to the portion anterior of the mandibular notch. Other regions will not be discussed.

The cranial bones or cranium form the main superior and posterior structure of the head. Their primary function is to house and protect the brain as well as the hearing and equilibrium organs (Tortora and Grabowski, 2004). The cranium is hollow and roughly spherical in shape, providing a robust structure. It is constructed of 8 individual bones, of which the frontal and temporal bones are of interest for this study. The spherically shaped *frontal* bone is located anteriorly and superiorly in the skull. It forms the superior wall of the orbits and articulates with nasal bone. The frontal bone contains internal cavities known as the frontal sinuses. The anterior extremity of the frontal bone is the frontal squama or forehead, which is slightly curved and predominantly lies in the vertical plane. The temporal bones are on the inferior lateral boundary of the cranium. They have a complex irregular shape with a squamous (flat) region forming the boundary of the cranium. Protruding anteriorly is the zygomatic process, which articulates with the zygoma to form the zygomatic arch (commonly the cheekbone), providing structural stability.

The facial skeletal assembly comprises 14 bones, and is approximately symmetrical in structure. The largest bone in the face is the *mandible* which is approximately U shaped, forming the lower jaw. There are two distinct regions of the bone, the *body* and the *rami* on each side of body. The body lies roughly in the transverse plane and contains *alveoli* which fixate the lower teeth. The ramus of mandible protrudes superio-posteriorly from the body at the *mandibular angle* on each side. It is elongated in structure providing significant strength in bending. There are two

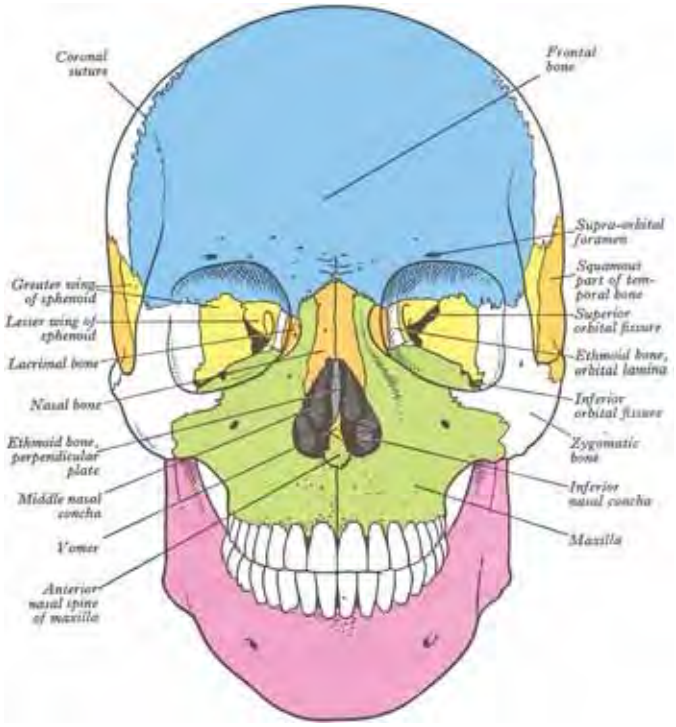

(a) Frontal view

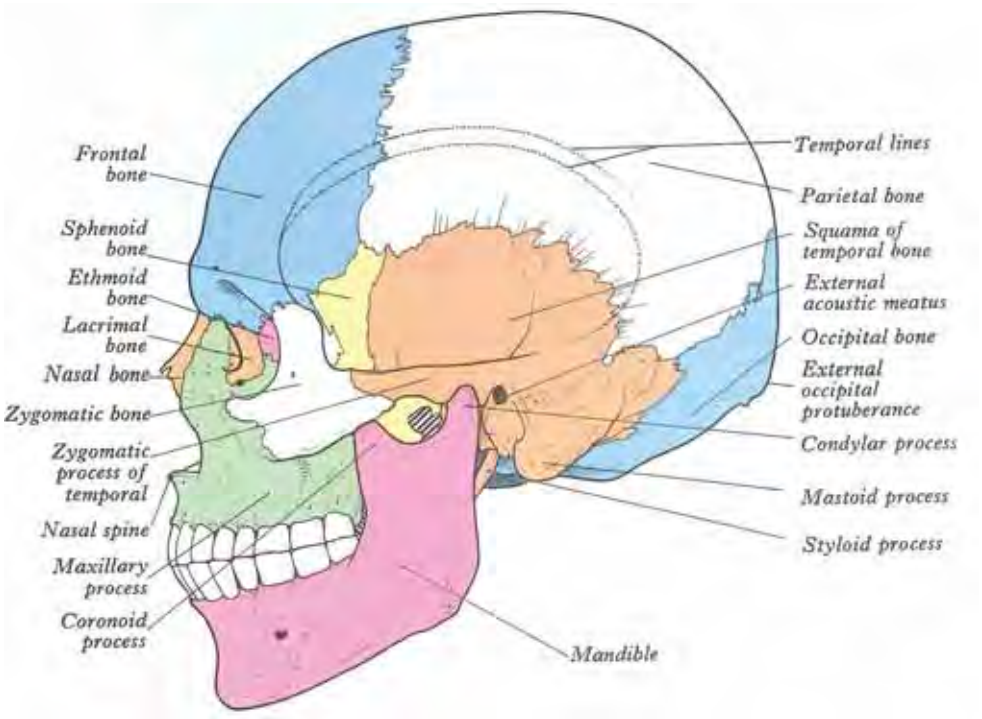

(b) Sagittal view

Figure 4.1: Frontal and sagittal views of the skull assembly showing individual bones (Williams *et al.*, 1995).

processes protruding superiorly from the rami, separated by the smooth *mandibular notch*. These are the coronoid process (anterior) and the *mandibular condyle* (posterior). The mandibular condyle articulates with the *mandibular fossa* of the temporal bone to form the Temperomandibular joint (TMJ). The coronoid process is an insertion point for the *temporalis* muscle used in chewing and speech.

The *maxilla* is formed from two medially fused maxillae. They are the central construct of the face. All facial bones except the mandible articulate with them. The maxillae form the upper jaw and mount the upper teeth. The *zygomatic processes* protrude laterally to articulate with the zygomatic bones. The maxillae also form the inferior medial border of the orbits.

The zygomatic bones, commonly known as the cheek bones, provide the underlying structure for the cheek and form the inferior boundary of the orbit. The zygomatic bones articulate with the zygomatic processes on both the temporal and the maxillae bones.

The nasal bones have an arched shape and for the bridge of the nose. The nasal bones articulate with the frontal bone superiorly, maxillae laterally, perpendicular plate of the ethmoid posteriorly. On the inferior side the nasal bones articulate with nasal cartilages.

Protruding medially into the nasal cavity, the complex, curved inferior nasal conchae are the largest of the turbinates and form part of the lateral wall of the nasal cavity.

4.3 Head and Facial Muscles

The muscles of the head and face have their origin and/or their insertion on the skull, shown in Figure 4.2. These muscles are broadly classified into two interrelated groups, namely the *muscles of mastication* and the *muscles of facial expression*. The muscles of facial expression are located superficially, whereas the muscles of mastication lie deep, adjacent to the bony structures of the skull. These form an interrelated network of muscles that allow the head and face to perform complex movements involved in critical life sustaining functions as well as communication.

4.3.1 Muscles of Mastication

The muscles of mastication are associated with the movement of the mandible during both mastication and speech. Several of the major muscles are described briefly. The *masseter* is a powerful muscle originating on the maxilla and zygomatic arch and inserting into the ramus of mandible. It acts to elevate and retract the mandible

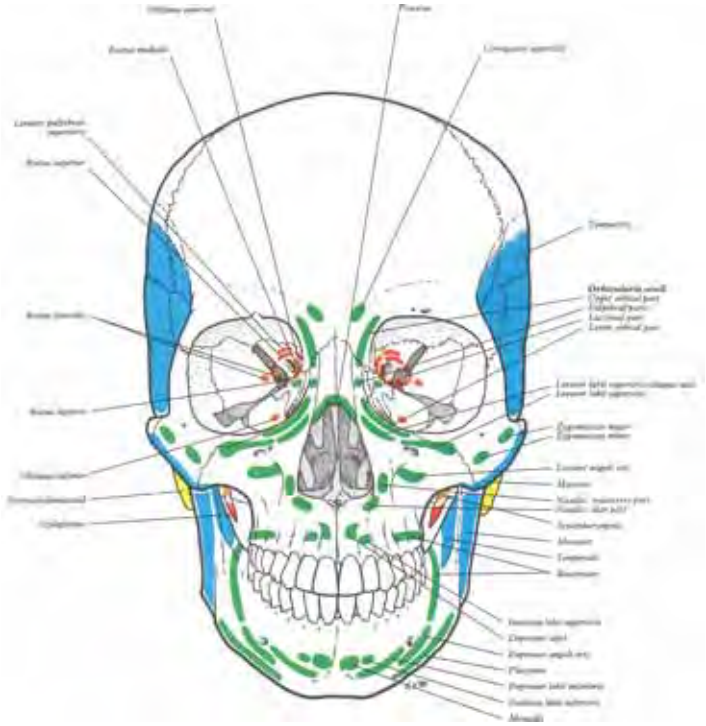

(a) Frontal view

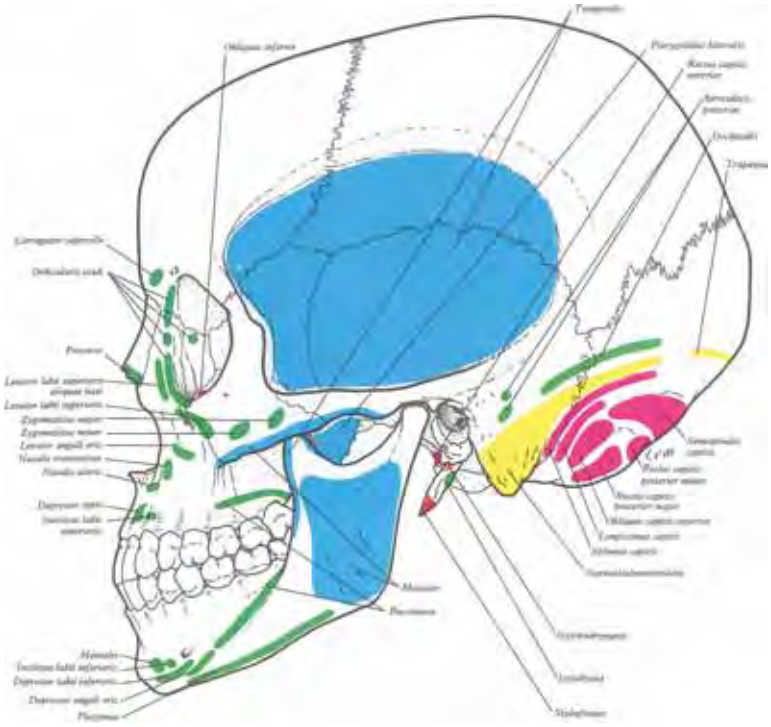

(b) Sagittal view

Figure 4.2: Frontal and sagittal views of the skull assembly showing muscle attachment locations (Williams *et al.*, 1995).

Table 4.1: Description of several muscles of facial expression (Tortora and Grabowski, 2004; Williams *et al.*, 1989b)

Muscle	Origin	Insertion	Action
Occipitalis	epicranial aponeurosis	Skin and muscles near eyebrows	move scalp backwards
Frontalis	nuchal lines posterior of skull	epicranial aponeurosis	move scalp forward, raise eyebrows, wrinkle forehead skin
Orbicularis Oculi	Medial orbit wall	muscles and skin	close eye, blink
Orbicularis Oris	muscles around the mouth	skin and fibrous modiolus at the side of the mouth	Close and protrude lips, compress lips against teeth
Zygomaticus major	Zygomatic bone	modiolis	moves corner of the mouth to smile and laugh
Zygomaticus minor	Zygomatic bone	muscle at upper lip	move the corner of the mouth *e.g.* in smiling
Buccinator	Maxilla & mandible	Orbicularis and skin of the lips	Draws cheeks against teeth, and move food in the mouth
Platysma	Fascia over the deltoid and pectoralis muscles	Mandible, skin of lower face, muscles around the corner of the mouth	Depress the mandible and outer part of lower lip

during mastication and speech. The *temporalis* originates in a broad connection with the temporal bone on the side of the skull. The muscle tapers to a tendon descending medial to the zygomatic arch before inserting into the coronoid process and medial surface of the ramus of mandible.

4.3.2 Muscles of Facial Expression

The muscles of facial expression are located superficially, with their origins located in the fascia or on the skull, whereas their insertions are located within the dermal layers. This functional arrangement allows for the active movement of the skin. This is important in a number of critical functions such as respiration, swallowing and protection as well as social functions such as speech and emotional expression. A selection of the major muscles of facial expression are briefly outlined in Table 4.1.

4.4 Surface Anatomy

The head can be divided into separate regions. Those covering regions of interest in the study are outlined in as follows:

Frontal region Covers the *frontal* bone up to the *coronal suture*

Nasal Covering the nose, medial to the infraorbital region and extending from the frontal region to the oral region at the upper lip.

Oral Surrounding the mouth, incorporating the upper and lower lips and lateral to the modiolus

Infra-orbital Lateral to the nose

4.5 Selected Facial Region Descriptions

Several regions of the face will be described in more detail as they are on the direct load path between the mask and the face, so their detailed structure is important when it comes to preparing the finite element model of the face.

4.5.1 Frontal Region

The frontal region covers the frontal bone, extending from the lower margin of the forehead to the coronal suture. It is characterised by the thin squamous planar-like layers of soft tissue, the *scalp*, which overlay the hard bony tissue. The underlying frontal bone can be palpated through the scalp. The scalp consists of five layers of tissue (Williams *et al.*, 1989b), skin, subcutaneous fibro-adipose tissue, aponeurosis and epicranius, subaponeurotic areolar tissue and pericranium.

4.5.2 Nasal Region

The nose is approximately tetrahedral in shape, descending anteriorly from the *root* at the bottom of the forehead. The tip of the nose is known as the *apex* which corresponds to the anthropometric landmark, *pronasale*. The inferior margin of the nose is characterised by the elliptical openings, nostrils or *nares*, which form the entrance to the nasal cavity and the respiratory system. The nares are bordered medially by the *nasal septum* and laterally by the *alar nasi* . The underlying structure of the nose is governed by bone and cartilaginous tissue. The nasal bone forms the root of the nose, blending into the nasal angle which is supported by the *septal cartilage*. This cartilage blends into the nasal bone superiorly and forms the nasal septum with the *vomer* and the *perpendicular plate of the ethmoid* posteriorly. The *lateral* cartilage descends from the nasal septum and is triangular in shape, giving structure to the flanks of the nose. The thin curved *major ala cartilages* are attached to the lateral cartilage and provide the support for the rounded shape of the lower *ala*. The tissue at the lower margin of the alar nasi at the opening of the nares consists of skin covering fibrous adipose tissue (Williams *et al.*, 1989c; Tortora and Grabowski, 2004).

The nasal skin is characteristically thin and loosely connected to the underlying tissue. This is particularly so at the root of the nose around the nasion, where the underlying nasal bone can be palpated. The skin becomes gradually thicker and is attached to the underlying structure towards the *ala* and *pronasale*.

4.5.3 Oral Region

The mouth, otherwise known as the *oral* or *buccal cavity* dominates the oral region of the face, and is approximately convex. The upper and lower lips form the margins of the mouth. The lips are folds of soft tissue which blend into the gums on the interior surface. Each lip is medially connected to the gums by a thin flexible *labial frenulum*, the upper frenulum is significantly larger than the lower. The upper lip is characterised by the *philtrum*, a tapered groove bordered by inferolaterally descending *philtrum ridges* from the nasal root to the red lip margin. Externally the lips are bounded by skin and mucosa externally and internally respectively, these enclose the *orbicularis oris*, adipose tissue vessels and nerves. The lips are continuous with the cheeks which form the lateral exterior boundary of the mouth. (Williams *et al.*, 1989d)

4.6 Summary

This section of the literature review has introduced the basic structure and function of the head assembly. In summary the skull, compared to the remainder of the head forms a rigid body which is the foundation for the superficial soft tissues. The soft tissues, in a gross sense consist of skeletal muscle, adipose or fatty tissue and the skin. The muscles are often categorised into two main groups, the muscles of mastication and the muscles of facial expression. The former are involved in mandibular movements for speech and chewing. The muscles of facial expression are unique in that they have their insertion into soft tissues to enable the complex facial movement. This arrangement has implications for the model structure in the face.

The nasal CPAP mask during therapy is positively located onto the face around the nose and forehead. Having considered the gross anatomy of the face and skull in the region of interest, it is important to turn attention to the mechanical properties of the soft tissues in the load path. This will include the skin, muscle and adipose tissue. Before outlining the mechanical properties of the soft tissues, the fundamental results of continuum mechanics will be introduced.

Chapter 5

Continuum Mechanics

This project is concerned with modelling living soft tissue and elastomers, both of which are highly compliant and also exhibit clear non-linear material properties. Therefore, it is important to introduce the relevant theory of continuum mechanics to provide the theoretical background to the analyses conducted in this project. The deformations encountered in this project are in the large deformation domain, so small strain simplifications cannot be made, and the deformation configuration of the body is significant to the equilibrium state.

5.1 Kinematics

Kinematics refers to the displacement or motion of a body, without reference to the nature of the body or the forces that cause the movement Oxf (2006). Therefore, in terms of continuum mechanics, kinematics refers to the state of deformation and strain in a body. Since the materials used in this project are highly compliant and deviate from the linear assumptions of small strains, it is necessary to introduce a theory of large deformation and large strain. Since the body in question is experiencing large strains and deformations, the difference between the reference and the deformed configuration is no longer negligible. Therefore, a number of different measures will be introduced which can characterise the material under deformations. The conventional continuum mechanics notation of denoting the *reference* (undeformed) configuration by the use of upper case letters ($\boldsymbol{X}$) whereas the *deformed* configuration is denoted with lower case letters ($\boldsymbol{x}$).

Consider a body in both a reference state and a deformed state with a point P and p with position vectors $\boldsymbol{X}$ and $\boldsymbol{x}$ respectively. The deformation gradient $\boldsymbol{F}$ maps

the reference configuration to the deformed configuration and contains information about rotations and displacements as follows,

$$x_i = X_i + u_i \tag{5.1}$$

$$\boldsymbol{F} = \frac{\partial \boldsymbol{x}}{\partial \boldsymbol{X}} = \boldsymbol{I} + \frac{\partial \boldsymbol{u}}{\partial \boldsymbol{X}} \tag{5.2}$$

where $\boldsymbol{X}$ and $\boldsymbol{x}$ are Cartesian position vectors of a point in the reference and deformed configurations respectively, and $\boldsymbol{u}$ is a displacement vector. The volumetric ratio of a deformation is the given by

$$dv = \det \mathbf{F} d\mathbf{X}^{(3)} \cdot \left(d\mathbf{X}^{(1)} \times d\mathbf{X}^{(2)} \right) \tag{5.3}$$

$$dv = \det \mathbf{F} dV \tag{5.4}$$

$$\det \mathbf{F} = \frac{dv}{dV} \tag{5.5}$$

The volumetric ratio is commonly denoted as J. The necessary and sufficient condition for the deformation to be incompressible or isochoric is:

$$J = \det \mathbf{F} = \frac{dv}{dV} = \lambda_1 \lambda_2 \lambda_3 = I_3 = 1 \tag{5.6}$$

Where the principal stretches of a deformed body are $\lambda_1, \lambda_2, \lambda_3$. This is equivalent to the third invariant I_3 of the stretch tensors $\mathbf{U}$ and $\mathbf{V}$.

The deformation gradient contains information about rotations as well as deformation. The right Cauchy Green deformation tensor, as its name suggests, is a measure of deformation calculated from $\boldsymbol{F}$,

$$\boldsymbol{C} = \boldsymbol{F}^T \boldsymbol{F}. \tag{5.7}$$

$\boldsymbol{C}$ is a symmetric tensor whose eigenvalues are the squares of the principal stretches of the material λ_i^2

The deformation gradient is also able to be decomposed into a symmetric stretch tensor and an orthogonal rotation tensor $\boldsymbol{R}$. The order of rotation and stretching operations is important and determines whether the stretch tensor is calculated with respect to the reference configuration or the deformed configuration.

$$\boldsymbol{F} = \boldsymbol{R}\boldsymbol{U} = \boldsymbol{v}\boldsymbol{R} \tag{5.8}$$

, where $\boldsymbol{U}$ is the *right stretch tensor* [1]with respect to the reference configuration, $\boldsymbol{v}$ is the *left stretch tensor* [2] with respect to the deformed or current configuration. The log or Hencky strain is then calculated directly from the right stretch tensor,

$$\epsilon = \ln \boldsymbol{U} \tag{5.9}$$

. Some manipulation shows that $\boldsymbol{C} = \boldsymbol{U}\boldsymbol{U}$.

5.1.1 Eigenvalues, Eigenvectors and Invariants

Any symmetric tensor, say $\boldsymbol{U}$, can be characterised by its eigenvalues and eigenvectors. These are calculated with from the well known equation

$$\det\left(\boldsymbol{C} - \lambda_i \boldsymbol{I}\right) = \boldsymbol{0} \tag{5.10}$$

, which leads to the characteristic cubic equation

$$\lambda^3 - I_1\lambda^2 + I_2\lambda - I_3 = 0 \tag{5.11}$$

The roots of this equation are the eigenvalues or principal values of the tensor. The eigenvalues of $\boldsymbol{U}$ and $\boldsymbol{v}$ are identical and are the principal stretches of the deformation. The associated eigenvectors define the orthogonal principal directions, however the eigenvectors of $\boldsymbol{U}$ and $\boldsymbol{v}$ will differ as $\boldsymbol{U}$ refers to the reference configuration and $\boldsymbol{v}$ refers to the deformed configuration. The coefficients I_1, I_2, I_3 are independent of the reference system and can be reduced to functions of the principal values. They are known as principal scalar invariants, and are given below for $\boldsymbol{U}$.

$$I_{U1} = \mathrm{tr}\boldsymbol{U} = \lambda_1 + \lambda_2 + \lambda_3 \tag{5.12}$$

$$I_{U2} = \mathrm{tr}\boldsymbol{U}^{-1}\mathrm{det}\boldsymbol{U} = \lambda_1\lambda_2 + \lambda_1\lambda_3 + \lambda_2\lambda_3 \tag{5.13}$$

$$I_{U3} = \mathrm{det}\boldsymbol{U} = \lambda_1\lambda_2\lambda_3 = J \tag{5.14}$$

The invariants of the right deformation tensor $\boldsymbol{C}$ are important for many constitutive models, so are presented below. The tensor $\boldsymbol{C}$ is given by $\boldsymbol{C} = \boldsymbol{U}\boldsymbol{U}$ the principal

[1]also known as the *material stretch tensor*
[2]also known as the *spatial stretch tensor*

values are the squares of the principal stretches, so the invariants are [3]

$$I_{C1} = \mathrm{tr}\boldsymbol{C} = \lambda_1^2 + \lambda_2^2 + \lambda_3^2, \tag{5.15}$$

$$I_{C2} = \mathrm{tr}\boldsymbol{C}^{-1} \det \boldsymbol{C} = \lambda_1^2\lambda_2^2 + \lambda_2^2\lambda_3^2 + \lambda_1^2\lambda_3^2, \tag{5.16}$$

$$\text{and} \quad I_{C3} = \det \boldsymbol{C} = \lambda_1^2\lambda_2^2\lambda_3^2 = J^2 \tag{5.17}$$

5.2 Stress

5.2.1 Introduction

In its simplest definition, stress is defined as force per unit area. Consider a body under the action of a force $\boldsymbol{f}$. If an arbitrary section plane cuts the body, $\boldsymbol{f}$ is resolved on that plane, containing components normal and tangential to the surface. Considering a small element of the surface, the force can be normalised by the area so that

$$\mathrm{d}\boldsymbol{f} = \boldsymbol{t}\mathrm{d}s = \boldsymbol{T}\mathrm{d}S \tag{5.18}$$

Where $\boldsymbol{t}$ is the Cauchy or true traction vector, which is the force per unit area in the deformed configuration acting over surface element $\mathrm{d}s$, and $\boldsymbol{T}$ is the 1st Piola Kirchoff or nominal traction vector, which is the force per unit area in the reference configuration acting over surface element $\mathrm{d}S$. These surface tractions are real physical loads in the case of boundary forces applied to the exterior of a body, *e.g.* from contact loading. They contain both shear and normal components.

5.2.2 Stress Tensor

In the case of a volume element with normal vectors parallel to the coordinate system (x_1, x_2, x_3), a nominal surface traction vector, $\boldsymbol{T}$, can be expressed with components acting along the coordinate directions for each of the orthogonal normal vector directions. This is shown in Figure 5.1.

A component is deemed to be positive if it acts on a face in the same direction as the outward normal of the same face, $\boldsymbol{n}$.It is convenient to arrange the components of the stress vectors according to the surface that they act on and the direction of the stress in the matrix as shown in Table 5.1. The first digit of the subscript refers to the surface that the stress acts on, while the second refers to the component direction of the stress.

[3] the subscript C is used here for differentiation from the invariants of the right stretch tensor

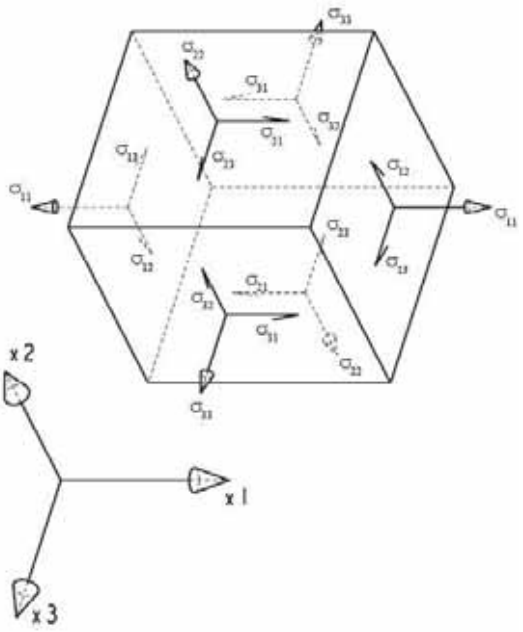

Figure 5.1: Stress tensor coordinate directions

	Stress Component Direction		
	1	2	3
Surface normal to x_1	σ_{11}	σ_{12}	σ_{13}
Surface normal to x_2	σ_{21}	σ_{22}	σ_{23}
Surface normal to x_3	σ_{31}	σ_{32}	σ_{33}

Table 5.1: Stress matrix arrangement

This is known as the Cauchy stress tensor and describes the three dimensional state of stress at a point in the deformed configuration. There is a simple and important relationship between the traction vector and the stress tensor, known as Cauchy's formula,

$$\boldsymbol{t} = \boldsymbol{\sigma n} \qquad t_i = \sigma_{ij} n_j \tag{5.19}$$

$$\boldsymbol{T} = \boldsymbol{PN} \qquad T_i = P_{ij} N_j \tag{5.20}$$

The stress tensor (stress matrix) is expressed as shown in table 5.1 above. This is the *Cauchy* or *true* stress tensor $\boldsymbol{\sigma}$. $\boldsymbol{P}$ is the first Piola Kirchoff stress tensor which will be expanded on in Section 5.3, $\boldsymbol{N}$ is the normal vector in the reference configuration.

5.2.3 Principal Stresses and Directions

The principal stresses and the corresponding orthogonal principal directions with respect to the deformed configuration in a body are the eigenvalues and eigenvectors respectively of the Cauchy stress tensor. Refer to Section 5.1.1 for details.

5.2.4 Mean and Deviatoric Stresses and Strains

The Cauchy stress and Hencky strain tensors can be additively decomposed into mean and deviatoric components, using the Cauchy stress as an example as follows;

$$\sigma_{ij} = \sigma_0 + \sigma'_{ij} \tag{5.21}$$

$$\sigma_0 = \frac{Tr\left(\sigma_{ij}\right)}{3} = \frac{I_1}{3} \tag{5.22}$$

$$\sigma'_{ij} = \sigma_{ij} - \sigma_0 \delta_{ij} \tag{5.23}$$

Where σ_0 is the mean stress, and σ'_{ij} is the deviatoric stress tensor. The mean stress acts evenly in all directions normal to the applied surface. This is equivalent to hydrostatic pressure in a fluid. Therefore, the mean stress of a tensor is often termed the hydrostatic component (Landau and Lifschitz, 1970; Fung, 1969). This is an invariant quantity, as the trace of a tensor is the first invariant. Therefore, the *mean stress is associated with volumetric strain*, while the *deviatoric stresses and strains are associated with constant volume (isochoric) distortions.*

5.3 Measures of Stress

In small deformation theory there is no significant difference between the reference area that a force acts on and the deformed area that the force acts over. Therefore, the nominal stress is simply the force acting over the reference area, however in the large deformation domain the difference between the reference configuration and the current configuration cannot be ignored. Therefore, additional measures of stress are needed to account for the material deformation.

The stress tensor that was derived in section 5.2.2 is known as the Cauchy or True stress tensor. This acts on the material in its current or deformed state, providing experimental challenges as it is often difficult or even impossible to obtain adequate measurements within an experiment of the deformed material. Therefore, it is desired to transform this stress into the reference configuration, which is usually defined or easily measured in experiments.

The 1^{st} Piola Kirchoff stress (1PK) is calculated such that the force applied in the reference configuration is the same as the force applied across a deformed surface by the Cauchy Stress. The Cauchy stress and 1^{st} PK stress are related by

$$P_{ij} = \sigma_{ik} J F^{-1}_{jk} \qquad \boldsymbol{P} = J\boldsymbol{\sigma}\boldsymbol{F}^{-T} \tag{5.24}$$

Conversely the Cauchy stress can be calculated in terms of the 1^{st} PK stress.

$$\sigma_{ij} = J^{-1} F_{jk} P_{ik} \qquad \boldsymbol{\sigma} = J^{-1}\boldsymbol{P}\boldsymbol{F}^{T} \tag{5.25}$$

The physical meaning of the 1st PK stress is that it is the actual force in the deformed configuration applied to the surface area in the reference configuration. This is the most convenient measure for experimentation, as force is usually obtained continually through a load cell or similar, whereas only the initial (reference) dimensions are known. Note that this tensor is not symmetric.

Although the 1st PK stress has a clear physical meaning and can be easily understood, there are some problems associated with it when developing constitutive relations. These include its non-symmetry and the fact the 1st PK stress does not form an energetically consistent pair with any of the measures of finite strain. Therefore, the 2nd Piola Kirchoff Stress Tensor was developed to overcome these problems. In the 2nd PK stress tensor, the Cauchy stress, modified by the volumetric ratio is mapped or pulled back to the reference configuration.

$$S_{ij} = J F^{-1}_{ik} F^{-1}_{jl} \sigma_{kl} = F^{-1}_{ik} P_{ki} \qquad \boldsymbol{S} = J\boldsymbol{F}^{-1}\boldsymbol{\sigma}\boldsymbol{F}^{-T} = \boldsymbol{F}^{-1}\boldsymbol{P} \tag{5.26}$$

By rearranging the we get the Cauchy and 1^{st} PK stresses as a function of the 2^{nd} PK stress

$$\sigma_{ij} = J^{-1} F_{ik} F_{jl} S_{kl} \qquad \boldsymbol{\sigma} = J^{-1}\boldsymbol{F}\boldsymbol{S}\boldsymbol{F}^{T} \tag{5.27}$$

$$P_{ij} = F_{ik} S_{kj} \qquad \boldsymbol{P} = \boldsymbol{F}\boldsymbol{S} \tag{5.28}$$

5.3.1 Physical Meaning and Implications

Cauchy Stress Tensor

As mentioned before the Cauchy stress tensor is a measure of the actual force in the deformed configuration acting over an area in the deformed configuration. Therefore, it is used in equations of equilibrium and motion [4]. The Cauchy stress tensor is work conjugate with the infinitesimal strain tensor.

1st Piola Kirchoff Stress Tensor

The 1st Piola Kirchoff stress tensor is a measure of the actual force in the deformed configuration acting over an area in the reference configuration. This is well suited to experimental work, since it is easy to monitor the actual load continuously through a load cell and to obtain measurements of the sample in the reference configuration. This is analogous to nominal or engineering stress in the small strain regime. The 1st PK stress tensor (T) is unsymmetric and is not work conjugate with any measure of strain. and to obtain measurements of the sample in the reference configuration. This is analogous to nominal or engineering stress in the small strain regime. The 1st PK stress tensor (T) is unsymmetric and is not work conjugate with any measure of strain.

2nd Piola Kirchoff Stress Tensor

The 2nd Piola Kirchoff stress tensor is an abstract measure of the applied force mapped into the reference condition and acting over an area in the reference condition. It has no physical meaning, but importantly it is work conjugate with the Green Lagrange strain tensor (E). Therefore, the following important relationship holds:

$$S_{ij} = \frac{\partial \Psi}{\partial E_{ij}} = 2\frac{\partial \Psi}{\partial C_{ij}} \tag{5.29}$$

.

5.4 Elastic Deformations

A material is said to be elastic if it behaves in such a way that if deformed under the action of a load, it will completely recover its reference state upon removal of the load. Therefore, for a perfectly elastic body, all of the strain energy stored in the deformed body is recovered upon unloading.

$$\mathrm{d}\Psi = \sigma_{ij} \cdot \mathrm{d}e_{ij} \tag{5.30}$$

This quantity is equal to the work done per unit volume in straining the body. This equation can be simply rearranged to determine the stress tensor,

$$\sigma_{ij} = \frac{\mathrm{d}\Psi}{\mathrm{d}e_{ij}} \tag{5.31}$$

Recall that both the true stress and strain tensors can be decomposed into hydrostatic and deviatoric stresses as well as volumetric and distortional (deviatoric) strains respectively. Therefore, the strain energy can also be determined as the sum of these components

$$\mathrm{d}\Psi = \sigma_0 \mathrm{d}V + \sigma_{ij}\prime \mathrm{d}e_{ij}\prime \tag{5.32}$$

Since the distortional and volumetric components are independent, this reduces to

$$\sigma_0 = \frac{\partial \Psi}{\partial V} \qquad\qquad \sigma_{ij}\prime = \frac{\partial \Psi}{\partial e_{ij}\prime} \tag{5.33}$$

. In many cases soft tissues and rubbers are assumed to be incompressible, so that all the strain energy is deviatoric and the volumetric component can be ignored.

5.5 Hyperelasticity

A material is said to be hyperelastic if it is able to withstand large fully recoverable elastic deformations Inc (2005). Typically hyperelastic materials display highly non linear mechanical behaviour and have been developed originally from the study of rubber (Mooney, 1940; Rivlin and Saunders, 1951). A hyperelastic material is characterised by the existence of a strain energy density function Ψ that is often expressed as a function of one of the measures of deformation.

5.5.1 Incompressibility

A further characteristic of hyperelastic materials is that they are usually incompressible or nearly incompressible. Therefore, under a general load inducing deformation, the volume will remain constant. This is known as an isochoric deformation. Recall also that stress and strain tensors can be decomposed to into volumetric and a distortional or isochoric components. The volumetric deformation can be extracted from the deformation gradient,

$$J = \det \boldsymbol{F} = \frac{\mathrm{d}v}{\mathrm{d}V} = \lambda_1 \lambda_2 \lambda_3 \tag{5.34}$$

For a fully incompressible material the volumetric ratio will be identically unity for all deformations, providing an extremely important identity.

$$J = \det \boldsymbol{F} = \lambda_1 \lambda_2 \lambda_3 = 1 \tag{5.35}$$

.

5.5.2 Isotropy

In general, hyperelastic materials may be anisotropic (Humphrey, 2003; Gasser *et al.*, 2006), but predominantly most elastomers due to the convoluted random orientation of their cross linked molecular chains possess isotropic properties in their resting state (Charlton *et al.*, 1994). For virtually all practical applications, elastomers can be considered to be isotropic.

5.5.3 Strain Energy Density Functions

In modelling the constitutive behaviour of any hyperelastic material, the determination of the strain energy density function Ψ is of fundamental importance. This continues to be an area of active research. Strain energy functions fall into two broad categories, these are phenomenological and structural. Phenomenological equations attempt to describe the behaviour of the material based solely on empirical observations of its behaviour. Following experimental observations a form of the strain energy function is chosen and material parameters are fitted. Usually the material parameters of the strain energy functions have no physical meaning and should not be thought of as properties. Structural equations on the other hand attempt to devise a strain energy function that is based on objective parameters that can be determined from the structural composition of the material. (Charlton *et al.*, 1994; Arruda and Boyce, 1993).

Rivlin Models

During the late 1940s and early 1950s Rivlin and co-workers produced an extensive set of papers outlining a general theory for large deformations of non linear highly elastic materials. Part of this work focussed on developing a general purpose theory for the strain energy function in rubber Rivlin and Saunders (1951).

Rivlin's form of the isotropic strain energy density function was developed as a function of the right stretch tensor ($\boldsymbol{C}$) invariants. Additionally he assumed that rubber was completely incompressible ($J = \lambda_1\lambda_2\lambda_3 = 1$).

$$\Psi\left(I_1, I_2\right) = \sum_{i+j=1}^{N} C_{ij}\left(I_1 - 3\right)^i \left(I_2 - 3\right)^j \tag{5.36}$$

where C_{ij} are material constants corresponding to order indices i, j and N is the order of terms to be included. In practice terms up to the second order are usually included.

Neo Hookean The Neo-Hookean model as it has come to be termed was developed by Treloar in 1943 Rivlin and Saunders (1951). It is a single parameter model, which can be developed by retaining only the first term of the Rivlin infinite series Boyce and Arruda (2000). The Neo Hookean strain energy density function is given by

$$\Psi\left(I_1, I_2\right) = \sum_{i+j=1}^{N=1} C_{ij}\left(I_1 - 3\right)^i \left(I_2 - 3\right)^j \qquad : i = 1, j = 0 \tag{5.37}$$

$$\Psi\left(I_1\right) = C_{10}\left(I_1 - 3\right) \tag{5.38}$$

$$C_{10} = \frac{\mu}{2} \tag{5.39}$$

It is important to note that in this case the material constant C_{10} does have a physical meaning. It is a multiple of the initial shear modulus μ of the material.

Mooney Rivlin The Mooney form of the strain energy density, while given as a function of the principal stretches is identical to the Rivlin equation with two first order terms.

$$\Psi\left(I_1, I_2\right) = \sum_{i+j=1}^{N=1} C_{ij}\left(I_1 - 3\right)^i \left(I_2 - 3\right)^j \qquad : i, j = 0, 1 \tag{5.40}$$

$$\Psi\left(I_1\right) = C_{10}\left(I_1 - 3\right) + C_{01}\left(I_2 - 3\right) \tag{5.41}$$

$$\mu = 2\left(C_{10} + C_{01}\right) \tag{5.42}$$

Once again the initial shear modulus (μ) is related to the Mooney Rivlin series coefficients.

By increasing the number of terms retained in the series it is possible to model increasingly complex non-linear constitutive behaviour, however this can come at the expense of computational resources and reliability as higher order models, beyond their potentially narrow region of fit, are prone to instability and rapid degradation of results. Other commonly used configurations of the model include three, five and nine parameter expansions. The three parameter model is used in this research as follows:

$$\Psi\left(I_1, I_2\right) = \sum_{i+j=1}^{N=2} C_{ij}\left(I_1 - 3\right)^i \left(I_2 - 3\right)^j \qquad : i, j = 0, 1 \tag{5.43}$$

$$\Psi\left(I_1\right) = C_{10}\left(I_1 - 3\right) + C_{01}\left(I_2 - 3\right) + C_{11}\left(I_1 - 3\right)\left(I_2 - 3\right) \tag{5.44}$$

5.5.4 Near Incompressibility

Each of the above models assume that the material is perfectly incompressible. While this assumption may well be valid, each of these models can be adjusted slightly to allow for near incompressibility. The procedure is very similar for all of the above models.

For an incompressible material, $J = 1$ identically. If not, the strain energy is associated with both volumetric and deviatoric (isochoric) deformations. The volumetric component is associated with the bulk behaviour of the material, whilst the deviatoric component is associated with the shear behaviour of the material. A compressible material is characterised by $J \neq 1$. To decompose Ψ a modified deformation gradient is formed such that

$$\det\bar{\boldsymbol{F}} = 1 \tag{5.45}$$

Where $\bar{\boldsymbol{F}}$ is the modified deformation gradient. Let,

$$\bar{\boldsymbol{F}} = J^{-1/3}\boldsymbol{F} \tag{5.46}$$

$$\bar{J} = \det\bar{\boldsymbol{F}} = \det J^{-1/3}\boldsymbol{F} = {J^{-1/3}}^3 \det\boldsymbol{F} \tag{5.47}$$

$$\bar{J} = \left(\lambda_1\lambda_2\lambda_3^{-1/3}\right)^3 \lambda_1\lambda_2\lambda_3 = \frac{\lambda_1\lambda_2\lambda_3}{\lambda_1\lambda_2\lambda_3} \tag{5.48}$$

$$\bar{J} = \det\bar{\boldsymbol{F}} = 1 \tag{5.49}$$

The modified principal stretches are given by

$$\bar{\lambda_i} = J^{-1/3}\lambda_i \tag{5.50}$$

Similarly the modified right Cauchy Green deformation tensor is given by

$$\begin{aligned}\bar{\boldsymbol{C}} &= \bar{\boldsymbol{F}}^T\bar{\boldsymbol{F}} \\ &= J^{-1/3}\boldsymbol{F}^T J^{-1/3}\boldsymbol{F} \\ &= J^{-2/3}\boldsymbol{F}^T\boldsymbol{F} \\ \bar{\boldsymbol{C}} &= J^{-2/3}\boldsymbol{C}\end{aligned} \tag{5.51}$$

The invariants used in the constitutive model are formed in the usual way.

5.6 Summary

This section has introduced the theory of large deformation continuum mechanics, hyperelastic modelling of incompressible elastomeric materials and a brief explanation of strain energy density functions. The theory provides background knowledge for discussion of the mechanical properties of soft materials

Chapter 6

Biological Tissues

6.1 Background

As outlined in Section 4, the face forms a very complex structure with layers of skin, fat and muscle supported on the bony scaffold of the skull. The mechanical loading scenario of the mask on the face places the skin in transverse compression and some shear. In order to accurately analyse and simulate the mechanics of this system, it is important to use or determine reasonable material properties. This chapter will briefly outline the structure and biomechanical properties of these tissues.

6.2 Bone

Bone is a hard calcified tissue. Its biomechanical functions in the skeleton include providing structure, protection and force transmission, manipulation and locomotion through the use of muscles. There are two broad categories of bone, cortical or compact bone, and trabecular or spongy bone. Bones themselves are classified by shape into long, flat, short and irregular. Cortical bone forms the exterior of all bones and the diaphysis (shaft) of long bones. Flat bones, as in the skull are primarily composed of trabecular bone sandwiched between cortical layers (Tortora and Grabowski, 2004).

Cortical or compact bone has a dense, highly organised, repetitive structure called Haversian systems or osteons. Each osteon consists of a central canal surrounded by lamellae (layers) of calcified matrix providing the structure of the bone. Spongy or trabecular bone on the other hand resembles a 3D scaffold of small columns. This arrangement is very light, minimising the inertia of the bone.

Experimental investigations into the mechanical properties of bone show that it is a non-linear, non-homogeneous, viscoelastic and anisotropic material (Duck, 1990). For low to moderate strains, the response can be assumed to be linear and that Hooke's Law applies. Assuming quasi-static loads from the CPAP mask, the

Table 6.1: Typical summary bone material properties, where $_L$ and $_T$ refer to the longitudinal and transverse directions respectively

		Elastic Modulus (E (GPa))	
Source	Parameter	Cortical	Trabecular
Nigg and Walter (1999)	E	20	1
Park and Lakes (1992)	E	17.2-18.6	0.09
Duck (1990)	E_L	17-20	-
Duck (1990)	E_T	6.9-13.4	-

viscous effects can be assumed to be negligible. As is common with all biological materials significant variability is encountered in the material properties determined. Some typical mechanical properties of bone are listed in Table 6.1.

Cortical bone is vastly stiff when compared to the soft tissues. It is therefore, considered rigid for modelling purposes in this study, however a value of $E = 19$GPa was used in the FEA models to evaluate a stable contact stiffness between the bone and the soft tissues.

6.3 Skin

The physiological purpose of the skin is multi-faceted. It is an extremely effective barrier shielding the body from the external environment. It performs the opposing tasks of providing mechanical protection for the internal organs of the body, while being flexible and not restricting motility of the body induced by the actions of the musculoskeletal system. The skin also is very hard wearing and forms the bearing surface for any mechanical interactions with the exterior of the body. Therefore, the transmission of any load from the body to an external object is transmitted through the skin in a predominantly compressive load pattern. The skin is a highly mobile material, yet it is also very tough, it is able to slide relatively freely over the underlying tissues while withstanding and transmitting loads and providing puncture and abrasion resistance.

Skin has a layered structure, consisting broadly of the epidermis, dermis and hypodermis. This is shown in figure 6.1. The epidermis forms an extremely thin layer of keratinised squamous cells. Hendriks *et al.* investigated the mechanical properties of the epidermis, as part of their study they measured the epidermal thickness to be in the range of 130-150 μm compared to the overall skin thickness on the forearm of 1-1.3mm (Hendriks *et al.*, 2006), this is about an order of magnitude thinner. than the dermal layer. Additionally their suction experiments and simulation showed that

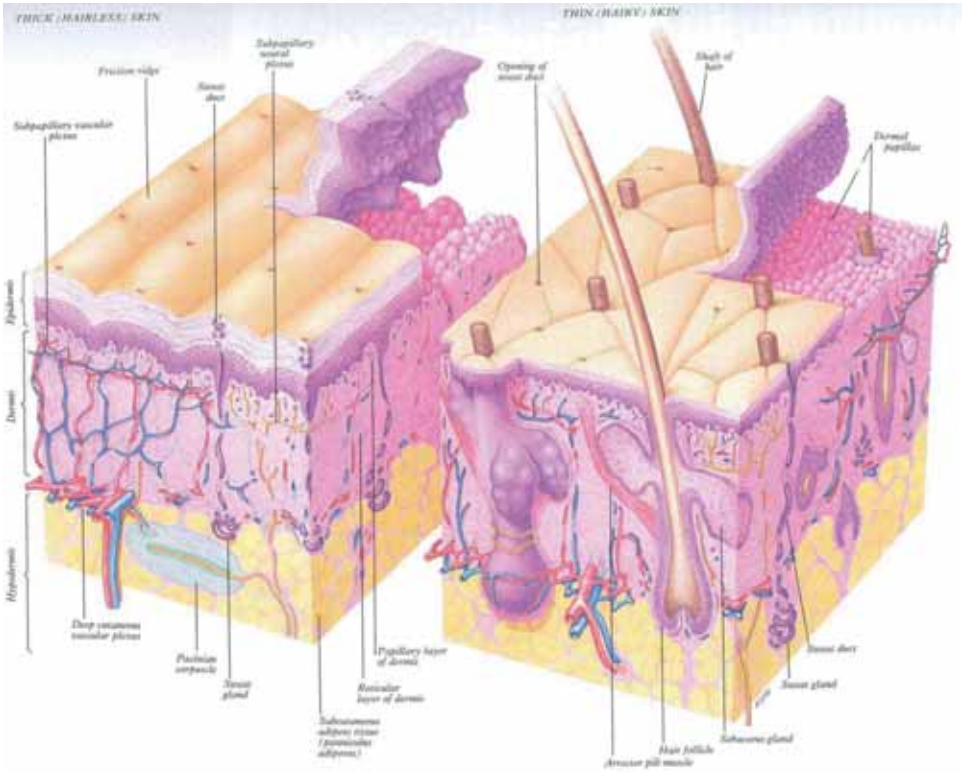

Figure 6.1: Skin structure (Williams *et al.*, 1989a)

the mechanical properties of the epidermis is about 3 orders of magnitude smaller than the dermal layer (Hendriks *et al.*, 2006).

The hypodermis, also known as the subcutis largely consists of adipose tissue. This provides a thermal barrier for insulation of the body and also acts as an elastic or flexible cushion upon which the dermis and epidermis rest (Rushmer *et al.*, 1966). Hendriks *et al.* (2003) estimated the mechanical properties of the hypodermis in tension and concluded that it was negligible compared to the properties of the skin overall. The properties of subdermal adipose tissue will be discussed further in Section 6.4.

The dermis layer provides most of the mechanical properties of the skin. It consists of fibres and proteoglycans embedded in a ground substance matrix. Collagen fibres comprise approximately 60-80% of the skin's dry mass with elastin fibres contributing about 4% (Lokshin and Lanir, 2009). It is well known that the stress/strain characteristics of skin exhibit 3 regions with increasing load, these are 1) low stiffness or toe region, 2) load bearing region with a large stiffness increase and 3) yielding and failure (Bischoff *et al.*, 2000; Fung, 1967, 1993; Dunn *et al.*, 1985). It is commonly accepted that the toe region is governed by the stretching and recovery of elastin fibres (Oxlund *et al.*, 1988), which are highly compliant, yet resilient, while the load bearing regions are governed by gradual recruitment of the

crimped collagen fibres as they straighten and begin to strain rather than unfold with increasing force. (Bischoff *et al.*, 2000; Fung, 1993; Lokshin and Lanir, 2009). The collagen and elastin fibres are oriented to lie in the plane of the skin. This provides skin with its significant mechanical strength and the capability to undergo large, recoverable deformations without the accumulation of damage. Considering the fibrillar arrangement of the load carrying members and their planar orientation skin predominantly acts like a membrane. This means that it is not able to effectively support bending or compressive loads.

Skin, as described above is a a layered structure, whose mechanical properties are governed by this structural arrangement. Extensive research has been undertaken to understand its mechanical properties using a range of experimental *in vivo* and *in vitro* methods, including tensile testing, biaxial testing, indentation, suction as well as inverse numerical analyses. Hyperelastic constitutive models have often been used to simulate the non-linear mechanical characteristics of the skin with the assumption of incompressibility common. Models used in addition to those described in Section 5.5.3 include various forms of the Rivlin series [1], Ogden [2] and the Arruda Boyce eight chain model [3] .

Lanir and Fung (1974a) performed one of the landmark studies into the mechanics of skin using a rabbit model. This was a series of biaxial and uniaxial *in-vitro* tensile tests. From this they demonstrated that skin is anisotropic, non-linear, viscoelastic, hysteretic and required preconditioning to stabilise. These tests were performed in plane and assumed incompressibility. The non linear and anisotropic nature of skin is shown in Figure 6.2. Further to these properties of skin, *in vivo*, it is preloaded in a state of biaxial tension. This is evident by the tendency of skin to retract from a cut. This tension has been mapped by Langer, and the contours of the principal stretches of the skin are known as Langer lines. This is a challenge for accurate modelling as it can be difficult to establish realistic initial boundary conditions. Kvistedal and Nielsen (2009) in a sophisticated experiment using a multi-axial test rig developed a two dimensional anisotropic membrane constitutive model of the skin *in-vivo*. This model captures the toe region and the sharp stiffening of the stress strain response both parallel and perpendicular to the Langer lines in human skin without altering the *in vivo* boundary and physiological conditions.

[1] extended Neo Hookean strain energy density function: $\Psi = C_{10}\left(I_1 - 3\right) + C_{11}\left(I_1 - 3\right)\left(I_2 - 3\right)$

[2] Ogden strain energy density function: $\Psi = \frac{\mu}{\alpha}\left(\lambda_1^{\alpha} + \lambda_2^{\alpha} + \lambda_3^{\alpha} - 3\right)$

[3] Arruda Boyce strain energy density function:
$\Psi = \mu\left[\frac{I_1-3}{2} + \frac{I_1^2-9}{20\lambda_L^2} + \frac{11\left(I_1^3-27\right)}{1050\lambda_L^4} + \frac{19\left(I_1^4-81\right)}{7000\lambda_L^6} + \frac{519\left(I_1^5-243\right)}{673750\lambda_L^8}\right]$

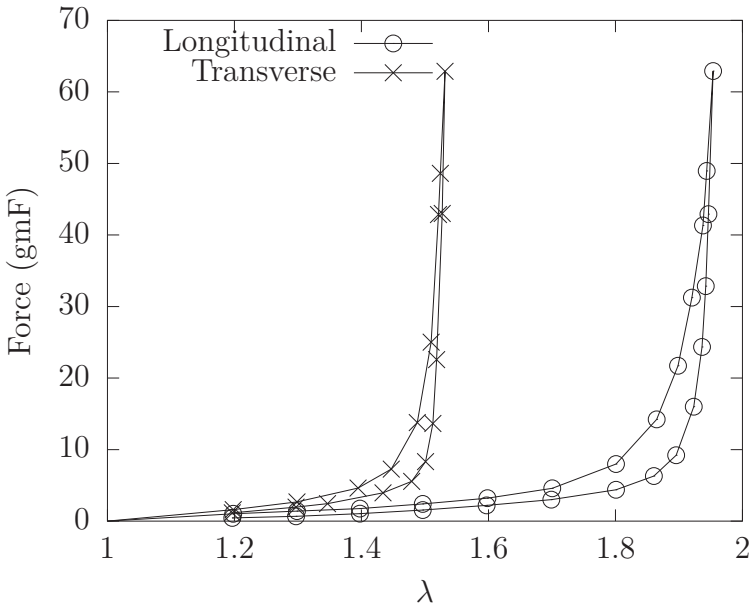

Figure 6.2: Force vs stretch curves in longitudinal and transverse directions, digitised from (Lanir and Fung, 1974b). Note the linear toe region governed by the compliant elastin fibres followed by the rapidly increasing stiffness as the crimped collagen straightens and is recruited into the load bearing of the skin

A brief survey of mechanical properties of skin is presented in Table 6.2. Most of the studies that have been listed have treated skin as a membrane and reported material parameters within the plane of the membrane. The skin is unable to resist bending and compression loads. The load bearing filaments of the dermis are arranged predominantly within the plane of the membrane, therefore providing significantly higher properties in the plane of the membrane compared to the transverse direction. External loads are applied to the skin through contact, which is a surface traction vector applying compression and shear to the skin. During CPAP therapy, the mask is positively located on the face applying a significant compressive traction. Therefore it is important for the modelling in this research that the transverse properties be considered. None of the more advanced material models presented in Table 6.2 consider loading in the thickness direction. Therefore, the properties of the indentation studies will be considered for further use in the study.

The study of Jachowicz *et al.* (2007) used an in-vivo indentation technique. This differs from many papers listed in Table 6.2 in that the load is applied transversely to the plane of the membrane. A spherical indenter was used to acquire force vs displacement data from the forearm and face. Hertzian contact theory was used to estimate the elastic moduli of the 10 subjects with results pooled. Results are reported at the forehead, which is a desired location for this study, therefore, the

Table 6.2: Skin published properties summary. Test types listed include suction (S), FEA, uniaxial tension (T), numerical (N), indentation (I) and unconfined compression (UC). The material models used in these studies include the Neo Hookean (NH), extended Neo Hookean (eNH), Ogden (O), stress-strain curves ($\sigma\epsilon$), Arruda Boyce (AB), non linear elastic (nlE), Hertzian (H) and inverse models (Inv). Parameters for the various constitutive models used are reported with their units if applicable. Finally an estimate of the initial elastic modulus is reported after converting the parameters, all values are converted into kPa.

Source	Test	Model	Tissue	Parameters		E estimate (kPa)
Hendriks *et al.* (2006)	S	NH	Epidermis	C_{01E}	0.11 kPa	0.66
			Dermis	C_{01D}	160 kPa	960
Hendriks *et al.* (2003)	S	eNH	Dermis	C_{10}	9.4 ± 3.6 kPa	28.2
				C_{11}	82 ± 60 kPa	
Oomens *et al.* (2003)	FEA	O	Dermis	μ	8 kPa	120
				α	10	
Dunn *et al.* (1985)	T	$\sigma\epsilon$	Dermis	E_T	650 kPa	650
				E_C	18900 kPa	18900
Bischoff *et al.* (2000)	N	AB	Skin	n	5.00e22m^{-3}	0.617
				N	1.1	
Delalleau *et al.* (2008)	S	nlE	Skin (toe)	E_T	41 – 131 kPa	
			Skin (collagen)	E_C	187 – 365 kPa	
Jachowicz *et al.* (2007)	I	H	Skin (arm)	E	7 – 33 kPa	33
			Skin (face)	E	7 – 16 kPa	16
Pailler-Mattei *et al.* (2008)	I	Inv	Dermis	E_D	35 kPa	35
			Hypodermis	E_H	2 kPa	2
Wu *et al.* (2007)	UC	$\sigma\epsilon$	Dermis	E_T	16.5 kPa	16.5
				E_C	712 kPa	712

facial skin elastic properties reported at the forehead are used subsequently for the remainder of this research.

6.4 Fat

Fat, or adipose tissue is a connective tissue consisting predominantly of adipocytes bound by vascular loose, or areolar, connective tissue. Adipose tissue concentrates much of the body's fat in the subcutaneous tissue among other preferential locations including the omentum and breasts. Functionally, adipose tissue acts as an energy reservoir, thermal insulator and as a mechanical load absorbing and distribution member, such as in the calcaneal fat pad under heel strike impact loading Williams *et al.* (1989a). Few studies have attempted to characterise the properties of subdermal fat, and have found its properties to be extremely compliant with in some cases negligible mechanical properties (Hendriks *et al.*, 2003). Subdermal fat is arranged in series with the skin forming an elastic foundation. Considering the idealisation

of springs in series the overall compliance of a structure is governed by the most compliant member, in this case the fat.

$$\frac{1}{k} = \frac{1}{k_{skin}} + \frac{1}{k_{fat}} + \frac{1}{k_{muscle}} \tag{6.1}$$

Therefore, the material properties of the subdermal fat will be a significant influence on the deformation of the composite of soft tissue as a whole. Since soft tissue deformation is commonly considered to be in the large deformation domain, the state of deformation will influence the structural stiffness and the load distribution. Therefore, for compressive loading, the mechanical behaviour of the subdermal fat should not be discounted.

In comparison to skin and muscle, there is a scarcity of mechanical property information on subdermal adipose tissue. Of this, much of the fatty tissue work has been focussed on the calcaneal fat pad and breast tissue (Miller-Young *et al.*, 2002; Samani *et al.*, 2003). The calcaneal fat pad is located in the heel and is important for load dissipation and shock absorption during locomotion, while breast tissue is comprised of primarily of both glandular and fatty tissue. Subdermal fat has received relatively little attention. In recent years through the use of FEA greater attention has turned to the simulation of load transmission through the discrete layers of soft tissue from contact loading on the skin. In numerous studies, the mechanical properties of fat tissue have been assumed or incorporated into a generic homogeneous material group (Linder-Ganz *et al.*, 2007; Oomens *et al.*, 2003).

The mechanical properties of subdermal fat have not been investigated extensively. Some studies have concluded that the properties are negligible (Hendriks *et al.*, 2003). These studies have primarily involved suction or some other loading mode that places the tissue in tension, which is then arranged in parallel to the dermal tissue. In this case, the effective in-plane modulus is additive, so it is a perfectly reasonable assumption. Hendriks *et al.* (2003) did make a rough estimate of the Neo Hookean parameter of subdermal fat in a layered FEA model ($C_{10_{Fat}} = 0.02$) kPa

Of the minimal investigative work that has been performed into the mechanical properties of fat, a brief summary of values from literature are reported in Table 6.3. Recently, work has increased on the micromechanics of adipose tissue (Comley and Fleck, 2010b,a) and the general mechanical properties of fat for the use in FEA simulation (Geerligs *et al.*, 2008, 2010).

Since the subdermal fat is on the load path for soft tissue placed in compression, it is important to mechanically characterise adipose tissue for use in FEA simulations of the soft tissue. The work of Geerligs *et al.* (2008) has commenced a systematic investigation into the mechanical properties of subdermal adipose tissue, however

Table 6.3: Summary of adipose tissue published properties

Source	Tissue	Type/Notes	Elastic/Initial Modulus (kPa)
Samani *et al.* (2007)	Breast	Inverse FEA	3.25 ± 0.91
Samani *et al.* (2003)	Breast	Inverse FEA	1.9
Samani and Plewes (2004)	Breast	MR5	0.305 ± 0.025
Azar *et al.* (2002)	Breast	Exponential	4.46
Erdemir *et al.* (2006)	Calcaneal Fat Pad	Ogden1	56
Miller-Young *et al.* (2002)	Calcaneal Fat Pad	MR2	0.02
Wearing *et al.* (2009)	Calcaneal Fat Pad	Secant	580
Geerligs *et al.* (2008)	Subdermal Fat	MR2	22.5

the linear assumption used in this exploratory work is inappropriate for the large deformations experienced. Therefore, in order to fill this gap in knowledge and provide material properties that are valid in the large deformation domain, an experimental and inverse FEA investigation was undertaken as part of this research. This is described in Chapter 9.

6.5 Muscle

Muscle is broadly categorised into three main types, skeletal, smooth and cardiac. Skeletal, or striated, muscle is of interest in this case. The main functions of skeletal muscle are to act on the skeletal system to generate body movements and stabilise posture. Skeletal muscle is a highly organised and specialised biological material with a hierarchical structure over a number of length scales, down to a fibrous structure. At the organ level, the muscle is contained by fascia, providing minimal a low friction surface which allows free movement of the muscles past surrounding tissue such as the skin. Within the muscle are bundles of muscle fibres. Within each muscle fibre is a group of axial fibres known as *myofibrils*, which in turn consist of an axially repeating arrangement of parallel interleaved thick (myosin) and thin (actin) protein filaments. These filaments are able to slide past each other and gradually increase or reduce fibre overlap depending on whether the muscle is contracting or lengthening. Each repeating arrangement is known as a sarcomere and is the level at which the mechanochemical reactions take place to contract the muscle or generate force. This repeating sarcomere arrangement leads to the characteristic striated pattern that is found in skeletal or striated muscle that is visible under microscopy. Remarkably two essentially independent research groups, led coincidently by Andrew Fielding Huxley and Hugh Huxley respectively, published simultaneously in Nature different landmark studies drawing the same conclusion that during contraction or force generation, the actin (thin) filaments are drawn into the arrangement of

myosin filaments (Huxley and Hanson, 1954; Huxley and Niedergerke, 1954). This is now commonly known as the sliding filament theory and is generally accepted as the kinematic mechanism by which muscle contract.

Considering the above description of the structure and arrangement of muscular tissue, mechanically muscle is considered to be transversely isotropic, with the isotropic plane transverse or normal to the muscle fibres. Muscle is an active tissue, capable of generating force, and not only passively responding to external forces applied to it. The modelling of muscle behaviour is of great interest in biomechanics for understanding the kinetics of the body, however for the application of CPAP masks, it is assumed that the muscles are acting passively. During sleep, skeletal muscle tone is drastically reduced, and eliminated during REM sleep with the exception of the orbital muscles and respiratory muscles of the trunk (Aserinsky and Kleitman, 1953; Berger, 1961).

While under CPAP therapy, the mask is at positive pressure with respect to the atmosphere, therefore, it is necessary for it to be positively located on the face. This will apply a compressive force to the skin and hence to the underlying muscles. The orientation of the muscles in the face essentially run parallel to the skin and skull. This means that the load applied to the muscle will be normal to the fibre direction, and can then reasonably be assumed to be acting normal to the fibre direction and acting within the plane of isotropy. Therefore, for these normal loads, the assumption of an isotropic material will be reasonable. As is common with many soft tissues, an assumption of incompressibility is made and hyperelastic models are commonly used.

Similarly to skin, there is voluminous study into the mechanics of skeletal muscle tissue, however despite decades of research there is relatively little work done on the passive transverse properties of muscle. This has begun to be addressed in recent years with the work of both Bosboom *et al.* (2001) and Van Loocke *et al.* (2006), who followed significantly different investigation paths.

Bosboom *et al.* (2001) performed a series of *in-vivo* quasi-static compression experiments on the tibialis anterior muscle of a rat model. The resting length of the muscle was marked before cutting the distal tendon. The muscle was then placed between heated platens (35–37^{O}C) and using a suture, stretched to the resting length prior to data acquisition. Inverse FEA using 2D plane stress elements was used to estimate material constants. The muscle material was modelled using a first order Ogden hyperelastic material with a first order Prony series for the viscous components,

Recently Van Loocke *et al.* (2006) used an *in-vitro* compression test method to acquire passive properties of porcine skeletal muscle at different angles to the fibre

direction. Their results were reported as a non-linear strain dependent moduli in a polynomial model of the form:

$$E_L = k_1 + k_2\epsilon + k_3\epsilon^2 \tag{6.2}$$

$$E_T = k_4 + k_5\epsilon + k_6\epsilon^2 \tag{6.3}$$

where E_L and E_T are the longitudinal (fibre) and transverse directions respectively. Oblique testing was used to derive shear terms in an elasticity or compliance matrix.

As mentioned previously, the contact loading on the face is essentially in the transverse plane of symmetry. Additionally due to the sliding filament arrangement of muscle, and the lack of muscle tone during sleep, there is minimal restraint on the tissue in the axial direction. Therefore, it will be assumed in this research that the muscle acts as an isotropic material with the elastic behaviour corresponding to that of the muscle in the transverse direction.

Muscle, as is common with other soft tissues, has a vast range property values published. This is the case for the passive transverse mechanical properties of muscle. The results from Bosboom *et al.* (2001) were fitted to a first order Ogden hyperelastic model with parameters of $\mu = 15.6$ kPa and $\alpha = 21.4$. The initial shear modulus from a first order Ogden model is given by $G_0 = \frac{\mu\alpha}{2} = 167$ kPa. This result differs by several orders of magnitude from that of Van Loocke *et al.* (2006), with an initial elastic modulus of $E_T = 2.25 \pm 0.007$ kPa, for the sake of comparison, this corresponds to an initial shear modulus of $G_0 = 0.88$ kPa assuming linear isotropy. This is at least two orders of magnitude difference, this could possibly be explained to some extent by the *in vivo* results not being atonic. This very wide range emphasises the need for further work in this area. The transverse results from Van Loocke *et al.* (2006) are used for reference in this research.

6.6 Cartilage

The entrance to the nasal cavity is separated by the nasal septum, which is predominantly the septal cartilage. This consists of semi rigid hyaline cartilage, which is a smooth, shiny, blue-white material with fine collagen fibres. Specialised forms of this cartilage are located at the bearing surfaces of bones (Tortora and Grabowski, 2004). Like the other tissues mentioned, there is a great body of literature regarding the mechanical properties of hyaline cartilage and its function as a bearing surface, however this is a different environment to the nasal cartilage, and there is only a small literature specifically addressing the nasal cartilage. Rotter *et al.* (2002) investigated the mechanical properties of nasal cartilage as a function of age, motivated

by uses for reconstructive surgery, using a confined compression method. They found that elastic modulus of the cartilage reduced with increasing age. The mean elastic modulus of nasal cartilage was reported as $E = 234$ kPa, which is approximately one quarter that reported for articular cartilage.

Chapter 7

Finite Element Analysis

7.1 Background

The mechanical scenario of the face/mask contact interactions have been introduced in Section 3.3.6. It is a challenging system to model with many complications including large deformations, non-linear contact, post buckling behaviour and non linear material properties. The finite element method is a numerical technique, originally developed for the analysis of structures that were too complicated or large to be analysed using classical methods (Cook *et al.*, 1989). The finite element method relies on a discretisation of the structure into small, simpler *finite elements* defined by nodal points, for which a solution can be easily obtained. Each of these finite elements is assembled into a global mesh connected at its nodes, where the individual behaviour of each element is influenced by its neighbours, thereby estimating the behaviour of the overall structure. Though FEA originated in the structural analysis field, it is a general purpose method that has been successfully used in many field approximation problems with different physics including heat transfer, fluid flow and electromagnetics among others. Structural analysis is the application of interest for this thesis.

A FEA solution consists of the solution of a large number of simultaneous equations in globally assembled matrices which solve for the active Degree of Freedom (DOF) of the elements. Loads and boundary conditions are applied to the relevant nodes and DOF to anchor or bound the solution, which in the case of a static structural analysis ensure that the assembled matrix is not singular and that a DOF solution vector is able to be calculated. In structural analyses the DOF are nodal displacements and element hydrostatic pressures in the case of mixed formulation elements. A constitutive relation is then used to estimate quantities such as stress or strain from the DOF results. Elements used to discretise and approximate a real structure could be an arbitrary arrangement of point (0D), beam or rod (1D), shell or membrane (2D) and solid (3D) elements as well as a range of specialised elements such as for detecting and handling contact interactions between separate

components. Elements are defined at nodal points, and field quantities are able to be estimated continuously within the element, therefore, approximating the full field of the overall assembly.

The process to perform a structural analysis consists of preprocessing, solving and postprocessing. Preprocessing refers to the preparation of the model including geometry preparation, meshing, load and boundary condition application and solution control settings and finally the output of an input file. The input file is then submitted to the solver and output files are generated. Postprocessing refers to the evaluation and examination of the results.

While FEA is a well known and mature technology, it is important to recognise that it is an approximation of reality, and its accuracy with respect to the real system that is being modelled must be assessed and evaluated. There are a wide variety of factors that influence the accuracy of a simulation. These relate to the mesh discretisation, correctness of boundary conditions, element behaviour, constitutive models used. Several of these are expanded briefly.

The size and quality of the mesh is critical to the solution. The process of mesh discretisation simulates a continuum with an assumed infinite number of particles and DOF (Cook *et al.*, 1989) with a finite number of DOF. As the number of DOF increases the model is better able to capture the geometry and behaviour of the system, at the cost of increased computational expense. Eventually the model response will plateau and become independent of further mesh refinement. At this point the mesh is said to be converged. Mesh shape is also important to the quality and stability of a solution. Element's performance degrades as their shapes depart from ideal primitives, for example by being stretched, skewed, warped or tapered. A common measurement of element quality for quadrilateral or hexahedral elements is the Jacobian Ratio, which reflects the distortion from parametric space of a perfect element to the element's actual configuration. Negative values indicate that the element has collapsed or inverted and will cause an error in solution.

Throughout its development FEA has placed extensive demands on computing resources, continually challenging the method with larger and more complicated problems as developments in software and hardware allowed. During this time, use of the method has expanded from its traditional origins in structural analysis across the entire spectrum of machine and civil design and mechanical analysis. As the sophistication of computational tools increased and the lines between biomedical research and traditional engineering roles blurred, interest arose in using computational methods such as FEA on biomedical problems. The method was initially adopted in orthopaedics where many of the same modelling assumptions are valid as for standard engineering analyses. Over recent years the biomechanical use of

structural FEA has proliferated to include the more challenging numerical problems of soft tissues mechanics with complex non linear constitutive models in the large deformation domain and the non-linear contact interactions with medical devices.

The use of FEA for biomechanical modelling presents exciting challenges in all aspects of the simulation workflow. Geometry is often complex, seldom generic, difficult to measure and obtain. Generation of an efficient, high quality mesh is also a challenge as many of the complex shapes encountered in the living world are difficult to fit mapped meshes to, often meaning that the pragmatic use of the overly stiff and undesired lower order tetrahedral element may be required (Beldie *et al.*, 2010). This is in addition to the complex resource heavy non-linear constitutive models that are often required to capture the physiological response.

Considering these issues related to the use of FEA in biomechanics the state of facial modelling will be briefly reviewed.

7.2 Medical Imaging and Finite Element Analysis

One of the major tasks in the preprocessing for any FEA simulation is the geometry preparation and meshing. In industrial applications it is common practice for three dimensional Computer Aided Design (CAD) geometry to be directly imported into the preprocessor for geometry editing if necessary and mesh generation. Anatomically based biomechanics models provide challenges in capturing both the complex exterior geomtry and the underlying mechanical structure of both the soft and hard tissues. Techniques such as laser scanning are very effective at capturing the exterior geometry of an anatomically based model, however they are unable to provide any information regarding the structure and arrangement of the underlying tissues. Medical imaging techniques such as Computed Tomography (CT) and MRI scanning are able to provide information regarding the underlying tissues. This data is in the form of a volumetric array populated with scalar valued voxels (volumetric pixels). Several steps are required to define the geometry for subsequent FEA simulation. These steps include segmentation, surface generation, and refinement.

Segmentation refers to allocation of the voxels to different material or volume groups. This can be achieved through manual and semi automatic methods. A volume may be segmented into many regions which sum to form the entire volume. The segmented data is often smoothed prior to further processing. Surfaces forming the boundaries of the segmented volumes are then created, often using a variant of the Marching Cubes algorithm (Lorensen and Cline, 1987; Young *et al.*, 2008).

The Marching Cubes algorithm fits a triangulated surface to the boundaries of the segmented volume. This is done by considering the connectivity of a cube and assigning low or high values to vertices depending on whether they are inside the surface or outside the surface. The surface passes through a voxel if at least one vertex is outside the surface and at least one vertex is inside the surface. A lookup table is then used to define the faceted connection topology. Due to symmetries, there are only 14 different topology configurations (Lorensen and Cline, 1987). These configurations are used to define a surface which may be of arbitrary shape and consist of non-manifold geometry such as T-intersections between different material groups. The resulting surface often contains a number of facets with a high aspect ratio, or small dihedral angles at sharp boundaries. These geometric irregularities, though of little concern for visualisation and measurement of volumes are critical for generation of meshes suitable for FEA. A smoothing process such as a Gaussian filter, Laplacian smoothing or Lloyd (Voronoi) relaxation can be used to create a triangular surface mesh with high quality regular shaped facets which is suitable to seed a volumetric FEA mesh for downstream analyses.

Over the last decade the use of MRI in conjunction with FEA has proliferated in many fields of biomechanics. A strength of MRI scanning is the high contrast displayed between different soft tissues, thus providing complex anatomically realistic surface geometry, accurate subdermal tissue distributions and the possibility of capturing the full domain behaviour *in vivo* during an experiment for model validation. Some biomechanical applications that have used MRI in conjunction with FEA include clinical knee mechanics (Peña *et al.*, 2005; Pena *et al.*, 2006; Tang *et al.*, 2011), breast deformation (del Palomar *et al.*, 2008; Samani *et al.*, 2001; Tanner *et al.*, 2006), cardiac mechanics (Augenstein *et al.*, 2005), pressure ulcer investigation (Ceelen *et al.*, 2008; Linder-Ganz *et al.*, 2007; Makhsous *et al.*, 2007) and the early stages of facial modelling which is outlined in Section 7.3.

The use of combined techniques such as MRI and FEA for patient specific simulation are in particularly relevant the recent recommendations for directions in pressure ulcer research where Bouten *et al.* (2003) encouraged a heirarchical approach over a range of length scales from the whole body down to the histological level. MRI coupled with FEA is able to simulate and investigate the state of load and deformation through the discrete subdermal tissues. These benefits are relevant to this project simulating the face under contact loading from the CPAP mask.

7.3 Facial Modelling

Despite the increasing use of FEA in biomechanics for several decades, only a handful of papers relating to the use of the method on the face were found in a broad keyword literature search prior to 1990 [1]. Early interest in facial modelling began in the animation industry with efforts to mimic facial expressions at the skin. Emphasis was placed on fast solution times and not on realistic discretisation of the underlying anatomy (Lee *et al.*, 1995). Keeve *et al.* (1998) proposed a similar fast solving facial model where a faceted skin surface was solved by a network of spring-mass-damper systems. This was used in a clinical setting to predict facial cosmetics after corrective surgery. Though this model had the great advantage of solving very quickly, which makes it very attractive in a clinical setting, it was also compared against a finite element model, which was found to be more precise, though at the expense of model preparation and run time.

The principal application for facial FEA modelling has been for orthognathic and facial reconstruction surgery, with particular emphasis on the cosmetic outcomes of surgery due to soft tissue displacement. Holberg *et al.* (2005) reported that even a simple 3D FEA model was superior in predicting the surgical outcomes when compared to a commercially available 2D surgical planning tool (Dentofacial Planner Plus). The model that was used in this study was greatly simplified, with non anatomical thickness and homogeneous soft tissues. More complex models with this purpose in mind have been developed by various groups around the world. Gladilin *et al.* (2004); Gladilin and Ivanov (2009) developed a tetrahedral facial models taking into account the layered soft tissue structure of the face consisting of the skin, muscle, fat [2] and bone and utilising large deformation theory and non linear material properties.

The research group of Chabanas *et al.* (2003) have developed an interesting series of models for the simulation of soft tissues in maxillofacial reconstructive surgery and to mimic facial expression. These models have been developed with the deployment over a range of subjects in mind *a priori*. A high quality, yet coarse predominantly hexahedral mesh was developed incorporating the dermal and hypodermal layers. Elements following the path of some of the primary muscles of facial expression were allocated to a muscle material property and the soft tissue was assumed to be rigidly fixed to the skull. Since the clinical application of surgical modelling is a patient specific process, this group has focussed on a mesh morphing or registration method which allows a generic mesh to be morphed onto patient specific geometry (Couteau

[1] Medline keyword search using ((FEA OR "finite element analysis") AND (face OR facial))
[2] fat material not included in (Gladilin *et al.*, 2004)

et al., 2000; Chabanas and Payan, 2000; Bucki *et al.*, 2010), greatly reducing the model development effort for the second and subsequent patients.

Mazza *et al.* (2007) have used a simple facial model to investigate the viscoplastic behaviour of skin as the body ages. This has been demonstrated through gravitational loading of the soft tissues and the evolution of strains and deformations in the facial tissue. Recently Barbarino *et al.* (2009) have developed a more advanced model of the lower portion of the face. Significant efforts were taken to consider the underlying anatomical structure of the lower face, taking into account a number of the muscles of facial expression and ensuring anatomically correct boundaries between the soft tissue and the underlying bone. Additionally the material constitutive models implemented in this model are capable of exhibiting some of the complex mechanical behaviours encountered in biological materials. This model was validated by comparing FEA results to facial holography measurements of a commensurate deformation state.

Beldie *et al.* (2010) has recently developed a half face model inferior to the sellion, assuming symmetry in the sagittal plane. This model has been developed to mimic facial expressions and simulate maxillofacial surgery. Notable features of this model include and anatomically correct skull as a support for the face and anatomic modelling of the muscles of facial expression and mastication. A custom constitutive model was also used for the muscles in the manner of Hill (1938) containing a contractile element, which allows the muscles to be activated to form facial expressions such as a smile. The complex geometry of the model necessitated the use of tetrahedral elements despite their well known stiff response. Over 2 million elements were used in the half model, creating a very large model.

The use of FEA in facial biomechanical analyses is a small, concentrated, but growing field. Models have been almost exclusively developed for use in the prediction of cosmetic outcomes for reconstructive or remedial maxillofacial surgery. Modelling has gradually increased in complexity particularly in the last decade, incorporating complex anatomically correct structures for both the skull and selected soft tissues. These complex models place high demands on available computing resources, and many major modelling assumptions are made depending on the purpose of the model.

Though sharing obvious similarities to the facial model that is required in this project, none of these models reviewed would be suitable for use. All of the models reviewed were constructed with the purpose of modelling an anterior movement of the skull and soft tissue, with the contact between the skull and soft tissues not considered, excepting the model of Beldie *et al.* (2010). The more advanced models

of Beldie *et al.* (2010); Barbarino *et al.* (2009) were truncated at the level of the eyes.

This thesis is concerned with the mechanical nature of the application of a CPAP mask being held onto the face. This has contact regions around the nose and on the forehead. These will compress the soft tissue onto the underlying skull and possibly allow sliding across the skull surface. To simulate realistically the CPAP mask on the face, the simplifications used in the models reviewed can not be made for this application. Therefore, it is necessary for the model of superficial tissues to extend to cover the full face height, and use the skull to provide underlying contact support. These tasks will be addressed in Section 10 where the model development is documented.

Part III

Magnetic Resonance Imaging of Continuous Positive Airway Pressure Therapy

Chapter 8

Magnetic Resonance Imaging of Continuous Positive Airway Pressure Therapy

8.1 Introduction

CPAP therapy has been shown to be a simple and effective treatment for OSAHS and other chronic conditions (Sullivan *et al.*, 1981; Marin *et al.*, 2005), however compliance to therapy is sub-optimal (Richard *et al.*, 2007). It is of clinical importance to increase the compliance to the therapy to ensure that the patient receives the full benefit of the treatment. Adverse events that have been reported from the use of CPAP include pain, discomfort, skin abrasions and degradation, erythema, irritated eyes from leaking air and a sore throat. A number of these are related to the fit of the mask and the transfer of loads between the mask and the face. Therefore, an understanding of the mechanics at the mask contact interface is required to create a conforming and comfortable system to improve clinical outcomes of the patient

8.2 Overview

To this end an experiment was devised with the aim of acquiring 3D geometric data from a range of subjects from the population by performing MRI scans in both a reference state and while wearing a pressurised nasal CPAP mask. These data will be used to generate and calibrate a finite element model of the face incorporating variable tissue thickness and layered material properties.

	BMI<25	BMI≥ 25
Age<50	n_{11}	n_{12}
Age≥ 50	n_{21}	n_{22}

Table 8.1: Age/BMI classification of participants

8.3 Experimental Design

Epidemiological studies have indicated that sleep apnoea and hence use of CPAP therapy increases in prevalence with age and obesity (Kirkness *et al.*, 2008; Smith *et al.*, 1985; Young *et al.*, 2002). Therefore, age and BMI were chosen as predictor variables in the experimental design space. These participant specific variables are easy to handle quantities that were able to be estimated at the recruitment stage to screen subjects to ensure that the participants were not disproportionately clustered in the experimental design space. The screening and spread of participants was aided by allocating them into high and low groups according to their age and BMI as shown in table 8.1.

8.4 Ethics

This study was granted approval by the Human Research Ethics Committee of the University of New South Wales (Approval No: HREC 07097), the Scientific Board at Prince of Wales Medical Research Institute and the Human Research Ethics Committee Executive at St Vincent's Hospital.

All participants were briefed about the study and given a participant information statement describing the study as well as a safety questionnaire issued by the medical imaging centre. All publishable information was anonymised. According to our ethics statement, all MRI scans were examined by a radiologist to check for any unexpected pathology. In the event that the MRI scans revealed an abnormality, a procedure was defined to notify the participant via their primary health care provider.

All clinical equipment that was be used in this experiment was approved for clinical use by the Therapeutic Goods Administration (TGA) and Food and Drug Administration (FDA).

Inclusion	Exclusion
age > 18 yrs	age < 18 yrs
Male	Female
Caucasian	Non Caucasian
Willing to give consent	Unwilling to give consent
Fluent in English	Not fluent in English
In general good health	In general poor health
	Presence of facial hair (prevents seal on mask)
	Claustrophobia
	Discomfort or distress with CPAP therapy
	Presence of contra-indications for MRI scan as screened by MRI safety questionnaire
	Presence of chronic medical conditions

Table 8.2: Inclusion and exclusion criteria for CPAP MRI study

8.5 Participants

Participants in this study are subject to the inclusion and exclusion criteria outlined in Table 8.2. Informed consent was provided by all participants. Participants were screened to ensure a broad range of the variables of age and BMI were included.

8.6 Procedure

8.6.1 Preliminary

A researcher contacted the participants and arranged a time to meet them at the MRI facility (POWMRI or St Vincent's Hospital) prior to MRI scanning. During this time the participant's height and mass were measured and personal details taken. For participants unfamiliar with the sensation of CPAP, an acclimatisation period was provided. The CPAP equipment used for the preliminary fitting and during the scanning experiment are listed in Table 8.3

8.6.2 Mask Fitting

All participants were fitted with identical commercially available nasal CPAP masks (ResMed UMII, Standard) as shown in figure 8.1a. In order to accurately simulate this experiment, it was important to measure the headgear tension to obtain a reasonable estimate of the force applied to the mask to positively locate it on the face. The mask was fitted to the face with headgear disengaged, connected to the

Table 8.3: Equipment list for CPAP MRI experiments consisting of the CPAP system, personal equipment supplied to each participant, mask fitting tools, preliminary anthropometric measurement items and pressure recording equipment

Item	Qty	Description
CPAP System		
Flow generator	1	ResMed CS2 flow generator. This is a powerful flow generator which is capable of supplying a pressure of 20 cm H_2O at a distance. This includes power cables.
Pressure tubing		Feedback signal to prevent mask leak alarm and pressure tapping.
Personal Equipment		
Adapter	1	19mm pressure tube port
CPAP Filter	1	Anti-bacterial CPAP filter to be placed at the inlet of the CPAP tubing. A new filter was supplied to each participant and discarded at the end of the experiment.
Tubing	10m	ϕ22mm tubing was used for each participant (2 off 2m, 2 off 3m). Tubing was washed, disinfected and dried prior to use.
Connectors	3	22mm connectors were required to assemble the 10m tubing length
Mask	1	ResMed UMII (standard size) nasal mask. Some participants in addition were scanned with the Activa LT nasal mask. Headgear has holes punched to allow for hooks from spreader bar
Mask Fitting		
Spreader bars	2	spreader bars with cables, hooks and suspended containers for calibrated weights.
Calibrated Masses		Calibrated mass set 5-200gm mass range.
Preliminary		
Tape measure	1	Used to measure height
Scales	1	Tanita scales to measure mass and estimate total body fat % by bio-impedance.
Pressure Recording		
ResMed Flow computer	1	In-house test instrument designed to measure flow rate and gauge pressure
Pressure tube	1	
Laptop computer	1	Data logging software is a Labview virtual instrument
USB/serial adapter	1	Flow computers are designed to communicate on the serial port, however the laptop used did not have a serial port.
Serial Cable	1	

flow generator (ResMed CS2) and brought up to operational pressure (10cm H_2O). The participant was then required to lie down on a bed with their head resting on a support to allow access to the headgear. A spreader bar was then suspended from each of the top and bottom headgear straps to enable the headgear to be tensioned by adding known masses to the bar. The mass was set by hand signals from the participant to indicate a level of comfort and mask sealing ability.

Due to the strong magnetic field, spatial field gradient and RF pulses in the Magnetic Resonance (MR) environment, readily available load cells were inappropriate for use due to safety and compatibility concerns, and did not comply with or had not been tested to the requirements of ASTM (ASTM, 2006a,b) to be MR *safe* or MR *conditional*. Furthermore traditional load cells have the capacity to interfere with the MR image acquisition process and induce undesirable artefacts in the output (Gassert *et al.*, 2008; Chapuis *et al.*, 2004). Alternative materials (Hidler *et al.*, 2005) or means of transducing or shielding sensors would therefore, be required to utilise force acquisition in the MR environment (Gassert *et al.*, 2008; Chapuis *et al.*, 2004; Tada *et al.*, 2002). Therefore, it was decided to measure the headgear tension at the time of fitting by applying calibrated masses to the headgear through a spreader bar.

The headgear was tensioned by gravitational loading. The spreader bars were designed so that the angle of the suspension cables were parallel to the headgear strap wrapping around the head. This ensured that the Velcro hooks of the strap were adjacent to the strap but not engaged. Refer to Figure 8.6 for a drawing of the spreader bars. Gravitational loading was applied to the spreader bars by the application of calibrated weights on the upper and lower bar simultaneously until indicated by the participant that a suitable seal and fit was achieved. The mass applied to each spreader bar was recorded on participant specific log sheets. Ideally this load was distributed evenly from left to right, however to account for asymmetric application of the headgear, digital photographs were taken from the superior aspect relative to the participant with a digital SLR camera. The 'ImageJ' image processing software was then used to extract the tension vectors in the transverse plane, assuming that any out of plane rotation is small ($cos\theta \approx 1$). This process is illustrated in figure 8.1b. After taking photographs, the Velcro was carefully engaged by the application of light normal pressure on the strap, the spreader bars were then carefully removed and the participant was instructed not to adjust the mask any further until the completion of the scan.

(a) ResMed Ultra Mirage II Nasal CPAP mask

(b) Gravitational headgear tensioning. A) Spreader bar, B) Calibrated masses and suspension containers, C) Head support, D) Tension only cables loading headgear, E) CPAP mask

Figure 8.1: ResMed UMII nasal CPAP mask and mask tensioning

8.6.3 Pressure Measurement

Simultaneous to the mask fitting, a recording of the internal mask gauge pressure relative to atmospheric pressure was made using the exact setup that would be used during the CPAP scan. The participant was undergoing CPAP therapy at a nominal pressure of 10cm H_2O. The pressure trace, sampled at 50 Hz, was recorded directly to a laptop computer via a LabView virtual instrument application interfacing with a ResMed Flow Computer through the serial port mounted on a USB2 adapter. The pressure tubing was connected to the pressure port incorporated into the mask frame.

The pressure trace provides the actual experienced pressure throughout the respiration cycle for the participant. The pressure recording is performed prior to scanning due to similar MR safety and compatibility reasons that applied to the headgear force measurement. For each measurement, the pressure tubing was disconnected for several seconds to provide a zero level to correct for sensor drift. The pressure

trace was used to check that the nominal pressure of 10cm H_2O was delivered to the participant for downstream analysis.

8.6.4 Magnetic Resonance Imaging Scans

All participants underwent a series of T1 anatomical MRI scans consisting of a reference scan and a CPAP scan using a Philips 3T Achieva MRI system. A consistent isometric voxel size (1mm × 1mm × 1mm) was used for all scans. Prior to the initial scan the participant's safety questionnaire was reviewed by the radiographer who then conducted a verbal interview and checked that metallic objects were removed in accordance with published safety guidelines (Kanal *et al.*, 2002; Shellock and Crues, 2004; Shellock and Spinazzi, 2008).

Scan Order

In all cases the CPAP MRI scan was performed first, this was followed by a relaxation period of at least 30 minutes to allow for the soft tissues to relax and return to their reference state prior to the reference scan being taken. This protocol was chosen through consideration of both convenience to the participant and optimal time efficiency when using the scanner. If a participant is unfamiliar to CPAP therapy it is important that they take some time prior to the scan to acclimatise to the sensation of breathing against positive airway pressure. If this were done before the reference scan, additional relaxation time would be required prior to the reference scan, and the mask would need to be fitted twice. Performing the CPAP scan first allows for the mask to be fitted once. The relaxation time can then be utilised to perform scans on other participants to avoid machine downtime. This also allows for an additional mask to be tested later in the scanning session without having to repeat the relaxation time. The optimum experimental procedure for three participants in a session is shown in figure 8.2, this highlights the scanner utilisation.

Reference MRI Scan

To perform the reference scan the participant was required to lie on the MRI gantry bed in a neutral supine position with the head oriented to look directly forward. SENSE Flex L coils were then carefully placed adjacent to the head and held loosely with a Velcro coated foam strap. An angled foam cushion was provided for the legs to allow the participant to lie in a comfortable position. The participant was provided with an alarm button and was able to communicate with the radiographer at all times.

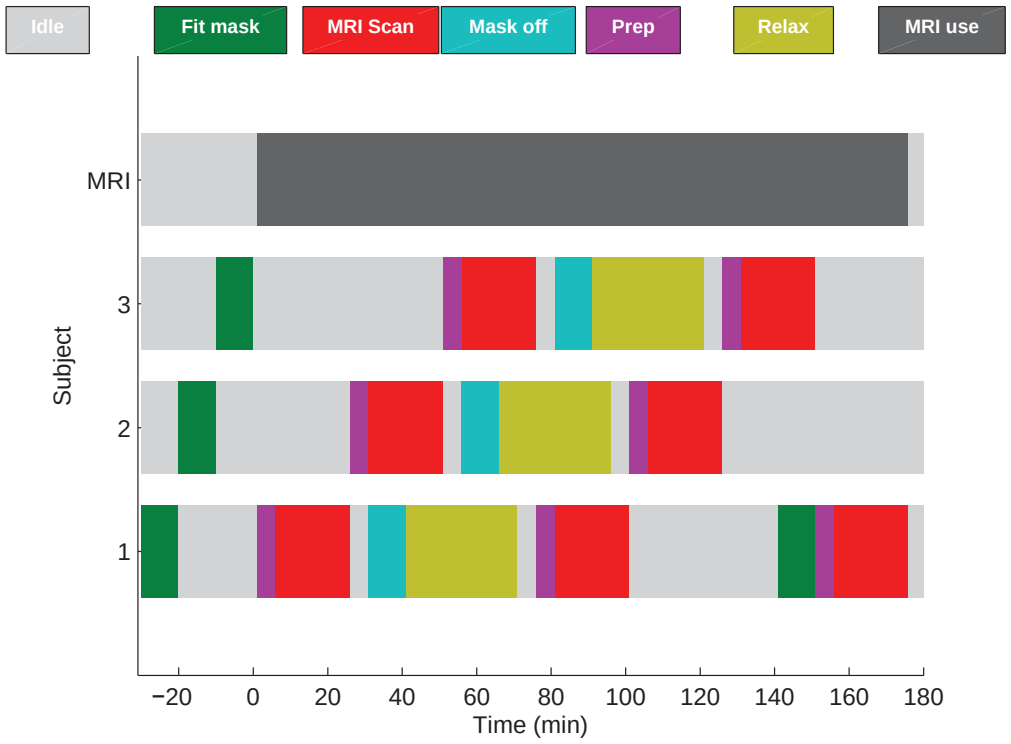

Figure 8.2: CPAP MRI utilisation and task timeline for three participants

The scan volume was set to cover the anterior portion of the head from approximately the top of the frontal bone down to the mandible at approximately the level of the menton. Anteriorly the volume was chosen to include the pronasale and to extend posteriorly to the occipital bone. Laterally the scan was defined to include the extents of the head. This resulted in a scan volume of approximately (varied from subject to subject) $180 \times 240 \times 240 \approx 10\,(10^6)$ voxels. Data was stored in 16 bit Digital Imaging and Communications in Medicine (DICOM) format (DICOM Standards Committee, 2007). Scan duration was approximately 15 minutes.

CPAP MRI Scan

The CPAP MRI scan was performed after the participant was fitted with the mask as described in section 8.6.3 without any further adjustment to the mask. To perform the CPAP scan the participant was required to lie on the MRI gantry bed in a neutral supine position with the head oriented to look directly forward. SENSE Flex L coils were then carefully placed adjacent to the head and held loosely with a Velcro coated foam strap. The flow generator was mounted outside the Faraday cage in the control room. The CPAP tubing (ϕ22mm)was passed through a plumbing hole in the wall. This was then arranged to run axially down the centre of the participant's body. CPAP pressure 10 cm H_2O was applied and participant comfort checked prior to

moving the gantry into the scanner bore. n. The participant was provided with an alarm button and was able to communicate with the radiographer at all times. The scan bounds were defined to be similar to the reference scan. Scan duration was approximately 15 minutes.

8.6.5 Mask Removal

After the completion of the CPAP MRI scan the participant was escorted to the preparation room, where a series of digital photographs were taken of the participant prior to removing the mask. The photographs were from the anterior, left and right aspect. The mask was then removed, the precise time of the removal was logged, and the series of photographs was repeated. The participant was then required to wait for 30 minutes tissue relaxation time prior to the commencement of the reference scan.

8.6.6 Reference Scan Processing

The DICOM scan volume was stored as 16 bit integers. Initially the volume was filtered using a 3D implementation of the non-linear anisotropic diffusion filter (Perona and Malik, 1990; Gerig *et al.*, 1992) in Matlab. This was chosen as it is an edge preserving filter, smoothing within regions and enhancing edge boundaries. The anisotropic diffusion filter is formulated according to Perona and Malik (1990); Gerig *et al.* (1992) as follows:

$$\frac{\partial}{\partial t} I(\boldsymbol{x}, t) = \operatorname{div}\left(c(\boldsymbol{x}, t)\, \nabla u(\boldsymbol{x}, t)\right) \tag{8.1}$$

$$c(\boldsymbol{x}, t) = \exp\left(-\left(\frac{|\nabla I(\boldsymbol{x}, t)|}{\kappa}\right)^2\right) \tag{8.2}$$

where $I(\boldsymbol{x}, t)$ is the greyscale intensity at position $\boldsymbol{x}$ and time (iteration) t. The scaling term c is adaptive tending towards zero as ∇I increases (*i.e.* an edge). The κ term tunes the filter to the edge strength and noise amplitude. Figure 8.3 shows an example of a slice from the raw and filtered volumes.

The AVIZO image processing package was used to process and manipulate the DICOM data. After importation of the filtered volume, a thresholding segmentation was performed over the whole head to label an enclosed volume. Gaussian smoothing was applied to the voxel allocation. An implementation of the marching cubes

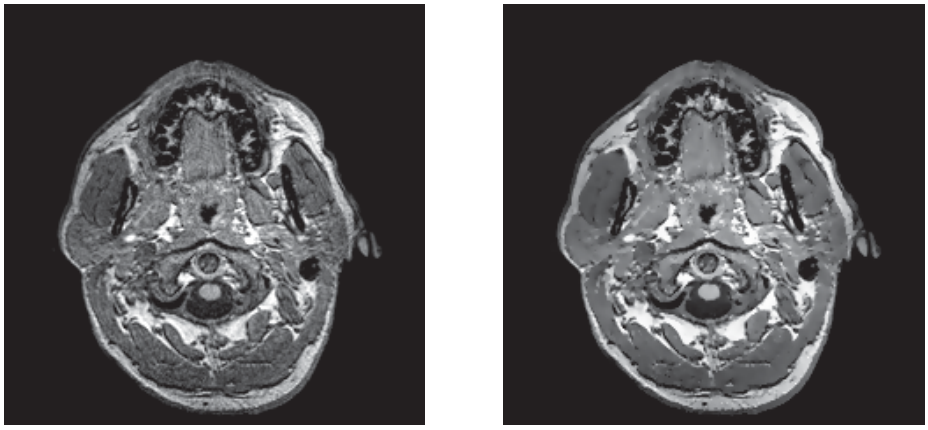

(a) As scanned with no further filtering.

(b) Filtered using the edge preserving anisotropic diffusion filter

Figure 8.3: Sample MRI transverse slice highlighting the postprocessing using the edge preserving filter

algorithm (Lorensen and Cline, 1987) was used to generate a manifold faceted surface. Laplacian smoothing was applied to the faceted surface to improve the quality of the surface facets.

Positioning and Orientation

The Frankfort Horizontal (FH) is commonly used in clinical practice to define a consistent horizontal positioning of the head. Looking straight ahead, the plane formed by the three landmarks, left porion (LP), right porion (RP) and left orbitale (LO) is oriented to be horizontal.

All participants are scanned with respect to a common, fixed coordinate system, however the positioning of participants will vary from scan to scan both between participants and between scans of the same participant. Therefore, it is important for consistency and downstream analysis to define a consistent particpant specific global coordinate system. This system was oriented in accordance with the recommendations of the International Society of Biomechanics for anatomical coordinate systems (Wu and Cavanagh, 1995). The X axis is oriented anteriorly, the Y axis superiorly, perpendicular to the FH plane, while the Z axis is given by $\boldsymbol{X} \times \boldsymbol{Y}$.

The position vector in the DICOM scan coordinate system of the patient coordinate system origin is located at the midpoint between the LP and RP as follows,

$$\boldsymbol{x}_{GCS} = \frac{\boldsymbol{x}_{LP} + \boldsymbol{x}_{RP}}{2} \tag{8.3}$$

The FH plane normal unit vector is defined by normalising the cross product between the vectors spanning the plane from the LP to the RP and LO respectively.

$$\boldsymbol{y} = (\boldsymbol{RP} - \boldsymbol{LP}) \times (\boldsymbol{LO} - \boldsymbol{LP}) \tag{8.4}$$

$$\boldsymbol{e_{2}}_{GCS} = \frac{\boldsymbol{y}}{\|\boldsymbol{y}\|} \tag{8.5}$$

The unit vector defining the $\boldsymbol{e_1}$ direction of the patient coordinate system is given by the projection of the vector from the origin to the projection of the nasion onto the FH plane. This is calculated by,

$$\boldsymbol{a} = \boldsymbol{N} - \boldsymbol{x_{GCS}} \tag{8.6}$$

$$\boldsymbol{b} = \boldsymbol{a} \cdot \boldsymbol{e_{2}}_{G}CS \tag{8.7}$$

$$\boldsymbol{e}_1 = \frac{(\boldsymbol{N} + \boldsymbol{b}) - \boldsymbol{x}_{GCS}}{\|(\boldsymbol{N} + \boldsymbol{b}) - \boldsymbol{x}_{GCS}\|} \tag{8.8}$$

$$\tag{8.9}$$

The coordinate system definition is completed by defining the $\boldsymbol{e_3}$ basis vector as

$$\boldsymbol{e}_3 = \boldsymbol{e}_1 \times \boldsymbol{e}_2 \tag{8.10}$$

.

The basis vectors were then used to define a rigid affine transformation matrix to reposition the scan volume. This is performed conveniently by decomposing the transformation to a translation followed by a rotation.

$$\boldsymbol{x} = \boldsymbol{x}\mathbf{TR} \tag{8.11}$$

A sample repositioned facial scan is shown in figure 8.4 with the patient coordinate system.

The scan volume was then resampled at the original resolution on this coordinate system.

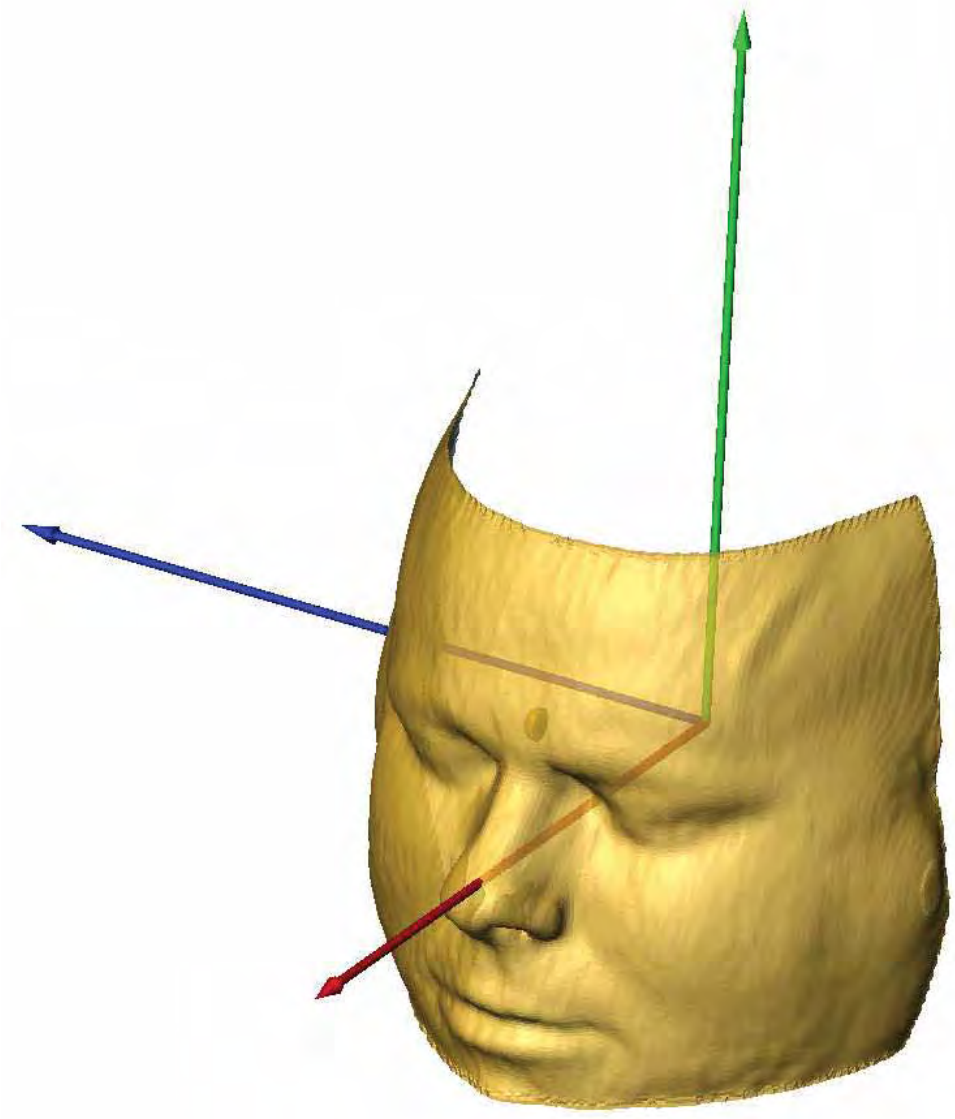

Figure 8.4: Subject specific coordinate system

Crop Model

Due to the extensive downstream processing requirements the scan volume was cropped to the region of interest. This is the anterior region of the face extending superiorly to include the forehead, posteriorly to the ramus of mandible and inferiorly to the mental region.

Segmentation

The voxels of the resampled region of interest were subsequently segmented or labelled to different materials or anatomical entities, namely skin, fat muscle and cartilage. Additionally the bones of the skull are segmented as their geometry defines the attachment of the muscles and acts as a rigid boundary for the general support of the soft tissues.

A mixture of techniques were used to segment the volume. Greyscale thresholding was used to define the entire volume. The skin material was defined by a 3D morphological erode operation of 3mm. The fat material was defined by a level set contour growing algorithm. The contour growth was initiated by seed points located the adiposus panniculus (cheek fatty deposits). The skull was a more complicated structure to reconstruct. Connected 3D (26 connectivity) voxels within a threshold range were initially assigned to the skull. Significant manual editing was required to complete the skull label or mask. This is in the form of manually labelling or painting voxels to the skull by tracing profiles or locally selecting greyscale regions using either threshold based region growing tools or level set contour development in local regions and merging the ensuing voxels with the skull material.

The small localised cartilage material was assigned by region growing methods in the nasal septum.

The remaining filler material was assumed to be muscular tissue, incorporating both the muscles of facial expression and the muscles of mastication.

The segmented volume was tidied up by the removal of any small islands, cavities and were subsequently smoothed with a Gaussian filter with a kernel size of 3 voxels.

Surface Extraction

Once the head was segmented to define the different materials, a marching cube like algorithm (Lorensen and Cline, 1987) as implemented in 'AVIZO' was used to generate a global non-manifold faceted surface with elements placed at the interfaces between the labelled materials, and also exterior to the face. The surfaces were then decimated and smoothed using a remeshing algorithm incorporating Lloyd

relaxation. Curvature proximity control was applied during the remeshing process by weighting the nodes with the scalar Gaussian curvature value at that point. This gradually refined the surface in regions of high curvature. The decimated surfaces consist of approximately 50000 triangles. The triangulated surfaces were also checked at this point to eliminate any triangle intersections and poor aspect ratio triangles. Though the surface as a whole is non-manifold with numerous T-connected edges at junctions of 3 materials (*e.g.* bone muscle and exterior), checks were performed to ensure that the portion of the surface enclosing a material volume formed a closed manifold. This allows the surface to be used easily for advancing front tetrahedral mesh generation. The nodal locations and connectivity matrix of the skin and skull surfaces were extracted from the global surface and saved separately for importation and subsequent analysis in Matlab.

8.6.7 CPAP Scan Processing

The processing of the CPAP scan was largely identical to the processing of the reference scan as outlined above in section 8.6.6. Differences in the process are described in the following paragraphs.

Registration

After importation of the DICOM volume into AVIZO, the CPAP scan was aligned or registered with the reference scan orientation. This was achieved through the registration module by maximising the correlation coefficient between the reference and CPAP scan for the overlapping region. The registration is a rigid affine transformation composed of a translation and a rotation, ensuring that there is no change in shape, only the position of the CPAP volume over the reference volume. The correlation coefficient between the two volumes is given by

$$r_{I_1,I_2} = \frac{\mathrm{cov}\left(I_1, I_2\right)}{\sigma_{I_1}\sigma_{I_2}} \tag{8.12}$$

The correlation coefficient is a function of the position of the CPAP scan over the reference scan. This is described by the 12 independent components of the rigid affine transformation matrix $\boldsymbol{T}$. Therefore, $r = r\left(T_{11}, T_{12}, T_{13}...T_{34}\right)$.

$$\boldsymbol{T} = \begin{bmatrix} T_{11} & T_{12} & T_{13} & T_{14} \\ T_{21} & T_{22} & T_{23} & T_{24} \\ T_{31} & T_{32} & T_{33} & T_{34} \\ 0 & 0 & 0 & 1 \end{bmatrix} \tag{8.13}$$

The registration transformation matrix is determined by maximising r_{I_1,I_2} with the 12 non-trivial elements of the transformation matrix $\boldsymbol{T}$ being independent variables. Since the registration optimisation was determined using gradient search methods it is sensitive to the start location. The start location was determined by treating the intensity values as mass density units, and then aligning the centres of mass of the volumes as well as the principal axes of the inertia tensor.

The CPAP scan was cropped to match the reference scan after registration has been performed. The scanned volume was also resampled onto the defined grid of the reference scan.

8.6.8 Surface Data Analysis

The reference and deformed facial surfaces were constructed from the DICOM scan data and stored as triangulated surfaces consisting of node or vertex coordinates and a connectivity matrix. Both surfaces were output after registration and position vectors are given with respect to the common global coordinate system aligned with the FH plane as described in section 8.6.6.

Since the surfaces have been overlaid by the registration process, it is possible to determine field measurements over surface domain.

Surface Definition

Each surface is defined by an array of nodal position vectors $\boldsymbol{x}$ and a connectivity matrix $\boldsymbol{E}$. The surface normal vectors can be calculated from the individual facets since each facet defines a plane. The facet normal was given by

$$\boldsymbol{n_{f}}_{f} = \frac{\boldsymbol{t_{a}}_{f} \times \boldsymbol{t_{c}}_{f}}{\left\| \boldsymbol{t_{a}}_{f} \times \boldsymbol{t_{c}}_{f} \right\|} \tag{8.14}$$

where $\boldsymbol{n_{f}}_{f}$ is the unit normal of surface facet f, and $\boldsymbol{t_{\alpha}}_{f}$ is the edge vector $\alpha = a, c$ of triangular facet f. This value is constant throughout the facet and changes discretely at facet edges creating a discontinuity. Facet nodes or vertices are of primary interest for performing calculations. Therefore, a means of estimating the surface normal

vector at the vertices was required. The arithmetic mean was calculated at each vertex,

$$\boldsymbol{n_{vi}} = \frac{\sum_{j=1}^{j=k} \boldsymbol{n_{fj}}}{\left\| \sum_{j=1}^{j=k} \boldsymbol{n_{fj}} \right\|} \tag{8.15}$$

where the nodal unit normal vector at node i, $\boldsymbol{n_{vi}}$ is calculated from the facet normals $\boldsymbol{n_{fj}}$ of the facets j attached to node i.

Surface Distance Map

Given the reference and deformed surfaces, it was now possible to calculate the displacement and distance fields from the reference surface to the deformed surface . In order to be consistent across the entire surface domain the distance field is calculated from the reference surface to the deformed surface along the reference surface normal at each vertex of the reference surface.

This surface distance field was calculated as follows. Consider two faceted surfaces S_A and S_B. The position vector of node i on S_A is $\boldsymbol{x_{Ai}}$, and the unit normal vector is $\boldsymbol{n_{vAi}}$. This can be written parametrically as a line,

$$\boldsymbol{l} = \boldsymbol{l_A} + (\boldsymbol{l_B} - \boldsymbol{l_A})\, t \tag{8.16}$$

where t is a parameter defining the position along the line. Similarly the surface facet definition using three points can define a plane parametrically,

$$\boldsymbol{P} = \boldsymbol{P_0} + (\boldsymbol{P_1} - \boldsymbol{P_0})\, u + (\boldsymbol{P_2} - \boldsymbol{P_0})\, v \tag{8.17}$$

The intersection of the plane and the line is found by equating the $\boldsymbol{l}$ and $\boldsymbol{P}$.

$$\boldsymbol{l} = \boldsymbol{P} \tag{8.18}$$

$$\boldsymbol{l_A} + (\boldsymbol{l_B} - \boldsymbol{l_A})\, t = \boldsymbol{P_0} + (\boldsymbol{P_1} - \boldsymbol{P_0})\, u + (\boldsymbol{P_2} - \boldsymbol{P_0})\, v \tag{8.19}$$

$$\boldsymbol{l_A} - \boldsymbol{P_0} = (\boldsymbol{l_A} - \boldsymbol{l_B})\, t + (\boldsymbol{P_1} - \boldsymbol{P_0})\, u + (\boldsymbol{P_2} - \boldsymbol{P_0})\, v \tag{8.20}$$

$$[\boldsymbol{l_A} - \boldsymbol{P_0}] = \begin{bmatrix} t & u & v \end{bmatrix} \begin{bmatrix} (\boldsymbol{l_A} - \boldsymbol{l_B}) \\ (\boldsymbol{P_1} - \boldsymbol{P_0}) \\ (\boldsymbol{P_2} - \boldsymbol{P_0}) \end{bmatrix} \tag{8.21}$$

Let

$$\boldsymbol{b} = [\boldsymbol{l_A} - \boldsymbol{P_0}] \tag{8.22}$$

$$\boldsymbol{p} = \begin{bmatrix} t & u & v \end{bmatrix} \tag{8.23}$$

$$\boldsymbol{A} = \begin{bmatrix} (\boldsymbol{l_A} - \boldsymbol{l_B}) \\ (\boldsymbol{P_1} - \boldsymbol{P_0}) \\ (\boldsymbol{P_2} - \boldsymbol{P_0}) \end{bmatrix} \tag{8.24}$$

Therefore, the parameters t, u, v are found as follows,

$$\boldsymbol{b} = \boldsymbol{pA} \tag{8.25}$$

$$\boldsymbol{bA}^{-1} = \boldsymbol{pAA}^{-1} \tag{8.26}$$

$$\boldsymbol{bA}^{-1} = \boldsymbol{pI} \tag{8.27}$$

$$\boldsymbol{p} = \boldsymbol{bA}^{-1} \tag{8.28}$$

.

Now any line will intersect a plane unless it is perpendicular to the surface normal. The intersection is simply found by substituting either t into equation (8.16) or u and v into (8.17). The intersection point will lie within the facet if the following conditions are met,

$$\begin{aligned} u &\geq 0 \\ v &\geq 0 \\ u + v &\leq 1 \end{aligned} \tag{8.29}$$

Considering the faceted facial surfaces, at each node i the line equation defines the surface normal. It is possible that the surface normal from S_1 can intersect 1 or more facets, or miss all facets. Therefore, it is necessary to include a search on S_2 to locate the facets that the normal vector intersects while meeting the criteria defined in equation (8.29), and then choose the facet with the minimum value for $|t|$. Since the normal vectors are of unit length,

$$d_i = t_i \tag{8.30}$$

t_i is equal to the signed perpendicular distance from S_1 to S_2. A vectorised version of this calculation was implemented in Matlab for use in this project.

8.7 Subject Data

Informed consent was obtained from $n = 25$ participants. Three participants were excluded, one prior to scanning due MRI safety issues. The other participants were excluded due to excessive artefacts in the MRI scans. The mean age of the participants was 47.8 ± 17.7 ($\mu \pm \sigma$)years with a range of 19 through to 73 years at the date of scanning . The mean BMI of participants was 26.0 ± 3.8kg/m^2 with a range of 17.7 through to 34.4 kg/m^2. The distribution of the age and BMI of the participants in the study are illustrated in Figure 8.5, and listed in Table 8.4.

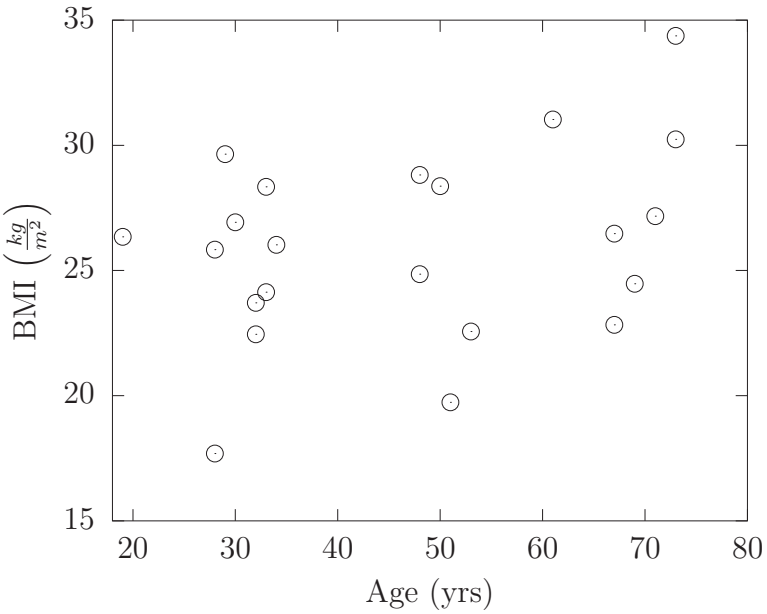

Figure 8.5: Scatter plot of BMI vs age for the included participants in the study.

8.8 Headgear Tension

The procedure used to fit the mask and estimate the headgear tension was introduced in Section 8.6.2. The upper and lower spreader bars including suspended containers to contain calibrated weights were weighed individually. Their masses are reported in Table 8.5.

The spreader bars are applied to the top and bottom headgear straps. Calibrated masses were applied to the suspended containers according to the participants comfort. The masses applied to the spreader bars for each of the participants are reported in Table 8.6. Note that for subject 2 a force gauge was used to apply the headgear tension rather than calibrated weights.

Table 8.4: Basic anthropometric data recorded from each subject prior to MRI scanning

Participant	Age yrs	Height m	Mass kg	BMI kg/m^2	Body Fat %
1	-	-	-	-	-
2	28	2.018	105.2	25.83	19.5%
3	-	-	-	-	-
4	-	-	-	-	-
5	19	1.840	89.2	26.35	19.5%
6	32	1.864	78	22.45	15.5%
7	30	1.953	102.7	26.93	26.0%
8	29	1.890	105.9	29.65	32.0%
9	50	1.792	91.1	28.37	27.5%
10	33	1.775	89.3	28.34	31.0%
11	33	1.738	72.9	24.13	18.5%
12	28	1.914	64.8	17.69	6.5%
13	61	1.850	106.2	31.03	26.0%
14	73	1.620	90.2	34.37	22.4%
15	53	1.795	72.7	22.56	8.1%
16	48	1.830	96.5	28.82	16.4%
17	67	1.775	83.4	26.47	21.2%
18	69	1.775	77.1	24.47	22.5%
19	73	1.824	100.6	30.24	30.5%
20	71	1.825	90.5	27.17	22.3%
21	67	1.833	76.7	22.83	9.7%
22	51	1.774	62.1	19.73	6.0%
23	34	1.684	73.8	26.02	12.0%
24	32	1.830	79.4	23.71	15.4%
25	48	1.793	79.9	24.85	20.7%

Table 8.5: Spreader bar mass

Spreader Bar	Weight (N)
1	0.883
2	0.888

A cable only able to resist tension was used to connect the spreader bar to the headgear straps. Using the known applied mass and the vectors measured from the superior aspect digital photographs, the forces required to satisfy static equilibrium,

$$\Sigma \boldsymbol{F} = \boldsymbol{0} \tag{8.31}$$

$$\Sigma \boldsymbol{M} = \boldsymbol{0} \tag{8.32}$$

were evaluated according to the free body diagram in Figure 8.6. To allow for the participants to have their head turned slightly to the side, θ_A is not assumed

Table 8.6: Headgear tension applied mass

Subject	m_{top} (gm)	m_{btm} (gm)
1	-	-
2	0	0
3	-	-
4	-	-
5	200	200
6	400	400
7	150	150
8	250	200
9	200	200
10	170	120
11	90	250
12	150	340
13	190	450
14	150	170
15	100	70
16	150	190
17	150	250
18	100	100
19	100	100
20	180	170
21	100	150
22	130	220
23	40	50
24	40	55
25	70	70

to equal θ_B. Moments were summed about central point of action of the applied masses to give,

$$\Sigma \boldsymbol{F} = \boldsymbol{F}_0 + \boldsymbol{F}_1 + \boldsymbol{F}_2 = 0 \tag{8.33}$$

$$\Sigma F_x = F_0 + F_1 cos\,(\theta_A) + F_2 cos\,(\theta_B) = 0 \tag{8.34}$$

$$\Sigma F_y = F_0 + F_1 sin\,(\theta_A) + F_2 sin\,(\theta_B) = 0 \tag{8.35}$$

$$F_{0Y} = mg + F_{bar} \tag{8.36}$$

$$\Sigma \boldsymbol{M} = (\boldsymbol{r}_1 \times \boldsymbol{F}_1) + (\boldsymbol{r}_2 \times \boldsymbol{F}_2) = 0 \tag{8.37}$$

$$\tag{8.38}$$

These equations were solved to determine the tensile load in the left and right cables. In the case that the subject had their head turned so that the load scenario is not symmetric, the applied headgear tension was taken to be the mean of the

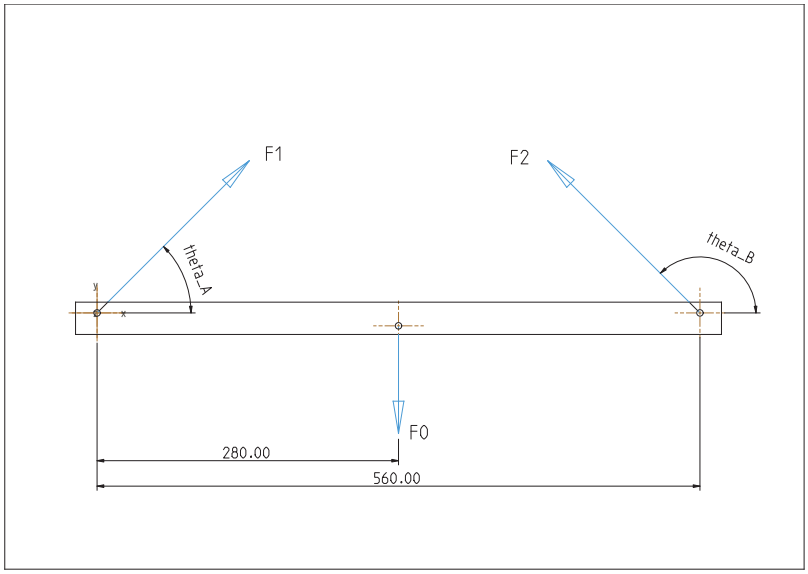

Figure 8.6: Spreader bar free body diagram

left and right values. The headgear acts like a membrane and is only able to resist loads in tension and does not support a bending moment. Therefore, only forces are transmitted from the headgear to the frame. As the headgear is threaded around the attachment locations, the applied load on the frame is determined by vectorial addition of the forces through the strands in the same manner as a rope around a pulley, as shown in Figure 8.1b. Friction was neglected in this estimation. Since the tension is assumed to act symmetrically the forces in the Z direction cancel. Therefore, the load in the sagittal plane applied from the headgear to the mask at each connection location is given by

$$F_{xy} = 2F\sin(\theta) \tag{8.39}$$

Within the sagittal plane the forces are resolved into the X and Y components by measuring the headgear line of action with respect to the FH plane from profile digital photographs of the participants, such as Figure 8.7. Therefore, the resultant applied force at each of the mask attachments is given by;

$$\begin{aligned}
\alpha_{top} &= \alpha_{FH} - \alpha_{HGtop} \\
\alpha_{btm} &= \alpha_{FH} - \alpha_{HGbtm} \\
\boldsymbol{F}_{top} &= F\begin{bmatrix} \cos(\alpha_{top}) & \sin(\alpha_{top}) & 0 \end{bmatrix} \\
\boldsymbol{F}_{btm} &= F\begin{bmatrix} \cos(\alpha_{btm}) & \sin(\alpha_{btm}) & 0 \end{bmatrix}
\end{aligned}$$

Figure 8.7: CPAP MRI participant showing the FH plane and the vectors of the headgear force resolved in the sagittal plane.

The mask headgear forces as estimated from the applied masses and digital photographs are outlined in Table 8.7. Over the sample population, the headgear force in the $\boldsymbol{x}$ direction is:

$$F_{XTop} = 2.27 \pm 0.81\text{N} \tag{8.40}$$

$$F_{XBtm} = 2.72 \pm 1.04\text{N} \tag{8.41}$$

8.9 Mask Configuration

The UMII nasal CPAP mask is designed to have an adjustable forehead support. The T-bar piece of the assembly has a cylindrical bearing surface, allowing the FHS to rotate about its axis, mounted on the frame. A profiled cantilevered spring is

Table 8.7: UMII Mask fitting summary data

Subject	FHS Pos'n	Tension (N)		F_{xy} (N)		Angle		Top Fmask (N)			Bottom Fmask (N)		
		Top	Btm	Top	Btm	Top	Btm	F_x	F_y	F_z	F_x	F_y	F_z
1	-	-	-	-	-	-	-	-	-	-	-	-	-
2		0.59	2.02	1.00	3.40	180	180	-1.0	0.0	0	-3.401	-	0
3	-	-	-	-	-	-	-	-	-	-	-	-	-
4	-	-	-	-	-	-	-	-	-	-	-	-	-
5		1.69	1.69	2.85	2.84	180	180	-2.849	0.0	0	-2.845	-	0
6	2	2.81	2.77	4.81	4.80	176.4	178.5	-4.763	-0.669	0	-4.731	-0.843	0
7	1	1.41	1.40	2.36	2.35	182.3	191.2	-2.354	-0.146	0	-2.296	-0.507	0
8	1	1.99	1.68	3.34	2.84	184.3	191.4	-3.336	-0.154	0	-2.804	-0.479	0
9	1	1.82	2.13	2.84	2.86	187.4	191.6	-2.842	-0.084	0	-2.846	-0.294	0
10	1	1.50	1.22	2.55	2.06	186.1	194.8	-2.516	-0.414	0	-1.963	-0.640	0
11	1	1.05	1.96	1.77	3.33	192.2	199.3	-1.757	-0.219	0	-3.234	-0.815	0
12	3	1.38	2.42	2.35	4.22	190.8	193.0	-2.335	-0.279	0	-4.167	-0.664	0
13	1	1.64	3.24	2.75	5.30	181.1	186.2	-2.749	-0.108	0	-5.256	-0.678	0
14	1	1.40	1.57	2.35	2.55	176.2	186.1	-2.350	0.080	0	-2.528	-0.354	0
15	2	1.12	0.95	1.86	1.57	186.6	193.2	-1.864	-0.018	0	-1.562	-0.197	0
16	3	1.41	1.65	2.35	2.75	188.8	192.3	-2.351	0.105	0	-2.751	-0.043	0
17	1	1.39	1.96	2.35	3.33	178.8	190.5	-2.354	0.040	0	-3.277	-0.617	0
18	1	1.11	1.11	1.86	1.87	189.2	196.1	-1.863	0.039	0	-1.859	-0.187	0
19	1	1.11	1.13	1.86	1.87	196.8	201.6	-1.863	-0.026	0	-1.859	-0.182	0
20	1	1.57	1.54	2.64	2.56	178.7	186.8	-2.637	0.208	0	-2.550	-0.158	0
21	1	1.11	1.40	1.86	2.36	182.6	190.5	-1.860	0.097	0	-2.351	-0.202	0
22	2	1.27	1.81	2.16	3.05	178.6	186.7	-2.146	0.212	0	-3.045	-0.130	0
23	3	0.76	0.82	1.28	1.38	191.7	196.9	-1.274	0.062	0	-1.377	-0.059	0
24	2	0.78	0.84	1.27	1.43	203.1	201.2	-1.269	-0.120	0	-1.424	-0.087	0
25	1	0.94	0.93	1.57	1.57	193.1	196.4	-1.565	-0.122	0	-1.560	-0.212	0

used to engage with four detent positions each at an increment of 13 deg within the adjustable arc range. Position 1 is when the articulation between the frame and the FHS is fully extended, whereas position 4 denotes the greatest flexion in the assembly. This has the effect of rotating the upper portion of the mask away from the face and changing the angle of contact in the nasal region. For more details refer to Section 3.3.6. The FHS position of the mask for each of the participants was determined from the digital photographs. This is reported in Table 8.7.

Prior to fitting, the participants were advised and shown the adjusting mechanism of the mask. The distribution of mask configurations chosen by the participants is shown in Figure 8.8. It was interesting to note that 59% (13) participants did not adjust the FHS from configuration 1, despite beimg demonstrated this feature, hence solely relying on the headgear tension adjustment to fit and seal their mask. This raises the question of how effectively patients are fitting the mask and exploring the range of fit to find a personally optimum configuration.

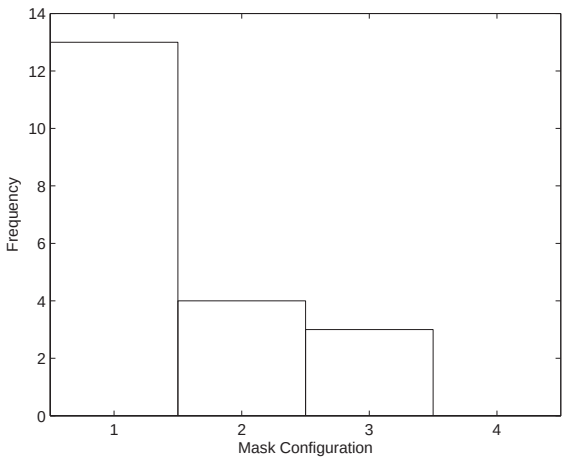

Figure 8.8: Frequency distribution of mask FHS configurations

Table 8.8: Summary statistics for basic anthropometric measurements (mm)

Variable	N	N*	μ	SE Mean	σ	Min	Q1	Median	Q3	Max
Nasal Width	22	3	37.0	0.7	3.5	31.6	34.4	36.1	40.3	44.3
Nasal Root Width	22	3	17.8	0.4	2.1	15.3	16.0	16.8	20.1	21.4
Nasal Height	22	3	53.8	0.8	3.8	47.2	51.2	54.1	55.7	63.2
Naso-labial Height	22	3	15.1	0.5	2.3	11.4	13.9	14.7	16.3	20.3

8.10 Results

8.10.1 Anthropometry

CPAP masks are designed and manufactured to fit a large range of people, so anthropometric variation must be taken into account. A number of anthropometric dimensions are considered in the design of a mask to address issues of fit, comfort, system performance and consumer sentiment such as obstructing vision. Of these, there are several key measurements that relate directly to the shape of the nasal region and are important to the design of nasal masks, these include nose width, nasal root width, nose height and naso-labial height. These dimensions are shown in Figure 8.10.

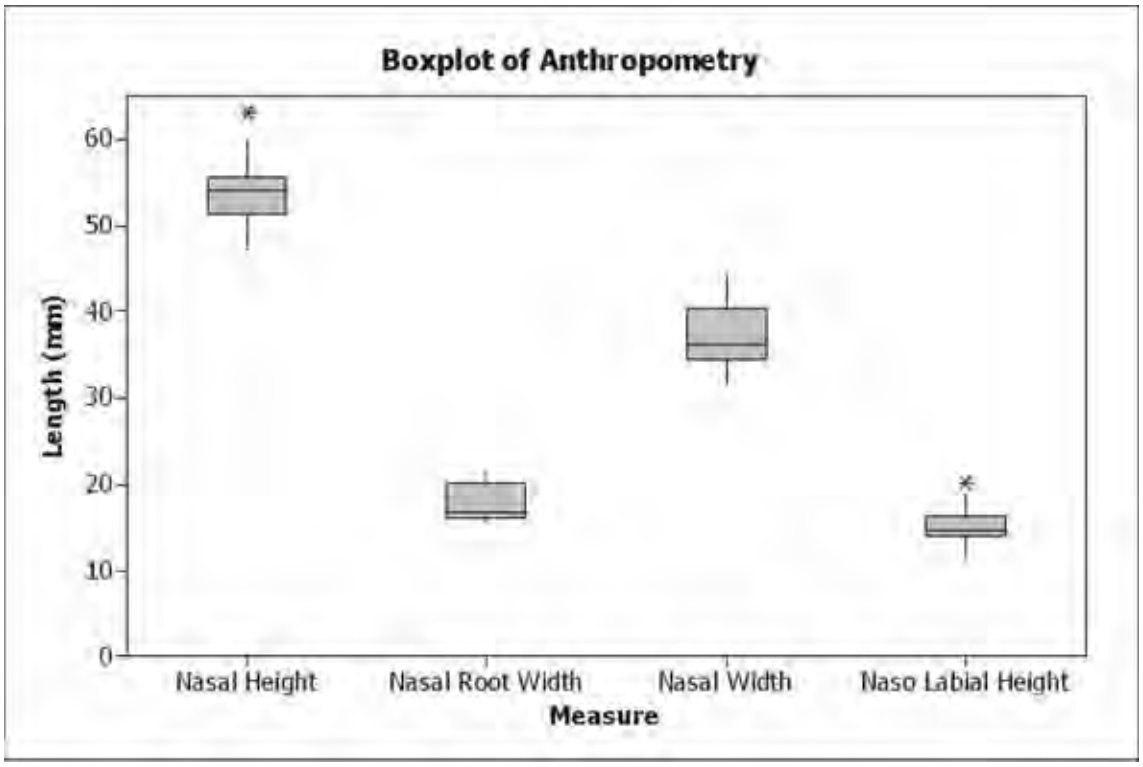

Figure 8.9: Boxplot of participant's nasal anthropometric data calculated from the reconstructed surfaces

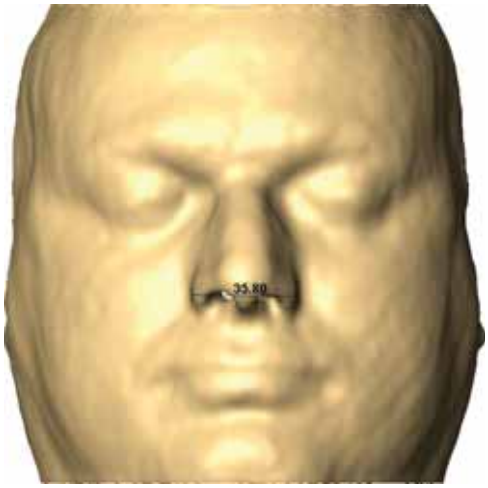

(a) Nose width: Distance between the lateral extremities of the alar nasi

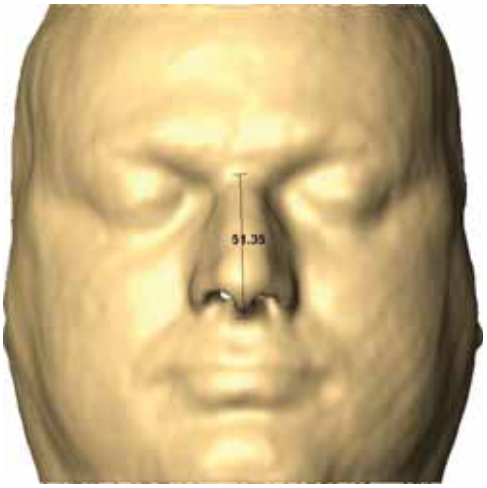

(b) Nose height: Distance between the subnasale and the sellion

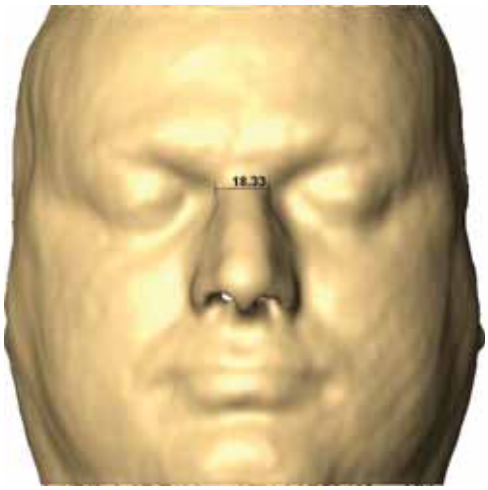

(c) Nasal root width: Width of the nasal root measured at a depth below the sellion equal to half the distance from the sellion to a line connecting the endocanthions

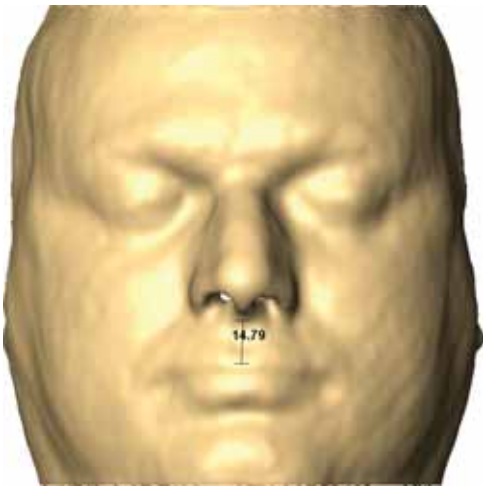

(d) Nasolabial height: Distance from the subnasale to the superior margin of the upper lip on the sagittal plane

Figure 8.10: Basic anthropometric measurement illustrations

Since the engagement of the mask on the face depends on the form of the underlying nasal geometry, these measurements were anticipated to influence the contact behaviour between the mask and face. Therefore, the above basic anthropometric measurements were determined from the reconstructed surfaces from the reference scan sets. Summary statistics for the participants of this study and their distribution are presented in Table 8.8 and Figure 8.9. The anthropometric variables are assumed to be normally distributed. These data will be used in the analysis of the FEA results to investigate their association with the contact result fields and parameters.

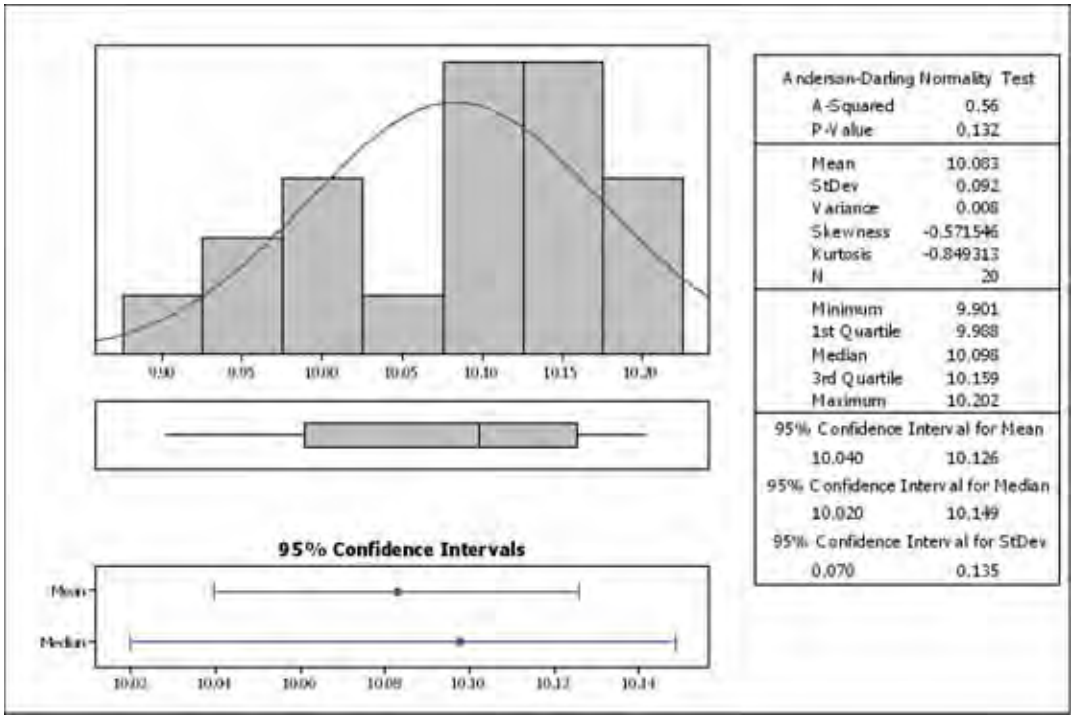

Figure 8.11: Summary data for CPAP pressure for the participants

8.10.2 Mask Pressure

The CPAP therapy pressure applied at the mask was recorded during the fitting of the mask. The mean pressure recorded across the participants is shown in Figure 8.11. The pressure across the participants was $10.08 \pm 0.09\text{cm}H_2O$. This is very close to the nominal value of 10cm H_2O, which will be used for downstream finite element modelling.

8.10.3 Deformation Field

The primary data source from this series of experiments was the DICOM data volume for each of the scans. Sample reference configuration and deformed configuration scans while undergoing CPAP therapy are shown in Figure 8.13. Inspection of these images from the MRI data set reveal several characteristics of the mask/face system. Firstly, although faint, the mask's cushion is visible allowing easy identification and localisation of regions compressed and deformed by the mask. Most evident for this subject is the deformation of the upper lip as the mask undercushion is compressed onto the face, indenting into the upper lip. This is shown in Figure 8.13d. This deformation in Subject 12 was approximately 7mm. The transverse section shows that the mask also noticeably indents the face at the side of the nose by a similar distance, and is approximately symmetrical. The forehead region

exhibits a noticeable, but much smaller deformation. These approximate patterns were evident across the experiment cohort.

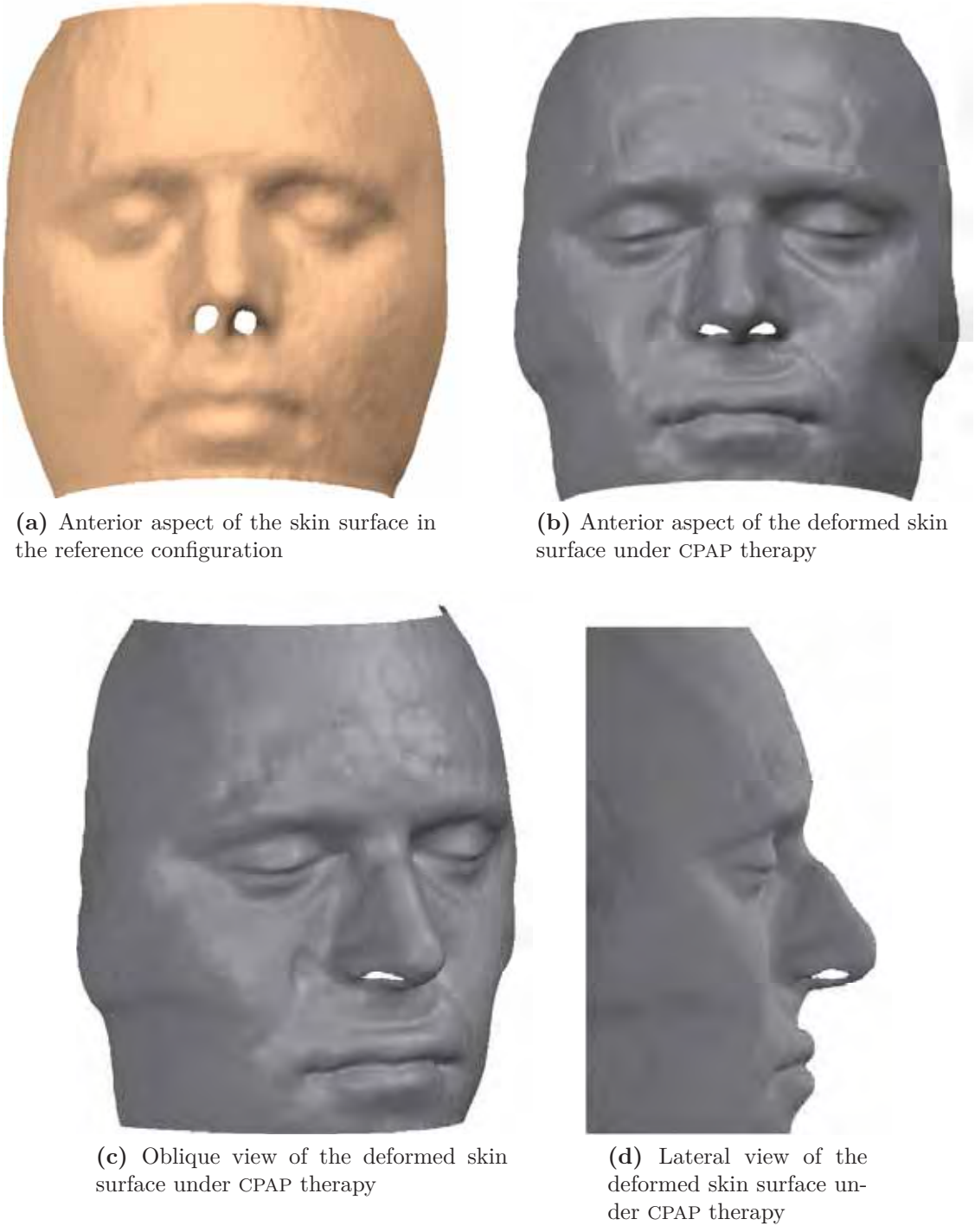

(a) Anterior aspect of the skin surface in the reference configuration

(b) Anterior aspect of the deformed skin surface under CPAP therapy

(c) Oblique view of the deformed skin surface under CPAP therapy

(d) Lateral view of the deformed skin surface under CPAP therapy

Figure 8.12: Sample reconstructions of the reference and deformed skin surfaces

Sample surface reconstructions of the face in the reference and deformed configurations are shown in Figure 8.12. These images show typical deformations encountered in this experiment. Initially these are qualitatively described. Upon the initial

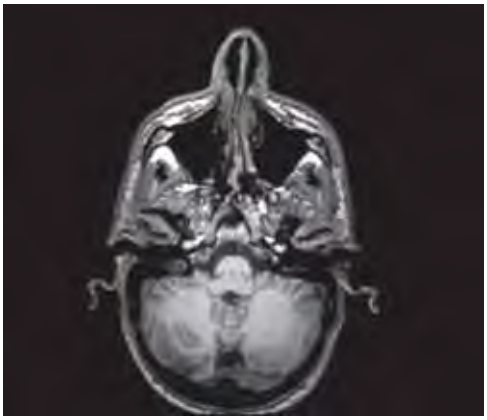

(a) Transverse section, reference configuration

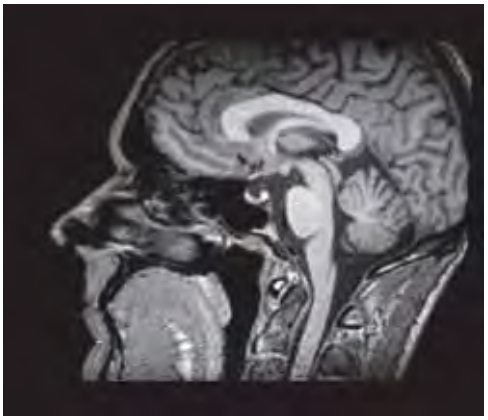

(b) Sagittal section, reference configuration

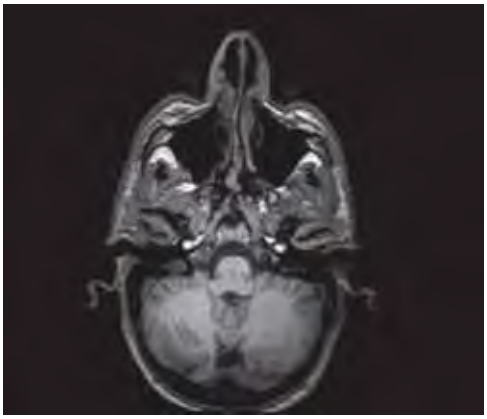

(c) Transverse section, deformed configuration

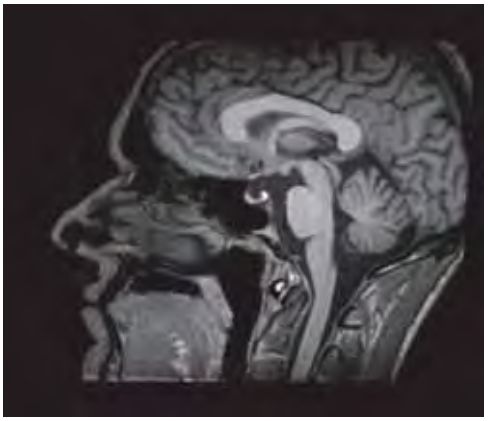

(d) Sagittal section, deformed configuration

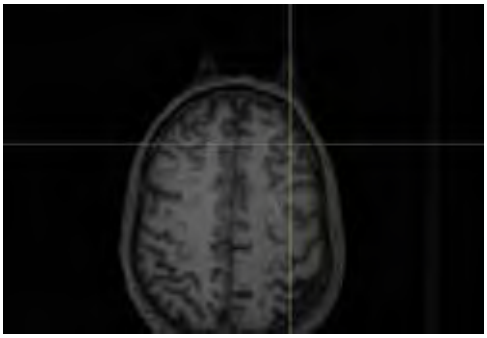

(e) Transverse section, deformed configuration through FHS

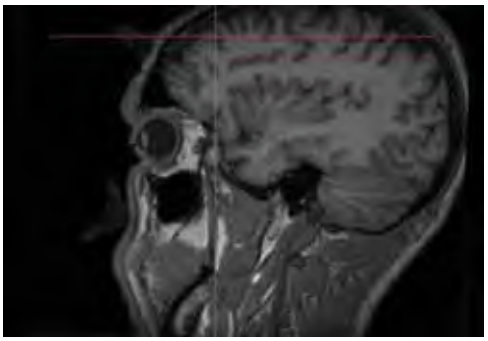

(f) Sagittal section, deformed configuration through FHS

Figure 8.13: Sample scan set showing subject 12 in the reference (a, b) and deformed (c, d, e, f) configurations. The indentation of the mask on the face can be seen in the deformed scans at the upper lip, each side of the nose and under the forehead support.

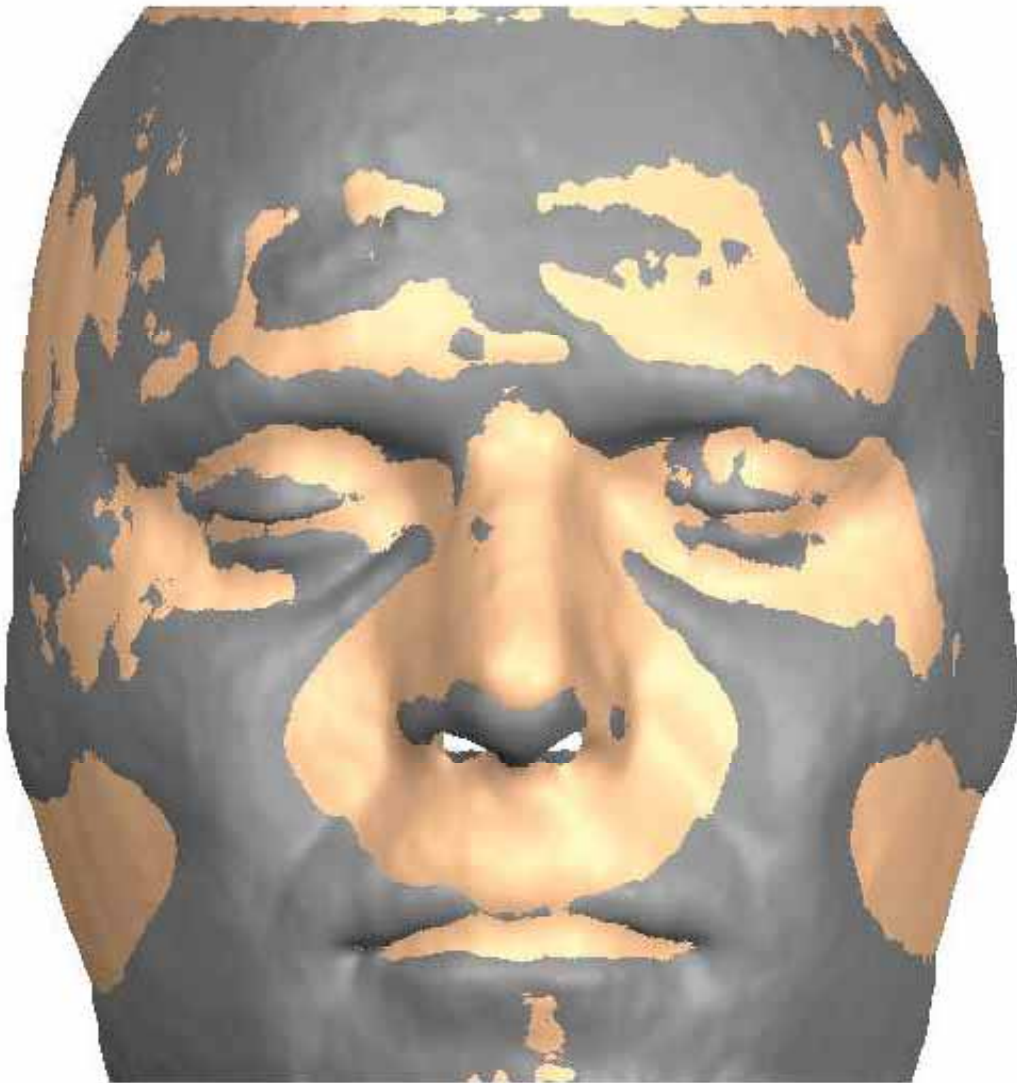

Figure 8.14: Overlay of the skin surface in the reference and the deformed conditions. This highlights regions that have been indented (skin colour) and those that have bulged out (grey)

observation of the sagittal MRI slices and the reconstructed deformed surfaces, the magnitude of the deformation particularly on the upper lip was surprising. Visual inspection of the deformed surfaces highlight deformations localised to the contact of the UMII mask. The upper lip and sides of the nose are noticeably indented. The upper lip indentation is relatively flat with a more abrupt run out at the vermilion border of the upper lip. The indentation at the sides of the nose are deep with an approximately cylindrical profile along their length. At the superior end, approaching the nasal root, the side indentations gradually flatten out and blend into a shallower depression which contours across the nasal bridge and joins to the side indentation at the other side of the nose.

The forehead exhibits a small deformation from the FHS pads. A faint outline of the FHS pads is visible as a depression. The final region that stands out from a visual inspection of the deformed surface is the lower headgear strap. In each model there are flat, straight depressed regions located bilaterally extending posteriorly and slightly inferiorly to the limit of the surfaces. This deformation is due to the headgear wrapping around the face and compressing the soft tissues beneath it, primarily the thick soft and mobile tissues of the cheeks in the buccal region of the face. The upper headgear strap however does not exhibit the same magnitude of deformation. This is due to the reduced thickness of the scalp tissue and the proximity to the underlying rigid support, whereas in the cheek region, the soft tissue is much thicker and suspended to span from the mandible to the maxilla, therefore, allowing a large lateral deformation as the tissue is compressed.

Figure 8.14 is an overlay of the registered surfaces showing both the deformed and reference configurations. This image provides a clear visualisation of the regions of the face where the mask has compressed the soft tissue, as the reference surface is visible above the deformed surface. Conversely adjacent to the compressed regions, the soft tissue can also be seen to bulge out and above the reference surface. Therefore, skin coloured regions define locations where the deformed surface has been compressed below the reference surface, grey regions are where the deformed surface has bulged out over the reference surface, while speckled regions denote those where the deformed and reference surfaces are close to coincident. These images show that the face is compressed from the mask cushion at the sides of the nose, at the bridge of the nose, under the forehead support and under the lower headgear straps. In order to maintain the volume of the soft tissue, it bulges and expands adjacent to the lower headgear strap, and adjacent to the compressed regions surrounding the nose. Figure 8.15 shows the same overlay from the anterior and lateral aspects, though enhancing the visualisation of the facial deformation by setting

(a) Anterior view of the reference and deformed surfaces

(b) Lateral view of the reference and deformed surfaces

Figure 8.15: Overlay of the reference (transparent) and deformed surfaces. The deformation field from the contact of the CPAP mask shows compressive deformations surrounding the nose including the upper lip, along the cheeks from the headgear and at the forehead support. The magnitude of the compressive deformation, particularly on the upper lip is striking.

the reference surface to be transparent, providing a datum to visually compare the deformed surface against.

The magnitude of the deformation is shown through the use of section plots as shown in Figure 8.16 for a representative participant. The normal deformation field was calculated for each of the participants according to the method outlined in Section 8.6.8. This is the distance from each node in the reference surface along its normal vector to its intersection with the deformed surface. The surface normal deformation map is a real scalar field across the domain of the surface. Negative values indicate that the deformed surface has been compressed below the reference surface, while positive values indicate that the deformed surface has bulged out above the reference surface.The section curves such as shown in Figure 8.16 allow more detailed local visualisation of the deformation experienced by the participant under CPAP therapy at 10cm H_2O.

The midsagittal section (Figure 8.16a) gives a good understanding of the main deformations experienced by the participant. The forehead region is only subjected to negligible deformations, as can be seen by the red and blue lines being almost coincident. It is important to note though, that the FHS incorporates a bridge between the pads which is convex in the anterior direction, so is actually not in contact on the midsagittal plane. Inspection of the forehead level transverse slice (8.16e shows that the compression is minimal at that location.

Table 8.9: ANOVA output for skin deformation across regions

Source	DF	SS	MS	F	P
ROI	3	85.43	28.48	11.81	0.000
Error	72	173.54	2.41		
Total	75	258.96			

$$S = 1.552 \quad R^2 = 32.99\% \quad R^2_{adj} = 30.20\%$$

Progressing inferiorly down the midsagittal slice the first noticeable difference between the reference and the deformed section curves is at the nasal bridge immediately inferior to the sellion (8.16b. In this region the soft tissue is broadly compressed over the nasal bone. This then blends into the nose (8.16c which is generally deformed by continuity as the tissues are compressed under the direct load path as well as shear factors from skin friction.

Below the nose at the upper lip (8.16d is the most notable deformation on the midsagittal plane. Here the undercushion of the mask directly bears on the upper lip, approximately at the level of the headgear attachment. Therefore, the applied headgear load is resisted in a large part by the upper lip undercushion. This results in the upper lip being compressed significantly with clear limits to the contact region, where the upper lip is folding around the indented tissue, as the skin surface is compressed. The magnitude of deformation in this region is in the order of up to 7mm.

The signed normal deformation map of the CPAP MRI is shown in Figure 8.17a. In the representative sample shown, this result quantifies the qualitative results that have been previously introduced.

The peak deformation data from the experiment is shown in Figure 8.18. A one way ANOVA analysis with Tukey comparisons was performed across the regions. A significant difference was found ($P < 0.01$), refer to Table 8.9. The comparisons showed that only the deformation across the bridge of the nose was significantly different. This result was expected as the soft tissue is much thinner in that location preventing excessive deformation magnitudes.

Since the original soft tissue thickness bounds the deformation field, the normal deformation results were normalised by the tissue thickness in the reference configuration (Figure 8.17b) to calculate a normal compression ratio, which is similar to compressive engineering strain. It is simply calculated as follows,

$$c_i = \frac{d_i}{t_i} \tag{8.42}$$

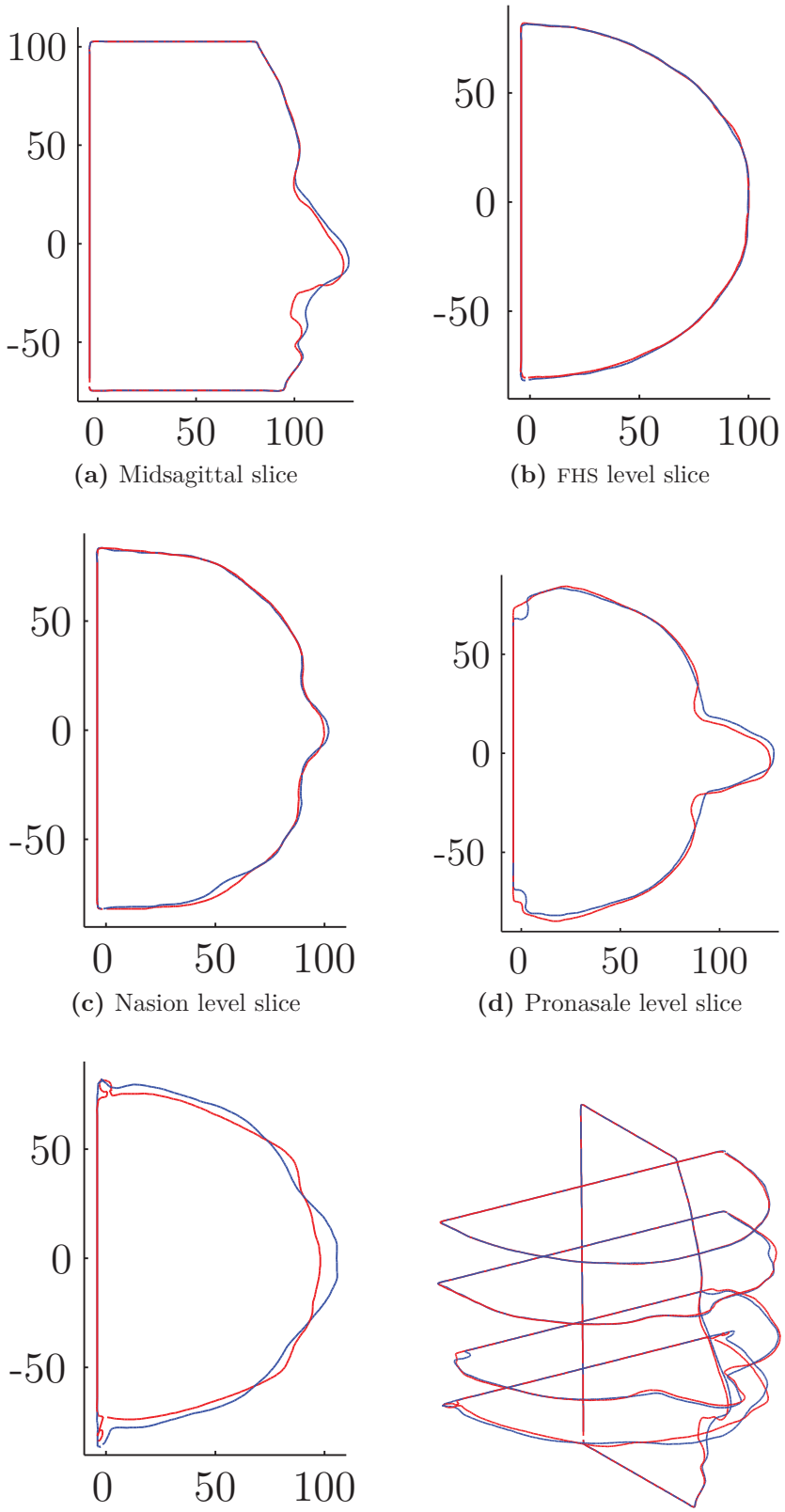

(a) Midsagittal slice

(b) FHS level slice

(c) Nasion level slice

(d) Pronasale level slice

(e) Mid philtrum level slice

(f) 3D view of slice planes

Figure 8.16: Reference (blue) and deformed (red) skin profiles. Dimensions are in mm.

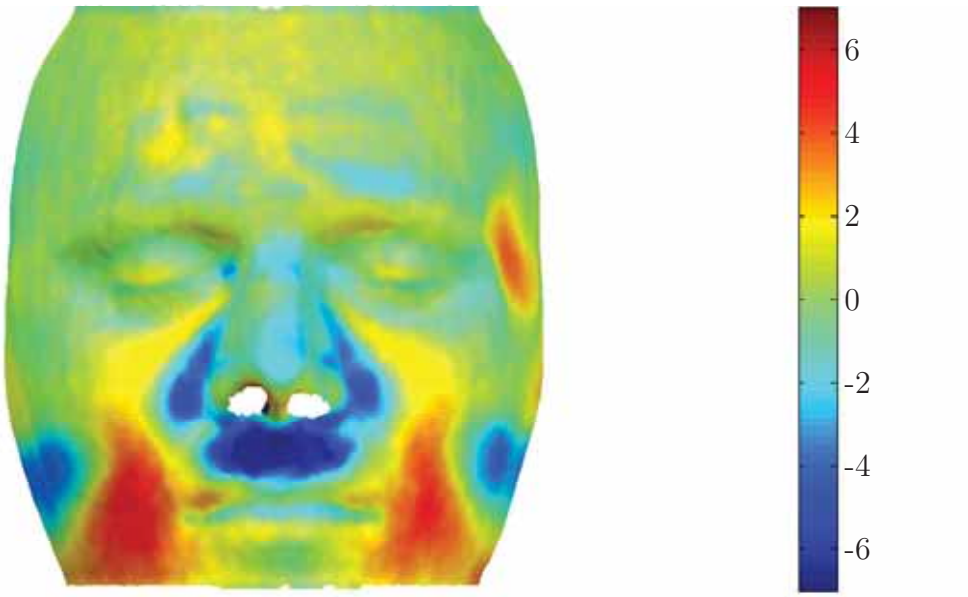

(a) Normal deformation field (mm) under CPAP therapy

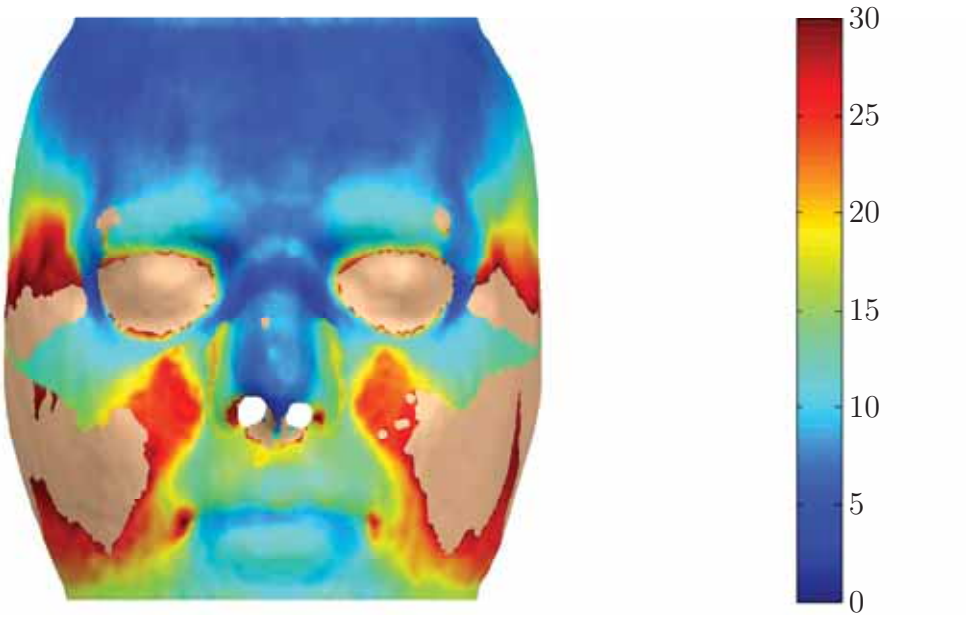

(b) Soft tissue thickness (mm)

Figure 8.17: Normal distance measurements

. Where c_i is the compression ratio, d_i is the normal deformation and t_i is the tissue thickness, all calculated at node i. The sign of c_i is such that a $c_i > 0$ when a material is compressed. The results of this normalisation are shown in Figures 8.19 and 8.20. Similarly a one way ANOVA analysis was used to look for significant differences in maximum compression in each of the regions. No significant difference was found at a 95% confidence level ($P = 0.327$), refer to Table 8.10.

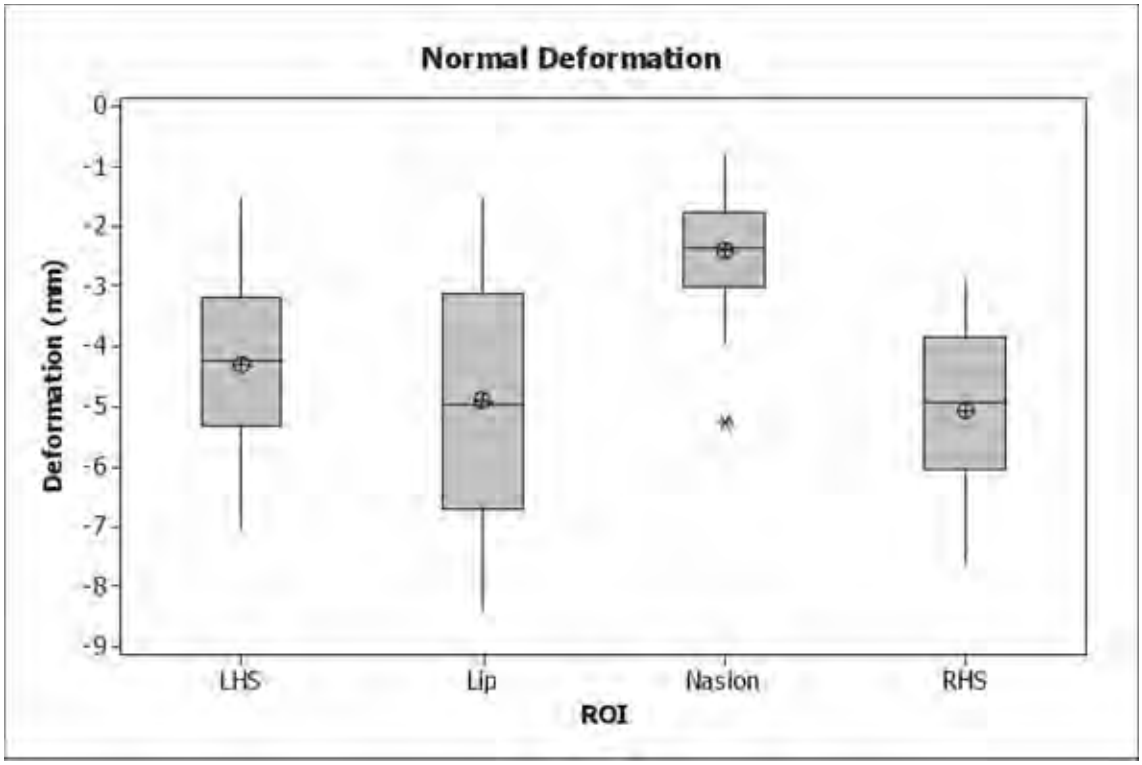

Figure 8.18: Normal deformation grouped by facial region

Table 8.10: ANOVA output for skin compression ratio across regions

Source	DF	SS	MS	F	P
ROI	3	0.0552	0.0184	1.17	0.327
Error	72	1.1325	0.0157		
Total	75	1.1877			

$S = 0.1254 \quad R^2 = 4.65\% \quad R^2_{adj} = 0.68\%$

This result confirms that the soft tissue around the face is thin enough to significantly influence the overall deformation field. Normalising by thickness shows that the peak compression ratio in each of the regions is similar. This effect is striking in when comparing the raw results in Figure 8.17a to Figure 8.19, where it can be seen that the normalised data highlights the compression of the tissue over the nasal bridge where deformations and thickness are small and also the upper lip where deformations and thicknesses are larger. In that particular case the compression ratio of the tissue at the sides is elevated, but not to the same level. This is a reflection of the variability that is associated with these parameters.

Additionally the participants in this experiment were able to adjust the headgear tension according to their own comfort, so the comparisons between people should take into account the applied headgear load. It was assumed that the tension in

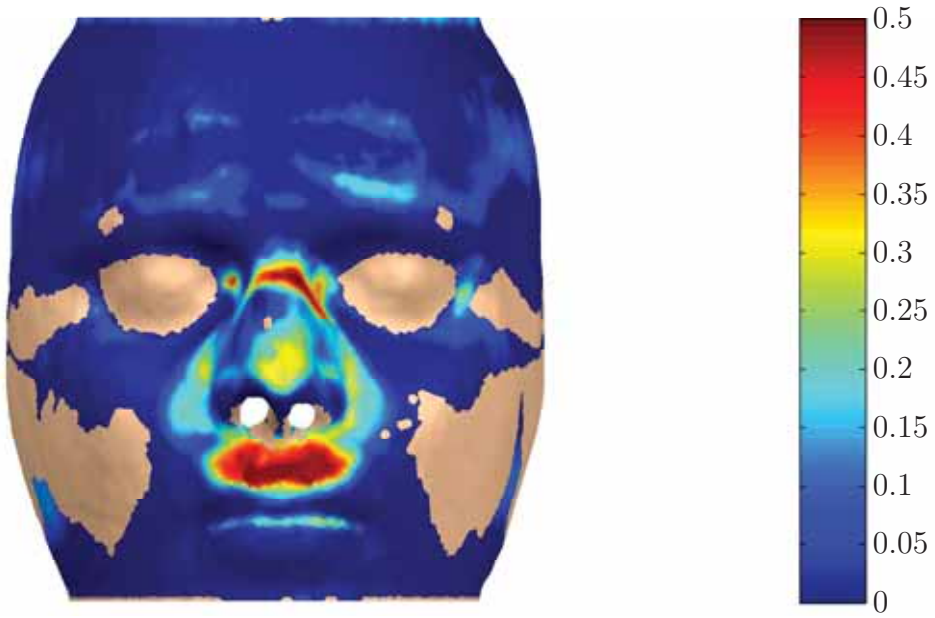

Figure 8.19: Sample compression ratio of the soft tissue.

Table 8.11: ANOVA output of deformation normalised by headgear tension

Source	DF	SS	MS	F	P
ROI	3	3.262	1.087	8.56	0
Error	72	9.149	0.127		
Total	75	12.411			

$$S = 0.3565 \quad R^2 = 26.28\% \quad R^2_{adj} = 23.21\%$$

the upper and lower straps were associated purely with the forehead and nasal regions respectively. Therefore, the nasal results were normalised once again by the headgear tension. No attempt was made to weight the individual regions according to the proportion of load resisted. The peak deformation/load results are shown in Figure 8.21. One way ANOVA with Tukey comparisons was used to compare the normalised results across the different regions, refer to Table 8.11. A significant difference was found with the region across the nasal bridge differing from all others with a smaller magnitude deformation per unit load.

The peak compression ratios normalised by headgear tension were likewise compared across the ROI of the face using the same one way ANOVA test at a level of $\alpha = 0.05$, these results are shown in Figure 8.22. The Compression ratio did not exhibit a significant difference between regions ($P = 0.347$).

In addition to identifying systematic differences in the facial deformations and compression ratios across the ROI, a primary *a priori* goal of this study was to investigate associations between the facial deformations and anthropometric parameters

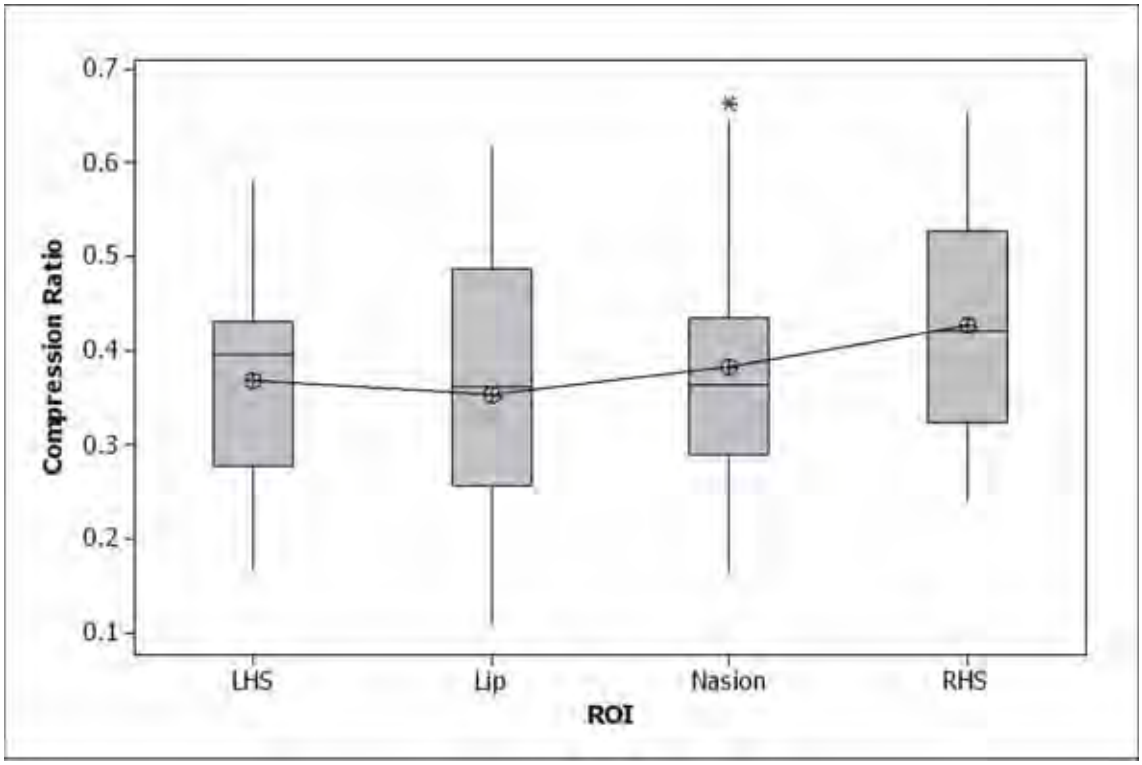

Figure 8.20: Soft tissue compression ratio by facial region

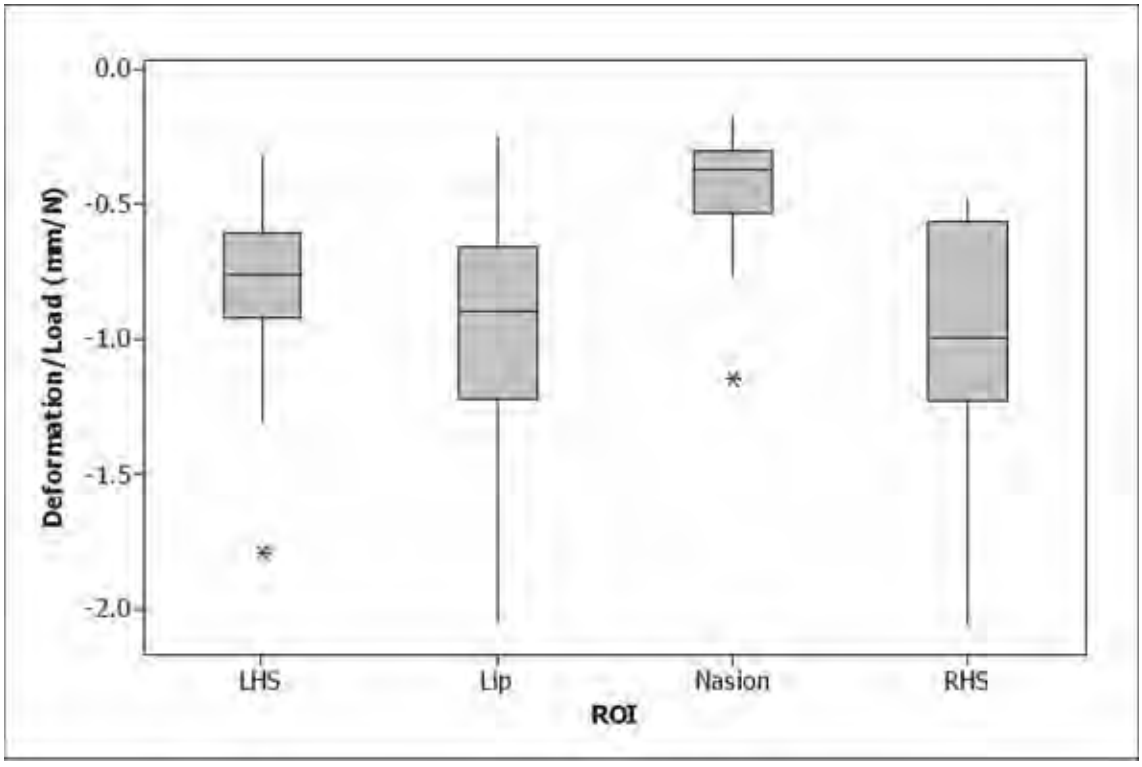

Figure 8.21: Facial deformations normalised by headgear tension, grouped by region

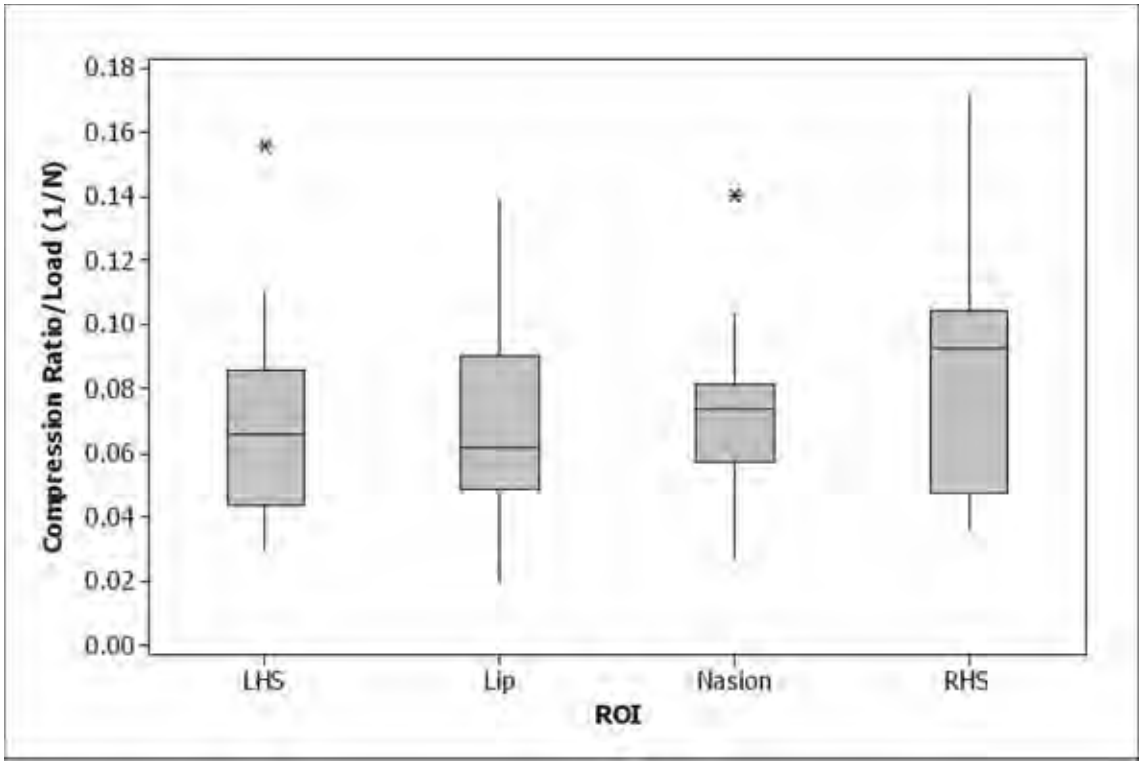

Figure 8.22: Facial compression ratios normalised by headgear tension, grouped by region

which vary between participants. Therefore, stepwise linear regression was used to investigate any associations between response and a set of predictor variables. The predictor variables used in the study incorporated the primary screening variables of age and BMI as well as the anthropometric measurements of nasal width, nasal height, nasal root width, and nasolabial height

Stepwise regressions were performed of the peak facial deformation normalised by headgear tension at the sides of the nose (pooled), the upper lip and around the nasion. The results are summarised in Table 8.12 and shown in Figures 8.23, 8.24 and 8.25.

The results from the stepwise regressions show that the normalised deformation is significantly associated with the BMI on the sides of the nose, the nasal height on the upper lip and nasion regions. The regression equations are listed in equations (8.43) to (8.45).

$$d_{0\ \text{side}} = 0.472 - 0.0519 \quad \text{BMI} \tag{8.43}$$

$$d_{0\ \text{lip}} = -3.76 + 0.0545 \quad \text{NH} \tag{8.44}$$

$$d_{0\ \text{ns}} = -3.05 + 0.0323 \quad \text{NH} + 0.0578 \quad \text{NLH} \tag{8.45}$$

Table 8.12: Summary data of the stepwise regression of normalised deformation and compression ratio on age, BMI, nasal width, nasal root width, nasal height and nasolabial height. ✓denotes predictor variables that were found to be significant at a level of $\alpha = 0.05$, * denotes predictor variables that approached significance, '-' denotes predictor variables that were not found to be significant. The probability values are reported for predictor variables found to be significant or approaching significance.

	Normalised Deformation			Normalised Compression		
Predictor Variable	Nasal Side	Lip	Nasion	Nasal Side	Lip	Nasion
Age	-	-	-	-	-	-
BMI	✓ $P < 0.01$	* $P = 0.067$	-	-	-	-
Nasal Width	-	-	-	✓ $P < 0.01$	* $P = 0.067$	-
Nasal Root Width	* $P = 0.064$	-	-	-	-	-
Nasal Height	-	✓ $P = 0.011$	✓ $P = 0.044$	✓ $P < 0.01$	✓ $P < 0.01$	-
Nasolabial Height	-	-	* $P = 0.083$	-	-	-
$r^2\%$	38.63	47.22	35.62	43.41	44.25	-

Note that the additional term approaching significance was included in the regression equation at the nasion as its non inclusion resulted in the regression on the nasal height alone not reaching significance.

The results from the stepwise regressions show that the normalised compression ratio at the sides of the nose are significantly associated with the nasal width ($P < 0.01$) and nasal height ($P < 0.01$); the normalised compression ratio at the upper lip was significantly associated with the nasal height ($P < 0.01$). The regression equations are listed in equations (8.46) to (8.47).

$$c_{0\ \text{side}} = 0.0589 + 0.00638\text{NW} - 0.00411\text{NH} \tag{8.46}$$

$$c_{0\ \text{lip}} = 0.259 - 0.00370\quad\text{NH} \tag{8.47}$$

8.11 Summary

The CPAP MRI experimental investigation has for the first time, to the best of the author's knowledge, measured and characterised the facial deformations experienced by CPAP users. Large deformations from the cushion were experienced at the upper lip (4.9 ± 1.8mm) and at the sides of the nose (4.6 ± 1.6mm). The deformation at the bridge of the nose was significantly lower (2.4 ± 1.0mm), however this was due

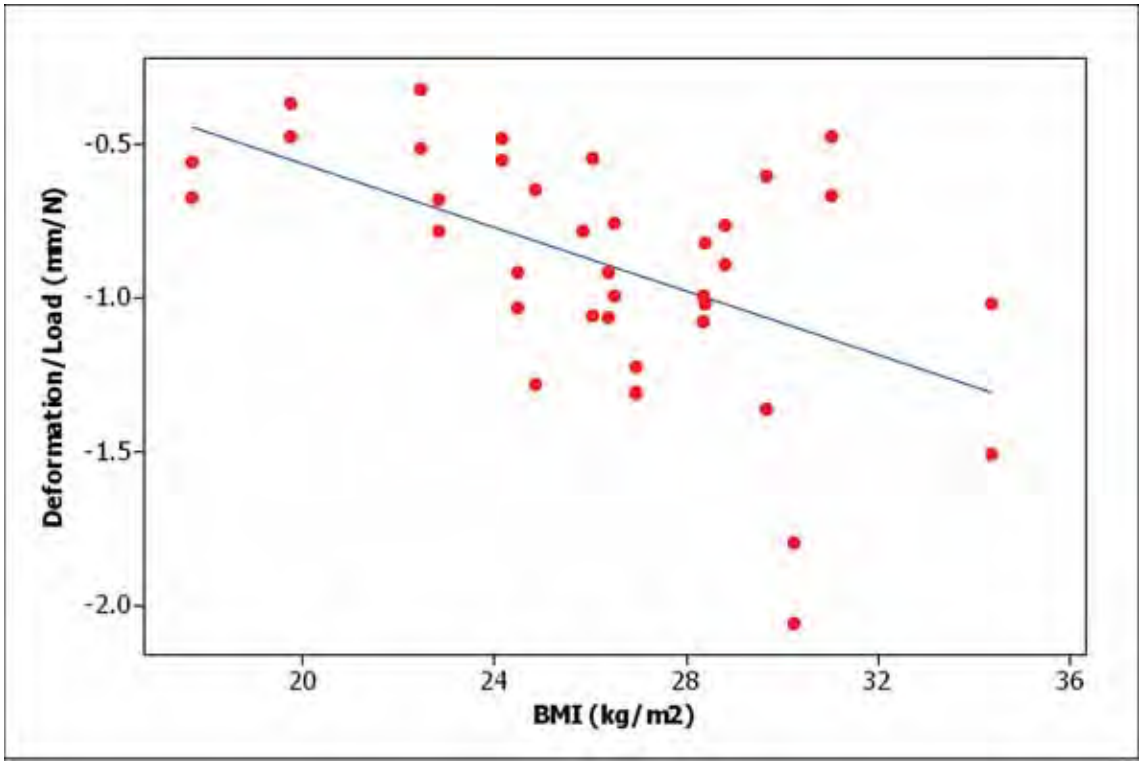

Figure 8.23: Normalised deformation vs BMI at the sides of the nose

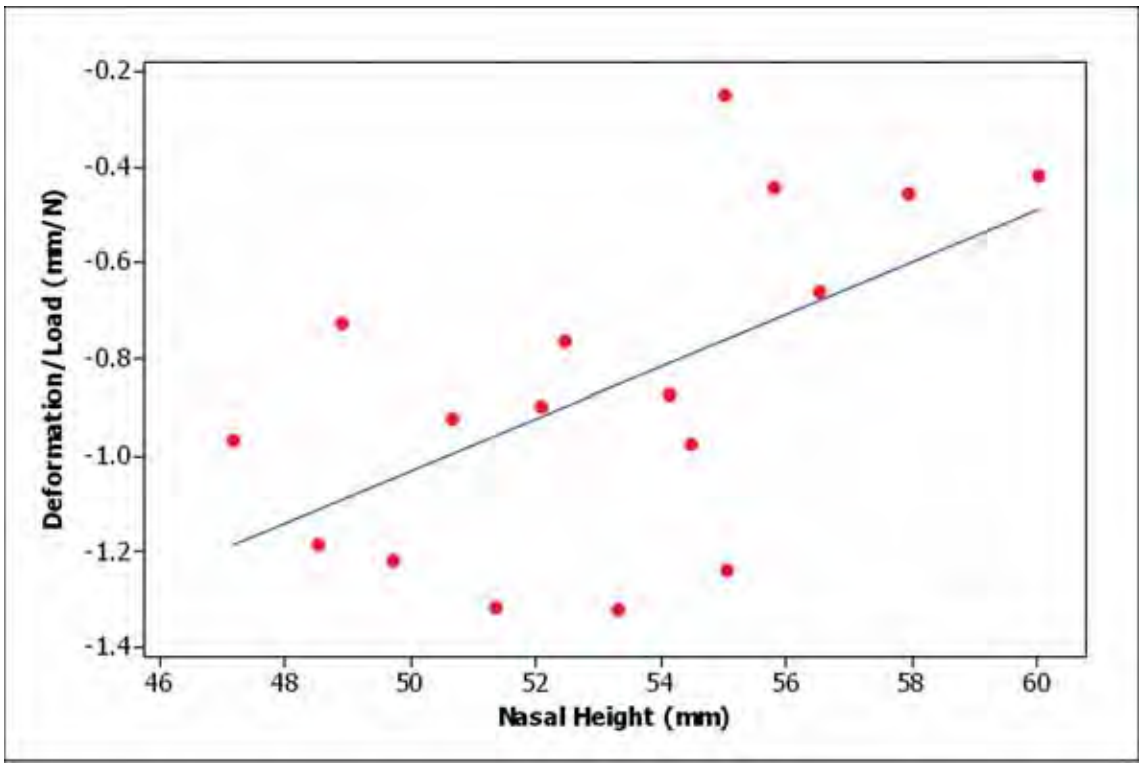

Figure 8.24: Normalised deformation vs nasal height at the upper lip

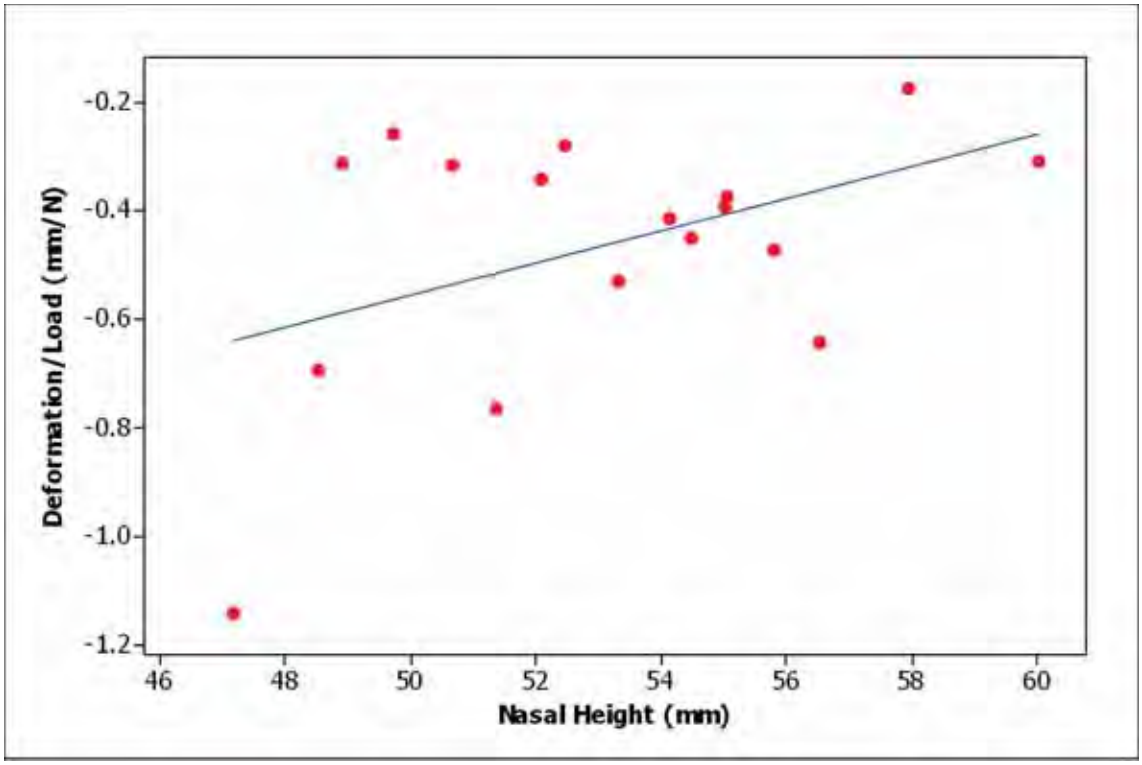

Figure 8.25: Normalised deformation vs nasal height at the nasal bridge

to the thinner soft tissue at this location. After normalising for tissue thickness and applied load, no significant difference was found between the normalised compression ratios at the side of the nose ($0.080 \pm 0.031\text{N}^{-1}$), the upper lip ($0.073 \pm 0.031\text{N}^{-1}$) and the nasion ($0.080 \pm 0.035\text{N}^{-1}$).

Associations were found using stepwise regression between the normalised compression ratio at the sides of the nose and the measurements of nasal width and nasal height. Additionally the normalised compression ratio at the upper lip was associated with the nasal height.

The information obtained during these experiments is very rich with data. It includes triangulated surfaces generated for the reference and CPAP scan volumes. These data sets form the basis for downstream FEA model development and subsequent validation against experimental results. The segmentation process provides information regarding the distribution of different skin, fat and muscle across the head and face. The distribution of the discrete material properties is important in determining the overall mechanical response to load. The mechanical properties of subdermal fat are investigated in Chapter 9, also forming an input to the FEA model development.

Part IV

Indentation

Chapter 9

Indentation

This chapter characterising the mechanical properties of subdermal fat for use in large deformation FEA simulations has been through the peer review process and published in the journal Biomechanics and Modelling in Mechanobiology. The text of this paper has been reproduced in this chapter. The author gratefully acknowledges the input of his co-workers and collaborators for this research. The individual contributions of each of the authors to this paper is outlined in Table 9.1. The citation for this paper is:

Sims, A.M.; Stait-Gardner, T.; Fong, L. *et al.* Elastic and viscoelastic properties of porcine subdermal fat using MRI and inverse FEA. *Biomech Model Mechanobiol*, 9(6):703–711, **2010**.

Table 9.1: Individual author contribution for Sims *et al.* (2010)

Author	Contribution
A. M. Sims	Ethics application, study design, protocol development, test rig design and manufacture, conduct experiments, image processing and 3D reconstruction, inverse FEA modelling, manuscript preparation
T. Stait-Gardner	NMR protocol development, conduct experiments, NMR sections of manuscript, manuscript review
L. Fong	Conduct experiments
J. W. Morley	Study design, manuscript review
W. S. Price	Study design, NMR expertise, manuscript review
M. Hoffman	Study design, project supervision, manuscript review
A. Simmons	Study design, project supervision, manuscript review
K. Schindhelm	Study design, project supervision, manuscript review

9.1 Introduction

Pressure sores are a significant clinical problem, resulting in the breakdown and potential necrosis of the skin and underlying tissue. The aetiology of pressure sores or ulcers is a focus of current investigation. The understanding of the mechanics of pressure ulcers was queried by Bouten *et al.* (2003). They proposed a multi-modal hierarchical structure for more detailed investigation into the mechanics of pressure ulcers over various length scales. This included pathophysiology under load and mechanics at the cellular level, and ranged through to the gross system response to the mechanical loading of the body through the interface of the skin.

Pressure sores are commonly classified as being superficial or DTI according to the National Pressure Ulcer Staging System (Black *et al.*, 2007; National Pressure Ulcer Advisory Panel, 1989). The dominant understanding for decades has been that pressure ulcers were caused by an applied contact pressure which exceeds capillary perfusion pressure (Landis, 1930). Subsequent investigations have shown that it is possible for DTI to be incurred without significant degradation of the skin (Nola and Vistnes, 1980) and that the localised state of stresses and strains play a more significant role than pressure alone. This is a particularly insidious condition as it allows for the DTI to progress extensively in the subdermal tissue before being discovered, potentially leading to sepsis.

The localised nature of stresses and strains in the body are functions of the applied load, local morphology and the constitutive behaviour of the soft tissue. The local morphology such as the proximity of a bony prominence or overall tissue thickness influences the local mechanical state of the soft tissue, for example through a stress concentration under the ischial tuberosity in the case of sitting.

Oomens *et al.* (2003) demonstrated through the use of finite element analysis (FEA) that the non homogeneity of tissue types has a strong influence on the mechanical state of the tissue. By its very nature, contact loading will have compressive and shear components. As the layers of superficial tissue are arranged in series, namely the skin, subdermal fat (or hypodermis) and the underlying muscle, they will all be on the load path as a load is transferred through to the bearing structure. Therefore in order to accurately simulate the mechanical behaviour of the superficial soft tissues in contact, it is necessary to consider their constitutive behaviour.

The mechanical behaviour of soft tissues has been the subject of much research over several decades. Skin has received, and continues to receive considerable attention, and it is now generally understood to be a specialised material exhibiting

non-linear elasticity, anisotropy and viscoelasticity (Lanir and Fung, 1974b). Similarly skeletal muscle has been the focus of a significant amount of research, including both active and passive properties. On the other hand, there is a paucity of information in the literature regarding the mechanical properties of adipose tissue or fat.

Adipose tissue is a connective tissue consisting predominantly of adipocytes bound by vascular loose, or areolar, connective tissue. Adipose tissue concentrates much of the body's fat in the subcutaneous tissue among other preferential locations including the omentum and breasts. Functionally, adipose tissue acts as an energy reservoir, thermal insulator and as a mechanical load absorbing and distribution member, such as in the calcaneal fat pad under heel strike impact loading (Williams *et al.*, 1989a). Subdermal fat, as previously mentioned, is arranged in series with the skin forming an elastic foundation. Considering the idealisation of springs in series the overall compliance of a structure is governed by the most compliant member. In this case this will be the subdermal fat. Therefore the material properties of the subdermal fat will be a significant influence on the deformation of the composite as a whole. Since soft tissue deformation is commonly considered to be in the large deformation domain, the state of deformation will influence the structural stiffness and the load distribution. Therefore for compressive loading, the mechanical behaviour of the subdermal fat should not be discounted.

Investigation into the mechanical properties of adipose tissue has been focussed on the calcaneal fat pad (Erdemir *et al.*, 2006; Miller-Young *et al.*, 2002) and breast tissue (Azar *et al.*, 2002; Samani *et al.*, 2003; Samani and Plewes, 2004). Incompressibility has been assumed, or in the case of linear models that the Poisson's ratio is near $\nu \approx 0.5$. Published values for the material properties of breast and calcaneal fat vary significantly. Various studies using different constitutive models by Samani et al have found that the mean elastic modulus of normal breast adipose tissue was in the range of $E = 3.25 - 3.6$ kPa (Samani and Plewes, 2004; Samani *et al.*, 2007), while Azar *et al.* (2002) using an exponential model reported an initial modulus of $E = 4.46$ kPa; Considering the calcaneal fat pad, Erdemir *et al.* (2006) using a first order Ogden model reported an initial shear modulus of 56 kPa, while Miller-Young *et al.* (2002) using a 2nd order Mooney Rivlin polynomial model determined an initial shear modulus of approximately 0.02 kPa, and recently Wearing *et al.* (2009) have reported an *in vivo* secant modulus of $E = 580 \pm 145$ kPa although this was calculated on the full tissue thickness. Even from this brief survey it can be seen that the material properties for adipose tissue vary widely in the literature and appear to be location specific. Turning now to subdermal fat, in only a few

studies, published mechanical property values range from $G = 0.02$ kPa (Hendriks *et al.*, 2006) through to $G = 7.5$ kPa (Geerligs *et al.*, 2008).

In this study, a confined indentation experiment was developed to estimate a minimal set of non-linear elastic and time dependent properties. Indentation was chosen as the experimental technique as it applies a compressive load which will be similar to *in vivo* contact loading. The experiment was performed within a high field Nuclear Magnetic Resonance (NMR) spectrometer providing cross sectional images of the sample as the primary data source. Image processing methods were used to extract experimental measurements from the test sample.

9.2 Materials and Methods

9.2.1 Tissue Preparation and Mounting

Superficial porcine soft tissue was excised from the abdomen immediately post mortem and then stored in an isotonic PBS solution within a thermally insulated container during transportation to the test site. Approval was obtained for the experiments (BRSC07/014).

For this study, cylindrical specimens ($n = 6$) of subdermal adipose soft tissue were cut using a sharp cylindrical borer. A scalpel was used to carefully trim any tissue remnants that were not cut cleanly. The natural thickness of the subdermal fat was maintained for the experiment.

The tissue samples were then placed in a cylindrical testing dish. A gelatine solution (10% by mass, in 0.1 M $CuSO_4 \cdot 5\,H_2O$) was then used to fill the remaining volume of the dish up to but not covering the top surface of the tissue sample, embedding it in an elastic media. This arrangement eliminated voids from the test and provided a known fixed boundary condition for subsequent FE simulation. The sample was allowed to set for 20 minutes. A prepared sample is shown in Figure 9.1a.

9.2.2 Test Rig Design

A custom test rig was required for this investigation. The Bruker Avance NMR spectrometer (wide bore, 11.7 T) used in this study has a small vertically oriented contained scanning volume. Placement in the spectrometer required that all materials used in the experiment did not interact with the strong magnetic fields present.

A custom test rig was developed, consisting of a 2 part housing (acetyl) and a lightweight indenter (Figure 9.1b). The indenter assembly consisted of an epoxy

sealed balsa wood body and a PTFE spherical tip with a radius of 4 mm. The housing base was profiled to snugly fit the coil sensor, additionally the indenter was self aligning to assist engagement, negating the need for spatial registration from test to test. The indenter was machined to engage with the body in a smooth running fit, additionally 3 evenly spaced axial grooves were machined into the body to allow air venting during engagement. The indenter body was designed to carry a filler material and apply a known gravitational load.

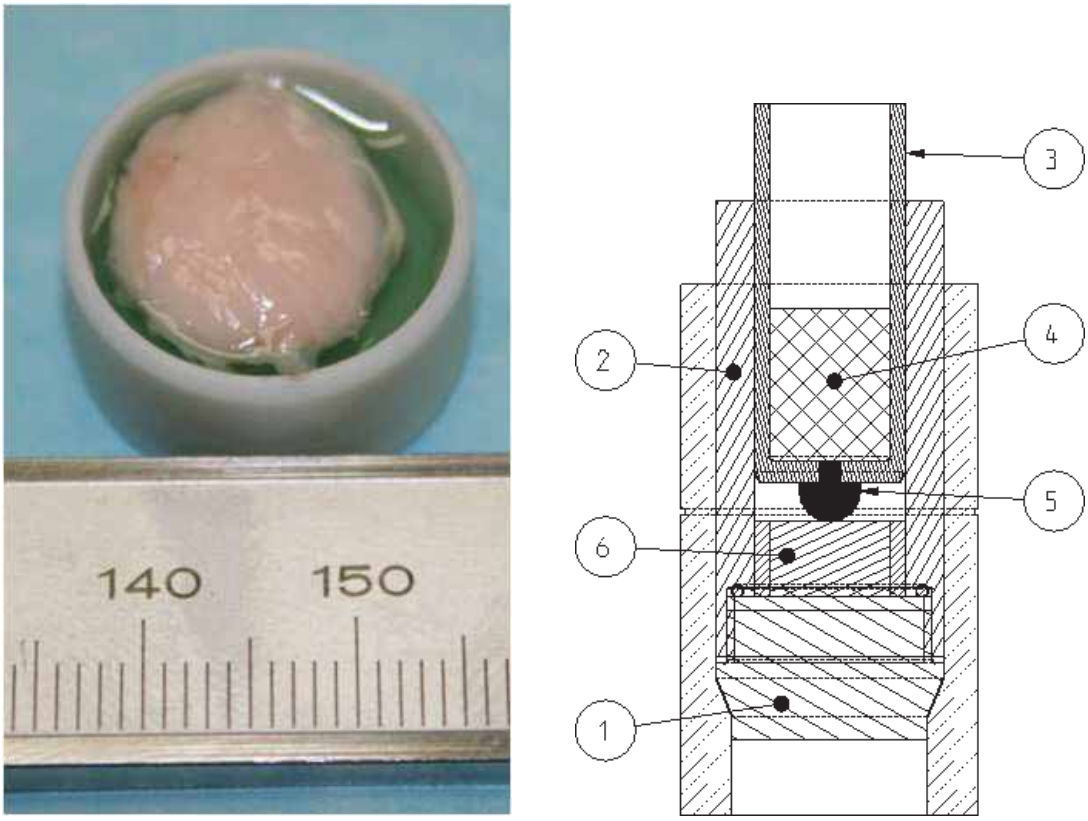

Figure 9.1: a) Mounted specimen; b) Indentation experiment schematic showing 1: profiled base, 2: cylindrical body, 3: indenter, 4: filler material, 5: spherical tip, 6: sample

9.2.3 Procedure

The embedded specimen was assembled into the test rig, and mounted into the MRI probe. This was inserted axially into the Bruker spectrometer and calibrated. A ^{1}H 3D volume scan was taken of the sample in the reference condition.

The indenter (2 g) was then applied to the sample ($t = 0$) and a series of orthogonal ^{1}H images was taken at regular intervals ($\Delta t = 30$ s) over 10 minutes. The voxel size for each of the scans of the sample was $0.1953 \times 0.1953 \times 0.5$ mm. The indenter was then removed (t_r) and the tissue allowed to relax for 10 minutes.

An identical series of orthogonal images was commenced at the removal of the load to track the relaxation of the sample. The mass applied by the indenter was then increased (5 g, 10 g) and the procedure repeated. Three load histories were used, (a) 2 g, 5 g (b) 2 g, 10 g and (c) 2 g, 5 g, 10 g.

Two different MRI scanning protocols were used in this study. These are the 3D scans and the 2D orthogonal section scans. The 3D scans are used to define the full 3D geometry of the test. In each case the DICOM output from these scans was used to segment the embedding gel and the soft tissue. Copper sulphate was included in the gelatine solution as a contrast agent to enhance the edge definition between the gelatine matrix and the fatty tissue layer in particular.

The 3D scan type was multi scan multi echo (MSME) with a repetition time of 3000 ms and an echo time of 3.0 ms. The approximate duration of a 3D scan was 384 s.

The shorter duration of 2D orthogonal scans (14 s) were compared to the 3D scans allows for the scanning period of $\Delta t = 30$ s, providing a history to investigate the time dependent response of the soft tissue. The 2D scan type was MSME with two mutually perpendicular scan planes (termed coronal and sagittal), a repetition time of 220.5 ms and and echo time of 3.0 ms.

9.2.4 Image Processing

The output from each of these scans was a DICOM series. In the case of the 3D scans it defined the scan volume, whereas for the 2D scans, the series corresponded to a time history through the same cross section. A representative time series of scans is shown in Figure 9.2. The voxel size for each of the scans of the sample was $0.1953 \times 0.1953 \times 0.5$ mm. DICOM images were filtered using a 2D anisotropic diffusion filter in order to preserve the image edge gradients defining material boundaries. The 2D section time series was segmented using ScanIP software (Simpleware) based on image intensity and Canny edge detection for the material boundaries.

The 3D volumes were reconstructed using ScanIP software. The level set method was used to define the overall volume of the sample. Interior voxels were assigned to material groups based on their greyscale intensity in conjunction with the edge detection based on the gradient image ($\nabla \cdot I$). The marching cubes algorithm was utilised to generate bounding surfaces. The model consists of discrete material volumes for the gel matrix, and the embedded adipose soft tissue sample within the test rig.

Each of the scans from the 2D orthogonal sets were collated into a time history at that spatial location. Each scan was similarly segmented based on greyscale

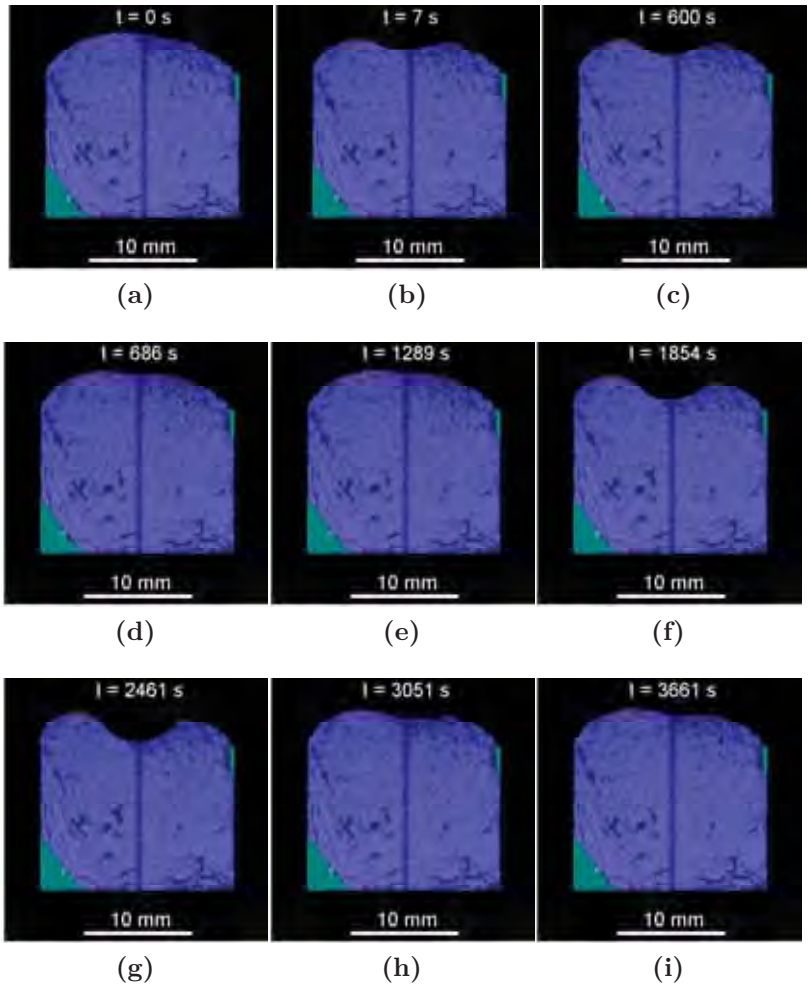

Figure 9.2: 2D ^{1}H MRI images (voxel size $0.1953 \times 0.1953 \times 0.5$ mm) of an adipose tissue sample from scan sequence showing indentation and relaxation history. a) Reference configuration, b & c) 2 g indentation period, d & e) Load removal and relaxation, f & g) 5 g indentation period, h) & i) Load removal and relaxation.

intensity. Matlab was then used to fit spline curves to the interfaces between each of the materials in the plane of the scan. The DICOM attribute Content Time or Image Time (DICOM Standards Committee, 2007) was used to determine the timestamp associated with each deformation configuration.

9.2.5 Derived Quantities

The vertical positions of the sample surface $y_t(t)$ were extracted at the intersection of the central axis of the sample and the spline curves to construct time histories for each series. The indentation was normalised by the reference height of the sample, this was calculated according to

$$z_{ind} = \frac{Y - y}{Y}. \tag{9.1}$$

Variables are assumed to be functions of time. The continuum mechanics convention of using upper case variables to refer to the reference configuration and lower case to refer to the deformed configuration has been used.

9.2.6 Inverse Finite Element Analysis

Model Description

An inverse FEA procedure was used to estimate the material properties of the soft tissue samples using ANSYS v11 and Matlab. The experiment was modelled as a 2D axisymmetric model with discrete materials used for the gel (elastic boundary) and fat. The 3D reconstructions of the gel/sample composite indicated that the samples were approximately cylindrical in shape, therefore idealised geometry was used for all of the samples except for one, which exhibited a convex superior surface. Sample specific models were developed by maintaining the known boundary of the sample dish and determining the respective fat tissue thickness and diameter in order to provide the correct material volumetric ratios and overall volume, as determined in Section 9.2.4 from the 3D reconstructions. The sample which exhibited a convex superior surface was profiled to match this surface and again dimensioned accordingly to provide the correct material volumetric ratios.

The axisymmetric cross section of the sample was meshed using 4 node planar quadrilateral elements. The indenter contact was modelled as a rigid profile, driven by a pilot node and assumed to be frictionless. Incompressible hyperelastic material properties were assumed for the fat, so mixed U/P element formulation was used to prevent volumetric locking. The contact interface was modelled using Lagrange multipliers to enforce the normal penetration tolerance constraint.

Large deformation theory was used for the model. The standard fundamental relations of solid continuum mechanics apply. The deformation gradient $\boldsymbol{F}$ maps the reference configuration to the deformed configuration.

$$\boldsymbol{F} = \frac{\partial \boldsymbol{x}}{\partial \boldsymbol{X}} = \boldsymbol{I} + \frac{\partial \boldsymbol{u}}{\partial \boldsymbol{X}} \tag{9.2}$$

where $\boldsymbol{X}$ and $\boldsymbol{x}$ are Cartesian position vectors of a point in the reference and deformed configurations respectively, and $\boldsymbol{u}$ is a displacement vector. The volumetric ratio $J = \det \boldsymbol{F}$ is identically 1 due to incompressibility. The right Cauchy Green deformation tensor is given by

$$\boldsymbol{C} = \boldsymbol{F}^T \boldsymbol{F}. \tag{9.3}$$

The eigenvalues of $\boldsymbol{C}$ are the squares of the principal stretches of the material λ_i^2. The invariants of $\boldsymbol{C}$ are given by

$$I_1 = \mathrm{tr}\boldsymbol{C} = \lambda_1^2 + \lambda_2^2 + \lambda_3^2, \tag{9.4}$$

$$I_2 = \mathrm{tr}\boldsymbol{C}^{-1} \det \boldsymbol{C} = \lambda_1^2\lambda_2^2 + \lambda_2^2\lambda_3^2 + \lambda_1^2\lambda_3^2, \tag{9.5}$$

$$\text{and} \quad I_3 = \det \boldsymbol{C} = \lambda_1^2\lambda_2^2\lambda_3^2 = J^2. \tag{9.6}$$

Symmetry conditions were enforced along the central axis, and all nodes in contact with the sample dish boundary were fully constrained in the x and y directions. The pilot node of the indenter was located on the central axis, and was constrained to only allow motion in the vertical (y) direction. The mesh and model setup used for the analyses is shown in Figure 9.3.

Material Properties

The gel material forming the elastic boundary of the samples was separately characterised using both tensile and compressive testing corrected to take into account friction according to Morriss *et al.* (2008). Refer to Appendices K, L and M for details of the testing performed and material property fitting. A three parameter Mooney Rivlin hyperelastic model (9.7) was used for the elastic component of the material

$$\begin{aligned} \Psi = C_{10}\left(I_1 - 3\right) + C_{01}\left(I_2 - 3\right) \\ + C_{11}\left(I_1 - 3\right)\left(I_2 - 3\right). \end{aligned} \tag{9.7}$$

A two element Prony series (9.8) ($k = 2$) was used to model the viscous component of the gel, with G_0 being the underlying shear elastic property and α_i being the series relative moduli where

$$G = G_0\left(\alpha_\infty + \sum_{i=1}^{k} \alpha_i \mathrm{e}^{-t/\tau_i}\right) \tag{9.8}$$

$$\alpha_\infty = 1 - \sum_{i=1}^{k} \alpha_i$$

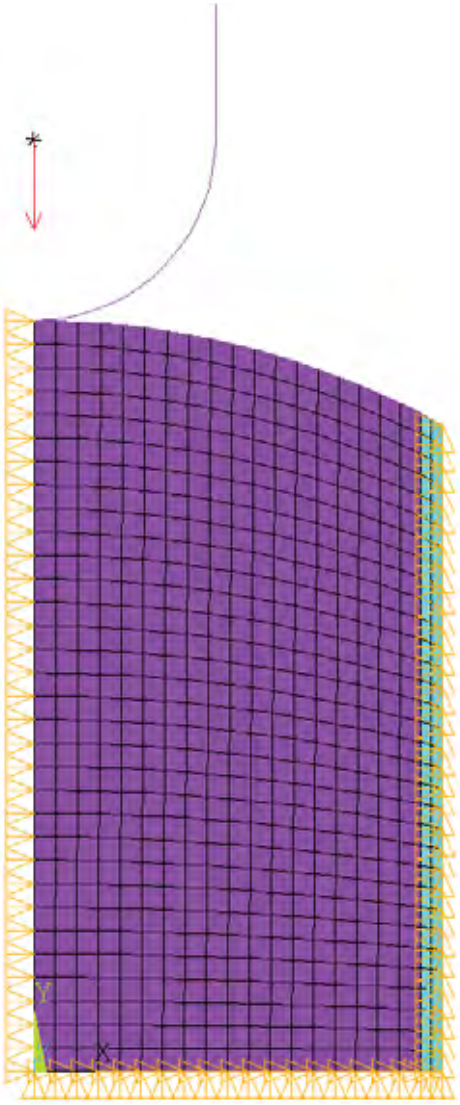

Figure 9.3: FEA mesh showing model for the convex profiled sample including the load and boundary conditions

Table 9.2: Gel Mooney Rivlin parameters

Parameter	Value
C_{10} (kPa)	0.43
C_{01} (kPa)	0.21
C_{11} (kPa)	0.012

The gel material properties are identified in Tables 9.2 and 9.3.

The simple Neo Hookean hyperelastic material model (9.9) was assumed for the subdermal fat. The viscoelastic behaviour was modelled with a single element Prony series (9.8) ($k = 1$). As these parameters form the independent variables for the non linear inverse analysis, the starting values must be chosen. The initial shear modulus $\mu = 0.5$ kPa was chosen arbitrarily. The initial values for the Prony series constants,

Table 9.3: Gel viscoelastic properties

i	1	2
α_i	0.21	0.044
τ_i (s)	245	21.2

the relative modulus α and the time constant τ were taken from the experimental curve fit

$$\Psi = \frac{\mu}{2}\left(I_1 - 3\right). \tag{9.9}$$

Optimisation

The model was solved quasi-statically using large deformation theory in a series of load steps with outputs synchronised to the scan times of the experiment throughout the duty cycles. The first of these steps applies or removes the load as a step function over a short time period. This corresponds to the instantaneous response of the material and is governed by the underlying elasticity (ANSYS Inc, 2005).

An inverse FEA procedure was used to estimate hyperelastic and viscoelastic material properties for subdermal fat in the load application and relaxation steps respectively. A non-linear least squares fitting routine was used to track and coordinate the solution. A user defined objective function was written to perform the following tasks: 1) write material properties to disk, 2) launch ANSYS as a batch process, ANSYS then reads the material properties, solves the model and writes out the normalised indentation results to file 3) read in ANSYS results to a model results vector and calculate norm of the residual vector $\boldsymbol{r}$. As mentioned previously only the loading portion of the experiment was considered. This was implemented by multiplying the experimental ($z_{ind\mathrm{E}}$) and model ($z_{ind\mathrm{F}}$) normalised indentation result vectors by a binary masking function γ.

$$\boldsymbol{r} = \gamma z_{ind\mathrm{E}} - \gamma z_{ind\mathrm{F}} \tag{9.10}$$

$$\gamma = \begin{cases} 0 & \text{if indenter is not applied,} \\ 1 & \text{if indenter is applied,} \end{cases}$$

Therefore the optimisation is defined as

$$\min_{\mu,\alpha,\tau} \|\boldsymbol{r}\|_2 \tag{9.11}$$

Parameter Study

The uniqueness of the parameter estimation can be assessed by altering the starting point to see if this influences the converged parameter estimate. Since the elastic component from the Neo Hookean model is a single parameter model, the convergence to the instantaneous response is assured. The viscous response in the Prony series is a function of both α and τ, so may be sensitive to starting values α_0, τ_0. Therefore a sample model was investigated by superimposing a random perturbation on the parameters' initial estimates for $n = 5$ iterations with an amplitude of up to 50% of the value.

3D FEA Comparison

As a check on the axisymmetric modelling assumption, the reconstructed geometry from one of the samples was generated into a 3 dimensional FEA model using a mapped mesh with 8 node hexahedral elements. Elements were allocated to the fat or gel material through a transformation mapping element gauss point coordinates with voxel indices. This simulation was also used to evaluate the feasibility of using a 3D model within an inverse analysis. The mesh is shown in Figure 9.6

9.3 Results and Discussion

9.3.1 Experimental

A time history of a representative sample is shown in Figure 9.4. From this several characteristics of the material behaviour can be inferred. Firstly the viscoelastic behaviour of the material is evident, as upon load application there is a clear initial response followed by a constant load creep towards an asymptotic value (Figure 9.4a). Additionally, upon load removal the corresponding behaviour can be seen as the tissue relaxes (Figure 9.4b). It is important to note at this point that there is a non recoverable portion of the deformation which is a function of the indentation load (Figure 9.4b). As an initial investigation of these results, a single constant exponential curve fitted to the data accounted for a large proportion of the recorded variation ($r^2 > 0.9$). This suggests that a simple single parallel element Prony series viscoelastic model will be appropriate to capture the viscous behaviour of the adipose tissue.

This normalised experimental data was used to calculate residuals for the inverse FE analysis which was used to estimate material properties.

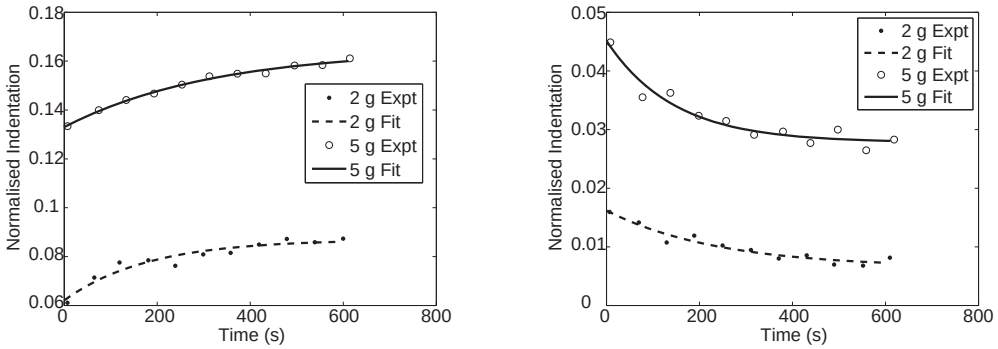

Figure 9.4: Representative experimental data of normalised indentation and corresponding curve fits during a) loading $\left(y = A\left(1 - \mathrm{e}^{-t/\tau}\right) + C\right)$, and b) relaxation $\left(y = A\mathrm{e}^{-t/\tau} + C\right)$

9.3.2 Finite Element Analysis Results

It was noted previously that the fat tissue underwent non recoverable deformations. This raises a limitation with this current study. Hyperelastic models assume that the deformation is elastic *i.e.* fully recoverable. Therefore this current model will not be able to capture this component of the material behaviour. For this study inverse analysis was only performed on the loading portion of the experimental data, and the relaxation component was not considered. The effect of the non recoverable deformation was incorporated in a dummy load step by applying a corresponding enforced displacement and updating the reference geometry to this configuration for the subsequent analysis.

The results from the inverse analyses yielded estimates for the shear modulus μ, relative modulus α and the time constant τ at each of the indentation loading levels. These are reported in Table 9.4. Data values which exceeded the median value by more than the interquartile range were considered to be outliers. This resulted in three values being excluded from the analysis ($\mu = 1.3, 2.2, 1.6$ kPa).

The shear modulus results lie within the broad range of published properties of adipose tissue of $\mu = 0.02 - 7.5$ kPa (Miller-Young *et al.*, 2002; Hendriks *et al.*, 2006; Geerligs *et al.*, 2008). The results from a representative sample and model are shown in Figure 9.5. Figure 9.5a indicates that the optimised parameters are able to simulate the indentation behaviour of superficial fat for the various indentations very well when μ is considered as a secant modulus.

Due to practicalities all the samples could not be taken from the same animal, and as a result there is some inherent variation in the results. The viscoelastic properties exhibited significantly greater relative variation than the elastic properties. However these data are encouraging considering the extremely soft nature of the material in question.

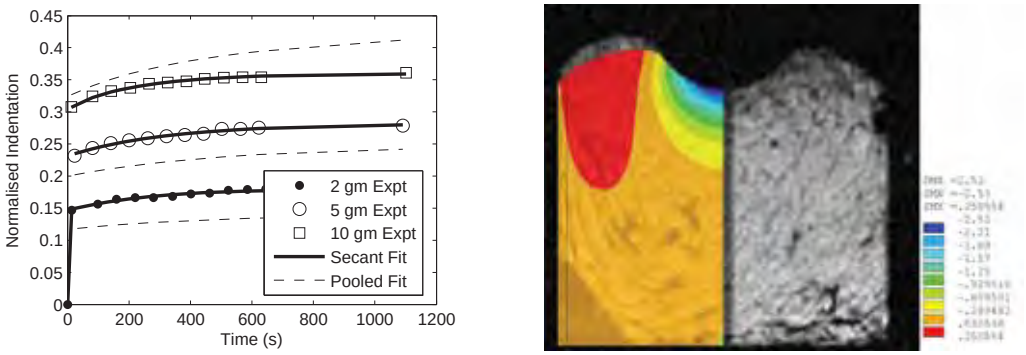

Figure 9.5: a) Normalised indentation vs time, experimental data and optimised FEA (secant and pooled properties) b) Overlay of MRI indentation scan and sample specific FEA model showing vertical displacement

Table 9.4: Optimised elastic and viscoelastic secant properties of subdermal fat (mean ± sd) Outliers were defined by values exceeding the median by more than the interquartile range

Mass (g)	n	μ (kPa)	α	τ (s)
2	5	0.21 ± 0.08	0.28 ± 0.08	217 ± 114
5	4	0.42 ± 0.25	0.22 ± 0.06	376 ± 188
10	3	0.52 ± 0.08	0.24 ± 0.11	189 ± 74

Table 9.5: Optimised elastic and viscoelastic properties of subdermal fat (mean ± sd), corresponding outliers as identified for Table 9.4 were removed

μ (kPa)	α	τ (s)
0.53 ± 0.31	0.39 ± 0.03	700 ± 255

Removal of the outliers greatly reduced the variation of the 2 g indentation results. After this treatment, the 5 g data exhibits the greatest variation. A one way analysis of variance was performed on the reduced data set. From this analysis, an increasing trend could be clearly be identified in μ with increasing indentation force, however it did not reach significance at a 95% confidence level ($p = 0.09$).

Additionally a set of parameters were calculated by pooling the loading levels for each of the samples in the residual calculation of the inverse analysis. After exclusion of the corresponding outliers these results are reported in Table 9.5 and Figure 9.5a. It can be clearly seen that the pooled fit, while optimum in an average sense does not agree as well as the secant data at specific load points.

The results from the parameter uniqueness study indicated that the relative modulus parameter was robust with respect to varying the starting point with $\alpha = 0.2453 \pm 0.0319$, while the time constant was sensitive to the starting value with $\tau = 245.1 \pm 78.9$.

Table 9.6: 2D and 3D sample optimised parameter comparison

Model	μ (kPa)	α	τ (s)
2D	0.241	0.18	635
3D	0.245	0.21	536
error	2%	17%	16%

3D FEA Results Comparison

As previously described, a commensurate 3D FEA model was compared to one of the 2D axisymmetric models. The comparative results from a 5 g indentation are shown in Table 9.6 and Figure 9.6. The 3D model was run within the same optimisation loop, however the objective function minimised on actual displacements, rather than normalised displacements in the 2D models. Excellent agreement was found between the 3D model and the 2D axisymmetric model for the shear modulus μ, while the viscous parameters agreed to within 17%. This error however is well within $\mu \pm \sigma$ from the 2D analysis. This both highlights the feasibility of using 3D models in optimisation loops judiciously, as well as validating the 2D axisymmetric assumption used.

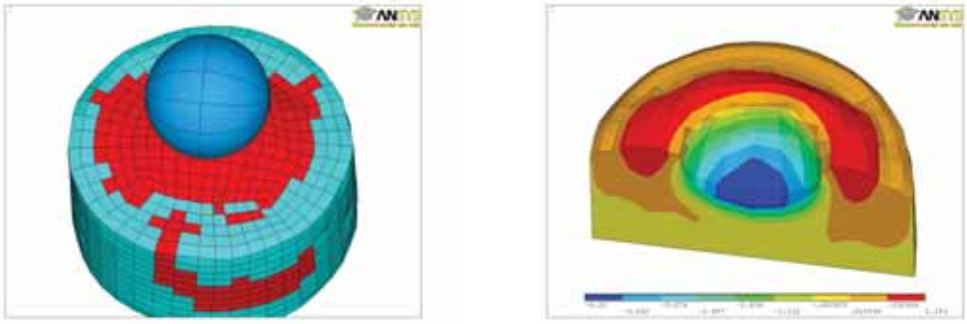

(a) **(b)**

Figure 9.6: a) 3D mesh of a cylindrical sample b) Capped section display of deformation

Of the viscoelastic properties the relative moduli α return the least variation. In contrast the time constant τ exhibited significant variation both across samples and when subject to different starting configurations. This is not surprising considering that the indentation is approaching an asymptote where any change in the time constant will not influence the overall result significantly. Due to the temporal resolution being limited by scan duration at $\Delta t = 30$ s there are not many data points in the initial stages of the creep and relaxation parts of the time history to more accurately capture this phenomenon. Ideally this could be improved by refining the temporal resolution, however using MRI this is not a simple matter

as there is a non-trivial trade off between temporal and spatial resolution. For instance improving spatial resolution by creating smaller voxels increases the number of scan locations. An isometric refinement by an integer factor β will increase the number of voxels by β^3, correspondingly increasing the number of scans (n_s) and the scan time. However the signal to noise ratio ζ also degrades with smaller voxels such that $\zeta \approx \sqrt{n_s}$. Therefore a voxel refinement of $\beta = 2$ results in a total time increase by a factor of approximately 64 to maintain the same signal to noise ratio. The variation in this parameter could be reduced by allowing an increased indentation time, and weighting the residual calculation more to the initial stage of the indentation. Despite this large variation in the time constant, it does not preclude the extraction of valuable material data as the time dependent response is a weak function of time.

9.4 Conclusions

The intent of this study was to address the paucity of information on the mechanical properties of subdermal fat, and to investigate the suitability of using magnetic resonance imaging as a means of acquiring both elastic and viscoelastic mechanical properties of extremely soft tissues. From this study we were able to successfully estimate secant material parameters for a Neo Hookean hyperelastic model, and the Prony series viscoelastic properties, as reported in Table 9.5 for three indentation loads. Additionally an average pooled set of material properties was estimated to give $\mu = 0.53 \pm 0.31$ $\alpha = 0.39 \pm 0.03$ and $\tau = 700 \pm 255$. These results fall within the range of published data. Viscoelastic material properties exhibited significant variability. Ideally this could be improved by refining the temporal resolution, however using MRI this is not a simple matter as there is a non-trivial trade off between temporal and spatial resolution as discussed in Section 9.3.2. Considering the available sampling rate, this could be improved by allowing a greater duration for the infinite time response to be approached and/or applying greater weighting to the initial data records of each indentation.

The secant Neo Hookean parameters identified that there is a trend of increasing modulus with increasing load, although this was not found to be significant at a 95% confidence level ($p = 0.09$). Additionally it can be seen that the pooled material parameter estimation is inferior to the specific solutions, suggesting that a more complex and highly configurable non-linear model such as the Ogden hyperelastic model would be a good candidate for future investigation as it is able to follow a more highly non linear load path.

This study did not attempt to address the unloading part of the curve, and it was noted that non recoverable deformations were encountered. A further direction for future work would be to consider the material as elastoplastic and quantify the extent of plasticity.

In summary these secant constitutive parameters provided close approximation of the mechanical behaviour for the all indentations. This indicates that the Neo Hookean model is adequate at low to moderate strains to model subdermal fat under a compressive load and a single element Prony series can capture the viscoelastic component of the material, however scope exists to develop or utilise a more complex material model that can incorporate a greater degree of non-linearity, such as the Ogden model. The material properties estimated in this paper can be used to improve FEA models of soft tissue in line with the recommendations of Bouten *et al.* (2003) to consider the heterogeneous nature of subdermal tissues.

The use of MR sections provides scope to develop this method to include the simultaneous estimation of the dermal/subdermal layered composite, or incorporate additional methods such as digital image correlation or MR tagging to develop more complex constitutive models. Additionally as MRI is a feasible technology for non invasive testing, this procedure could lead to the development of an *in vivo* testing regime.

Part V

Finite Element Analysis of Continuous Positive Airway Pressure Therapy

Chapter 10

Finite Element Analysis of Continuous Positive Airway Pressure Therapy

10.1 Introduction

This chapter shows the development and validation of a FEA model of the face and mask used during CPAP therapy. The modelling techniques and assumptions used to develop the model are outlined. The validation of the model includes a mesh refinement study, equilibrium and energy balances before finally comparing the simulation results to the experimental results using a field comparison in the regions of interest.

10.2 Background

CPAP has been shown to be a simple, effective and non-invasive treatment for obstructive sleep apnoea Sullivan *et al.* (1981). As outlined in section 3.3.1 OSA can be considered to be a passive process. The soft tissues of the oropharynx are acted upon by a body force, gravity, the pressure difference across the wall and muscle tone. During sleep, paralysis or atonia is induced, hence, only the mechanical properties of the soft tissue and its structure maintain patency of the oropharynx. While CPAP provides a clear clinical benefit, some patients find compliance with the therapy difficult. This is due to factors such as comfort, poor mask fit, claustrophobia, leaking and noise among others.

Therefore, it is clinically important to understand the nature of the contact pressures and load paths in this interface. The interface is between two compliant bodies, the skin and underlying soft tissues and the LSR components of the mask, namely the cushion and the FHS. It is particularly attractive to consider this problem

using FEA because it is an extremely difficult phenomenon to measure reliably *in vivo*. To this end, subject specific 3D FEA models of the patients wearing the CPAP mask were developed. This section of the thesis considers the development and validation of these models and evaluates independently the face and the mask models.

Sophisticated design techniques are used in the development of mask systems to allow them to fit, conform to the shape of the face, seal effectively and be comfortable. Despite great benefits to patients, comfort and fit still remain an issue (Pepin *et al.*, 1995). Facial measurements that are used to design masks are taken in the reference configuration (without wearing a mask). The contact interface is one between two compliant bodies, large deformations are experienced, so a deformed equilibrium position will be adopted by the system of the face/mask. Since this mechanical scenario falls in the large deformation regime, the load distribution, contact areas and hence contact pressures will be dependent on the final equilibrium position adopted. The purpose of this model is to simulate the application of the mask on the face while undergoing therapy, and, hence, extract information about the contact behaviour and load distribution.

10.3 Modelling Strategy and Development

Initially, considering the quasi-static nature of the mask engagement, and the magnitude of deformations experienced, the static implicit non-linear FEA method was chosen for simulating this scenario using ANSYS. It was understood at the outset that the wrinkling, or post buckling behaviour of the mask membrane would require either numerical or mechanical stabilisation in order to allow for the Newton-Raphson method to successfully converge to a stable solution in the region of the instabilities.

To a large extent this was achieved through a number of techniques including pressurising the mask membrane to place it in a state of tension and hence avoid the possibility of the membrane buckling. This had the unintended consequence of inducing a snap through instability in the membrane. These were in turn able to be restrained by controlling the engagement of the mask onto the face and guiding the initialisation of the contact regions to ensure that the snap through region was in closed contact and therefore, able to eliminate the snap through instability. The use of such techniques allowed for significant progress to be made in engaging the mask onto the face. However as the mask engagement progressed, new regions of instability were recruited into the model, leading to numerical problems, such as non

convergence of the Newton-Raphson residuals or for excessive element distortions and inversions to be encountered which caused the solution to terminate, an example of this is shown in Figure 10.1a. Common regions of difficulty encountered were wrinkling of the membrane in the vicinity of the naso-labial sulcus or in regions of high facial curvature under contact conditions where interactions with the face and undercushion generated dominant compressive membrane stresses which were unable to be resisted. Additionally the terminating ends of the undercushion were susceptible to local buckling, as were the swept transition regions of the undercushion blending from the sides to the labial region of the mask, this is shown in Figure 10.1b.

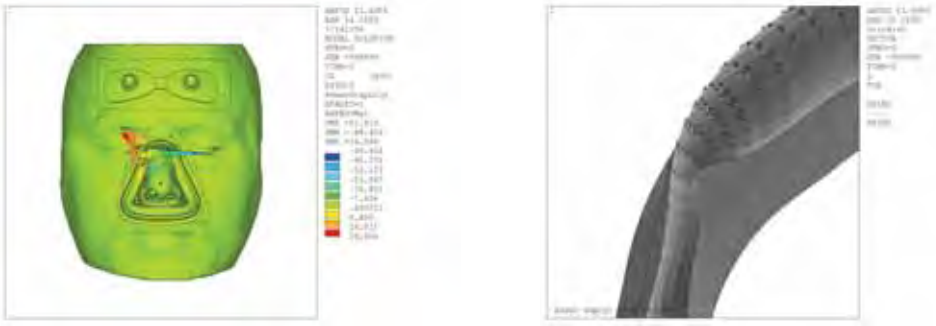

(a) Distorted elements in the membrane

(b) Pinch point in the undercushion swept profile just prior to model termination

Figure 10.1: FEA model development results using the implicit method in ANSYS.

Unfortunately after significant time and effort this resulted in asymptotic development of the face/mask FEA model, and the mask was not able to fully engage. At this point the decision was made to switch the FEA modelling method from the implicit method (ANSYS) to the explicit method using LS-DYNA. The explicit method treats this quasi-static problem as a slow dynamic solution, such that

$$\boldsymbol{m\ddot{x}} + \boldsymbol{c\dot{x}} + \boldsymbol{kx} - \boldsymbol{F} = \boldsymbol{0} \tag{10.1}$$

In this case, as this is a quasi-static analysis, the contributions from the inertial and damping components are negligible once static equilibrium is approached. The explicit solution algorithm used by LS-DYNA is a central difference algorithm where the calculated property is the nodal accelerations. The explicit time integral is calculated as follows,

$$\boldsymbol{M}\boldsymbol{a}^n = \boldsymbol{P}^n - \boldsymbol{F}^n + \boldsymbol{H}^n \tag{10.2}$$

where $\boldsymbol{M}$ is the diagonal lumped mass matrix, $\boldsymbol{a}^n$ is the nodal acceleration vector at time $t = n$, $\boldsymbol{F}^n$ is the stress divergence vector and $\boldsymbol{H}^n$ accounts for hourglass

stiffness effects. This can be simply rearranged to calculate the acceleration vector,

$$\boldsymbol{a} = \boldsymbol{M}^{-1} \left(\boldsymbol{P}^n - \boldsymbol{F}^n + \boldsymbol{H}^n \right) \tag{10.3}$$

This calculation is greatly simplified with the diagonal mass matrix since $\boldsymbol{M}_{ii}^{-1} = \frac{1}{\boldsymbol{M}_{ii}}$. Using the initial conditions, the accelerations are integrated to give the nodal velocities,

$$\boldsymbol{v}^{n+1/2} = \boldsymbol{v}^{n-1/2} + \boldsymbol{a}^n + \Delta t^n \tag{10.4}$$

.

Similarly the nodal displacements are calculated from the initial previous state and the velocities.

$$\boldsymbol{u}^{n+1} = \boldsymbol{u}^n + \boldsymbol{v}^{n+1/2} + \Delta t^{n+1/2} \tag{10.5}$$

where the time increment is given by

$$\Delta t^{n+1/2} = \frac{(\Delta t^n + \Delta t^{n+1})}{2} \tag{10.6}$$

Therefore, the nodal position vectors for the next increment are updated to

$$\boldsymbol{x}^{n+1} = \boldsymbol{x}^0 + \boldsymbol{u}^{n+1} \tag{10.7}$$

10.4 Ultra Mirage II CPAP Mask Models

Nasal CPAP masks are used for the treatment of obstructive sleep apnoea, they are typically an assembly consisting of the following components:

1. Adjustable frame
2. Cushion
3. Forehead support (FHS)
4. Headgear
5. Tubing and Attachments

10.4.1 Mask Assembly Model

The UMII mask was modelled as an assembly with the cushion and FHS components prepared individually and assembled into a top level model, and spatially positioned with respect to the mask coordinate system, the affine transformation matrices describing each component's position with respect to the UMII coordinate system are listed in F. The mating surface for the elbow swivel connection was chosen as a convenient location for the UMII reference coordinate system, it is a flat, circular surface which is centred on the mid-sagittal plane, approximately at the level of the nasal bridge. The coordinate system was oriented according to the ISB recommendations for standardisation (Wu and Cavanagh, 1995) ($\boldsymbol{X}$-anterior, $\boldsymbol{Y}$-superior, $\boldsymbol{Z} = \boldsymbol{X} \times \boldsymbol{Y}$-lateral to the right). This is shown in figure 10.2. This coordinate system orientation is approximately parallel to the global coordinate system used on the facial models, allowing for simple manipulation when the models are brought together.

As the polycarbonate frame is relatively rigid when compared with the cushion and FHS, it was assumed to be a rigid body governed by a pilot node at its centre of mass. Therefore, the frame was modelled as a nodal based rigid body with an assigned inertia tensor at the frame's centre of mass, refer to Appendix B for the calculation of the mask frame inertia tensor. Nodal sets were defined on both the cushion and FHS at the connections to the frame. The pilot node at the centre of mass of the frame was used to apply resultant forces to the frame.

Figure 10.2: UMII frame and reference coordinate system

10.4.2 Cushion

As previously described, the cushion is a complex lofted shape. The coordinate system of the cushion is defined again in the same orientation as the ISB recommendations (Wu and Cavanagh, 1995). This is shown in figure 10.3.

The *body* and *undercushion* have been meshed using fully integrated 8 node HEX elements. The degenerate edge of the undercushion was modelled by a row of wedge elements. The lofted surface of the membrane was modelled using variable thickness shell elements using reduced integration. The connection between the cushion body and the membrane was made using kinematic constraints tying both the translational DOF u_x, u_y, u_z and rotational DOF of the shell to the displacements of the nodes across the interface surface. The mesh of the UMII cushion is shown in Figure 10.4.

10.4.3 Forehead support

The FHS was located with respect to the TBar coordinate system. The FHS is adjustable around a pin jointed connection on the mask frame, with detents pitched at 13.33 deg. Refer to Appendix F for the calculation of transformation matrices.

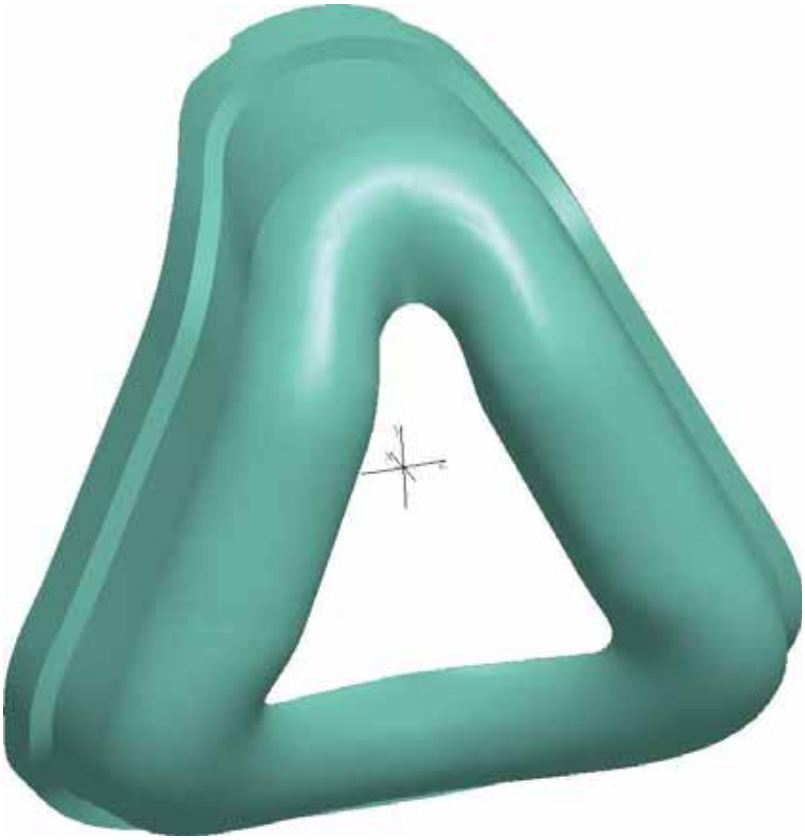

Figure 10.3: UM2 standard cushion and reference coordinate system

The FHS was modelled with 8 node fully integrated HEX elements. The TBar the connection region is rotated around an oblique axis, a rotational sweep was used to mesh this region. Refer to Figure 10.5

10.4.4 Headgear

The headgear for the mask is a one piece laminated composite textile component. It is manufactured from a material known as Breathe-O-Prene ™, which is a layered construction of polyurethane foam with an outer layer of nylon and spandex. The layers are thermally bonded to form a contiguous textile material that is able to both breathe and wick moisture away from the skin (ResMed Inc, 2011). Additionally, Velcro tabs are thermally bonded to the textile to provide a fastening method. As described in Section 8.6.2

The headgear was modelled using fully integrated membrane shell elements (LS-DYNA formulation 9). The thickness ($t = 2.8$mm) and profile of the elements was assumed to be constant. To increase modelling efficiency, only the anterior portion of the face and head was modelled. No attempt was made to model the wrapping of

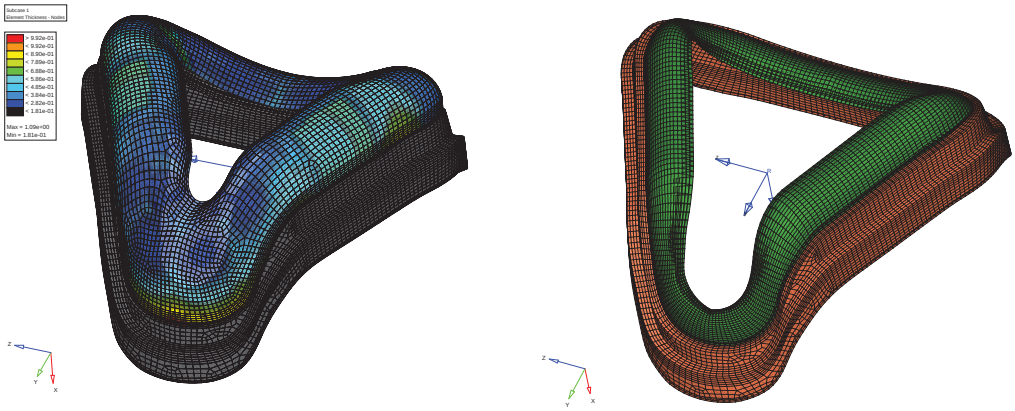

(a) UMII mesh showing membrane variable thickness shells

(b) UMII mesh showing body and undercushion

Figure 10.4: UMII cushion mesh

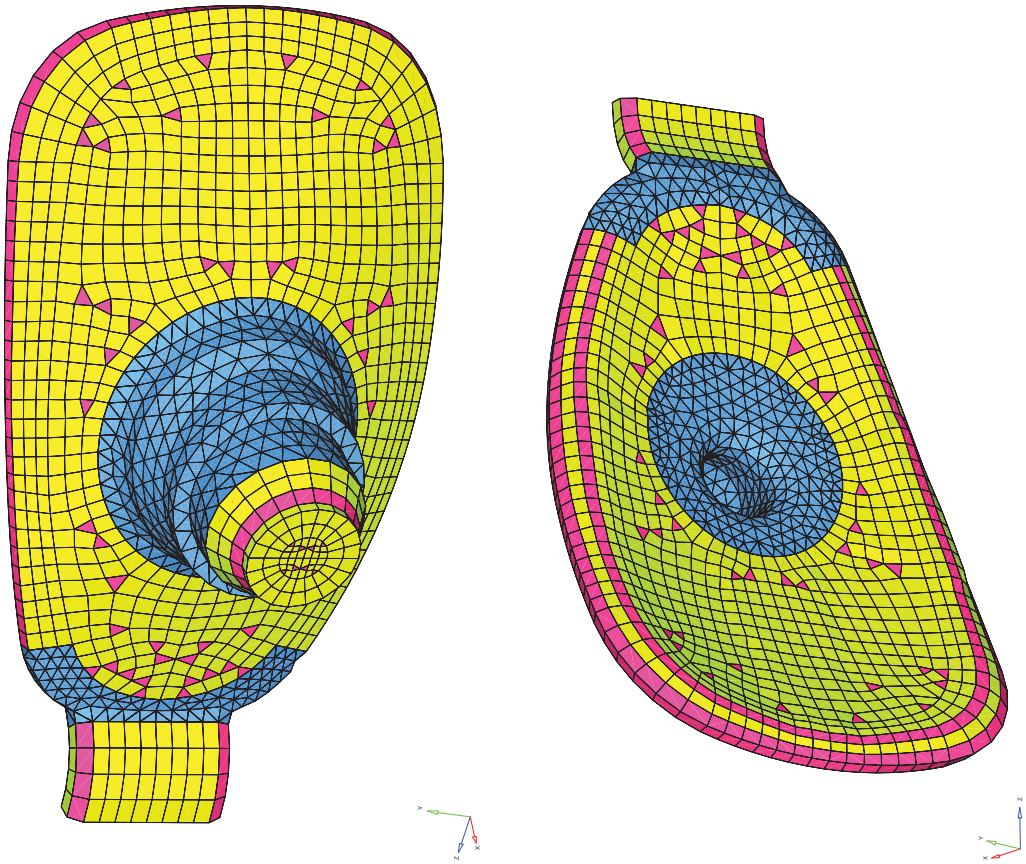

(a) **(b)**

Figure 10.5: a) FHS attachment b) FHS pad

the headgear around the posterior portion of the head, and the interaction between the strands. The headgear was modelled as 4 independent straps.

In order to avoid distortions from the application of point loads, nodal rigid bodies were defined at each end of the straps. The middle node across each of the ends was assigned as the independent node in the constraint. The mask end was connected to the frame nodal rigid body via a frictionless spherical joint between the master node of the headgear rigid body and one of the slave nodes of the frame rigid body. This ensured that forces and not moments were transferred between the frame and the headgear. The free end was used for the application of the headgear tension estimated in Section 8.8 and specified in Table 8.7. This was done either via force control through the application of a point load history or using velocity control to quickly engage the mask prior to switching to force control to settle to the static equilibrium deformation state.

10.4.5 Ultra Mirage II Mask Contact Definition

Contact interactions were defined for various sections of the mask cushion. The contact regions were defined for interaction between a) the membrane and the undercushion which is the principal load path, b) the membrane and the external surfaces of the mask body and c) self contact of the membrane if it folds onto itself. Within LS-DYNA, the newer automatic contact algorithm was used for all these interfaces. The automatic contact surfaces search for contact on both the +ve and −ve surface normal directions of shell elements. The penalty method is used for the contact surfaces in the mask model. Due to the compliant nature of the materials used, the `SOFT` contact formulation is used for each of the definitions. When using the `SOFT` formulation the penalty stiffness is calculated according to the timestep used in the explicit integration step.

$$k\left(t\right) = 0.5 * SLSFAC * SFS\left(\frac{m_1 m_2}{m_1 + m_2}\right)\left(\frac{1}{\Delta t_c\left(t\right)}\right)^2 \tag{10.8}$$

,

where $SLSFAC$ is a global scale penalty scale factor [1], SFS, SFM are scale factors for the slave and master segments respectively, m_i are the segment masses of the slave and master segments and Δt_c is the contact timestep [2]. A similar relation exists for the master segment.

[1] Default $SLSFAC = 0.1$ (LSTC, 2010)

[2] $\Delta t_c = 1.05\Delta t_0$ which is the initial timestep. If at any time the current explicit timestep $\Delta t > \Delta t_c$, Δt_c is reset to $\Delta t_c = 1.05\Delta t$

Table 10.1: UMII LSR material properties for a 3 parameter Mooney Rivlin model.

Property	Value	
ρ	$1.12\,(10^{-3})$	g/mm^3
ν	0.499	
C_{10}	$0.4489\,(10^{6})$	Pa
C_{01}	$-0.3198\,(10^{6})$	Pa
C_{11}	$0.2781\,(10^{6})$	Pa

As per the UMII models, a nominal static and dynamic friction coefficient of $\mu_s = \mu_d = 0.1$ was used.

10.4.6 Material Properties

Liquid Silicone Rubber

The mask cushion and FHS are manufactured from a clear compliant silicone rubber, Dow Corning LSR (94-595HC). The LSR exhibits the typical characteristics of rubber materials of near incompressibility. Therefore, hyperelastic modelling of the material behaviour is appropriate. The material properties were determined by fitting a non linear strain energy density function to mechanical test results across a range of independent testing modes according to the recommendations of (Ogden *et al.*, 2004), refer to Appendix C. This was subsequently modified slightly to provide a better fit to the mechanical behaviour of the cantilevered spring of the undercushion under compressive loading, which is the dominant mode in the mask from the interface with the face. Refer to Appendices D and E for details. A three parameter Mooney Rivlin model was used to model the mask material properties. The near incompressibility of the elastomer was modelled by assuming a Poisson's ratio close to the incompressible limit of $\nu = 0.5$. The density ($\rho = 1.12\,(10^{-3})$ g/mm^3)was taken from manufacturer's published data sheets. The material parameters used are outlined in Table 10.1. The strain energy function of the three parameter Mooney Rivlin model is given by

$$\Psi = C_{10}\,(I_1 - 3) + C_{01}\,(I_2 - 3) + C_{11}\,(I_1 - 3)\,(I_2 - 3) \tag{10.9}$$

Breath-O-Prene

The material properties of the headgear were tested internally at ResMed and were found to have an elastic modulus of $E \approx 1$MPa.

10.5 Face Models

10.5.1 Geometry Preparation and Mesh Strategy

The MRI volume data acquired from the CPAP MRI experimental study, were segmented using AVIZO to allocate voxels to one of a number of materials, namely skin, fat, muscle and cartilage as well as materials for the skull consisting of the mandible and the cranium. This was described in detail in Section 8.6.6. Additionally null materials named *Exterior* were also generated to define limits on the enclosed volume. Triangular faceted surfaces were extracted from the boundaries between these material groups, and define an enclosed volume for each of these materials. This faceted surface can then be used to seed tetrahedral meshes using for example the advancing front method for use in subsequent FEA simulations.

The soft tissues on the human face form an extremely complex freeform geometric shape. Therefore, the use of tetrahedral elements is very attractive as they offer the advantage of easily being able to fill an arbitrary volume of complex shape. Unfortunately linear tetrahedral elements often exhibit overly stiff behaviour and are prone to shear and volumetric locking which can pathologically stiffen the structure and degrade solution quality (LSTC, 2006; Cook *et al.*, 1989). Therefore, a hybrid meshing strategy was used for this study.

Several methods of hybrid meshing were investigated for this project. These include the use of traditional CAD based mesh generation, image based meshing methods such as the enhanced volumetric marching cubes outlined by Young *et al.* (2008) and hex core remeshing. The CAD based mesh generation has the advantage of generating high quality elements mapped to geometry, however for complicated geometry this method can be laborious and time consuming. The image based meshing method is linked to the underlying voxel structure of the scan volume. The hybrid mesh is generated by voxel meshing in the interior of the model and then dividing the voxels at a boundary that the isosurface passes through according to a lookup table based on the intersection topology. This has the benefit of being quick and extremely robust with regular element quality. Hexahedral elements are attempted to be extended to the boundaries of the model, subject to mesh quality criteria. Regions of high curvature on the boundary are meshed with tetrahedral elements, which transition to the hexahedral core of the mesh. Hex core remeshing modifies the interior of a tetrahedral volume by either developing a cartesian grid mesh transitioning to a tetrahedral mesh or combining tetrahedral elements to form hexahedrons. The outer layers of the mesh remain as tetrahedral elements. As the region of interest in this scenario is the nasal region, which is of high curvature with

thin soft tissue depth over the skull, any of the hex core mesh options would result in a purely tetrahedral mesh of only 2 or 3 elements through the thickness within the region of interest around the nose. This region will be under compressive contact loading from the mask, so adequate capture of the stress or strain gradients and large deformations around the contact region will require a greater mesh density and higher quality elements. Therefore, the more laborious CAD based meshing method was adopted for the model, which provides increased mesh density and high quality elements in and near the contact regions. First order elements were used for both the hexahedral mesh and also the tetrahedral mesh. This ensured that, despite the boundaries not being topologically compatible, the same degrees of freedom were active at each of the shared nodes and no special handling was required.

Each of the manifold boundaries of the skull, skin, cartilage and nares were exported individually on the same global coordinate system. A reverse engineering step was then used to fit Non Uniform Rational B-Spline (NURBS) CAD surfaces to the geometry for each of these volumes using Geomagic ®. Initial Graphics Exchange Specification (IGES) surfaces were created for each of the components. Enclosed volumes were converted into solid bodies. The CAD geometry was subsequently imported into HyperMesh ®for hybrid mesh generation. Boolean operations were used to generate topologically consistent models of the face and skull where connectivity to partitioning surfaces in adjoining volumes is shared. This ensures that the mesh in adjacent volumes is compatible and that nodes are shared between elements in the adjacent volumes.

The facial model was divided into regions for meshing. These are the forehead, nasal, anterior, mandibular, left and right sides. The forehead region was defined by a plane normal to the global Y axis passing through the glabella. The mandibular region was similarly defined by a plane normal to the Y axis below the inferior level of the ramus of mandible to form a mappable region. The nasal region is bounded by the margin of the nasal cavity on the maxilla and nasal bones, and inferiorly by the projection from the base of the nose to the maxilla. The anterior region surrounds the nasal region and is bounded inferiorly by the mandibular region, superiorly by the forehead region and laterally by a curve proceeding from the exocanthion inferiorly down the lateral margin of the orbit to the inferior margin of the zygomatic arch before following the blend into the maxilla and inferiorly to the plane defining the mandibular region. The left and right regions are bounded medially by the previously described bounding surface of the anterior region. The superior and inferior borders are given by the parallel planes through the glabella and mandible. The posterior boundary of these regions is a plane normal to the global X axis passing through the saddle on the ramus of mandible midway between

the *coronoid process* and the *head of mandible*. The partitioning of the soft tissue volume into mappable regions is shown in Figure 10.6.

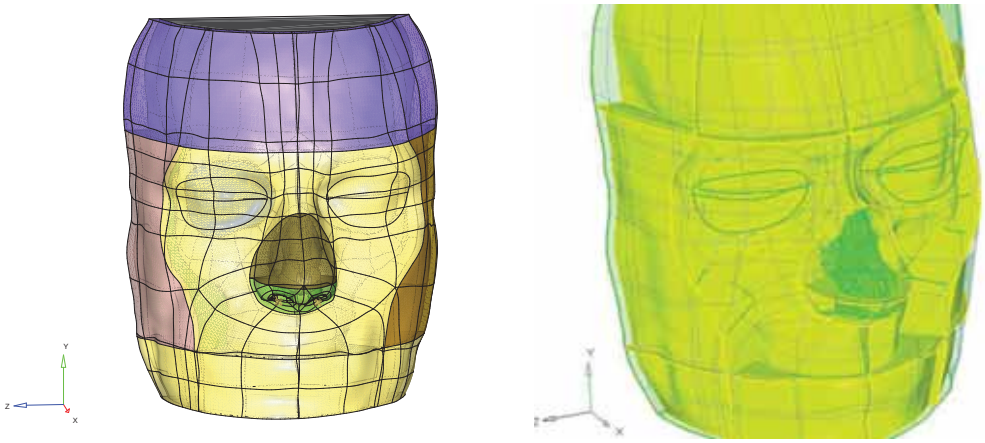

(a) Facial soft tissue partitioned into mappable and tetrahedral mesh regions

(b) View showing shared partition surfaces separating regions in solid yellow

Figure 10.6: Sample soft tissue geometry

10.5.2 Face Mesh

The skin was assumed to be of constant thickness ($t = 3$mm) after inspection of the MRI data in the left and right regions. Additionally the thickness of the skin was locally adjusted in some regions remote to the region of interest to ensure topological consistency of the hexahedral mesh over subject specific abnormalities such as bony prominences or dents.

A coarse hexahedral mesh (1^{st} order, 8 nodes) was initially mapped to the forehead, anterior and mandibular regions as well as the skin on the left and right sides. A nominal element size of 2mm was used throughout the model. A mesh refinement study was performed to ensure that an appropriate mesh density was used in the region of interest radiating out from the nose. This study is described in Section 10.11.1. The result of the mesh refinement study indicated that a 1mm mesh size was appropriate for this model, and meshes were revised and subsequently prepared accordingly.

Due to the complicated and varying shape of the participant's noses in this study, the nasal region was modelled using tetrahedral elements (1^{st} order, 4 nodes). The nasal region consists of the nares, nasal cartilage and the soft tissue overlying the nose. Since the bony material of the skull has an elastic modulus of several orders of magnitude greater than the soft tissue, it acts to shield any of the interior tissues from a load path. Therefore, the posterior margin of the nasal region is taken at the

depth of the maxilla at the nasal cavity and does not protrude further posteriorly. The nostrils are modelled and extend to this level. The full airway is not modelled. Similarly the cartilage and soft tissues are modelled to the same extent. The nominal mesh size of the tetrahedral region is 1.0mm, curvature proximity meshing was used for the nasal region to refine the surface seed mesh in high curvature regions.

The lateral regions on the left and right consist of highly complex geometry that are most efficiently modelled using tetrahedrons (1^{st} order, 4 nodes). These incorporate the volume bordered by the ramus of mandible, the zygomatic arch, the orbit and the temporal bones. As mentioned previously the skull acts to shield the soft tissues deep to them from externally applied loads. Therefore, these deep tissues are not modelled and interpolated surfaces were defined as a boundary to enclose a volume of the superficial tissues, allowing the deep tissues to be neglected. The left and right soft tissue regions were seeded with the surfaces of the hexahedral mapped mesh so that nodes and degrees of freedom are shared between the hexahedral and tetrahedral meshes. In some cases in local regions the hexahedral mesh provided a poor element seed, in this case the tetrahedral mesh was prepared independently and tied contacts were used to constrain the meshes together. Since the side regions are remote to the region of interest a larger element size was used (3 mm) for the sake of computational efficiency. Curvature and proximity refinement were used to ensure fidelity to the extracted geometry and discretisation deviations from the prepared geometry was minimised.

Since the models were prepared with shared topology between the solid volumes, nodes will be shared across this boundary, ensuring that the meshes are compatible if like elements types are connected (hex to hex or tet to tet) or at least share DOF for dissimilar element types. This is exploited in the generation of the skull tetrahedral mesh. As the skull is modelled as a rigid body, the elements are not used in the stress calculation algorithms at all, however the surface facets can be used for contact calculations as is the case in this model. The skull - soft tissue interface is modelled as a frictionless contact surface. Therefore, in order to minimise the risk of initial penetrations between the skull and the soft tissue shared nodes are used to seed the enclosed volume of the skull. The advancing front method was then used to fill the volume with tetrahedral elements. Mesh expansion was used to increase element size away from the boundary of the material. The skull was then detached from the soft tissues to allow relative movement between the two components.

10.5.3 Material Properties

Material Allocation

After meshing the soft tissues, it was required to allocate the elements to their correct material group. This was done on an element by element basis according to the segmentation already performed using AVIZO. This task was implemented using Matlab by estimating each element's centroid location in space, and affine transformation matrix was then calculated to transform this location from global cartesian coordinates to voxel index coordinates. The real indicial coordinates were rounded to provide index values. The voxel index integer values were assumed to refer to the centre of the voxel in accordance with the DICOM standard (Committee, 2007). The voxel indices were then used to look up the allocated material of the voxel that the centroid falls within. The element was allocated to this material group. A transfer file was written and then imported back into Hypermesh to overwrite the element associations and assign elements to the correct material groups. A sample mesh is shown in Figure 10.7.

Skin

The dominant loading mode on the skin is compressive, normal to its surface through the contact regions between the face and mask, as it is positively located on the face to both seal and resist lift of from internal pressurisation. The majority of constitutive testing and modelling that has been performed on the skin is in the plane of the membrane, leaving the normal direction unconstrained with deformation governed by the incompressibility assumption. Numerous models have been proposed for the non-linear behaviour of skin, however for the current application, these are inadequate. Examples include the Arruda and Boyce (1993) which was implemented for skin by Bischoff *et al.* (2000), however as this is an isotropic model, this mechanical behaviour is also applied in the normal direction which results in an excessively stiff response under compressive loading. Anisotropic models have been proposed by Tong and Fung (1976), Lanir (1983) and more recently Kvistedal and Nielsen (2009). Though capturing the non-linear and anisotropic behaviour of the skin, these models are two dimensional and do not consider out of plane loadings. Additionally the primary purpose of this analysis was to develop subject specific models, the extensive work required to develop and validate a suitable 3D anisotropic constitutive model made this impractical and worthy of a project itself. Therefore, it was decided to utilise a linear material property which was tuned for the compressive properties of skin. The published values of Jachowicz *et al.* (2007) were used for the initial

(a) Subject specific mesh of the skull and nasal cartilage. Element edges are not shown for clarity

(b) Subject specific mesh of the soft tissue showing the muscle (red) and fat (grey) materials

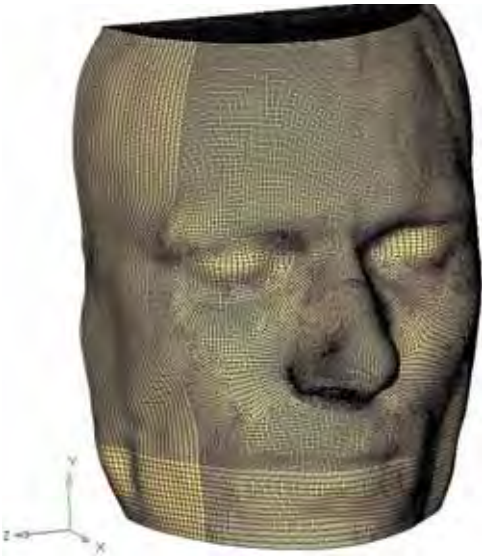

(c) Subject specific mesh of the soft tissue showing the skin layer

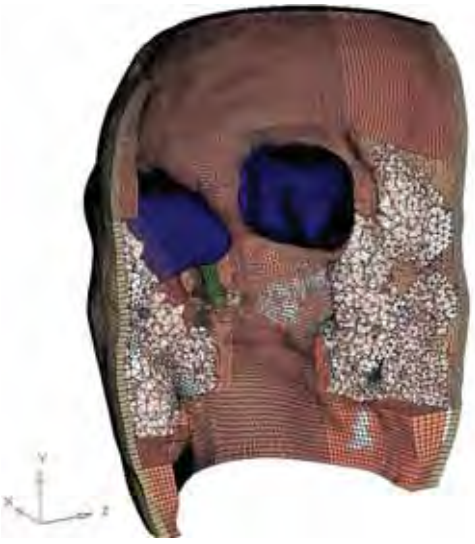

(d) Reverse view of the mesh with the skull not shown and the muscle tetrahedrons transparent. Note the concentration of fat in the cheek region

Figure 10.7: Sample subject specific mesh showing illustrating the hybrid meshing approach adopted and the layered arrangement of the soft tissues supported by the rigid skull.

Table 10.2: Nominal mechanical properties of skin used in the face models

Parameter	Value	Notes
E (Pa)	16000	(Jachowicz *et al.*, 2007)
ν	0.45	Assumed, reduced from incompressibility limit for stability
ρ (g/mm^3)	0.001	Skin

Table 10.3: Mechanical properties of fat used in the face models

Parameter	Value	Notes
C_{10} (Pa)	265	(Sims *et al.*, 2010)
ρ (g/mm^3)	0.0009	(Duck, 1990)

properties as they were acquired from a compressive test applied to the forehead of subjects, matching both the mode of testing and region of the body. The skin properties used in the nominal models are shown in Table 10.2

Fat

The hyperelastic properties used in these analyses for the subdermal adipose tissue are specified in Table 10.3. These values were determined from a series of experiments performed on porcine subdermal adipose tissue. The samples were loaded in compression and an inverse FEA procedure was used to estimate both the elastic and visco-elastic parameters of the materials. This study is defined in detail in Chapter 9.

Muscle

Muscle is a complex material with a transversely isotropic arrangement arising from the ordered fibrous nature of the material. The muscles in the facial region consist of the muscles of mastication and the muscles of facial expression. These are arranged to lie under the skin with the fibre direction approximately parallel to the skin, therefore, the compressive load path is in the plane of isotropy, transverse to the fibre direction. It was assumed that the muscle tissue was relaxed for the simulation. Few studies have investigated the passive transverse properties of skeletal muscle. Van Loocke *et al.* (2006) investigated the mechanical behaviour of passive muscle in compression at various orientations from the fibre to the transverse directions. They used this set of data to populate an anisotropic elasticity matrix with strain dependent moduli. In a different study, Bosboom *et al.* (2001) investigated the *in vivo* compressive passive transverse mechanical properties of rat tibialis anterior muscle

Table 10.4: Mechanical properties of muscle used in the face models

Parameter	Value	Notes
C_{10} (Pa)	287	Derived from (Van Loocke *et al.*, 2006)
C_{20} (Pa)	529	Derived from (Van Loocke *et al.*, 2006)
ρ (g/mm^3)	0.0011	(Duck, 1990)

and fitted the results to an Ogden isotropic hyperelastic model. It is important to note that the stress/strain response of these two studies differ remarkably. This could be due to incomplete inhibition of muscle tone during anaesthesia and the differences in in vivo test conditions (Bosboom *et al.*, 2001) compared to explanted, trimmed samples (Van Loocke *et al.*, 2006). Considering this vast range of published mechanical properties, the use of both material properties were investigated in the FEA model during development. Using the mechanical properties from the study of Bosboom *et al.* (2001) resulted in small and widely distributed deformations indicating that this material property was too rigid. The material properties derived from Van Loocke *et al.* (2006) in comparison provided a much deeper and more localised deformation which matched the experimental results much better. Therefore, the passive transverse load characteristic from the study by Van Loocke *et al.* (2006) was used for the simulations. In order to use these data, they were digitised and then a Yeoh hyperelastic model was fitted using a non-linear least squares method. Since the Yeoh model is dependent only on the 1^{st} strain invariant, it is less susceptible to spurious deformations in alternate deformation modes. The incompressible strain energy density function is given by,

$$\Psi = C_{10}\left(I_1 - 3\right) + C_{20}\left(I_1 - 3\right)^2 \tag{10.10}$$

The robustness of the model was checked for alternate deformation modes by deforming a sample block in tension, pure shear and biaxial tension. All models were stable. Therefore, the Yeoh model fitted to the passive transverse test data of Van Loocke *et al.* (2006) was used in the CPAP FEA simulations. The nominal parameters for the model are shown in Table 10.4. The Yeoh model is isotropic, this simplifying assumption was accepted for these models as the primary load path is in the transverse plane of symmetry and muscle stonia during sleep provides minimal restraint on the sliding filaments of the muscle. This assumption is outlined in more detail in Section 6.5.

Table 10.5: Mechanical properties of nasal cartilage used in the face models

Parameter	Value	Notes
E (Pa)	234000	(Rotter *et al.*, 2002)
ν	0.45	Assumed, reduced from incompressibility limit for stability
ρ (g/mm^3)	0.001	(Duck, 1990)

Nasal Cartilage

The nasal cartilage was modelled as a linear elastic material in line with the study of Rotter *et al.* (2002). The mechanical properties of the nasal cartilage material model are shown in Table 10.5.

10.5.4 Facial Contact Interfaces

Skull - Soft Tissue Contact

The skull provides a rigid foundation that supports the soft tissues, however apart from muscle insertions, the superficial soft tissues are free to slide over the skull, as can be readily observed by palpation. Therefore, to accurately model the mechanics of the soft tissue on the face it is important to consider the contact interfaces in the facial model. Three contact regions are defined in the model. These are the interfaces between the skull and soft tissues, the upper and lower lips and a numerical stabilisation region known as interior contact which helps to resist element inversions under extreme deformations.

The skull to soft tissue contact was defined in LS-DYNA as a segment based version (`SOFT=2`) of the penalty contact formulation. In this case the contact algorithm considers the contact element as a whole and not just node by node penetrations, therefore, penetrations are distributed loads across all nodes in the segment. The soft formulations determines the penalty stiffness for the segment based on explicit timestep stability criteria rather than the elastic properties of the underlying materials. LS-DYNA does allow for release of contact if the interpenetration of the segments is too great, the nodes exceeding a threshold are released. This allows for failure modelling. It was noticed during the development of the model that under the FHS contact, a number of soft tissue nodes were penetrating the skull and being released. This was undesirable and was addressed by scaling the penalty stiffness of the skull-soft tissue contact interface using the parameters SFS and SFM. The calculation penalty contact stiffness for the slave side is given by (LSTC, 2006),

Table 10.6: Skull to soft tissue contact

Description	Contact surface between the skull and soft tissue.
Type	Automatic Surface to Surface
Algorithm	Penalty, Segment based
Scale Factors	$SFS = SFM = 4.0$
Friction	0.0
Initial State	Penetrations ignored

Table 10.7: Labial contact

Description	Contact between the upper and lower lips
Type	Automatic Surface to Surface
Algorithm	Penalty, Segment based
Scale Factors	$SFS = SFM = 1.0$
Friction	0.0
Initial State	Penetrations ignored

$$k\left(t\right) = 0.5 * SLSFAC * SFS\left(\frac{m_1 m_2}{m_1 + m_2}\right)\left(\frac{1}{\Delta t_c\left(t\right)}\right)^2 \tag{10.11}$$

,

where $SLSFAC$ is a global scale penalty scale factor [3], SFS, SFM are scale factors for the slave and master segments respectively, m_i are the segment masses of the slave and master segments and Δt_c is the contact timestep [4]. A similar relation exists for the master segment.

Labial Contact

The opening of the mouth is adjacent to the region of interest, and hence needed to be modelled with care. The opening of the mouth was modelled by detaching the upper elements at the level of the lips from the lower elements. The free surface was then used to generate a contact interface. The segment based algorithm was used and friction was neglected. Refer to Table 10.5 for details.

Interior Contact

Due the the very soft nature of the materials being used in this model, the avoidance of inversion of elements during the engagement of the mask is a challenge in this

[3] Default $SLSFAC = 0.1$ (LSTC, 2010)

[4] $\Delta t_c = 1.05\Delta t_0$ which is the initial timestep. If at any time the current explicit timestep $\Delta t > \Delta t_c$, Δt_c is reset to $\Delta t_c = 1.05\Delta t$

Table 10.8: Interior contact

Description	Numerical aid to resist inverted elements under extreme deformations
Type	Interior
Algorithm	Penalty

project. Assisting in this regard is the interior contact algorithm which was activated for the tetrahedral elements in the model. The interior contact algorithm activates when the material is compressed to a stretch of 0.2. At this point penalty stiffness is added to the elements to help resist element inversion and solution termination. Refer to Table 10.8 for details.

10.5.5 Boundary Conditions

In the CPAP FEA assembly model, the face is constrained and the mask's position is determined by equilibrium conditions. Therefore, the constraints on the face were assigned within the face sub model. The applied boundary conditions were as follows.

X Symmetry

The posterior margin of the model is defined by a cut normal to the X axis midway between the *coronoid process* and the *head of mandible*. A symmetry condition normal to the $\boldsymbol{X}$ axis was applied to this cut surface This surface was constrained as shown in Figure 10.8a.

Y Symmetry

The upper and lower borders of the model normal to the $\boldsymbol{Y}$ axis were similarly constrained with a symmetry condition. This is shown in Figure 10.8a

Fully Fixed Skull and Cartilage

As mentioned previously the skull forms a rigid foundation for the soft tissues. In LS-DYNA the skull was modelled as a rigid body and fully constrained at its centroid.This is included in the rigid material card.

The nasal cartilage is continuous with the skull. Posteriorly this is through the perpendicular *vomer* bone. This provides fixation at to the nasal cartilage at the posterior region. Therefore, the trim surface of the cartilage is applied as fully fixed boundary condition to the displacement DOFs asshown in Figure 10.8b.

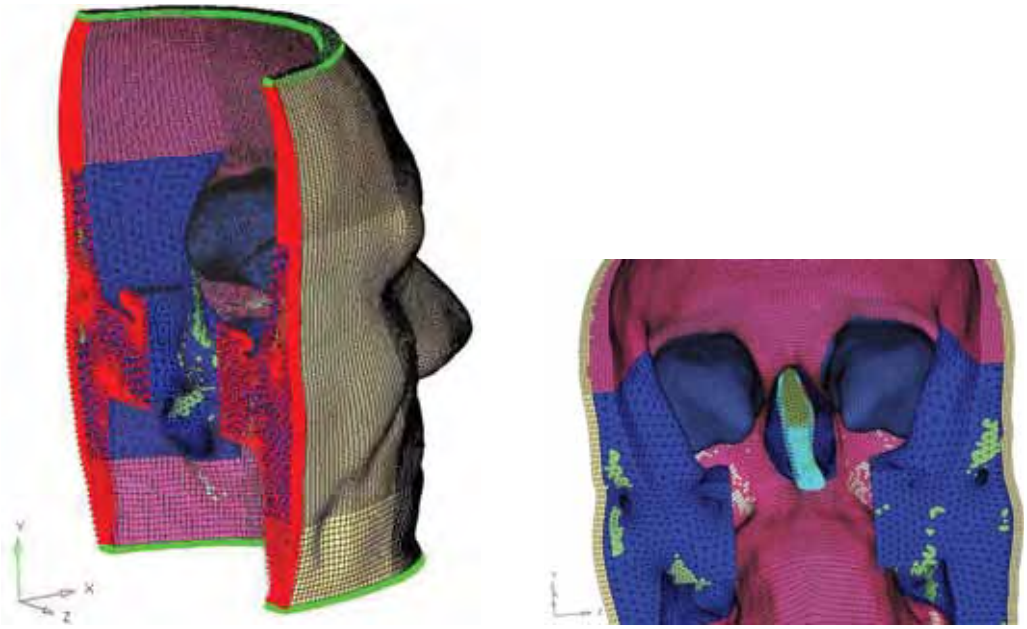

(a) $\boldsymbol{X}$ (red) and $\boldsymbol{Y}$ (green) planar constraints

(b) Fully fixed constraint applied to the cartilage

Figure 10.8: Boundary conditions on extremity surfaces. red: $\boldsymbol{X}$, green: $\boldsymbol{Y}$, cyan: Fully fixed

Table 10.9: Muscle attachment constraint descriptions

Muscle	Location
Masseter	Zygomatic arch
	Ramus of mandible
Temporalis	Temporal bone
	Coronoid process of mandible
Buccinator	Mandible
Nasalis	Nasal bone (inferior margin)
Levator anguli oris	Maxilla
Orbital Group	Medial portion of orbit
Depressor labii inferioris	Mandible
Incisivus labii superioris	Maxilla

Additional soft tissue nodes were spatially constrained to mimic the insertion of various individual muscles from the muscles of facial expression and mastication groups. These nodes were fully constrained in all spatial DOFs. The muscle groups that were constrained are shown in Figure 10.9. Locations were selected based on muscle attachment diagrams from Gray's Anatomy (Williams *et al.*, 1989e).

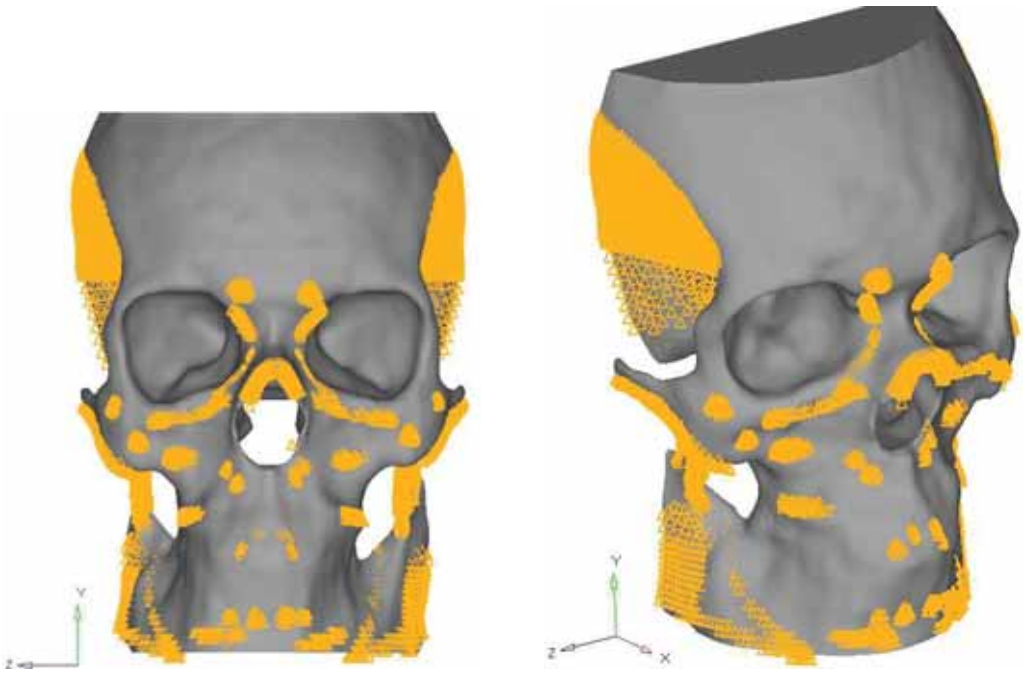

(a) (b)

Figure 10.9: Muscle attachment constraints.

10.6 Top Level Assembly Models

The mask and face models have been independently prepared with respect to their own local coordinate systems, the anatomically defined system of the facial model was used as the global origin for the top level assembly models. To create a top level assembly model of a patient undergoing CPAP therapy, the appropriate configuration mask model was then imported into the top level FEA assembly model. The mask was approximately positioned with the FHS located anteriorly just clear of the forehead and vertically to ensure that the cushion of the mask engages directly with the upper lip, avoiding significant contact with the nasal septum or pronasale during engagement. Additionally the mask was oriented such that the FHS would engage first and act as a pivot while the mask engaged with the nasal region of the face. The headgear elements were rotated to match up with the approximate level orientation of the headgear from the profile photographs of the participants. In the event of intersections between the headgear and the head, the headgear elements were rotated to be lateral to the head to remove any penetrations. The top level assembly model is shown in Figure 10.10

10.6.1 Face / Mask Assembly Contact Definitions

The interaction between the mask and the face are central to these simulation. The mask and face interact through contact interfaces in different anatomical regions. These are the nasal, forehead, cheek and the temporal regions.

Face / Membrane Contact

The primary interface of interest between the face and the mask is the nasal region. The `SOFT` penalty formulation was used for this interface with the penalty stiffness based on a stability criterion rather than the underlying stiffness of the elements. To aid portability from model to model, the exterior surfaces of the soft tissue elements were selected if they were enclosed in a selection volume. This allowed the contact segment set definition to be independent of the index numbers of the elements involved. The membrane consists of variable thickness shell elements with a minimum thickness of approximately 0.35mm. This very thin shell does cause difficulties with the penalty contact algorithm which uses the underlying thickness to determine the maximum allowable penetration prior to releasing nodes from contact. In accordance with LS-DYNA recommendations the contact parameter `SFST`=2 was used to scale the thickness of the shells used in the contact calculations by a factor of

Table 10.10: Face to membrane contact definition

Description	Contact surface between the nasal region of the face and the membrane of the mask.
Type	Automatic Surface to Surface
Algorithm	Penalty, Soft formulation
Scale Factors	$SFST = 2.0$
Friction	0.1
Initial State	No penetrations

2 to correspond to the minimum recommended shell contact thickness of $0.6-0.7$mm (LSTC, 2011). This resolved the issue with nodes being released from contact.

A significant assumption that has been made for this contact interface is regarding the friction. A Coulomb friction model was used. Since this is a quasi-static model the static and dynamic friction coefficients were assumed to be equal with a value of $\mu_S = \mu_D = 0.1$. This value is reduced from published values of skin on silicone with a frictional coefficient estimated in the range of $0.47 \geq \mu_D \geq 0.57$ with the exception of the palmar skin with a significantly higher value of $\mu_D = 0.93$ (Zhang and Mak, 1999). Additionally, unpublished testing estimated the static coefficient of friction between skin and the LSR used in the masks to be greater than unity ($\mu_s > 1.0$) (ResMed Inc).

The application of a high Coulomb static friction coefficient in line with the findings of Zhang and Mak (1999) was investigated. The large sliding encountered during the engagement and settling of the mask on the face presented difficulties when solved using a high coefficient of friction. This was manifest in highly distorted elements as the shear component of the surface traction induced excessive deformations in elements in or near the contact interface, which in turn caused the solution to terminate. Therefore, as mentioned previously the simulations were modelled with a nominal friction coefficient of $\mu_S = \mu_D = 0.1$. While it is acknowledged that this assumption is a departure from physiological conditions, the influence of this is reduced by the settling and adjustment process that the participants use when placing and adjusting the mask, and the repeated pressure swings encountered each respiratory cycle. The extreme deformations encountered with a high coefficient of friction are also attributable to the simple soft model for skin that was used for the simulations that did not account for the biaxial locking behaviour of skin as the collagen fibres are straightened and recruited into load bearing.

Table 10.11: Forehead to FHS contact definition

Description	Contact surface between the forehead region of the face and the FHS of the mask.
Type	Automatic Surface to Surface
Algorithm	Penalty, Soft segment based formulation
Scale Factors	-
Friction	0.4
Initial State	No penetrations

Table 10.12: Head to headgear strap contact definition

Description	Contact surface between the head and the headgear straps of the mask.
Type	Automatic Surface to Surface
Algorithm	Penalty, Soft segment based formulation
Scale Factors	-
Friction	0.1
Initial State	No penetrations

Forehead / FHS Contact

The forehead is also an important contact region as it defines a major load path supporting the mask. The nature of the contact here is simpler than the nasal region as the contact is approximately normal to the surface in an easily mapped mesh, and a large engagement stage is not required, allowing for a more realistic friction coefficient of $\mu_S = \mu_D = 0.4$ to be used. The segment based penalty method was used for this contact definition.

Head / Headgear Contact

The final contact to describe in the model is between the head and the forehead. Four of these regions were defined for each of the upper, lower, left and right straps. The segment based algorithm was used, which assists in distributing the loads at the straps wrap around sharp edges at the posterior end of the model. A nominal friction coefficient of $\mu_S = \mu_D = 0.1$ was used.

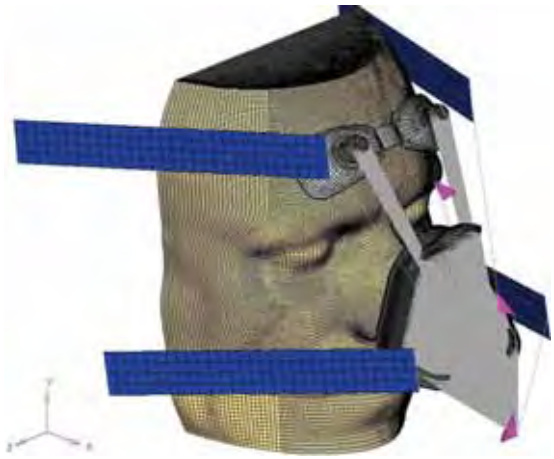

(a) 3D view of CPAP FEA mesh

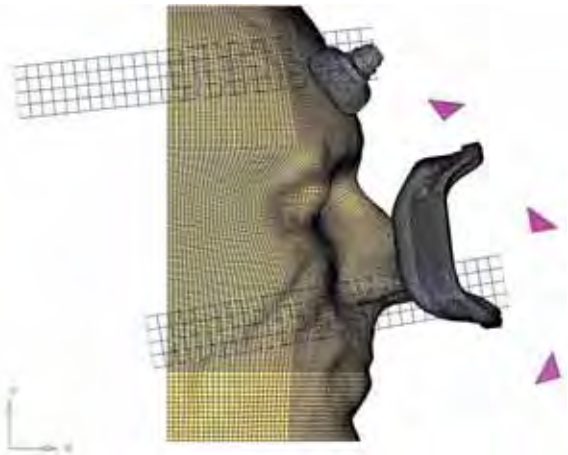

(b) Lateral view of CPAP FEA mesh

(c) Anterior view of CPAP FEA mesh

Figure 10.10: Sample CPAP FEA model

10.7 Assembly Applied Loads

The simulation of nasal CPAP therapy requires the engagement of the mask on the face as well as the application of realistic therapeutic loads. The model was assumed to be quasi-static. The loads applied to the model are due to gravity, headgear tension and the CPAP pressure.

10.7.1 Gravitational Load

A simplifying assumption was made for the application of the gravitational component loads applied to the face by the mask. The load was applied as an equivalent force/couple system at the independent node of the mask frame rigid body. The load was calculated at the centre of mass of the mask and assumed to act in the $-X$ direction of the global coordinate system. The gravitational force incorporated the inertia of the frame and tube calculated in Appendices A and B ($m = 97$g) and the mass of the deformable LSR components extracted from the mass properties of the mask model ($m = 26.5$g),

$$m = 26.5 + 97.0 = 123.5\text{g} \tag{10.12}$$

$$\boldsymbol{g} = \begin{bmatrix} -9806.7 & 0 & 0 \end{bmatrix} \text{mm/s}^2 \tag{10.13}$$

$$\boldsymbol{F}_g = m\boldsymbol{g} \tag{10.14}$$

$$= \begin{bmatrix} -1.211 & 0 & 0 \end{bmatrix} 10^6 \mu\text{N} \tag{10.15}$$

Since the load was applied at the independent node of the nodal rigid body, it is offset from the centre of mass of the mask. Therefore, a couple was required to generate a statically equivalent load,

$$\boldsymbol{M}_g = \boldsymbol{r} \times \boldsymbol{F}_g \tag{10.16}$$

where $\boldsymbol{r}$ is the vector from the independent node to the centre of mass of the mask. The gravitational moment was calculated on the approximate final position of the mask when stabilised and was assumed to remain constant throughout the simulation. The moment arm varies according to the position of the TBar on the mask. The applied moments are specified in Table 10.5.

The inertial force was applied to the model as a static load rather than as a body force due to the influence of mass scaling on the overall result. Mass scaling was used in the model to bring the run time down to a practical level. Since the

Table 10.13: UMII gravitational moment loads according to FHS position

FHS Position	Moment ($10^6 \mu$Nmm)
1	$\begin{bmatrix} 0 & 0 & 21.29 \end{bmatrix}$
2	$\begin{bmatrix} 0 & 0 & 20.89 \end{bmatrix}$
3	$\begin{bmatrix} 0 & 0 & 20.38 \end{bmatrix}$
4	$\begin{bmatrix} 0 & 0 & 19.80 \end{bmatrix}$

explicit integration algorithm is conditionally stable, the timestep is required to be less than a critical value which is known as the Courant criterion and corresponds to the period of time a wave takes to propagate across the smallest element dimension in the model. Considering the wave equation, this can be seen to be a function of element size, mass density and material properties. For an undamped system, the critical timestep is given by $t_c = 2/\omega_{max}$. This is governed by the maximum element natural frequency (LSTC, 2006). Mass scaling is a commonly used technique in explicit analysis that allows the run time to be shortened by artificially increasing the density of the elements and increasing t_c. This has the undesired result of increasing the contributions of the inertial term ($\boldsymbol{M}\ddot{\boldsymbol{x}}$) and the body force ($g \int_V \rho \mathrm{d}V$) in the equation of motion. Therefore, the kinetic energy of the system must be monitored to ensure that the artificial mass is not altering the energy of the system significantly (LSTC, 2011). In the case of a quasi-static analysis the kinetic energy should be a small fraction of the internal or strain energy. As equilibrium is reached the time dependent terms in the equation of motion approach zero and the state of the model is purely a function of its deformation and the influence of mass scaling is minimal. However as body forces are dependent on density the use of mass scaling can alter the static equilibrium. This was noticed during model development where small element edges on the transition regions of the undercushion exhibited significant mass increase and this excess mass distorted the contact forces between the face and the mask. Impractical run times were encountered without the use of mass scaling, therefore, a modelling decision was made to remove inertial loading from the model, neglecting gravitational accelerations and applying the equivalent load as a force couple system, thereby conserving the correct load paths and magnitudes for the contact interfaces between the face and the mask.

10.7.2 Headgear Load

Nodal point loads were applied to the independent nodes of each of the straps for the headgear. The force was applied in the $-X$ direction with the straps being free to adopt an equilibrium position laterally. The vertical position of the straps was

constrained to match approximately with the strap positions on each of the participants. Models were prepared corresponding to the subject specific experimental conditions. The forces applied to the straps are outlined in Table 8.7 (p 98).

The headgear forces were applied to the model as a ramp hold function. The load was increased gradually over 0.25s simulation time. The load was then held constant for the remainder of the simulation. This corresponded to the way the experiment was set up with force control being used to adjust the tension in the mask according to patient preference. The static equilibrium of the pressurised mask on the face was the endpoint of this analysis. To further advance this model the headgear could have been constrained after equilibrium to mimic the engaging of the Velcro tabs for.

In order to allow comparison between subjects, a further set of models was prepared with each subject using the mean headgear tension results. The mean headgear forces applied were,

$$\boldsymbol{F}_{top} = \begin{bmatrix} -2.173 & 0 & 0 \end{bmatrix} 10^6 \mu\text{N} \tag{10.17}$$

$$\boldsymbol{F}_{btm} = \begin{bmatrix} -2.564 & 0 & 0 \end{bmatrix} 10^6 \mu\text{N} \tag{10.18}$$

$$\tag{10.19}$$

10.7.3 Headgear Enforced Displacement

In order to speed up the mask engagement process with the face, the motion of the pilot nodes at each of the ends of the headgear membranes was controlled using a prescribed velocity in the X degree of freedom. The overall enforced displacement from the prescribed velocity is given by

$$\boldsymbol{x} = k_i \int_0^t \dot{\boldsymbol{x}} \mathrm{d}t, \tag{10.20}$$

where k_i is a scale factor and $\boldsymbol{x}$ is defined as a function of time. It was convenient to choose a function with the following definition.

$$v_x(t) = \begin{cases} 20t & : 0 \leq t < 0.05 \\ 1 & : 0.05 \leq t < 1.0 \\ 21 - 20t & : 1.0 \leq t < 1.05 \\ 0 & : 1.05 \leq t \leq 1.1 \\ - & : 1.1 < t \end{cases} \tag{10.21}$$

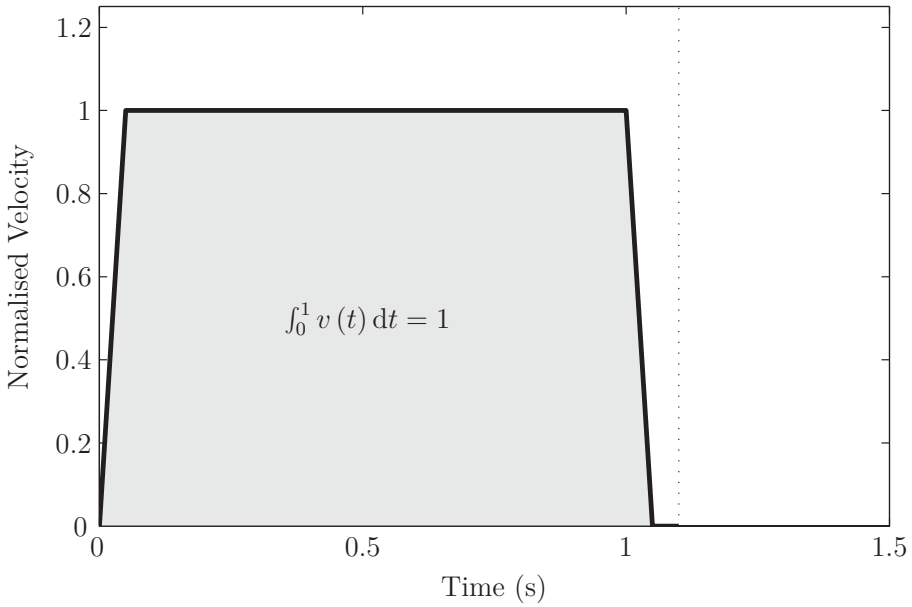

Figure 10.11: Prescribed velocity

Since the area under the curve is equal to 1, the scale factor corresponds to the enforced displacement as shown in Figure 10.11. Unwanted transient effects were avoided by ramping the velocity to and from zero. The scale factors were chosen based on previous force controlled runs. After engaging the mask with the face, the prescribed velocity control was removed at $t = 1.1$s, at which point the mask is force controlled and settles to equilibrium governed by the headgear tension.

10.7.4 CPAP Pressure Therapy Load

The CPAP therapy pressure was chosen to be set at 10cm H_2O for this experiment model. It is critical that a consistent unit system (mm, g, s) be used for the analyses. This requires pressure to be in units of Pascals. Therefore, the pressure applied to the air contact regions is

$$P = 980.67\text{Pa} \tag{10.22}$$

The CPAP therapy pressure acts on the interior surfaces of the mask, possibly a small portion of the external surface of the membrane that is on the high pressure side of the seal with the face and is not held in intimate contact with the underlying face, and the face within the bounds of the sealed region on the face. Note that the membrane is assumed to be predominantly in intimate contact with the nose at the end of the engagement stage, therefore allowing the contact pressure to be applied to the internal surface of the membrane. Figure 11.3a shows that the membrane is in intimate contact with the nose with the exception of some wrinkles, which

Table 10.14: UMII Frame pressure force resultant applied at the mask frame centre of mass for a pressure of P=10 cm H_2O

	X	Y	Z	Magnitude
$\boldsymbol{f}_{\text{cg}}$ $(10^6\mu\text{N})$	0.1188	-2.3074	-0.0346	2.311
$\boldsymbol{m}_{\text{cg}}$ $(10^6\mu\text{Nmm})$	-0.1145	1.9402	-129.7664	129.78

only cover a small portion of the area, reinforcing this assumption. The interior surfaces of the mask that the pressure is directly applied to as a segment load are the membrane and the internal surfaces of the cushion from the connection with the membrane, over the undercushion to the level of the groove that interfaces with the frame. Beyond this the frame is modelled as a nodal rigid body, and hence does not have any inherent geometry, however the projected area of the frame enclosing the volume must be accounted for. Therefore, the effect of the internal pressure on the frame is resolved back to a force/couple system applied at the independent node of the rigid body, similar to the application of the gravitational load. Importantly the CPAP pressure equivalent load is applied as a follower force and moment, so that the direction of the forces and moment updates with the motion of the mask as it engages and settles on the face mesh. The calculation of the pressure equivalent load is outlined in Appendix G, and are shown in Table 10.6. The equivalent pressure force was calculated with respect to the mask frame inertial coordinate system.

The load is applied using the `LOAD_NODE_POINT` card in LS-DYNA with one card for each of the component directions listed in Table 10.6. This is scaled with reference to a normalised load profile curve, which synchronises with the load history of the applied pressure.

10.7.5 Load Staging

The loads are applied to the mask in order to engage the mask and let it settle into an equilibrium configuration. These are applied over an arbitrary 2.5s simulation time, which was chosen as a balance of reasonable solution time, is of the same order as the events that are being simulated and does not induce a spurious dynamic response in the model which needs to decay. The simulation can be divided into 4 sections, namely engagement, mask stabilisation, pressure application, final stabilisation.

The engagement stage initialises the model. During this stage the mask is rapidly engaged with the face applying gravitational loads which remain constant over the entire solution, headgear forces which were ramped initially and then held constant for the entire solution. The engagement stage was aided by prescribed velocities helping to quickly bring the mask into place and minimise kinetic energy. The mask

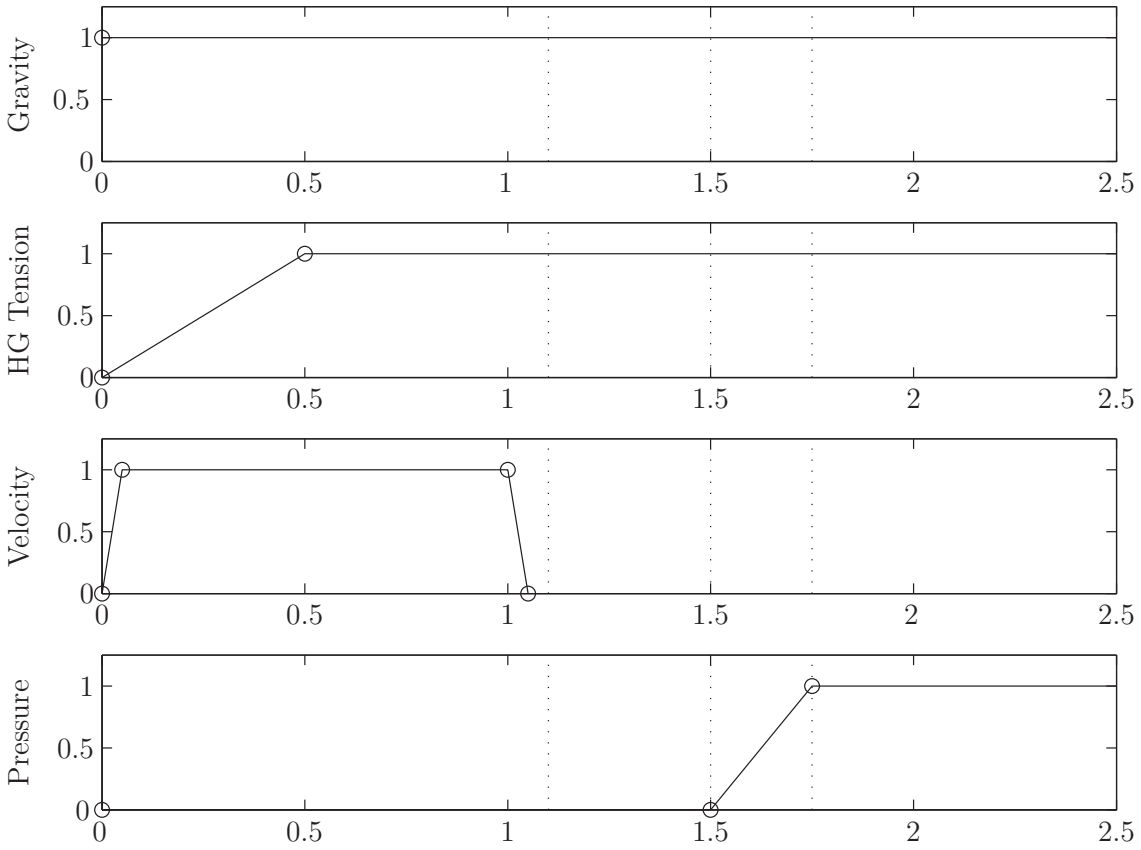

Figure 10.12: Time history of the loads applied to the CPAP FEA model. All curves are normalised so that the actual magnitude and sign of the load is given by the scale factor in the `*LOAD_` card. Vertical dotted lines indicate demarcations between load stages engagement, stabilisation, pressure application and final stabilisation. Note that the prescribed boundary condition is removed at $t = 1.1$s, not simply set to zero, which would act as a fixed constraint.

stabilisation stage is a period of constant load commencing with the removal of the headgear prescribe velocity constraint which allows the mask to settle. Following this the mask is pressurised using a ramped load and finally held constant to stabilise. This is shown in Figure 10.12.

10.8 Simulation Settings and Job Submission

The models were solved using the explicit FEA method with LS-DYNA. During the solution, a number of controls were set. Principal among these was the use of a stiffness based hourglass control on reduced integration elements. Stiffness as opposed to viscous based hourglass control was used due to the quasi-static nature of the simulation. The termination time was set to $t_{end} = 2.5$s. Mass scaling was used to enforce a minimum timestep of $\Delta t = 7.2\mu$s. The mass scaling algorithm adjusted the density of elements with a default calculated timestep of $\Delta t_e < \Delta t$. The adjusted elements were primarily in the undercushion of the mask. Global damping

was applied to the model to damp oscillations and allow the model to approach static equilibrium.

The models were solved using the high performance computer, VAYU at the National Computing Infrastructure (NCI). VAYU is a 64 bit Linux system The models were run in shared memory mode using 64bit architecture on 8 parallel CPUs in a temporary scratch directory. Models were submitted through the PBS batch queueing system. Each model was checkpointed and killed at regular intervals then resubmitted recursively and restarted until the termination time was reached. This was done to break the models into smaller jobs which are processed through the queue more quickly and use computational resources more efficiently. The large models using the above computational resources took up to 30 hours of wall time to solve.

Binary nodal results were output for accelerations, velocities and displacements as well as contact forces and boundary reactions. Binary element results that were written to file include the stress and strain tensors. These results were output at a coarse interval of 0.15s prior to the pressure application stage, at which point the results interval was reduced to 0.05s. In addition a series of ascii result files were also generated to capture history data throughout the solution. These included nodal motion results, total energy summations, material specific energy summations, joint resultant forces and contact region resultant forces.

10.9 Postprocessing

After each simulation was completed, the FEA results were prepared for comparison with the experimental results. This was done by importing a triangulated surface mesh of the FEA skin surface in the reference configuration into Matlab along with the corresponding experimental surfaces. The deformed nodal coordinates output from LS-DYNA were read into Matlab, therefore, providing a surface mesh in the reference and deformed configurations. The surface normal deformation was calculated using the same method as was used for the experimental results as outlined in Section 8.6.8. In order to enable comparison between the FEA and experimental mesh, the results of one must be mapped onto the other. In this case it was chosen to map the FEA results onto the experimental surface mesh using a linear isoparametric interpolation method. A sample set of FEA and experimental results are shown in Figure 10.13.

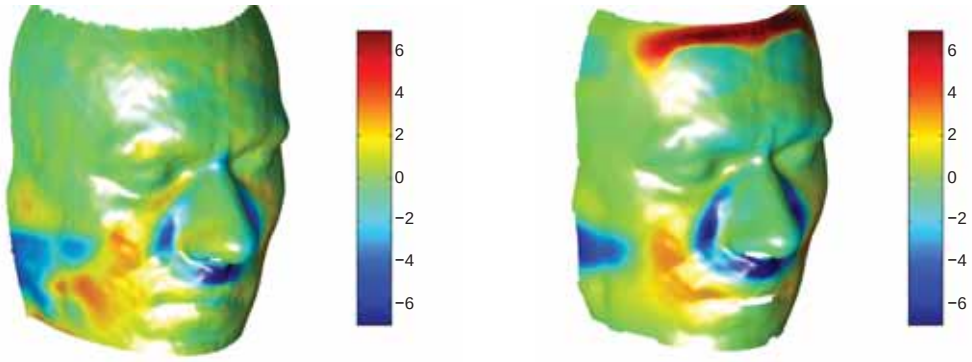

(a) Experimental signed normal deformation field (mm)

(b) FEA signed normal deformation field (mm)

Figure 10.13: Experimental and FEA comparison

10.10 Regions of Interest

The primary ROI in the simulations is the nasal region. This in turn for reporting of results can be subdivided into four smaller ROIs are in four regions around the nose. These are the upper lip, left base of the nose, right base of the nose and the nasion. The landmarks were then used to seed an ellipsoid selection region with each cluster of 4 landmarks defining the $\boldsymbol{a}$ and $\boldsymbol{b}$ axes of the ellipsoid. The third axis was chosen to be large to ensure that local surface curvature did not eliminate portions that lie off the plane of the $\boldsymbol{a}$ and $\boldsymbol{b}$, yet not so large as to include backfacing surfaces from a further intersection with the ellipsoid. The placement of the ROI landmarks is outlined in Table 10.15 and shown in Figure 10.14.

The above defined regions are used to report and compare results from the FEA and experimental data sets. The nodal values and interpolated fields were also used to approximate surface integrals using Gaussian quadrature of scalar result fields. The surface integral was calculated as outlined in Appendix I.

Calculated quantities of interest are the deformation field, and contact parameters such as pressure and area.

Table 10.15: Region of interest landmark descriptions

Landmark	Region	Description
1	Upper Lip	On the RHS nasolabial sulcus at the level of the mid-philtrum
2	Upper Lip	On the LHS nasolabial sulcus at the level of the mid-philtrum
3	Upper Lip	Approximately on the mid-sagittal plane at the base of the nasal septum
4	Upper Lip	Approximately on the mid-sagittal plane immediately superior to the margin of the upper lip
5	RHS	Laterally Adjacent to the RHS ala
6	RHS	On the line from point 5 to the RHS endocanthion at the level of the soft tissue fold above the orbitale
7	RHS	Offset from the midpoint of 5 and 6 on the surface of the nose, used to orient selection ellipsoid
8	RHS	Offset from the midpoint of 5 and 6 towards the orbitale on the skin superficial to the maxilla, used to orient selection ellipsoid
9	LHS	Laterally Adjacent to the LHS ala
10	LHS	On the line from point 9 to the LHS endocanthion at the level of the soft tissue fold above the orbitale
11	LHS	Offset from the midpoint of 9 and 10 on the surface of the nose, used to orient selection ellipsoid
12	LHS	Offset from the midpoint of 9 and 10 towards the orbitale on the skin superficial to the maxilla, used to orient selection ellipsoid
13	Nasion	Right endocanthion
14	Nasion	Left endocanthion
15	Nasion	Glabella
16	Nasion	On the midsagittal plane offset equally below the nasion as the glabella is above the nasion

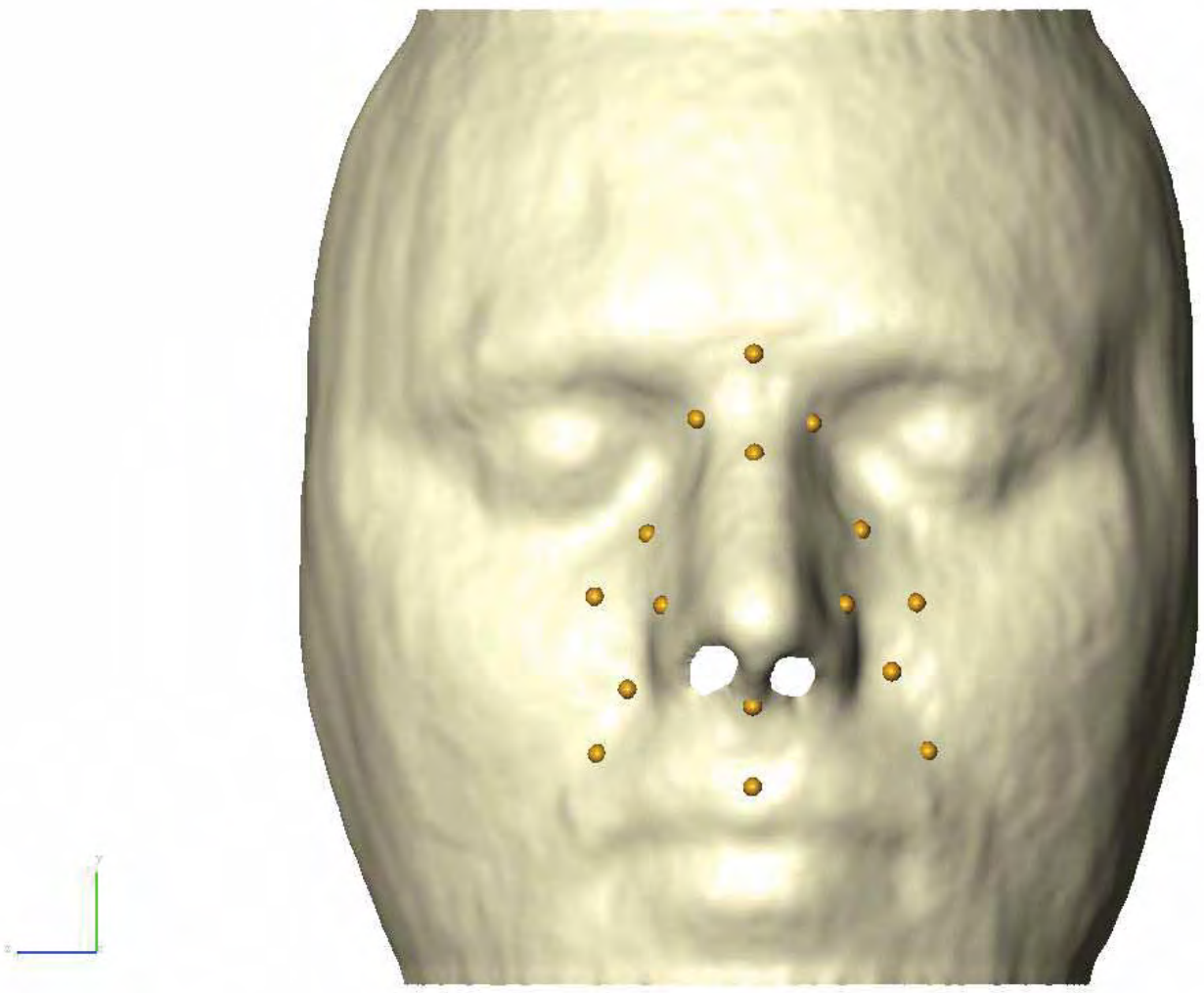

Figure 10.14: Sample subject showing anatomical landmarks used to define ROIs

10.11 Validation

A number of model validation exercises were performed in the development of the CPAP FEA models. These were a mesh refinement study, evaluation of the quasi-static assumption and a balance of applied loads.

Subject 12 was chosen for this evaluation of the modelling strategy. This participant was one of the extreme data points based on BMI. Subject 12 had the lowest BMI of all the participants ($BMI = 17.7\text{kg/m}^2$). Additionally this subject chose to fit the face mask with a very high headgear tension of 2.42N on the lower straps This was anticipated to create the most challenging model scenario with little room for load dissipation through the soft tissue thickness to the underlying rigid skull, and potentially large compressive strains being encountered.

10.11.1 Mesh Refinement Study

In order to assure that an appropriate element size was used for the FEA models a systematic mesh refinement study was performed on the region of interest, namely the nasal region and its surrounds. Subject 12 was chosen as the face mesh to use for this task, and this was the participant with the lowest BMI and hence leanest body structure. This was anticipated to be the most challenging modelling scenario with reduced tissue bulk in the facial region leading to lower soft tissue thickness. For mapped meshing this will reduce element quality as the elements flatten with a reduced overall thickness dimension. The aspect ratio increases away from the ideal value of 1 for a cube.

A systematic series of analyses were performed on a series of meshes for subject 12 with element sizes in the region of interest given in Table 10.5. The facial meshes that were used in the mesh refinement study are shown in Figure 10.15.

The initial model was developed with a nominal surface mesh size of 2mm in the nasal region. A free meshing algorithm was used to generate the mesh. This was then mapped to the volume bounded by the skull surface. The nose itself was map meshed. This is not in the primary load path after the mask is fully engaged with

Table 10.16: Subject 12 mesh refinement study: element edge length and number of elements through the thickness of soft tissue in the nasal region

Simulation	Edge Length (mm)	No. Elem thickness
1	2	9
2	1	9
3	0.5	12

the face, therefore, this region was maintained at a constant element size (1mm). For the 2mm and 0.5mm mesh sizes, the interface between the face and nose was modelled using a tied constraint. The mesh was not refined in the thickness direction between run 1 and 2, as the mesh refinement significantly improves the aspect ratio and hence quality of the elements. The refinement to 0.5mm refines the elements to approximately maintain the aspect ratio of the elements in the upper lip which increase in aspect ratio with mesh refinement.

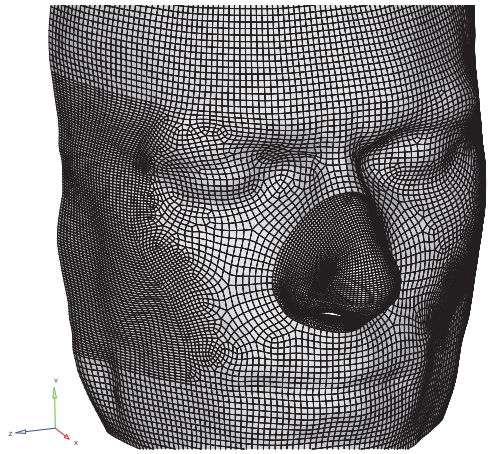

(a) Subject 12 - 2mm nominal mesh size

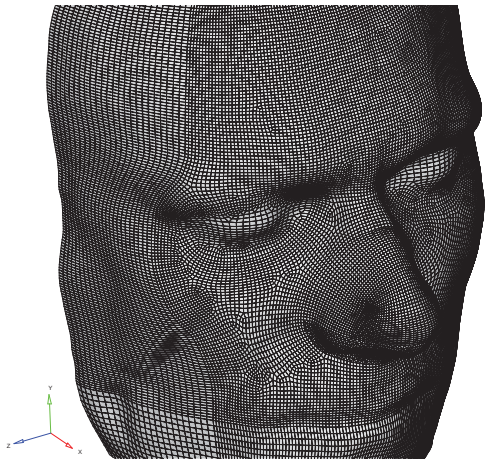

(b) Subject 12 - 1mm nominal mesh size

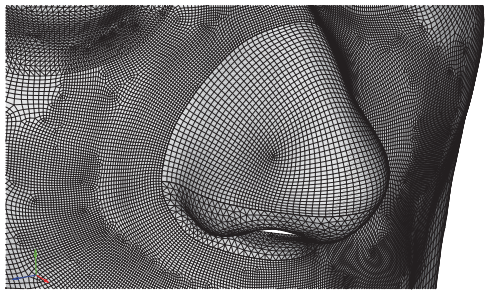

(c) Subject 12 - 0.5mm nominal mesh size

Figure 10.15: Subject 12 mesh refinement mesh iterations

As described in Section 10.5.5, symmetry boundary conditions are applied to the posterior, superior and inferior trim surfaces to represent the continuum interface with the adjacent material. The skull was considered to be a fully fixed rigid body. Muscle attachments to the skull were fully fixed. The UMII mask was positioned so that there were no initial penetrations with the face. The history of loads applied to mask are shown in Figure 10.16. The prescribed velocity was used to quickly engage the mask with the face. The enforced displacement from the prescribed velocity is given by

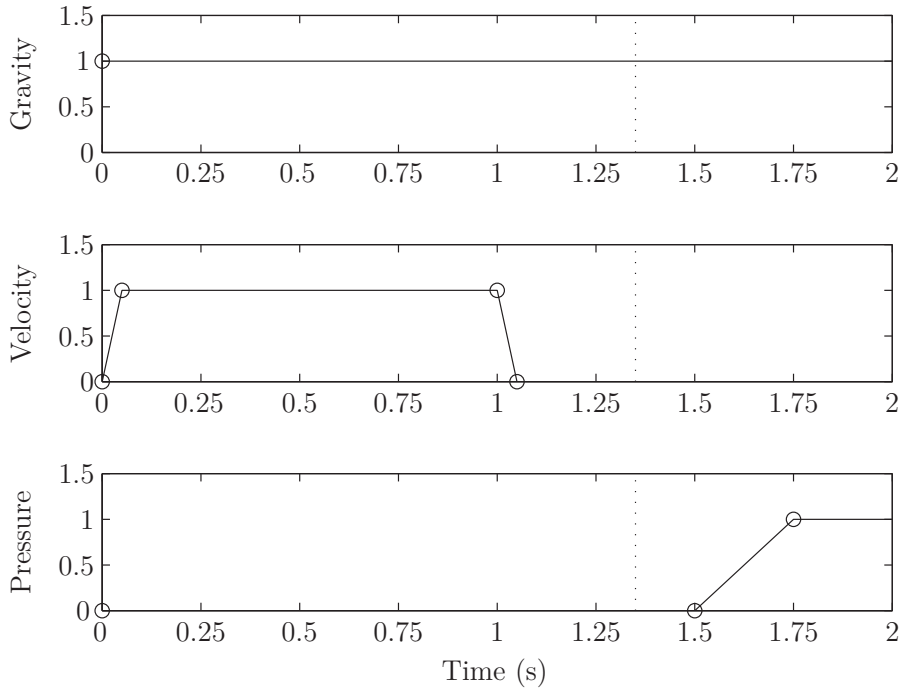

Figure 10.16: Time history showing normalised loads applied to the CPAP FEA model. Internal LS-DYNA scale factors were applied to the normalised curves to specify each load. Gravity was applied constantly throughout the solution. The mask was engaged on the face quickly using a prescribed velocity boundary condition on the head gear strap end nodes. The area under the velocity curve was chosen to be unity so that the scale factor would define the enforced displacement precisely. The CPAP pressure loads were applied after the mask was fully engaged with the face. The vertical dotted line at $t = 1.35s$ is the time that the refinement comparison was performed

$$\boldsymbol{x} = k_i \int_0^t \dot{\boldsymbol{x}} \mathrm{d}t, \tag{10.23}$$

, where k_i is a scale factor. Since the area under the curve is equal to 1, the scale factor corresponds to the enforced displacement. Unwanted transient effects were avoided by ramping the velocity to and from zero. The scale factors were chosen based on rigid series force controlled runs. After engaging the mask with the face, a period is allowed until $t = 1.5$s for transients to decay and static equilibrium conditions to be established. At a solution time of $t = 1.5$s the CPAP pressure of 10 cmH_2O is applied and sustained. The pressure is ramped over 0.25s.

Each of the models were solved with a termination time of $t = 2.5$s. The 2mm and 1mm mesh models solved to completion. The 0.5mm mesh model solved to t=1.4s before a distorted element caused a numerical instability in the solution. However inspection of the total kinetic energy traces from each of the runs indicate that the model is essentially in static equilibrium after $t = 1.3$s with the mask fully engaged on the face. Therefore, results at this timestamp prior to the termination

Table 10.17: Displacement convergence

		Philtrum		LHS		RHS	
Run	Mesh Size	Ux (mm)	% error	Ux (mm)	% error	Ux (mm)	% error
1	2	-7.81	-	-6.17	-	-6.10	-
2	1	-7.87	0.7%	-6.22	0.9%	-6.21	1.8%
3	0.5	-7.69	2.3%	-6.38	2.4%	-6.32	1.7%

Table 10.18: Pressure Convergence

		Philtrum		LHS		RHS	
Run	Mesh Size	P (kPa)	% error	P (kPa)	% error	P (kPa)	% error
1	2	9.27	-	8.18	-	7.49	-
2	1	9.69	4.3%	10.58	22.7%	10.39	27.9%
3	0.5	10.55	8.2%	11.01	3.9%	10.78	3.6%

of the 0.5mm mesh size model can be used for the purpose of evaluating mesh convergence.

Results

The mesh convergence study was performed by comparing primary outputs (nodal displacements) at landmarks of interest and the principal derived quantity of interest, namely contact pressure, in the nasal region for the various models. Results are compared in three regions. These are the philtrum, and adjacent to the nose on the left and right hand sides.

The displacement results converge to well within 5% even at the coarse 2mm mesh size. The contact pressure results on the other hand exhibit much greater sensitivity to mesh size. Averaged nodal contact pressures are shown in Figure 10.17. Both fringe plots and plots of approximately coincident [5] nodal paths for each of the three regions considered are shown. From these results, the 2mm mesh size does not capture the variation or peaks in contact pressure across the contact region that the finer meshes do. In this case the contact pressure was effectively averaged as the nodal reaction forces are distributed over a much larger area. In contrast the 1mm and 0.5mm meshes were able to capture the same characteristics of the contact interface. These include corresponding peak locations and contact pressure profiles in each of the locations. The variation of results from the 2mm mesh to the 1mm mesh was large with a change in contact pressure of over 20% for each side of the nose. The philtrum however shows a small relative difference

[5]The nodal paths are not identical as the underlying geometry in these areas was in the interior of a surface patch and did not follow a surface boundary curve. The free meshing algorithm used paved each mesh slightly differently to optimise element quality

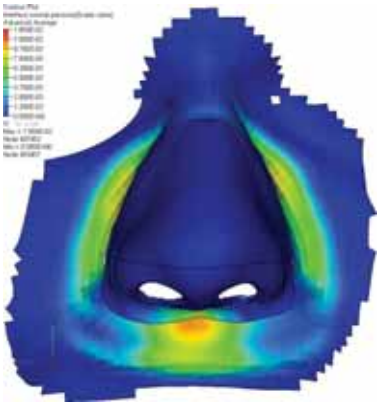

(a) Contact pressure, 2mm mesh

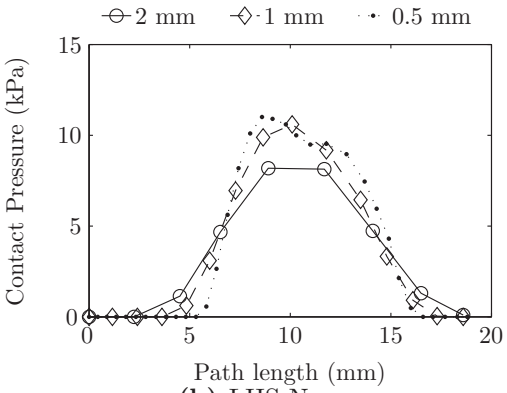

(b) LHS Nose

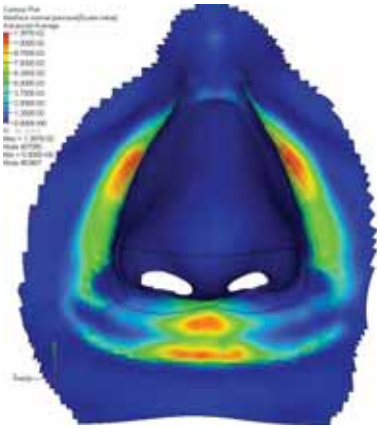

(c) Contact pressure, 1mm mesh

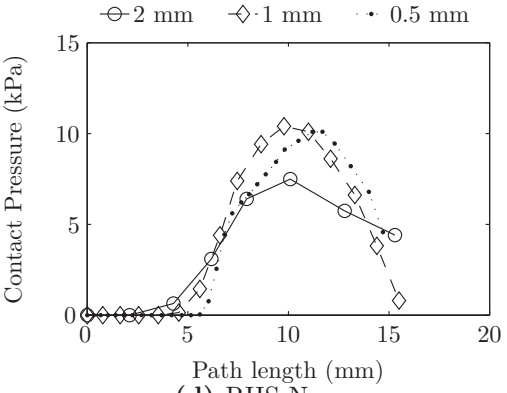

(d) RHS Nose

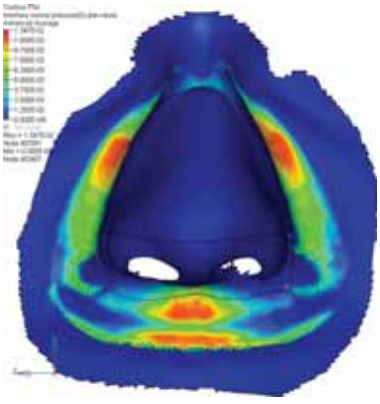

(e) Contact pressure, 0.5mm mesh

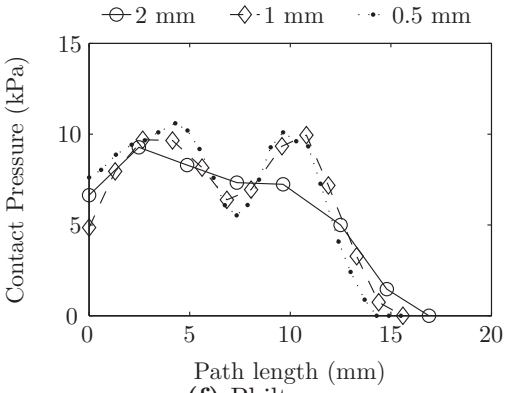

(f) Philtrum

Figure 10.17: Subject 12 contact pressure mesh refinement results

Table 10.19: Solution Summary data

Run	Mesh Size (mm)	WallTime (hr)	NCPUs	Nodes	Elements
1	2	3.75	8	302794	764121
2	1	5.06	8	428065	922164
3	0.5	8.96	8	764882	1218236

between the 2mm and 1mm mesh, however though the magnitude of these results are close, the plots in Figures 10.17a and 10.17f show that the 2mm mesh inadequately captures the contact pressure profile as the inferior contact pressure peak was not captured. The 1mm and 0.5mm meshes both captured this pressure profile, and agreed to well within 10%. All other locations indicated discrepancies between the 1mm and 0.5mm meshes less than 5%.

Discussion

Therefore, from this series of analyses it can be seen that the 2mm mesh size is inadequate as it fails to capture the contact pressure field adequately, as it smooths over some peaks and troughs and tends to underestimate contact pressures on the whole. The 1mm and 0.5mm meshes were shown to capture the same contact pressure characteristics across the entire field. In particular this was most notable on the philtrum where two distinct peaks in contact pressure are identifiable. These correspond to load paths from the undercushion and the body of the cushion where the membrane is folded respectively. The numerical results from the 1mm and 0.5mm models agree to within 8% and on the side of the nose, to within 5%.

A further consideration in the choice of mesh size for the facial models is solution efficiency. The computational demands of each solution are outlined in Table 10.8. Computational demands increase significantly with mesh refinement. There is an increase in solution time of over 75% with the mesh refinement from 1mm to 2mm. This resulted in no change in the nature of the contact detected, and a mesh refinement discrepancy of less than 10% and less than 5% adjacent to the nose.

The instability encountered in the 0.5mm model was manifest with distorted shell elements in the membrane close to the edge of the contact area where it is sandwiched between the undercushion and the face. In this location this was in the vicinity of the shell/solid tied connection, where the shell assumption used for the membrane results in a local sharp edge as the shell connects to the solid on its mid surface, and is hence offset accordingly. This allows an artefact of the nodes on the sharp edge to potentially come into contact with the membrane or face and generate a local disturbance due to artificial concentrated nodal loads.

This analysis has shown that a mesh size of 1mm is adequate to capture the contact pressure field of the nasal mask. Further refinement beyond this reveals minimal mesh dependence with variations in results of only 3-8% at the expense of 75% in computational demands and solution time, and increased sensitivity to disturbances due to the enhanced influence of localised effects due to modelling assumptions. Therefore, in light of these considerations a mesh size of 1mm was chosen for use with all the facial models in this project.

10.11.2 Kinetic Energy Considerations

The engagement of the mask and application of therapy pressure was considered to be a quasi-static problem. This was solved using a fully non-linear dynamic algorithm. Therefore, in order for the quasi-static assumption to be met kinetic energy component must be negligible. Pursuant to the mesh refinement study, the 1mm mesh model was run to completion. The internal and kinetic energies were compared in Figure 10.18. It can be seen that the strain energy stabilises and that the kinetic energy approaches asymptotically towards zero at the equilibrium position. The ratio of the kinetic energy to the internal strain energy indicates that the contribution of kinetic energy is less than 1%. Therefore, this modelling strategy adequately reaches a stable static equilibrium deformed configuration.

10.11.3 Force Balance

The load path from the mask to the face is defined through the contact regions between the face and mask. These include the anterior nasal region, forehead and lateral regions in contact with the headgear. A balance of the applied loads excluding the CPAP pressure and the output contact force reaction forces were used to validate the setup of the model. The CPAP pressure loads were excluded from this validation check as it is very difficult to manually account for the pressure loading on the interior surfaces of the mask, particularly that component that applies to the membrane as this is partially decoupled from the mask, so pressures applied to the membrane are transferred to the face directly, while the pressure acting on the remainder of the frame and cushion reduces the contact force as it tends to lift off the face. Therefore, for this model validation task, the pressure load was not included.

The dominant loading is in the X direction. The loads in the Y and Z directions were not controlled. The sum of applied loads in the X direction were compared to the recovered reaction forces from the contacts between the face and mask of 14.5 N.

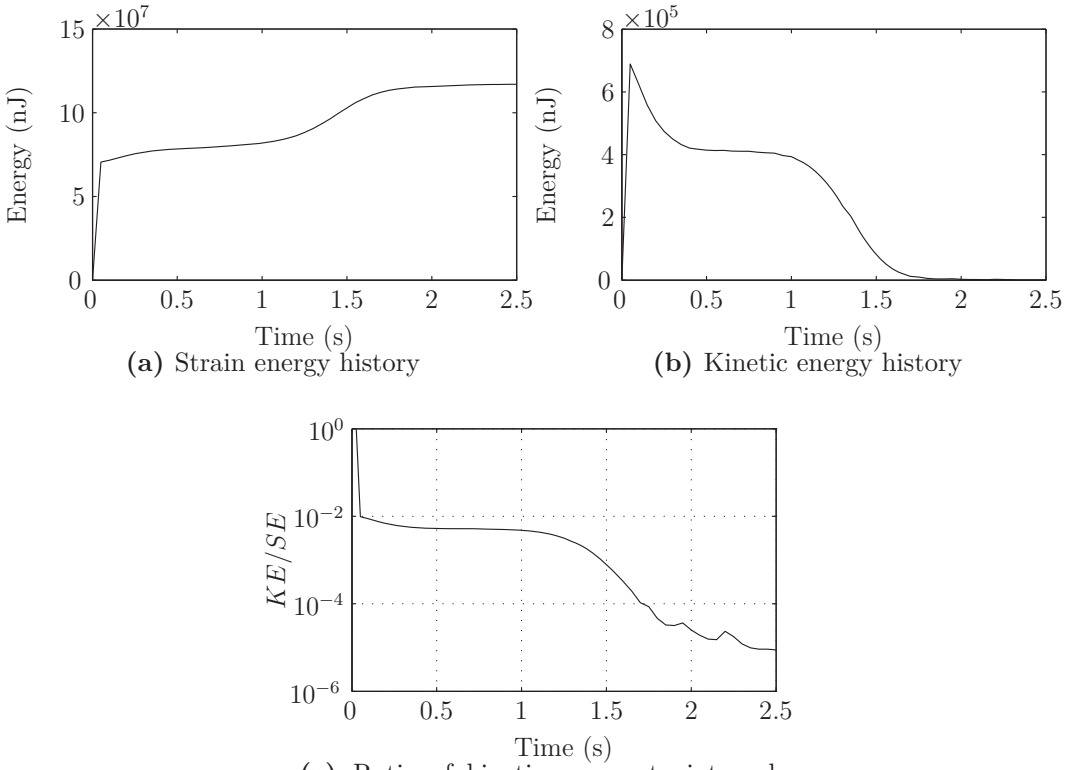

(a) Strain energy history

(b) Kinetic energy history

(c) Ratio of kinetic energy to internal strain energy. Kinetic energy is a small fraction of the internal energy validating the quasi-static nature of the simulation

Figure 10.18: Comparison between internal strain energy and the kinetic energy of the CPAP FEA simulation

These agree to within a close margin of 2.5%. Therefore, the boundary conditions and load paths of the model represent the physical scenario.

10.11.4 Comparison to Experimental Results

The refined model was then solved according to the experimental conditions recorded for that user. The mask was successfully engaged with the face and pressurised to simulate the application of the mask and the CPAP therapy. The FEA nodal displacement results were used to export the deformed geometry. The same algorithm that was used to calculate the experimental signed normal deformation field was used on the simulation results and then interpolated onto the experimental reference mesh. This allows comparison between the experimental and simulation results. Figure 10.19 shows the experimental and FEA results prior to processing the FEA results to provide compatible results to compare.

The overall behaviour of the model corresponds to the behaviour captured in the experiment. There is a prominent indentation around the nasal region incorporating the upper lip as well as the left and right sides of the nose. The nasion has reduced deformation due to the reduced tissue thickness in that region. Laterally the headgear causes a depression in the cheeks, which are also reflected in the experimental results. A qualitative difference of note between the experimental and simulation results can be seen in the forehead region in Figure 10.19. The simulation results show the contact interface of the FHS indenting into soft tissue on the forehead, which is evident on the experimental results. The FEA results however take into account the sliding of the scalp over the frontal bone, whereas the experimental results calculate the deformation normal to the reference configuration of the face at each node, which does not incorporate the tangential motion of the sliding surface. A further difficulty encountered in this model is that the upper limit of the MRI scanned volume only just included the forehead support pads of the mask as the signal began to attenuate. Therefore, the upper boundary of the model was close to the FHS. In order to approximate the presence of solid material beyond the boundary of the model, a symmetry condition normal to the Y direction was applied. Due to the proximity of the FHS contact with the upper boundary, an artifact was introduced into the model which caused the soft tissue to bow away from the skull in an excessive departure from anatomical reality. While the presence of this wrinkling and buckling of the soft tissue on the forehead above the FHS has been observed in the course of this project, this is limited by the aponeurosis of the occipitofrontalis muscle wrapping fully over the top of the skull. In the model, as it terminates just superior to this region the tissue cannot dissipate this deformation over the entire path of the muscle, so the tissue must bulge and lift off from the skull. Removing the upper constraint and allowing free sliding in this region was investigated, however this proceeded to cause numerical problems as elements were distorted by the localised concentrated forces from the edge of the skull. Therefore, it was decided for stability considerations to maintain the upper boundary condition as this is remote to the primary region of interest, which is the nasal region.

The signed normal deformation field was calculated for the simulation results. This is shown along with the signed experimental results in Figure 10.20. It can be seen that the simulation model replicates the primary features of the mechanics evident in the experimental results, with the exception of the region above the FHS where the tissue has buckled and moved away from the frontal bone, as previously described. Despite this artefact, the normal displacement is a much better measure of correlation between the simulation and experimental data sets. The deformation

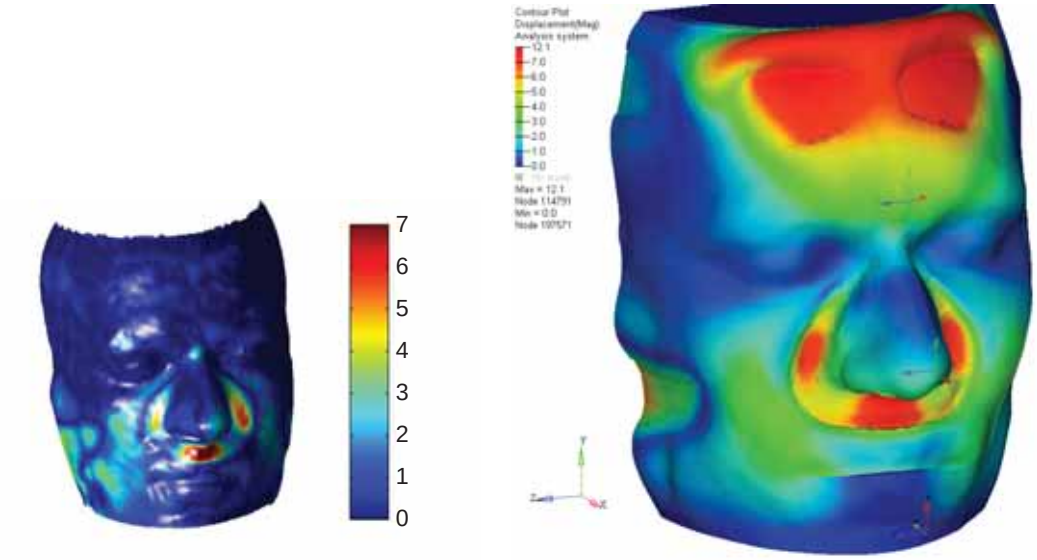

(a) Subject 12 experimental results showing the magnitude of the normal displacement deformation under CPAP therapy.

(b) Subject 12 FEA nodal displacement magnitude

Figure 10.19: Experimental and raw FEA deformation results. Note that these quantities are not yet commensurate and cannot be directly compared.

was interpolated onto the experimental surface mesh for direct comparison and calculation of residuals.

The models were specifically compared in the regions of interest previously defined. Both surface and point based metrics were calculated to compare the FEA and experimental data. Root Mean Square (RMS) values of the scalar result fields and residuals were calculated for each of the ROIs consisting of n sampled points. The calculation for residuals is given as,

$$r_{rms} = \sqrt{\frac{\sum_{i=1}^{n} r_i^2}{n}} \tag{10.24}$$

Node based weighting was used to generate pooled results for the residual scalar field. This was then used to provide a single pass material property refinement for each of the subject specific deformable models prepared for this study. The weighted ROI residual metric r_w was given by

$$r_w = \frac{\sum_{a=1}^{n} N_a r_{a\,rms}}{\sum_{a=1}^{n} N_a} \tag{10.25}$$

The results for this participant's initial simulation are shown in Table 10.8. In this case the initial estimate of the material properties applied to the face have

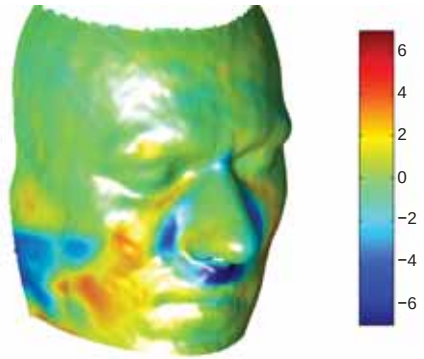

(a) Experimental signed normal deformation field (mm)

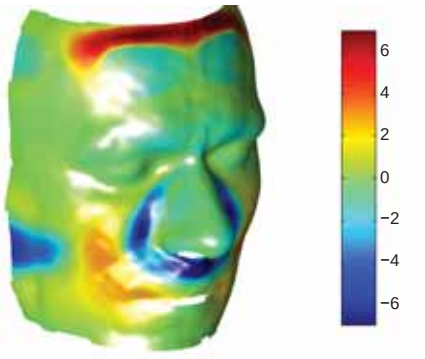

(b) FEA signed normal deformation field (mm)

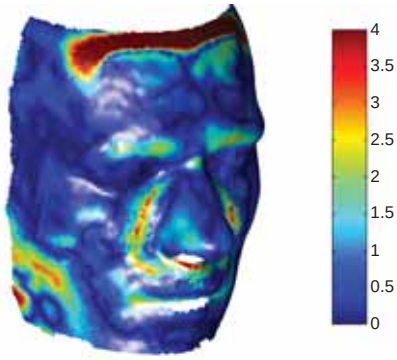

(c) Residual magnitude between experimental and FEA results (mm)

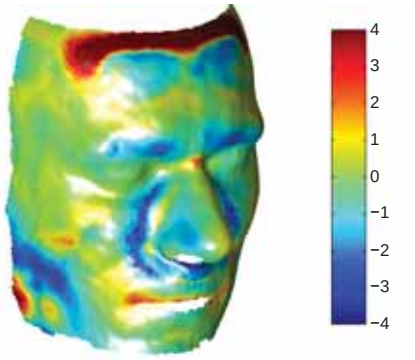

(d) Signed residuals between experimental and FEA results (mm). -ve values indicate that the FEA results have been compressed to a greater degree than the experimental results.

Figure 10.20: Experimental and FEA comparison

Table 10.20: Subject 12 experimental and simulation results

ROI	N	$u_{expt\,min}$ mm	$u_{FEA\,min}$ mm	u_{FEA} at $u_{expt\,min}$ mm	r_{rms} mm
Lip	400	-7.50	-10.84	-10.15	1.96
LHS	284	-5.85	-7.61	-6.93	1.62
RHS	307	-4.66	-7.02	-6.94	1.59
NS	117	-2.86	-1.53	-0.79	0.94
					$r_w = 1.66$

resulted in the mask compressing the soft tissue beyond the deformed state of the face. Therefore, in order to tune the simulation for this subject the mechanical properties local to the regions of interest must be increased.

This has been done using a material parameter perturbation and then using that to provide a single pass material property adjustment. Since the subdermal fat deposits are located laterally to the ROIs around the nasal region and experimental

Table 10.21: Subject 12 material property adjustment summary

	Skin	Muscle (Yeoh)	
α	E (Pa)	C10 (Pa)	C20 (Pa)
1	16000	287.19	529.53
1.15	18400	330.27	608.96
1.479	23664	424.75	783.17

data was obtained for subdermal adipose tissue, the material property adjustment was performed on the skin and muscle material models.

A global material adjustment was made using a common scale factor. The run times of the models and inherent variability of the mechanical properties of soft tissue made a multi factor material localised material property adjustment impractical and the material property adjustment was made as follows.

Let α be a scaling factor such that the relevant material properties C are given by $C = \alpha C_0$. The material properties were perturbed and the model resubmitted with $\alpha = 1.15$. A linear extrapolation was used to adjust the material parameters for the participant based on the sensitivity of the residual weighted RMS values.

$$\hat{r_w} = m\alpha + b \tag{10.26}$$

$$m = \frac{\Delta r_w}{\Delta \alpha} \tag{10.27}$$

$$b = r_{w1} - m\alpha \tag{10.28}$$

$$\tag{10.29}$$

The material property estimation was extrapolated to a target weighted RMS value of $\hat{r_w} = 1.0$mm and the updated scale factor was given by,

$$\hat{\alpha} = \frac{\hat{r_w} - b}{m} \tag{10.30}$$

Therefore, the initial and perturbed properties for the skin and muscle materials are shown in Table 10.21. The improvement in the full field residuals can be seen in Figure 10.21. At this point the model was accepted for further use in the project. This single pass procedure was applied to all of the deformable models used in this project.

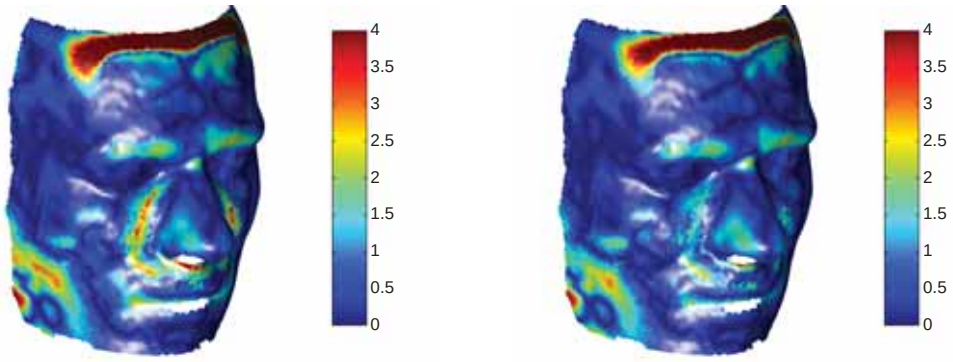

(a) Initial residual magnitude (mm)

(b) Adjusted residual magnitude (mm)

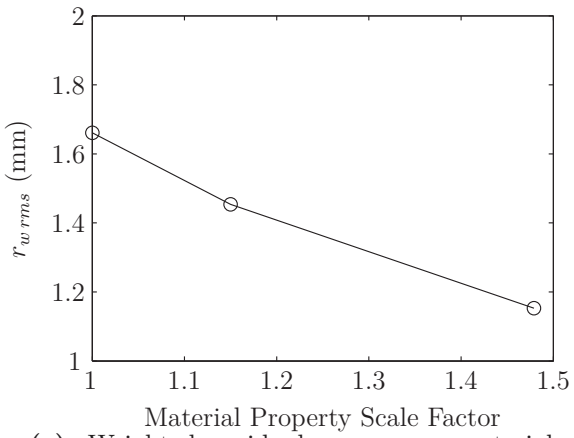

(c) Weighted residual $r_{w\,rms}$ vs material property scale factor α

Figure 10.21: Residual improvement with material property adjustment

10.12 Conclusion

This chapter has documented the development and validation of a subject specific CPAP FEA model using the explicit FEA method. The model was developed taking as inputs the reference geometry from the CPAP MRI experiments (Section 8)and the mechanical properties of the subdermal adipose tissue from the indentation experiment (Section 9).

The validation process for the CPAP FEA models consisted of a mesh refinement study, force and energy balances as well as ROI comparisons between the experimental and simulation results. The mesh refinement study revealed that a nominal mesh size of 1mm was refined enough to capture the physics of the simulated scenario. The energy and equilibrium balances confirmed that the quasi-static assumption is valid. Finally the comparison to experimental results across the ROIs has validated that the model is able to simulate the mechanics of the mask engaged on the face. Therefore, this development process and strategy was replicated for a modest sample

of ($N = 5$) participant specific models. This model series and corresponding results are described in Section 11.

Chapter 11

Deformable CPAP Finite Element Analysis Model Series

11.1 CPAP Finite Element Analysis Setup

Using the modelling strategy described in Chapter 10 as a series of six deformable FEA models were developed. These models included the participants with the extreme values of BMI, which range from 17 to 35 kg/m^2. Figure 11.1 shows the face meshes used for the extreme values of BMI encountered in this study. The models were set up to to simulate the subject specific experimental conditions that were experienced while capturing the deformation fields.

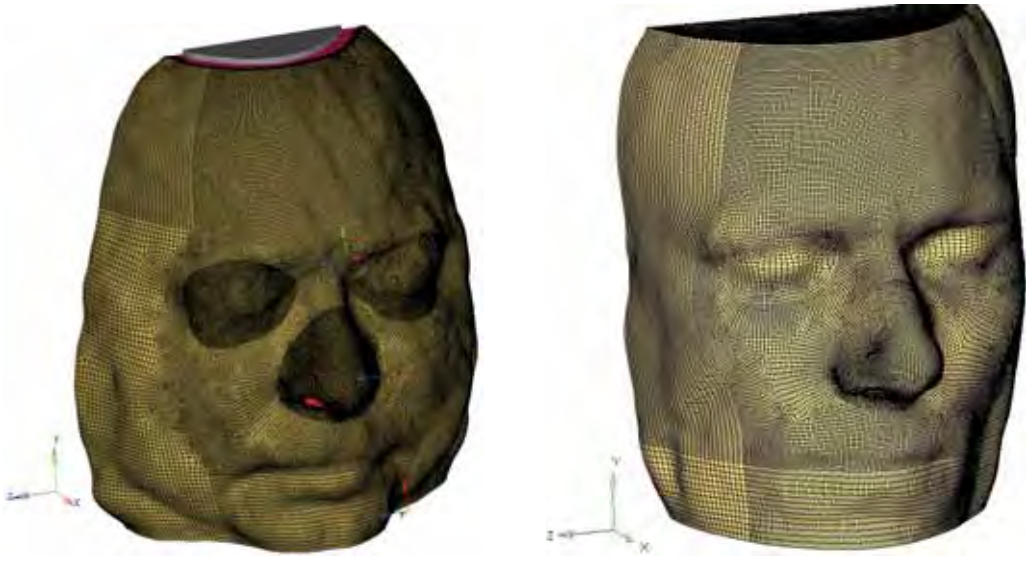

(a) Mesh of participant with BMI=35 kg/m^2

(b) Mesh of participant with BMI=17 kg/m^2

Figure 11.1: Meshes of extreme body compositions used in the study

The same postprocessing and material property adjustment steps were applied for each of the deformable models as was outlined in sections 10.4.2, 10.4.3 and 10.4.4. The single pass material property adjustment results are shown in Figure

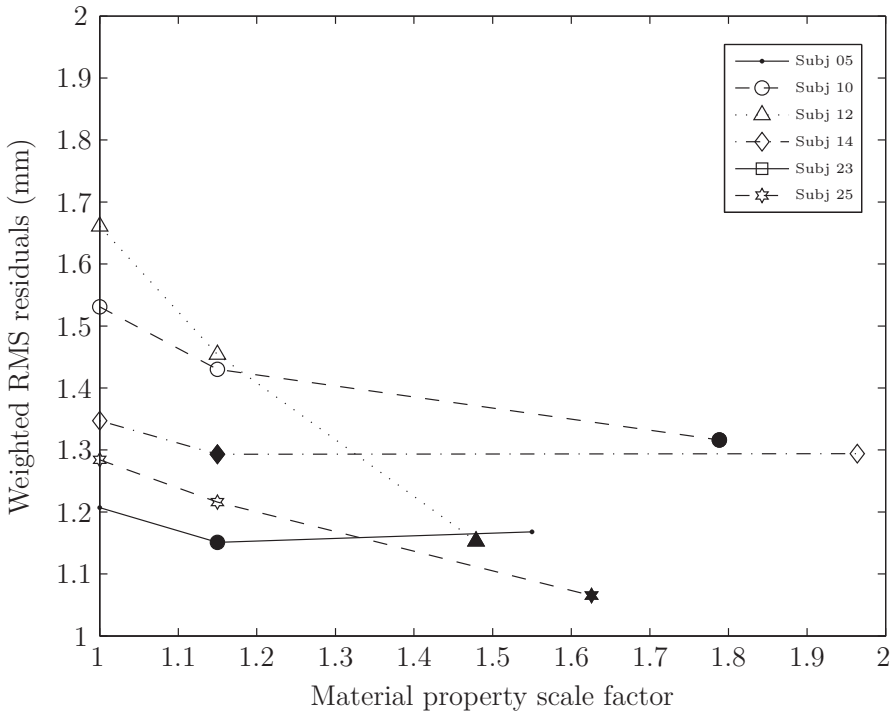

Figure 11.2: Weighted RMS values of the ROIs from the deformable models. The lowest of the residual values was chosen for further modelling. This is indicated by the solid markers

11.2. The minimum RMS residual value was chosen for use in subsequent models. Considering the diverse group of participants in this study, and the published observations that mechanical properties of soft tissues change with age (Agache *et al.*, 1980; Mazza *et al.*, 2007), an allowance was made to coarsely tune the models to each participant and allow for biological variation between participants. The range of values used is well within the broad range of mechanical properties published in the biomechanics literature, as can be seen by reference to Sections 6.3 and 6.5.

11.2 Results

The results from the experimental configuration models are described in this section for each of the participants, one will be in full detail, while the remainder at a level that highlights their characteristics, due to similarity in results.

11.2.1 Subject 5

Subject 5 was the youngest of the participants, aged 19 years at the date of scanning, and had a BMI of 26.3. The mask was applied to the face with headgear tensions above the median for both the top and bottom straps. The upper limit of the MRI volume was located close to the level of the FHS. The solid boundary condition being

so close to the line of action of the contact force vector for the upper limit of the model prevented any significant sliding in the Y direction and any associated bulging away from the skull. Soft tissue was seen to bulge out from the frontal bone laterally adjacent to the FHS bilaterally. This is due to the material being deformed laterally from the forehead contact and being constrained by the temporalis muscle origin. During engagement, the FHS contacts with the forehead first early in the solution and then acts as a pivot as the cushion engages with the face. The membrane first made contact with the face on the side of the nose. Significant load is applied to the nasal region, once the undercushion begins to engage with the membrane and face. This load is concentrated at the terminating taper of the undercushion on the side of the nose. As the mask further engages, the cantilevered spring of the undercushion is gradually engaged and bends about its connection to the mask body. As the mask is engaging, an additional load path is created when the contact between the upper lip and membrane engages. The membrane deforms to conform to the profile of the nose. The membrane is sandwiched between the undercushion and the nose on the sides of the nose and the upper lip. The compressive load path from the undercushion to the skin on the sides of the nose indents the cushion into the face and similarly causes the membrane to locally wrap around the undercushion and bulge away from the nose adjacent to the load path on the medial side. Additionally the nasal contour is a doubly curved surface and hence is non developable. Therefore, it is impossible for the mask to conform precisely to the underlying skin surface without considerable deformation. In conforming to a non developable surface a membrane will buckle and wrinkle, particularly in regions of high curvature or transitions from one region to another. This is evident in the CPAP FEA model of the membrane as it buckles and folds away from the skin, radiating out from the *subalare* bilaterally. This is a transition between the three major load paths in the mask, namely the left and right sides of the nose and the upper lip. The material joining these regions is less constrained and is able to deform out of plane to accommodate the engagement of the face on the mask. Further wrinkles were noted near the nasion, bulging around the superior extent of the undercushion's contact. As the mask further engages, the membrane is tensioned and its stresses increase as it forms closely to underlying shape of the nose. This is particularly evident on the free edge of the membrane, across the nasal bridge and in the subnasal region. The buckling and wrinkling induced during engagement persist as the membrane was tensioned, with notable out of plane deformations present bilaterally at the nasal bridge and at the root of the nose radiating out bilaterally from the *subalare* landmarks towards the nasolabial sulcus. The out of plane deformations at the bottom of the cushion are severe with the membrane folding over completely, and inducing an adjacent out

of plane deformation due to curvature continuity of the material. This buckling of the membrane results in regions of the projected contact area of the mask on the face having extremely low contact pressure or even being out of contact, as can be seen in Figure 11.3b. This is undesirable for maintaining an effective seal for CPAP therapy.

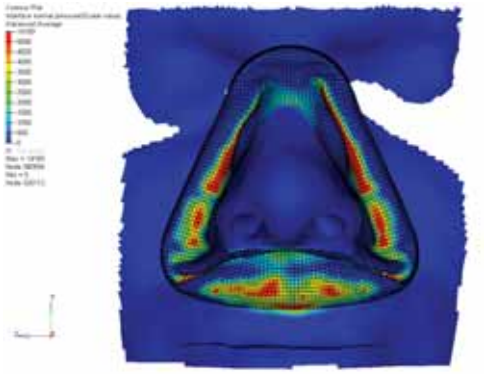

(a) Contact pressure between the membrane and the face prior to pressurisation. Note the buckling of the membrane at the nasion, and then more prominently radiating out from the *subnasale*.

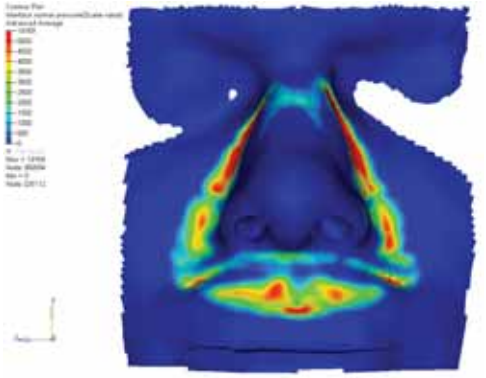

(b) Contact pressure (Pa) between the membrane and the face prior to pressurisation. Note the distinct double bands of low contact pressure propagating from the *subnasale*.

(c) Vector plot of the major principal membrane stress showing the tensile loading in the deformed mask membrane.

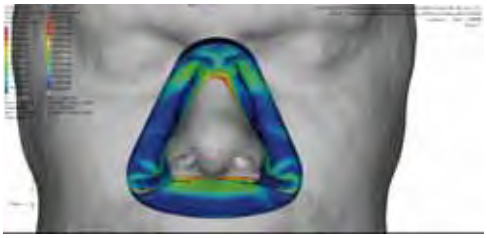

(d) Overlay of major principal membrane stresses with their corresponding vector plots

Figure 11.3: Subject 5 results prior to therapy pressure application

As the pressure was applied to the mask, the contact pressure increased as the membrane was pressed directly onto the face. This caused the membrane to form more closely to the underlying nasal geometry. The contact pressure was increased all over the region, with particular increases located on the nasal bridge and upper lip. Additionally, low level contact pressures are able to be detected outlining the contact area. The buckling of the membrane at the level of the upper lip resulted in a distinct region of low contact pressure on each side of the mask potentially providing an air path for a leak if this seal is disturbed. Since the material was wrinkled prior to the application of pressure, the pressure caused the membrane to

completely fold on itself and self contact, generating a ridge that cannot be removed passively. This is shown in Figure 11.4a. It can also be seen that the mask has indented into the upper lip soft tissue, and the membrane has bottomed out on the mask body. This is shown by an abrupt indentation into the upper lip, this is accompanied by the lip folding around the cushion and lifting away from the lower lip slightly.

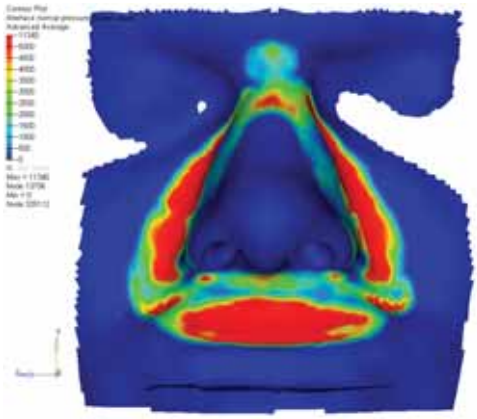

(a) Contact pressure after application of CPAP therapy pressure

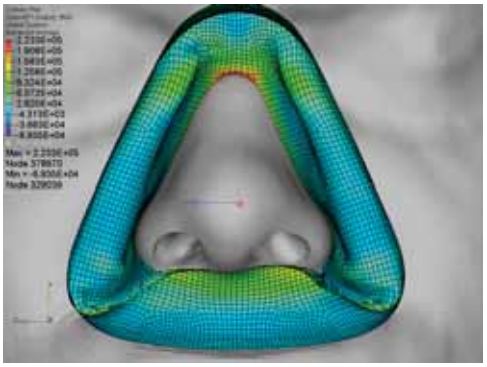

(b) Major principal stress in the membrane after application of the CPAP therapy pressure. Note that the membrane has completely folded back on itself on both sides, providing a potential egress path for leaking air.

Figure 11.4: Subject 5 results including CPAP therapy pressure

The full field residual results for subject five indicate that there is generally a good agreement between the simulation and experimental results. Notable locations with increased residuals within the nasal region of interest are the left hand side of the nose, the nasion and the vermilion margin. The FEA results for the LHS of the nose did not indent as deeply into the face as the experimental results and was located more towards the lower end of the nose. The nasion results from the FEA did not deform to the same extent as the experimental results, while the results at the vermilion border of the upper lip indicate that the FEA model has deformed beyond the experimental results, though this particular location is subject to the geometry approximation of the lips.

11.2.2 Subject 10

Subject 10 was aged 33 with a BMI of 28.3 kg/m^2 at the date of scanning. Headgear tensions were close to the median value for the top strap and below the median for the bottom strap. Similarly to subject five, the FHS made contact initially, providing

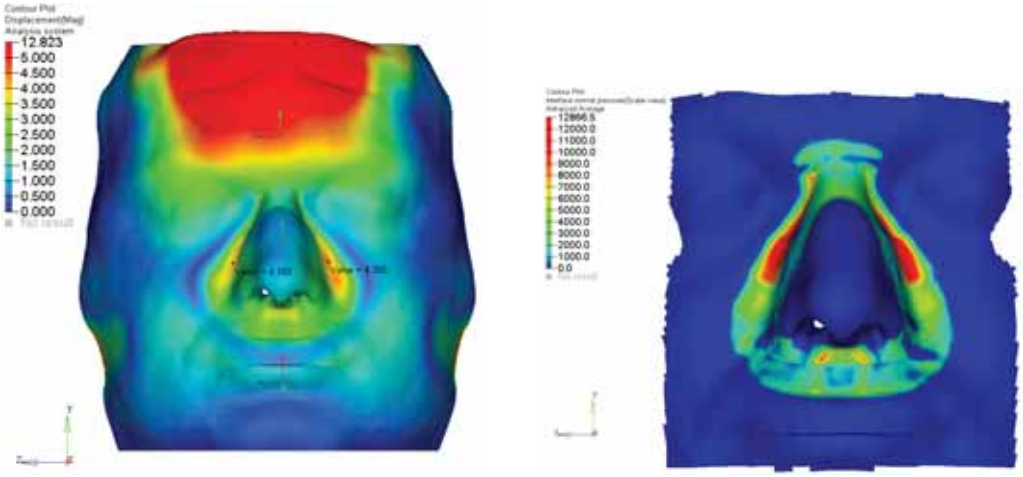

(a) Displacement magnitude (mm) including the artifact at the forehead from the tissue sliding over the frontal bone and bulging due to the solid material constraint at the top plane

(b) Contact pressure after application of CPAP therapy pressure

Figure 11.5: Subject 10 results including CPAP therapy pressure

a fulcrum as the mask engaged. As the membrane contacts the nose, wrinkling was induced radiating from the nasion on each side as well as the transition from the sides to the upper lip region of the mask on each side. With further engagement, the undercushion gradually bends and provides a dominant load path along the sides of the nose. Prior to the mask being pressurised, it has engaged with the face. The membrane has conformed to the profile of the nose, with the wrinkled regions now fully developed with a symmetric fold in the membrane superior to the nasion, and lateral folds propagating from each of the alar. The most significant facial deformation to this point was on the upper portion of the side of the nose (4.25mm). After the pressure was applied the membrane was pressed into the face, this had the effect of flattening the membrane folds near the alar significantly, however the pressure acting on the membrane folds at the nasion caused this completely fold over and undergo self contact. The equilibrium configuration of the mask (Figure 11.5) shows that the deformations are greatest on the sides of the nose, and that the contact pressure was concentrated at the upper ends of the undercushion on the side of the nose. Significantly reduced contact pressures and even open contact were observed beneath membrane wrinkles, potentially providing a leak path.

11.2.3 Subject 12

Subject 12 was aged 28 with a BMI of 17.7 kg/m^2 at the date of scanning. This was the participant with the lowest BMI. The mask was applied with headgear tensions

well above the median of the group that was tested. Prior to the application of the pressure, the mask engaged with the same progression described above. Particular to this participant was that the induced wrinkling in the membrane at the nasion was reduced, and did not fold over. The membrane did buckle at the alar on each side. Additionally the high headgear load caused the membrane to completely fold over on the upper lip and bottom out providing a direct load path from the body of the mask to the face. Upon application of the therapy pressure to the model, the membrane was inflated and conformed very closely to the facial profile. The membrane has not folded over in any other location than the upper lip. Regions of lower contact pressure are located propagating from the alar nasi on each side of the face. The highest pressure for this subject was located on the upper lip due to the membrane folding over and forming a direct load path to the upper lip from the mask body.

11.2.4 Subject 14

Subject 14 was aged 73 with a BMI of 34.4 kg/m^2 at the date of scanning. This was the participant with the highest BMI. The progressive deformation during engagement was consistent with the detailed description above. Prior to the application of pressure, buckling of the membrane was encountered superior to the nasion and extending laterally below the alar nasi. The application of pressure did not eliminate the wrinkles from the membrane. Regions of low contact pressure are located underneath the wrinkles or folds of membrane superior to the nasion and extending laterally from the region of the alar nasi. Additionally the wider nose of this participant resulted in the translation of the load path further towards the top of the nose, this is evident by a reduced general contact pressure across the upper lip, and moving the peak contact pressure location in the superior direction, towards the terminal ends of the undercushion.

11.2.5 Subject 25

Subject 25 was aged 48 with a BMI of 24.9 kg/m^2 at the date of scanning. The headgear tensions for this participant were below the median for the group. The engagement of the mask on the face resulted in the same engagement pattern as was detailed previously. Wrinkling of the membrane was induced at the nasion and propagating from the alar nasi. The application of pressure reduced the extent of deformation in the buckled regions, but did not flatten them out to conform to the face completely. The nasion region had a persistent wrinkle bowing away from

the skin which extended fully across the nasal bridge, but not to the interior of the mask, so should not be a path for air egress. The local buckling at the alar nasi were similarly pressed into the nose, but not to the extent that the out of plane deformations were flattened to conform to the facial profile. Regions of low contact pressure exist at the alar buckled regions, with a potential leak path of low pressure extending from the interior of the mask to the atmosphere. The peak contact pressures were located at the sides of the nose under the load path from the cantilevered spring of the undercushion.

11.2.6 Collated Results

The CPAP FEA models provide a number of useful results relating to the contact between the face and the mask. Of primary interest are the contact pressure and contact area. The contact pressures were averaged at the nodes to generate a continuous scalar field over the contact surface. For each model in the experimental configuration, results were extracted for the left and right hand sides of the nose as well as the upper lip, nasion and forehead regions. The peak contact pressures were extracted for each of the regions after the model had stabilised. The contact pressure thresholds were used to reselect within each region, the nodes with a pressure exceeding 1 Pa, 980 Pa and 5000 Pa. Elements were then selected that were connected to these nodes. These selected regions correspond to the total contact area between the face and mask, the area of the face where the contact pressure exceeds the CPAP therapy and a region of higher contact pressure identifying primary load paths.

Gaussian quadrature was used to approximate the integral of a scalar field (ϕ) over the selected faceted surface region as outlined in Appendix I. The mean contact pressure applied over each of these regions in the deformed configuration was calculated according to equation (10.23),

$$\bar{p} = \frac{1}{A}\int_A p \mathrm{d}A \tag{11.1}$$

$$\approx \sum_{j=1}^{n} A_j \sum_{i=1}^{3} p_{ij} W_i \tag{11.2}$$

where n is the number of elements in the faceted surface, j is the element index, A_j is the area of facet j, A the area of the whole surface being integrated, W_i the weighted factors for Gaussian quadrature, p_{ij} the contact pressure for node i on element j and $\bar{p}$ the mean pressure over the surface. This measure was used

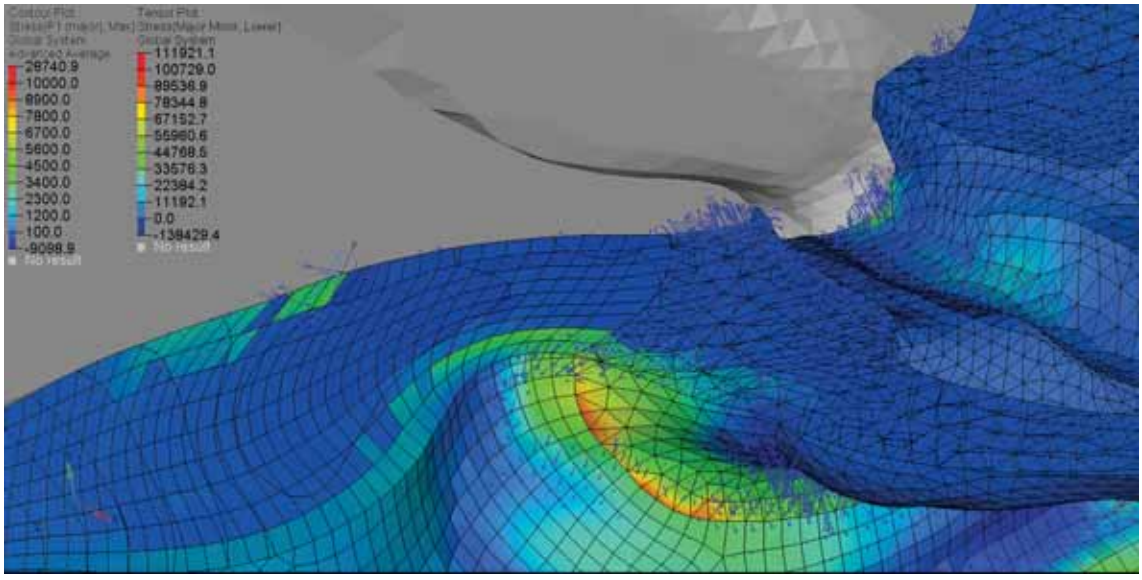

Figure 11.6: Transverse cross section at the level of the pronasale landmark of Subject 12. This shows the maximum principal stress contour as well as the principal stress tensors. Scales are set so that saturated blue regions are compressive. This shows that tensile stresses secondary to the deformation are localised to the skin layer.

for comparison against different configurations of models, to avoid distortion from localised effects. Contact areas were also calculated in the deformed configuration.

The contact pressure fringe from the simulations are presented graphically in Figures 11.7 through 11.11 at each of the threshold levels (1 Pa, 980 Pa, 5000 Pa) for the deformable models in the experimental configuration. For all of these models the fringe plots are saturated at 10000 Pa, which is twice the highest selection threshold.

The maximum and minimum principal stress results were checked examined to check for secondary loads paths induced due to the compression of the mask onto the face. These stresses indicated that the loading was dominated by the primary compressive load path. There was a small secondary tensile load induced in the skin where it was placed into tension as it bent around the deformed shape of the mask.in the transverse direction. This load was localised to the skin, the deeper layers of fat and muscle were had a Progressing through to the deeper muscles, the maximum (most tensile) principal stress was in compression or only marginally positive, that the loading is dominated by compression from the compressive intermediate and minimum principal stresses. This can be seen in Figure 11.6.

Figure 11.12 presents the distribution of the maximum contact pressures for each of the facial regions in a boxplot in the experimental configuration. Figure 11.13a presents the distribution of the mean contact pressure acting over the contact areas grouped by facial region and threshold level. One thing to note in Figure 11.13a is that the contact pressure for the nasion at the 5000 Pa threshold level results in

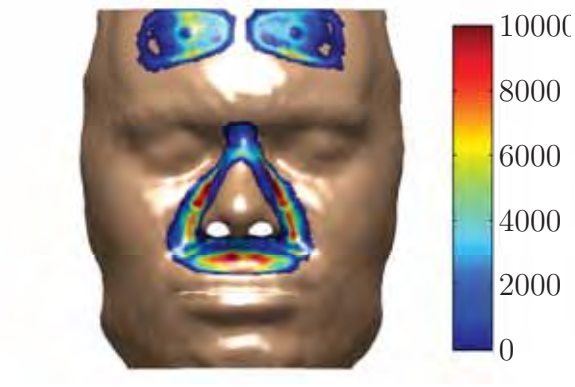

(a) Contour of contact pressure showing total mask contact area

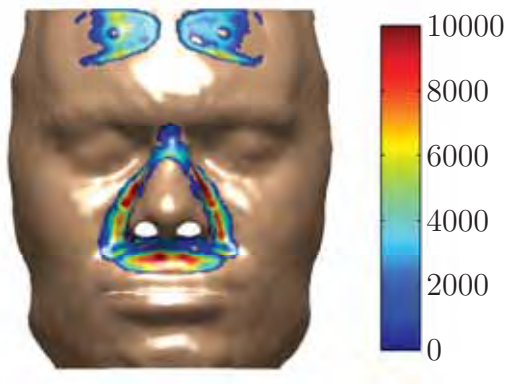

(b) Contour of contact pressure showing contact area such that $P > 980$Pa

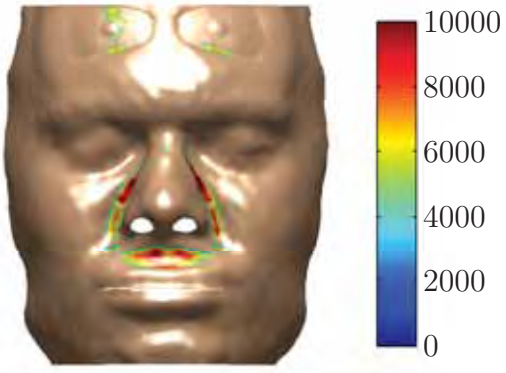

(c) Contour of contact pressure showing contact area such that $P > 5000$Pa

Figure 11.7: Subject 5 mask contact pressures (Pa)

mean pressures that are actually below 5000 Pa. This is because this region is small and the surface integral includes the facets which are connected to the few nodes above the threshold. This includes the weighted contribution from the surrounding nodes below the threshold, hence reducing the mean value across the surface below the original nodal selection threshold. Figure 11.13b presents the contact areas similarly grouped by region and contact area. The integrated results will be used to compare regions against alternate configurations of models.

A visual inspection of these data reveal characteristics in the contact parameters. A large range was observed in the contact pressure in the lip region. The same ranking relationships were seen between regions at different threshold levels, suggesting that the scalar field is relatively smooth, and is not unduly influenced by extreme values. The left and right hand regions are similar suggesting that there is not a significant difference in the mean contact pressure between the left and right hand sides of the faces. These same patterns are exhibited in the boxplots of the maximum contact pressure results, where the left and right sides are similar in

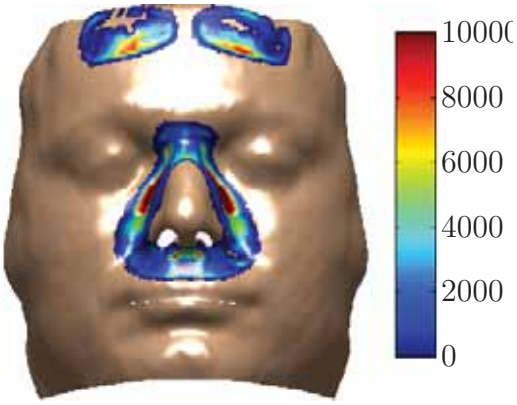

(a) Contour of contact pressure showing total mask contact area

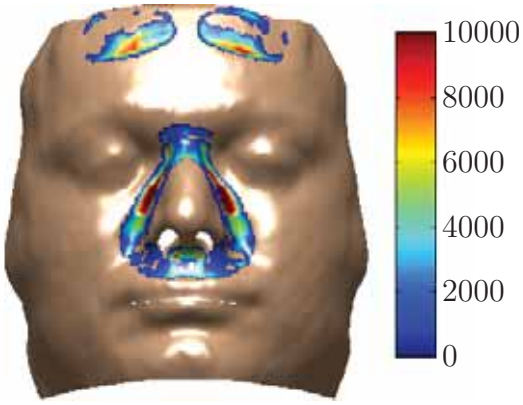

(b) Contour of contact pressure showing contact area such that $P > 980$Pa

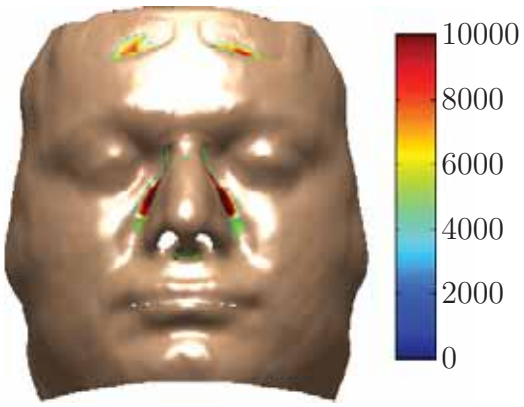

(c) Contour of contact pressure showing contact area such that $P > 5000$Pa

Figure 11.8: Subject 10 mask contact pressures (Pa)

magnitude and distribution, the lip exhibits a high range of data and the contact pressure at the nasion is lower.

A one way ANOVA test was performed with facial region as the factor and a null hypothesis that the mean of each group is equal ($H_0 : \mu_1 = \mu_2 = ... = \mu_n$) and an alternative ($H_1$) that the means of all the groups are not all equal at confidence level of 95%. H_0 was rejected ($P < 0.01$) so a significant difference in mean contact pressure was found across the regions. Tukey comparisons were performed (95% confidence level) between the nasal groups, which indicate that the nasion contact pressure was significantly different from the other groups. The left and right hand side region's contact pressures were not significantly different.

A similar ANOVA test for equal mean areas across regions at a threshold of 5000Pa indicated that the null hypothesis ($H_0 : \mu_1 = \mu_2 = ... = \mu_n$) can be rejected ($P = 0.002$). Tukey comparisons indicated that the nasion region was the only region with a significantly different area. That the nasion region contact area differs from the others is a trivial result as the selection region was much smaller than the

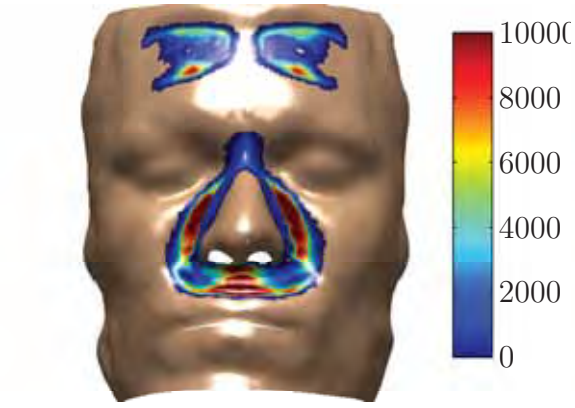

(a) Contour of contact pressure showing total mask contact area

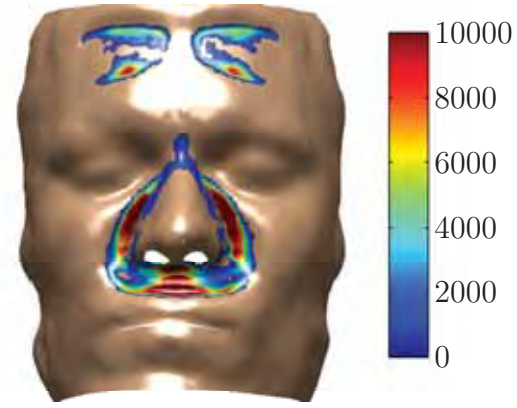

(b) Contour of contact pressure showing contact area such that $P > 980$Pa

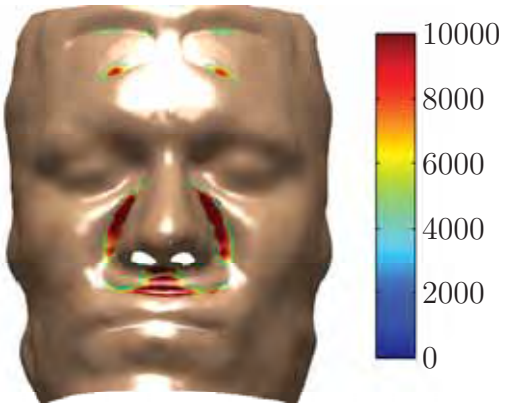

(c) Contour of contact pressure showing contact area such that $P > 5000$Pa

Figure 11.9: Subject 12 mask contact pressures (Pa)

others initially. The main result of interest from this analysis is that the left and right hand areas are similar, so we cannot reject symmetry of the primary results.

The contact pressure results at the 1Pa threshold highlights the entire contact area of the mask on the face and contains the higher thresholded results as subsets. These plots are helpful identifying the pattern of contact pressure on the various models. Several characteristics are evident. The contact pressure on the forehead conforms closely to the shape of the mask's FHS, even to the point that surface features such as the raised pad's central cores are seen on the pressure traces. The forehead contact pressure was concentrated towards the lower margin of the FHS. In all subjects the left and right hand sides of the nose contained regions of higher pressure corresponding to load path from the undercushion directly onto the membrane and then the face. The lip region exhibited varying contact pressures and area. The other primary output from this presentation of the data is the presence of low contact pressure regions. It is understandable that low contact pressure regions are seen to be desirable, however this is not necessarily the case. One of the challenges

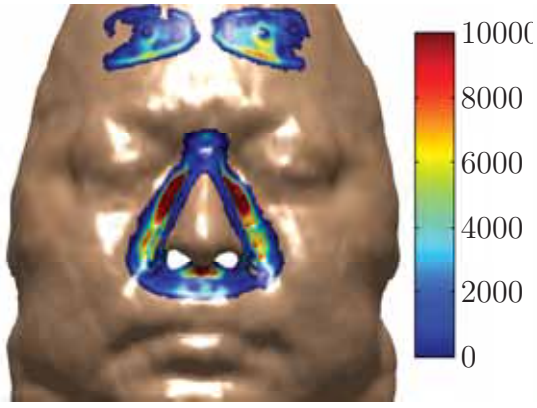

(a) Contour of contact pressure showing total mask contact area

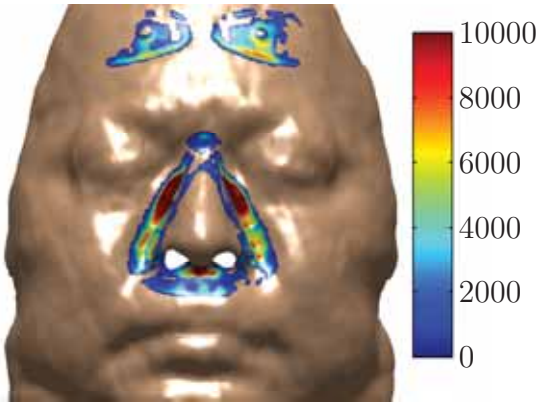

(b) Contour of contact pressure showing contact area such that $P > 980$Pa

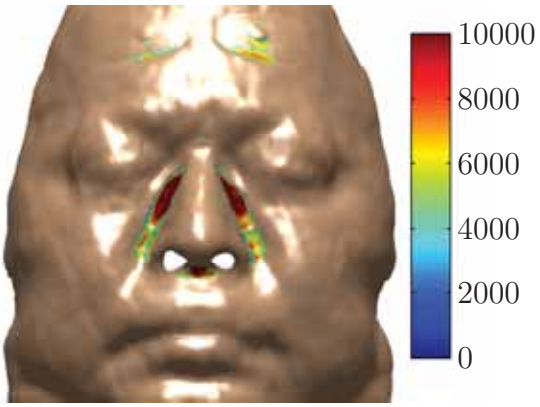

(c) Contour of contact pressure showing contact area such that $P > 5000$Pa

Figure 11.10: Subject 14 mask contact pressures (Pa)

with CPAP therapy is sealing of the mask against leaks. Low contact pressure regions are potential leak paths for the pressurised air. Leaks are one of the main causes of patient complaint/antipathy against using CPAP therapy. In all subjects there was a low pressure region radiating out from the *alar nasi* corresponding to the corner transition between the upper lip and side regions. The nasion is another region of interest for contact pressure in these models. For the UMII mask used, it differs to the other nasal regions in that there is no undercushion providing a direct load path in this region. The nasion topologically, is a saddle point with curvature in orthogonal directions locally forming a non developable surface. Therefore, the contact pressure in this region relies solely on the membrane deforming and conforming to the underlying geometry under the applied therapy pressure and the deformation induced as the membrane is stretched as the mask engages with the face as a whole. This results in local buckling and regions of reduced contact pressure.

The contact pressure fringes thresholded at 980 Pa corresponds to the CPAP therapy pressure of 10 cm H_2O. This fringe only colours contact pressures greater

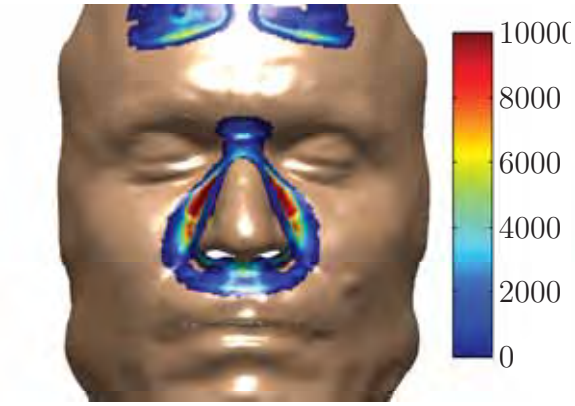

(a) Contour of contact pressure showing total mask contact area

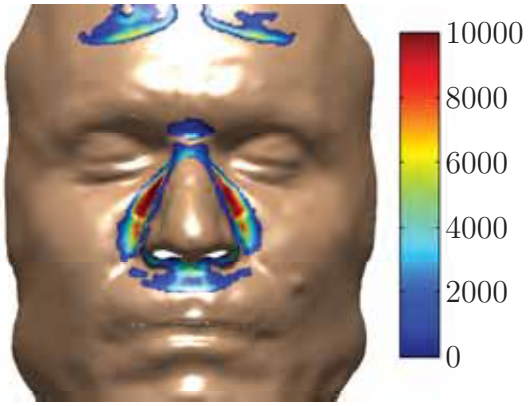

(b) Contour of contact pressure showing contact area such that $P > 980$Pa

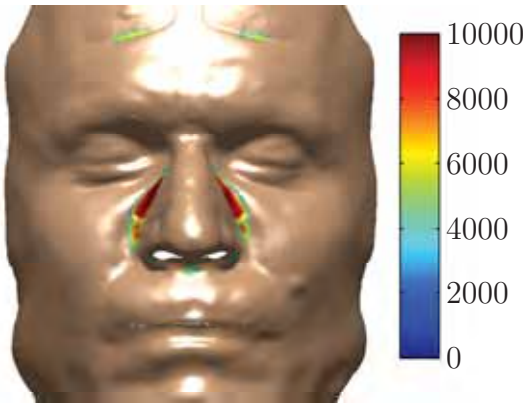

(c) Contour of contact pressure showing contact area such that $P > 5000$Pa

Figure 11.11: Subject 25 mask contact pressures (Pa)

than the therapy pressure. The entire volume of the mask and airway is considered to be at this elevated pressure. Unless the membrane edge is sealed against the face, it is possible that the pressure could act on the external side of the membrane and locally reduce the contact pressure and gradually propagate a leak path by lifting the membrane off the face. The mechanics of this situation could lead to an unsteady state occasionally encountered where tonal vibrations are induced at the membrane/face interface through the repeated build up and release of pressure between the face and membrane. Therefore, this slightly higher thresholded region identifies possible regions where leaks may develop, rather than clear paths.

The 5000 Pa threshold isolates the primary load paths form the mask to the face. As mentioned previously, these were consistently present approximately symmetrically on the left and right hand sides of the nose. High contact pressure load paths were also encountered on the upper lip, though these were much more variable in nature from these models.

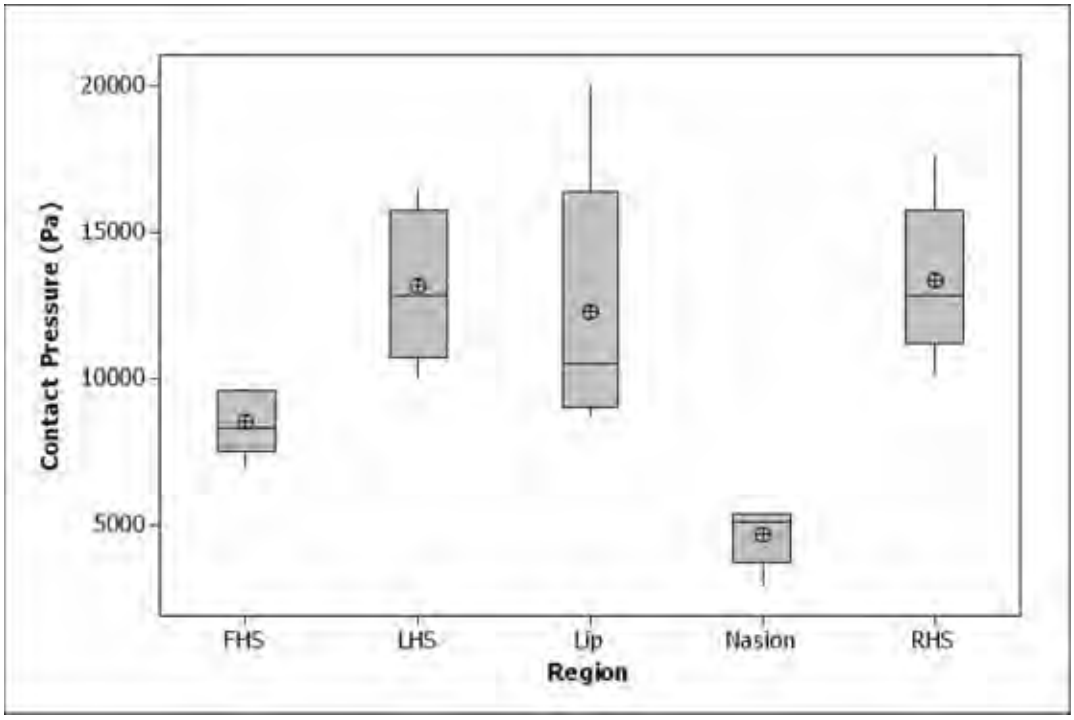

Figure 11.12: Boxplot of maximum contact pressures in each of the facial contact regions for the deformable FEA model in the experimental configuration

The independent variables for the experiment were age and BMI. In addition the headgear loading is an independent continuous variable that was subject chosen during the experiment. Therefore, associations were tested using stepwise multilinear regression between the predictor variables age, BMI and headgear tension [1] at a 95% confidence level. As no significant difference was found between the left and right nasal regions, these data were pooled. Figure 11.14 shows how the mean contact pressure $\bar{p}_{5000}$ varies with age, BMI and applied load. Although the number of samples is very small, some patterns were evident. The mean contact pressure appears to follow a parabolic pattern when plotted against the BMI of participants, while weak associations were seen when plotted against age and load.

Preliminary significant associations were found between the applied force ($P = 0.032$) and the age ($P = 0.01$) for the mean contact pressure in the left and right sides of the nose, refer to Table 11.1 for details. In this configuration, the BMI was not found to be a significant factor in the regression. The regression equation is

$$\bar{p}_{5000} = 5620 + 21.3a + 344F_x \tag{11.3}$$

[1] The bottom strap headgear tension was used for the nasal regions and the top strap headgear tension was used for the forehead region

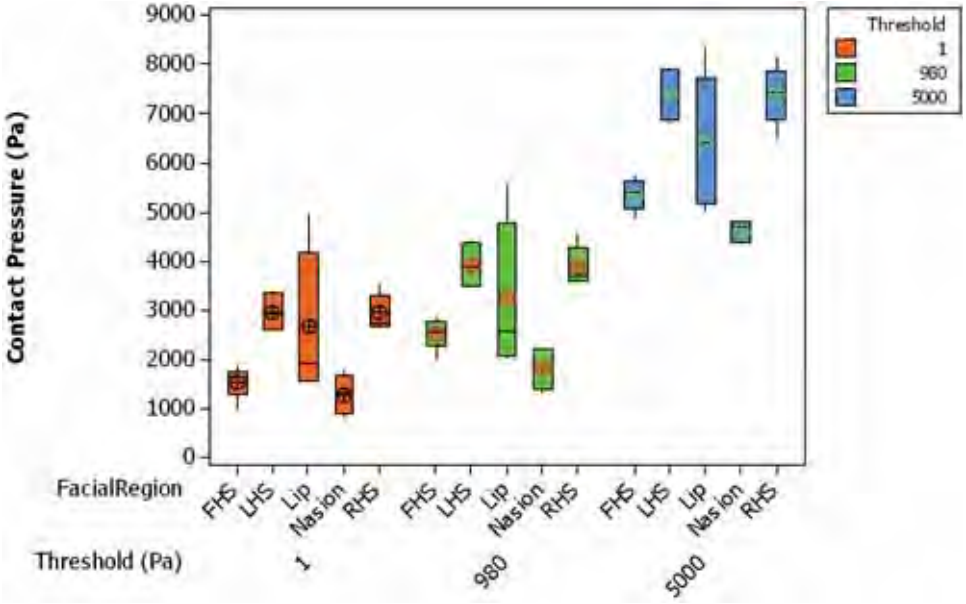

(a) Boxplot of contact pressure (Pa) at different pressure thresholds by facial region.

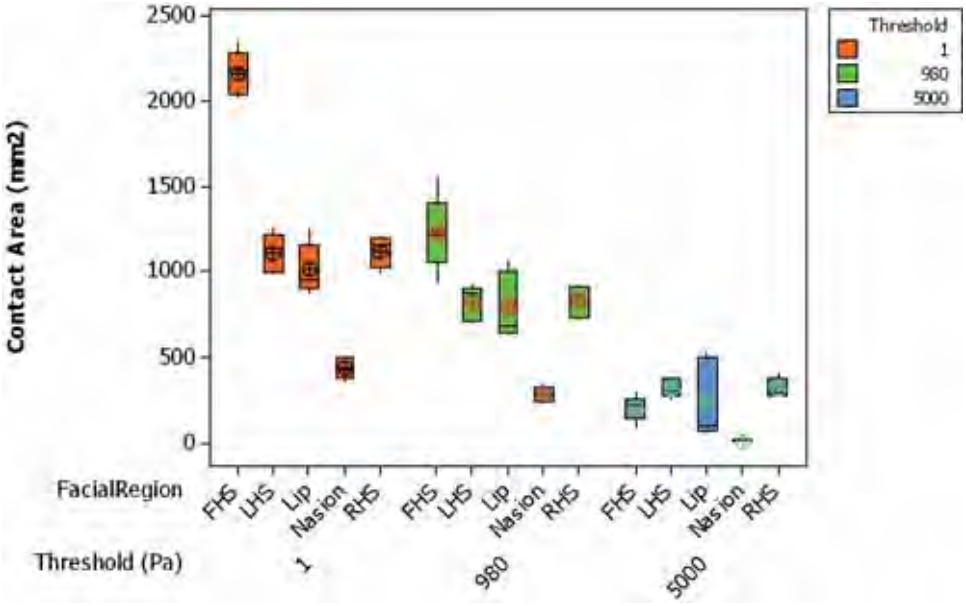

(b) Boxplot of contact areas $\left(\mathrm{mm}^2\right)$ at different pressure thresholds by facial region.

Figure 11.13: Contact parameters from the deformable FEA models in the experimental configuration

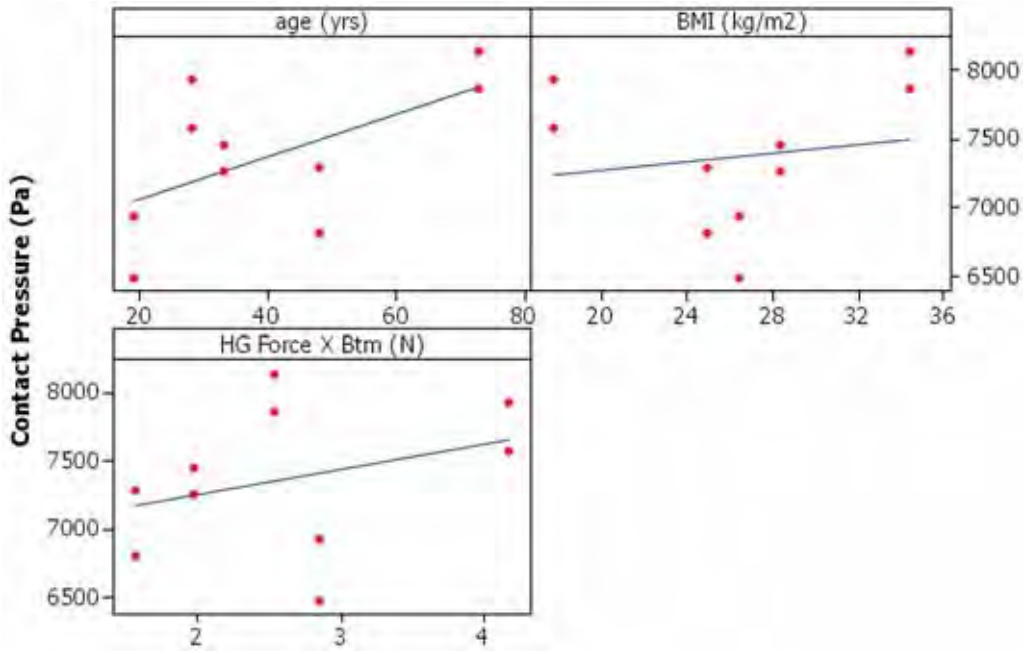

Figure 11.14: Scatter plot of mean contact pressure ($P > 5000$) for the pooled data set from the left and right hand sides of the nose against the independent variables of age, BMI and headgear tension.

where a is the age in years and F_{xbtm} is the X component for the headgear force in the bottom straps.

Table 11.1: Contact pressure regression output at the sides of the nose

Predictor	Coef	SE Coef	T	P
Constant	5620.2	495.3	11.35	0
age (yrs)	21.33	6.121	3.48	0.01
HG Force X Btm (N)	344.1	129.3	2.66	0.032

$$S = 341.961 \quad R^2 = 67.4\% \quad R^2_{adj} = 58.1\%$$

Analysis of Variance

Source	DF	SS	MS	F	P
Regression	2	1690979	845489	7.23	0.02
Residual Error	7	818561	116937		
Total	9	2509539			

The same process was followed for the mean contact pressure at the lip at the 5000Pa threshold level. The raw data is shown in Figure 11.15. Again it is acknowledged that sample size is low. The step wise regression found significant factors of the age and headgear loading, refer to Table 11.2 for details. A strong linear correlation was found at the upper lip with the applied load, which dominates this regression. The regression equation is

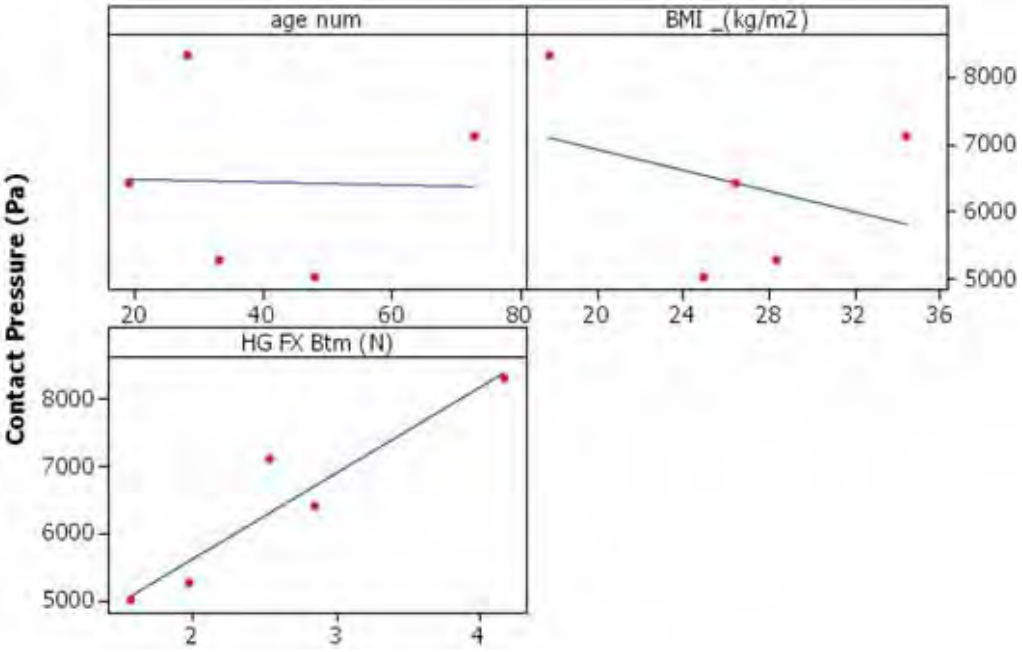

Figure 11.15: Scatter plot of mean contact pressure ($P > 5000$) at the upper lip against the independent variables of age, BMI and headgear tension.

$$\bar{p}_{lip} = 1748 + 22.7a + 1447F_x \tag{11.4}$$

Table 11.2: Contact pressure regression output at the upper lip

Predictor	Coef	SE Coef	T	P
Constant	1747.8	262.2	6.67	0.022
age num	22.67	3.24	7	0.02
HG FX Btm (N)	1447.05	68.43	21.15	0.002

$S = 127.979 R^2 = 99.6\% R^2_{adj} = 99.1\%$

Analysis of Variance

Source	DF	SS	MS	F	P
Regression	2	7330152	3665076	223.77	0.004
Residual Error	2	32757	16379		
Total	4	7362909			

No significant regression coefficients were found for the contact pressure on the nasion and the forehead.

It is important to note that the influence of the headgear loads dominate the effects from the inherent patient variables of BMI and age. Therefore, in order to investigate these parameters, the simulation samples must be controlled for headgear tension. This is addressed in Section 11.3.

11.3 Mean Headgear Tension Analyses

To this point the CPAP FEA models have been validated and then run to simulate the experimental conditions that the participants experienced. One of the prime purposes of this study is to estimate the dependence of contact parameters on anthropometric variables. In order to ensure a good fit of the mask to the face, participants were allowed to fit the mask according to their own level of comfort. As a result, the headgear tensions varied significantly from participant to participant. The primary outputs of interest for this study are the contact parameters such as interface contact pressure. As pressure is force per unit area, it is obvious that the use of different headgear tensions holding the mask onto the face will confound the sensitivity of the contact pressure to anthropometric variations alone. Therefore, it is necessary to control for headgear tension to eliminate its effects from the analysis of results across the sample. To achieve this, the models prepared in the experimental configuration were adjusted to be all run with identical headgear tensions.

11.3.1 Model Descriptions

The models used were prepared as described in Chapter 10. Validated meshes and material properties were used, identical to the experimental configuration model series described in 11.2. The only change for these models is the magnitude of the headgear forces.

The headgear forces recorded from the participant controlled fitting of the mask is reported in Table 8.7. These data are repeated graphically in Figure 11.16.

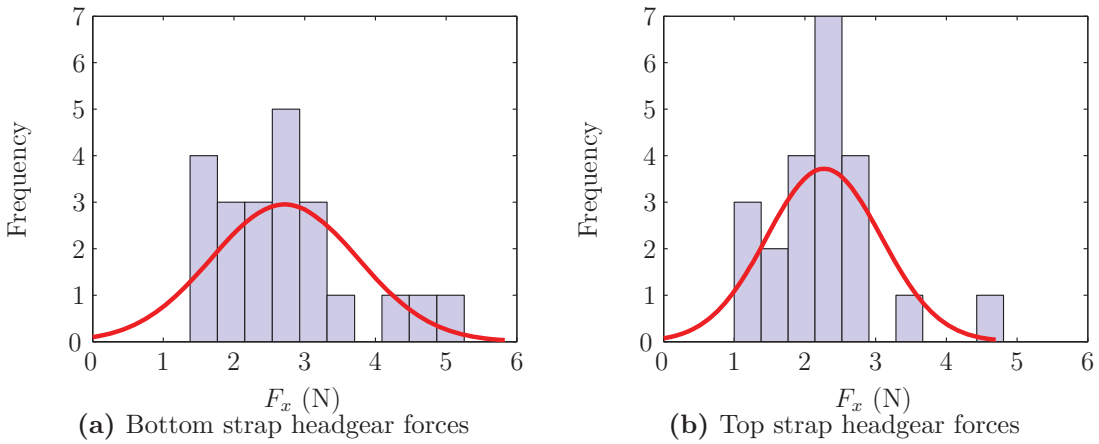

(a) Bottom strap headgear forces **(b)** Top strap headgear forces

Figure 11.16: Distribution of the X (anterior/posterior) component of headgear forces. Fitted normal distribution curves are also shown

The summary statistics of the headgear loads are given below. Note that $n = 19$ instead of 22 for these summaries. This is because the image based data was not available for 3 of the subjects.

Table 11.3: Headgear tension summary statistics.

Variable	Strap	N	μ	SE Mean	σ	Min	Q1	Median	Q3	Max
F_x HG (N)	Btm	19	2.564	0.225	0.982	1.377	1.859	2.528	3.045	5.256
	Top	19	2.173	0.123	0.536	1.269	1.86	2.335	2.516	3.336
F_y HG (N)	Btm	19	-0.3425	0.056	0.2441	-0.8152	-0.6168	-0.2123	-0.1582	-0.0432
	Top	19	-0.0446	0.0373	0.1625	-0.4142	-0.1461	-0.026	0.08	0.2123

Therefore, the loads applied to the headgear are

$$F_{top} = (-2.173, -0.04, 0)\,\text{N} \tag{11.5}$$

$$F_{btm} = (-2.564, -0.34, 0)\,\text{N} \tag{11.6}$$

11.4 Results - Mean Headgear Tension

The results from the mean headgear tension are described briefly below.

11.4.1 Subject 5

The mean headgear tension simulation results are similar in nature to the experimental configuration, refer to Figure 11.17. The same contact pressure patterns are present in the mean tension model compared to the experimental configuration. In particular the same buckling of the membrane is present at the alar nasi, providing the same localised pressure reduction and leak path. The peak values are reduced in the mean headgear model. The peak contact pressure in this model is 10580 Pa located at the left hand side of the nose, compared to 11340 Pa in the experimental configuration.

11.4.2 Subject 10

The mean headgear results for subject 10 (Figure 11.18) are qualitatively identical to the experimental configuration described in Section 11.2.2. The membrane has buckled, folding over completely across the nasion and bulging out from the skin surface propagating out from the alar nasi. The magnitude of the contact pressures has increased at the left and right hand sides of the nose.

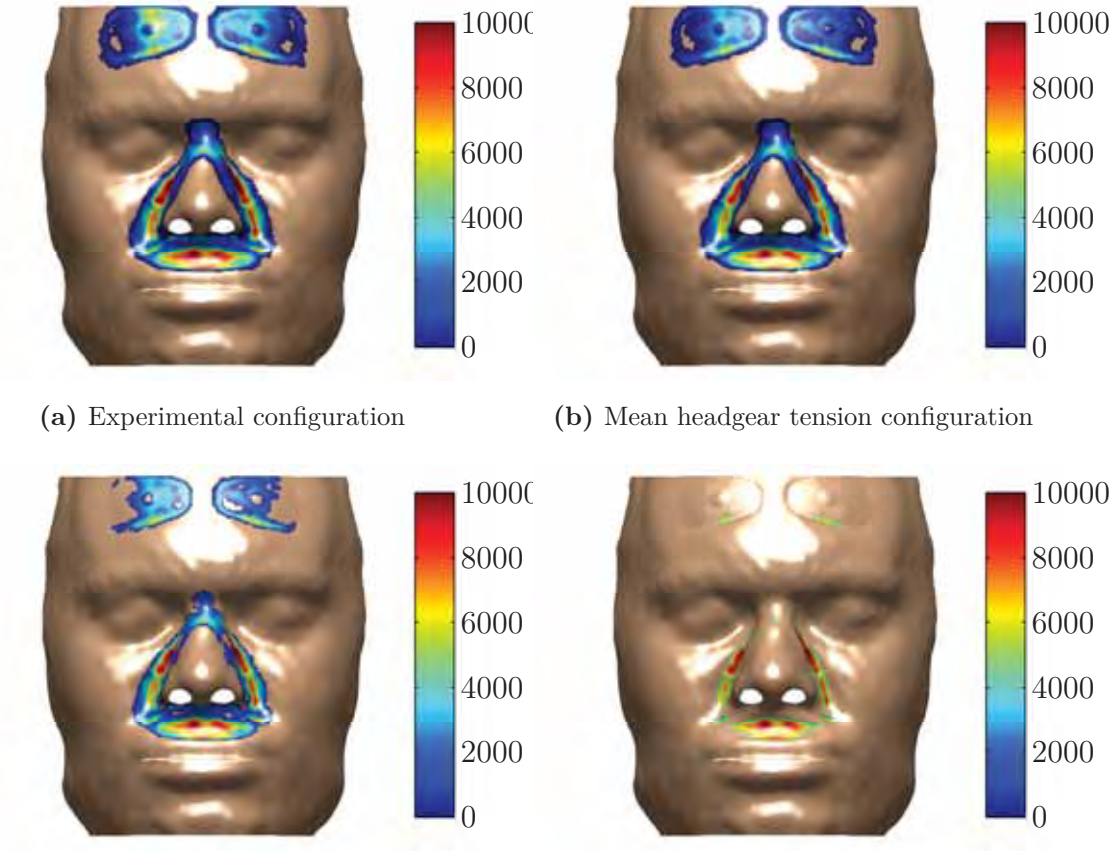

(a) Experimental configuration

(b) Mean headgear tension configuration

(c) Mean headgear tension configuration, 980 Pa threshold

(d) Mean headgear tension configuration, 5000 Pa threshold

Figure 11.17: Subject 5 mask contact pressures (Pa)

11.4.3 Subject 12

The mean headgear tension results for subject 12 differ markedly from the experimental configuration. This is because this participant used a very high headgear tension to apply loads, so the mean tension reduced the load on the lower strap by approximately 40 %. The peak contact pressures and areas above the 5000 Pa threshold were reduced. In particular the load borne by the upper lip was markedly reduced as the load was redistributed and carried preferentially by the left and right hand sides, though with a reduced pressure magnitude. This is shown in Figure 11.19.

11.4.4 Subject 14

The mean headgear results for subject 14 (Figure 11.20) are very similar to those for the experimental configuration. The deformed configuration of the mask on the face qualitatively matches the results from the experimental configuration. Local

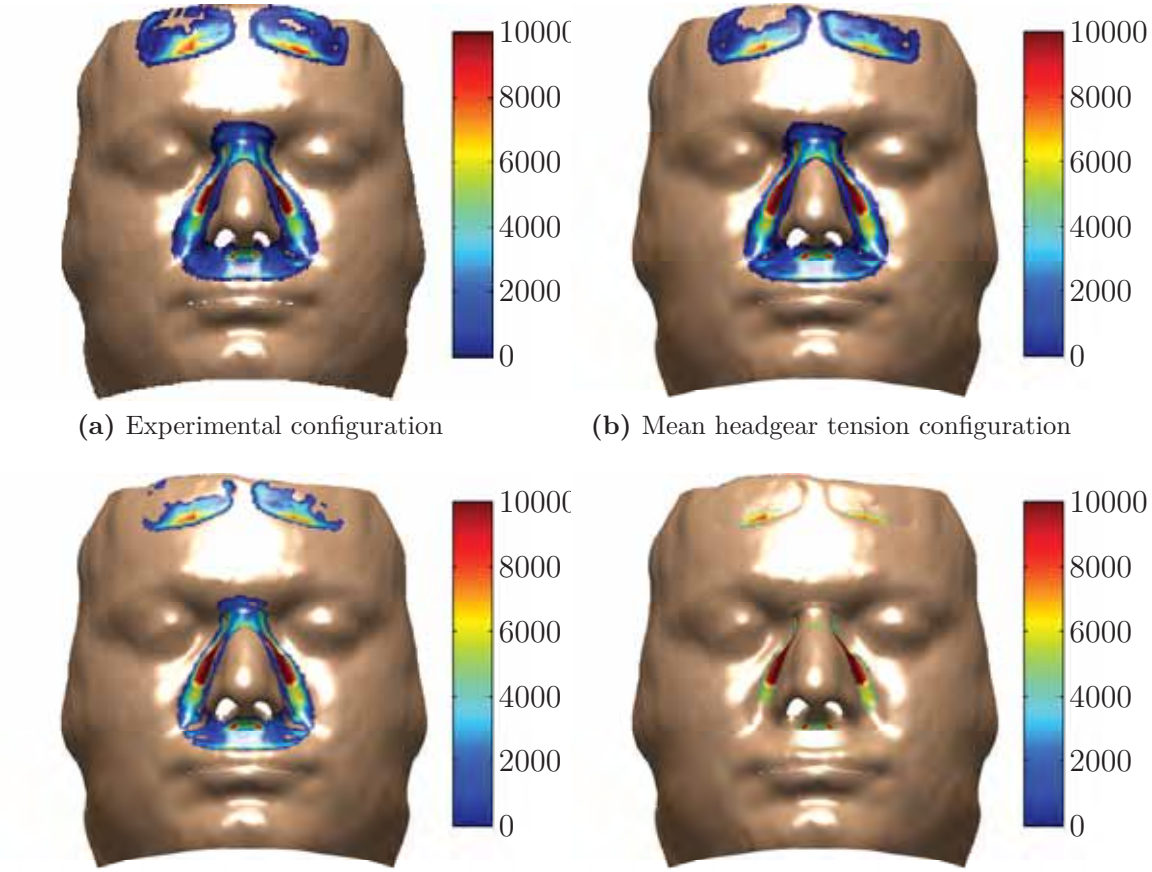

(a) Experimental configuration

(b) Mean headgear tension configuration

(c) Mean headgear tension configuration, 980 Pa threshold

(d) Mean headgear tension configuration, 5000 Pa threshold

Figure 11.18: Subject 10 mask contact pressures (Pa)

buckling is evident at the nasion, where bilateral wrinkles are observed propagating laterally and superiorly, though not crossing the entire contact zone of the membrane. Local bulging was observed on the sides of the nose as well as buckling radiating from the alar nasi. Refer to Section 11.2.4.

11.4.5 Subject 25

The mean headgear tension results for subject 25 (Figure 11.21) qualitatively corresponded closely to the experimental configuration. The contact pressures are increased for the mean tension simulation, and greater weighting is applied to the sides of the nose and the forehead. Refer to Section 11.2.5.

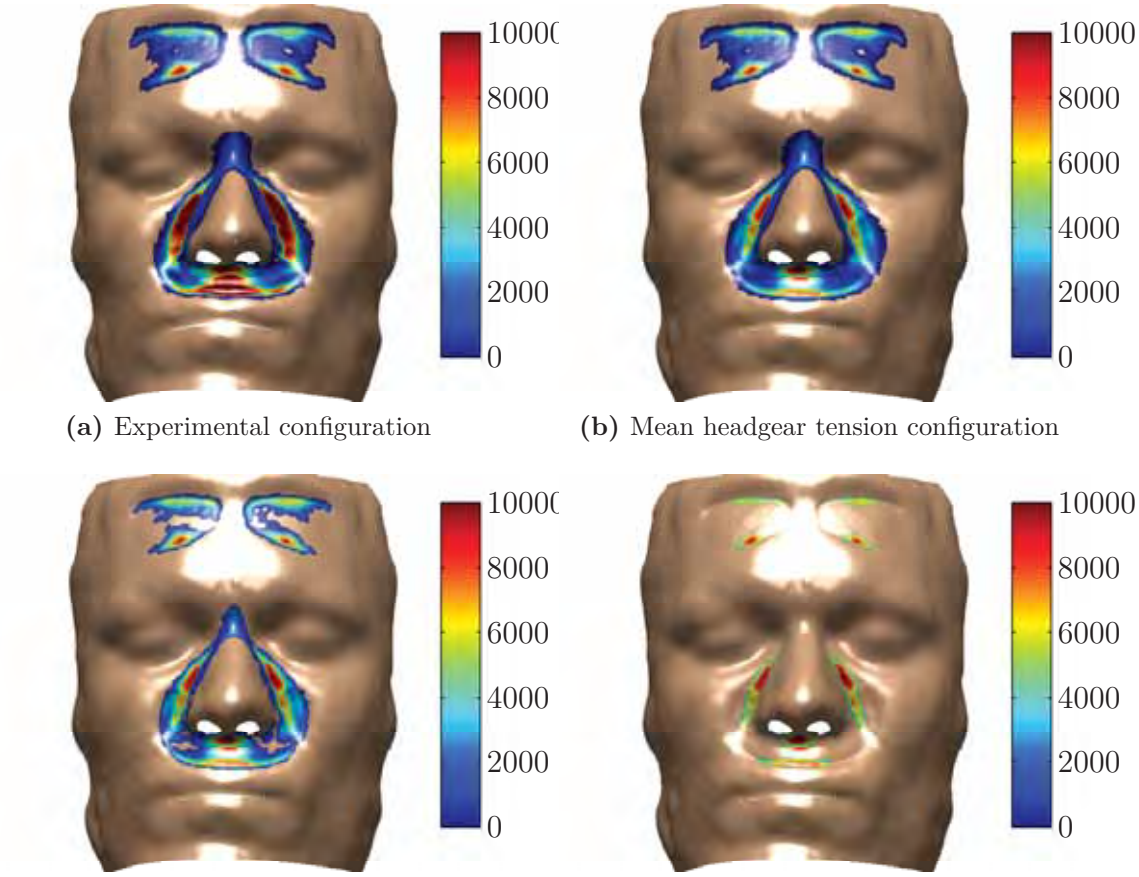

(a) Experimental configuration

(b) Mean headgear tension configuration

(c) Mean headgear tension configuration, 980 Pa threshold

(d) Mean headgear tension configuration, 5000 Pa threshold

Figure 11.19: Subject 12 mask contact pressures (Pa)

11.4.6 Collated Results

Each model in the mean headgear tension series is identical except for the facial meshes and the corresponding mask positioning. Therefore, the variation in the results is assumed to be due to the anthropometric variation among the sample.

A preliminary visual inspection of the collated data, presented in Figures 11.22 and 11.23, reveal several data trends. The maximum peak and mean pressures are located in the left and right hand sides of the nose. The contact pressure on the left and right hand sides are approximately of the same level and distribution. In the same manner as for the experimental configuration, a one way ANOVA test was evaluated of the mean contact pressure at the 5000 Pa threshold level, with facial region as the factor. The null hypothesis tested was that the means of the groups are equal ($H_0 : \mu_1 = \mu_2 = ... = \mu_n$) versus the alternative (H_1) that the means of all the groups are not all equal at confidence level of 95%. H_0 was rejected ($P < 0.01$) so all of the means are not considered equal. Tukey comparisons were performed (95% confidence level) to between the nasal groups. This test indicated, that the

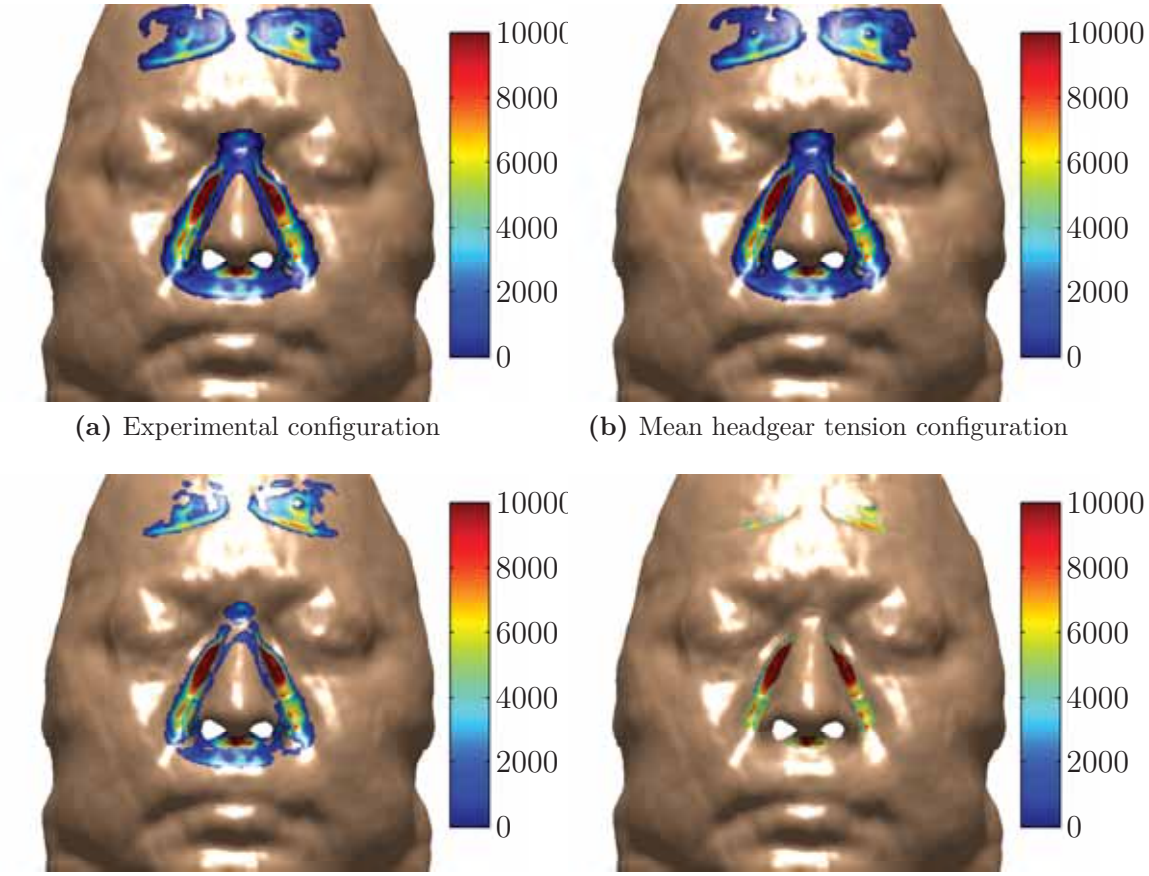

(a) Experimental configuration

(b) Mean headgear tension configuration

(c) Mean headgear tension configuration, 980 Pa threshold

(d) Mean headgear tension configuration, 5000 Pa threshold

Figure 11.20: Subject 14 mask contact pressures (Pa)

nasion contact pressure was significantly different to the left and right hand sides of the nose, though not the lip region. Consistent with the experimental configuration hypothesis that the means of the left and right hand sides are equal, cannot be rejected. Therefore, these results can be pooled for statistical analyses.

The lip region in the mean headgear tension analysis series exhibited a much narrower data distribution than in the experimental configuration. Considering that this analysis series held the headgear tension constant, this highlights the strong dependence of the lip region's contact parameters on the headgear load, which was identified in Section 11.2.6.

To investigate the sensitivity of contact pressure on the primary anthropometric independent variables, the contact mean pressure at the 5000Pa threshold level was regressed on the predictor variables of the age, participant BMI and the measures of nasal width, nasal height, nasal root width and naso-labial height in a stepwise manner. Only the BMI was found to be a significant factor, refer to Table 11.4.

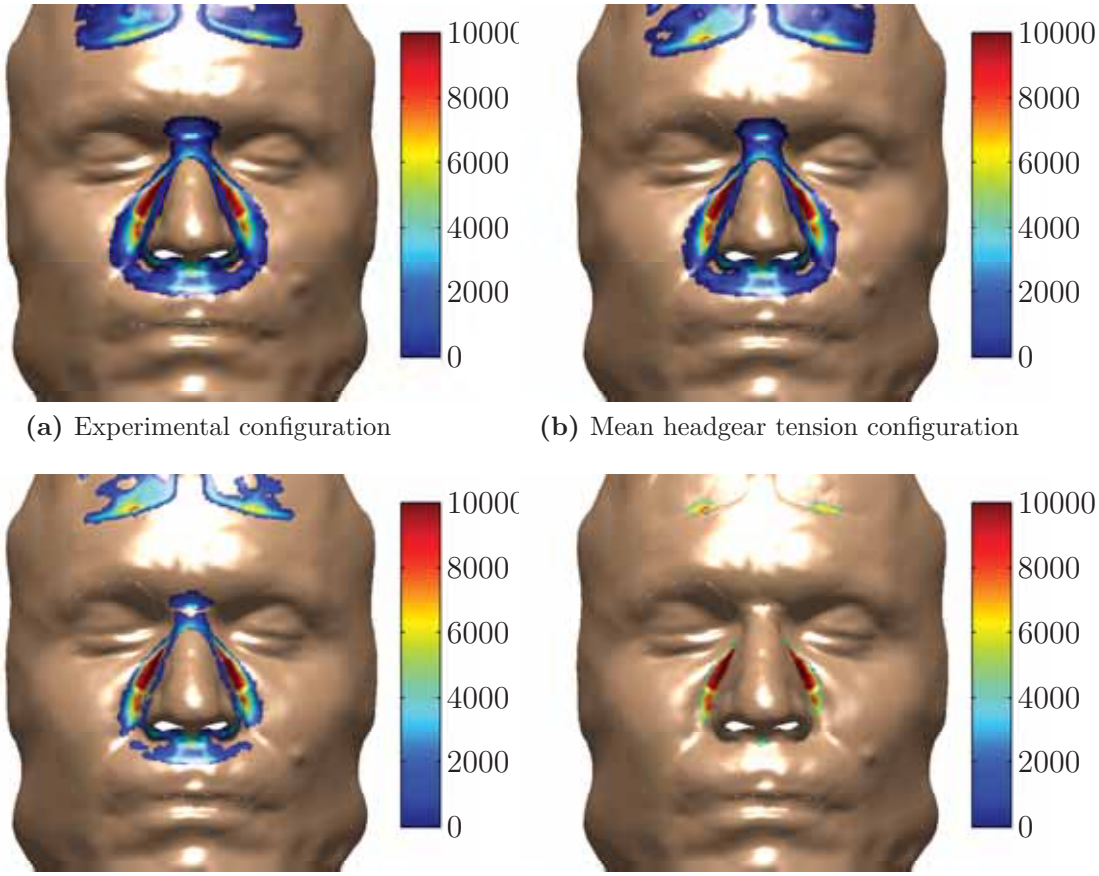

(a) Experimental configuration

(b) Mean headgear tension configuration

(c) Mean headgear tension configuration, 980 Pa threshold

(d) Mean headgear tension configuration, 5000 Pa threshold

Figure 11.21: Subject 25 mask contact pressures (Pa)

Therefore, the regression equation of $\bar{p}_{5000}$ on BMI for the pooled data for the left and right sides of the nose is;

$$\bar{p}_{5000} = 4159 + 115\text{BMI} \tag{11.7}$$

This regression equation accounts for 61% of variation in contact pressure in the sampled data.

The same regression process was used to evaluate the sensitivity of the contact pressure on the lip to the primary independent variables of age, BMI and the measures of nasal width, nasal height, nasal root width and naso-labial height. No significant association was found. It is acknowledged that the small sample size does limit the power of the investigation in this case. When this result is compared against the strong dependence found for this region on the lower strap tension, it is safe to conclude that in the lip region the contact pressure is much more strongly influenced by the strap tension than anatomical variation.

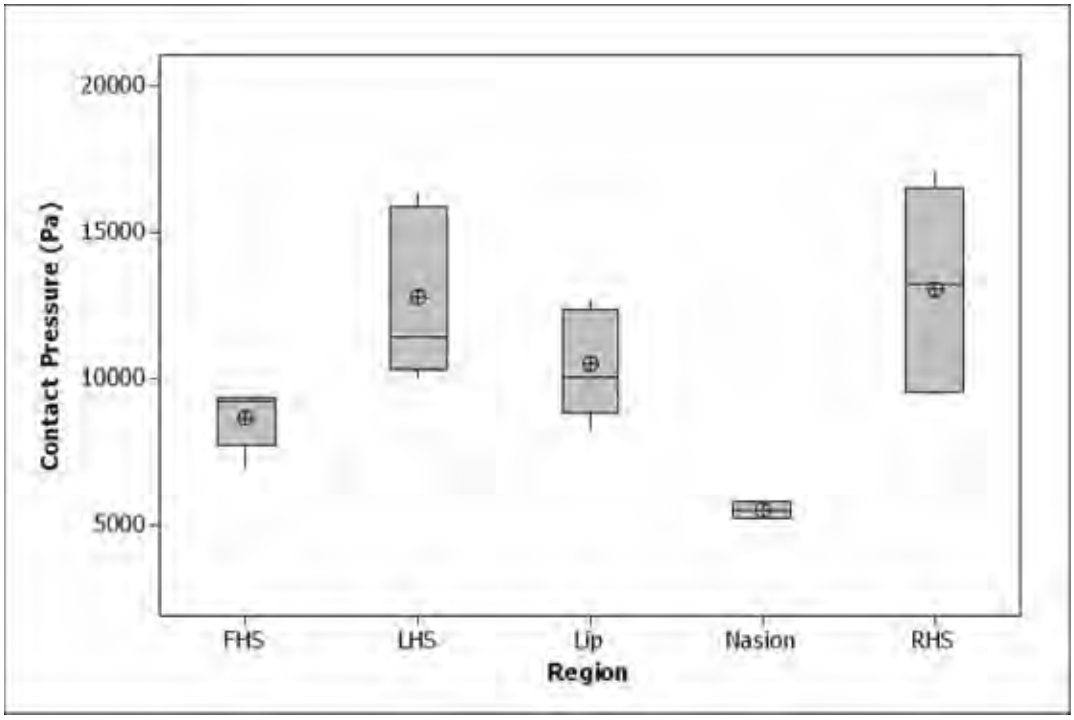

Figure 11.22: Boxplot of maximum contact pressures in each of the facial contact regions for the deformable FEA model in the mean headgear tension configuration

Table 11.4: Contact pressure regression output at the sides of the nose, mean headgear tension

Predictor	Coef	SE Coef	T	P
Constant	4158.8	876	4.75	0.001
BMI	115.31	32.6	3.54	0.008

$S = 556.252 \quad R^2 = 61.0\% \quad R^2_{adj} = 56.1\%$

Analysis of Variance

Source	DF	SS	MS	F	P
Regression	1	3870558	3870558	12.51	0.008
Residual Error	8	2475327	309416		
Total	9	6345885			

Similar to the lip region, the same regression process was used to evaluate the sensitivity of the contact pressure at the forehead region against age, BMI and the facial measurements. No significant dependency was found on anatomic variability.

11.5 Summary

The deformable model series have been developed, tuned and validated against physical test results. A series of simulations was performed controlling for headgear

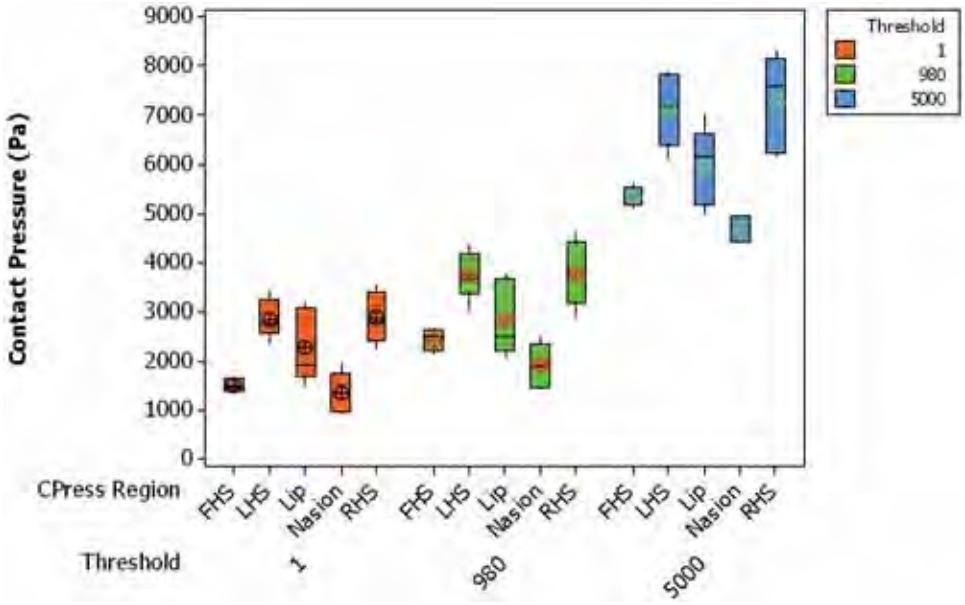

(a) Boxplot of contact pressure (Pa) at different pressure thresholds by facial region.

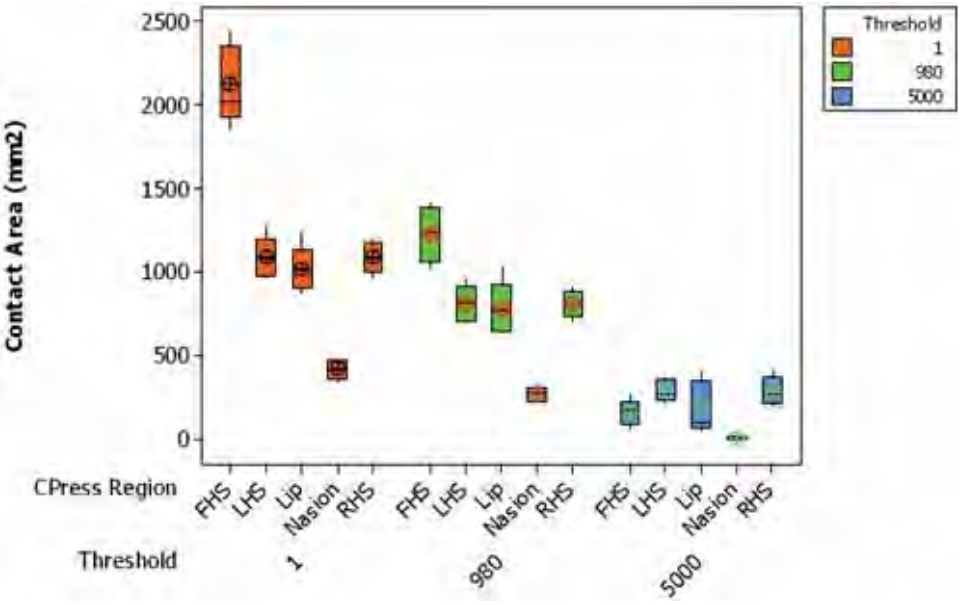

(b) Boxplot of contact areas $\left(\mathrm{mm}^2\right)$ at different pressure thresholds by facial region.

Figure 11.23: Contact parameters from the deformable FEA models in the mean headgear tension configuration

to investigate the subject to subject variability. Stepwise regression revealed an association between the contact pressure at the side of the nose and BMI. No other significant associations were found. This completes the deformable models with the UMII mask. Chapter 12 builds on this work by using an alternate mask with different mechanics on one of the validated face models.

Chapter 12

Activa LT Finite Element Analysis Models

12.1 Introduction

Chapters 10 to 14 of the CPAP FEA study have documented the development and validation of a range of FEA models. These include the individual components and assembly model of the ResMed UMII standard size nasal CPAP mask as well as the development of MRI based subject specific three dimensional deformable hybrid models and subject specific rigid facial profile models. This study has successfully demonstrated that the deformable and rigid finite elements models have been able to simulate the mechanical behaviour of the face and mask under CPAP therapy using the UMII mask. The models exhibited realistic mask behaviour. The mask successfully engaged on the face, capturing local buckling and postbuckling behaviour observed in use. The facial deformations calculated in the models agreed both qualitatively and quantitatively with the facial deformations measured using the MRI scans. A single pass optimisation was used to tune the material properties of each deformable subject specific mesh to reduce the residuals between the experimental and simulation data.

Considering the above model development and validation, the FEA models have been calibrated using the UMII mask and have replicated the experimental conditions encountered during the MRI scans. This provides confidence that the explicit FEA method is able to be reliably used to estimate difficult to measure parameters such as contact pressure or deep soft tissue states of stress and strain in these models. Since the models have been developed and calibrated to the same experimental data, the question remains about the generality of the models used. Therefore, it was planned to perform a preliminary evaluation of the predictive capability of the facial models by considering an the behaviour of an alternate mask on the face.

To meet this requirement one of the participants underwent a third scan wearing an alternate mask. The result set from this scan was quarantined and not used in

(a) Activa LT mask fully assembled. Note the expandable gusset near the base of the cushion of the mask

(b) Exploded view of the Activa LT nasal CPAP mask

Figure 12.1: ResMed Activa LT mask

any model tuning or calibration. The Activa LT was chosen as the alternate mask as it is still a nasal mask with contact and load paths in the same regions of the face as for the models developed, but significantly different in design and mechanical behaviour. Therefore, the mask swap in the assembly model is not simply a like for like swap, and allows the predictive ability of the model to be tested.

12.2 Activa LT Mask Description

The ResMed Mirage Activa LT mask is shown in Figure 12.1. In order to accommodate a range of facial shapes, it is available in four sizes; small, medium, large and large wide. The medium size mask was used in this study.

Like the UMII mask, the Mirage Activa LT consists of a frame, cushion, FHS, headgear, tubing and attachments.

The frame is moulded from polycarbonate (Makrolon 2458) and incorporates the mounting for the FHS T-bar into a single component. The FHS and cushion are manufactured from LSR. Since, as for the UMII, the frame is considerably stiffer than the compliant FHS and cushion, the frame along with the T-bar was modelled as a single rigid body. A swept groove locates the cushion on the mask, as a profiled clip positively locks it into position. The FHS is connected to the frame via the T-Bar. The frame/T-Bar connection is a variable piston joint which is adjusted by

a the anteriorly positioned dial driving a locating thread. Bilateral clip housings are located laterally towards the base of the frame. These are the fastening locations for the headgear.

The cushion is a complex component that can be considered in five regions:

Base The base of the mask that attaches to the frame.

Gusset A single folded expanding gusset. This acts to partially decouple the base from the body and undercushion to make the fit more robust to movement, misalignment, and to respond passively to pressure changes.

Body The bulk of the mask, which supports the undercushion. This is markedly taller in the Activa LT mask.

Undercushion This is continuous with the body and is essentially a complex swept 3D cantilevered spring with a varying section profile, approximating a C-section. This acts as a non linear spring during engagement and under load.

Membrane This is a lofted membrane surface with varying thickness. In large parts it is very thin (0.35mm) and acts to conform to the underlying facial shape and billow under a transverse pressure difference.

The FHS is the same component as used in the UMII mask. The previously developed FHS mesh was re-used in the Activa LT mask.

12.2.1 Mask Assembly Model

The Activa LT model was prepared using the same assembly hierarchy as the UMII mask. The Activa LT mask was modelled as an assembly with the cushion and FHS component meshes prepared individually then assembled into a top level model. These components were spatially positioned with respect to the mask coordinate system, the affine transformation matrices describing each component's position with respect to the mask's coordinate system are listed in appendix J. The Activa LT mask coordinate system is located on the sagittal midplane near the apex of the mask footprint and the connection to the frame. It is oriented with the X axis to the left of the subject, Y upwards and Z anteriorly. This is shown in Figure 12.2.

As previously mentioned the frame was assumed to be rigid compared to the compliant cushion and FHS. Therefore, the frame was modelled as a nodal based rigid body governed by a pilot node at its centre of mass and an assigned inertia tensor also calculated with respect to the frame's centre of mass. Refer to appendix

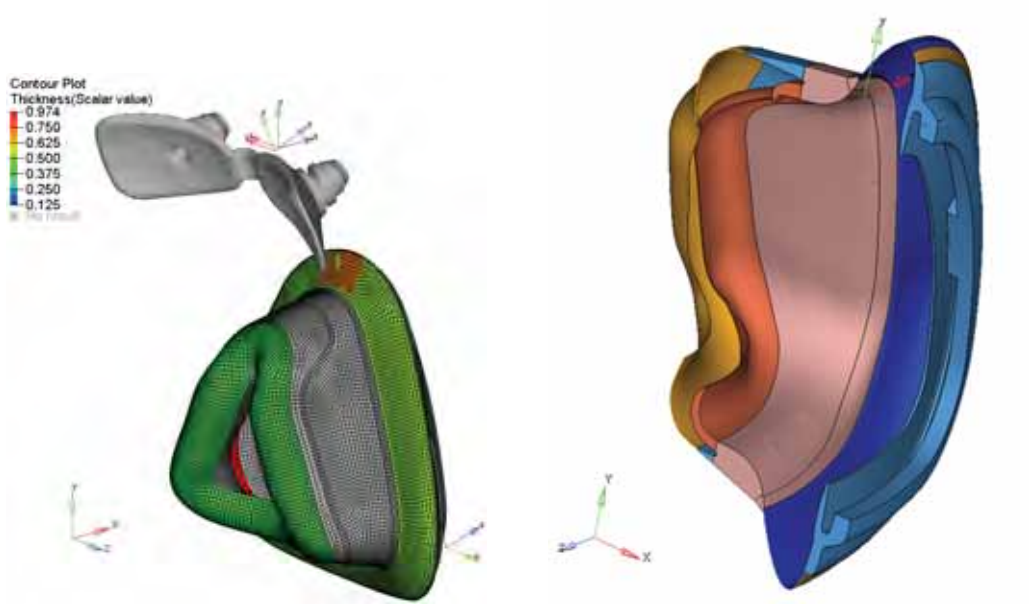

(a) Activa LT mesh showing the cushion and the FHS. The shell elements of the cushion are contoured according to their thickness scale (mm)

(b) Activa LT cushion mesh cross section. The regions of the cushion are identified; Base - light blue region around the cushion clip, Gusset - deep blue and gold shell elements, Body - large pink coloured region bulk of the mask attached to the gusset, Undercushion - orange swept cantilevered section, Membrane - gold shell lofted surface mesh and light blue tapered solid transition region

Figure 12.2: Activa LT and cushion mesh

J for the calculation of the mask frame inertia tensor. Nodal sets were defined on both the cushion and FHS at the connections to the frame. The pilot node at the centre of mass of the frame was used to apply resultant forces to the frame. The nodal rigid body and its connections are outlined in Figure 12.3.

12.2.2 Cushion

The Activa LT cushion is a very complex lofted shape, which is shown in figures 12.2b.

A high quality primarily QUAD/HEX mesh was developed for the cushion. The *base, body, membrane base* and *undercushion* have been meshed using fully integrated 8 node HEX elements. The degenerate edge of the undercushion was modelled by a row of wedge elements. The *gusset* and the lofted surface of the *membrane* were modelled using reduced integration shell elements. The connection between the

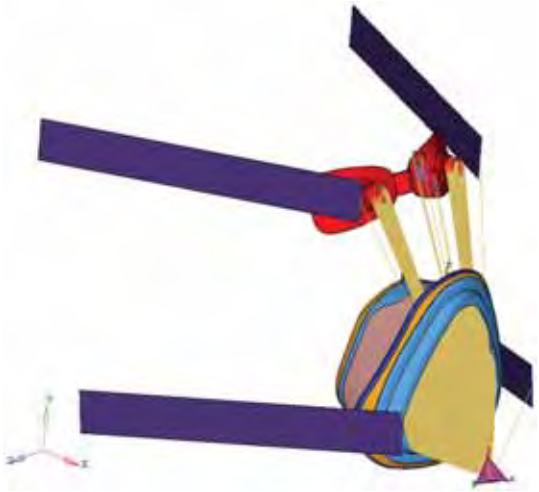

Figure 12.3: Activa LT mesh showing the nodal rigid body and its connections to model the frame. The independent or master node is located at the centre of mass

shells and solid elements were made using kinematic constraints tying both the translational DOF u_x, u_y, u_z and rotational DOF of the shell to the displacements of the nodes across the interface surface. The connection between the membrane base and the body of the mask was made using kinematic constraints tying the translational degrees of freedom of both sides of the interface. The mesh of the Activa LT cushion is shown in Figure 12.4.

12.2.3 Forehead support

The FHS in the Activa LT is identical to the FHS in the UMII model. The FHS was modelled with 8 node fully integrated HEX elements. Refer to section 10.4.3 and Figure 10.5 for details.

12.2.4 Headgear

The headgear in the Activa LT is identical to that in the UMII model. The headgear was modelled using fully integrated shell membrane elements. Refer to section 10.4.3 for details.

12.2.5 Activa LT Mask Contact Definition

The Activa LT mask contains a number of intra model contact regions. These follow the pattern of the UMII mask with the addition of the gusset self contact.

Contact regions were defined for interaction between the membrane and the undercushion as well as the gusset self contact. The LS-DYNA automatic contact algorithm was used for these interfaces, which searches for contact on both sides

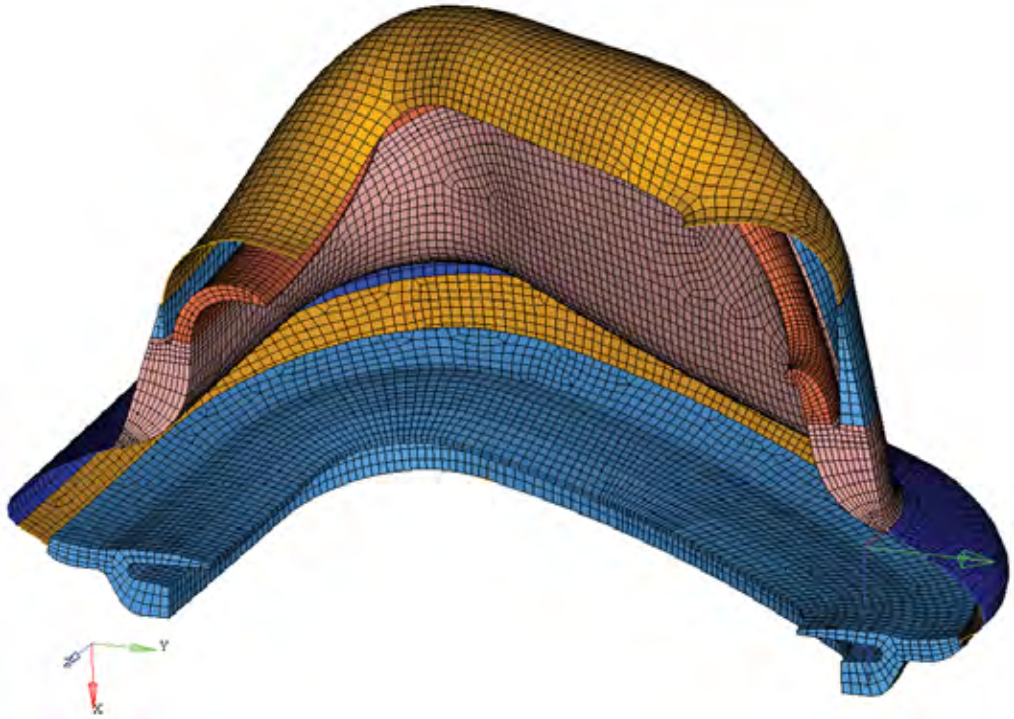

(a) Activa LT cushion cross section showing the interior, undercushion and base of the cushion. Note the constrained connection between the body and membrane base

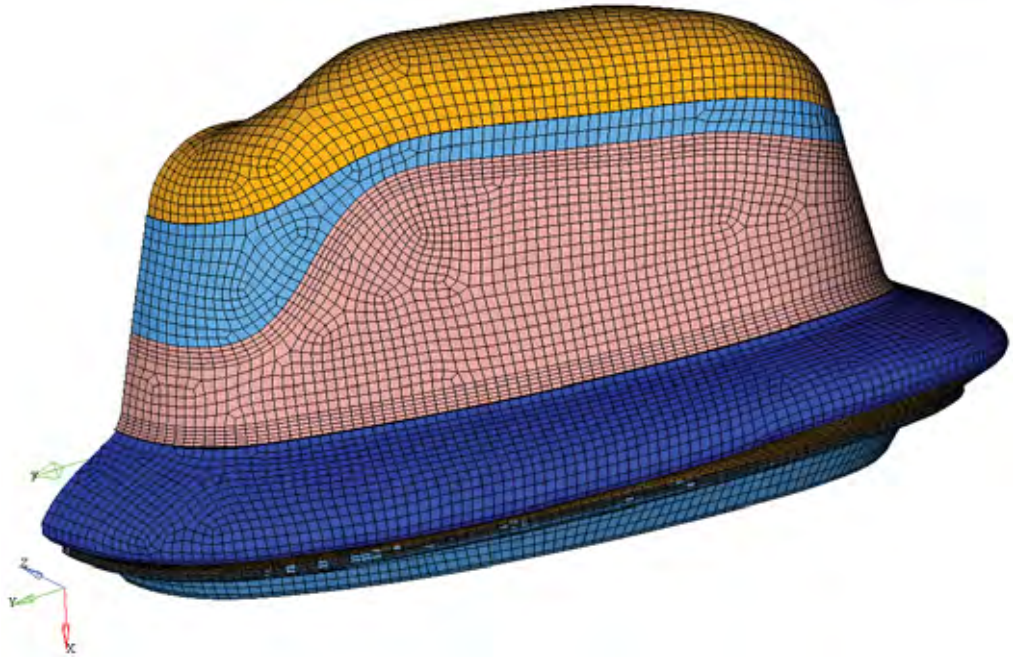

(b) Activa LT cushion mesh showing the exterior of the mask

Figure 12.4: Activa LT mesh images

Table 12.1: LSR material properties for a 3 parameter Mooney Rivlin model

Property	Value	
ρ	$1.12\,(10^{-3})$	g/mm^3
ν	0.499	
C_{10}	$0.4489\,(10^{6})$	Pa
C_{01}	$-0.3198\,(10^{6})$	Pa
C_{11}	$0.2781\,(10^{6})$	Pa

of shell elements. The penalty method is used for the contact surfaces in the mask model. Due to the compliant nature of the materials used, the `SOFT` contact formulation is used for each of the definitions. When using the `SOFT` formulation the penalty stiffness is calculated according to the timestep used in the explicit integration step.

12.2.6 Material Properties

Liquid Silicone Rubber

The Activa LT cushion is manufactured from the same LSR as the UMII, therefore, the material properties for the cushion and FHS were identical to those used in the UMII mask. The Dow Corning 94-595HC material was modelled with a 3 parameter Mooney Rivlin model as follows;

$$\Psi = C_{10}\,(I_1 - 3) + C_{01}\,(I_2 - 3) + C_{11}\,(I_1 - 3)\,(I_2 - 3) \tag{12.1}$$

The parameters of the model are reported for convenience in Table 12.1.

Breath-O-Prene

The headgear properties were identical to those used in the UMII model.

12.3 Face Model

Subject 25 was was scanned with both the UMII and the alternate Active LT nasal CPAP masks. Therefore, the facial mesh for subject 25, as outlined in Section 10.4 was re-used for the alternate mask CPAP assembly mask model. This mesh is shown in Figure 12.5.

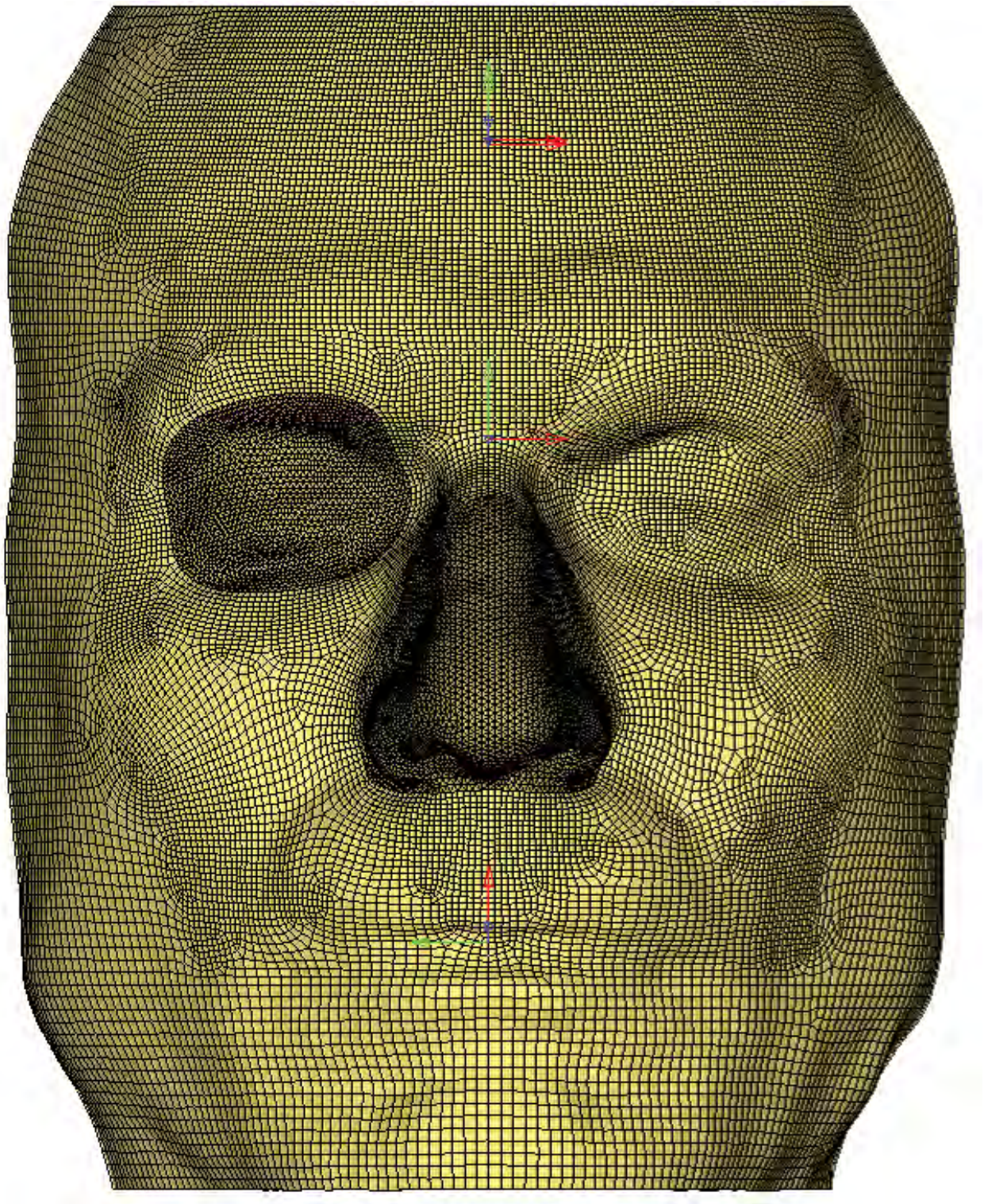

Figure 12.5: Subject 25 facial mesh consisting of a high quality mapped HEX mesh with the nose and right eye using TET elements

12.4 Assembly Model

Having independently prepared the face and the mask model, these were both assembled into a top level assembly model. The global coordinate system coincided with the origin of the face. The mask was positioned in the top level model so that there was a very small clearance between the face and the membrane of the mask. The mask was positioned to ensure that the membrane engaged with the upper lip and was not prematurely engaging with the nasal septum during the engagement phase. The top level assembly model is shown in Figure 12.6.

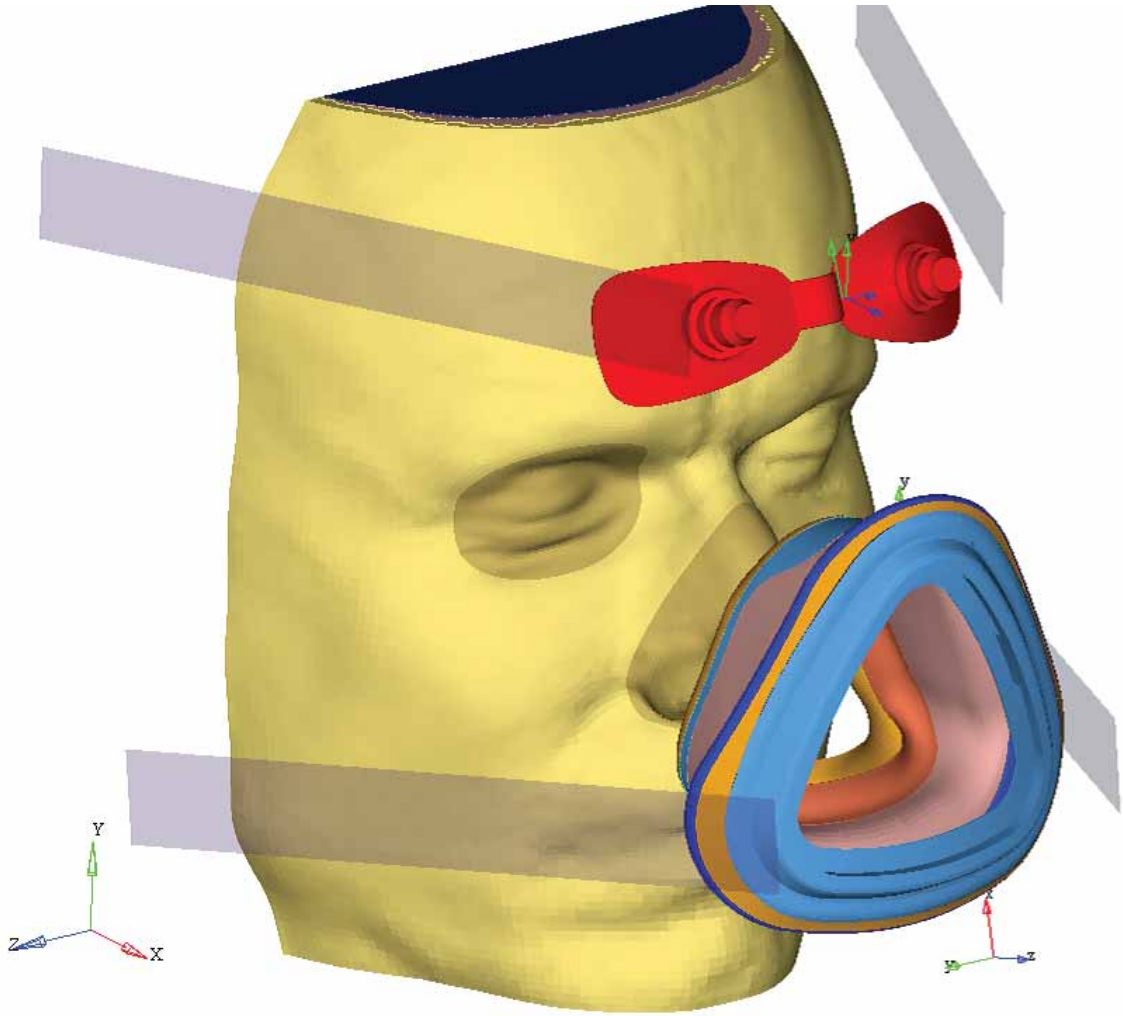

Figure 12.6: Top level assembly mesh with the Activa LT. For clarity, the rigid elements of the frame are not shown

12.5 Loads and Boundary Conditions

The same loading strategy was used for the Activa LT model as for the UMII model. The loads applied to the model consist of gravity, headgear tension and the CPAP therapy pressure. The gravitational load was applied as point load at the centre of mass of the frame and attachments. The constant gravitational load applied was as follows;

$$F_x = -1.426\text{N} \tag{12.2}$$

The headgear loads which were calculated from the applied weights during the fitting stage of the CPAP MRI were applied to the pilot nodes on the headgear.

$$\boldsymbol{F_{top}} = [-1.57, 0, 0] \tag{12.3}$$

$$\boldsymbol{F_{btm}} = [-0.88, 0, 0] \tag{12.4}$$

The CPAP pressure was applied as surface segment loads to the interior of the mask, including the gusset. The pressure was applied using a ramp function at $t = 1.5s$ as per the UMII model to allow the contact between the face and mask to be well engaged before inflating the cushion. This is necessary to prevent snap through of the membrane. The applied pressure was

$$P = 980\text{Pa} \tag{12.5}$$

Since the mask frame was modelled as a nodal rigid body and not included in the physical model, the action of the CPAP pressure on the rigid frame was not included in the segment loads. Therefore, the action of the therapy pressure was applied to the model as a concentrated force on the pilot node of the frame rigid body synchronously with the segment based pressure loads. The pilot node is located at the frame centre of mass, which forms the origin of the inertial coordinate system which is aligned with the principal moments of inertia of the rigid body, refer to Appendix J. The concentrated loads were applied as follower force and moments that moved with the frame. The equivalent pressure loads applied to the model with respect to the cushion coordinate system orientation were;

$$\boldsymbol{f}_{\text{csh}} = \begin{bmatrix} 0.1188 & -2.3074 & -0.0346 \end{bmatrix} \text{N} \tag{12.6}$$

$$\boldsymbol{m}_{\text{csh}} = \begin{bmatrix} -0.1145 & 1.9402 & -129.7664 \end{bmatrix} \text{Nmm} \tag{12.7}$$

Refer to Appendix H for details.

12.6 Simulation Settings and Job Submission

The Activa LT simulations were solved using the explicit method with LS-DYNA. All solution settings and parameters were identical to the UMII models. Refer to section 10.4.1 for a fuller description. The models were solved on the VAYU supercomputer at the NCI in shared memory mode using 64bit architecture on 8 parallel CPUs in a temporary scratch directory. Models were submitted through the PBS batch queueing system. Each model was checkpointed and killed at regular intervals then resubmitted recursively and restarted until the termination time was reached.

Binary nodal results were output for accelerations, velocities and displacements as well as contact forces and boundary reactions. Binary element results that were written to file include the stress and strain tensors. These results were output at a coarse interval of 0.15s prior to the pressure application stage, at which point the results interval was reduced to 0.05s. In addition a series of ascii result files were also generated to capture history data throughout the solution. These included nodal motion results, total energy summations, material specific energy summations, joint resultant forces and contact region resultant forces.

12.7 Results

The Activa LT mask was successfully engaged on the face, the kinetic energy of the system as a whole had decayed to less than 1% of the peak kinetic energy during the engagement phase. The quasistatic assumption for this simulation was valid with a ratio of kinetic energy to internal strain energy of

$$\frac{KE}{SE} < 0.001$$

The fully engaged mask is shown in Figure 12.7 along with the experimental configuration for this subject. The close similarity between the simulation and experimental results are clear. There is a small difference that is noticeable, namely that the mask is sitting slightly lower in the experimental configuration than the simulation results. This will be discussed towards the end of the chapter.

The FEA results for the CPAP simulation with the Activa LT mask are shown graphically in Figures 12.7 to 12.10. These results show that the soft tissue is deformed in particular on the side of the face from the headgear straps, the forehead and around the nose. The peak displacement magnitude in the model was at the posterior margin of the model at the headgear strap (3.7mm). Around the nose, the peak displacement was 2.3mm at the ridge of the philtrum, 2.0mm at the side of the

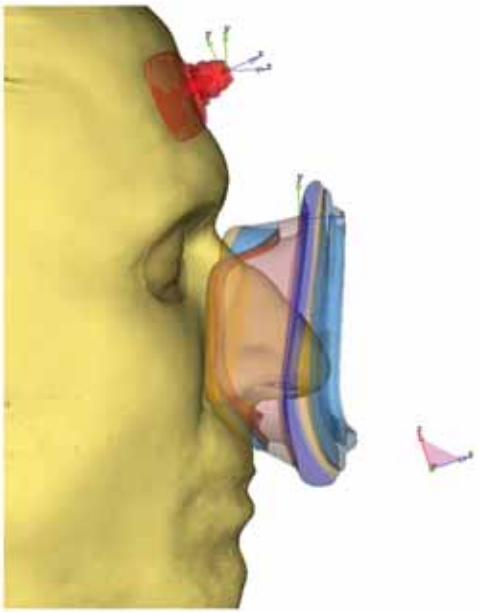

(a) Fully engaged mask model on the face. Note that this image includes loads from gravity (anterior - posterior direction), inertial effects from the tube and the applied therapy pressure

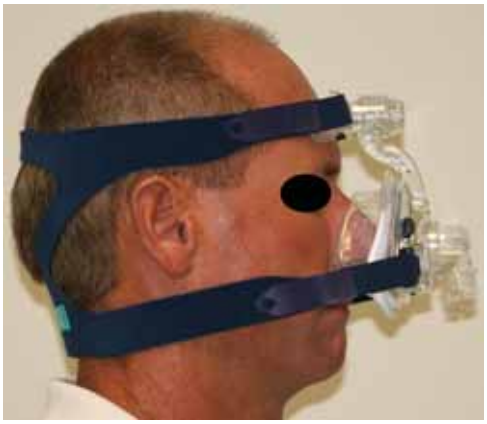

(b) Subject 25 experimental configuration using the Activa LT mask. Note that since the subject is standing up the gravitational load is in the inferior - superior direction and does not include tube mass, and since the mask is disconnected the therapy pressure load is absent

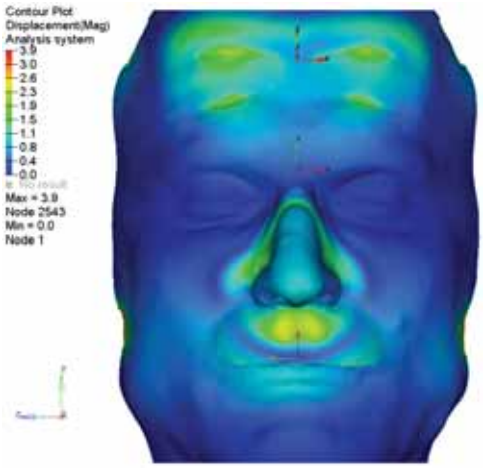

(c) FEA results

Figure 12.7: Images showing the engaged Activa LT mask on the face in both the simulation and the experiment

nose and 2.3mm at the top of the FHS. These results are not yet commensurate with the experimental data, which is reported in terms of the projected distance between the reference and deformed surfaces normal to the reference surface. The deformed surface of the simulation results were processed using the same algorithm as the experimental data to prepare commensurate data. Figure 12.9 shows a comparison

Table 12.2: Subject 25 Activa LT residual results

ROI	N	$\bar{r}_{rms}$ mm
Lip	319	1.07
LHS	82	0.76
RHS	84	2.12
NS	52	0.59
Weighted		1.14

between the experimental and simulation data sets. There is close agreement between the two data sets across the whole surface, as is highlighted by the unsigned and signed residual plots in Figures 12.9c and 12.9d respectively. These results show that there is very close agreement across the surface domain with the exception of the right hand side at the right hand side of the nose. To evaluate the effectiveness of the model to simulate the CPAP experiment, the mean residual was calculated for the identical regions of interest as used in the UMII mask. These were pooled into a weighted mean residual value. The regional mean residuals are summarised in Table 12.2.

From the results, good correlation occurs between the simulation and the experimental results in all regions except for the right hand side of the nose. Figure 12.8 shows that the experimental configuration for this participant was positioned obliquely, leading to greater deformation of the right hand side of the face. The FEA simulation corresponding to this experiment was prepared symmetrically. This explains the increased residuals on the right hand side. Even considering this discrepancy, the residuals between the experimental and simulation results are within the range of RMS weighted residuals encountered during modelling while using the the UMII mask. This comparative analysis provided evidence that the facial model as prepared for the UMII model series FEA is valid to use to predict the mechanical interaction not only for the UMII mask but also alternate masks with markedly different mechanics.

Considering that the comparison between the simulation and experimental results was favourable, this model can be used with confidence to provide pilot results for the contact between a deformable model of the face and the Activa LT mask.

The contact pressure results of the alternate mask simulation using the medium Activa LT mask are shown in Figure 12.10 and Table 12.3.

The Activa LT contacted the face on the forehead and surrounding the nose. This can be seen in Figure 12.10a. The forehead deformed conforming to the shape of the FHS. The load was evenly distributed between the upper and lower portions

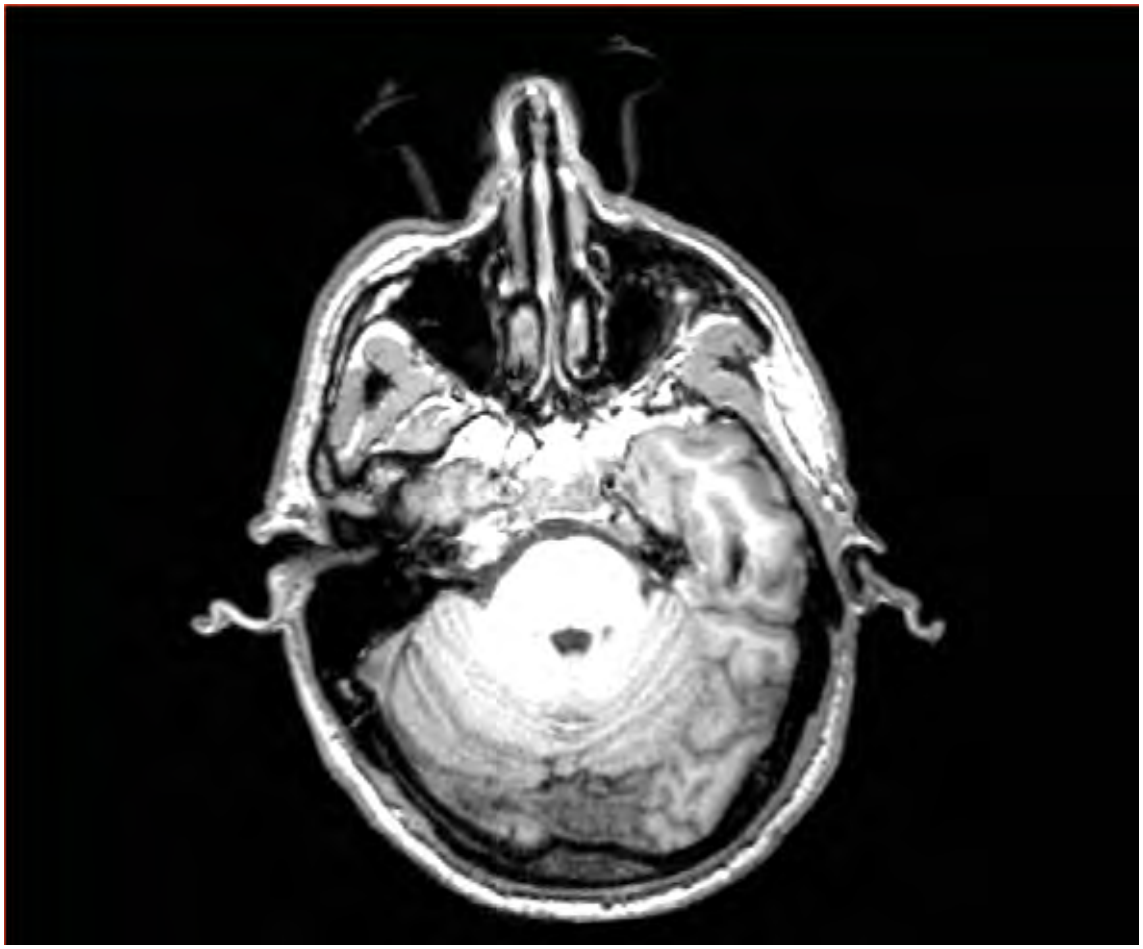

Figure 12.8: MRI scan slice of Subject 25 while using the Activa LT mask. This image is viewed from the inferior aspect so the right hand side of the body is on the left side of this image. Note that the mask is being worn obliquely with the right hand side being deformed significantly more than the left hand side.

Table 12.3: Subject 25 Activa LT mean contact pressure and contact area results on the facial regions of interest

ROI	$\bar{P}$ (Pa)			P_{max} (Pa)	A_C $\left(\text{mm}^2\right)$		
Threshold (Pa)	0	980	5000	-	0	980	5000
Total Nose	1136	1770	5791	10953	2949	1705	77
LHS	944	1497	-	-	745	416	-
RHS	1020	1600	4184	5107	791	441	3
Lip	991	1510	4031	5077	1129	648	4
Nasion	3063	3802	6052	10953	197	157	65
Forehead	1006	2141	4735	6511	1848	762	52

of the FHS. This is in contrast to many of the UMII simulations, where the angle of the FHS weighted the contact towards the lower edge.

Around the nasal region the contact pressures in this case are distributed much more evenly than has been exhibited in the UMII mask. This is shown in Figures 12.10a to 12.10c where the range of pressure values shown are significantly reduced, and the large region on the side of the nose of elevated contact pressure is absent.

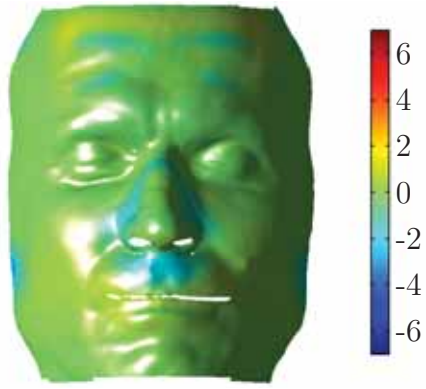

(a) Subject 25 FEA results showing the magnitude of the normal displacement deformation under CPAP therapy.

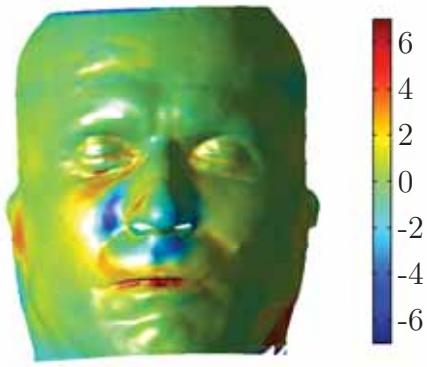

(b) Subject 25 experimental results showing the magnitude of the normal displacement deformation under CPAP therapy.

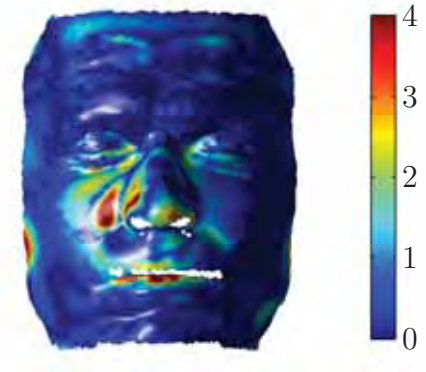

(c) Subject 25 unsigned residuals.

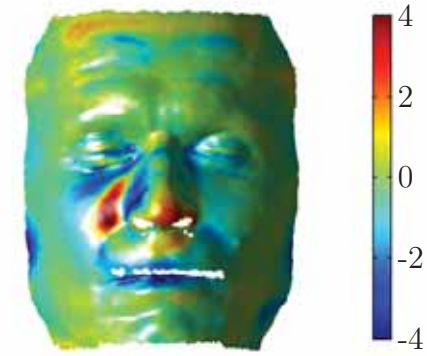

(d) Subject 25 signed residuals.

Figure 12.9: Subject 25 Experimental and FEA normal deformation magnitude (mm)

It is notable that the location of the peak contact pressure in this case was found on the bridge of the nose, whereas for the UMII mask the peak contact pressures and hence dominant load paths were through the side of the nose.

The contact between the soft tissue and the underlying skull can be seen in Figure 12.10d. The peak contact pressure ($P_C = 11194$Pa) at this interface is located at the transition between the nasal cartilage and the nasal bone. This is directly under the peak contact pressure at the skin/mask interface. There is an elevated region of pressure ($P_C \approx 5000$Pa) on the maxillae surrounding the nasal orifice. The contact pressure on the flat regions of the maxillae surrounding the are relatively even at a reduced level of approximately 2000Pa. The applied load from the forehead support is reacted by the contact with the skull beneath the interface. It can be seen that the contact pressure boundary here is not as distinct as the load is distributed through the soft tissue to the frontal bone.

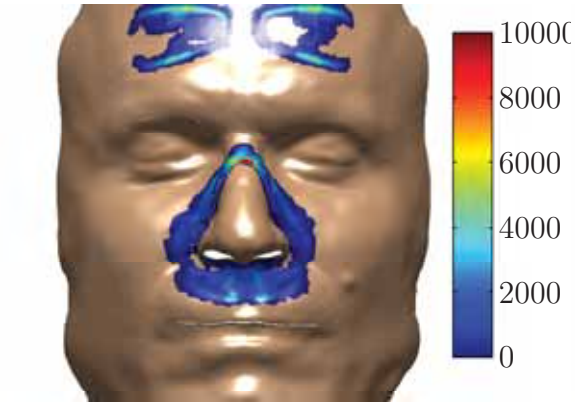

(a) Contour of contact pressure showing total mask contact area

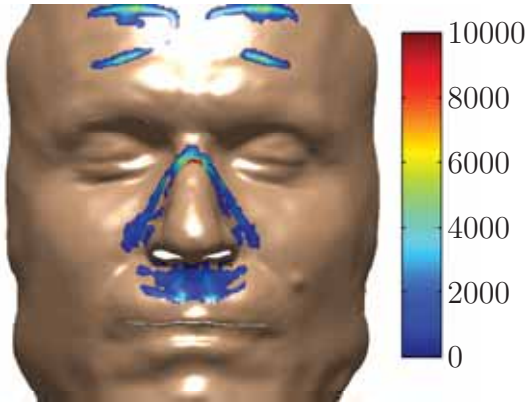

(b) Contour of contact pressure showing contact area such that $P > 980$Pa

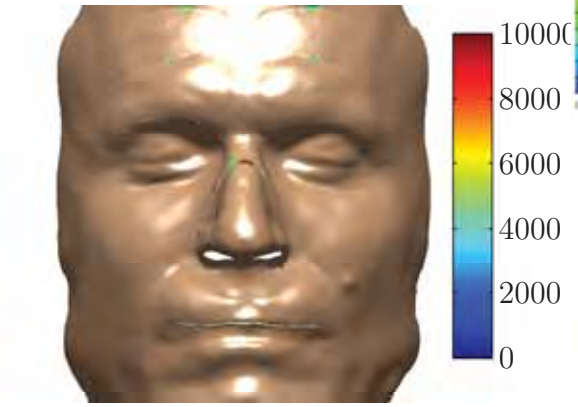

(c) Contour of contact pressure showing contact area such that $P > 5000$Pa

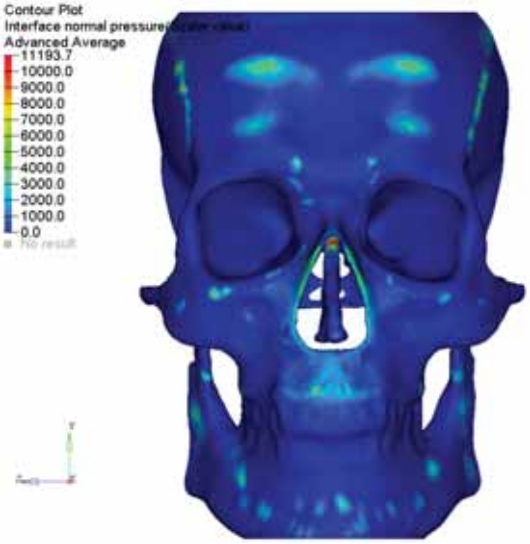

(d) Skull contact pressure (Pa). Note peak contact pressure is located near where the nasal septal cartilage blends into the nasal bone.

Figure 12.10: Subject 25 contact pressure results with the Activa LT mask

12.8 Discussion

The Activa LT simulation (alternate mask) was intended to challenge the facial model prepared as part of the deformable models series. This challenge evaluated the usefulness of the simulation as a predictive tool beyond the tuned specific application. One original participant underwent a third scan with an alternate mask. The resulting data set was quarantined and used only to establish differences between experiment and simulation. This utilised the normal deformation algorithm outlined in Sections 8.6.8 and 10.9.

The results the Activa LT simulation are very encouraging. Without tuning the facial model (used in the UMII model series,) the simulation of the mask/face system in the experimental configuration returned a weighted RMS residual of only 1.14mm. This weighted residual incorporates the discrepancy from the oblique position of the mask during the scan.

This excellent result provides evidence and confidence that the deformable facial model is valid, and the assembly modelling technique may be used to reliably predict complex mechanical behaviours in mask/face systems. The whole system operates within a large deformation regime. It incorporates non-linear contact for both the skull/soft-tissue and mask/face interfaces.

Considering that the model is validated across masks with different designs, it is possible to compare the mechanical behaviour of the facial interface using the Activa LT with that of the UMII mask. The results from these analyses indicate that the nature of load path from the mask to the face is different. The UMII results are characterised by pressure concentrations at the side of the nose, whereas the Activa LT mask provided a more even distribution with only a small area of concentration near the edge of the membrane across the bridge of the nose. The gusset included in the Activa LT mask body has decoupled the facial interface with the cushion from the mask frame to some extent. This has allowed the mask to adopt a stable equilibrium configuration on the face with the load distributed evenly. These are all advantages for the Activa LT over the older UMII mask. The pressure concentration at the nasal bridge is due to the seal membrane being strained and conforming to the shape of the nose. The same effect is noticeable in the UMII mask, though in this case it was dominated by the undercushion load path. It was noticed that the participant positioned the Activa LT mask lower on the face compared to the UMII mask; this explains the increased value of contact pressure in this location, as the nose widens inferiorly from the nasion causing increased strain in the membrane on the Activa LT. This might well be reduced if that mask were positioned slightly higher, without significantly comprimising the reduced contact pressures around the

nose. Therefore, these analyses have been able to identify the superior interface load transfer characteristics of the Activa LT compared to the UMII mask on the whole as well as explain the mechanics of the peak contact pressure at the nasal bridge.

The correlation with experimental results is particularly valuable. It allows modelling to be informative for the critical early stages of mask design and development and predictive of the mechanical behaviour of mask/face systems prior to physical prototyping. To the author's knowledge this is the first development that is capable of providing such information on deformable facial models simulating CPAP.

This simulation demonstrated the utility of the deformable models to predict the mask/face system. The current design process does not take facial deformation into account. Therefore, it is desirable to quantify the influence of the rigid assumption on the mask/face system. Attention will now turn to the development of rigid facial models enabling comparisons between deformable and rigid facial models.

Chapter 13

Rigid CPAP Finite Element Analysis Model Series

13.1 Introduction

In addition to the deformable series of models that were described in Section 11, a parallel series of models was developed corresponding to the experimental configuration, however in this case, the face was considered to be a rigid body. This modelling strategy aligns with the existing mask design and development process, where anthropometric data from faces in the reference condition are used to dimension and design masks without considering the nature of deformation of the face while under therapy. The modelling process for the rigid model series differs slightly from the deformable series.

13.2 Rigid Face Model

The rigid facial profile model development commences at the triangular faceted surface output from the MRI 3D reconstruction step. The smoothed faceted surface was decimated to give a mean element edge size of approximately 1.0mm or less. This corresponds to the element size used in the deformable models. The faceted surface was exported as an Stereolithography (STL) file. This was in turn imported into the FEA preprocessor, Hypermesh ®, to initialise a triangular surface mesh.

The triangular surface mesh was extruded 1mm towards the interior of the face, ensuring that the exterior surface of the mesh was coincident to the original triangular mesh, This process generated a mesh of pentahedral wedge solid elements. Since the soft tissue was regarded as rigid, element shape metrics were not of critical importance, as the elements were not able to deform. Therefore, a check was performed to ensure that the extrusion process did not result in any inverted elements and that all elements were valid. As the face was considered rigid, for these

analyses there was no need to model any of the soft tissues beneath the surface of the skin. A thin single layer solid mesh was used, rather than the shell mesh to simplify the contact interactions further downstream, and not to offset the actual contact interface surface from the skin. An example of the rigid facial profile model is shown in Figure 13.1.

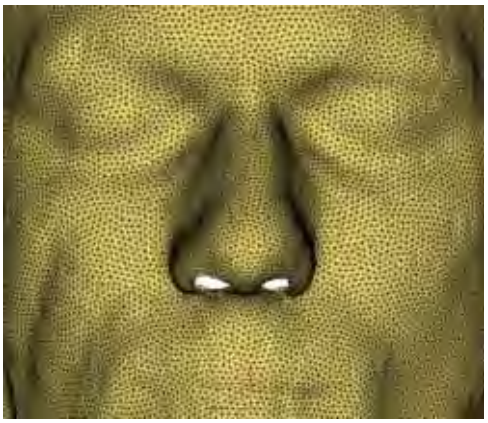

(a) Close up of the smoothed single layer solid mesh seeded with a triangular surface mesh

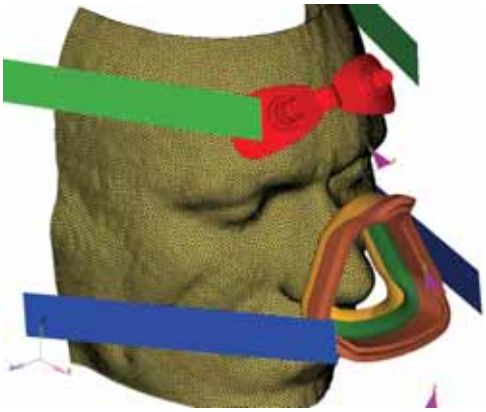

(b) CPAP FEA rigid model with UMII mask positioned ready for engagement on the face. Magenta triangular elements are for visualisation only and indicate coordinate system locations and track deformations

Figure 13.1: Rigid CPAP FEA model details

13.2.1 Material Properties

The face was assigned to the rigid material property, `*MAT_RIGID (*MAT_020)`, in LS-DYNA. This greatly reduces computational demands as elements assigned to rigid materials are bypassed for element calculations and element based history result storage (LSTC, 2010). The material properties entered for the The primary input required for the `*MAT_RIGID` material model is the density, which is used to calculate correct inertial properties. The material properties assumed for the rigid soft tissue are outlined in Table 13.1. The density in the rigid body is used primarily to calculate the inertia tensor of the rigid body. The linear elastic properties for a rigid body are used to calculate the penalty contact stiffness for interaction with other components. As with the deformable models, the head was constrained, since all the nodes in the rigid body move in concert, only a master point need be constrained. This facility is provided with the `*MAT_RIGID` model by allowing for the constraint of the rigid body's centre of mass in all six degrees of freedom.

Table 13.1: Assumed rigid soft tissue material properties

Property	Value
ρ	0.001g/mm^3
E	$20.0\,(10^3)\,\text{Pa}$
ν	0.45
Constraint	Fully constrained at centre of mass

13.3 Top Level Assembly Models

The rigid top level assembly models were developed using the same procedure as has been previously described in Section 3.3.6, however in this case the rigid skin mesh was used in place of the deformable facial model. The UMII mask model was assembled into the model using the same configuration and positioning as for the deformable series for corresponding runs. For those subjects that did not have deformable models prepared, the same positioning procedure of the mask was used.

13.3.1 Rigid Face / Mask Assembly Contact Definitions

The contact interfaces and their definitions between the face and the mask were identical to those described for the deformable models in Section 10.6.1. The contact regions in between the face and mask are;

- Face / Membrane - refer to Table 10.10
- Forehead / FHS - refer to Table 10.11
- Head / Headgear (Top left) - refer to Table 10.12
- Head / Headgear (Top right) - refer to Table 10.12
- Head / Headgear (Bottom left) - refer to Table 10.12
- Head / Headgear (Bottom right) - refer to Table 10.12

13.3.2 Rigid Model Applied Loads and Boundary Conditions

The loads applied to the rigid model correspond to the experimental configuration as outlined in Table 8.7 (p 98).

The individual loads applied to the models are given as follows;

- Gravitational load - refer to Section 10.7.1
- Headgear load - refer to Section 10.7.2
- Headgear enforced displacement - refer to Section 10.7.3
- CPAP pressure therapy load - refer to Section 10.7.4

The load staging used in the rigid series if models was identical to the deformable models, refer to Section 10.7.5.

The DOF boundary conditions applied to the rigid models are similar to those used in the deformable models. The difference is that the constraints to fully fix the rigid face were applied to the model through the rigid material definition, rather than as a nodal DOF constraint set. Otherwise the boundary constraints were identical to the deformable series. A prescribed velocity was used to quickly engage the mask onto the face prior to releasing this constraint and allowing to approach equilibrium.

13.4 Simulation Settings and Job Submission

The rigid series of models were solved using the explicit method on the VAYU supercomputer at the NCI using the same settings as outlined in Section 10.4.1.

13.5 Postprocessing

The deformation field obviously has no value for the rigid series of models and was not considered. The contact results from the rigid models were processed in an identical manner to the deformable series. The scalar contact pressure field was integrated over the contact area at each of the threshold pressures of 1Pa, 980Pa and 5000Pa. These results correspond to the experimental configuration and are able to be directly compared to quantify the influence of assuming the face is rigid, as is the current mask design practice.

13.6 Results - Experimental Configuration

Rigid models were prepared for all of the valid data sets acquired during the CPAP MRI. A total of $N = 25$ participants were recruited. Of these, 3 participants were excluded either due to non correctable artefacts in the original scan data, or last

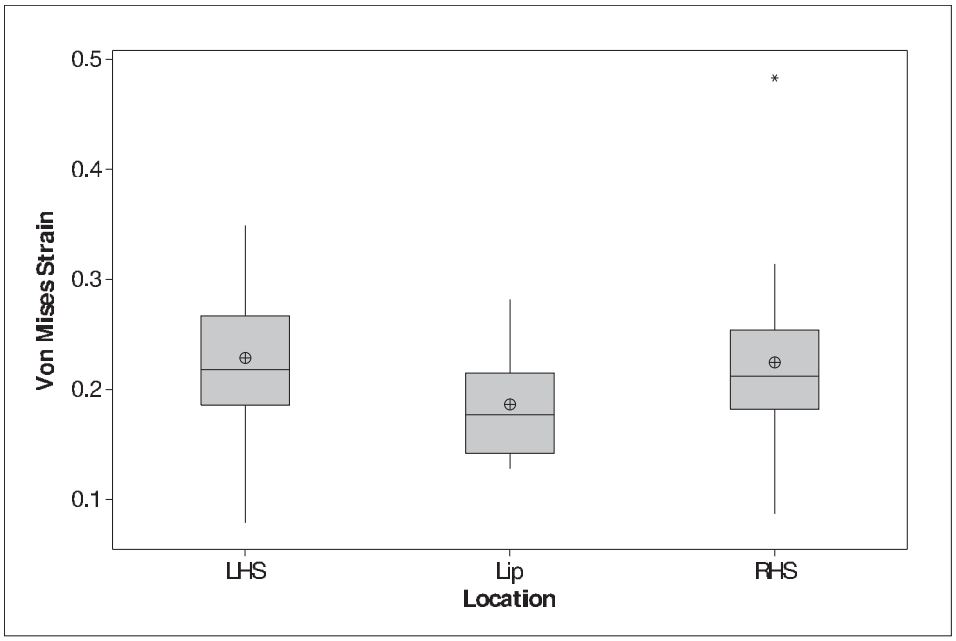

Figure 13.2: Mask cushion Von Mises equivalent strains

minute removal of the participant from the study due to safety concerns in the high magnetic fields of the MRI environment. Therefore, the final data set of $N = 22$ were available for analysis.

Qualitatively the engagement of the mask on the rigid facial profiles matched the engagement on the deformable profile. The FHS engaged first and acted as a fulcrum as the cushion engaged with the face. The membrane of the cushion first engaged on the sides of the nose. The undercushion then progressively engaged along the sides of the nose before coming into contact at the philtrum. The addition of the CPAP therapy pressure loading on the mask acted to inflate the membrane and even out the pressure between the face and the membrane in the regions where it has not buckled. Again similar to the deformable model there is some buckling and wrinkling of the membrane propagating from the alar nasi landmarks. The effect of this is evident in a contact pressure fringe plot showing paths of low contact pressure across the contact of the membrane from the alar nasi.

The von Mises equivalent strain was calculated from the Hencky strain tensor. Representative results are shown for Subjects 12 and 14 in Figures 13.3 and 13.4 respectively. These subjects were chosen for graphical presentation of representative results as they are the participants with the extreme values of BMI providing markedly different facial shapes. Additionally for consistency, subject 12 was used as an example during model development and validation.

The strains recovered from the mask cushions for the rigid series of models in the experimental configuration are represented as boxplots in Figure 13.2. The peak

(a) Experimental configuration

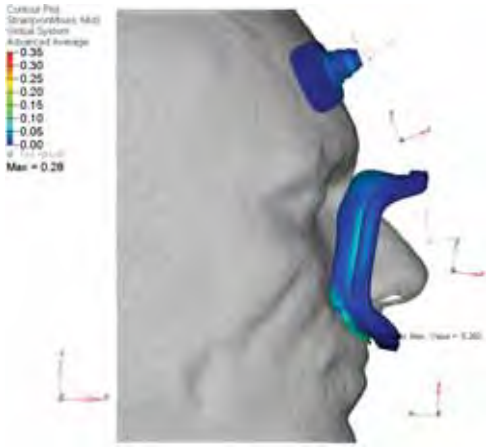

(b) Fully engaged mask on rigid facial profile

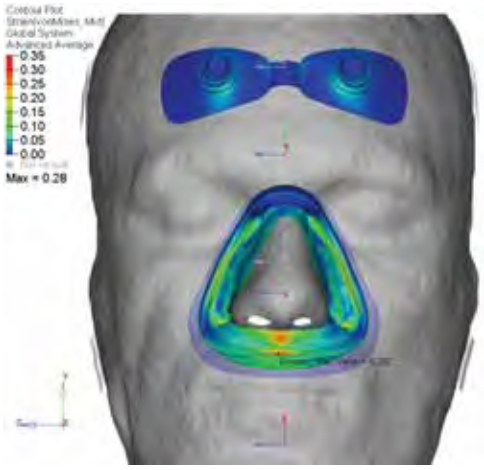

(c) Mask strain

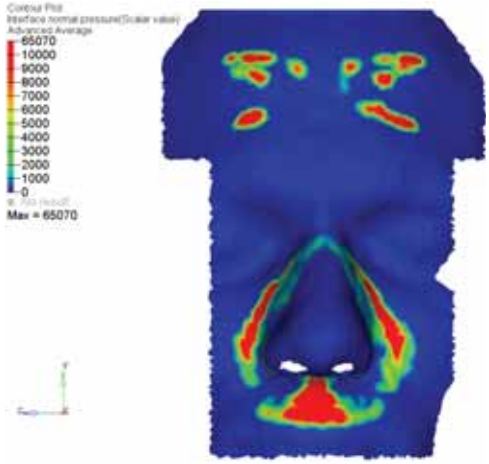

(d) Contact pressure saturated at 10 kPa. Note the regions of reduced pressure below the membrane wrinkles

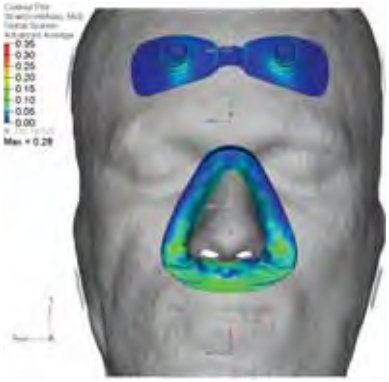

(e) membrane fully engaged. Note buckled membrane propagating from the alar nasi.

Figure 13.3: Sample results from Subject 12

(a) Experimental configuration

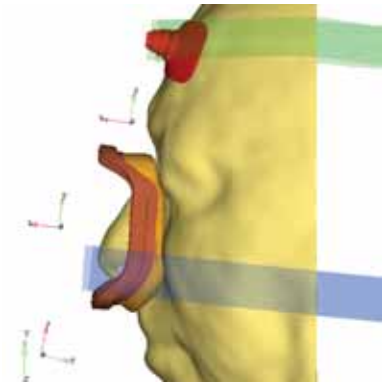

(b) Fully engaged mask on rigid facial profile

(c) Mask strain

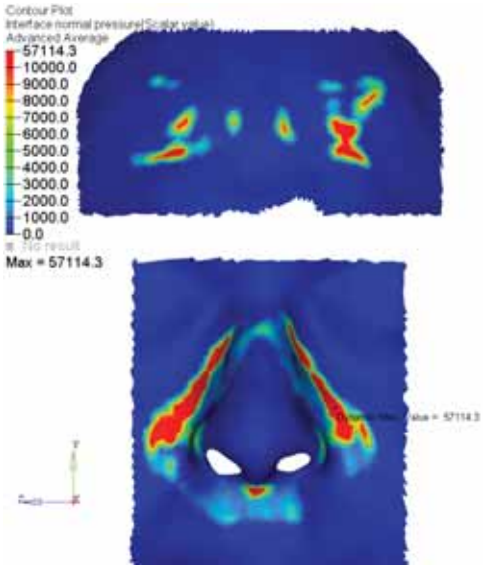

(d) Contact pressure saturated at 10 kPa. Note the regions of reduced pressure below the membrane wrinkles

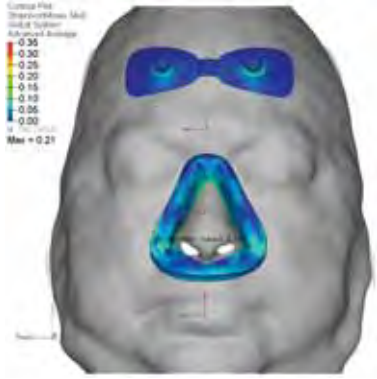

(e) membrane fully engaged. Note buckled membrane propagating from the alar nasi.

Figure 13.4: Sample results from Subject 14

equivalent strain in the undercushion of the mask for the rigid model experimental series was $\sigma_{VM} = 0.35$ one outlier was found for subject 19 [1].

The contact pressures between the face and the mask for subjects 12 and 14 are shown in Figures 13.3d and 13.4d as well as Figures 13.5 and 13.6 where the contact pressures are thresholded at 0 Pa, 980 Pa and 5000 Pa. These samples are shown as representative of the extreme body structures within the study. The dominant features of the interface between the face and mask are the regions of high pressure under the deformed cantilevered spring of the undercushion on each side of the face. The upper lip is another significant region of contact pressure. Due to the rigid facial profile, the pressures calculated concentrate around the prominent ridge of the philtrum. In comparing these results it can be seen that the contact pressure on the upper lip of subject 14 was significantly lower, shifting the resultant centre of pressure upwards, to increase the portion of the load that is borne through the left and right sides of the undercushion in preference to the labial region. In each case, the buckling of the membrane was evident propagating from the alar nasi, creating regions of low contact pressure or even open contact, providing a potential leak path.

Peak contact pressure results were found to vary significantly across the sample. As noted above, the peak contact pressure was concentrated around the ridge of the philtrum. This is an artefact of the rigid assumption. As contact is made, the penalty algorithm applies a spring force to the node proportional to the interference between the slave and the master elements. In the case of a two deformable bodies interfering, both bodies deform to adopt a contact region, which will increase the contact area and act to smooth and distribute the contact pressure over a larger area. In the case of a finite element discretisation, this will recruit more contact elements and nodes into the region distributing the load and reducing both the penetration and hence penalty force at individual nodes. For the rigid assumption however, the facial profile does not deform, and is subject to undistributed concentrations around prominent anatomical locations such as the philtrum and nasolabial ridges as the penetration and forces are not distributed during deformation. Additionally this forces excessive deformation to be carried by the deformable member of the contact pair increasing the internal loading in this component. For this reason, the contact pressure results for the rigid series will only refer to the integrated mean pressures and not absolute peak values which are highly dependent on the rigid body assumption.

[1] An outlier was classified as any value exceeding the third quartile by 1.5 times the interquartile range

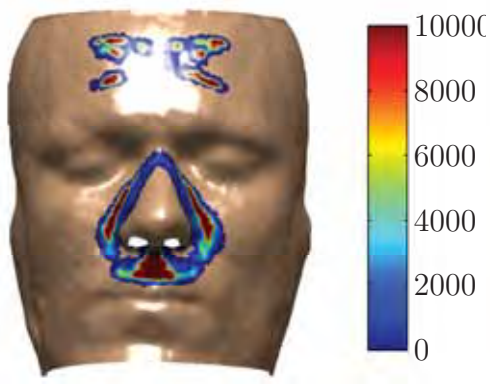

(a) Contour of contact pressure showing total mask contact area

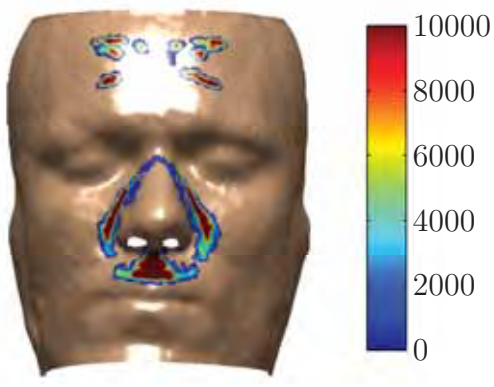

(b) Contour of contact pressure showing contact area such that $P > 980$Pa

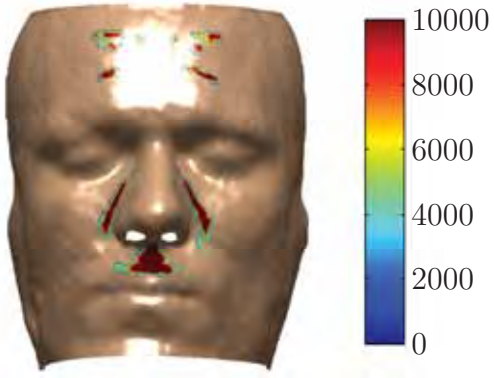

(c) Contour of contact pressure showing contact area such that $P > 5000$Pa

Figure 13.5: Subject 12 mask contact pressures (Pa)

The collated results from the experimental configuration model series are presented graphically in Figure 13.7. The same one way ANOVA test, as used in the deformable models was applied to the data from the rigid model series. The null hypothesis that the mean contact pressure (5000 Pa threshold) at each location is equal ($H_0 : \mu_1 = \mu_2 = ... = \mu_n$) was rejected ($P < 0.01$). Tukey comparisons indicate that the contact pressure at the nasion is significantly different, lower, to the regions of the lip and both sides of the nose. No significant difference was found between the lip and the sides of the nose. As mentioned in Section 11.2.6, the participant specified headgear tension confounds the investigation into the sensitivity of the contact parameters on anatomical variations, and must be taken into account.

For the experimental configuration of the rigid model series, the contact pressure at the 5000Pa threshold level at each of the nasal regions and forehead was regressed in a stepwise manner on age (yrs), BMI (kg/m^2) and headgear tension (F_{XBtm}) or (F_{XTop}). Data from the left and right sides of the nose were pooled as the hypothesis

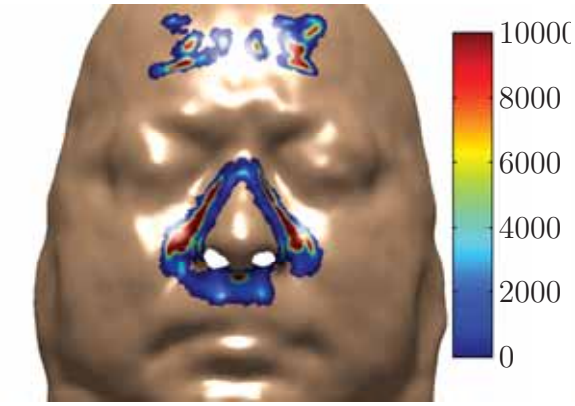

(a) Contour of contact pressure showing total mask contact area

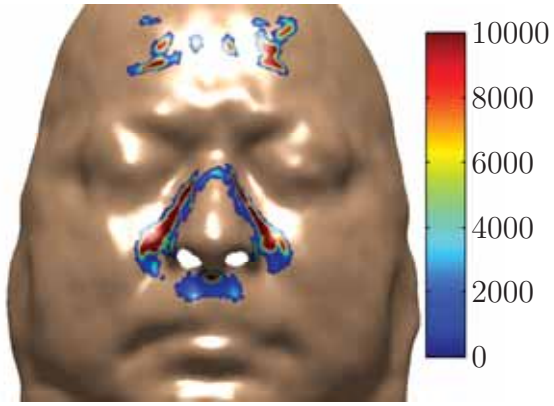

(b) Contour of contact pressure showing contact area such that $P > 980$Pa

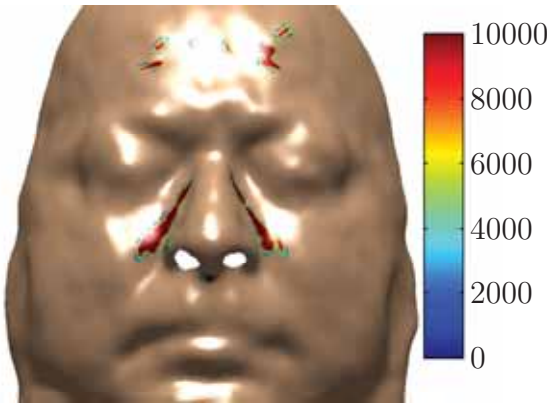

(c) Contour of contact pressure showing contact area such that $P > 5000$Pa

Figure 13.6: Subject 14 mask contact pressures (Pa)

Table 13.2: Summary of contact pressure ($P > 5000$) predictor variables for the various facial regions. Check marks (✓) denote significant factors, crosses (✗) denote factors not reaching significance, dashes (-) denote variables not included in stepwise regression

	Predictors				
Region	Age	BMI	HG Top	HG Btm	Nasal Width
Sides	✓	✓	-	✓	✗
Lip	✗	✗	-	✗	✗
Nasion	✗	✗	-	✗	✗
FHS	✗	✗	✓	-	✓

that their means were equal could not be rejected. Table 13.2 identifies which of the predictor variables are significant at each of the regions.

The regression equation of the mean contact pressure ($P > 5000$) on the sides of the nose is given by

$$P_{5000\text{side}} = -7754 + 134\text{age} + 347\text{BMI} + 1315F_{XBtm} \tag{13.1}$$

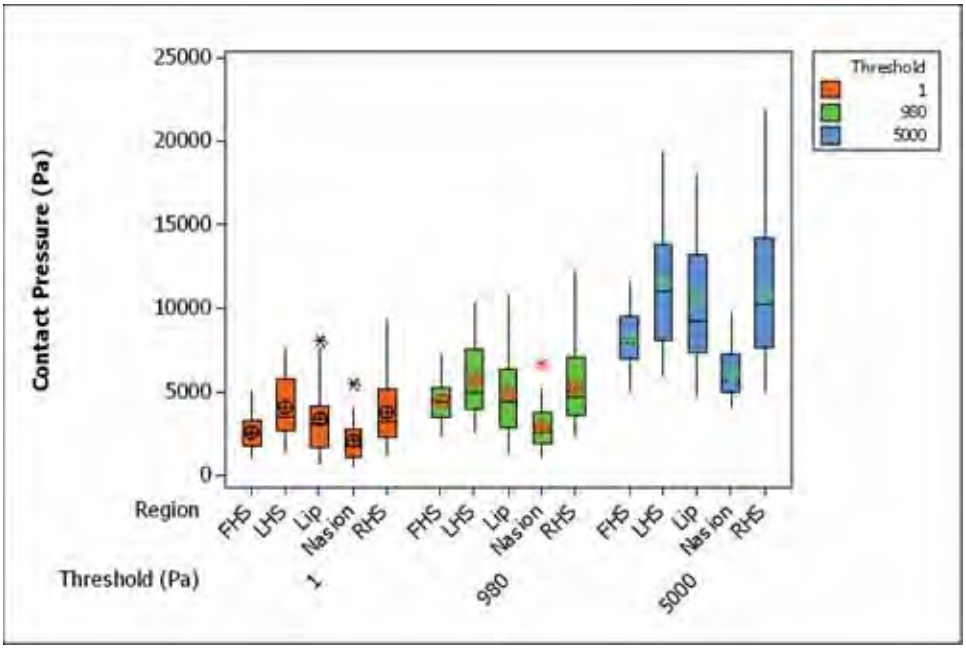

(a) Boxplot of contact pressure (Pa) at different pressure thresholds by facial region.

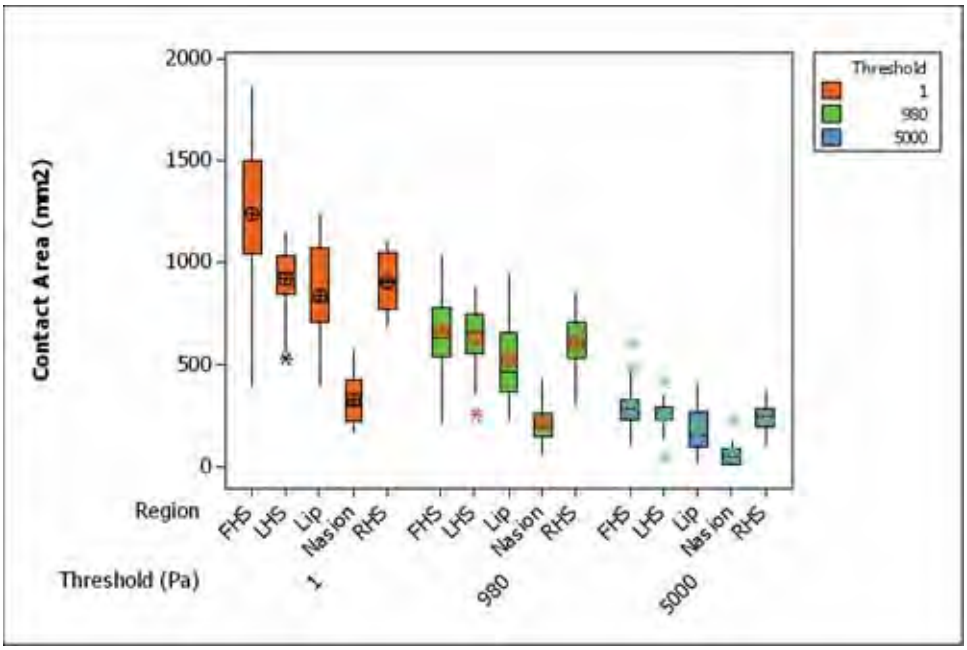

(b) Boxplot of contact areas $\left(\text{mm}^2\right)$ at different pressure thresholds by facial region.

Figure 13.7: Contact parameters from the rigid FEA models in the experimental headgear tension configuration

This model accounts for 60.5% (r^2) of the variation, refer to Table 13.3. Correlations between the predictor variables were checked visually by plotting each of the predictor and response variables against each other in a matrix plot (Figure 13.8) and by evaluating the Pearson correlation coefficient matrix of the variables. No strong correlation was identified between any of the predictor variables.

Table 13.3: Contact pressure regression output at the sides of the nose, rigid face, experimental headgear tension

Predictor	Coef	SE Coef	T	P
Constant	-7754	3104	-2.5	0.017
age	133.9	24.41	5.48	0
BMI (kg/m2)	346.8	113.3	3.06	0.004
HG FX Btm (N)	1315.4	395.9	3.32	0.002

S = 2643.13 R-Sq = 60.5% R-Sq(adj) = 57.6%

Analysis of Variance

Source	DF	SS	MS	F	P
Regression	3	4.29E+08	1.43E+08	20.46	0
Residual Error	40	2.79E+08	6986125		
Total	43	7.08E+08			

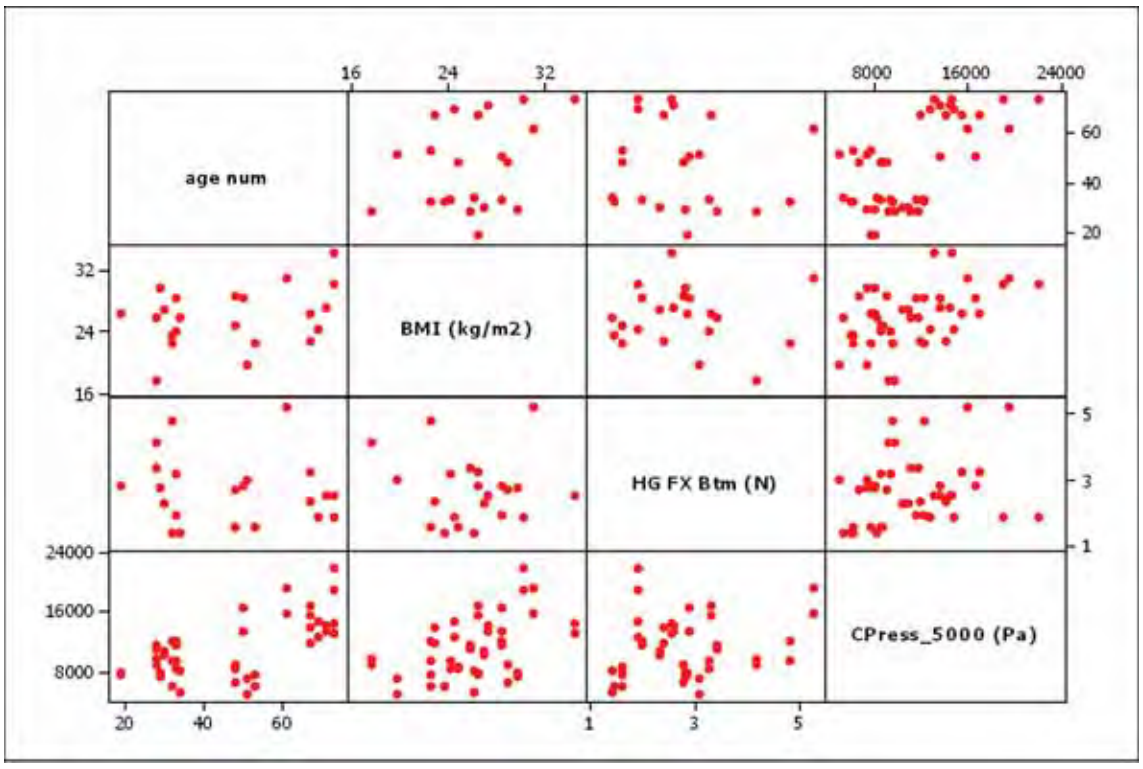

Figure 13.8: Matrix plot of the predictor and response variables for the regression of contact pressure at the side of the nose on age, BMI and headgear tension

The regression equation of the mean contact pressure ($P > 5000$) on the forehead is given by

$$P_{5000\text{FHS}} = 11790 - 1634F_{XTop} - 201w_N \tag{13.2}$$

This model accounts for 70.1% (r^2) of the variation of the contact pressure at the forehead, refer to Table 13.4 for details. Once again a matrix plot, Figure 13.9, along with the Pearson coefficient was used to investigate the correlation of the predictor variables. No high level of correlation was found. The data represented in Figure 13.9 reveals a slight association of the contact pressure with respect to nasal width, while a stronger association is shown between contact pressure and headgear tension in the top strap.

Table 13.4: Contact pressure regression output at the forehead, rigid face, experimental configuration

Predictor	Coef	SE Coef	T	P
Constant	11790	2575	4.58	0
HG FX Top (N)	-1633.9	284	-5.75	0
NasalWidth	-200.6	66.06	-3.04	0.007

$S = 1051.40 \quad R^2 = 70.1\% \quad R^2_{adj} = 67.0\%$

Analysis of Variance

Source	DF	SS	MS	F	P
Regression	2	49239944	24619972	22.27	0
Residual Error	19	21003482	1105446		
Total	21	70243426			

For the experimental configuration of simulation, the stepwise regression procedure did not find a significant association at the 95% confidence level between the predictor variables and the mean contact pressure over the lip and nasion regions at the 5000 Pa threshold.

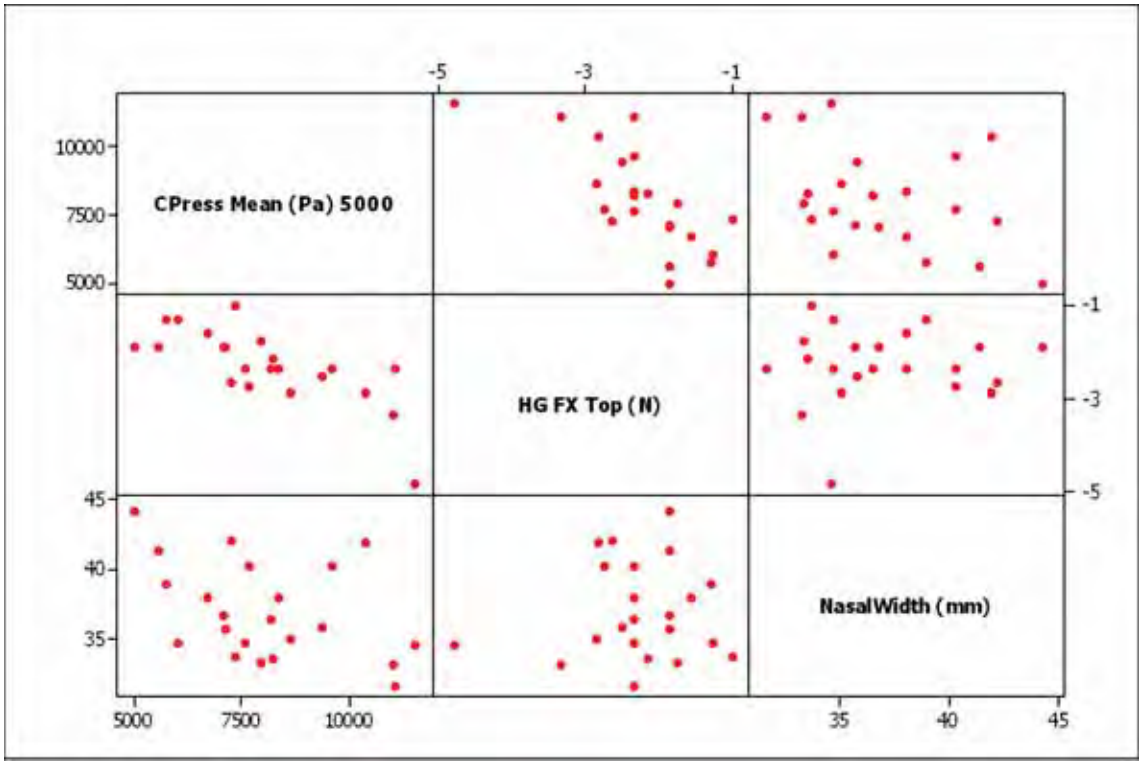

Figure 13.9: Matrix plot of predictor and Contact pressure $P > 5000$ response at the forehead

13.7 Mean Headgear Tension Analyses

The rigid model series has been developed in parallel with the deformable series to identify the differences between assuming the face is rigid and allowing the face to deform and adopt an equilibrium configuration. As was mentioned in Section 11.3, it is important to assess the variability of the contact results independent to the headgear tensions. Therefore, a corresponding series of models were developed using the meshes from the rigid model series with the mean headgear tensions calculated across the subject sample.

13.7.1 Model Descriptions

The models used were prepared as described in Chapter 13. The meshes and material properties were used were identical to the experimental configuration model series described in 13.2. The only change for these models is the magnitude of the headgear forces.

The headgear forces recorded from the participant controlled fitting of the mask is reported in Table 8.7. The mean loads applied to the headgear are identical to those applied in the deformable model series.

$$F_{top} = (-2.173, -0.04, 0)\,\mathrm{N} \tag{13.3}$$

$$F_{btm} = (-2.564, -0.34, 0)\,\mathrm{N} \tag{13.4}$$

13.8 Results - Mean Headgear Tension

The mean headgear tension results from the rigid model series once again are similar in form to the experimental configuration series. Refer to Sections 11.4 and 13.6 for a qualitative description of the mask engagement. Representative contact results are once again presented for subjects 12 and 14 in Figures 13.10 and 13.11. The results for Subject 12 in the mean tension configuration exhibit the same characteristics as the experimental configuration, with a prominent pressure concentration located centrally at the upper lip on the philtrum and bilaterally at the sides of the nose. The mean headgear tension is markedly less than the experimental configuration for this subject. This is evident in the reduced high pressure contact areas. This is most notable at the philtrum where the tapered high pressure region is reduced by approximately 30%. As mentioned previously, for subject 14, the mean headgear tension is very close to the experimental configuration, so there are not the clear

noticeable differences in the contact pressure contours between the model series for this participant.

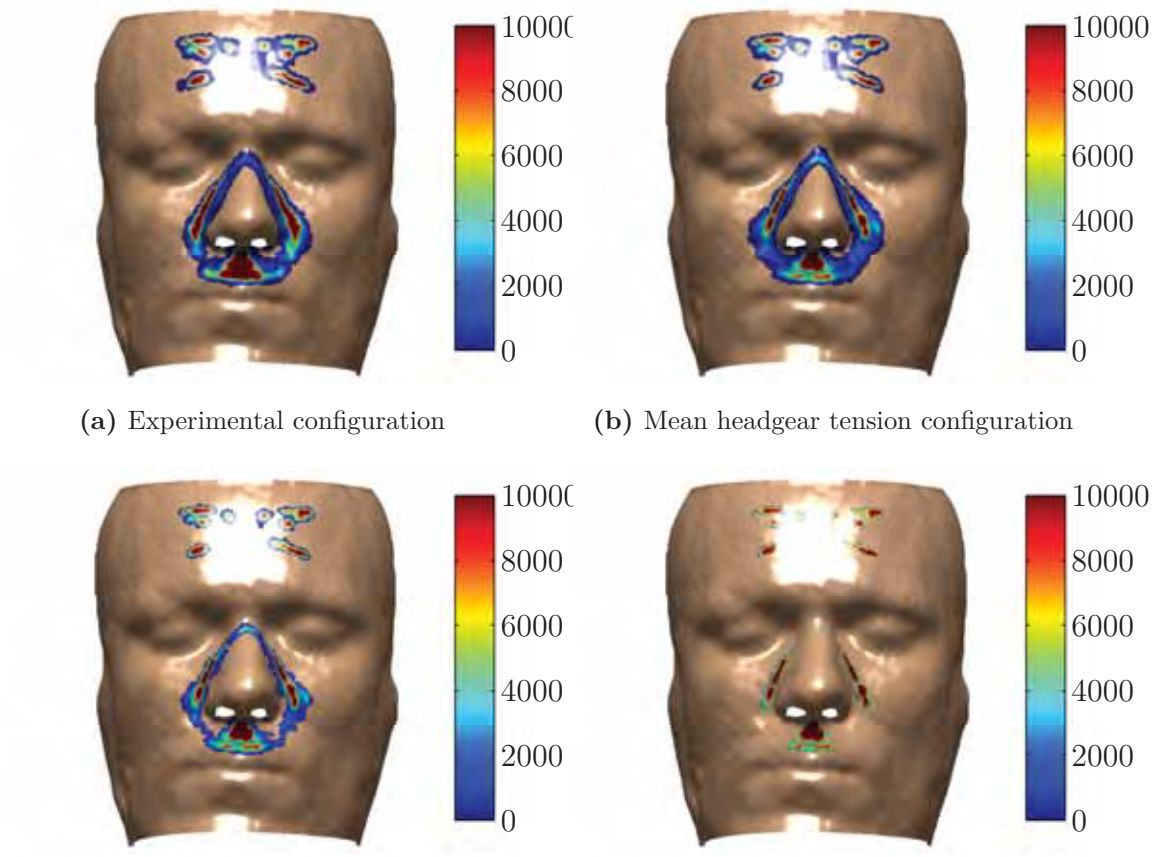

(a) Experimental configuration

(b) Mean headgear tension configuration

(c) Mean headgear tension configuration, 980 Pa threshold

(d) Mean headgear tension configuration, 5000 Pa threshold

Figure 13.10: Subject 12 mask contact pressures (Pa) for the rigid series of models in the experimental and mean headgear tension configurations

The distribution of contact pressure and areas across the facial regions at different contact pressure threshold levels (1Pa, 980Pa and 5000Pa) are shown in Figure 13.12. These results indicate a wide scatter in mean contact pressure above the 5000Pa threshold at the lip and sides of the nose. Once again a one way ANOVA test was used to evaluate the null hypothesis that the means of the contact pressures at each of the locations were equal ($H_0 : \mu_1 = \mu_2 = ... = \mu_n$). H_0 was rejected at the 95% confidence level $P < 0.01$. Again Tukey comparisons were performed between groups. The nasion region was found to be significantly different to the lip and sides of the nose with a lower mean contact pressure for the region. The contact pressure at the forehead significantly differs from the sides of the nose, but not the nasion or lip.

A similar ANOVA test was not performed on the contact areas at the 5000 Pa threshold level, as the original selection regions varied greatly in size, generating a

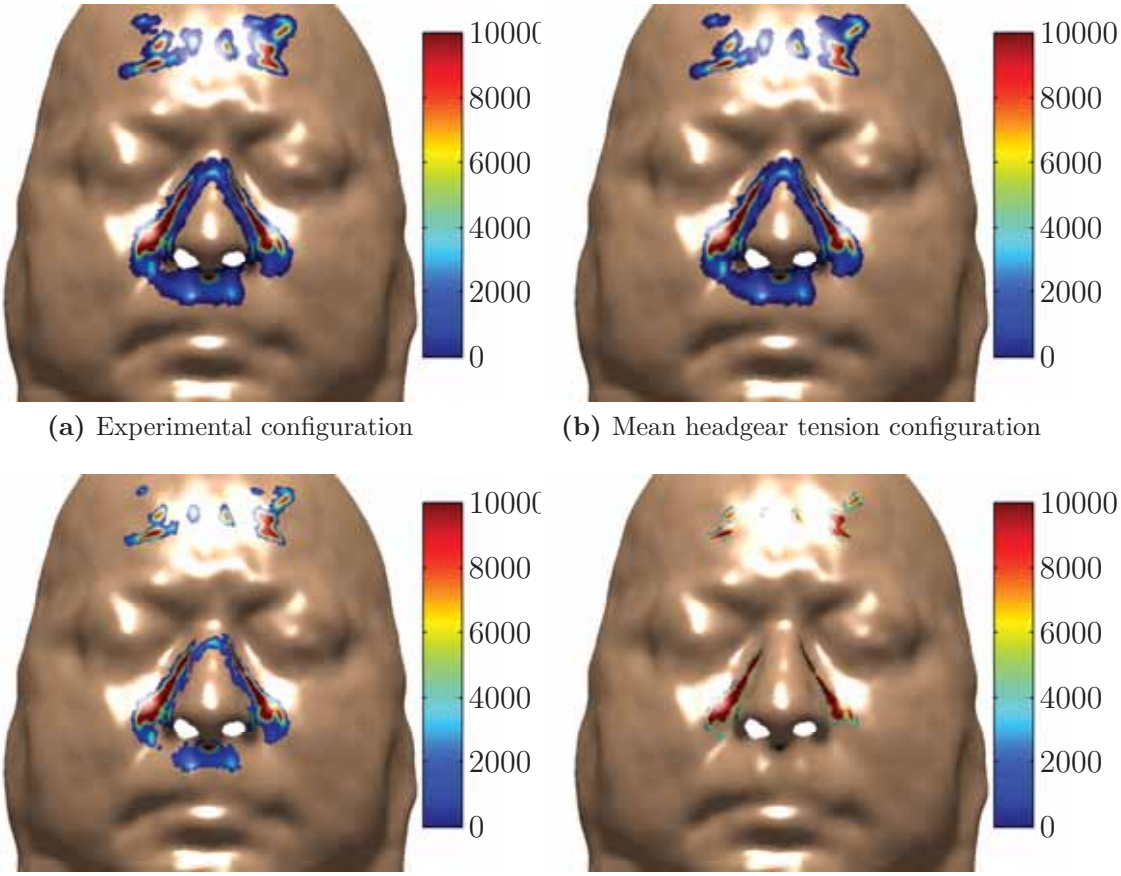

(a) Experimental configuration

(b) Mean headgear tension configuration

(c) Mean headgear tension configuration, 980 Pa threshold

(d) Mean headgear tension configuration, 5000 Pa threshold

Figure 13.11: Subject 14 mask contact pressures (Pa) for the rigid series of models in the experimental and mean headgear tension configurations

trivial result. These results are of best use for direct comparison between series with corresponding solutions.

Linear regression was used to look for dependencies of the contact pressure on the independent experimental variables of age and BMI as well as the anthropometric variables for the facial regions defined. The contact pressure data at the sides of the nose were pooled for regression analysis. At the mean headgear tension the regression equation of contact pressure on age and BMI is

$$\bar{p}_{5000} = -2378 + 137\text{age} + 263\text{BMI} \tag{13.5}$$

Significant associations were found between the contact pressure, age and BMI below. This model accounts for 56.6% of mean contact pressure variation at the sides of the nose, refer to Table 13.5.

The contact pressure at the sides of the nose was cross plotted along with its predictor variables in a matrix plot in Figure 13.13. A positive correlation trend

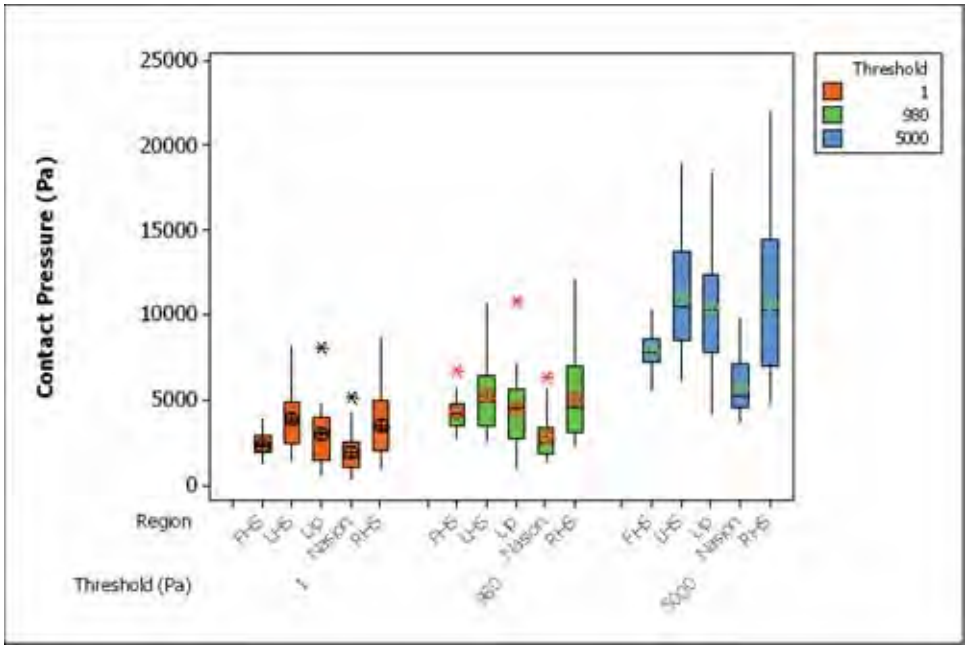

(a) Boxplot of contact pressure (Pa) at different pressure thresholds by facial region.

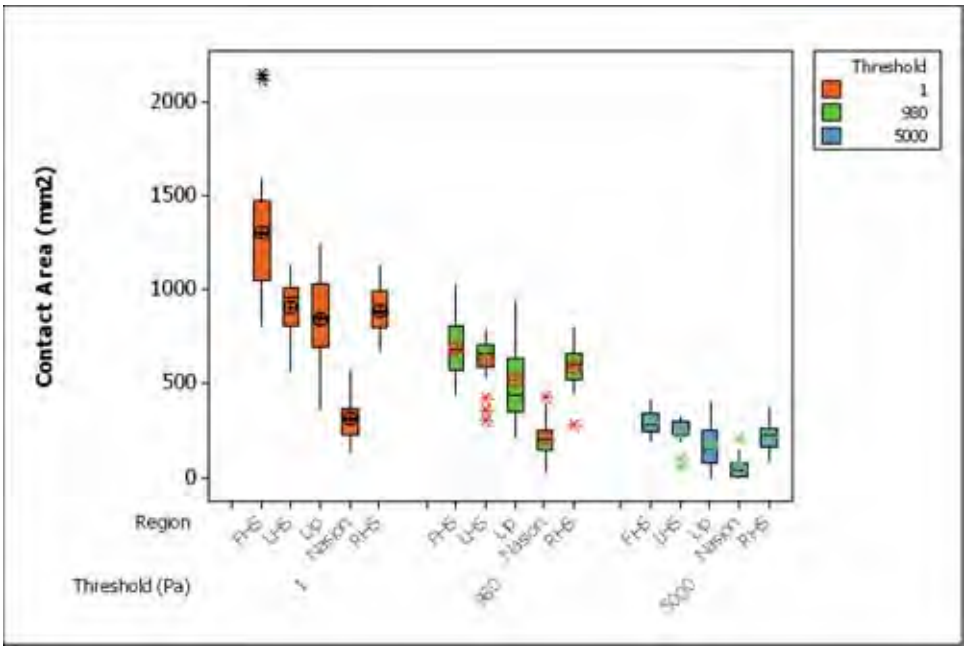

(b) Boxplot of contact areas $\left(\text{mm}^2\right)$ at different pressure thresholds by facial region.

Figure 13.12: Contact parameters from the rigid FEA models in the mean headgear tension configuration

Table 13.5: Contact pressure regression output at the sides of the nose, rigid face, mean headgear configuration

Predictor	Coef	SE Coef	T	P
Constant	-2378	2747	-0.87	0.392
age	136.66	23.61	5.79	0
BMI	263	110.1	2.39	0.022

$S = 2570.35 \quad R^2 = 56.6\% \quad R^2_{adj} = 54.5\%$

Analysis of Variance

Source	DF	SS	MS	F	P
Regression	2	3.54E+08	1.77E+08	26.76	0
Residual Error	41	2.71E+08	6606690		
Total	43	6.24E+08			

was observed between the contact pressure and the age (row 3,column 1) with a correlation coefficient of $r = 0.71$. Additionally a positive correlation was found between the contact pressure and the participant's BMI (row 3, column 2) with a correlation coefficient of $r = 0.46$.

A statistically significant association was found at the nasion (refer to Table 13.6 and Figure 13.14) and forehead (refer to Table 13.7 and 13.15) with respect to the nasal height. No significant associations were found between the independent variables and anthropometric measures and the contact pressure at the lip at the 95% confidence level. The regression equation at the nasion region is;

$$P = -4622 + 194NH \tag{13.6}$$

Table 13.6: Contact pressure regression output at the nasion, rigid face, mean headgear tension configuration

Predictor	Coef	SE Coef	T	P
Constant	-4622	4353	-1.06	0.302
NasalHeight	194.4	80.89	2.4	0.027

$S = 1400.94 \quad R^2 = 24.3\% \quad R^2_{adj} = 20.1\%$

Analysis of Variance

Source	DF	SS	MS	F	P
Regression	1	11334855	11334855	5.78	0.027
Residual Error	18	35327417	1962634		
Total	19	46662271			

The regression equation at the forehead is given by

$$P = 14723 - 126NH \tag{13.7}$$

Table 13.7: Contact pressure regression output at the forehead, rigid face, mean headgear tension configuration

Predictor	Coef	SE Coef	T	P
Constant	14723	3366	4.37	0
NasalHeight	-126.06	62.43	-2.02	0.057

$S = 1087.64 \quad R^2 = 16.9\% \quad R^2_{adj} = 12.8\%$

Analysis of Variance

Source	DF	SS	MS	F	P
Regression	1	4823565	4823565	4.08	0.057
Residual Error	20	23659040	1182952		
Total	21	28482605			

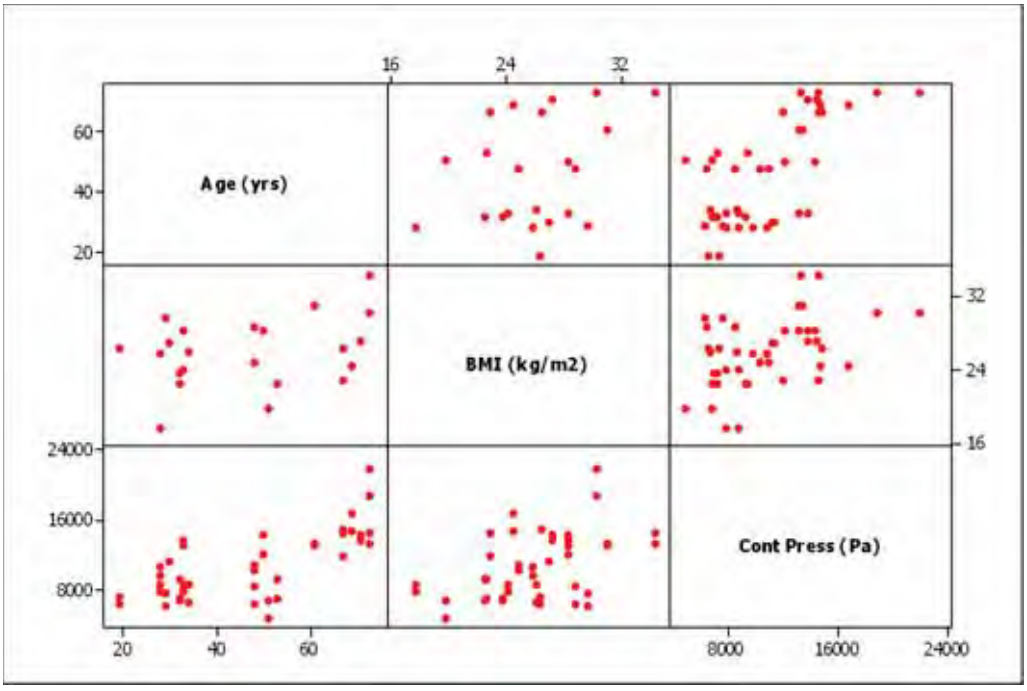

Figure 13.13: Matrix plot of the predictor and response variables for the regression of contact pressure at the side of the nose on age and BMI with all headgear tensions constant at the mean value

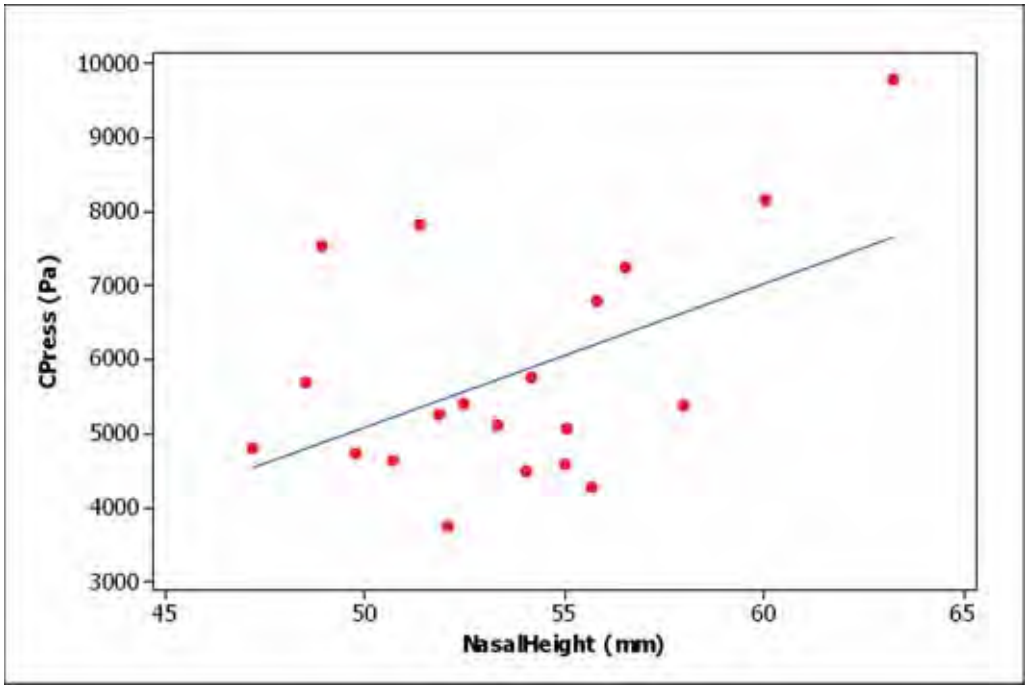

Figure 13.14: Contact pressure at the nasion vs nasal height in mean headgear configuration

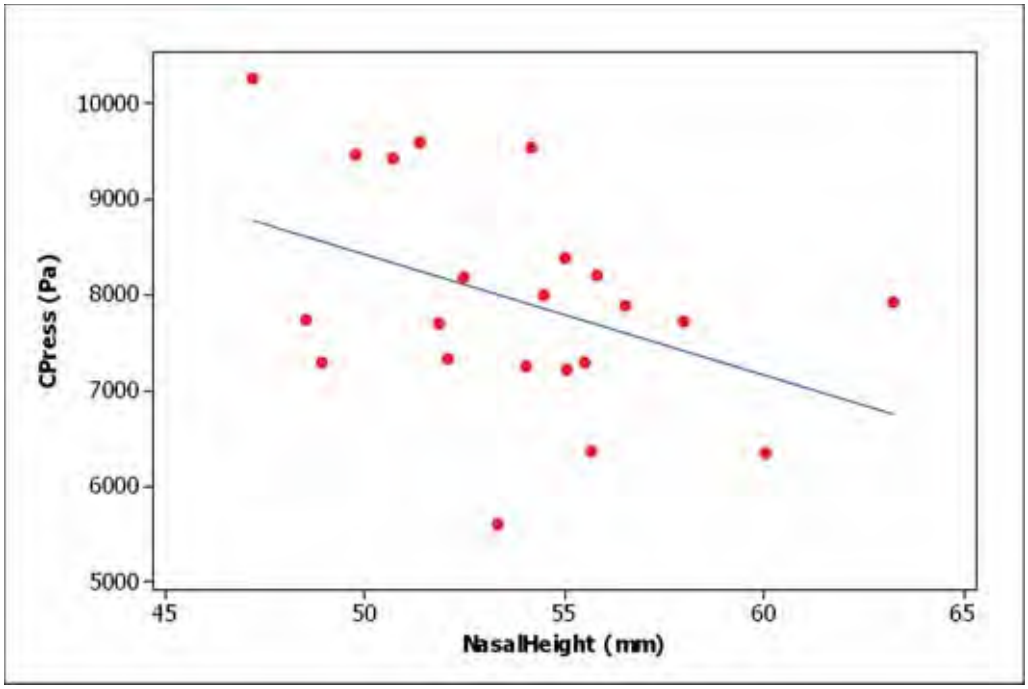

Figure 13.15: Contact pressure at the forehead vs nasal height in mean headgear configuration

13.9 Discussion

This section has developed and presented results from the rigid series of facial models which correspond to the current design process for CPAP masks. Some associations

were found between the contact pressure and age, BMI at the sides of the nose. Associations were also found between the contact pressure at the nasion and forehead with nasal height in the mean headgear tension configuration. These results now provide a data set that can be used for comparison against the deformable data. This will allow estimation of the effect that the rigid assumption has on the facial contact parameters.

Chapter 14

Comparison Between Deformable and Rigid Finite Element Analysis Models

14.1 Introduction

Chapters 11 and 13 outlined the development of the deformable and rigid FEA model series respectively. The rigid series of models reflect the assumed behaviour of the face during the mask development process. Mass produced CPAP masks such as the UMII have been designed and developed from anthropometric studies of subjects in the reference condition. Facial profiles are used to guide the cushion form to closely follow that of the face. While sophisticated tools and techniques are used to develop the complex free form shapes of the masks that contact the face from the reference condition, the deformed configuration of the face engaged with a mask has not been considered in the design of the masks. This study seeks to commence filling this void and to identify the influence that the rigid face assumption has on the contact interface between the face and the mask. This serves the dual purposes of developing a more realistic model of the mechanical interface and evaluating the similarities, differences and hence usefulness of rigid modes into the future.

14.2 Model Descriptions

Deformable models were prepared for a subsample ($N_{def} = 5$) of the participants ($N = 22$) in the CPAP MRI experimental study. The reconstructed faceted surface of the face was used to prepare a hybrid mesh consisting of hexahedral and tetrahedral elements. Hexahedral elements were used on the anterior region of the face providing high quality shaped elements in the region of interest for the face/mask contact. The elements were allocated to either skin, fat or muscle material groups by looking up

the corresponding location in the segmented face voxel array. The mask was pre-engaged on the face using velocity control before releasing and allowing to settle using force control through the headgear straps.

The rigid models were prepared for the every available subject. Three participants were excluded after recruitment due to either safety concerns with the scanning process or artefacts in the scans that prevented geometry reconstruction. Therefore, the number of samples available was $N = 22$.

The rigid series models were identical to the deformable series in terms of their mask positioning, loading and control. The only difference was that the rigid face mesh was a single layer extruded from the reconstructed faceted surface.

14.3 Deformable and Rigid Face Comparisons

One of the prime objectives of this study at the outset was to evaluate the influence of the rigid assumption on simulation contact results. Three parameters were investigated to determine if there was a significant effect from the rigid assumption, and its nature. These were the mean face/mask contact pressure at at the 5000 Pa threshold value at each of the regions of interest around the nose and the forehead.

Since the deformable model sample was a subset of the rigid model, the corresponding models in each series are paired observations. This allowed for a paired t-test be used to evaluate whether there is a significant influence between the means of the corresponding participants in the rigid and deformable series. Comparisons were performed at each of the regions of interest, namely the sides of the nose (pooled data), the upper lip, nasion and the forehead.

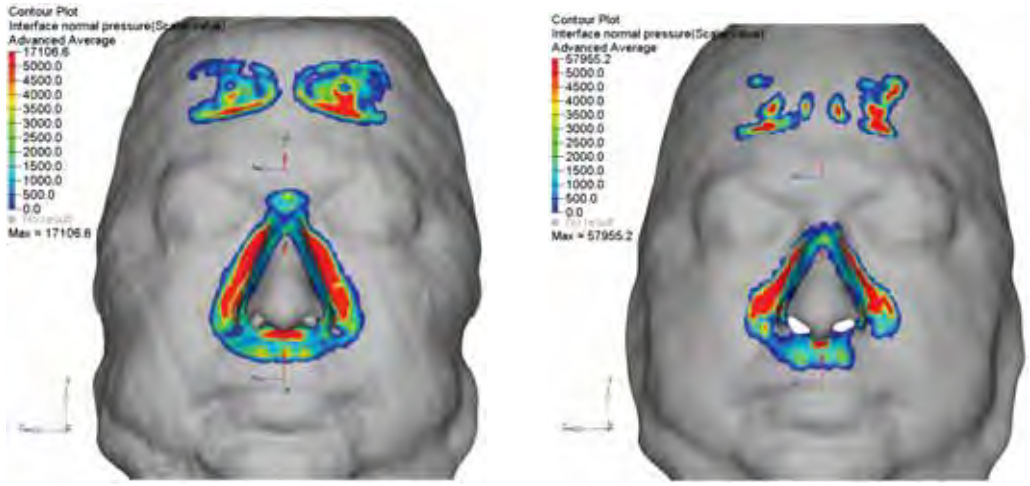

(a) Sample deformable model contact pressure (Pa) $P > 1$ Pa

(b) Sample rigid model contact pressure (Pa) $P > 1$ Pa

Figure 14.1: Contact pressure on deformable and rigid models.

The mean contact pressures above the 5000 Pa threshold level were compared for the participants in the deformable model series and the corresponding rigid model series. Figure 14.1 shows a fringe plot of the contact pressure for a sample deformable and rigid model. The null and alternative hypotheses for the comparison are

$$H_0 : \mu_{rgd} = \mu_{def}$$
$$H_1 : \mu_{rgd} > \mu_{def}$$

The mean contact areas above the 5000 Pa threshold level were compared for the participants in the deformable model series and the corresponding rigid model series. The null and alternative hypotheses for the comparison are

$$H_0 : \mu_{rgd} = \mu_{def}$$
$$H_1 : \mu_{rgd} \neq \mu_{def}$$

The peak Von Mises strain (ϵ_{VM}) were compared for the participants in the deformable model series and the corresponding rigid model series. The strain values are reported for the undercushion and FHS. Since the undercushion terminates and blends into the cushion body at the superior end of each side of the nose, the undercushion does not extend to the nasion, so this region is not considered. The null and alternative hypotheses for the comparison are

$$H_0 : \mu_{rgd} = \mu_{def}$$
$$H_1 : \mu_{rgd} > \mu_{def}$$

In each case the null and alternative hypotheses were tested at the $\alpha = 0.05$ level.

The results for these comparisons are presented in Table 14.1 and Figures 14.2 to 14.4. Significant differences in the contact pressure were found at each of the regions except for the nasion. Therefore, at the sides of the nose, the upper lip and the forehead, the null hypothesis H_0 ($\mu_{rgd} = \mu_{def}$)was rejected in favour of the alternative hypothesis H_1 ($\mu_{rgd} > \mu_{def}$).

This test assumed a normal distribution of the samples. Due to the low number of samples the normal assumption of normality is not robust. Therefore, in addition to the t-test the corresponding non-parametric Wilcoxon signed rank test was evaluated for the data.

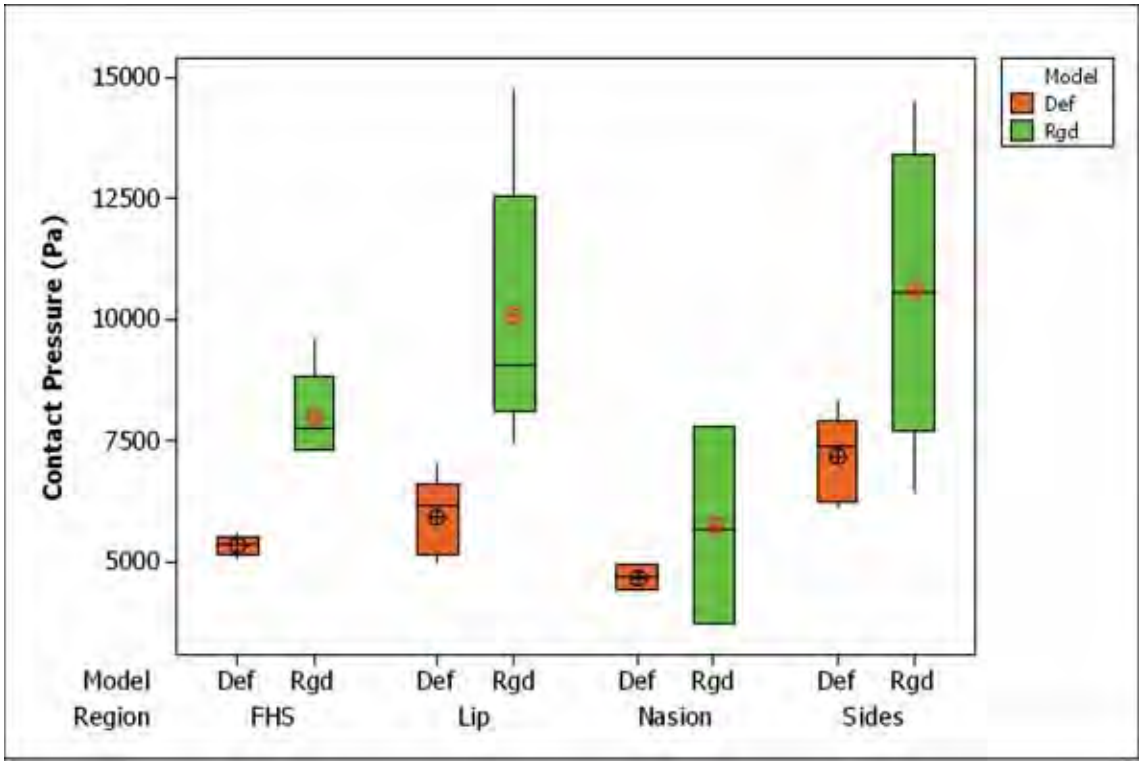

Figure 14.2: Contact pressures in the rigid and deformable models

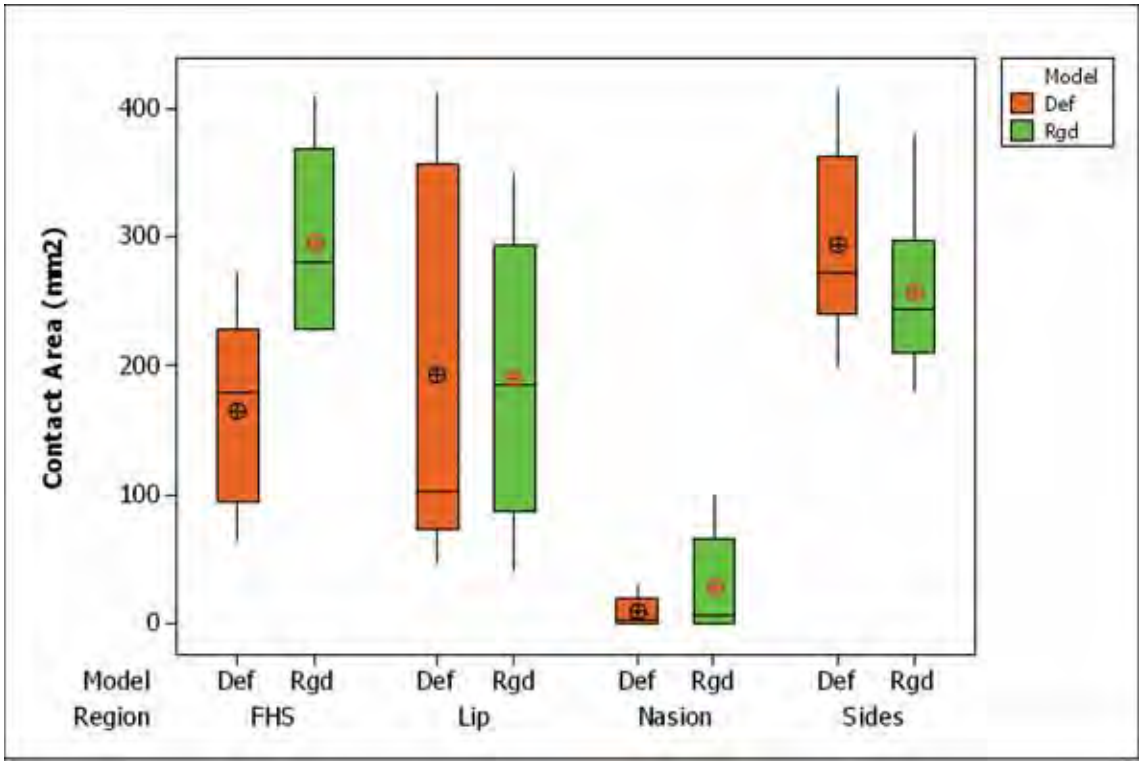

Figure 14.3: Contact area in the rigid and deformable models

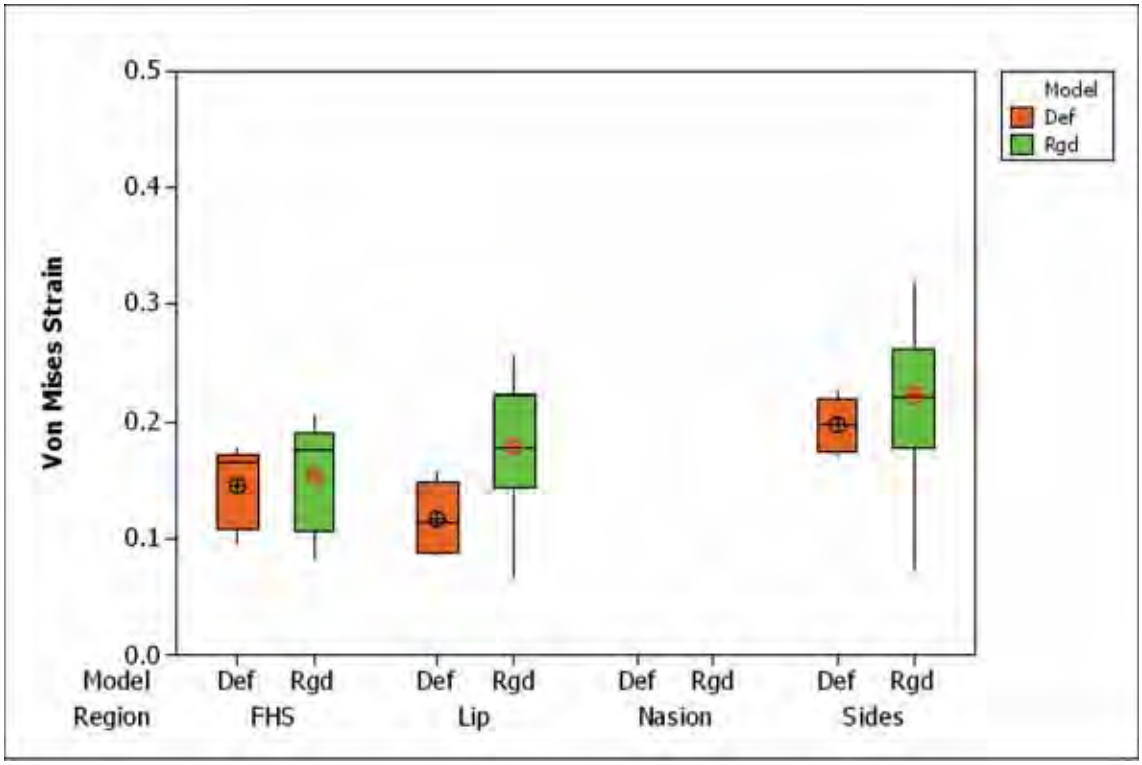

Figure 14.4: UMII mask strains in rigid and deformable masks

Table 14.1: Results from the t-test comparison of corresponding results in the rigid and deformable series of models. P levels identified with (*) denote a significant difference in means where the null hypothesis is rejected at a 95% confidence level.$\bar{P}_c$ is the mean contact pressure, A_c is the contact area and ϵ_{VM} is the Von Mises strain

ROI	Model	$\bar{P}_c$ Pa	P level ($\alpha = 0.05$)	A_c mm^2	P level ($\alpha = 0.05$)	ϵ_{VM}	P level ($\alpha = 0.05$)
Sides Pooled	Deformable	7194	0.000*	294.2	0.053	0.1984	0.002*
	Rigid	10624		256.6		0.2251	
Upper Lip	Deformable	5940	0.015*	193	0.926	0.1168	0.012*
	Rigid	10079		189.1		0.1786	
Nasion	Deformable	4813	0.144	27.5	0.238	-	-
	Rigid	6747		8.3		-	
Forehead	Deformable	5343	0.001*	165.2	0.024*	0.1446	0.121
	Rigid	7989		295.4		0.1540	

Table 14.2: Results from the non-parametric Wilcoxon signed rank test comparison of corresponding results in the rigid and deformable series of models. P levels identified with (*) denote a significant difference in means where the null hypothesis is rejected at a 95% confidence level. $\Delta\bar{P}_c$ is the *median* difference in mean contact pressure (rigid - deformable), ΔA_c is the *median* difference in contact area (rigid - deformable) and $\Delta\epsilon_{VM}$ is the *median* deifference in Von Mises strain

ROI	Test	$\Delta\bar{P}_c$ Pa	P level ($\alpha = 0.05$)	ΔA_c mm^2	P level ($\alpha = 0.05$)	$\Delta\epsilon_{VM}$	P level ($\alpha = 0.05$)
Sides Pooled	Rgd − Def	3344	0.004*	-34.49	0.067	0.0265	0.011*
Upper Lip	Rgd − Def	3746	0.03*	-16.19	0.787	0.0580	0.030*
Nasion	Rgd − Def	1934	0.186	10.02	0.201	-	-
Forehead	Rgd − Def	2570	0.03*	118.8	0.059	0.0105	0.209

The null and alternative hypotheses for the non-parametric Wilcoxon signed rank test for the comparison of contact pressures are

$$H_0 : \text{median}\,(X_{rgd} - X_{def}) = 0$$
$$H_1 : \text{median}\,(X_{rgd} - X_{def}) > 0$$

The null and alternative hypotheses for the non-parametric Wilcoxon signed rank test for the comparison of contact areas are

$$H_0 : \text{median}\,(X_{rgd} - X_{def}) = 0$$
$$H_1 : \text{median}\,(X_{rgd} - X_{def}) \neq 0$$

The null and alternative hypotheses for the non-parametric Wilcoxon signed rank test for the comparison of mask undercushion strains are

$$H_0 : \text{median}\,(X_{rgd} - X_{def}) = 0$$
$$H_1 : \text{median}\,(X_{rgd} - X_{def}) > 0$$

The results of the non-parametric test are presented in Table 14.2

These non-parametric results confirm those from the paired t-test for the contact pressure comparisons. The null hypothesis ($H_0 :$ median $(X_{rgd} - X_{def}) = 0$) that the medians were equal was able to be rejected in favour of the alternative ($H_1 :$ median $(X_{rgd} - X_{def}) > 0$) hypothesis at a confidence level of 95% for the sides of the nose, the upper lip and the forehead. These results are identical to those obtained from the t-test, though without making any assumptions about the distribution of the data.

The influence of the rigid assumption on the contact area above a pressure threshold is not as clear. Differences approaching significance using the non-parametric

Wilcoxon test were found at the forehead ($P = 0.059$) and on the sides of the nose ($P = 0.067$). Using the t-test, the forehead found a significant difference ($P = 0.024$) and approaching significance at the sides of the nose ($P = 0.053$). It can be seen from Figure 14.3 that the sign of the difference changes in these locations. At the side of the nose the deformable model series returned a greater contact area above the threshold pressure than in the rigid model series. The simulation results however show that the rigid model returned a higher contact area above threshold at the forehead. There are opposing effects that are balanced to determine the final contact area. The deformable model conforms to the shape of the contacting body, this distributes the load over a greater contact area. This tends to reduce the contact pressure. Therefore, considering the thresholded contact area, the deforming body acts to increase the contact area that the load is distributed over, but the distributed load reduces the pressure and correspondingly the area above the threshold pressure. This explains why the thresholded contact area in the deformable model may be either higher or lower than the corresponding thresholded contact area in the rigid model.

The von Mises strain in the LSR components of the mask were similarly compared in the undercushion at the sides of the nose, the upper lip and the forehead support. These non-parametric results confirm those from the paired t-test for the mask strain comparisons. The null hypothesis ($H_0 :$ median $(X_{rgd} - X_{def}) = 0$) that the medians were equal was able to be rejected in favour of the alternative ($H_1 :$ median $(X_{rgd} - X_{def}) > 0$) for the sides of the nose ($P = 0.011$) and the upper lip ($P = 0.030$). The rigid profile of the face ensures that all of the strain energy of the system is in the mask and not shared with the soft tissues of the face, explaining the increased mask strain in the rigid series models.

14.4 Discussion

This analysis has compared the contact pressure, contact area and Von Mises mask strain across paired observations in a number of ROIs on the face. The contact pressure in the rigid model series was found to be significantly higher than the deformable series at the side of the nose, upper lip and forehead. Similarly the mask strain was found to be significantly higher in the rigid model series compared to the deformable series at the sides of the nose and the upper lip. This difference is due to the influence of the rigid facial soft tissue assumption. The rigid model corresponds to the current design processes where anthropometric data from facial profiles in the reference condition are used to define key dimensions and shapes of the mask. The

compliance and deformation of the face is not considered. The deformable models correspond to the real situation, allowing for the sliding of soft tissue over the skull and the compression of the soft tissue layers. The results of the contact simulations for the deformable models are of great interest as design inputs since they allow an estimation of the actual behaviour of the face under therapy.

The deformable FEA models are computationally intensive, where as the rigid FEA models have much reduced preprocessing and solving computational demands. This makes the rigid model series of practical interest for a number of reasons. Firstly the reduced preprocessing requirements of the rigid series mean that it is feasible to perform numerous iterations as a mask design develops. Since the rigid facial profile does not require any information about the subdermal tissue and bone structure, there is no need for complex medical imaging data acquisition modes such as MRI or CT scanning. Extremely fine resolution surface geometry can be easily and non-invasively obtained from a laser scan, from which it is possible to simply generate a shell mesh and then a single layer of extruded shell elements. This process can be automated, which feasibly opens up the possibility of iterating through a database of facial scans to generate large sample population based stochastic FEA information.

Considering these applications, it is highly desirable to exploit the rigid facial models as much as possible. Although the paired comparisons between the rigid and deformable model have indicated that the rigid models exhibit higher strains and contact pressures than the deformable series, associations have not been established. It is desirable to be able to infer or estimate the actual mean contact pressure from the over estimated rigid facial profile results. To estimate this the contact pressure of the deformable model series was plotted against the contact pressure in the rigid series in Figures 14.5 to 14.7 at the sides of the nose, the upper lip and the forehead respectively. From these plots, a clear positive trend was evident between the mean contact pressure results from the deformable and rigid model series at the sides of the nose. Similarly a positive trend was observed at the forehead, while no clear trend was evident at the upper lip of the model.

Linear regression was used to evaluate the relationship between the variables. The regression equation at the sides of the nose is given in (14.1), which indicates a significant relationship between the contact pressure in the rigid and deformable models ($P = 0.0$). This model accounts for over 80% of the variation at this location in mean contact pressure, refer to Table 14.3 and Figure 14.5.

$$P_{5000d\ side} = 4453 + 0.258 P_{5000r\ side} \tag{14.1}$$

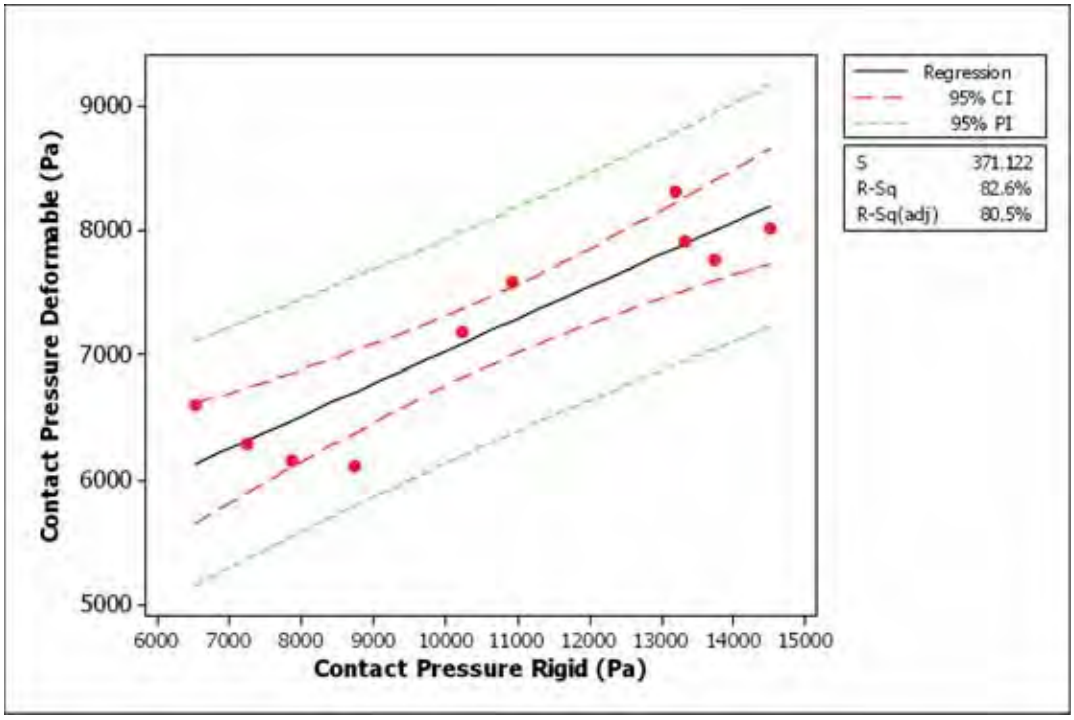

Figure 14.5: Linear regression of contact pressure at the side of the nose in the deformable model on the corresponding variable in the rigid model.

Table 14.3: Regression summary of association between rigid and deformable models at the side of the nose

Predictor	Coef	SE Coef	T	P
Constant	4453.3	459.4	9.69	0
Rgd CP Mean 5000 Sides	0.25796	0.04181	6.17	0

$S = 371.122 \quad R^2 = 82.6\% \quad R^2_{adj} = 80.5\%$

Analysis of Variance

Source	DF	SS	MS	F	P
Regression	1	5244034	5244034	38.07	0
Residual Error	8	1101851	137731		
Total	9	6345885			

The regression of the mean deformable contact pressure on the mean rigid contact pressure at the upper lip could not identify a significant relationship between these variables at this location ($P = 0.869, r^2 = 0.01$), this can be seen in Figure 14.6

At the forehead, a positive trend was identified between the mean contact pressure in the deformable and the rigid models, however the association did not reach significance at the 95% level ($P = 0.148$). This model accounted for 55% of the variation in the response variable. The regression equation and analysis results are listed below and in Table 14.4.

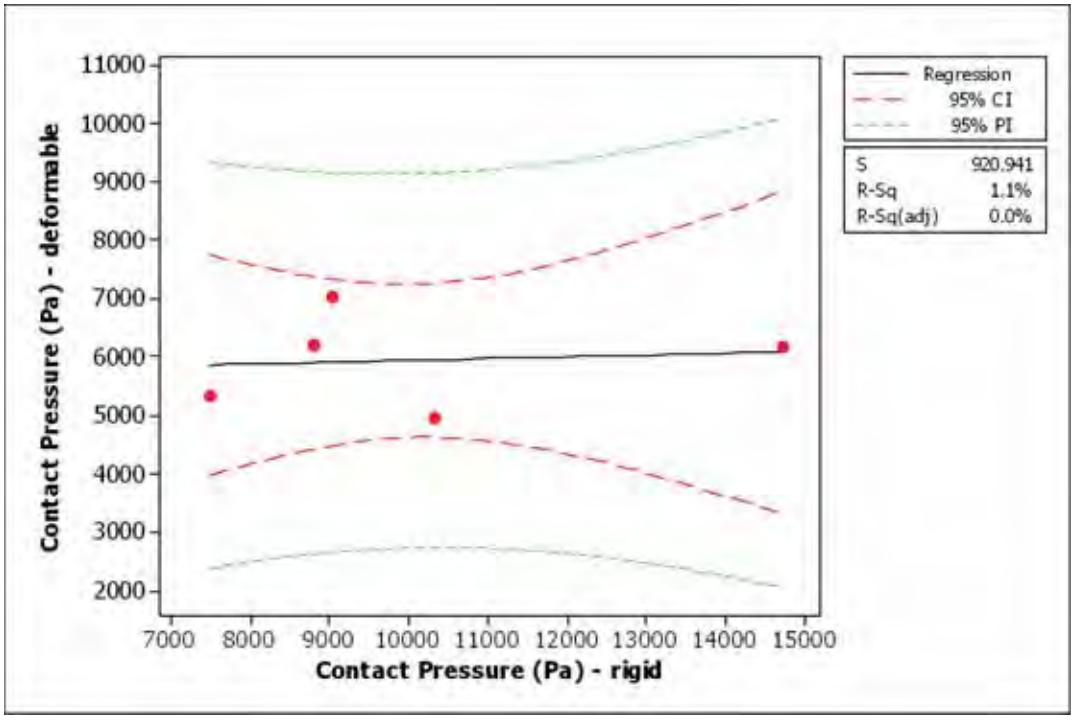

Figure 14.6: Linear regression of contact pressure at the upper lip in the deformable model on the corresponding variable in the rigid model.

$$P_{5000d\ FH} = 4120 + 0.153 P_{5000r\ FH} \tag{14.2}$$

Table 14.4: Regression summary of association between rigid and deformable models for contact pressure at the forehead

Predictor	Coef	SE Coef	T	P
Constant	4119.6	636	6.48	0.007
Rgd CP Mean 5000 FHS	0.15316	0.07916	1.93	0.148

$S = 149.607 \quad R^2 = 55.5\% \quad R^2_{adj} = 40.7\%$

Analysis of Variance

Source	DF	SS	MS	F	P
Regression	1	83782	83782	3.74	0.148
Residual Error	3	67146	22382		
Total	4	150928			

Considering the contact areas between the two model series, the tests for differences were approaching significance at the forehead and sides of the nose. These regions were investigated for associations of the contact area in the deformable model as the response to the corresponding contact areas in the rigid model series as predictor variables. Figure 14.8 plots the contact area at the forehead in the deformable model against the same variable in the rigid model. Linear regression was used. The regression equation at the forehead is

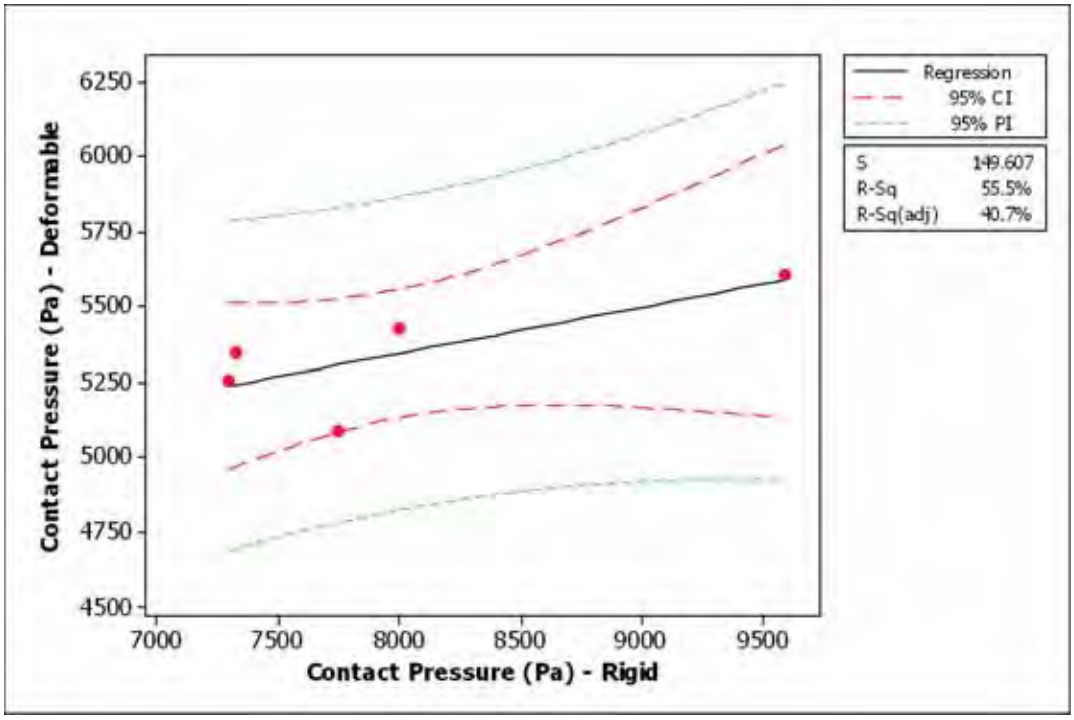

Figure 14.7: Linear regression of contact pressure at the forehead in the deformable model on the corresponding variable in the rigid model.

$$A_{5000d\ FH} = 40 + 0.423 A_{5000r\ FH} \tag{14.3}$$

The regression analysis is reported in Table 14.5, and indicates that this linear model only accounts for approximately 18% of the variation, and the association with the contact area in the rigid model did not reach significance ($P = 0.481$).

Table 14.5: Regression summary of association between rigid and deformable models for the contact area at the forehead

Predictor	Coef	SE Coef	T	P
Constant	40.2	159.8	0.25	0.818
ContArea (mm2) 5000 FHS	0.4232	0.527	0.8	0.481

$S = 80.6506 \quad R^2 = 17.7\% \quad R^2_{adj} = 0.0\%$

Analysis of Variance

Source	DF	SS	MS	F	P
Regression	1	4196	4196	0.65	0.481
Residual Error	3	19514	6505		
Total	4	23709			

The relationship between the contact areas at the sides of the nose in the deformable and rigid model series is shown in Figure 14.9. A positive linear trend

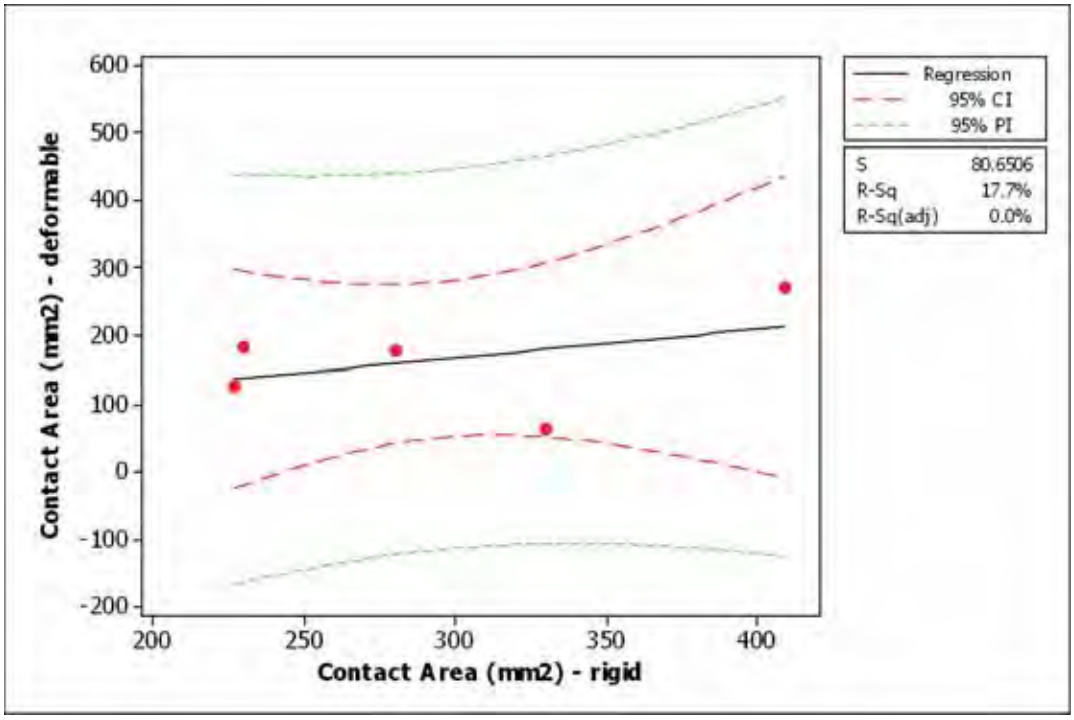

Figure 14.8: Linear regression of contact area at the forehead in the deformable model on the corresponding variable in the rigid model.

is evident in this graph. The linear regression equation of contact area in the deformable model on the the corresponding variable in the rigid model series is given by

$$A_{5000d\ Side} = 91.8 + 0.789 A_{5000r\ Side} \tag{14.4}$$

A significant association was found between the contact areas in the rigid and deformable model series at these locations ($P = 0.029$). This linear regression model accounts for approximately 47% of the variation in the deformable contact area at the sides of the nose. Refer to Table 14.6 for details.

Table 14.6: Regression summary of association between rigid and deformable models for the contact area at the side of the nose

Predictor	Coef	SE Coef	T	P
Constant	91.78	78.26	1.17	0.275
CA mm2 5000 Sides	0.7888	0.2974	2.65	0.029

$S = 54.9422 \quad R^2 = 46.8\% \quad R^2_{adj} = 40.1\%$

Analysis of Variance

Source	DF	SS	MS	F	P
Regression	1	21238	21238	7.04	0.029
Residual Error	8	24149	3019		
Total	9	45387			

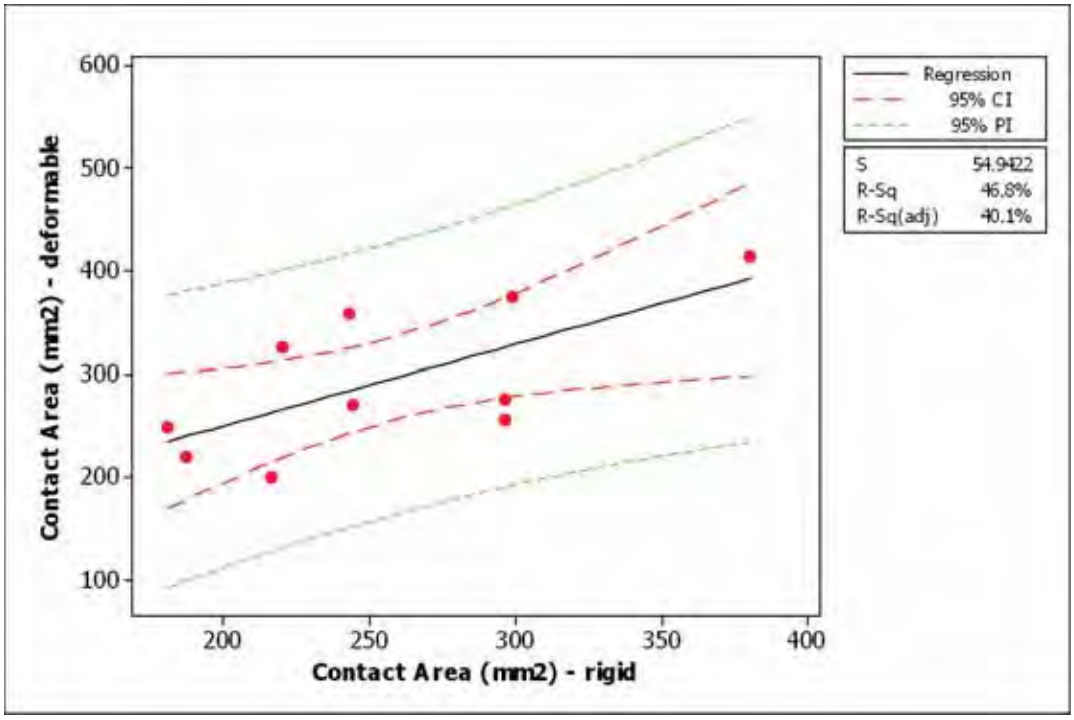

Figure 14.9: Linear regression of contact area at the side of the nose in the deformable model on the corresponding variable in the rigid model.

The mask Von Mises strain was also investigated using linear regression for the presence of associations between the rigid and deformable model series. Figure 14.10 plots the deformable model series against the rigid model series for ϵ_{VM} at the side of the nose. A significant association ($P = 0.000$) was found between $\epsilon_{VM\ d}$ and $\epsilon_{VM\ r}$ (refer to Table 14.7). The linear model accounts for approximately 87% of the variation between the model series. The regression equation is

$$\epsilon_{VM\ d} = 0.0867 + 0.496\epsilon_{VM\ r} \tag{14.5}$$

Table 14.7: Regression summary of association between rigid and deformable models of undercushion strain at the side of the nose

Predictor	Coef	SE Coef	T	P
Constant	0.0867	0.01558	5.57	0.001
RgdStrainVM Sides	0.4962	0.06819	7.28	0

$S = 0.00841728$ $R^2 = 86.9\%$ $R^2_{adj} = 85.2\%$

Analysis of Variance

Source	DF	SS	MS	F	P
Regression	1	0.003752	0.003752	52.95	0
Residual Error	8	0.000567	7.09E-05		
Total	9	0.004318			

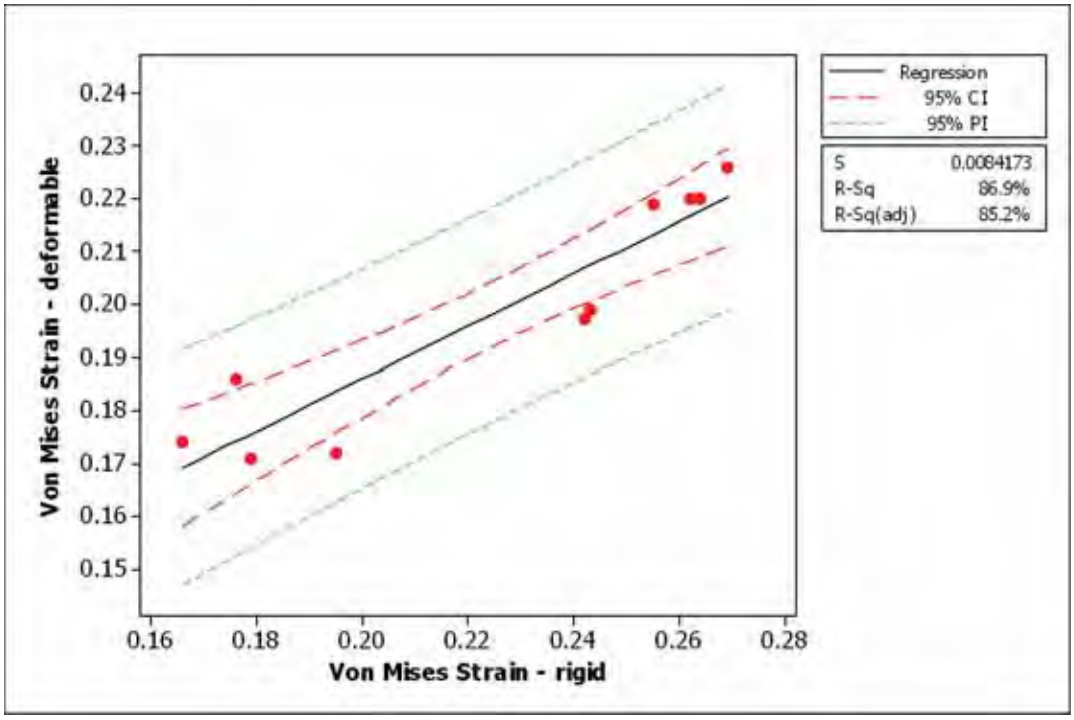

Figure 14.10: Linear regression of ϵ_{VM} at the side of the nose in the deformable model on the corresponding variable in the rigid model.

The Von Mises strain at the upper lip region, as shown in Figure 14.11 was similarly examined, but a significant association between the mask strains in the rigid and deformable models was not found ($P = 0.234$). Figure 14.12 shows the peak mask strains in the FHS of the deformable series against the peak mask strain in the rigid model series. A significant association was found between the strains in the FHS ($P = 0.003$), refer to Table 14.8 for details. The regression equation and analysis follow.

$$\epsilon_{VM\ d} = 0.03495 + 0.7120\epsilon_{VM\ r} \tag{14.6}$$

Table 14.8: Regression summary of association between rigid and deformable model FHS strain

Predictor	Coef	SE Coef	T	P
Constant	0.03495	0.0122	2.87	0.064
RgdStrainVM FHS	0.71204	0.07625	9.34	0.003

$S = 0.00736811$ $R^2 = 96.7\%$ $R^2_{adj} = 95.6\%$

Analysis of Variance

Source	DF	SS	MS	F	P
Regression	1	0.004734	0.004734	87.21	0.003
Residual Error	3	0.000163	5.43E-05		
Total	4	0.004897			

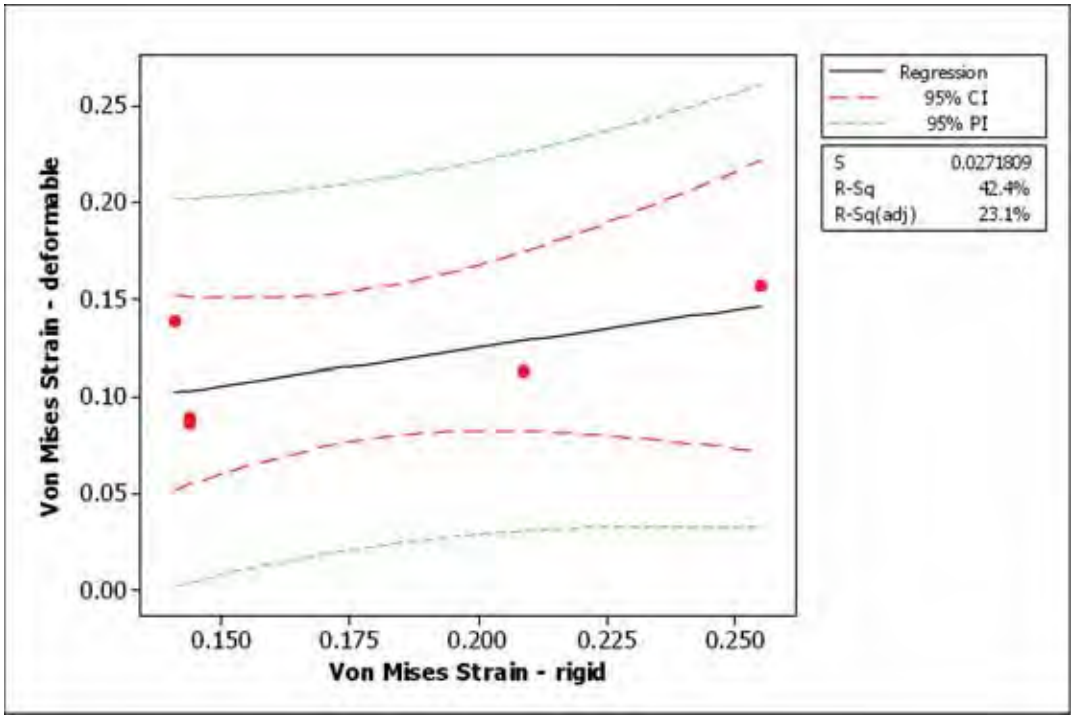

Figure 14.11: Linear regression of ϵ_{VM} at the upper lip in the deformable model on the corresponding variable in the rigid model.

This linear model fits these data excellently accounting for 97% of the variation.

14.5 Conclusion

These regression analyses have interrogated commensurate quantities of contact pressure, contact area and mask Von Mises strain across the rigid and deformable model series. Significant associations have been found for a number of variables. These are summarised in Table 14.1.The presence of significant linear regression equations indicated that it could be feasible to extract a rough estimate of the actual contact pressures, area and strain from the rigid model series. Trends were identified but did not reach statistical significance at the lip and forehead for the contact pressure. It is acknowledged that the small sample size of deformable models is a factor in this, and an increased sample size is expected to further reinforce these associations.

The identification of significant associations is important from a practical point of view, as it opens up the avenue of considering the contact parameters and strains in the mask on a wide range of subjects. As the associations have had positive correlation coefficients, the rigid model series are very well suited to comparative or ranking of design choices or comparative evaluation of fit over a large populations

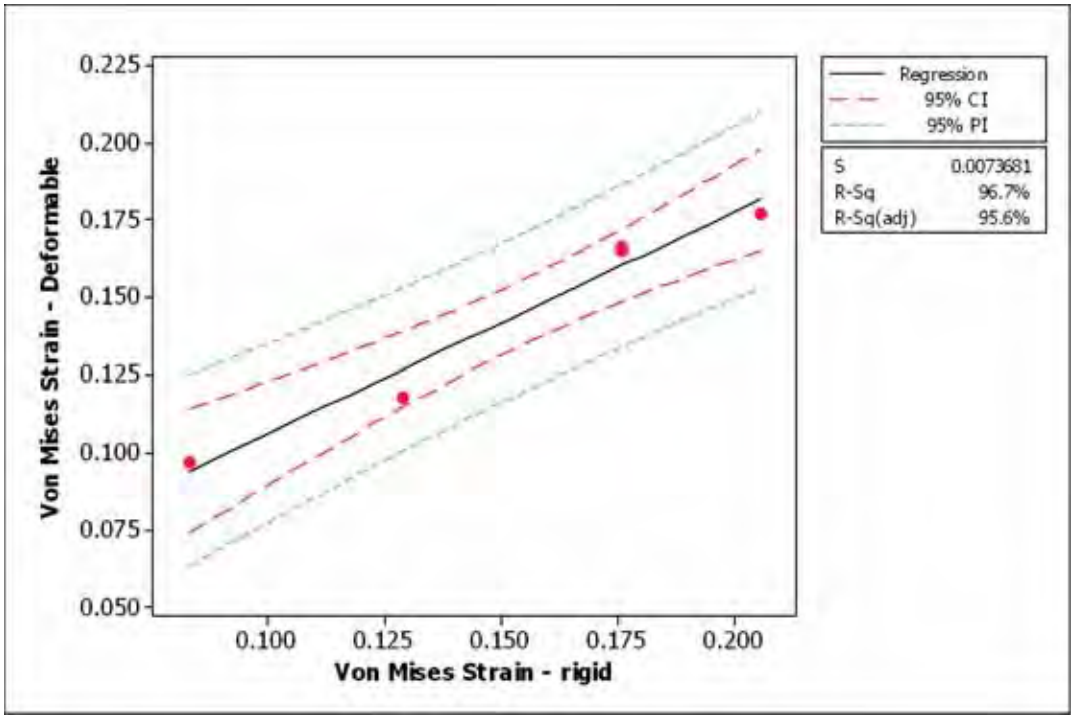

Figure 14.12: Linear regression of ϵ_{VM} in the FHS deformable model on the corresponding variable in the rigid model.

Table 14.9: Summary of regression results, ✓indicates that there was a significant association between the rigid and deformed model series, * indicates an identified trend which has not reached statistical significance in this small sample

Region	Pressure	Area	Strain
Sides	✓	✓	✓
Lip	-	*	-
Nasion	-	-	-
Forehead	*	-	✓

sample. Furthermore the development of rigid models only require facial profile data, and not subdermal detail, non invasive and cheap laser scanning methods are appropriate rather than expensive and time consuming medical imaging modalities such as MRI or CT scanning. Therefore, provided the significant implications of the non physiological assumption of a rigid face are understood, the rigid model series does provide an expedient method to compare and evaluate CPAP mask fit and as part of the development process of a more complicate gold standard deformable model.

Chapter 15

Sensitivity Studies

15.1 Introduction

Two series of models have been developed in this FEA study of nasal CPAP masks on a range of participant's faces. These are the deformable facial mesh series and the rigid facial mesh series. By maintaining consistent loading and boundary conditions across the subjects, anthropometric sourced variation in the contact pressure was able to be investigated and associations found. This leaves an obvious source of variation and sensitivity that must be addressed in this study, namely the sensitivity to the loading and boundary conditions themselves. The loads applied to the system as identified in Section 10.7 consist of the CPAP therapy pressure, the mask headgear tension and the weight of the mask assembly and a portion of the tubing supplying the air.

While under active therapy, the supplied air was simulated to be at an elevated constant pressure [1]. The pressure load is applied to the interior surfaces of mask frame and cushion. This has the effect of causing the mask to lift off from the face. Therefore, the headgear tension is required to preload the system so that the mask remains positively located on the face and that adequate sealing pressure is maintained at the skin/mask interface. In addition to these opposing loads, the weight of the mask acts in the direction pressing the mask onto the face.

The gravitational loading from the mask is a body force and remains constant. The headgear tension and the CPAP therapy pressure on the other hand are continuously variable. The headgear is able to be adjusted according to personal preference, as was allowed in the original experiment of this study. The CPAP therapy pressure may vary for a number of reasons. As mentioned above, the static pressure normally swings during the respiration cycle. The therapy pressure is prescribed on a personal basis after a titration sleep study to ensure that the minimum pressure is applied to the airway to maintain patency. A further variation in pressure may arise from the

[1] In reality the static pressure in the mask swings around the set point throughout the respiratory cycle, dropping on inspiration and increasing during exhalation

flow generators themselves. Some flow generators such as the ResMed S8 Autoset ®flow generator among others incorporate a patient usability feature known as a "ramp". This slowly ramps the supplied pressure from a small value to the therapy pressure over a number of minutes so that the patient can fall asleep with minimal airway pressure and then this is imperceptibly ramped up to therapy pressure, thus avoiding many patient discomfort issues. The point of this is that the two primary loading inputs governing the nature of the contact interface are the headgear tension and the therapy pressure.

15.2 Sensitivity Study Models

Due to the minimal number of independent variables being investigated, it was feasible to investigate the effects of the factors in a series of 2×2 full factorial numerical experiments. This allowed for the evaluation of the sensitivity of the contact results to each of the independent variables of headgear tension and CPAP therapy pressure, as well as their interaction.

A full factorial study was prepared for a single representative sample (subject 12) to investigate the sensitivity of the contact pressure to the CPAP therapy pressure and headgear tension.

15.3 Factorial Definition

The input files for the factorial simulations were prepared using the HyperStudy package by Altair. The models were organised into a small master file containing only loads and property definitions, with references to include files for solver settings, database settings and the meshes for the face and mask. This structure allowed for the paramaterisation of the top level master file without the extensive processing demands of the entire model.

15.3.1 Loads and Boundary Conditions

The mean headgear configuration model series forms the basis for this sensitivity study. The levels of the factors in the experiment are scaled relative to the mean headgear tension configuration. The scaling factors are specified in Table 15.1

Table 15.1: Factorial DOE arrangement showing levels of the controlled variables as scale factors with respect to values from the mean headgear tension model series

Run	Pressure	Tension
1	0.9	0.9
2	0.9	1.5
3	1.5	0.9
4	1.5	1.5

15.3.2 Postprocessing

Since the meshes used in the factorial study were identical to mesh from the corresponding model from the deformable series, the nasal region definitions were reused for this series of models. Nodes and elements within the contact regions were reselected to the 1 Pa threshold for plotting to include the entire contact area and then 5000 Pa for peak contact pressure comparisons. The results from the CPAP pressure threshold varies accordingly, as this defines the contact area that exceeds the therapy pressure and is compressed enough to maintain contact if the pressurised air were to infiltrate between the face and the membrane of the mask and act to pry them apart.

15.4 Results

The results from the sample deformable model are presented graphically as a series of fringe plots in Figure 15.1 and interaction plots in Figure 15.2.

Visual inspection of the fringe plots indicate the same general contact patterns across the factorial experiment. Peak contact regions were consistently located on the sides of the nose, on the upper lip and to a lesser extent at the lower margin of the forehead region. Comparing the four different runs, the contact pressure fringe plots are visually similar between Figures 15.1a and 15.1c in the first column of the plot array, and also Figures 15.1b and 15.1d in the 2nd column of the plot array. In each case these similar pairs correspond to holding the headgear tension constant at the low and high level respectively and varying the CPAP therapy pressure. Only slight differences in the mean contact pressure were observed at the sides of the nose $\left(\frac{\Delta \bar{P}_c}{\bar{P}_c} < 0.01\right)$ after a 60% change in contact pressure.

Considering the rows of the plot matrix, which correspond to maintaining the CPAP therapy pressure constant while varying the headgear tension. In this case it can be seen that the contact area above the 5000 Pa threshold is significantly increased with the 60% variation in headgear tension. This indicates that the overall

load transferred to the face through this load path is increased. The variation of the mean contact pressure with the headgear tension change increases approximately 20% with a tension change of approximately 60%. A similar trend was observed at the upper lip. This information is presented graphically in the interaction plot in Figures 15.2a and 15.2b. This indicates a strong dependency of the mean contact pressure on the headgear tension both for the sides of the nose and the upper lip, as the lines for each of the the levels of headgear tension are at markedly different values of the response variable, contact pressure. Looking at the change in therapy pressure, the response values of contact pressure are approximately constant at the sides of the nose, indicating at most a weak dependency of contact pressure on therapy pressure when compared to headgear tension. The degree of interaction between the two independent variables at the sides of the nose is able to be graphically estimated from the interaction plot. The fact that the lines for each of the levels of headgear tension are approximately parallel indicate that there is little interaction between the variables in this location.

The mean contact pressure on the upper lip at low headgear tension shows a slight positive sensitivity to therapy pressure, while at high tension the contact pressure is essentially independent of the therapy pressure. This difference of behaviour in response to the independent variables is evident in the interaction plot where the lines are not parallel indicating that there is some level of interaction between the independent variables.

The contact area at the side of the nose is similarly sensitive and positively correlated to the headgear tension. Some interaction between the tension and therapy pressure is indicated as the lines are not parallel. At high headgear tension, the contact area above the threshold increases with therapy pressure, while it is approximately constant at low tension. The contact area at the upper lip differs in response to the other variables described, as the contact area is negatively correlated to therapy pressure. Interaction is indicated between the independent variables as the lines are not parallel, with the response to therapy pressure being stronger at lower headgear tension.

15.5 Discussion

The loads applied to the face from the mask arise from the weight of the mask, the headgear tension and CPAP therapy pressure. Of these the pressure and tension are variable, which were examined in this study. The internal pressure acts on the internal wetted area to lift the mask off the face, tending to reduce the contact

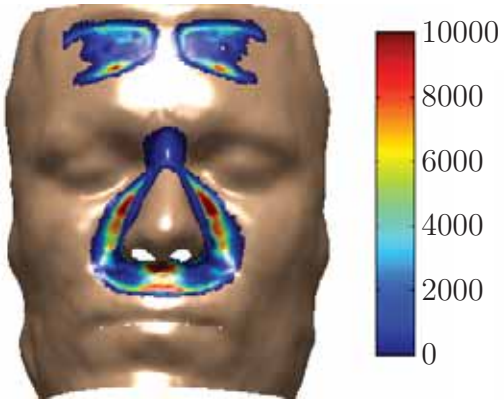

(a) CPAP Pressure factor = 0.9, Headgear tension factor =0.9

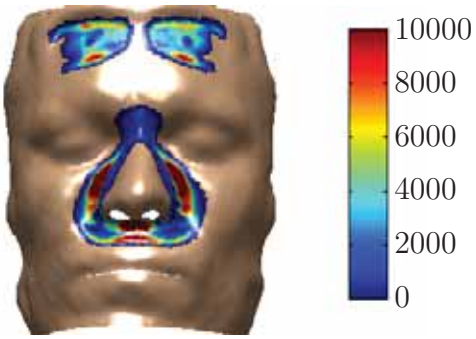

(b) CPAP Pressure factor = 0.9, Headgear tension factor =1.5

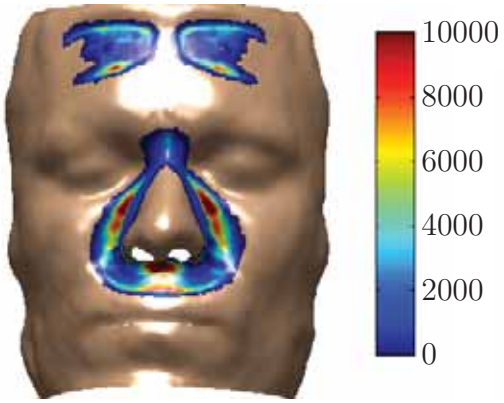

(c) CPAP Pressure factor = 1.5, Headgear tension factor =0.9

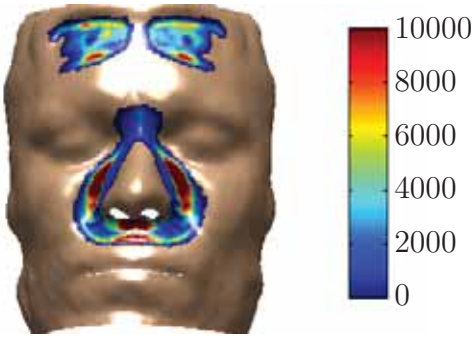

(d) CPAP Pressure factor = 1.5, Headgear tension factor =1.5

Figure 15.1: Subject 12 mask contact pressures over a 2x2 factorial variation of CPAP therapy pressure and headgear tension

pressure and area. Parts of the mask, however, such as the membrane, due to their compliant nature are essentially mechanically decoupled from the remainder of the frame and cushion. While the action of the therapy pressure acts to lift the mask as a whole off the face, locally the pressure will act to press the membrane onto the face. This is particularly evident at the upper lip, which is approximately at the level of the line of action of the lower headgear strap. If the therapy pressure is increased, lifting the mask off the face, this displacement and rotation pivots about the headgear contact region. Due to the maximal moment arm from the fulcrum to the lower portion of the mask at the upper lip, the displacement at the lip will be greatest, leading to a reduction in contact area. At a high headgear tension, the mask undercushion is sufficiently preloaded such that the contact area does not begin to disengage to any significant degree. This effect can be seen by the contact area response shown in Figure 15.2d. Considering the mechanics of the contact pressures, there are competing effects being balanced. An increase in pressure will

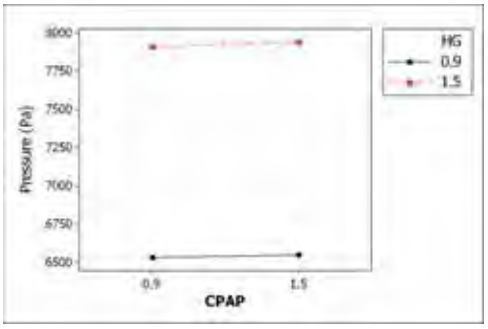

(a) Mean contact pressure $P > 5000$ Pa, sides of nose

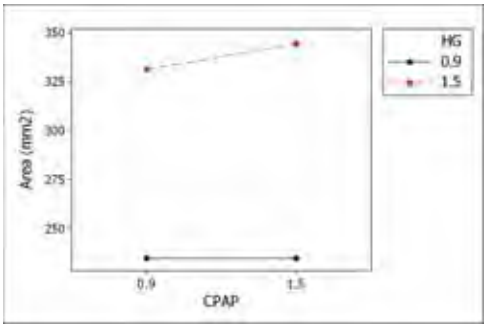

(b) Contact area $P > 5000$ Pa, pooled sides of nose

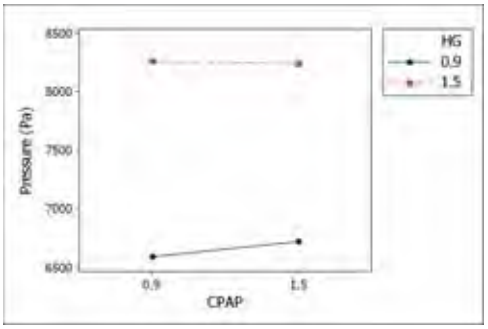

(c) Mean contact pressure $P > 5000$ Pa, lip region

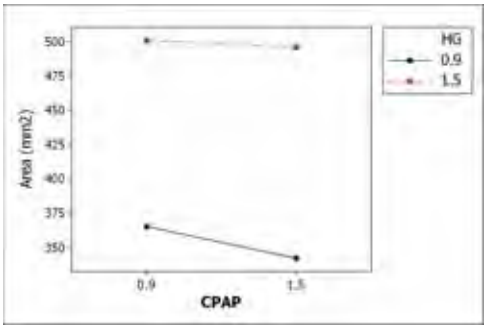

(d) Contact area $P > 5000$ Pa, lip region

Figure 15.2: Interaction plots of the response variables, mean contact pressure and contact area, subject to the factors of headgear tension and CPAP therapy pressure

tend to lift the mask off the face and reduce contact pressure, while simultaneously the increased pressure has a direct load path through the membrane to the face, which will tend to increase contact pressure. In the case of the the upper lip of subject 12, with the headgear tension held constant at the low level, these opposing effects are seen in the magnitudes of the contact pressure fluctuations. The uniform therapy pressure increased by 588 Pa which resulted in an increase in mean contact pressure of 126 Pa. These contact pressure values are of the same order and are able to be accounted for by these CPAP therapy pressure variation ranges.

The contact at the sides of the nose have a reduced moment arm from the fulcrum at the FHS compared to the upper lip, so the tendency to lift off the face is reduced at that location. Additionally, the flanks of the nose engage with the undercushion much earlier during the engagement of the mask. Further, the gradient of the adjacent flanks of the nose are are oriented in more closely with the Z (lateral) axis than the X anterior-posterior axis as is encountered at the upper lip. Therefore, a displacement in the X direction is accompanied by a much smaller displacement in the Z axis, which will prevent the undercushion from unloading significantly.

Previously the contact area above a threshold contact pressure was identified, along with contact pressure, as being strongly dependent on headgear tension. The response of the contact area to the independent variables of headgear tension and therapy pressure differs in pattern from that of the contact pressure. The degree of interaction between the variables is increased for contact area, with the contact area on the side of the nose increasing markedly more with therapy pressure at high tension than at low tension. Contrastingly on the upper lip the contact area has a negative correlation with therapy pressure, as an increase in pressure forces the mask off the face.

This study has investigated the sensitivity of the contact pressure and contact area of the mask on the side of the nose and the upper lip to the headgear tension and the CPAP therapy pressure. These are the two variable components of the total load on the mask. A two factor full factorial numerical experiment was prepared using the LS-DYNA FEA model for subject 12 from the deformable model series as a template. Due to numerical processing expense only a single participant was used for this study. This allows trend data to be extracted, which is of primary importance, but not the variation of results across a sample of participants. The contact pressure and area on this model were both found to be be positively correlated and sensitive to changes in headgear tension. The contact pressure at the side of the face was found to be essentially independent of moderate changes of therapy pressure. There are opposing effects from the pressure acting to both lift the mask off the face, reducing the contact pressure, and, directly pressing the membrane onto the face increasing the contact pressure. The contact pressure at the upper lip is positively correlated to the therapy pressure with some interaction with the headgear tension, with the influence of the therapy pressure reducing at higher headgear tensions. The contact area at the side of the nose is influenced by interactive effects between both variables, with the influence of the contact pressure increasing at higher tensions. The contact area on the lip is negatively correlated with contact pressure. Interaction effects are present with the response to variations in therapy pressure more marked at lower tensions.

Part VI

Recommendations and Conclusions

Chapter 16

Summary and Conclusions

At the outset of this research, the aims of the project were to quantify the facial deformations experienced by the patient during nasal CPAP therapy, and to simulate the contact interactions between the face and the mask. This was expressed through the hypothesis stated in Section 2.1.

> "That MRI and FEA can be used to effectively simulate the mechanical and contact conditions experienced by patients while undergoing CPAP therapy."

The first conclusion that can be drawn from this research, is that this hypothesis can be accepted. The various experimental and simulation streams that have formed this body of work, have all successfully combined to prepare and validate finite element models of the face and mask system in contact.

Using anatomical MRI scans of the participants both in the reference condition and the deformed condition, the deformation of the face while under therapy was able to be measured across the full field of the face. The impressions from the mask cushion, FHS and straps were all evident on the face. Of particular interest were the results in the nasal region. This was divided into four subregions, the left and right sides of the nose, upper lip and the nasion. The peak deformation measured was 8.4mm at the upper lip. The deformations measured at these locations are summarised in Table 16.1. The deformation at the nasion region was significantly smaller than at the other locations due to the small tissue thickness in that region. The deformation was normalised by the tissue thickness to give the compression ratio, which is similar to the nominal compressive strain. The peak compression ratio of $\epsilon_{CMP} = 0.664$ was measured at the nasion, no significant difference was found between regions. Normalising for tissue thickness highlights the compression particularly in the thin tissues across the nasal bridge, which corresponds to the site of skin degradation in some published case studies (Sleilati *et al.*, 2008; Smurthwaite and Ford, 1993). When the compression ratio was further corrected for the applied load to give the normalised compression ratio ϵ^*_{CMP}, there was no significant

difference between locations. Linear regression found associations between the deformation and BMI at the side of the nose ($P < 0.01, r^2 = 38.6\%$) and also between the nasal height at both the upper lip ($P = 0.011, r^2 = 47.2\%$) and nasion regions ($P = 0.044, r^2 = 35.6\%$). Linear regression associations were also found between the nasal width and height and the normalised compression at the side of the nose ($P_{NW} < 0.01, P_{NH} < 0.01, r^2 = 43.4\%$)as well as an association between the nasal height and the normalised compression at the upper lip ($P < 0.01, r^2 = 44.3\%$).

Table 16.1: Summary results ($\mu \pm \sigma$) for facial deformation δ, compression ratio ϵ_{CMP} and compression ratio normalised by headgear load ϵ^*_{CMP} at the regions of interest around the nose.

ROI	δ (mm)	ϵ_{CMP}	ϵ^*_{CMP} (N^{-1})
LHS	4.2 ± 1.5	0.366 ± 0.112	0.073 ± 0.028
Lip	4.9 ± 1.8	0.361 ± 0.133	0.073 ± 0.031
Nasion	2.4 ± 1.0	0.397 ± 0.139	0.080 ± 0.035
RHS	5.0 ± 1.6	0.423 ± 0.129	0.086 ± 0.034

Successful measurement of the facial deformations has for the first time, to the author's knowledge, quantified the extent of facial deformation experienced by CPAP users. This measurement provided a valuable resource that was used in both model development and validation.

Using the information from the CPAP MRI study, two series of models were prepared, one with a deformable mesh corresponding to the experimental data, and the other with a rigid facial profile which corresponds to the assumptions currently used in mask design where facial deformation is not taken into account. From these analyses a number of conclusions may be drawn. Firstly, the deformable facial models were able to successfully engage with the face and could be validated across several regions of interest. The validated models may then be used to estimate difficult to measure quantities such as contact parameters, in this case, between the face and the mask. This highlights the utility of the finite element method for this task. However many challenges were encountered in the development of these models, one of the most significant was resolving the instabilities and post buckling behaviour induced in the mask, and its interaction with the face. This was resolved through the use of the explicit finite element method. Therefore despite the fact that these models were considered to be quasi-static, it was concluded that the explicit finite element method is the appropriate solution method to use for this class of problem.

The results from the deformable series of models controlled for headgear tension indicated that the maximal peak contact pressure ($\mu \pm \sigma$) was located at the

sides of the nose (7.2 ± 0.88kPa). The other facial regions ranked in order of descending mean contact pressure are the upper lip (5.9 ± 0.8kPa), FHS (5.3 ± 0.2kPa) and finally the nasion region (4.7 ± 0.3kPa). Linear regression did not identify any particular anthropometric dimension associated with the contact pressures at the various regions. This could be influenced by the small sample size. Linear regression however, did identify a significant association between the contact pressure at the side of the nose and BMI, and the contact pressure at the upper lip was shown to have a positive correlation between the headgear load and contact pressure as it is directly on the load path to the strap clip locations.

Paired comparisons between the corresponding models of the rigid series and deformable model series allowed for the rigid assumption to be tested. A conclusion of this work is that the rigid assumption significantly influences the nature of the contact between the face and the mask as well as the the nature of the load distribution. Significant reductions in calculated contact pressure were found at the sides of the nose (3.4 kPa), the upper lip (4.1 kPa) and at the forehead (2.6 kPa) in the deformable model series compared to the rigid series. Although the rigid assumption influences the contact parameters it does not imply that the rigid facial models do not provide useful information for the analyst. Important linear associations were found between the contact pressure in the deformable models and the contact pressure in the rigid models at the sides of the nose, additionally significant reductions of pressure were consistently found across the samples used at the upper lip and forehead. This verifies that the rigid models could be effectively used for comparative studies or to infer some approximate prediction of deformable contact pressure. The rigid modelling technique is very attractive from a designers point of view as the model development and run time are reduced to a fraction of that required for the deformable models. In particular the rigid model development is able to be automated to a point where only minimal user interaction is required. This opens up the valuable possibility of acquiring large scale predictive contact data from specific demographics, which would be of great utility for designing masks for specific cross sections of the population.

Considering both the rigid and deformable modelling techniques, both can be used to gain great insight into mask/face interactions. Both are suitable for the mask design process assuming that suitable computing power is available, which is increasingly common. The rigid model is highly suited to comparative modelling and fast design iterations, stochastic population based studies and for simulated Design of Experimentss (DOEs) with large numbers of factors or levels. In this study, considerable effort has been spent developing and validating the deformable modelling process. Fortunately for ongoing work, much of this work does not need to

be repeated and future model development will be a far simpler process. Individual study centres will likely develop meshes that are able to be re-used in future studies saving considerable work and providing paired data that will be simple to analyse for differences and improvements in design. The increased computational expense of the deformable models may make them inappropriate for very high speed design iterations across many factors, but they are reasonable for use during product design and will provide a rich source of data regarding the interface and fit of the masks on the face. This will be particularly relevant for future detailed study into localised mechanics such as the state of loading and deformation around the nasion.

The variable loads applied to the face from the mask and therapy are the headgear load and the therapy pressure. A sensitivity study varying these loads found that the contact pressure was dominated by the headgear tension rather than the therapy pressure.

The reliability of the explicit FEA method for simulation of nasal CPAP was enhanced by the alternate mask study. An alternate mask with significantly different stiffness characteristics was substituted into one of the models previously solved in the deformable series, and compared to a quarantined data set from the original CPAP MRI study. The residuals between this study and the experiment were within the range of the tuned models from the deformable series. The significance of this result is that the modelling strategy is not only valid for the deformable series that was tuned to the experimental data, but also for an alternate case with no further adjustment. This emphasises the suitability of the explicit FEA method to simulate the contact of nasal CPAP masks on the face.

The results of this research are extremely encouraging and provide a foundation to incorporate facial deformation into the early stages of future CPAP mask designs. There are a number of assumptions that were made in this model that provide scope for further development. These include the low value for the friction coefficient between the face and the mask, more complex, realistic material models, consideration of the full respiration cycle among others. This naturally leads into recommendations for future work to build on this study.

Chapter 17

Recommendations for Future Work

One of the major assumptions that was made in this study was that the Coulomb friction coefficient between the face and the mask was arbitrarily set at $\mu = 0.1$ for stability purposes. This is an unrealistic value, and an obvious source of further development in this modelling strategy. The use of a more realistic value was investigated briefly during this research and found to cause problems with shearing in the skin layer elements. The skin was modelled isotropically, so accommodating the realistic transverse modulus according to Jachowicz *et al.* (2007) was at the expense of reduced stiffness in the membrane plane, not to mention the sharply non-linear locking characteristics of skin as the collagen fibres straighten as they are loaded. A high friction coefficient between the skin and the mask will have the effect of drawing the skin with the mask as it is engaged and will require the locking behaviour of skin allow sliding of the mask over the skin. The implementation of a constitutive model incorporating the three dimensional micro-mechanics of the of the skin taking into account the composite nature of the ground substance and fibrous components. A more realistic constitutive model of the skin would allow realistic skin friction and shear stresses to be estimated. These parameters are likely of great importance addressing the occasional adverse event of skin breakdown after using nasal masks for CPAP therapy or non invasive ventilation. This future development of this work would also be directly relevant for further research into pressure ulcer and DTI mechanics potentially providing great and broad clinical benefit.

A logical extension of the work is to consider CPAP therapy as a dynamic process and track the solution through a full respiratory cycle monitoring the effect on the face and the fit of the mask through pressure fluctuations experienced during a breathing cycle. This model extension could also be used to extend the modelling process to alternate therapy modalities such as bi-level and ventilation processes with expiratory pressure relief, increased pressures and pressure swings. A further benefit of modelling the full dynamic process is to more extensively consider the interactions of between headgear tension, preload and therapy pressure.

Extending beyond the realm of just considering the raw simulation results, mask design would be assisted if a scalar, objective measure or index of comfort or fit could be developed. In the field of pressure ulcer research, Gefen (2008) proposed the compression intensity index, $CII = \sqrt{\frac{w_{body}}{Rt}}$, which incorporates body weight w_{body}, bone radius of curvature R and tissue thickness t as a risk analysis tool for pressure sores. Gefen's work considers geometry, external loading and tissue bulk, these influences are similar to the scenario encountered CPAP masks. Even further benefit could be attained if an objective measure could be correlated to subjective feedback of clinical patients participating in device trials to relate contact mechanics to patient perception of comfort.

Considering the rigid face model series, the technology and computing power now makes it feasible to automate a series of finite element moderately complex solutions across a very large number of samples. This would make available population specific predictions of fit with sample sizes large enough to provide high power for alternate design considerations.

The research presented in this thesis has focussed on nasal CPAP masks. The same insight from contact simulation is available to full face masks and nasal pillows. There are other complications associated with these masks, such as mandibular movement for full face masks, but these are problems which are presently being addressed in other fields of biomechanics and should not provide too great a hurdle. Nasal pillows masks may in fact be less susceptible to buckling as they are in a more constrained environment, so implicit methods may be suitable for consideration of this type of mask.

A brief consideration of future directions from this thesis has identified a range of both long term and short term developments of this work. These range from adding sophistication and capturing more detail in the model through to large scale implementation of some of the work that has been presented in this thesis. All of these recommendations for future work feed into the continual process of increasing understanding of the face/mask interface and using this knowledge to design better and more comfortable masks, which will remove some of the obstacles to compliance to therapy.

In the introduction to this thesis it was stated that this research was intended to open the investigation into the nature of contact interactions between the face and CPAP masks as a foundation for more sophisticated biomechanical analyses in the future. This thesis has begun to address issues related to the contact interactions between the face and the mask and has outlined a number of areas where this work can be further developed. A major achievement of this work is that now the influence of the rigid facial assumption has been quantified and these methods are able to be

used to consider facial deformations in the design of future masks, which it is hoped are more comfortable and pleasant to use and deliver tangible health and well-being benefits to both CPAP patients and their families.

Appendices

Appendix A

Tube Force Effects

Inspection of experimental photographs indicate that the tubing is supported by resting on the subject's torso. At some point it leaves the body and is supported by the interference fitting between the tube and the swivel, which is connected to the mask. As the subject is lying in the supine position, the primary loading on the tube is gravitational.Another source of load is from tube bending or stretching. The nature of this loading over the dimension scale in question is summarised below as well as how this is will be considered in FEA models.

A.1 Method

The length of unsupported tube was estimated from digital photographs taken during the experiments by tracing the unsupported length of the curve using a polyline converted into a best fit spline on the image and scaling this according to the known length of the mask. This was performed in the ImageJ image analysis software. This is shown in Figure A.1. The length of the curve shown is 350mm.

The applied load was investigated by resting a CPAP tube on a rigid surface fixed to the frame of an Instron mechanical testing machine. The tube was fixed at a distance of (350) mm) from its end which was aligned with the crosshead of the Instron. A thread was looped around the tube and connected to the load cell (50N). The load cell was calibrated and balanced without load. The crosshead then raised the tube end by 18.4mm which was sufficient to support the tube back to the level of the fixation. This was repeated 3 times and the load cell force was recorded. The mass of the tube was also measured with an analytical balance.

A.1.1 Results

Results are tabulated in Table A.1. The basic measurements of the tube portion were

Figure A.1: Red curve indicates unsupported length of tube estimation using ImageJ software

$$m = 37.65\text{g}$$
$$l = 348\text{mm}$$
$$\phi_{OD} = 23$$
$$\phi_{ID} = 19$$

Note that the diameters given are overall diameters measured across the spiral pattern of the tube. Assumptions will be made for inertial calculations to treat this as a nominal cylinder.

Reading	Force (N)
1	0.388
2	0.391
3	0.385
mean $\pm\sigma$	0.388 ± 0.003

Table A.1: Force measured to raise an end of a tube to a length of ($l = 350$mm) from a surface supporting it.

The weight of the sector of the tube that was elevated was:

$$
\begin{aligned}
F &= mg \\
&= 37.65\left(10^{-3}\text{kg}\right) \times 9.80665\text{ms}^{-2} \\
F &= 0.369\text{N}
\end{aligned}
$$

A.2 Conclusion

The flexible nature of the tube at this length scale has minimised the cantilever spring effect of the tubing. Therefore from this analysis, at this length it can be seen that 95% of the load required to support the end of the tube is provided by the mass of the tube. Therefore an assumption will be made that for FE modelling the influence of the tube and connectors will be assumed to be through inertial effects.

Appendix B

Ultra Mirage II Inertia

Since the mask frame is a significantly stiffer than the compliant LSR interface materials of the mask, the mask assembly is considered as a rigid body for FEA. As a transient solution method was used and body loads are significant, it is important to correctly account for the mass distribution of the rigid body.

The UMII mask is able adopt 4 configurations according to the rotational position of the T-Bar. Therefore the inertial properties were determined for each case.

B.1 Method

B.1.1 Mask Assembly

Each component of the assembly was weighed using an analytical balance and recorded. The solid 3D CAD (Pro/ENGINEER) models of each component were used to provide the inertial properties of the assembly in the various configurations.These were compared to the measured component. Inertial properties of the assembly from the CAD system were scaled so that the CAD mass matched the measured mass.

The CAD mass property results were calculated for each part with respect to their master coordinate system. The assembly results were calculated with respect to the UMII coordinate system which is oriented approximately parallel to the global anatomical coordinate system. CAD principal inertia results I_1, I_2, I_3 are ordered in increasing magnitude such that $I_1 \leq I_2 \leq I_3$. Consistent units (mmNs) were used for FEA analysis, and the inertial properties here are reported in this unit system, therefore mass is reported in Tonnes. The centroidal system is oriented so that I_1, I_2 and I_3 are the principal moments of inertia about the centroidal X, Y and Z axes.

Inertial properties were entered in the FEA model using principal values about the centroidal coordinate system.

Table B.1: Measured and calculated masses of UM2 mask assembly and components

Component	Mass 10^{-6} T	CAD Mass 10^{-6} T	Correction Scale Factor
Frame	17.8	17.2	1.04
Tbar	10.3	10.0	1.04
Cushion Clip	3.6	3.8	0.96
Circlip	0.6	0.6	1.02
Vent Cover	3.0	3.1	0.94
Elbow	13.2	13.6	0.97
Swivel	7.3	7.3	1.00
HG Clip LHS	1.8	1.9	0.91
HG Clip RHS	1.8	1.9	0.91
Tube (305 mm)	19.9	19.9	1.0
Tube End	17.8	17.8	1.0
Total	97.0	97.0	-

B.1.2 Tube Section

The centre of mass of the mask assembly took into account the mask assembly and about 350mm of the tube assembly. This was estimated from images of The tube assembly will be assumed to consist of a composite body of two cylinders, namely the tube and its terminating connection. The tube assembly was assumed to be rigidly connected to the mask at the swivel and is oriented along the axis of the swivel and on the midplane.

The properties of the tube were estimated from measurements taken from a portion of tube. Ideal geometry was assumed.

B.2 Results

B.2.1 Mask Assembly Mass

The mass of the mask components is reported in Table B.1

The position vector of the centre of mass $\bar{\boldsymbol{x}}$ for each configuration is presented in Table B.2.

The principal inertia tensors of the mask assembly in the centroidal coordinate system as calculated by the CAD model are defined in equations (B.1) to (B.4) below.

Table B.2: Centre of mass coordinates for UMII nasal mask for each T-Bar configuration

Configuration	X	Y	Z
1	2.20	-56.52	0.074
2	1.52	-56.63	0.074
3	0.89	-56.89	0.074
4	0.33	-57.29	0.074

Inertia Tensor Position 1 - Straightest

$$I = \begin{bmatrix} 0.0444 & 0 & 0 \\ 0 & 1.1796 & 0 \\ 0 & 0 & 1.1828 \end{bmatrix} \tag{B.1}$$

Inertia Tensor Position 2

$$I = \begin{bmatrix} 0.0471 & 0 & 0 \\ 0 & 1.1782 & 0 \\ 0 & 0 & 1.1842 \end{bmatrix} \tag{B.2}$$

Inertia Tensor Position 3

$$I = \begin{bmatrix} 0.0506 & 0 & 0 \\ 0 & 1.1727 & 0 \\ 0 & 0 & 1.1822 \end{bmatrix} \tag{B.3}$$

Inertia Tensor Position 4 - Angled

$$I = \begin{bmatrix} 0.0544 & 0 & 0 \\ 0 & 1.1636 & 0 \\ 0 & 0 & 1.1769 \end{bmatrix} \tag{B.4}$$

B.2.2 Transformation Matrices

The transformation of the coordinates of position vector of a fixed location *from* the Centre of Gravity (CG) reference frame *to* the UMII master reference frame is given by equation (B.5)

$$\boldsymbol{x}^* = \boldsymbol{x}\boldsymbol{A}, \tag{B.5}$$

where $\boldsymbol{x}$ is the position row vector of the location in the original coordinate system (CG), $\boldsymbol{x}^*$ is the position row vector transformed into the alternate system (UMII), and $\boldsymbol{A}$ is the affine forward transformation matrix.

Position 1

$$\boldsymbol{A_1} = \begin{bmatrix} -0.09765 & 0.99522 & -0.00044 & 0 \\ -0.99486 & -0.09763 & -0.02707 & 0 \\ -0.02699 & -0.00221 & 0.999633 & 0 \\ 2.200735 & -56.5173 & 0.074072 & 1 \end{bmatrix} \tag{B.6}$$

Position 2

$$\boldsymbol{A_2} = \begin{bmatrix} -0.1059 & 0.9944 & -0.0004 & 0 \\ -0.9943 & -0.1059 & -0.0150 & 0 \\ -0.0150 & -0.0012 & 0.9999 & 0 \\ 1.5234 & -56.6259 & 0.0741 & 1 \end{bmatrix} \tag{B.7}$$

Position 3

$$\boldsymbol{A_3} = \begin{bmatrix} -0.11337 & 0.993553 & -0.00043 & 0 \\ -0.99351 & -0.11337 & -0.00972 & 0 \\ -0.00971 & -0.00067 & 0.999953 & 0 \\ 0.88924 & -56.8878 & 0.074072 & 1 \end{bmatrix} \tag{B.8}$$

Position 4

$$\boldsymbol{A_4} = \begin{bmatrix} -0.11947 & 0.992837 & -0.00043 & 0 \\ -0.99281 & -0.11947 & -0.00699 & 0 \\ -0.00699 & -0.00041 & 0.999976 & 0 \\ 0.33263 & -57.2889 & 0.074102 & 1 \end{bmatrix} \tag{B.9}$$

Appendix C

Liquid Silicone Rubber Mechanical Testing

The material used for the cushion and forehead support in the ResMed masks is Dow Corning LSR 94-595 HC ®. It is a silicone elastomer. Elastomers commonly exhibit non linear mechanical behaviour associated with very large, incompressible deformations. This material is appropriately modelled using incompressible hyperelastic material models. A series of mechanical tests were performed in order to characterise the behaviour of the LSR under a range of load states.

C.1 Introduction

The aim of this experiment and analysis is to determine using inverse finite element analysis (FEA) non linear material properties for Dow Corning Liquid Silicone Rubber 94-595HC ®, which is used to manufacture the CPAP mask cushion and FHS components.

A material is termed hyperelastic if it is capable of withstanding very large recoverable mechanical deformations. Hyperelastic materials commonly exhibit incompressibility, whereby these large deformations are associated with very small variations in material volume. Additionally these materials exhibit a non linear stress-strain characteristic.

This provides some complications in determining an appropriate constitutive model for structural simulation, as due to the incompressibility of the material, the state of stress is not unique to a particular strain state (ANSYS Inc, 2005). Since most of the hyperelastic models that have been developed are phenomenological models (Treloar *et al.*, 1976) (*i.e.* models are based on regression and do not take into account the physical structure of the material) it is important to test in multiple modes of deformation, as it is not guaranteed that a good model fit in one deformation mode will translate to another (ANSYS Inc, 2005). Therefore it is commonly

regarded as good practice when using such phenomenological models to consider at least two independent testing modes when possible (Ogden *et al.*, 2004; ANSYS Inc, 2005). The primary independent test modes (and equivalent deformation modes) are uniaxial tensile extension (biaxial compression), pure shear using planar extension and compression (biaxial tension).

The mechanical behaviour of elastomers typically exhibits a number of characteristics that need to be taken into account when performing testing. These include hysteresis and preconditioning. In general the loading and unloading paths of an elastomer will differ as energy is dissipated internally, this is hysteresis. The energy dissipation is the nett area under the loading and unloading force vs displacement curves. Preconditioning on the other hand is characterised by the sample following different loading curves each cycle of a repeating load history. In general the first cycle deformation will be stiffer and require more energy than subsequent cycles. After a few cycles the sample is preconditioned and the load path is essentially constant from cycle to cycle, the sample is said to be preconditioned or stabilised. Residual damage is accrued in the sample, so that the reference state of the sample is shifted to a different location. Interestingly if the magnitude of the load cycle is increased, the next cycle follows the stabilised path to the original load level, then the continuation of the initial stiffer load curve beyond the stabilised point, the material can then be preconditioned again. Therefore when extracting data for mechanical characterisation, it is important to choose the appropriate portion of the load history. Considerations include:

- Loading or unloading portion of the curve
- Initial or preconditioned curve
- Anticipated strain level

Compressive testing is kinematically equivalent to equibiaxial tension. Unfortunately the direct use of compressive data is hindered by the indeterminate boundary condition given by the platen friction. This results in a non uniform stress and strain field, which is evident by barrelling of test samples under compressive loading due to shear stresses at the sample/platen interface. Coupled with the use of numerical simulation, the effect of the friction can be accounted for, hence improving test data.

In order to characterise the material, the standard independent deformations of tension, planar tension and compression were performed. The undercushion of the mask acts as a cantilevered spring and and is the primary load bearing mechanism. Therefore in order to test the material in a loading configuration that mimics the in use load, a bending test was performed using samples cut from new mask cushions.

C.2 Governing Equations and Variables

The following measured and derived quantities are used to present the results and for subsequent calculations. Note that *UPPER CASE* kinematic variables denote the reference configuration, and *lower case* kinematic variables denote the deformed or current configuration.

Force (P) Measured load (N) applied to the sample

Engineering Strain (e) Measured nominal strain from the non contact extensometer

$$e = \frac{\Delta L}{L} \tag{C.1}$$

Stretch Ratio (λ_i) Principal stretch ratio in the i direction

$$\lambda_i = \frac{l_i}{L_i} = e + 1 \tag{C.2}$$

Incompressibility Constant volume maintained throughout arbitrary deformations

$$\lambda_1 \lambda_2 \lambda_3 = 1 \tag{C.3}$$

1st Piola Kirchoff Stress (T) Applied load in the i direction normalised by the reference area normal to the j direction, also known as Engineering Stress

$$T_{ij} = \frac{P_i}{A_j} \tag{C.4}$$

Cauchy Stress (σ) Applied load in the i direction divided by current or deformed area normal to the j direction, also known as true stress

$$\sigma_{ij} = \frac{P_i}{a_j} \tag{C.5}$$

$$= \frac{P_i}{\frac{A_j}{\lambda_i}} = \lambda_i \frac{P_i}{A_j} \tag{C.6}$$

$$\sigma_{ij} = \lambda_i T_{ij} \tag{C.7}$$

C.3 Uniaxial Tension

The uniaxial tension deformation mode is set up using a standard tension test. The sample is long elongated in the direction of testing and maintains a constant cross

Table C.1: Tensile test equipment list

Item	Qty	Comment
Dow Corning LSR 94-595HC samples	4	ASTM D412 dumbbells
Instron 5542 Mechanical Tester	1	
Pneumatic Grips	2	
Instron AVE Non Contact Video Extensometer	1	
Gauge template	1	
Marker	1	

section in the gauge region. The sample is allowed to freely deform under the applied deformation. Therefore the deformation gradient for this mode of testing is;

$$\boldsymbol{F} = \begin{bmatrix} \lambda & 0 & 0 \\ 0 & \frac{1}{\sqrt{\lambda}} & 0 \\ 0 & 0 & \frac{1}{\sqrt{\lambda}} \end{bmatrix} \tag{C.8}$$

C.3.1 Equipment and Materials

The equipment and materials used in this experiment are outlined in Table C.1.

C.3.2 Preparation

ASTM D412C ($n = 4$) dumbbell samples were punched from a blank sheets ($180 \times 180 \times 3$ mm) manufactured from Dow Corning LSR 94-955HC.

Dimensions of the gauge region were nominally $25 \times 6 \times 3$ mm.

The width of each sample was measured in three locations using a pair of digital vernier callipers. The mean value was used for downstream calculations. The thickness of each sample was measured in three locations using a digital thickness gauge. The mean value was used for downstream calculations.

Two gauge marks were placed on each sample using a marking template. The gauge length was approximately 25mm and was precisely determined during the experiments by the video extensometer.

C.3.3 Protocol

The following procedure was followed for each sample. The load cell was balanced prior to mounting. The sample was mounted first into the top grip. The cross head position was adjusted so that the sample was in the correct location, and the

lower grip was engaged. This caused the sample to deform slightly and placed the sample in a small compression. The fine adjust was used to position the crosshead at the zero load location. The gauge length was then reset and the test protocol commenced.

The test protocol preconditioned the sample by subjecting it to 5 precycling loops followed by an extension test. The extension speed was held constant on both the rising and falling ramps (60mm/min). The samples were tested to a nominal stretch of $\lambda = 1.25$.

C.3.4 Processing

The LSR in the masks experiences cyclic loading from the pressure change during the respiration cycle through to forces applied due to body movements. Therefore it is appropriate to utilise data from stabilised or preconditioned test results. Therefore the final loading curve data will be extracted for analysis and material model development. The data was adjusted to account for the altered reference condition as follows:

At the beginning of the test the gauge length was measured by the non contact extensometer (L_0). This was written to the data file for each sample. The width (W_0)and thickness (T_0) were measured in the reference state prior to testing. After extracting the final load curve, the start of the load curve was detected by locating the rising edge with a threshold of 0.01N. This is the stabilised reference configuration. The engineering strain (e_0) at this location was used to define the preconditioned stretch λ_0

$$\lambda_0 = 1 + e_0 \tag{C.9}$$

Therefore the preconditioned gauge length is adjusted as follows:

$$L = \lambda_0 L_0 \tag{C.10}$$

In order to meet the incompressibility kinematic constraint, the cross sectional area must be adjusted also,

$$\lambda_{W0} = \lambda_{T0} = \frac{1}{\sqrt{\lambda_0}} \tag{C.11}$$

$$A_0 = W_0 T_0 \tag{C.12}$$

$$A = WT = \frac{W_0}{\sqrt{\lambda_0}} \frac{T_0}{\sqrt{\lambda_0}} \tag{C.13}$$

$$A = \frac{A_0}{\lambda_0} \tag{C.14}$$

Where A, L, W, T refer to the adjusted preconditioned reference state, and L, W, T correspond to the principal dimensions $X = [X_1, X_2 X_3]$ in the reference coordinate system.

C.4 Pure Shear - Planar Tension

The pure shear deformation mode is set up using a planar tension test. The sample is short (direction of testing), wide and thin. The sample is rigidly constrained at each end, this can be seen in Figure C.1. This restricts the lateral deformation. Therefore the stretch ratio $\lambda_2 = 1$ throughout testing. Therefore the deformation gradient for this mode of testing is;

$$\boldsymbol{F} = \begin{bmatrix} \lambda & 0 & 0 \\ 0 & 1 & 0 \\ 0 & 0 & \frac{1}{\lambda} \end{bmatrix} \tag{C.15}$$

C.4.1 Equipment and Materials

The equipment and materials used in this experiment are outlined in Table C.2.

C.4.2 Preparation

Six ($n = 6$) wide samples were punched from a blank sheets ($180 \times 180 \times 1$ mm) manufactured from Dow Corning LSR 94-955HC.

Dimensions of the gauge region were nominally $180 \times 10 \times 1$ mm.

The width of each sample was measured in three locations using a pair of digital vernier callipers. The mean value was used for downstream calculations. The

Figure C.1: Planar tension test

Table C.2: Planar tensile test equipment list

Item	Qty	Comment
Dow Corning LSR 94-595HC samples	6	Wide samples
Instron 5542 Mechanical Tester	1	
Planar Tension grips	2	
Pneumatic Grips	2	
Sample cutter	1	
Instron AVE Non Contact Video Extensometer	1	
Gauge template	1	
Marker	1	

thickness of each sample was measured in three locations using a digital thickness gauge. The mean value was used for downstream calculations.

Two gauge marks were placed on each sample using a marking template. The gauge length was approximately 10mm and was precisely determined during the experiments by the video extensometer.

Table C.3: Compression test equipment list

Item	Qty	Comment
Dow Corning LSR 94-595HC samples	5	Cylindrical samples
Instron 5542 Mechanical Tester	1	
Compression platens	2	Emery paper coated platens for fixed boundary condition

C.4.3 Protocol

The following procedure was followed for each sample. The load cell was balanced prior to mounting. The sample was mounted first into the planar tension grips. The cross head position was adjusted so that the sample was in the correct location, and the lower grip was engaged. The fine adjust was used to position the crosshead at the zero load location. The gauge length was then reset and the test protocol commenced.

The test protocol preconditioned the sample by subjecting it to 5 precycling loops followed by an extension test. The extension speed was held constant on both the rising and falling ramps (60mm/min). The samples were tested to a nominal stretch of $\lambda = 1.25$.The planar tension test is shown in Figure C.1.

C.4.4 Processing

Refer to Section C.3.4 for processing details.

C.5 Compression

A semi-confined compression test was used to establish a compressive deformation in the test sample. Friction at the platen interface however complicates this test, and steps were taken to account for it. Instead of trying to minimise the friction and assume a uniform state of strain, a rough platen was used to create *semi-confined* compression tests by applying a no-slip boundary condition to the platen interfaces. This allows for post-hoc correction of the experimental data to determine uniform stress vs strain data. The deformation gradient of a uniform compression deformation field is identical to that for uniaxial tension (C.8), except that $\lambda < 1$.

C.5.1 Equipment and Materials

The equipment and materials used in this experiment are outlined in Table C.3.

C.5.2 Preparation

Six ($n = 5$) cylindrical samples were moulded ($\phi 25 \times 20$ mm) from Dow Corning LSR 94-955HC.

C.5.3 Protocol

The following procedure was followed for each sample. The load cell was balanced prior to testing. The sample was placed on the lower platen. The cross head position was adjusted so that the sample was almost in contact. The gauge length was then reset and the test protocol commenced.

The test protocol preconditioned the sample by subjecting it to 5 compressive precycling loops followed by a compressive test. The extension speed was held constant on both the rising and falling ramps (10mm/min). The samples were tested to a nominal stretch of $\lambda = 0.75$.

C.5.4 Processing

Similarly to Section C.3.4, the final loading curve was extracted from the load history. Due to preconditioning the stabilised origin was determined, and reference geometry was updated to this configuration. Due to the effect of the no-slip boundary condition at the platens, a uniform state of strain was not established, so direct measured quantities, force (N) and displacement (mm) are reported for use with subsequent numerical treatment.

C.6 Results

The results from the various mechanical tests are shown graphically in Figure C.2.

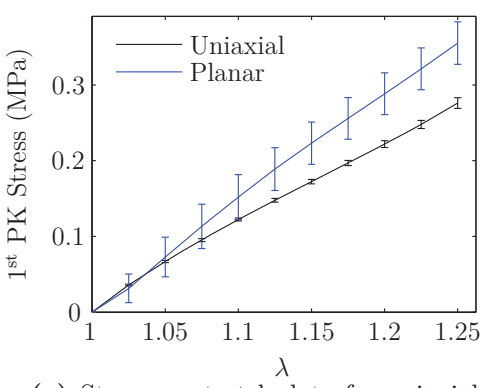

(a) Stress vs stretch data for uniaxial tension and planar tension to a stretch of $\lambda_1 = 1.25$

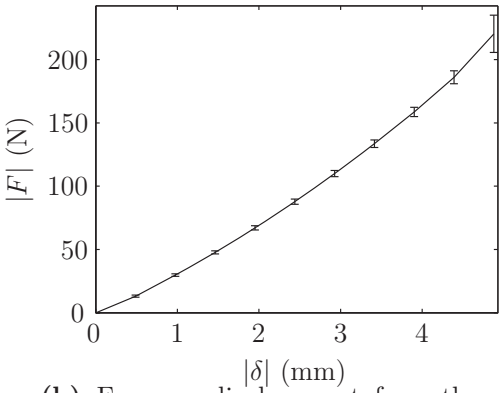

(b) Force vs displacement from the semi defined compression test

Figure C.2: LSR mechanical test results to a nominal strain of ±0.25

Appendix D

Ultra Mirage II Undercushion Bending

D.1 Purpose

The purpose of this test was to determine the force-deflection characteristics of the UMII undercushion cantilevered spring. These data are to be used to validate the material model of the LSR material that is used for the mask in a deformation mode that is similar to usage conditions.

D.2 Introduction

As the mask is brought into contact with the face, the membrane essentially conforms to the face, while the undercushion provides the dominant load path between the face or membrane and the mask frame. The undercushion comes into contact in various locations with the membrane (sandwiching it between the face and the undercushion) or the skin directly in some cases depending on the geometry of the face and the positioning of the mask. The undercushion of the mask acts as a non-linear cantilevered spring, designed to gradually increase in stiffness as it is deflected.

This test allows for the measurement of cushion force-deflection characteristic curve from a production sample in a mode that is similar to in use conditions.

D.3 Materials and Equipment

The consumables and test equipment required for this test are outlined in Table D.1

Table D.1: LSR bending test equipment

Item	Qty	Comments
UM2 Nasal Mask Standard	5	Unused production masks
Scalpel	1	
Straight edge cutting jig	1	
Instron 5543 Mechanical Testing Machine	1	
50N Load cell	1	
Compression platen	1	Rough finish for non slip boundary condition
Mounting jig	1	Fastens rigidly to Instron tie rod
Vernier Callipers	1	
Bluehill 2 Software	1	Data logging and experimental control

D.4 Protocol

D.4.1 Sample Preparation

Using a scalpel, cut the cushion into 2 parts down the axis of symmetry (sagittal plane), then on each side carefully trim using the scalpel and cutting jig a 10mm long sample from the straight portion of the mask on the flank of the nose where the section does not change along this direction. Carefully trim the membrane from the sample so that it does not interfere with the compression platen. Following the preparation of the sample, measure the length of the sample using a vernier calliper in three (3) locations. The mean length is used for normalising results.

D.4.2 Specimen Mounting

If pneumatic grips are installed on the Instron testing machine, ensure that the pressure is relieved and remove the grips from the machine. If the 50N load cell is not installed remove the currently installed load cell and install and calibrate the 50N load cell. Mount the compression platen on the lower rod by fastening the adapter and screwing in the platen including the rough non-slip insert.

Load the sample into the custom mounting jig and fasten locating screws, then transfer and install the jig on the upper Instron rod. Manually adjust the location of the crosshead to bring the sample almost but not quite into contact, balance the load cell and reset the gauge length.

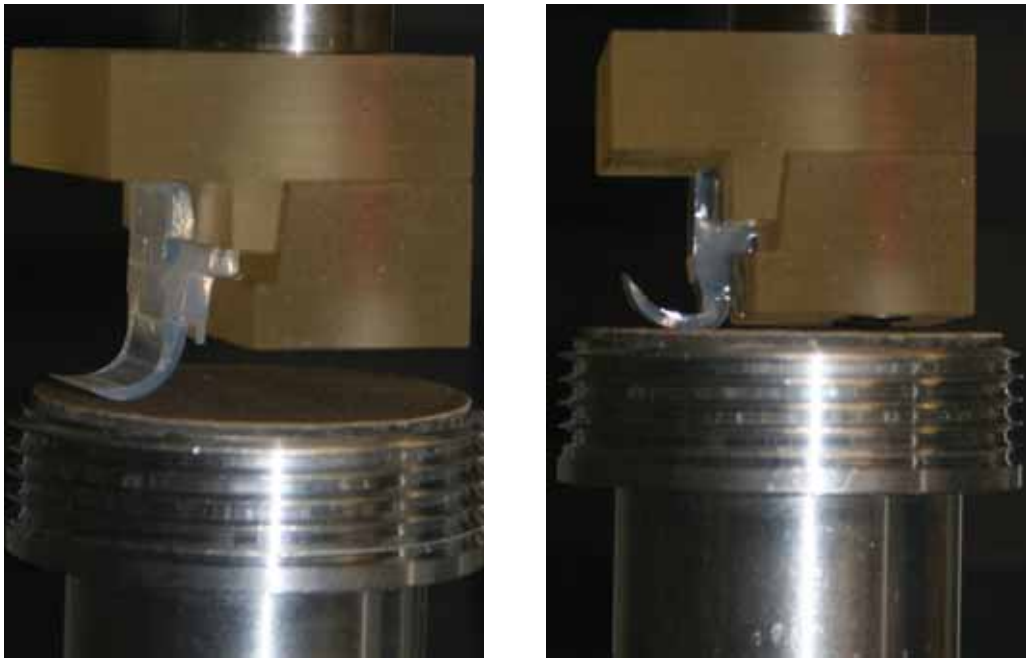

(a) (b)

Figure D.1: a) Reference state of undercushion sample b) Deformed state of undercushion sample

D.4.3 Test Procedure

A compression test method was used. The test speed was set to be constant at 5mm/min. The compression was limited to -4mm from the gauge point. The sample was preconditioned with 5 load/unloading cycles, before the test load application. At completion the head was returned to the gauge point. The head was moved up to allow room to manipulate the sample. The jig was removed from the rod and the next sample installed. The head was returned to the gauge point and the test was repeated for each sample.

D.5 Results

Preconditioned results from the final cycle were taken for each of the samples ($n = 10$). A threshold force magnitude of 0.01N was used on the falling edge of the signal to define the initiation of contact. The origin of the extracted data was offset to this location. The raw results normalised by the length of the sample are presented in Figure D.2.

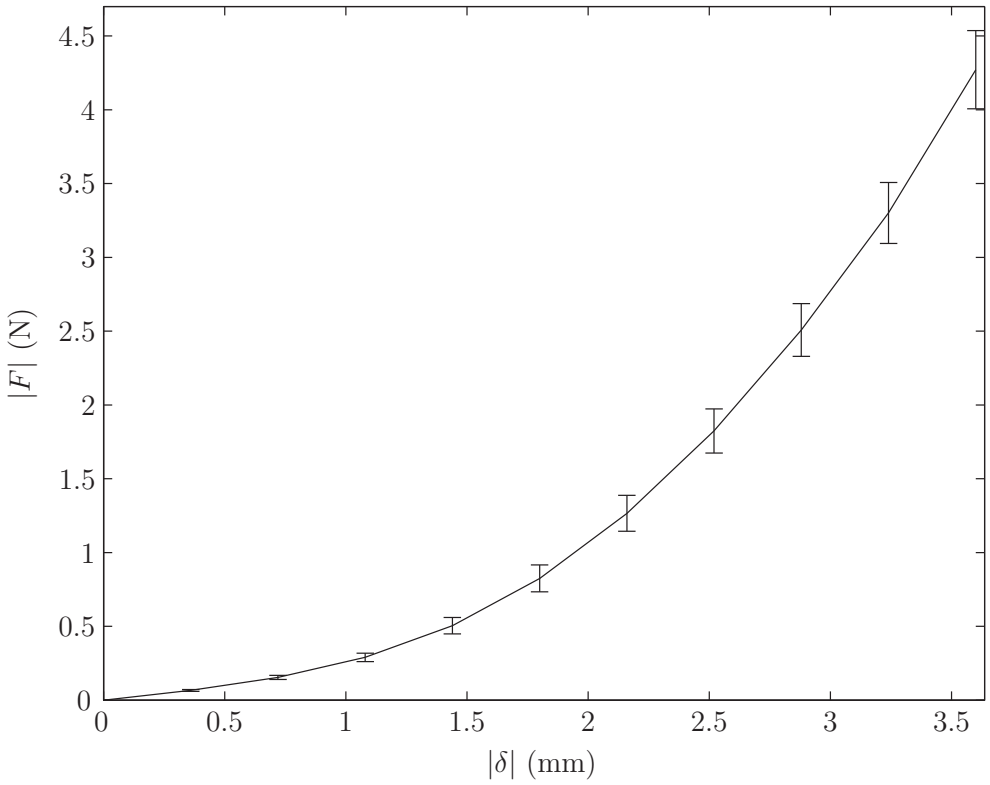

Figure D.2: UMII undercushion bending stabilised force vs compressive displacement (mean $\pm\sigma$)

D.5.1 Undercushion Bending FEA

FEA models were prepared ANSYS and LS-DYNA to validate the material model used to simulate the mask in a loading scenario which is similar to the patient use situation. In ANSYS, both a 3D and 2D generalised plane strain model were developed for comparison.

Mesh

The CAD geometry of the UMII mask used to generate a mapped mesh of the undercushion and body. The length of the model was 10mm to correspond with the performed test. First order hexahedral elements (SOLID185) were predominantly used for the mesh. The mesh was refined to determine the maximum acceptable element size to capture the force/displacement characteristic of the cushion. The mesh used is shown in Figure D.3. Since incompressible hyperelastic materials were used, the mixed U/P element formulation was used to avoid volumetric locking.

The 2D model was prepared by sectioning the 3D geometry and meshing using PLANE182 elements. Using generalised plane strain a nominal length of 10mm was used for the simulation to correspond to the experiment.

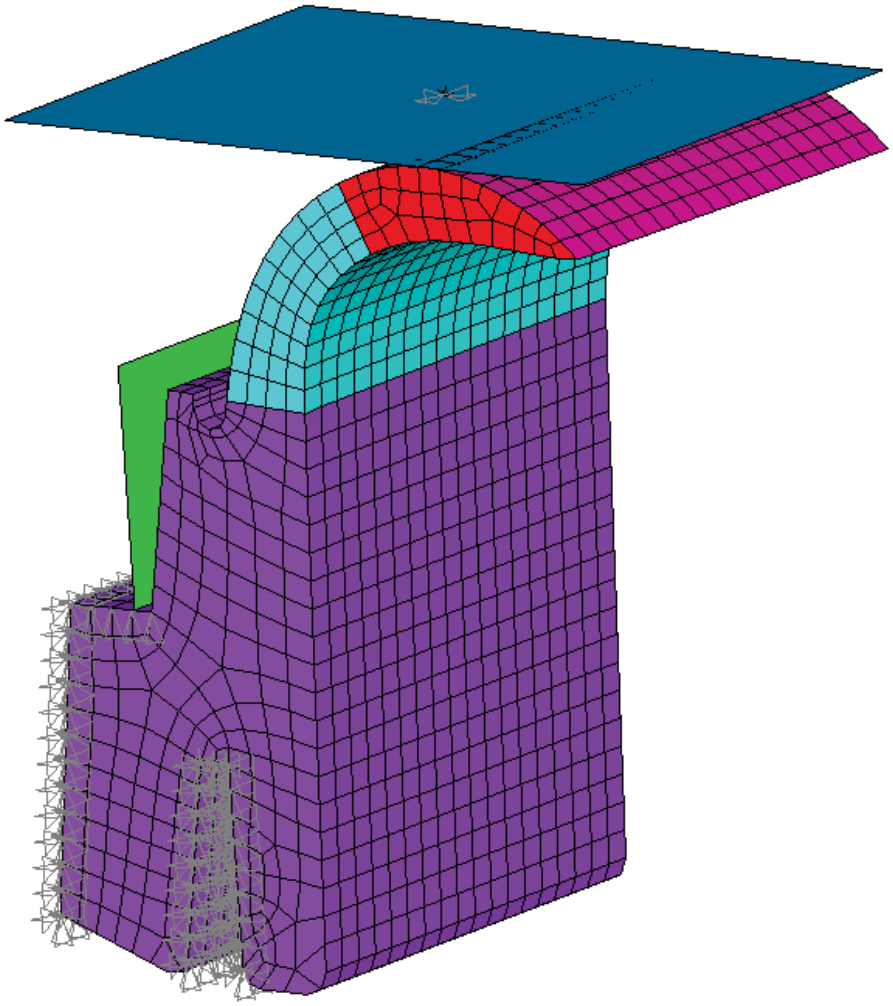

Figure D.3: Mesh for bending simulation

Material Properties

Prior to this work, an 5 parameter Mooney Rivlin material model was developed for the LSR. Unfortunately this was derived from a stabilised strain state far in excess of the operating strain in the mask, so is of suspect utility in the deformation range that is anticipated in this study. However in order to evaluate the suitability of the model and to estimate the strain range that is likely to be experienced in the load scenario, this model was used.

The LSR was modelled using a five parameter Mooney Rivlin incompressible hyperelastic model. The strain energy function is given by

$$\begin{aligned}\Psi = {} & C_{10}\left(I_1 - 3\right) + C_{01}\left(I_2 - 3\right) \\ & + C_{20}\left(I_1 - 3\right)^2 + C_{11}\left(I_1 - 3\right)\left(I_2 - 3\right) + C_{02}\left(I_2 - 3\right)^2\end{aligned} \tag{D.1}$$

Table D.2: LSR Mooney Rivlin hyperelastic parameters

Parameter	Value (MPa)
C_{10}	5.71E-02
C_{01}	0.11451
C_{20}	2.20E-02
C_{11}	-3.00E-02
C_{02}	4.96E-03

Table D.3: ANSYS contact settings

	Platen	Jig
Algorithm	Aug. Lagrange	
Friction	Rough	Frictionless
Stiffness Update	Each iteration	
Normal Stiffness Factor (FKN)	1	
Initial Adjustment	Close gap/Reduce pen	None
Initial Status	Closed	Open

The material parameters for the LSR are shown in Table D.2.

Contact

Two contact regions were defined in the simulation. These model the rough compression platen surface and the constraint of the jig. These can be seen in Figure D.3. The Augmented Lagrange method was used to enforce the contact constraint. The contact settings used are summarised in Table D.3

Loads and Boundary Conditions

Jig Supports The surfaces of the cushion that are held by the jig were assumed to be fully fixed

	X	Y	Z
Disp	0	0	0
Rot	-	-	-

Compression Platen An enforced displacement ($y = -5$mm) was applied to the pilot node of the platen contact surface. The test was performed to a 3.6mm enforced displacement.

Table D.4: Analysis settings

Setting	Value
Type	Static
Non-linear geometry	On
Newton Raphson Method	Full
Solver	Sparse
Auto Timestep	On
Substeps	50,200,25
F convergence	0.005
U convergence	0.05

	X	Y	Z
Disp	0	-3.6	0
Rot	0	0	0

Jig Surface The jig side contact surface was fully constrained.

	X	Y	Z
Disp	0	0	0
Rot	0	0	0

Analysis

The analysis was run using the sparse solver and utilised the full Newton Raphson method and large deformation theory. Convergence testing was performed using the $L2$ norm of the residual loads and displacement increment. The solution settings are shown in Table D.4. The simulation reached completion.

D.5.2 Results

The deformation pattern of the undercushion model can be seen to match the behaviour in the physical test in Figure D.4.

The vertical reaction force vs displacement results for the ANSYS model is shown in Figure D.5. At deformations above 2mm the LSR model matches the experimental results excellently, however this is not the case in the initial part of the load curve. At lower deformations, the FEA model is too stiff and significantly overestimates the force applied by a factor of up to 2.

In order to estimate the state of strain in the mask undercushion during use, a FEA model of the mask engaged with a rigid face was solved using LS-DYNA. The maximum Von Mises strain was $\epsilon = 0.25$. This is shown in Figure D.6.

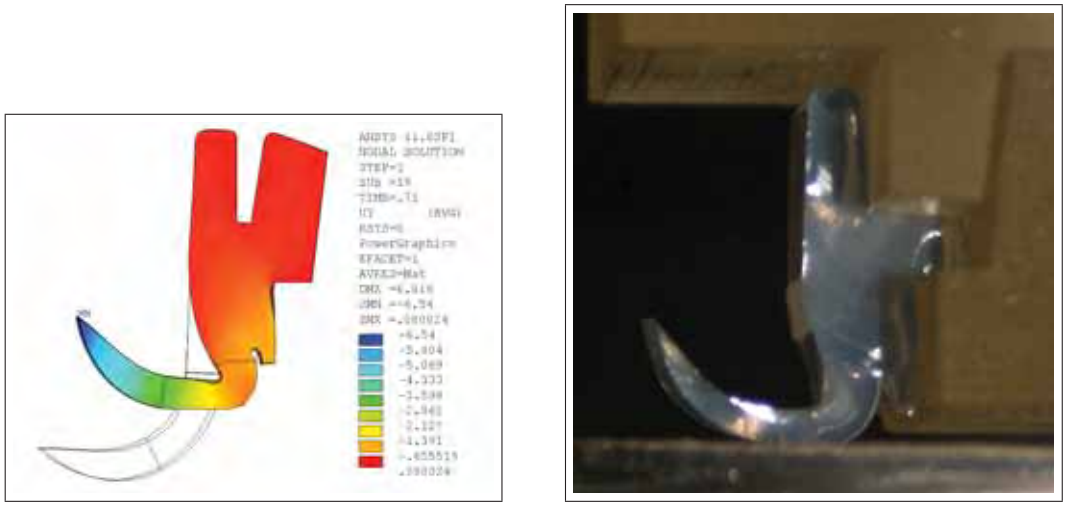

(a) **(b)**

Figure D.4: Deformed configuration of the UMII undercushion from a) simulation and b) experiment

Therefore the 2D model was interrogated to determine that $\epsilon_{\mathrm{VM}}(1.66) = 0.25$. This is shown in Figure D.7. Therefore in order to more closely match hyperelastic model to the recorded behaviour of the LSR undercushion, the bending deformation of the undercushion will be taken into account up to 1.8mm.

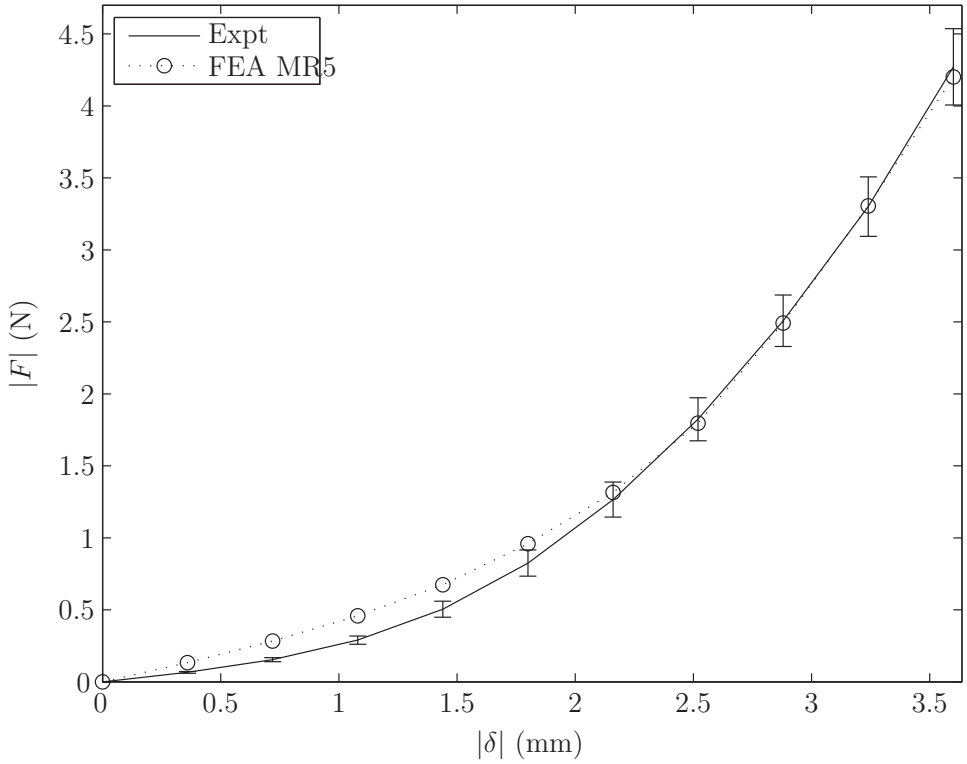

Figure D.5: Force vs displacement curves for experimental results and FEA model

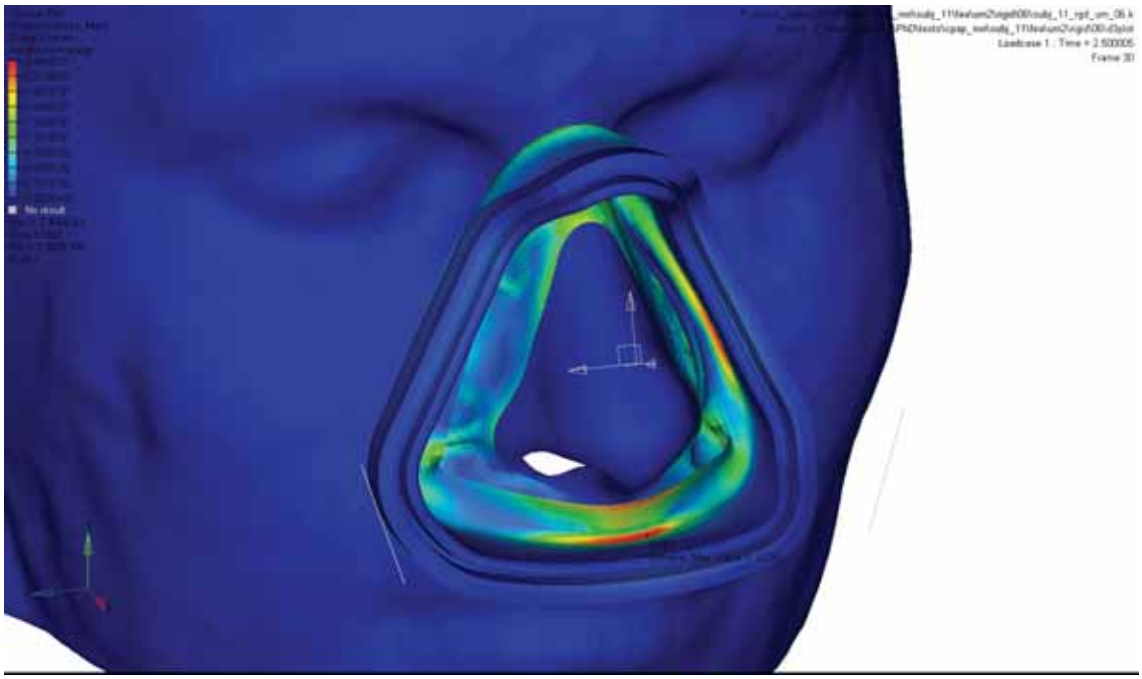

Figure D.6: Von Mises strain in a sample mask use model

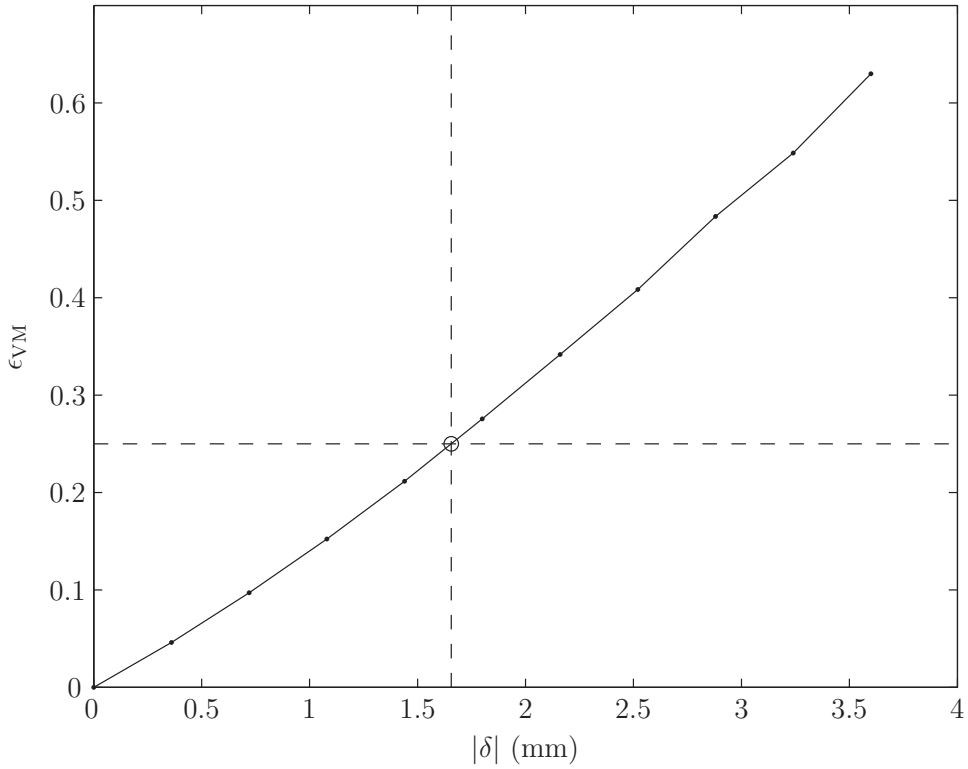

Figure D.7: FEA results for Strain vs displacement of the 2D model. $\epsilon = 0.25$ is indicated on the plot

Appendix E

Liquid Silicone Rubber Hyperelastic Model Fitting

E.1 Introduction

Mechanical testing has been performed on LSR samples in uniaxial tension, planar tension (pure shear), compression (Appendix C) and cantilevered bending (Appendix D). The cantilevered bending test was conducted using samples cut from new masks from the production line. The other tests were performed with samples manufactured from simple geometric test pieces.

Mechanical testing has been performed on samples of LSR to develop a hyperelastic material model. This is done on simple geometric shapes in uniform strain fields. Since hyperelastic models are generally phenomenological rather than physical, it is good practice to perform material curve fitting on at least two independent deformation states (Ogden *et al.*, 2004; ANSYS Inc, 2005).

The results of the cantilevered bending test in C as shown in Figure D.2 indicate that the existing model is too stiff in the strain range of interest. Therefore a new curve fit is required for the mechanical model of the LSR bending.

To analytically characterise the tested material under compression, a uniform strain field needs to be established. Friction at the platen/sample interface introduces shear stresses at the surface and prevents a uniform deformation. This is evident from the bulging or barrelling of compressive samples. This will have the effect of increasing the strain energy for a given compressive deformation, possibly overestimating the stiffness of the material.

FEA provides an opportunity to numerically mimic an experiment and allows for the frictional boundary conditions to be replicated and accounted for to improve the material model Wu *et al.* (2004); Morriss *et al.* (2008). In order to do this it is important that the frictional boundary condition be replicated in the FEA model. This is most easily done if a non slip boundary condition is enforced. This corresponds to the rough platens that were used in Appendix C and D.

Since a uniform stress and strain field are not established in the semi-confined compression test nor the bending test, it is best to fit to the experimental data of force (N) and displacement (mm) instead of directly using stress (MPa) and strain (mm/mm). Therefore the optimisation will consider pooled data of different dimensional quantities.

E.2 Optimisation

The *lsqcurvefit* function in the Matlab Optimization Toolbox was used to coordinate a non linear least squares optimisation. In order to not distort the optimisation by the order of magnitude differences between the stress/strain and force/displacement data, normalised residuals were used. For each mode (i), a normalised residual vector ($\boldsymbol{r}$) was calculated with vector elements given as follows:

$$\boldsymbol{r}\left(x\right)_i = \frac{y\left(x\right)_{\mathrm{M}} - y\left(x\right)_{\mathrm{E}}}{y\left(x\right)_{\mathrm{E}}} \tag{E.1}$$

The pooled 2-norm of the residual vectors over N test modes was used as the objective function to minimise as follows;

$$e = \sum_{i=1}^{N} \boldsymbol{r_i}^T \boldsymbol{r_i} = \left\|\boldsymbol{r}_i\right\|_2 \tag{E.2}$$

Weighting to the different curves or even regions of curves can be applied to this on an element by element basis through the incorporation of a diagonal weighting matrix $\boldsymbol{W}$ as follows;

$$e = \sum_{i=1}^{N} \boldsymbol{r_i}^T \boldsymbol{W}_i \boldsymbol{r_i} \tag{E.3}$$

$$\boldsymbol{W}_i = \boldsymbol{w}_i \boldsymbol{I} \tag{E.4}$$

Therefore in order to fit material properties to the LSR in the loading range of interest the following minimisation was performed.

$$e = \min_{\text{Coeffs}} \left(\sum_{i=1}^{N} \boldsymbol{r_i}^T \boldsymbol{W}_i \boldsymbol{r_i} \right) \tag{E.5}$$

Four modes of testing were pooled in the residual calculation. This is outlined in Table E.1.

Table E.1: Pooled optimisation description

N	Test Mode	Type	Ordinate Unit
1	Tension	Analytical	MPa
2	Planar tension	Analytical	MPa
3	Semi confined compression	Numerical FEA	N
4	UM2 Bending	Numerical FEA	N

E.3 Results

A range of different hyperelastic strain energy functions were used in the optimisation. The results of these are presented in Table E.2.

Table E.2: Pooled optimisation results

Model Type	**Material Coefficients**	**Residual Norm**
MR2	$C_{10} = 0.178$ $C_{01} = -0.032$	4.77
MR3	$C_{10} = 0.4489$ $C_{01} = -0.3198$ $C_{11} = 0.2781$	2.59
ArrudaBoyce	$\mu = 0.1793$ $\lambda_L = 1.4489$	2.43

The Mooney Rivlin 3 parameter model provided the best fit to the pooled data without any additional weighting. The results of this are shown in Figure E.1.

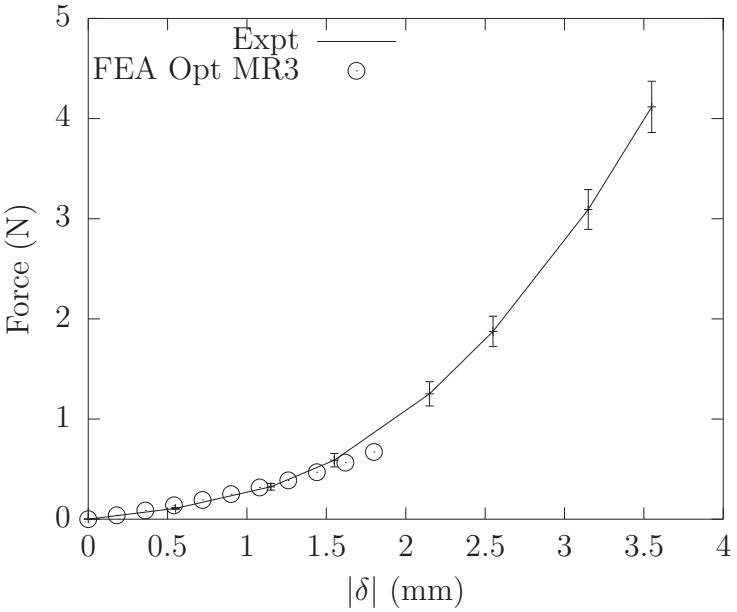

Figure E.1: Fitted LSR 3 parameter hyperelastic model FEA results compared to experimental results

Appendix F

Ultra Mirage II Spatial Transformation Matrices

F.1 Cushion Coordinate System

The coordinate system of the cushion is defined again in the same orientation as the ISB recommendations (Wu and Cavanagh, 1995). This is shown in figure 10.3. The transformation matrix from the cushion coordinate system to the UM2 reference system is as follows [1] [2]:

$$\mathbf{A_{csh}} = \begin{bmatrix} 0.998401 & 0.056531 & 0 & -37.481245 \\ -0.056531 & 0.998401 & 0 & 3.748344 \\ 0 & 0 & 1 & -0.000003 \\ 0 & 0 & 0 & 1 \end{bmatrix} \tag{F.1}$$

T-Bar Coordinate System

The coordinate system of the T-Bar is located on the axis of the neck pivot. This can take a number of orientations depending on the detent position of the T-Bar. The T-Bar reference coordinate system is chosen to be oriented approximately in line with UM2 system when T-Bar is at the straightest setting as shown in figure F.1.

[1] In Pro/ENGINEER the transformation matrix is given as in the form:

$$\boldsymbol{x\prime} = \mathbf{A}\boldsymbol{x}^T$$

[2] Note that the 4^{th} row $\begin{bmatrix} 0 & 0 & 0 & 1 \end{bmatrix}$ needs to be added to compute the affine transform. This matrix is output from the Analysis/Measure/Transform. The coordinate systems are chosen as follows:

1^{st} **Coordinate System** Coordinate System that vectors are transformed into

2^{nd} **Coordinate System** Coordinate System that vectors are transformed from

Figure F.1: UM2 T-Bar and coordinate system

The transformation matrix from the T-Bar coordinate system to the UM2 coordinate system in the straight position is given by:

$$\mathbf{A_{TBar}} = \begin{bmatrix} 0.999730 & -0.023227 & 0 & -26.000210 \\ 0.023227 & 0.999730 & 0 & 48.661617 \\ 0 & 0 & 1 & 0 \\ 0 & 0 & 0 & 1 \end{bmatrix}$$

Now the T-Bar can adopt 4 different angular positions, each pitched at 13.33° as shown in table F.1. These pure rotations can be simply used to calculate the composed transformation matrix. The T-Bar rotates about the Z axis of its coordinate system. Therefore the rotation matrix for this transformation can be calculated as follows.

$$\mathbf{R_{TBar}} = \begin{bmatrix} cos(\theta) & -sin(\theta) & 0 & 0 \\ sin(\theta) & cos(\theta) & 0 & 0 \\ 0 & 0 & 1 & 0 \\ 0 & 0 & 0 & 1 \end{bmatrix} \tag{F.2}$$

Table F.1: T-Bar Angular Locations

Position	Rotation	Comments
0	0°	Straight
1	13.33°	
2	26.67°	
3	40.00°	Angled

Therefore the full transformation matrix is calculated by the composition of the original transformation and the T-Bar rotational position.

$$\mathbf{T_{TBar}} = \mathbf{A_{TBar}}\mathbf{R_{TBar}} \tag{F.3}$$

$$\boldsymbol{x\prime} = \mathbf{T_{TBar}}\boldsymbol{x} \tag{F.4}$$

Forehead Support Coordinate System

The FHS coordinate system used for this analysis is located on the midplane in both the sagittal and transverse directions as shown in figure F.2. It is mounted on the T-Bar, and as such the transformation matrix can be composed from subsequent transformation operations.

The transformation matrix from the FHS coordinate system to the T-Bar coordinate system is as follows.

$$\mathbf{A_{F\rightarrow T}} = \begin{bmatrix} 1 & 0 & 0 & -5.29 \\ 0 & 1 & 0 & 37.00509 \\ 0 & 0 & 1 & 0 \\ 0 & 0 & 0 & 1 \end{bmatrix}$$

This can be composed with the T-Bar transformation to give:

$$\mathbf{T_{FHS}} = \mathbf{T_{TBar}}\mathbf{A_{F\rightarrow T}} \tag{F.5}$$

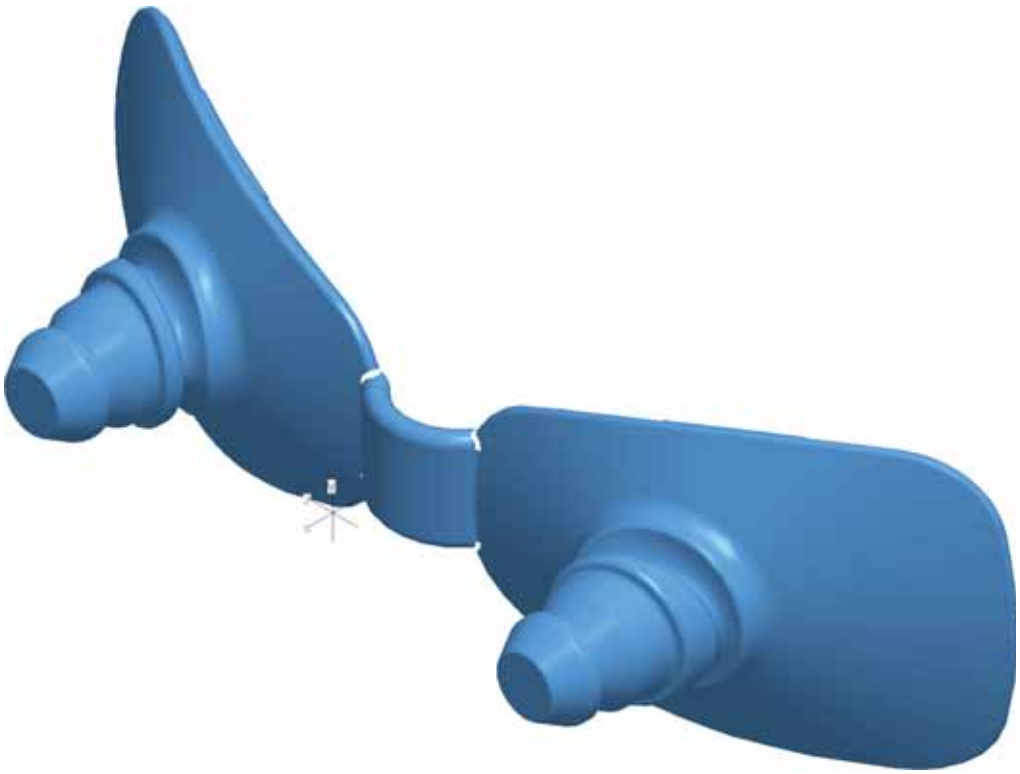

Figure F.2: UM2 Forehead Support and coordinate system

Appendix G

Ultra Mirage II Pressure Force Calculation

G.1 Introduction

The applied CPAP pressure acts on the internal surfaces of the mask and tubing. The CPAP pressure was applied to the internal surfaces of the cushion including the membrane, however as the frame of the mask, which contains a significant portion of surface area for the pressure to act on, was modelled as a rigid body idealisation, the pressure load was not applied to the mask body. Therefore the equivalent force couple of the pressure acting on the projected area of the mask must be applied to the independent node of the mask frame's nodal rigid body.

The frame essentially encloses the volume anterior to the cushion of the mask. The resultant load acting on the frame is a follower force with respect to the movement of the frame. Therefore the applied load was calculated at and with respect to the UM2 coordinate system, and applied to the mask as a force / couple system at the mask rigid body's centre of mass.

The geometry of the masks is complex, consisting of 3D lofted and blended surfaces, making analytical determination of the centre of pressure difficult. Therefore CAD geometry and FEA was used to estimate the equivalent force couple system from.

G.2 Finite Element Analysis Model

A curve demarking the limits of the modelled cushion was extracted from the 3D CAD model. A NURBS surface was generated, bounded by this curve. This is shown in Figure G.1. The surface was imported into the ANSYS v12.1 FEA analysis package. The global coordinate system of the model coincided with the UMII coordinate system. The FEA model was prepared using the Nmms consistent unit system.

G.2.1 Mesh

A fine mesh of thin quadrilateral shell elements (Shell181) was generated on the surface. This is shown in Figure G.1a.

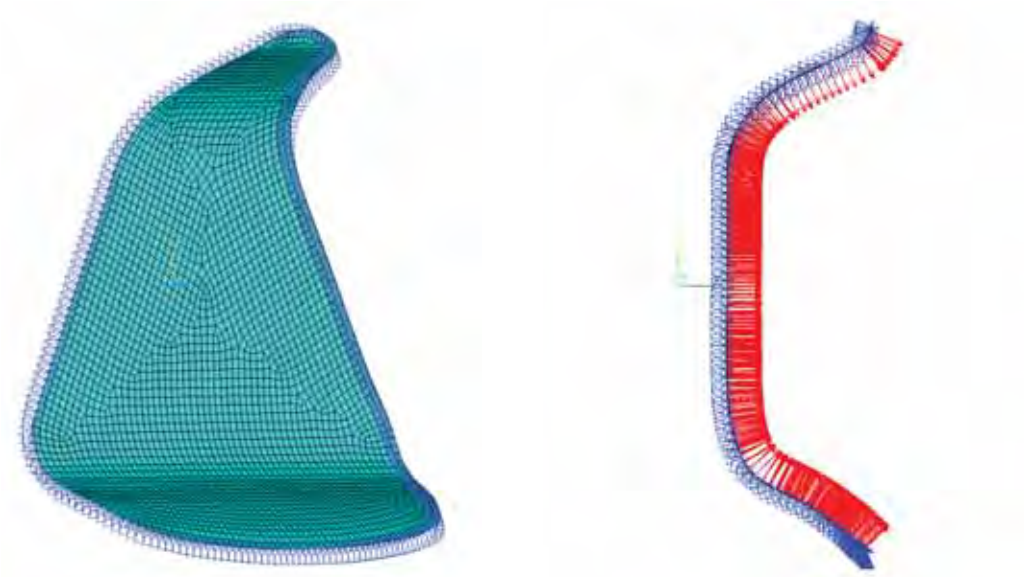

(a) Shell mesh of bounding surface for rigid body of the UMII mask. Edges are fully constrained

(b) side on view showing pressure load applied to shell faces

Figure G.1: UMII frame surface for equivalent pressure load evaluation

G.2.2 Material Properties

Since the purpose of this model is to only estimate reaction loads, an arbitrarily assigned material property is acceptable provided that the small strain and small deformation approximations are valid. Therefore steel mechanical properties (manufacturer's default material allocation) were arbitrarily assigned to the shell model.

G.2.3 Loads and Boundary Conditions

Fully Fixed

All nodes on the bounding edges of the surface were fully fixed as specified in Table G.1.

CPAP Pressure

The faces of the shell elements were all applied with the CPAP pressure of 10cm H_2O. The hydrostatic pressure of a column of water is simply given by

Table G.1: Fully fixed boundary edges

	X	Y	Z
Disp	0	0	0
Rot	0	0	0

Table G.2: UMII Frame pressure force resultant applied at the cushion origin for a pressure of P=10 cm H_2O

	X	Y	Z	Magnitude
$\boldsymbol{f}_{\text{csh}}$ (N)	2.258	0.491	0.0	2.311
$\boldsymbol{m}_{\text{csh}}$ (Nmm)	0.0	0.0	19.42	19.42

$$P = \rho g h \tag{G.1}$$

Therefore the pressure corresponding to a $h = 1$ cm H_2O with $\rho = 1000\frac{\text{kg}}{\text{m}^3}$ and $g = 9.81\frac{\text{m}}{\text{s}^2}$ is

$$P_{1\text{cm}} = 1000\frac{\text{kg}}{\text{m}^3} \times 9.81\frac{\text{m}}{\text{s}^2} \times 1\text{cm} \quad \frac{1}{100}\frac{\text{m}}{\text{cm}} \tag{G.2}$$

$$= 98.0665\text{Pa} \tag{G.3}$$

Since the model is prepared in the mmNs unit system, this must be converted to MPa. Therefore,

$$P_{1\text{cm}} = 9.80665\left(10^{-5}\right)\text{MPa} \tag{G.4}$$

Finally this unit value is scaled to give the pressure load applied to the surface:

$$P_{10\text{cm}} = 9.80665\left(10^{-4}\right)\text{MPa} \tag{G.5}$$

G.2.4 Analysis Settings

This simulation was run as a linear static analysis.

G.2.5 Results

The summed reaction results from the pressure application (10 cm H_2O) are summarised in Table G.2. Moments were taken about the cushion origin.

For inclusion into the mask model, the force is referred to the mask coordinate system.

The force is referred to the UMII coordinate system by the rotational components of an affine transformation matrix between the cushion and UMII coordinate systems.

$$\boldsymbol{f}_{\mathrm{UM2}} = \boldsymbol{A}_{\mathrm{rot}} \boldsymbol{f}_{\mathrm{csh}} \tag{G.6}$$

$$= \begin{bmatrix} 2.2821 & 0.3626 & 0 \end{bmatrix} \tag{G.7}$$

Since the Z axes of the UMII and cushion coordinate systems are parallel, the transformation of the moment is trivial, and is added to the moment due to the offset. The position vector is determined by transforming the local coordinates of the cushion coordinate system's origin $(0, 0, 0)$ to be expressed with respect to the UMII coordinate system.

$$\boldsymbol{r} = \boldsymbol{A}\boldsymbol{r}_{\mathrm{csh}} \tag{G.8}$$

$$= \boldsymbol{A} \begin{bmatrix} 0 & 0 & 0 \end{bmatrix} \tag{G.9}$$

$$\tag{G.10}$$

Therefore, with both the moment arm and the force vectors expressed in the UMII coordinate system, the moment can be calculated as follows:

Therefore the moment referred to the UMII coordinate system is

$$\boldsymbol{m}_{\mathrm{UM2}} = \boldsymbol{m}_{\mathrm{csh}} + (\boldsymbol{r} \times \boldsymbol{f}_{\mathrm{UM2}}) \tag{G.11}$$

$$= 19.42 + -22.14 \tag{G.12}$$

$$= -2.728\mathrm{Nmm} \tag{G.13}$$

G.3 Load Application to Rigid Body

Since this load is due to applied pressures, it must be applied to the mask model in concert with the pressure loading on the interior surfaces of the mask. The load is applied at the rigid frame independent or pilot node. Since this is a rigid body, the relative location of the application and point of action is a constant offset from the UMII coordinate system. Therefore an equivalence force couple was determined as follows.

In LS-DYNA, a follower force is defined by the movement of three nodes during the solution. The cross product of the vectors from the application point to the other

two nodes defines a normal vector which is the line of action for the follower force. Null shell elements were included in the nodal rigid body to define the normals. These null shell elements were aligned with the basis planes of the inertial principal coordinate system. Therefore the forces and moments need to be transformed into the inertial system for entry, and then assigned to the principal planes of the system.

Similar to the above calculations, the loads are transformed to the CG coordinate system.

$$\boldsymbol{f}_{\mathrm{CG}} = \boldsymbol{A}_{\mathrm{CGrot}} \boldsymbol{f}_{\mathrm{UM2}} \tag{G.14}$$

$$= \begin{bmatrix} 0.1188 & -2.3074 & -0.0346 \end{bmatrix} \mathrm{N} \tag{G.15}$$

The applied moment at the centre of mass pilot node with respect to the inertial coordinate system was determined as follows. The moment vector resolved at the UMII origin first was transformed to be expressed with respect to the inertial coordinate system.

$$\boldsymbol{m}_{\mathrm{CG-UM2}} = \boldsymbol{A}_{\mathrm{CGrot}} \boldsymbol{m}_{\mathrm{UM2}} \tag{G.16}$$

$$= \begin{bmatrix} 0.0012 & 0.0409 & -2.7234 \end{bmatrix} \mathrm{Nmm} \tag{G.17}$$

Finally the couple was added to the transformed moment vector as follows, with the moment arm being the vector from the CG origin to the UMII origin with respect to the CG coordinate system. This is simply calculated as the transformation of the UMII origin position vector into the CG system.

$$\boldsymbol{r}_{CG} = \begin{bmatrix} 0.0 & 0.0 & 0.0 & 1 \end{bmatrix} \boldsymbol{A}_{\mathrm{CG}} \tag{G.18}$$

Therefore the transformed and referred moment vector is given by,

$$\boldsymbol{m}_{\mathrm{CG}} = \boldsymbol{m}_{\mathrm{CG-UM2}} + (\boldsymbol{r}_{CG} \times \boldsymbol{f}_{\mathrm{CG}}) \tag{G.19}$$

$$= \boldsymbol{m}_{\mathrm{CG-UM2}} + \begin{bmatrix} -0.1134 & 1.9811 & -132.4898 \end{bmatrix} \tag{G.20}$$

$$\boldsymbol{m}_{\mathrm{CG}} = \begin{bmatrix} -0.1145 & 1.9402 & -129.7664 \end{bmatrix} \mathrm{Nmm} \tag{G.21}$$

Table G.3: UMII Frame pressure force resultant applied at the mask frame centre of mass for a pressure of P=10 cm H_2O

	X	Y	Z	Magnitude
$\boldsymbol{f}_{\text{cg}}$ (N)	0.1188	-2.3074	-0.0346	2.311
$\boldsymbol{m}_{\text{cg}}$ (Nmm)	-0.1145	1.9402	-129.7664	129.78

Therefore the summary of the loads applied to the CPAP FEA model from the pressure acting on the non modelled components of the mask are outlined in Table G.3. These results are for 10 cm H_2O, scale as necessary for different pressures.

Appendix H

Activa LT Pressure Force Calculation

H.1 Introduction

This section follows the same procedure as Appendix . Refer there for a full description.

H.2 Finite Element Analysis Model

A curve demarking the limits of the modelled cushion was extracted from the 3D CAD model. A NURBS surface was generated, bounded by this curve. This is shown in Figure H.1. The surface was imported into the ANSYS v12.1 FEA analysis package. The global coordinate system of the model coincided with the Activa LT Mask coordinate system. The FEA model was prepared using the SI consistent unit system.

H.2.1 Mesh

A fine mesh of thin quadrilateral shell elements (Shell181) was generated on the surface. This is shown in Figure H.1a.

H.2.2 Material Properties

Since the purpose of this model is to only estimate reaction loads, an arbitrarily assigned material property is acceptable provided that the small strain and small deformation approximations are valid. Therefore steel mechanical properties (software's default material allocation) were arbitrarily assigned to the shell model.

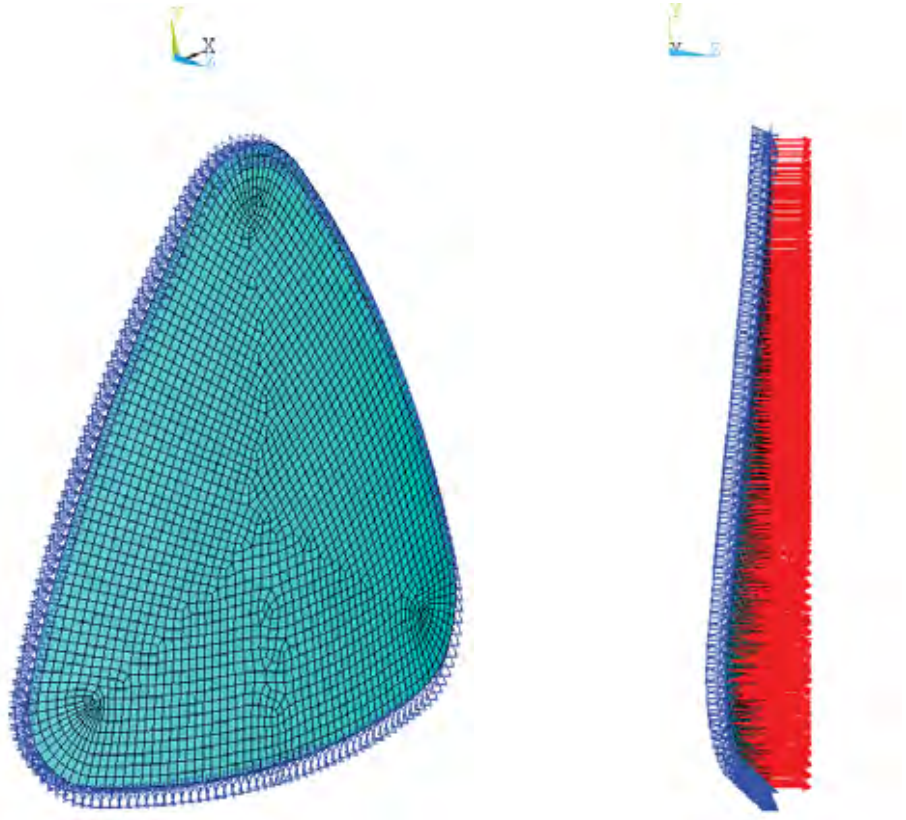

(a) Shell mesh of bounding surface for rigid body of the Activa LT mask. Edges are fully constrained

(b) side on view showing pressure load applied to shell faces

Figure H.1: Activa LT frame surface for equivalent pressure load evaluation

Table H.1: Fully fixed boundary edges

	X	Y	Z
Disp	0	0	0
Rot	0	0	0

H.2.3 Loads and Boundary Conditions

Fully Fixed

All nodes on the bounding edges of the surface were fully fixed as specified in Table H.1.

CPAP Pressure

The faces of the shell elements were all applied with the CPAP pressure of 10cm H_2O. The hydrostatic pressure of a column of water is simply given by

Table H.2: Activa LT frame pressure force resultant applied at the cushion origin for a pressure of P=10 cm H_2O

	X	Y	Z	Magnitude
$\boldsymbol{f}_{\text{csh}}$ (N)	0.0	0.0	2.0651	2.0651
$\boldsymbol{m}_{\text{csh}}$ (Nmm)	-81.03	0.0	0.0	81.03

$$P = \rho g h \tag{H.1}$$

Therefore the pressure corresponding to a $h = 1$ cm H_2O with $\rho = 1000\frac{\text{kg}}{\text{m}^3}$ and $g = 9.81\frac{\text{m}}{\text{s}^2}$ is

$$P_{1\text{cm}} = 1000\frac{\text{kg}}{\text{m}^3} \times 9.81\frac{\text{m}}{\text{s}^2} \times 1\text{cm} \quad \frac{1}{100}\frac{\text{m}}{\text{cm}} \tag{H.2}$$

$$= 98.0665\text{Pa} \tag{H.3}$$

Since this model is prepared in SI units, the units of Pa are appropriate for this model.

Finally this unit value is scaled to give the pressure load applied to the surface:

$$P_{10\text{cm}} = 980.665\text{Pa} \tag{H.4}$$

H.2.4 Analysis Settings

This simulation was run as a linear static analysis.

H.2.5 Results

The summed reaction results from the pressure application (10 cm H_2O) are summarised in Table H.2. Moments were taken about the cushion origin, which is coincident with the mask origin.

For inclusion into the mask model, the force is referred to the mask inertial system which is positioned at the frame centre of mass with axes oriented to align with the principal inertia axes.

The force is referred to the Activa LT inertial coordinate system by the rotational components of an affine transformation matrix between the cushion and Activa LT coordinate systems. The affine transformation matrix is reported in (J.4)

$$\boldsymbol{f}_{\mathrm{UM2}} = \boldsymbol{A}_{\mathrm{rot}}\boldsymbol{f}_{\mathrm{csh}} \tag{H.5}$$

$$= \begin{bmatrix} -0.55018 & 0.005508 & 1.9905 \end{bmatrix} \tag{H.6}$$

The transformation of the moment requires the consideration of the moment arm offset from one coordinate system to another. The position vector is determined by transforming the local coordinates of the mask's system's origin $(0, 0, 0)$ to be expressed with respect to the inertial coordinate system.

$$\boldsymbol{r} = \boldsymbol{A}\boldsymbol{r}_{\mathrm{csh}} \tag{H.7}$$

$$= \boldsymbol{A}\begin{bmatrix} 0 & 0 & 0 \end{bmatrix} \tag{H.8}$$

$$\tag{H.9}$$

Therefore with both the moment arm and the force vectors expressed in the UMII coordinate system, the moment can be calculated as follows:

Therefore the moment referred to the UMII coordinate system is

$$\boldsymbol{m}_{\mathrm{UM2}} = \boldsymbol{m}_{\mathrm{csh}} + (\boldsymbol{r} \times \boldsymbol{f}_{\mathrm{UM2}}) \tag{H.10}$$

$$= 19.42 + -22.14 \tag{H.11}$$

$$= -2.728\mathrm{Nmm} \tag{H.12}$$

H.3 Load Application to Rigid Body

Since this load is due to applied pressures, it must be applied to the mask model in concert with the pressure loading on the interior surfaces of the mask. The load is applied at the rigid frame independent or pilot node. Since this is a rigid body, the relative location of the application and point of action is a constant offset from the UMII coordinate system. Therefore an equivalence force couple was determined as follows.

In LS-DYNA, a follower force is defined by the movement of three nodes during the solution. The cross product of the vectors from the application point to the other two nodes defines a normal vector which is the line of action for the follower force. Null shell elements were included in the nodal rigid body to define the normals. These null shell elements were aligned with the basis planes of the inertial principal

coordinate system. Therefore the forces and moments need to be transformed into the inertial system for entry, and then assigned to the principal planes of the system.

Similar to the above calculations, the loads are transformed to the CG coordinate system.

$$\boldsymbol{f}_{\mathrm{CG}} = \boldsymbol{A}_{\mathrm{CGrot}} \boldsymbol{f}_{\mathrm{UM2}} \tag{H.13}$$

$$= \begin{bmatrix} 0.1188 & -2.3074 & -0.0346 \end{bmatrix} \mathrm{N} \tag{H.14}$$

The applied moment at the centre of mass pilot node with respect to the inertial coordinate system was determined as follows. The moment vector resolved at the UMII origin first was transformed to be expressed with respect to the inertial coordinate system.

$$\boldsymbol{m}_{\mathrm{CG-UM2}} = \boldsymbol{A}_{\mathrm{CGrot}} \boldsymbol{m}_{\mathrm{UM2}} \tag{H.15}$$

$$= \begin{bmatrix} 0.0012 & 0.0409 & -2.7234 \end{bmatrix} \mathrm{Nmm} \tag{H.16}$$

Finally the couple was added to the transformed moment vector as follows, with the moment arm being the vector from the CG origin to the UMII origin with respect to the CG coordinate system. This is simply calculated as the transformation of the UMII origin position vector into the CG system.

$$\boldsymbol{r}_{CG} = \begin{bmatrix} 0.0 & 0.0 & 0.0 & 1 \end{bmatrix} \boldsymbol{A}_{\mathrm{CG}} \tag{H.17}$$

Therefore the transformed and referred moment vector is given by,

$$\boldsymbol{m}_{\mathrm{CG}} = \boldsymbol{m}_{\mathrm{CG-UM2}} + (\boldsymbol{r}_{CG} \times \boldsymbol{f}_{\mathrm{CG}}) \tag{H.18}$$

$$= \boldsymbol{m}_{\mathrm{CG-UM2}} + \begin{bmatrix} -0.1134 & 1.9811 & -132.4898 \end{bmatrix} \tag{H.19}$$

$$\boldsymbol{m}_{\mathrm{CG}} = \begin{bmatrix} -0.1145 & 1.9402 & -129.7664 \end{bmatrix} \mathrm{Nmm} \tag{H.20}$$

Therefore the summary of the loads applied to the CPAP FEA model from the pressure acting on the non modelled components of the mask are outlined in Table H.3. These results are for 10 cm H_2O, scale as necessary for different pressures.

Table H.3: UMII Frame pressure force resultant applied at the mask frame centre of mass for a pressure of P=10 cm H_2O

	X	*Y*	*Z*	Magnitude
$\boldsymbol{f}_{\text{csh}}$ (N)	0.1188	-2.3074	-0.0346	2.311
$\boldsymbol{m}_{\text{csh}}$ (Nmm)	-0.1145	1.9402	-129.7664	129.78

Appendix I

Numerical Integration Over a Faceted Surface

I.1 Introduction

The experimental and much of the FEA results are presented as fields varying over an arbitrary surface in 3D space. The manifold surfaces are composed of adjoining linear triangular facets. Varying results are calculated and stored at nodal locations. These nodal values were interpolated between the nodes using an isoparametric representation, that is the element's geometry and field quantities use the same interpolation (Cook *et al.*, 1989), which is a weighting based on nodal values.

At times it is desirable to determine the integral of an arbitrary scalar field ϕ over a surface,

$$\int_A \phi \mathrm{d}A \tag{I.1}$$

Using area coordinates, an arbitrary point P divides a triangle of area A into 3 sub areas, namely A_1, A_2 and A_3. Using the ratio of areas, the following are defined (Cook *et al.*, 1989)

$$\xi_i = \frac{A_i}{A} \tag{I.2}$$

As the areas must sum up to A, the following holds:

$$\xi_1 + \xi_1 + \xi_3 = 1 \tag{I.3}$$

For a linear triangle the shape functions are therefore

$$\boldsymbol{N} = \begin{bmatrix} \xi_1 & \xi_2 & \xi_3 \end{bmatrix} \tag{I.4}$$

Since isoparametric coordinates are used, the Jacobian matrix is required to transform from Cartesian to isoparametric coordinates. Since linear triangles are

Table I.1: Gaussian Quadrature Data for triangular regions (Cook *et al.*, 1989)

NumPts	Gauss Pt (ξ_1, ξ_2, ξ_3)	Weights (W_i)
3	$\left(\frac{2}{3}, \frac{1}{6}, \frac{1}{6}\right)$	$\frac{1}{3}$

used, the edges are straight and no midside nodes are specified, all the elements of the Jacobian matrix are identical. For a triangle, the determinant of the Jacobian matrix, $J = |\boldsymbol{J}|$ is constant with a value

$$J = 2A \tag{I.5}$$

Therefore, using Gaussian quadrature the integral over a triangular surface is approximated by:

$$\int_A \phi \mathrm{d}A \approx \frac{1}{2} \sum_{i=1}^{n} \phi_i J_i W_i \tag{I.6}$$

Since the determinant of the Jacobian matrix is constant within the triangle, and considering (I.5), this simplifies to (Cook *et al.*, 1989)

$$\int_A \phi \mathrm{d}A \approx \frac{J}{2} \sum_{i=1}^{n} \phi_i W_i \tag{I.7}$$

$$\approx A \sum_{i=1}^{n} \phi_i W_i \tag{I.8}$$

This was implemented in Matlab for use in this project. The code is as follows:

Contents

- Calculate interpolated Gauss Points
- Calculate Quadrature for Triangles and Surface

```
function [Integral, Area] = fn_gaussquad_tria(nodes, faces, field)

% FUNCTION fn_gaussquad_tria
% USAGE:
% [Integral, Area] = fn_gaussquad_tria(nodes, faces, field)
% This function calculates the surface integral of a scalar field over a
% triangular faceted surface using Gaussian Quadrature with 3 Gauss Points.
%
% INPUT
% nodes - [n,3] Matrix containing row position vectors for each node
```

```
% faces - [m,3] Connectivity containing a row vector for each element with
%               the index of each node.
% field - [n,1] Vector of scalar field that is to be integrated over the
%               surface. There should be 1 value for each node. Data should
%               be real numbers.
%
% OUTPUT
% Integral -    Scalar value of the quadrature over the surface.
% Area -        Scalar value of the overall surface area of the entire
%               surface.

% Faces is a connectivity matrix indexing into the node array.
n_elems = size(faces,1);     % number of elements to integrate over


% Gaussian Quadrature weighting factors for each of the gauss points for
% corner
GaussWeight = 1/3;

% Isoparametric area coordinates of the Gauss Pts which are then used in
% the quadrature.
GaussLoc = repmat([2/3 1/6 1/6], n_elems, 1);

% Position vectors of node
P0 = nodes(faces(:,1),:);
P1 = nodes(faces(:,2),:);
P2 = nodes(faces(:,3),:);

A_vec = P1-P0;
B_vec = P2-P0;

% Calculate Jacobian and Triangle Area
Area = zeros(n_elems)';
J = Area;

normVec = cross(A_vec, B_vec,2);
J = sqrt(sum(normVec.^2,2));

area = J/2;
```

Calculate interpolated Gauss Points

```
% Nodal Values of field
phi_node = zeros(n_elems,3);
for a=1:n_elems
    phi_node(a,:) = [field(faces(a,1)) field(faces(a,2)) field(faces(a,3))];
end

% Interpolate nodal values to Gauss pts
phi_gauss = [sum(phi_node.*GaussLoc,2)  ...
             sum(phi_node.*(circshift(GaussLoc,[0,1])),2) ...
             sum(phi_node.*(circshift(GaussLoc,[0,2])),2)];
```

Calculate Quadrature for Triangles and Surface

```
% Calculate the field integrated over each element
integral = (J/2).*sum(phi_gauss*GaussWeight,2);

% Sum over all elements
Integral = sum(integral);
Area = sum(area);

end
```

Appendix J

Activa LT Inertia

Since the mask frame is significantly stiffer than the compliant LSR interface materials of the mask, the mask assembly is considered as a rigid body for FEA. As a transient solution method was used and body loads are significant, it is important to correctly account for the mass distribution of the rigid body.
The Activa LT mask is able to be adjusted by the dial which advances or retracts the FHS. Since this mask is only used for a single instance of a comparative model, only the inertial properties for the configuration used will be calculated. Subject 25 used the Activa LT mask in the fully retracted position as shown in Figure J.1.

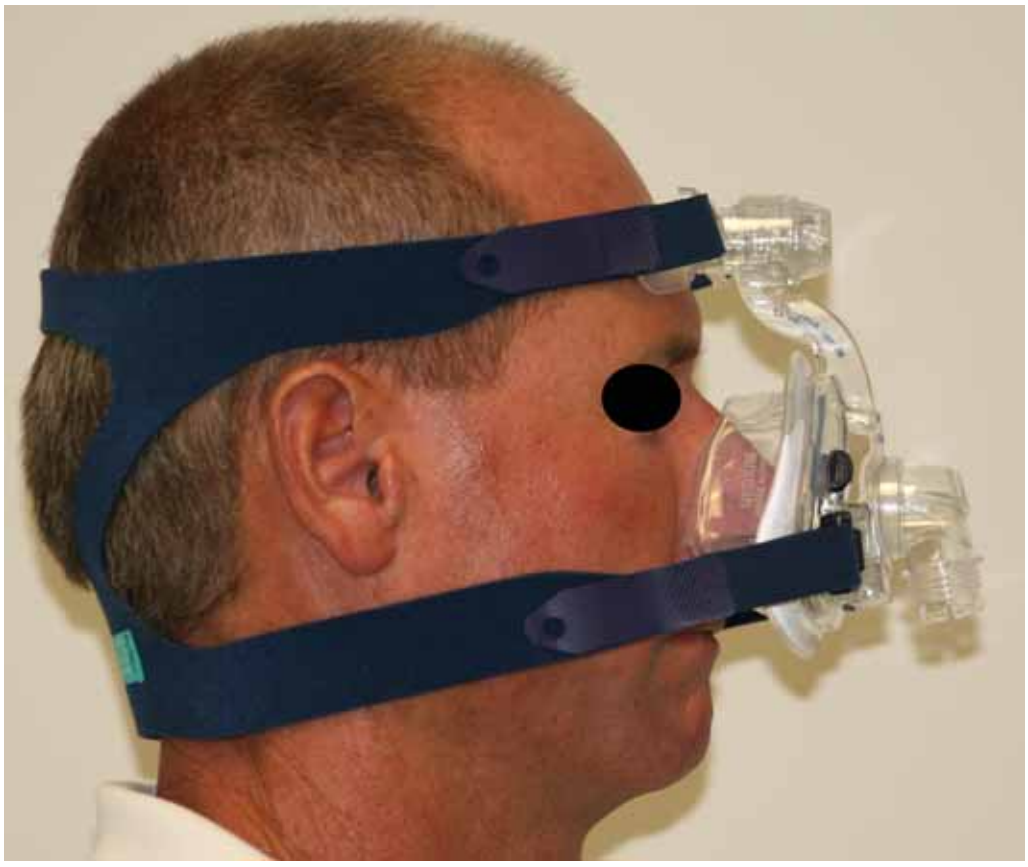

Figure J.1: Subject 25 wearing Activa LT mask with the FHS in the retracted position

J.1 Method

J.1.1 Mask Assembly

Each component of the assembly was weighed using an analytical balance and recorded. The solid 3D CAD (Pro/ENGINEER) models of each component were used to provide the inertial properties of the assembly in the various configurations.These were compared to the measured component. Inertial properties of the assembly from the CAD system were scaled so that the CAD mass matched the measured mass. In this case as the CAD and measured masses agreed to within 1%, the CAD properties were used for the inertial properties of the FEA model.
The CAD mass property results were calculated for each part with respect to their master coordinate system. The assembly results were calculated with respect to the Activa LT mask coordinate system which is oriented with the X axis to the left of the subject, Y upwards and Z anteriorly. CAD principal inertia results I_1, I_2, I_3 are ordered in increasing magnitude such that $I_1 \leq I_2 \leq I_3$. Consistent units (mm g s) were used for FEA analysis, and the inertial properties here are reported in this unit system, therefore mass is reported in grams and forces in μN. The centroidal system is oriented so that I_1, I_2 and I_3 are the principal moments of inertia about the centroidal X, Y and Z axes.
Inertial properties were entered in the FEA model using principal values about the centroidal coordinate system.

J.1.2 Tube Section

The tube portion of the inertia is identical to the UMII mask. Refer to Appendix B for details.

J.2 Results

J.2.1 Mask Assembly Mass

The mass of the mask components is reported in Table J.1
The position vector of the centre of mass $\bar{\boldsymbol{x}}$ for the fully retracted configuration of the frame (ex cushion and FHS)is as follows:

Table J.1: Measured and calculated masses of Activa LT mask assembly and components

Component	Mass	CAD	Correction Scale Factor
	g	g	
Frame	50.8	50.5	1.00
Cushion Clip	3.3	3.3	1.00
Port Cover	0.9	0.9	1.02
HG Clip	1.8	2.0	0.88
HG Clip	1.8	2.0	0.88
Swivel	7.3	7.3	1.00
Tube	37.8	37.8	1.00
	103.6	103.8	1.00

$$\boldsymbol{x}_{cg} = \begin{bmatrix} 0.0 & -78.46 & 35.76 \end{bmatrix} \tag{J.1}$$

The principal inertia tensors of the mask assembly in the centroidal coordinate system as calculated by the CAD model are defined in equations (J.1) to (J.2) below.

Inertia Tensor Fully Retracted

$$I = \begin{bmatrix} 40544 & 0 & 0 \\ 0 & 1359445 & 0 \\ 0 & 0 & 1362082 \end{bmatrix} \tag{J.2}$$

J.2.2 Transformation Matrices

The transformation of the coordinates of position vector of a fixed location *from* the CG reference frame *to* the Activa LT master reference frame is given by equation (J.3)

$$\boldsymbol{x}^* = \boldsymbol{x}\boldsymbol{A}, \tag{J.3}$$

where $\boldsymbol{x}$ is the position row vector of the location in the original inertial coordinate system (CG), $\boldsymbol{x}^*$ is the position row vector the same location transformed into the alternate system, namely the mask (Activa LT) system, and $\boldsymbol{A}$ is the affine forward transformation matrix.

$$\boldsymbol{A} = \begin{bmatrix} 6.8e-005 & 0.96386 & -0.26642 & 0 \\ -1 & 8.08e-4 & 2.667e-3 & 0 \\ 2.786e-3 & 0.26642 & 0.96385 & 0 \\ 7.449e-3 & -78.456 & 35.758 & 1 \end{bmatrix} \tag{J.4}$$

Appendix K
Buoyancy Artefact

K.1 Introduction

K.2 Aim

The aim of this experiment is to acquire tensile test data for the 10% gelatine material used in tissue indentation experiments. This experiment is performed using the recommendations developed previously.

K.3 Hypothesis

This experiment acquires mechanical data for 1 material to be used as an input for subsequent work. There is no hypothesis to test.

K.4 Equipment

The equipment required for this experiment are as follows

- Instron 5543 mechanical testing machine
- 50 N load cell
- Non contact video extensometer
- Immersion bath
- Pneumatic grips
- Warm water bath for melting
- sample moulds
  - 10mm × 2mm × 1mm
  - ASTM C - 3mm thick

Table K.1: Consumables required for gelatin compressive testing

Item	Quantity	Description
10% gelatine		10% Gelatine solution by mass prepared
Syringe	1	Fill moulds
Marking pen or similar	1	Mark samples for non contact extensometer
Glass sheet	2+	Base and cover to mould samples
Cover slips	1/mould	Cover mould to get smooth surface
Parafilm or similar	-	Non stick interface to assist demoulding
PDMS solution	1	Mould lubricant

K.5 Consumables

The consumables required for this experiment are outlined in Table K.1

K.6 Protocol

K.6.1 Sample Preparation

1. Place the gelatine preparation into the 60°C water bath to melt prior to moulding
2. Apply parafilm to glass base
3. Smear PDMS over the moulds and base as a lubricant to assist demoulding
4. Using a syringe, fill the moulds taking care to avoid introducing air bubbles
5. Place cover over mould (glass sheet or cover slip)
6. Place in the freezer and allow to set for at least 30 minutes

K.6.2 Pre Test

1. Turn on mechanical testing machine
2. Calibrate video extensometer and load cell
3. Fill the immersion bath

4. Turn on the pneumatic supply (Lift: ≈ 50psi, Grips: ≈ 20psi)

K.6.3 Test

1. Remove sample from freezer
2. Apply gauge marks on the sample
3. Remove sample from the mould and transport with minimal handling to the testing machine
4. Mount in the upper grip
5. Balance the load cell
6. Close the lower grip
7. Raise the immersion bath
8. Commence tensile test

K.6.4 Tensile Test Description

The test was performed in two stages. The first stage allows for thermal equilibrium to be reached by holding the sample in the immersion bath for 5 minutes prior to commencing sample extension (5 mm/min). The test was terminated by sample fracture. The experiment is shown in figure K.1.

K.7 Results

The results from the samples are outlined in table K.2 and presented graphically in figure K.2.

K.8 Discussion

Previous experiments have encountered difficulties in obtaining valid data for the gelatine material. This experiment was able to acquire valid test data for 2 samples. The results from sample 1 show that there is a a discrete jump in force as soon as the cross head starts moving ($t = 300$ s). A further discrete jump in force was observed at $t \approx 460$s. The sample fractured at $t \approx 500$. It can be seen that the force recorded continues to rise. Therefore it is hypothesised that this is an artefact caused by the

Figure K.1: 10% gelatine test setup. Note that the upper grip is fitted with a collar to prevent the air bubble build-up artifact

Table K.2: Sample Observations

Sample	Type	Valid Data	Comments
1	ASTM C	✓	Sample failed in gauge region. A sudden spike was noticed in the gauge region at the start of crosshead movement. Tensile load continued to increase after sample had fractured
2	Excluded	x	-
3	Blank	✓	Turned off AVE for blank runs
4	Excluded	x	-
5	Blank	✓	Regular sawtooth pattern corresponding to a build-up of bubbles which are released periodically. This needs to be prevented as the magnitude is significant for very soft materials.
6	Blank	✓	Sleeve created to prevent bubble build-up. Sleeve prevented the build-up and release of bubbles
7	Excluded	x	-
8	ASTM C	✓	Liquid paper used as specimen marker

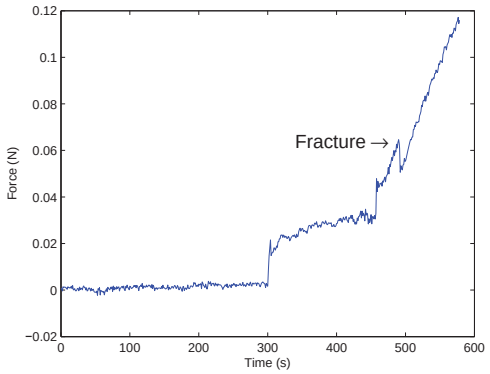

(a) Sample 1 raw data showing increasing load beyond fracture

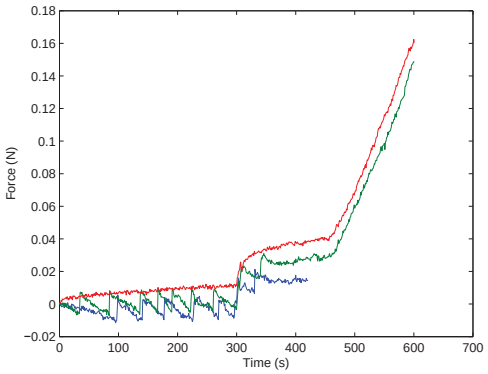

(b) Blank runs for artefact determination

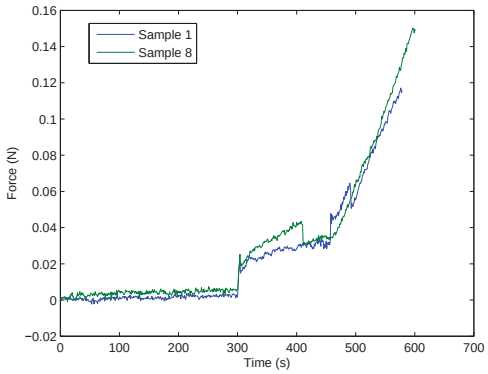

(c) Uncorrected test data

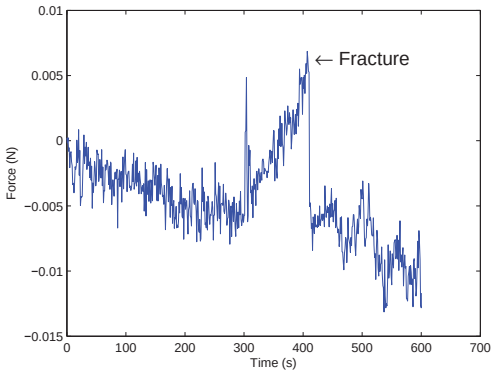

(d) Sample 5 corrected test data

Figure K.2: Buoyancy artefact and correction

raising of the crosshead which in turn gradually pulls the grips out of the immersion bath, reducing the buoyancy of the grips and transferring this force to the load cell. It is planned to characterise this artefact, so that it can be subtracted from the raw data.

K.8.1 Buoyancy Artefact

To investigate the nature of the artefact, a series of blank runs were performed [1]. Samples 3 and 5 exhibited a regular sawtooth pattern of a gradually decreasing load followed by a step increase in load, repeating at a period of approximately 50s. This was determined to be from a fluctuation in the buoyancy of the grips due to the gradual build up and release of an air bubble from the bled air in the lower grip on a facet on the underside of the top grip. A sleeve was fashioned to fit over the grip

[1] Video extensometer was turned off and a commensurate displacement was used to control the experiment

to cover the facet and prevent this air bubble from accumulating. The sleeve was manufactured from the barrel of a 60ml syringe. The fitted sleeve can be seen on the barrel of the upper grip in figure K.1.
Sample 6 (blank) was run with the grip sleeve fitter. The results from sample 6 showed that the sawtooth pattern was eliminated. Visual inspection also confirmed that the air bubble build up was prevented with the sleeve fitted. There was a drift in the equilibrium phase of the test. Repeated tests will be required to have a reliable artefact correction. The buoyancy artefact has a noted change in gradient at about $t \approx 470$. This corresponds to the main casting of the grip body starting to be lifted out of the immersion bath, rather than the extension rod with constant cross section.

K.8.2 Pilot Data

The final sample from this test was run with the grip sleeve in place. Therefore the test data can be corrected for the buoyancy artefact by subtracting the artefact from the raw data as follows

$$P^{*}(t) = P(t) - P_{artefact}(t)$$

The result from this correction is shown in figure K.2d. The negative slope of the equilibrium phase of the test is caused by the sensor drift noted in sample 6. Due to the very soft nature of the samples this does however have the effect of highlighting the noise associated with the measurement, which is a significant portion of the mean signal. This will have to be accounted for in future testing.

K.9 Conclusion

This test has shown that the freezing method greatly facilitates handling of these samples, and allows for valid tensile data to be acquired using an immersion bath and non contact extensometer. Difficulties are still encountered marking the specimens, but these do not appear to prevent the acquisition of valid data.
The buoyancy artefact identified in this test needs to be accounted for in any future tests. Since this artefact has an irregular profile, it is *essential* that it be determined individually for each test configuration, and that the same zero point be used for all samples as well as the repetitions of the blank artefact characterisation runs.

Appendix L
Gelatine Mechanical Testing

L.1 Aim

The aim of this experiment is to acquire tensile test data for the 10% gelatine material used in tissue indentation experiments, taking into account the buoyancy artifact. This experiment was performed using the recommendations developed previously from studying the buoyancy artefact described in Appendix K.

L.2 Hypothesis

This experiment acquires mechanical data for 1 material to be used as an input for subsequent work. There is no hypothesis to test.

L.3 Equipment

The equipment required for this experiment are as follows

- Instron 5543 mechanical testing machine
- 50 N load cell
- Non contact video extensometer
- Immersion bath
- Pneumatic grips
- Upper grip sleeve to prevent air build-up while immersed
- Warm water bath for melting
- sample moulds
  - 10mm × 2mm × 1mm
  - ASTM C - 3mm thick

L.4 Consumables

The consumables required for this experiment are as follows

Item	Quantity	Description
10% gelatine		10% Gelatine solution by mass prepared
Syringe	1	Fill moulds
Marking pen or similar	1	Mark samples for non contact extensometer
Glass sheet	2+	Base and cover to mould samples
Cover slips	1/mould	Cover mould to get smooth surface
Parafilm or similar	-	Non stick interface to assist demoulding
PDMS solution	1	Mould lubricant

L.5 Protocol

L.5.1 Sample Preparation

1. Place the gelatine preparation into the 40°C water bath to melt prior to moulding
2. Apply parafilm to glass base
3. Smear PDMS over the moulds and base as a lubricant to assist demoulding
4. Using a syringe, fill the moulds taking care to avoid introducing air bubbles
5. Place cover over mould (glass sheet or cover slip)
6. Place in the freezer and allow to set for at least 30 min

L.5.2 Pre Test

1. Turn on mechanical testing machine
2. Calibrate video extensometer and load cell
3. Fill the immersion bath

4. Turn on the pneumatic supply (Lift: ≈ 50psi, Grips: ≈ 20psi)

L.5.3 Buoyancy Artifact Correction

Prior to running the test protocol a series of blank runs must be performed to assess the artifact that is recorded from the system's self weight and movement. In order to do this an identical test procedure (refer to L.5.5) is followed for a number of samples to provide enough data to generate and augmented average for the artifact's effect. It is important to ensure that the pneumatic grips are closed for the blank tests, as this will also include the effect of air in the pneumatic chamber and any pressure relief bleeding.
Since this is a test run with no sample, the loads will be very low. This will mean that noise will need to be taken into account in the processing. This will be done by pooling the results to give and augmented average and then using a digital low pass filter to further reduce the noise.

L.5.4 Test

1. Remove sample from freezer
2. Apply gauge marks on the sample
3. Remove sample from the mould and transport with minimal handling to the testing machine
4. Mount in the upper grip
5. Balance the load cell
6. Close the lower grip
7. Raise the immersion bath
8. Commence tensile test as per L.5.5

L.5.5 Tensile Test Description

The test was performed in two stages. The first stage allows for thermal equilibrium to be reached by holding the sample in the immersion bath for 5 min prior to commencing sample extension (5 mm/min). The test was terminated by sample fracture. The experiment is shown in figure L.1.

Figure L.1: 10% gelatine test setup. Note that the upper grip is fitted with a sleeve to prevent the air bubble build-up artifact

L.6 Results

L.6.1 Artifact Baseline

Eight (8) blank tests were performed for artifact characterisation. The results from the artifact correction tests are outlined in table L.1 and presented graphically in figure L.2.

Table L.1: Baseline test runs

Sample	Valid Data	Comments
1	x	Pneumatic grips not activated
2	✓	-
3	✓	-
4	✓	-
5	✓	-
6	✓	-
7	✓	-
8	x	Outlier

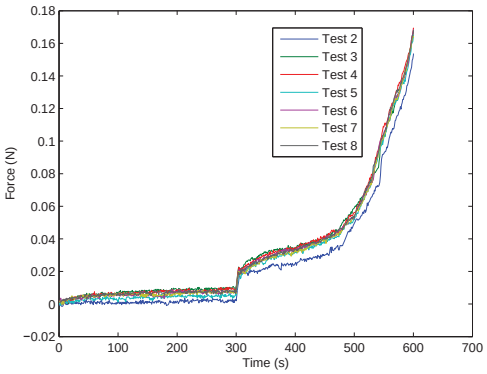

(a) Artifact data from 7 tests, Test 2 is an outlier

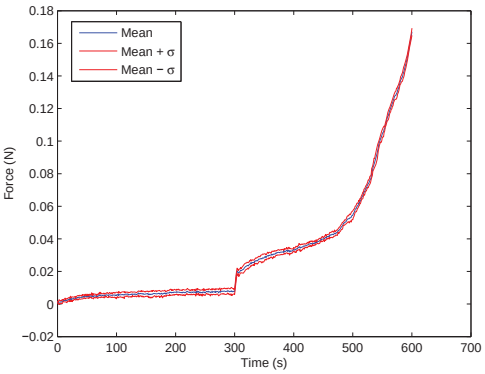

(b) Artifact baseline mean $\pm\sigma$

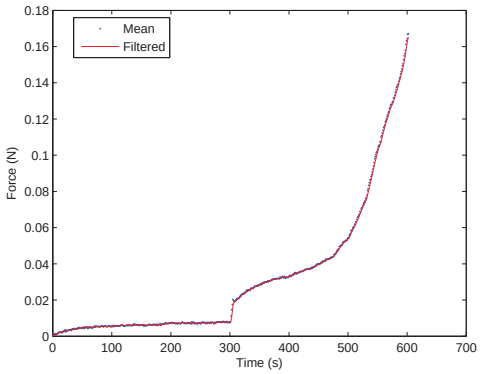

(c) Filtered artifact baseline (Low pass, $K = 1$, $\xi = 0.5$, first order)

Figure L.2: Buoyancy artefact correction calculations

L.6.2 Gelatine Tensile Tests

Valid data was obtained from ten (10) ASTM ASTM (1998) dumbbell samples. The results from the tensile tests are outlined in table L.2 and presented graphically in figure L.3.

The data was corrected and normalised to account for the test artefacts as follows. A * superscript will denote corrected or adjusted values, and for upper case values will refer to the reference configuration:

The filtered artifact baseline was subtracted from the raw signal of each of the samples and offset to after the impulse from the crosshead commencing moving at time t_0.

Sample	Valid Data	Comments
1	✓	-
2	✓	-
3	✓	Fractured in middle
4	✓	Fractured in middle
5	✓	Fractured in middle
6	✓	Fractured in middle
7	✓	Fractured in middle
8	✓	Fractured in middle
9	x	Excluded
10	✓	Fractured in middle
11	x	Excluded
12	✓	Fractured in middle

Table L.2: Gelatine tensile test runs

$$
\begin{aligned}
t^* &= t - t_0 \\
F_i^*\left(t^*\right) &= F_i\left(t\right) - f\left(t\right) && t \geq t_0 \\
F_i^*\left(t^*\right) &= 0 && t < t_0
\end{aligned}
\tag{L.1}
$$

The gauge length has been recorded at the start of the thaw phase of the test and has been used to calculate the engineering strain from the video extensometer throughout the test. Therefore the reference configuration of the sample needs to be reset to its current configuration at the start of crosshead movement.

$$
\begin{aligned}
l\left(t_0\right) &= \lambda\left(t_0\right) L \\
&= \left(1 + e\left(t_0\right)\right) L \\
L^* &= l\left(t_0\right)
\end{aligned}
\tag{L.2}
$$

The material is assumed to be isotropic and completely incompressible, therefore the product of the principal stretches is identically

$$
\lambda_1 \lambda_2 \lambda_3 = 1 \tag{L.3}
$$

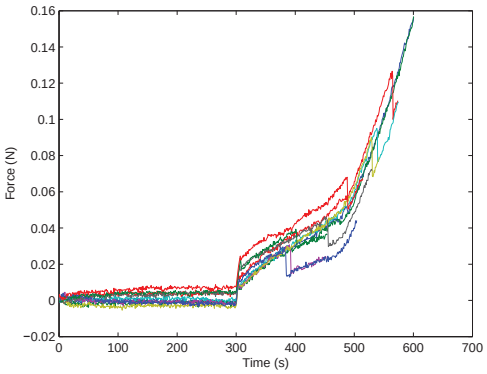

(a) Gelatine raw tensile data

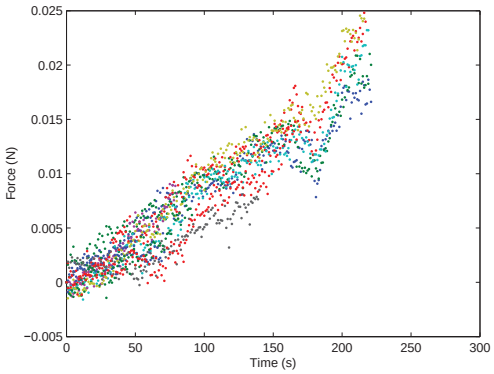

(b) Corrected gelatine tensile data

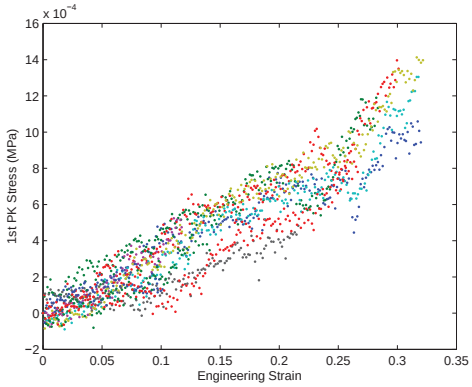

(c) 1st PK Stress vs Engineering strain

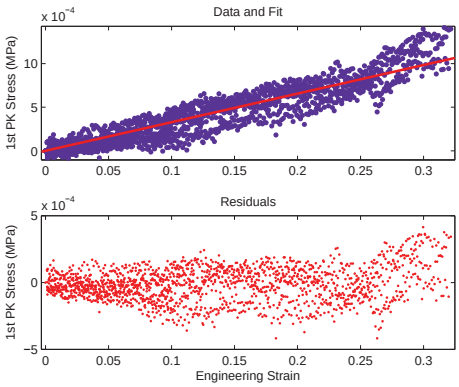

(d) Linear fit of stress vs engineering strain data

Figure L.3: Gelatine tensile testing results

Therefore the corrected stretch and area is given by

$$\lambda^* = \frac{l}{L^*}$$
$$a = \frac{A}{\lambda_1}$$
$$A^* = a(t_0)$$

Therefore the 1^{st} Piola Kirchoff stress (T) and deformation measures updated to the start of the crosshead movement are

$$T = \frac{F^*}{A^*} \tag{L.4}$$
$$\lambda^* = \frac{l}{L^*} \tag{L.5}$$
$$e^* = \lambda^* - 1 \tag{L.6}$$

The stress and strain data were used to determine a linear relationship between the $1st$ PK stress and the engineering strain. These variables were chosen as they scaled easily to the units of force and displacement, where they will be used for inverse FEA material characterisation.
A linear relationship was found between the stress and the strain, forcing it to pass through the origin as follows:

$$T = p_1 x \tag{L.7}$$

The value and 95% confidence interval for p_1 is

$$p_1 = 3.278\left(10^{-3}\right) \qquad 3.241\left(10^{-3}\right) < p_1 < 3.316\left(10^{-3}\right)\text{MPa}$$

A clear trend is indicated by these data, however the residuals are large with respect to the mean value of the data ($SSE = 2.601e-005$, $r^2 = 0.8583$). This is due to the relatively large magnitude of the noise in the corrected signal as the artifact correction only subtracts the mean.

L.7 Discussion

This experiment has been able to successfully acquire tensile test data for the 10% solution of gelatine. This has been corrected to account for buoyancy artefacts from the immersion test. A linear model has been found to be adequate to represent the relationship between stress and stretch. This does not imply by any means that the material properties are linear, only that a linear relationship was found between the engineering strain and the 1^{st} Piola Kirchoff stress. This is a large deformation problem and will need to be modelled as such taking into account both geometric and material non linearities. The results from this experiment will be used to provide multi modal data for hyperelastic curve fitting of the gelatine material.

Appendix M

Gelatin Mechanical Properties using Inverse Finite Element Analysis

M.1 Introduction

The aim of this analysis is to determine using inverse finite element analysis (FEA) non linear material properties for 10% gelatine, which is used as an elastic boundary in other tests.

A material is termed hyperelastic if it is capable of withstanding very large recoverable mechanical deformations. Hyperelastic materials commonly exhibit incompressibility, whereby these large deformations are associated with very small variations in material volume. Additionally these materials exhibit a non linear stress-strain characteristic.

This provides some complications in determining an appropriate constitutive model for structural simulation, as due to the incompressibility of the material, the state of stress is not unique to a particular strain state ANSYS Inc (2005). Since most of the hyperelastic models that have been developed are phenomenological models Treloar *et al.* (1976) (*i.e.* models are based on regression and do not take into account the physical structure of the material) it is important to test in multiple modes of deformation, as it is not guaranteed that a good model fit in one deformation mode will translate to another ANSYS Inc (2005). Therefore this report will simultaneously consider uniaxial tensile extensions and compression. ANSYS Inc (2005).

M.1.1 Governing Equations and Variables

The following measured and derived quantities are used to present the results and for subsequent calculations. Note that *UPPER CASE* kinematic variables denote

the reference configuration, and *lower case* kinematic variables denote the deformed or current configuration.

Force (P) Measured load (N) applied to the sample

Engineering Strain (e) Measured nominal strain from the non contact extensometer

$$e = \frac{\Delta L}{L} \tag{M.1}$$

Stretch Ratio (λ_i) Principal stretch ratio in the i direction

$$\lambda_i = \frac{l_i}{L_i} = e + 1 \tag{M.2}$$

Incompressibility Constant volume maintained throughout arbitrary deformations

$$\lambda_1 \lambda_2 \lambda_3 = 1 \tag{M.3}$$

1st Piola Kirchoff Stress (T) Applied load in the i direction normalised by the reference area normal to the j direction, also known as Engineering Stress

$$T_{ij} = \frac{P_i}{A_j} \tag{M.4}$$

Cauchy Stress (σ) Applied load in the i direction divided by current or deformed area normal to the j direction, also known as true stress

$$\sigma_{ij} = \frac{P_i}{a_j} \tag{M.5}$$

$$= \frac{P_i}{\frac{A_j}{\lambda_i}} = \lambda_i \frac{P_i}{A_j} \tag{M.6}$$

$$\sigma_{ij} = \lambda_i T_{ij} \tag{M.7}$$

M.2 Inverse Finite Element Analysis

Inverse finite element modelling was used to fit material properties to the experimental results. This is done by minimising the an objective function which calculates the norm of the residuals between the model results and the experimental data. Ogden *et al.* showed that superior model fits were achieved with the use of pooled

residual calculations which take into account multiple modes of deformation Ogden *et al.* (2004). Therefore models incorporating both tensile and compressive data will considered simultaneously when fitting model data.
Due to the sensitive nature of the gel material being tested, during the compression test, it was extremely difficult to eliminate, or reduce significantly enough, friction from the sample platen interface. Therefore a *no slip/bonded* condition was enforced in the test (refer to test performed 21 Nov 2008).
Since the compression test will enforce a no slip condition a uniaxial state of stress and deformation will not be set up. Therefore in order to correctly use normalised stress/stretch data, this will need to be accounted for by referring data back to the mid-plane, the only location of the sample subject to an orthogonal state of deformation Miller (2005); Klingbeil and Shield (1966). Moriss *et al.* have shown that converged numerical models provide more reliable material properties than these analytical techniques for the compression of very soft materials at moderate to high strains Morriss *et al.* (2008).
Therefore this simulation uses commensurate data from the experiments that can be pooled across both samples from different testing modes. Specifically, the optimisation will be performed using the acquired force data from each of the tests which will be compared to the reaction forces calculated in the FEA models which will be set up to mimic the experiments.

M.2.1 Material Model

Common to both FEA models will be that material that is used. This will be varied iteratively throughout the simulation. A Hyperelastic model will be used with a mixed U/P element formulation to avoid volumetric locking due to material incompressibility. The material coefficients are the independent variables in the optimisation. Several different hyperelastic material models were trialled.

M.2.2 Tensile Model

A 3D solid model was created in ANSYS using 8 node HEX elements (Solid185)to simulate a uniaxial tensile test. Only the gauge region of the sample is modelled, so end effects are assumed to be negligible. Symmetry about all 3 planes was assumed for modelling simplicity and numerical efficiency. Therefore a $\frac{1}{8}$ model was developed. Tensile set and the Mullins effect was accounted for by comparing the FEA model back to experimental results after they had been offset to a stabilised origin (refer to test performed 7 Jan 2009).

The model was constructed using a consistent MMNS unit system. The test piece modelled is $30 \times 6 \times 3$mm.
The results from the FEA model will need to be scaled to match the experiment. Two of the symmetry planes reduce the cross sectional area carrying the load, while the third halves the length of the sample. Therefore the following scaling relations are used:

$$P_{expt} = 4P_{FEA} \tag{M.8}$$

$$\Delta L_{expt} = 2\Delta L_{FEA} \tag{M.9}$$

Element Definition

The material being tested was modelled with *SOLID185* elements. The keyoptions defined for this element type are shown in table M.1. Since this is modelling a uniform stress and stretch field, there are no gradients to consider and a coarse mesh is suitable.

Table M.1: Keyoptions for element type 1

Key Option	Value	Description
6	1	Mixed U/P formulation

Loads and Boundary Conditions

Symmetry - X Midplane ($x = 0$).

	X	*Y*	*Z*
Disp	0	-	-
Rot	N/A	0	0

Symmetry - Y Midplane ($y = 0$).

	X	*Y*	*Z*
Disp	-	0	-
Rot	0	-	0

Symmetry - Z Midplane ($z = 0$).

	X	*Y*	*Z*
Disp	-	-	0
Rot	0	0	-

Enforced displacement The simulation is displacement controlled. So the loads on the sample are applied by an enforced displacement on the upper surface of the model.

$$e = 0.35\text{mm} \tag{M.10}$$

$$\delta y = e\frac{L}{2}$$

$$= 10.5\text{mm} \tag{M.11}$$

	X	Y	Z
Disp	-	10.5	-
Rot	-	-	-

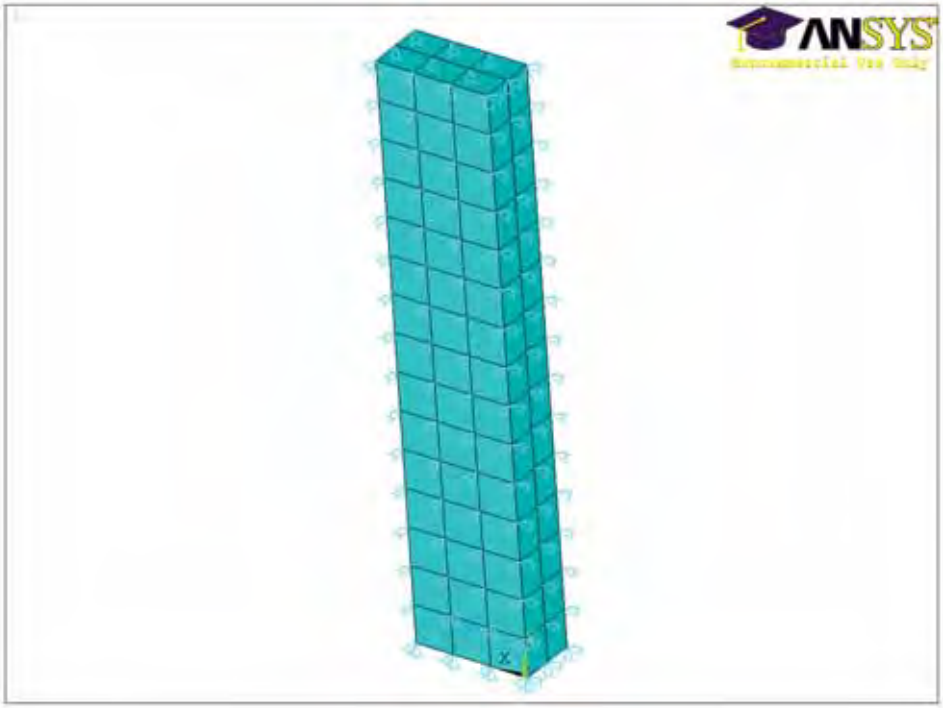

Figure M.1: Tensile FEA model and boundary conditions

M.2.3 Compression Model

A 2D axisymmetric finite element model was developed in ANSYS to mimic the compression test with a no slip boundary condition. The no slip boundary condition

was incorporated into the model using rigid contact elements rather than simply using DOF constraints, as there is the possibility due to the bulging of the sample that the side walls might come into contact with the platen and provide a varying load path. This is accounted for by using a contact surface extending beyond the sample. Contact surfaces consist of paired groups of elements designated as *contact* and *target* elements. Symmetry was assumed at the midplane of the sample. The sample is a cylinder, modelled in the XY plane. The dimensions are the mean calculated values from the gel compression test.
The model was constructed using a consistent MMNS unit system.

$$\phi = 25\text{mm}$$
$$2H = 18.2666\text{mm}$$

The model was solved in 2 major steps to take into account the offset origin from the precycling. This was completed as follows:

Compressive set Solve for compression to the stabilised origin $\delta H = -1.2408$mm as calculated in preconditioning of the compression experiment (7 Jan 2009)

Update mesh Update the model so that the new reference configuration is the stabilised geometry for the compression test.

Compression test Solve for the compression test

The elements that were used in the model are outlined in table M.2.

Element Type	Name	Description	Comments
1	Plane183	2D 6/8 node planar element	Test sample
2	Targe169	2D contact target element	Contact
3	Conta172	2D contact element	Contact

Table M.2: Element type definitions

Element Definition

The gel material being tested was modelled with triangular *plane183* elements. High order triangular elements are used due to the high skew quadrilateral elements at the corner of the platen interface as the side wall is deformed due to compression and becomes horizontal at the platen. Although the material properties are unknown, it is assumed that they will take the form of a hyperelastic model. This requires the

use of the mixed U/P element formulation. The keyoptions defined for this element type are shown in table M.3

Key Option	Value	Description
3	1	Axisymmetric
6	1	Mixed U/P formulation

Table M.3: Keyoptions for element type 1

Contact Definition

A rigid-deformable contact pair was defined for the platen/sample interface (element types 2 and 3 in table M.1). Rough contact is used to ensure the no slip condition at the platen. A pilot node is used to apply a known deflection to the platen rigid element. The contact elements cover the top surface of the sample and extend down the external side to allow for them to come into contact as the material bulges. The contact parameters take their default settings with the exception of those listed in tables M.4, M.5 and M.6:

	Value	Name	Description
Real Constant Set	2	-	Identifies contact pair
Contact ET	2	Targe169	2D rigid target
Target ET	3	Conta171	2D contact

Table M.4: Platen/sample contact summary

Element Type	Key Option	Value	Description
2-Target	2	0	Auto Boundary conditions for rigid target
	TSHAP	Line	2 node line rigid element
3-Contact	1	0	DOF: x, y
	2	0	Algorithm: Augmented Lagrange
	5	0	Automated offset - no adjustment
	9	0	Include both initial penetration or gap and offset
	10	1	Update stiffness each substep
	12	1	Rough

Table M.5: Contact keyoptions

Real Set	No.	Name	Value	Description
2	3	FKN	1	Normal penalty stiffness factor
	4	FTOLN	0.1	Penetration tolerance factor
	5	ICONT	0	Initial contact closure
	6	PINB	-2	Pinball region
	10	CNOF	0	Contact surface offset

Table M.6: Contact real constant settings

Loads and Boundary Conditions

Symmetry - Centreline Due to axisymmetry the centreline must be fixed in the x direction. This is shown in figure M.1

	X	*Y*	*Z*
Disp	0	-	N/A
Rot	N/A	N/A	0

Symmetry - Z Midplane $z = 0$. This is shown in figure M.1

	X	*Y*	*Z*
Disp	-	0	N/A
Rot	N/A	N/A	0

Enforced displacement The simulation is displacement controlled. So the loads on the sample are applied by an enforced displacement on the platen pilot node. This is in 2 steps as follows:

Preconditioning The following enforced displacement is applied to the platen to precondition the sample. This is determined by the offset at the stabilised origin from the experiment.

	X	*Y*	*Z*
Disp	0	-1.2408	N/A
Rot	N/A	N/A	0

Compression The following enforced displacement is applied to the platen to compress the sample. This corresponds to the a normalised compression of 0.5.

	X	*Y*	*Z*
Disp	0	-4.1219	N/A
Rot	N/A	N/A	0

M.2.4 Material Properties

The mechanical material properties of the gel are initially unknown. A various hyperelastic constitutive laws were trialled to model the material. The strain energy density function for the fully incompressible material models trialled are:

Mooney Rivlin 2 Parameter

$$W = C_{10}\left(I_1 - 3\right) + C_{01}\left(I_2 - 3\right) \tag{M.12}$$

$$\mu = 2\left(C_{10} + C_{01}\right) \tag{M.13}$$

where C_{10} and C_{01} are material constants which are to be fitted to the test results and μ is the initial shear modulus.

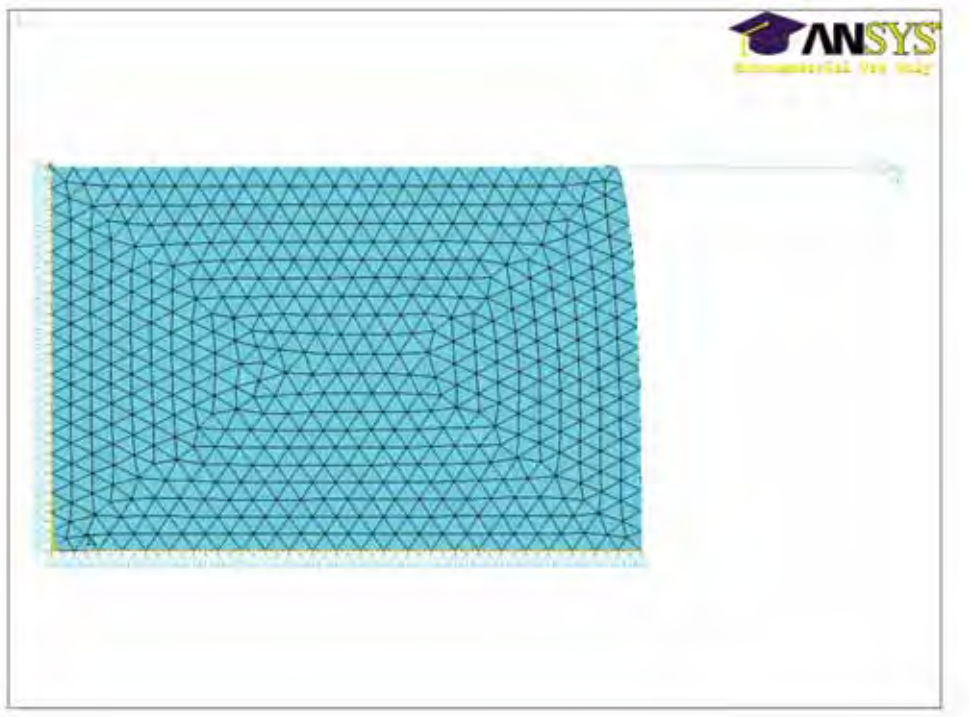

Figure M.2: Preconditioned axisymmetric compression model

Mooney Rivlin 3 Parameter

$$W = C_{10}(I_1 - 3) + C_{01}(I_2 - 3) + C_{11}(I_1 - 3)(I_2 - 3) \tag{M.14}$$

where C_{10}, C_{01} and C_{11} are material constants which are to be fitted to the test results.

Ogden

$$W = \sum_{i=1}^{N} \frac{\mu_i}{\alpha_i}(\lambda_1^{\alpha_i} + \lambda_2^{\alpha_i} + \lambda_3^{\alpha_i}) \tag{M.15}$$

where μ_i and α_i are material constants which are to be fitted to the test results, and N is the order of the model. Second and third order Ogden models were trialled.

M.2.5 Solution

This FE model is solved iteratively using the optimisation toolbox in Matlab [1]. An objective function calculates the residuals between vectors containing reaction forces of the FEA model and the measured test results at corresponding displacements. The 2-norm of the residuals is minimised as by adjusting the material parameters *e.g.* C_{10} and C_{01}.

$$\epsilon = \|\boldsymbol{P_{FEA}} - \boldsymbol{P_{EXPT}}\|_2 \tag{M.16}$$

$$\epsilon = f(\text{parameters...}) \tag{M.17}$$

The solution parameters for the FEA model are shown in table M.7.

Results

The results from the fitted simulation are shown in figure M.3
As recorded in table M.8, the Mooney Rivlin models have provided the best fit for the data from the tensile and no-slip compression experiments. The 3 parameter

[1] For various configurations the functions used were *fminunc, fmincon, lsqcurvefit*

Table M.7: FEA solution parameters

Parameter	**Preconditioning**	**Compression**
Analysis Type	Static	Static
Non-Linear Geometry	On	On
Load Steps	1	10
Max Substeps	100	10
Force Convergence	0.005	0.005
Displacement Convergence	0.05	0.05

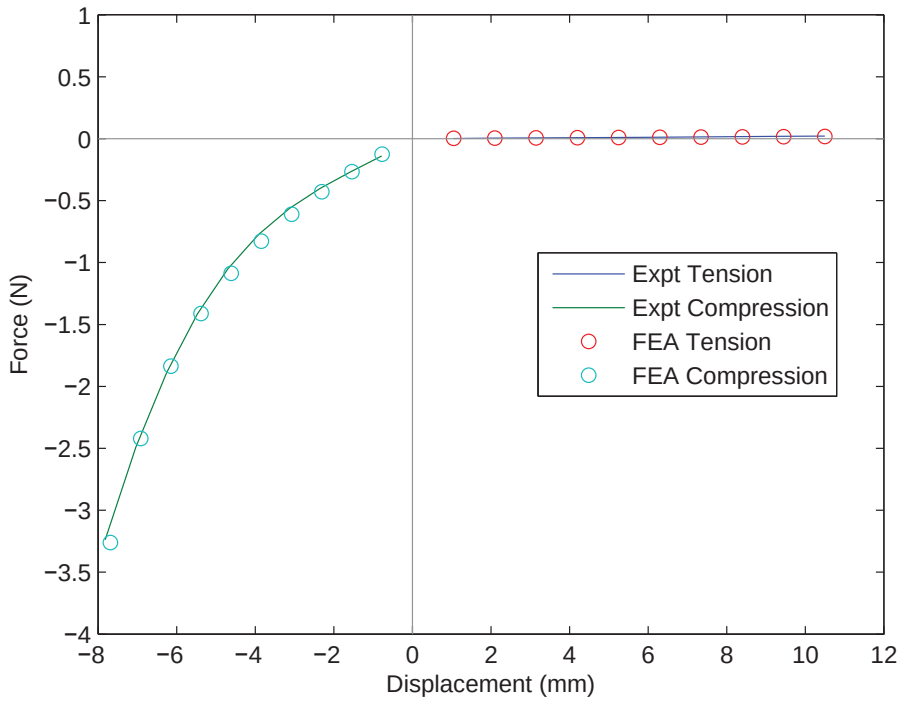

Figure M.3: Force vs Displacement FEA model fit

Table M.8: Inverse FEA results

Model Type	**Material Coefficients**	**Residual Norm**
MR2	$C_{10} = 0.4346\,(10^{-3})$	1.447
	$C_{01} = 0.2213\,(10^{-3})$	
MR3	$C_{10} = 0.4317\,(10^{-}3)$	1.308
	$C_{01} = 0.2115\,(10^{-}3)$	
	$C_{11} = 0.01155\,(10^{-}3)$	
Ogden2	$\alpha_1 = 0.1627$	2.0754
	$\mu_1 = 1.2872\,(10^{-3})$	
	$\alpha_2 = -0.19738$	
	$\mu_2 = -0.012410$	
Ogden3	$\alpha_1 = 0.081469886$	2.0749
	$\mu_1 = 4.5544271\,(10^{-3})$	
	$\alpha_2 = 0.097637738$	
	$\mu_2 = 0.019200310$	
	$\alpha_3 = 0.081602716$	
	$\mu_3 = 5.1944781\,(10^{-3})$	

Mooney Rivlin model returned the lowest residual and provided the best fit for both data sets in this situation. The fitted material parameters are:

$$\begin{aligned} C_{10} &= 0.4317\left(10^{-}3\right) \\ C_{01} &= 0.2115\left(10^{-}3\right) \\ C_{11} &= 0.01155\left(10^{-}3\right) \end{aligned} \tag{M.18}$$

The norm of the residuals is:

$$\|\epsilon\|_2 = \left(10^{-3}\right) \tag{M.19}$$

Therefore using equation (M.13), the initial shear modulus is:

$$\mu = 0.6559\,(10^{-3})\ \text{MPa}$$

The compression test and FEA simulation are shown in figure M.4.

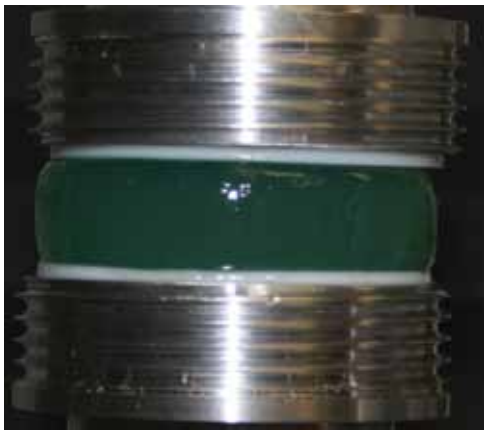

(a) Compression test

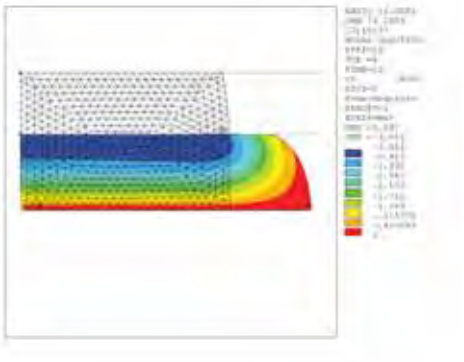

(b) FEA simulation results, vertical displacement

Figure M.4: Compression test of gel sample with rough boundary conditions and corresponding FEA simulation results

References

Oxford English Dictionary. Oxford University Press, Oxford, **2006**.

ISO 17510-1; Sleep apnoea breathing therapy - Part 1: Sleep apnoea breathing therapy equipment. **2007**a.

ISO 17510-2; Sleep apnoea breathing therapy - Part 2: Masks and application accessories. **2007**b.

Agache, P.G., Monneur, C., Leveque, J.L. and Rigal, J.D.: Mechanical properties and young's modulus of human skin in vivo. *Arch Dermatol Res*, 269(3):pages 221–232, **1980**.

American Academy of Sleep Medicine Task Force: Sleep-related breathing disorders in adults: recommendations for syndrome definition and measurement techniques in clinical research. The Report of an American Academy of Sleep Medicine Task Force. *Sleep*, 22(5):pages 667–689, **1999**.

ANSYS Inc: Chapter 4. structures with material nonlinearities. In *ANSYS Inc. Theory Reference*. ANSYS Inc., Canonsburg, PA, **2005**.

Arruda, E.M. and Boyce, M.C.: A 3-dimensional constitutive model for the large stretch behavior of rubber elastic-materials. *Journal of the Mechanics and Physics of Solids*, 41(2):pages 389–412, **1993**.

Aserinsky, E. and Kleitman, N.: Regularly occurring periods of eye motility, and concomitant phenomena, during sleep. *Science*, 118(3062):pages 273–274, **1953**.
URL `http://www.jstor.org/stable/1680525`

ASTM: *D412-98a: Standard Test Methods for Vulcanized Rubber and Thermoplastic Elastomers - Tension*. ASTM, West Conshohocken, PA, **1998**.

ASTM: *F2052-06: Standard Test Method for Measurement of Magnetically Induced Displacement Force on Medical Devices in the Magnetic Resonance Environment*. ASTM, West Conshohocken, PA, **2006**a.

ASTM: *F2213-06: Standard Test Method for Measurement of Magnetically Induced Torque on Medical Devices in the Magnetic Resonance Environment*. ASTM, West Conshohocken, PA, **2006**b.

Augenstein, K.F., Cowan, B.R. *et al.*: Method and apparatus for soft tissue material parameter estimation using tissue tagged magnetic resonance imaging. *Journal of Biomechanical Engineering-Transactions of the Asme*, 127(1):pages 148–157, **2005**.
URL <GotoISI>://000227971600016

Azar, F.S., Metaxas, D.N. and Schnall, M.D.: Methods for modeling and predicting mechanical deformations of the breast under external perturbations. *Med. Image Anal.*, 6(1):pages 1–27, **2002**.

Babu, A.R., Herdegen, J. *et al.*: Type 2 diabetes, glycemic control, and continuous positive airway pressure in obstructive sleep apnea. *Arch Intern Med*, 165(4):pages 447–452, **2005**. doi:10.1001/archinte.165.4.447.

Banabilh, S.M., Suzina, A.H. *et al.*: Craniofacial obesity in patients with obstructive sleep apnea. *Sleep Breath*, 13(1):pages 19–24, **2009**. doi:10.1007/s11325-008-0211-9.

Barbarino, G.G., Jabareen, M. *et al.*: Development and Validation of a Three-Dimensional Finite Element Model of the Face. *Journal of Biomechanical Engineering-Transactions of the ASME*, 131(4), **2009**. doi:10.1115/1.3049857.

Beldie, L., Walker, B. *et al.*: Finite element modelling of maxillofacial surgery and facial expressions–a preliminary study. *Int J Med Robot*, 6(4):pages 422–430, **2010**. doi:10.1002/rcs.352.

Berger, R.J.: Tonus of extrinsic laryngeal muscles during sleep and dreaming. *Science*, 134(3482):page 840, **1961**.
URL http://www.jstor.org/stable/1707772

Berlowitz, D.R. and Brienza, D.M.: Are all pressure ulcers the result of deep tissue injury? a review of the literature. *Ostomy Wound Manage*, 53(10):pages 34–8, **2007**.

Bischoff, J.E., Arruda, E.M. and Grosh, K.: Finite element modeling of human skin using an isotropic, nonlinear elastic constitutive model. *J. Biomech.*, 33(6):pages 645–52, **2000**.

Bixler, E., Vgontzas, A. *et al.*: Effects of age on sleep apnea in men . i. prevalence and severity. *Am. J. Respir. Crit. Care Med.*, 157(1):pages 144–148, **1998**.

Black, J., Baharestani, M. *et al.*: National pressure ulcer advisory panel's updated pressure ulcer staging system. *Dermatol. Nurs.*, 19(4):pages 343–9, **2007**.

Bosboom, E.M.H., Hesselink, M.K.C. *et al.*: Passive transverse mechanical properties of skeletal muscle under in vivo compression. *J. Biomech.*, 34(10):pages 1365–1368, **2001**.
URL <GotoISI>://000170925600016

Bouten, C.V., Oomens, C.W., Baaijens, F.P. and Bader, D.L.: The etiology of pressure ulcers: skin deep or muscle bound? *Arch. Phys. Med. Rehabil.*, 84(4):pages 616–9, **2003**.

Boyce, M.C. and Arruda, E.M.: Constitutive models of rubber elasticity: A review. *Rubber Chemistry and Technology*, 73(3):pages 504–523, **2000**.
URL <GotoISI>://000089293800006

Bucki, M., Lobos, C. and Payan, Y.: A fast and robust patient specific finite element mesh registration technique: Application to 60 clinical cases. *Medical Image Analysis*, 14(3):pages 303 – 317, **2010**. doi:10.1016/j.media.2010.02.003.

Ceelen, K.K., Stekelenburg, A. *et al.*: Validation of a numerical model of skeletal muscle compression with mr tagging: a contribution to pressure ulcer research. *J Biomech Eng*, 130(6):page 061015, **2008**. doi:10.1115/1.2987877.
URL `http://dx.doi.org/10.1115/1.2987877`

Chabanas, M., Luboz, V. and Payan, Y.: Patient specific finite element model of the face soft tissues for computer-assisted maxillofacial surgery. *Med. Image Anal.*, 7(2):pages 131–51, **2003**.

Chabanas, M. and Payan, Y.: A 3d finite element model of the face for simulation in plastic and maxillo-facial surgery. In *Medical Image Computing and Computer-Assisted Intervention - Miccai 2000*, volume 1935 of *Lecture Notes in Computer Science*, pages 1068–1075. Springer-Verlag Berlin, Berlin, **2000**.
URL `<GotoISI>://000171938700111`

Chai, C.L., Pathinathan, A. and Smith, B.: Continuous positive airway pressure delivery interfaces for obstructive sleep apnoea. *Cochrane Database of Systematic Reviews*, (4):page CD005308, **2006**.

Chapuis, D., Gassert, R. *et al.*: Design of a simple mri/fmri compatible force/torque sensor. *Intelligent Robots and Systems, 2004. (IROS 2004). Proceedings. 2004 IEEE/RSJ International Conference on*, 3:pages 2593–2599 vol.3, **2004**. doi:10.1109/IROS.2004.1389799.

Charlton, D.J., Yang, J. and Teh, K.K.: Review of methods to characterize rubber elastic behavior for use in finite element analysis. *Rubber Chemistry and Technology*, 67(3):pages 481–503, **1994**.

Comley, K. and Fleck, N.A.: A micromechanical model for the young's modulus of adipose tissue. *International Journal of Solids and Structures*, 47(21):pages 2982 – 2990, **2010**a. doi:10.1016/j.ijsolstr.2010.07.001.

Comley, K. and Fleck, N.A.: The toughness of adipose tissue: measurements and physical basis. *Journal of Biomechanics*, 43(9):pages 1823 – 1826, **2010**b. doi:10.1016/j.jbiomech.2010.02.029.

Committee, D.S.: Part 6: Data dictionary. In *Digital Imaging and Communications in Medicine (DICOM)*. National Electrical Manufacturers Association, Rosslyn, **2007**.

Cook, R.D., Malkus, D.S. and Plesha, M.E.: *Concepts and Applications of Finite Element Analysis*. John Wiley & Sons Ltd, **1989**.

Couteau, B., Payan, Y. and Lavallee, S.: The mesh-matching algorithm: an automatic 3d mesh generator for finite element structures. *J. Biomech.*, 33(8):pages 1005–1009, **2000**.

Culebras, A.: *Clinical Handbook of Sleep Disorders*. Butterworth-Heinemann, **1996**.

del Palomar, A.P., Calvo, B. *et al.*: A finite element model to accurately predict real deformations of the breast. *Med. Eng. Phys.*, 30(9):pages 1089 – 1097, **2008**. doi: DOI:10.1016/j.medengphy.2008.01.005.
URL `http://www.sciencedirect.com/science/article/B6T9K-4S1BX8X-1/2/9ee92fb3ad55dd3e28844666e3494923`

Delalleau, A., Josse, G. *et al.*: A nonlinear elastic behavior to identify the mechanical parameters of human skin in vivo. *Skin Res Technol*, 14(2):pages 152–164, **2008**. doi:10.1111/j.1600-0846.2007.00269.x.

Dempsey, J., Veasey, S., Morgan, B. and CP., O.: Pathophysiology of sleep apnea. *Physiological Reviews*, 90(1):pages 47–112, **2010**.

DICOM Standards Committee: Part 3: Information object definitions. In *Digital Imaging and Communications in Medicine (DICOM)*. National Electrical Manufacturers Association, **2007**.

Douglas, N., White, D. *et al.*: Respiration during sleep in normal man. *Thorax*, pages 840–844, **1982**. doi:10.1136/thx.37.11.840.

Duck, F.A.: *Physical Properties of Tissue, A Comprehensive Reference Book*. Academic Press, **1990**.

Dunn, M.G., Silver, F.H. and Swann, D.A.: Mechanical analysis of hypertrophic scar tissue: structural basis for apparent increased rigidity. *J Invest Dermatol*, 84(1):pages 9–13, **1985**.

Durán, J., Esnaola, S., Rubio, R. and Iztueta, A.: Obstructive sleep apnea-hypopnea and related clinical features in a population-based sample of subjects aged 30 to 70 yr. *Am J Respir Crit Care Med*, 163(3 Pt 1):pages 685–689, **2001**.

Erdemir, A., Viveiros, M.L., Ulbrecht, J.S. and Cavanagh, P.R.: An inverse finite-element model of heel-pad indentation. *J. Biomech.*, 39(7):pages 1279–1286, **2006**.

Flegal, K.M., Carroll, M.D., Ogden, C.L. and Curtin, L.R.: Prevalence and trends in obesity among us adults, 1999-2008. *JAMA: The Journal of the American Medical Association*, 303(3):pages 235–241, **2010**. doi:10.1001/jama.2009.2014.

Fung, Y.C.: Elasticity of soft tissues in simple elongation. *Am J Physiol*, 213(6):pages 1532–1544, **1967**.
URL `http://ajplegacy.physiology.org`

Fung, Y.C.: *A First Course in Continuum Mechanics*. Prentice-Hall, Eaglewood Cliffs, NJ, **1969**.

Fung, Y.C.: *Biomechanics: Mechanical Properties of Living Tissues*. Springer-Verlag, New York, 2nd edition, **1993**.

Gasser, T., Ogden, R. and Holzapfel, G.: Hyperelastic modelling of arterial layers with distributed collagen fibre orientations. *Journal of The Royal Society Interface*, 3(6):pages 15–35, **2006**. Doi:10.1098/rsif.2005.0073.
URL `http://dx.doi.org/10.1098/rsif.2005.0073`

Gassert, R., Chapuis, D., Bleuler, H. and Burdet, E.: Sensors for applications in magnetic resonance environments. *Mechatronics, IEEE/ASME Transactions on*, 13(3):pages 335–344, **2008**. doi:10.1109/TMECH.2008.924113.

Geerligs, M., Peters, G.W. *et al.*: Does subcutaneous adipose tissue behave as an (anti-)thixotropic material? *Journal of Biomechanics*, 43(6):pages 1153 – 1159, **2010**. doi:DOI:10.1016/j.jbiomech.2009.11.037.

Geerligs, M., Peters, G.W.M. *et al.*: Linear viscoelastic behavior of subcutaneous adipose tissue. *Biorheol.*, 45(6):pages 677–688, **2008**.

Gefen, A.: The compression intensity index: a practical anatomical estimate of the biomechanical risk for a deep tissue injury. *Technol Health Care*, 16(2):pages 141–149, **2008**.

Gerig, G., Kubler, O., Kikinis, R. and Jolesz, F.: Nonlinear anisotropic filtering of mri data. *Medical Imaging, IEEE Transactions on*, 11(2):pages 221–232, **1992**. doi:10.1109/42.141646.

Gladilin, E. and Ivanov, A.: Computational modelling and optimisation of soft tissue outcome in cranio-maxillofacial surgery planning. *Comput Methods Biomech Biomed Engin*, 12(3):pages 305–318, **2009**. doi:10.1080/10255840802529925.

Gladilin, E., Zachow, S., Deuflhard, P. and Hege, H.C.: Anatomy- and physics-based facial animation for craniofacial surgery simulations. *Medical & Biological Engineering & Computing*, 42(2):pages 167–70, **2004**.

Hendriks, F., Brokken, D. *et al.*: The relative contributions of different skin layers to the mechanical behavior of human skin in vivo using suction experiments. *Med. Eng. Phys.*, 28(3):pages 259–266, **2006**.

Hendriks, F.M., Brokken, D. *et al.*: A numerical-experimental method to characterize the non-linear mechanical behaviour of human skin. *Skin Research & Technology*, 9(3):pages 274–83, **2003**.

Hidler, J., Mbwana, J. and Zeffiro, T.: Mri compatible force sensing system for real-time monitoring of wrist moments during fmri testing. *Rehabilitation Robotics, 2005. ICORR 2005. 9th International Conference on*, pages 212–214, **2005**. doi:10.1109/ICORR.2005.1501087.

Hill, A.V.: The heat of shortening and the dynamic constants of muscle. *Proceedings of the Royal Society of London. Series B, Biological Sciences*, 126(843):pages pp. 136–195, **1938**.
URL `http://www.jstor.org/stable/82135`

Holberg, C., Schwenzer, K. and Rudzki-Janson, I.: Three-dimensional soft tissue prediction using finite elements. part i: Implementation of a new procedure. *Journal of Orofacial Orthopedics*, 66(2):pages 110–21, **2005**.

Humphrey, J.D.: Continuum biomechanics of soft biological tissues. *Proceedings of the Royal Society of London Series a-Mathematical Physical and Engineering Sciences*, 459(2029):pages 3–46, **2003**.
URL `<GotoISI>://000180376800001`

Huxley, A.F. and Niedergerke, R.: Structural changes in muscle during contraction; interference microscopy of living muscle fibres. *Nature*, 173(4412):pages 971–973, **1954**.

Huxley, H. and Hanson, J.: Changes in the cross-striations of muscle during contraction and stretch and their structural interpretation. *Nature*, 173(4412):pages 973–976, **1954**.

Inc, A.: *ANSYS Inc. Theory Reference*. ANSYS Inc„ Canonsburg, PA, **2005**.

Ip, M.S.M., Lam, B. *et al.*: Obstructive sleep apnea is independently associated with insulin resistance. *Am J Respir Crit Care Med*, 165(5):pages 670–676, **2002**.

Jachowicz, J., McMullen, R. and Prettypaul, D.: Indentometric analysis of in vivo skin and comparison with artificial skin models. *Skin Res Technol*, 13(3):pages 299–309, **2007**. doi: 10.1111/j.1600-0846.2007.00229.x.

Jones, D.J.M., Braid, G.M. and Wedzicha, J.A.: Nasal masks for domiciliary positive pressure ventilation - patient usage and complications. *Thorax*, 49(8):pages 811–812, **1994**.
URL `<GotoISI>://A1994PB70700017`

Kakkar, R.K. and Berry, R.B.: Positive airway pressure treatment for obstructive sleep apnea. *Chest*, 132(3):pages 1057–1072, **2007**.
URL `<GotoISI>://000249742100050`

Kanal, E., Borgstede, J.P. *et al.*: American college of radiology white paper on mr safety. *Am. J. Roentgenol.*, 178(6):pages 1335–1347, **2002**.
URL `http://www.ajronline.org`

Keeve, E., Girod, S., Kikinis, R. and Girod, B.: Deformable modeling of facial tissue for craniofacial surgery simulation. *Computer Aided Surgery*, 3(5):pages 228–38, **1998**.

Kirkness, J.P., Schwartz, A.R. *et al.*: Contribution of male sex, age, and obesity to mechanical instability of the upper airway during sleep. *J Appl Physiol*, 104(6):pages 1618–1624, **2008**. doi:10.1152/japplphysiol.00045.2008.

Klingbeil, W. and Shield, R.: Large-deformation analyses of bonded elastic mounts. *ZEITSCHRIFT FUR ANGEWANDTE MATHEMATIK UND PHYSIK*, 17(2):pages 281–305, **1966**.

Kribbs, N.B., Pack, A.I. *et al.*: Objective measurement of patterns of nasal cpap use by patients with obstructive sleep apnea. *Am Rev Respir Dis*, 147(4):pages 887–895, **1993**.

Kvistedal, Y. and Nielsen, P.: Estimating material parameters of human skin in vivo. *Biomechanics and Modeling in Mechanobiology*, 8:pages 1–8, **2009**. doi:10.1007/s10237-007-0112-z.

Landau, L.D. and Lifschitz, E.M.: *Theory of Elasticity*, volume 7 of *Course of Theoretical Physics*. Pergamon Press, Oxford, 2nd english edition, **1970**.

Landis, E.M.: Micro injection studies of capillary blood pressure in human skin. *Heart*, 15(15):pages 209–228, **1930**.

Lanir, Y.: Constitutive equations for fibrous connective tissues. *J. Biomech.*, 16(1):pages 1–12, **1983**.

Lanir, Y. and Fung, Y.C.: Two-dimensional mechanical properties of rabbit skin. i. experimental system. *J. Biomech.*, 7(1):pages 29–34, **1974**a.

Lanir, Y. and Fung, Y.C.: Two-dimensional mechanical properties of rabbit skin. ii. experimental results. *J. Biomech.*, 7(2):pages 171–82, **1974**b.

Lawati, N.M.A., Patel, S.R. and Ayas, N.T.: Epidemiology, risk factors, and consequences of obstructive sleep apnea and short sleep duration. *Prog Cardiovasc Dis*, 51(4):pages 285–293, **2009**. doi:10.1016/j.pcad.2008.08.001.

Lee, R.W.W., Petocz, P. *et al.*: Prediction of obstructive sleep apnea with craniofacial photographic analysis. *Sleep*, 32(1):pages 46–52, **2009**.

Lee, Y., Terzopoulos, D. and Waters, K.: Realistic modeling for facial animation. In *Proceedings of the 22nd annual conference on Computer graphics and interactive techniques*, SIGGRAPH '95, pages 55–62. ACM, New York, NY, USA, **1995**. doi:http://doi.acm.org/10.1145/218380.218407.

Lee-Chiong Jr, T.: *Sleep Medicine: Essentials and Review*. Oxford University Press, **2008**.

Lindberg, E., Berne, C. *et al.*: Cpap treatment of a population-based sample–what are the benefits and the treatment compliance? *Sleep Med*, 7(7):pages 553–560, **2006**. doi:10.1016/j.sleep.2005.12.010.

Linder-Ganz, E. and Gefen, A.: The effects of pressure and shear on capillary closure in the microstructure of skeletal muscles. *Ann Biomed Eng*, 35(12):pages 2095–2107, **2007**. doi:10.1007/s10439-007-9384-9.

Linder-Ganz, E., Shabshin, N., Itzchak, Y. and Gefen, A.: Assessment of mechanical conditions in sub-dermal tissues during sitting: a combined experimental-mri and finite element approach. *J. Biomech.*, 40(7):pages 1443–1454, **2007**. doi:10.1016/j.jbiomech.2006.06.020.

Lojander, J., Brander, P.E. and Ammala, K.: Nasopharyngeal symptoms and nasal continuous positive airway pressure therapy in obstructive sleep apnoea syndrome. *Acta Oto-Laryngologica*, 119(4):pages 497–502, **1999**. ISI Document Delivery No.: 218ND Times Cited: 9 Cited Reference Count: 24.
URL `<GotoISI>://000081557900016`

Lokshin, O. and Lanir, Y.: Viscoelasticity and preconditioning of rat skin under uniaxial stretch: Microstructural constitutive characterization. *Journal of Biomechanical Engineering*, 131(3):031009, **2009**. doi:10.1115/1.3049479.

Lorensen, W.E. and Cline, H.E.: Marching cubes: A high resolution 3d surface construction algorithm. *Computer Graphics (ACM)*, 21(4):pages 163 – 169, **1987**.

LSTC: *LS-DYNA Theory Manual*. LSTC, **2006**.

LSTC: *LS-DYNA Keyword User Manual, Version 971/ Rev 5*. LSTC, **2010**.

LSTC: Ls-dyna users guide. **2011**.
URL http://www.dynasupport.com/tutorial/ls-dyna-users-guide

Makhsous, M., Lim, D. *et al.*: Finite element analysis for evaluation of pressure ulcer on the buttock: development and validation. *IEEE Trans Neural Syst Rehabil Eng*, 15(4):pages 517–525, **2007**. doi:10.1109/TNSRE.2007.906967.
URL http://dx.doi.org/10.1109/TNSRE.2007.906967

Marin, J.M., Carrizo, S.J., Vicente, E. and Agusti, A.G.N.: Long-term cardiovascular outcomes in men with obstructive sleep apnoea-hypopnoea with or without treatment with continuous positive airway pressure: an observational study. *Lancet*, 365(9464):pages 1046–1053, **2005**. doi:10.1016/S0140-6736(05)71141-7.

Mazza, E., Papes, O. *et al.*: Simulation of the aging face. *J Biomech Eng*, 129(4):pages 619–623, **2007**. doi:10.1115/1.2746388.

Mihaescu, M., Mylavarapu, G., Gutmark, E.J. and Powell, N.B.: Large eddy simulation of the pharyngeal airflow associated with obstructive sleep apnea syndrome at pre and post-surgical treatment. *Journal of Biomechanics*, **2011**. doi:10.1016/j.jbiomech.2011.06.006.

Miller, K.: Method of testing very soft biological tissues in compression. *J. Biomech.*, 38(1):pages 153–158, **2005**.
URL http://www.sciencedirect.com/science/article/B6T82-4CBVKMR-1/2/80201db162da0f716e4feb6a4074625d

Miller-Young, J.E., Duncan, N.A. and Baroud, G.: Material properties of the human calcaneal fat pad in compression: experiment and theory. *J. Biomech.*, 35(12):pages 1523–31, **2002**.

Mooney, M.: A theory of large elastic deformation. *Journal of Applied Physics*, 11(9):pages 582–592, **1940**.
URL <GotoISI>://000200097300003

Morriss, L., Wittek, A. and Miller, K.: Compression testing of very soft biological tissues using semi-confined configuration - a word of caution. *J. Biomech.*, 41(1):pages 235–238, **2008**. doi:10.1016/j.jbiomech.2007.06.025.

Mortimore, I.L., Whittle, A.T. and Douglas, N.J.: Comparison of nose and face mask cpap therapy for sleep apnoea. *Thorax*, 53(4):pages 290–292, **1998**.
URL <GotoISI>://000073334300013

National Pressure Ulcer Advisory Panel: Pressure ulcers prevalence, cost and risk assessment: consensus development conference statement–the national pressure ulcer advisory panel. *Decubitus*, 2(2):pages 24–28, **1989**.

National Transportation Safety Board: Brief of incident. Technical Report SEA08IA080, National Transportation Safety Board„ **2009**.
URL http://www.ntsb.gov/ntsb/brief.asp?ev_id=20080222X00229\&key=1

Nigg, B.M. and Walter, H.: *Biomechanics of the Musculo-skeletal System*. Wiley, **1999**.

Nino-Murcia, G., McCann, C.C. *et al.*: Compliance and side effects in sleep apnea patients treated with nasal continuous positive airway pressure. *Western Journal of Medicine*, 150(2):pages 165–9, **1989**.

Nola, G.T. and Vistnes, L.M.: Differential response of skin and muscle in the experimental production of pressure sores. *Plast. Reconstr. Surg.*, 66(5):pages 728–733, **1980**.

Ogden, R.W., Saccomandi, G. and Sgura, I.: Fitting hyperelastic models to experimental data. *Computational Mechanics*, 34(6):pages 484–502, **2004**.
URL `<GotoISI>://000225184500005`

Oomens, C.W.J., Bressers, O.F.J.T. *et al.*: Can loaded interface characteristics influence strain distributions in muscle adjacent to bony prominences? *Comput. Methods Biomech. Biomed. Eng.*, 6(3):pages 171–80, **2003**.

Oxlund, H., Manschot, J. and Viidik, A.: The role of elastin in the mechanical properties of skin. *J. Biomech.*, 21(3):pages 213–8, **1988**.

Pailler-Mattei, C., Bec, S. and Zahouani, H.: In vivo measurements of the elastic mechanical properties of human skin by indentation tests. *Med. Eng. Phys.*, 30(5):pages 599–606, **2008**.

Park, J.B. and Lakes, R.S.: *Biomaterials, An Introduction*. Plenum Press, **1992**.

Peña, E., Calvo, B. *et al.*: Finite element analysis of the effect of meniscal tears and meniscectomies on human knee biomechanics. *Clin Biomech (Bristol, Avon)*, 20(5):pages 498–507, **2005**. doi: 10.1016/j.clinbiomech.2005.01.009.
URL `http://dx.doi.org/10.1016/j.clinbiomech.2005.01.009`

Pena, E., Calvo, B., Martinez, M.A. and Doblare, M.: A three-dimensional finite element analysis of the combined behavior of ligaments and menisci in the healthy human knee joint. *J. Biomech.*, 39:pages 1686–1701, **2006**.
URL `http://www.sciencedirect.com/science/article/B6T82-4GHRC7B-1/2/ac49db45dbccdda82959139fcd95379e`

Pepin, J.L., Leger, P. *et al.*: Side effects of nasal continuous positive airway pressure in sleep apnea syndrome. study of 193 patients in two french sleep centers.[see comment]. *Chest*, 107(2):pages 375–81, **1995**.

Peppard, P.E., Young, T., Palta, M. and Skatrud, J.: Prospective study of the association between sleep-disordered breathing and hypertension. *N Engl J Med*, 342(19):pages 1378–1384, **2000**. doi:10.1056/NEJM200005113421901.

Perona, P. and Malik, J.: Scale-space and edge detection using anisotropic diffusion. *Pattern Analysis and Machine Intelligence, IEEE Transactions on*, 12(7):pages 629–639, **1990**. doi: 10.1109/34.56205.

Punjabi, N.M., Sorkin, J.D. *et al.*: Sleep-disordered breathing and insulin resistance in middle-aged and overweight men. *Am J Respir Crit Care Med*, 165(5):pages 677–682, **2002**.

Rechtschaffen, A., Kales, A. *et al.*: *A Manual of Standardized Terminology, Techniques amd Scoring System for Sleep Stages of Human Subjects*. Public Health Service, U.S. Government Printing Office, Washington D.C., **1968**.

ResMed Inc: Static friction coefficient between LSR and the plantar skin.

ResMed Inc: Ultra Mirage ^{TM}II - Technology. **2011**.
URL `http://www.resmed.com/us/products/ultra_mirage_ii_nasal/ultra-mirage-technology.html?nc=patients\&sec=true`

Richard, W., Venker, J. *et al.*: Acceptance and long-term compliance of ncpap in obstructive sleep apnea. *Eur Arch Otorhinolaryngol*, 264(9):pages 1081–1086, **2007**. doi:10.1007/s00405-007-0311-3.

Rivlin, R.S. and Saunders, D.W.: Large elastic deformations of isotropic materials. vii. experiments on the deformation of rubber. *Philosophical Transactions of the Royal Society of London. Series A, Mathematical and Physical Sciences*, 243(865):pages 251–288, **1951**.

Robinson, G.V., Stradling, J.R. and Davies, R.J.O.: Sleep . 6: obstructive sleep apnoea/hypopnoea syndrome and hypertension. *Thorax*, 59(12):pages 1089–1094, **2004**. doi:10.1136/thx.2003.015875.
URL `http://dx.doi.org/10.1136/thx.2003.015875`

Rotter, N., Tobias, G. *et al.*: Age-related changes in the composition and mechanical properties of human nasal cartilage. *Archives of Biochemistry & Biophysics*, 403(1):pages 132–40, **2002**.

Rushmer, R.F., Buettner, K.J.K., Short, J.M. and Odland, G.F.: The skin. *Science*, 154(3747):pages 343–348, **1966**.
URL `http://links.jstor.org/sici?sici=0036-8075%2819661021%293%3A154%3A3747%3C343%3ATS%3E2.0.CO%3B2-0`

Ryan, C.F. and Love, L.L.: Mechanical properties of the velopharynx in obese patients with obstructive sleep apnea. *Am J Respir Crit Care Med*, 154(3 Pt 1):pages 806–812, **1996**.

Samani, A., Bishop, J., Luginbuhl, C. and Plewes, D.B.: Measuring the elastic modulus of ex vivo small tissue samples. *Phys. Med. Biol.*, 48(14):pages 2183–2198, **2003**.

Samani, A., Bishop, J., Yaffe, M.J. and Plewes, D.B.: Biomechanical 3-d finite element modeling of the human breast using mri data. 20(4):pages 271–9, **2001**. Samani A Bishop J Yaffe MJ Plewes DB United States Journal Article Research Support, Non-U.S. Gov't Research Support, U.S. Gov't, Non-P.H.S.

Samani, A. and Plewes, D.: A method to measure the hyperelastic parameters of ex vivo breast tissue samples. *Phys. Med. Biol.*, 49(18):pages 4395–4405, **2004**.

Samani, A., Zubovits, J. and Plewes, D.: Elastic moduli of normal and pathological human breast tissues: an inversion-technique-based investigation of 169 samples. *Phys. Med. Biol.*, 52(6):pages 1565–1576, **2007**.

Schlosshan, D. and Elliott, M.W.: Sleep . 3: Clinical presentation and diagnosis of the obstructive sleep apnoea hypopnoea syndrome. *Thorax*, 59(4):pages 347–352, **2004**.

Schwartz, A.R., Gold, A.R. *et al.*: Effect of weight loss on upper airway collapsibility in obstructive sleep apnea. *Am Rev Respir Dis*, 144(3 Pt 1):pages 494–8, **1991**.

Shellock, F.G. and Crues, J.V.: Mr procedures: biologic effects, safety, and patient care. *Radiology*, 232(3):pages 635–652, **2004**. doi:10.1148/radiol.2323030830.

Shellock, F.G. and Spinazzi, A.: Mri safety update 2008: part 2, screening patients for mri. *AJR Am J Roentgenol*, 191(4):pages 1140–1149, **2008**. doi:10.2214/AJR.08.1038.2.

Shiomi, T., Guilleminault, C., Stoohs, R. and Schnittger, I.: Leftward shift of the interventricular septum and pulsus paradoxus in obstructive sleep apnea syndrome. *Chest*, 100(4):pages 894–902, **1991**.

Sims, A.M., Stait-Gardner, T. *et al.*: Elastic and viscoelastic properties of porcine subdermal fat using mri and inverse fea. *Biomech Model Mechanobiol*, 9(6):pages 703–711, **2010**. doi: 10.1007/s10237-010-0207-9.

Sin, D.D., Mayers, I., Man, G.C.W. and Pawluk, L.: Long-term compliance rates to continuous positive airway pressure in obstructive sleep apnea: a population-based study. *Chest*, 121(2):pages 430–435, **2002**.

Sleilati, F.H., Stephan, H.A., Nasr, M.W. and Riachy, M.A.: An unusual pressure sore of the nasal bridge. *Br J Oral Maxillofac Surg*, 46(5):pages 411–412, **2008**. doi:10.1016/j.bjoms.2007.10.003.

Smith, P.L., Gold, A.R. *et al.*: Weight loss in mildly to moderately obese patients with obstructive sleep apnea. *Ann Intern Med*, 103(6 (Pt 1)):pages 850–5, **1985**.

Smurthwaite, G.J. and Ford, P.: Skin necrosis following continuous positive airway pressure with a face mask. *Anaesthesia*, 48(2):pages 147–148, **1993**.
URL `<GotoISI>://A1993KL84200014`

Sullivan, C.E., Issa, F.G., Berthon-Jones, M. and Eves, L.: Reversal of obstructive sleep apnoea by continuous positive airway pressure applied through the nares. *Lancet*, 1(8225):pages 862–5, **1981**.

Tada, M., Sasaki, S. and Ogasawara, T.: Development of an optical 2-axis force sensor usable in mri environments. *Sensors, 2002. Proceedings of IEEE*, 2:pages 984–989 vol.2, **2002**. doi: 10.1109/ICSENS.2002.1037244.

Tang, S.Y., Souza, R.B. *et al.*: Local tissue properties of human osteoarthritic cartilage correlate with magnetic resonance t(1) rho relaxation times. *J Orthop Res*, 29(9):pages 1312–1319, **2011**. doi:10.1002/jor.21381.
URL `http://dx.doi.org/10.1002/jor.21381`

Tanner, C., Schnabel, J.A. *et al.*: Factors influencing the accuracy of biomechanical breast models. *Medical Physics*, 33(6):pages 1758–1769, **2006**. ISI Document Delivery No.: 058TW Times Cited: 0 Cited Reference Count: 31.
URL `<GotoISI>://000238688500025`

Tong, P. and Fung, Y.C.: The stress-strain relationship for the skin. *J Biomech*, 9(10):pages 649–657, **1976**.

Tortora, G.J. and Grabowski, S.R.: *Introduction to the Human Body*. John Wiley and Sons, 6 edition, **2004**.

Treloar, L.R.G., Hopkins, H.G., Rivlin, R.S. and Ball, J.M.: The mechanics of rubber elasticity [and discussions]. *Proceedings of the Royal Society of London. Series A, Mathematical and Physical Sciences*, 351(1666):pages 301–330, **1976**.

Van Loocke, M., Lyons, G.C. and Simms, C.K.: A validated model of passive muscle in compression. *Journal of Biomechanics*, 39(16):pages 2999 – 3009, **2006**. doi:DOI:10.1016/j.jbiomech.2005.10.016.

Verse, T.: Side effects of nasal cpap ventilation therapy. *Hno*, 48(9):pages 706–715, **2000**. URL `<GotoISI>://000089511800014`

Walczak, T. and Chokroverty, S.: *Sleep Disorders Medicine: Basic Science, Technical Considerations and Clinical Aspects*, chapter Electroencephalography, Electromyography and Electrooculography: General Principles and Basic Terminology, pages 95–117. Butterworth-Heinemann, **1994**.

Wearing, S.C., Smeathers, J.E. *et al.*: Bulk compressive properties of the heel fat pad during walking: a pilot investigation in plantar heel pain. *Clin. Biomech.*, 24(4):pages 397–402, **2009**.

Williams, P.L., Berry, M.M. *et al.*, editors: *Gray's Anatomy*, chapter 6 Skeletal System, pages 425–736. Churchill Livingstone, 37th edition, **1995**.

Williams, P.L., Warwick, R., Dyson, M. and Bannister, L.H., editors: *Gray's Anatomy*. Churchill Livingstone, 37 edition, **1989**a.

Williams, P.L., Warwick, R., Dyson, M. and Bannister, L.H., editors: *Gray's Anatomy*, chapter 5 Myology, pages 546–659. Churchill Livingstone, 37 edition, **1989**b.

Williams, P.L., Warwick, R., Dyson, M. and Bannister, L.H., editors: *Gray's Anatomy*, chapter 7 Neurology, pages 859–1244. Churchill Livingstone, 37 edition, **1989**c.

Williams, P.L., Warwick, R., Dyson, M. and Bannister, L.H., editors: *Gray's Anatomy*, chapter 8 Splanchnology, pages 1245–1475. Churchill Livingstone, 37 edition, **1989**d.

Williams, P.L., Warwick, R., Dyson, M. and Bannister, L.H., editors: *Gray's Anatomy*, chapter 3 Osteology, pages 268–458. Churchill Livingstone, 37th edition, **1989**e.

Wolkove, N., Baltzan, M. *et al.*: Long-term compliance with continuous positive airway pressure in patients with obstructive sleep apnea. *Can Respir J*, 15(7):pages 365–369, **2008**.

Wu, G. and Cavanagh, P.R.: Isb recommendations for standardization in the reporting of kinematic data. *J. Biomech.*, 28(10):pages 1257–61, **1995**.

Wu, J.Z., Cutlip, R.G., Andrew, M.E. and Dong, R.G.: Simultaneous determination of the nonlinear-elastic properties of skin and subcutaneous tissue in unconfined compression tests. *Skin Research and Technology*, 13(1):pages 34–42, **2007**.
URL `http://www.blackwell-synergy.com/doi/abs/10.1111/j.1600-0846.2007.00182.x`

Wu, J.Z., Dong, R.G. and Smutz, W.P.: Elimination of the friction effects in unconfined compression tests of biomaterials and soft tissues. *Proceedings of the Institution of Mechanical Engineers Part H-Journal of Engineering in Medicine*, 218(H1):pages 35–40, **2004**.
URL `<GotoISI>://000220037500004`

Young, P., Beresford-West, T. *et al.*: An efficient approach to converting three-dimensional image data into highly accurate computational models. *Philosophical Transactions of the Royal Society A: Mathematical, Physical and Engineering Sciences*, 366(1878):pages 3155–3173, **2008**. doi: 10.1098/rsta.2008.0090.

Young, T., Palta, M. *et al.*: The occurrence of sleep-disordered breathing among middle-aged adults. *New England Journal of Medicine*, 328(17):pages 1230–1235, **1993**. doi:10.1056/NEJM199304293281704.

Young, T., Peppard, P.E. and Gottlieb, D.J.: Epidemiology of obstructive sleep apnea: a population health perspective. *American Journal of Respiratory & Critical Care Medicine*, 165(9):pages 1217–39, **2002**.

Zhang, M. and Mak, A.F.: In vivo friction properties of human skin. *Prosthet Orthot Int*, 23(2):pages 135–141, **1999**.